DIEGO HAYASHI ALONSO

Topology optimization for 2D swirl flows with application in the design of a ventricular assist device

São Paulo

2022

DIEGO HAYASHI ALONSO

Otimização topológica para escoamentos 2D girantes com aplicação no projeto de um dispositivo de assistência ventricular

Versão corrigida

Tese apresentada à Escola Politécnica da Universidade de São Paulo como pré-requisito para obtenção de título de Doutor em Ciências.

Área de concentração:
Engenharia de Controle e Automação Mecânica

Orientador:
Prof. Dr. Emílio Carlos Nelli Silva

São Paulo

2022

Autorizo a reprodução e divulgação total ou parcial deste trabalho, por qualquer meio convencional ou eletrônico, para fins de estudo e pesquisa, desde que citada a fonte.

Este exemplar foi revisado e corrigido em relação à versão original, sob responsabilidade única do autor e com a anuência de seu orientador.

São Paulo, 30 de Maio de 2022

Assinatura do autor: Diego Hayashi Alonso

Assinatura do orientador: Emilio Carlos Nelli Silva

Catalogação-na-publicação

Alonso, Diego Hayashi
Topology optimization for 2D swirl flows with application in the design of a ventricular assist device / D. H. Alonso – versão corr. – São Paulo, 2022.
441 p.

Tese (Doutorado) - Escola Politécnica da Universidade de São Paulo. Departamento de Engenharia Mecatrônica e de Sistemas Mecânicos.

1. Otimização topológica. 2. Bomba Tesla. 3. Hemólise. 4. Trombose. 5. Turbulência. I. Universidade de São Paulo. Escola Politécnica. Departamento de Engenharia Mecatrônica e de Sistemas Mecânicos II.t.

DIEGO HAYASHI ALONSO

Topology optimization for 2D swirl flows with application in the design of a ventricular assist device

Corrected version

Thesis submitted to the Polytechnic School of the University of São Paulo in partial fulfillment of the requirements for the degree of Doctor of Science.

Concentration area:
Control and Mechanical Automation Engineering

Advisor:
Prof. Dr. Emílio Carlos Nelli Silva

São Paulo

2022

ALONSO, D. H.**Topology optimization for 2D swirl flows with application in the design of a ventricular assist device**. 2022. 441 p. Thesis (Doctor of Science) – Polytechnic School, University of São Paulo, São Paulo, 2022.

Evaluated in: São Paulo, _____ ____ , 2022

Examination committee

Prof. Dr. _____

Institution: _____

Judgement: _____

Prof. Dr. _____

Institution: _____

Judgement: _____

Prof. Dr. _____

Institution: _____

Judgement: _____

Prof. Dr. _____

Institution: _____

Judgement: _____

Prof. Dr. _____

Institution: _____

Judgement: _____

ACKNOWLEDGEMENTS

I would first like to thank my advisor, Prof. Dr. Emílio Carlos Nelli Silva, for the guidance, attention, discussions and suggestions during the development of this work and also for the constant support and dedication.

I would like to thank all colleagues from the Multiphysics Systems Optimization Laboratory (MSOL) for the academic discussions, suggestions and support. More specifically, I would like to thank Francisco Oliveira for the help in printing and post-processing the 3D printed parts.

I would like to thank my family, for all the immeasurable support and help in all aspects throughout these years.

I would also like to thank FAPESP for the financial support of this research under grant 2017/27049-0, which is part of the thematic project "Electromagnetic propeller systems for implantable artificial heart and mechanical circulatory support devices" ("*Sistemas Propulsores Eletromagnéticos para Coração Artificial Implantável e Dispositivos de Suporte Circulatório Mecânico*", under grant 2013/24434-0).

I would like to extend the thanks to RCGI (Research Centre for Greenhouse Gas Innovation) for infrastructure and computational resources.

To finalize, I would like to give a big thanks to all who directly or indirectly contributed to the development of this work.

ABSTRACT

Ventricular Assist Devices (VADs) substitute or temporarily assist the heart and blood circulation by means of a small-scale blood pump. Due to the operation with blood, their designs aim to minimize blood damage (hemolysis and thrombosis) and maximize the performance (i.e., more efficient pumping). For that, the topologies of the rotor and the volute play a major role. In this research, the rotor is based on the 2D swirl concept, which considers swirling axisymmetric flow, being represented mainly by the Tesla pump. In a Tesla pump, the boundary layer (viscous) effect pumps the fluid, which may lead to less blood damage than bladed pumps (pumping based on the variation of linear momentum). However, the obtained efficiency is normally low, which may be improved by using the topology optimization method. Therefore, in this research, the topology optimization method is implemented for the 2D swirl flow model, also considering a non-Newtonian model for blood (Carreau-Yasuda) and hemolysis/thrombosis models to quantify the blood damage. Furthermore, the 2D swirl flow topology optimization is extended to the Wray-Agarwal turbulence model (WA2018), which presents advantages from the simulation and topology optimization points-of-view. The solid material is modeled as a porous medium with permeability controlled by the topology optimization. The numerical implementation is performed mainly through the FEniCS platform, by using the dolfin-adjoint library for the automatically derived adjoint model, and also relying on the OpenFOAM® software for considering higher-speed flows, turbulence and 3D simulations. For the optimization, the IPOPT and TOBS solvers are considered. The optimized designs are interpreted and fabricated through additive manufacturing, and then experimentally evaluated.

Keywords: Topology optimization. Tesla pump. Hemolysis. Thrombosis. Turbulence.

RESUMO

Dispositivos de Assistência Ventricular (DAVs) substituem ou auxiliam temporariamente o coração e a circulação sanguínea por meio de uma bomba de sangue de pequena escala. Devido à sua operação com sangue, os seus projetos visam minimizar o dano ao sangue (hemólise e trombose) e maximizar o desempenho (i.e., bombear de forma mais eficiente). Para isso, as topologias do rotor e da voluta têm um papel de destaque. Nesta pesquisa, o rotor é baseado no conceito de escoamento 2D girante, que consiste em escoamento axissimétrico rotativo, sendo representado principalmente pela bomba Tesla. Em uma bomba Tesla, o fluido é bombeado pelo efeito da camada limite (viscosidade) e não pela variação de quantidade de movimento linear (como em bombas de palhetas), o que pode levar a um menor dano ao sangue. Porém, a eficiência obtida é normalmente baixa, mas que pode ser aumentada utilizando o método de otimização topológica. Assim, nesta pesquisa, o método de otimização topológica é implementado para o modelo 2D de escoamento girante, também considerando um modelo não-Newtoniano para o sangue (Carreau-Yasuda) e modelos de hemólise/trombose para quantificar o dano ao sangue. Além disso, a otimização topológica de escoamento 2D girante é estendida para o modelo de turbulência de Wray-Agarwal (WA2018), que possui vantagens dos pontos-de-vista de simulação, e otimização topológica. O material sólido é modelado como um meio poroso com permeabilidade controlada pela otimização topológica. A implementação numérica é feita principalmente usando o *software* FEniCS, por meio da biblioteca dolfin-adjoint para a derivação automática do modelo adjunto, e também é usado o *software* OpenFOAM® para considerar escoamentos de alta velocidade, turbulência e simulações 3D. Para a otimização, os otimizadores IPOPT e TOBS são considerados. Os projetos otimizados são interpretados e fabricados por manufatura aditiva, e então avaliados experimentalmente.

Palavras-chave: Otimização topológica. Bomba Tesla. Hemólise. Trombose. Turbulência.

LIST OF FIGURES

Figure 1.1 – Types of VAD implantation. 56
Figure 1.2 – Some blood pump models for VADs. 58
Figure 1.3 – Typical blood (static) pressure values in the human body. The LVAD and RVAD positions are also illustrated (a BiVAD would correspond to both LVAD and RVAD positions) (BONOW *et al.*, 2012; GREYSON, 2010). ("RA" stands for Right Atrium, "RV" stands for Right Ventriculum, "LA" stands for Left Atrium, "LV" stands for Left Ventriculum). 60
Figure 1.4 – Representation of the relationship between energy dissipation, vorticity, hemolysis and thrombosis. 64
Figure 1.5 – Representation of the 2D swirl flow model. 65
Figure 1.6 – Some examples of 2D swirl flow devices. 66
Figure 1.7 – Tesla principle exemplified for a two-disk Tesla pump ($\boldsymbol{v}_1$ and $\boldsymbol{v}_2$ are the velocities of fluid on the inlet and on the outlet, respectively). . 67
Figure 1.8 – Spiral movement of fluid inside a Tesla pump and main components, according to the geometry initially proposed by Tesla (1913a). . . 67
Figure 1.9 – Illustration of the flow in a Tesla pump compared to the flow in a bladed centrifugal pump (H is the pressure head, Q is the flow rate, and n is the rotation of the rotor in rpm). 68
Figure 1.10 – Tesla wind turbine proposed by Fuller (2010). 69
Figure 1.11 – Discflo (2000)'s Tesla pump (for hard-to-pump applications). . . . 69
Figure 1.12 – Alternative designs for Tesla-type devices. 71
Figure 1.13 – Some axisymmetric designs of Tesla-type devices compared to the traditional (*straight inlet*) design. 72
Figure 1.14 – Axial designs from the Tesla principle. 72
Figure 1.15 – Some commercial extracorporeal Tesla pump models. 75
Figure 1.16 – Possible ways to model a Tesla pump rotor. 76
Figure 1.17 – *Spacers* or *arms* positioned on Tesla pump rotor disks. 77
Figure 1.18 – Simplified configuration of the rotor and the volute in a VAD, showing the terminology that is used for some parts of the volute – *tongue* and *discharge nozzle*. 77

Figure 1.19 – Types of casing design for centrifugal pumps (the rotor is represented illustratively by a gray circle and is represented with, illustratively, different external diameters for each type of casing). 78
Figure 1.20 – Types of volute-type casing. 78
Figure 1.21 – Some types of volute cross sections. 80
Figure 1.22 – Examples of optimization methods applied to the design of a Tesla pump rotor in the 2D swirl flow model. 81
Figure 1.23 – Sequence of a design approach using topology optimization. . . . 86
Figure 2.1 – Possible behaviors of non-Newtonian fluids. 96
Figure 2.2 – Limit of the continuum hypothesis for blood flow inside tubes of different diameters. 97
Figure 2.3 – Carreau-Yasuda model for blood flow. 100
Figure 2.4 – Types of boundaries in the computational domains. 106
Figure 2.5 – Some approaches for defining the boundary conditions for the outlet.107
Figure 2.6 – Some LBB-stable finite elements (lowest-order versions). 116
Figure 2.7 – Finite element interpolation for the turbulent variables. The interpolation of the reciprocal wall distance (G) is indicated as ℓ_w, for the figure to be more generic – i.e., ℓ_w may be computed from other wall distance equations (YOON, 2016; SÁ *et al.*, 2021). 117
Figure 2.8 – Characteristic dimension selected for the Reynolds number of the volute. 126
Figure 2.9 – Finite element interpolation for the blood damage indices (also used for the auxiliary variables used in their computations). 128
Figure 2.10 – Finite element interpolation for the pseudo-density. 145
Figure 2.11 – Illustration of Borrvall and Petersson (2003)'s inverse permeability material model. 146
Figure 2.12 – 3D interpretation of the porosity of the 2D swirl flow model as porous medium particles. 148
Figure 2.13 – Darcy and Forchheimer effects in a porous medium. 149
Figure 2.14 – Material model for the non-Newtonian viscosity. 152
Figure 2.15 – Example of pattern repetition for two repeated zones. 160
Figure 2.16 – Schematic illustration of the application of a Helmholtz filter. 162

Figure 2.17 – Illustration of the thresholding technique applied to an optimized topology. 165
Figure 2.18 – Illustration of an example of thresholding (for a nodal design variable).166
Figure 2.19 – Illustration of a smoothing technique applied to an optimized topology.167
Figure 2.20 – Example of the procedure to reinclude a sharp edge of the original mesh after smoothing, through CSG. 169
Figure 2.21 – Internal and external corners with $\gamma_{\mathrm{c,int}}$ indicated for each case. . . 170
Figure 2.22 – Illustration of an example of mesh smoothing by generation of contours (for a nodal design variable). 172
Figure 2.23 – Possible choices to define the point cloud (the points of the point cloud are represented in green color, while the recognized contour is represented in red color. The other symbols are the same as Fig. 2.24). 173
Figure 2.24 – Illustration of an example of mesh smoothing by point cloud (for a nodal design variable). 174
Figure 3.1 – Flowchart of the implementation of the topology optimization method.181
Figure 3.2 – Relaxation of the linearized inequality constraint bound ($\Delta c_{\mathrm{ineq},i}(\alpha)$). 185
Figure 3.3 – Flowchart showing the approaches for deriving the adjoint model (based on Farrell *et al.* (2013) and Funke (2013)). 187
Figure 3.4 – Interfacing between the adjoint model and the forward model with *FEniCS TopOpt Foam*, outlining the main differences/similarities between FEniCS/dolfin-adjoint and OpenFOAM® 196
Figure 3.5 – Diagram illustrating the computation of the sensitivities when using OpenFOAM® and the *FEniCS TopOpt Foam* library for the fluid flow simulation. 197
Figure 3.6 – Representation of 2D and 2D swirl computational domains in FEniCS and OpenFOAM® (the specific boundary conditions "`wedge`" are presented separately, because they are imposed separately on each *almost parallel* face with respect to the 2D plane in OpenFOAM®). 198
Figure 3.7 – Diagram illustrating the conversion of variables between OpenFOAM® and FEniCS. 200

Figure 3.8 – An example of boundary conditions in FEniCS and OpenFOAM® for the pressure-velocity formulation. 201
Figure 3.9 – Representation of a computational domain with cyclic boundary conditions. 202
Figure 3.10 – Mixing plane approach for the pressure and the velocity in the simulation of the designed prototypes. 204
Figure 3.11 – Circumferential averaging examples, for cylinder-shape and disk-shape mixing planes. 205
Figure 4.1 – Possible driving systems (for simplicity, the driving magnets are depicted as rectangles in darker brown color). 208
Figure 4.2 – Possible bearing configurations. 209
Figure 4.3 – Approximated analysis for the pressures in the case the motor is mechanically coupled through the shaft in the lower side of the figure. 210
Figure 4.4 – Illustration of the *pattern stacking* approximation. 212
Figure 4.5 – Side of the shaft of the external motor. 212
Figure 4.6 – Labyrinth seal design for 2 labyrinths. 213
Figure 4.7 – Some possibilities for the design of the inlet around the shaft. . . . 216
Figure 4.8 – Blockage ratio and the dimensions used to compute it. 218
Figure 4.9 – Some possibilities for the fluid below the rotor (the spacing is exaggerated to facilitate visualization). 220
Figure 4.10 – Typical flow in the clearance below the rotor. 220
Figure 4.11 – 3D views of the prototype. 221
Figure 4.12 – Projected/section views of the prototype. 221
Figure 4.13 – Exploded view of the prototype, showing its components and assembly. 222
Figure 4.14 – Rotors considered in the experiments, where the brown dashed lines indicate the position where the central shaft is attached. The rotation viewed from above the rotors is clockwise. 222
Figure 4.15 – Washout hole in the rotor (inclined hole with diameter equal to 2 mm), illustrated from the rotor cross-section that crosses it. 223
Figure 4.16 – Schematic view of the fluid flow circuit. 223
Figure 4.17 – Fabricated prototype. 225
Figure 4.18 – Photo showing the experimental setup. 225

Figure 5.1 – *Crossed triangular elements* (triangular elements distributed in rectangular partitions). 229
Figure 5.2 – Research fronts being considered for topology optimization and further results. 229
Figure 5.3 – Design domain for the nozzle. 233
Figure 5.4 – Mesh used in the design of the nozzle. 234
Figure 5.5 – Effect of the wall rotation in the design of the nozzle. 235
Figure 5.6 – Convergence curve for the nozzle optimized for 20 rpm wall rotation. 236
Figure 5.7 – Plot of the relative velocity field ($|\boldsymbol{v}| = \sqrt{v_r^2 + v_\theta^2 + v_z^2}$ (m/s)) in logarithmic scale for 20 rpm wall rotation (maximum Reynolds number of 420) (the boundary line of the optimized topology is indicated with a gray thick line). 236
Figure 5.8 – Topology optimization result of the nozzle for 20 rpm wall rotation (the pressure and velocities are computed in the post-processed result). 237
Figure 5.9 – Design domain for the hydrocyclone-type device. 238
Figure 5.10 – Effect of the inlet rotation in the design of the hydrocyclone-type device. 239
Figure 5.11 – Convergence curve for the hydrocyclone-type device optimized for 10 rpm inlet rotation. 240
Figure 5.12 – Topology optimization result of the hydrocyclone-type device for 10 rpm inlet rotation (the pressure and velocities are computed in the post-processed result). 241
Figure 5.13 – Model for the optimization of a horizontal inlet Tesla pump, considering an inlet zone outside the design domain. 243
Figure 5.14 – Mesh for the optimization of a horizontal inlet Tesla pump. 243
Figure 5.15 – Relative energy dissipation (Φ_{rel}) for the optimized topologies of a horizontal inlet Tesla pump for different rotations and different $\kappa_{\theta,\max}$ values in relation to $\kappa_{r,\max} = \kappa_{z,\max}$. 244
Figure 5.16 – Pressure head (H) and isentropic efficiency (η_s) for the optimized topologies of a horizontal inlet Tesla pump with $\kappa_{\theta,\max}$ 100 times lower than $\kappa_{r,\max} = \kappa_{z,\max}$ for different rotations. 245

Figure 5.17 – Convergence curve for the objective function value of a horizontal inlet Tesla pump for 0.5 L/min and 500 rpm. 246
Figure 5.18 – Topology optimization result of the horizontal inlet Tesla pump for 500 rpm and 0.5 L/min (the pressure and velocities are computed in the post-processed mesh). 246
Figure 5.19 – Models for the optimization of a vertical inlet Tesla pump. 248
Figure 5.20 – Mesh for the optimization of a vertical inlet Tesla pump. 249
Figure 5.21 – Convergence curve for the objective function value (relative energy dissipation) of a one-channel Tesla pump for 500 rpm and 0.5 L/min (the circles indicate the beginning of a new step of iterations, by changing parameters and restarting the IPOPT algorithm; the squares indicate change in the rotation of the disks). 250
Figure 5.22 – Topology optimization result of the one-channel Tesla pump for 500 rpm and 0.5 L/min (the pressure and velocities are computed in the post-processed mesh). 251
Figure 5.23 – Convergence curve for the objective function value (relative energy dissipation) of a two-channel Tesla pump for 500 rpm and 0.5 L/min.252
Figure 5.24 – Topology optimization result of a two-channel Tesla pump for 500 rpm and 0.5 L/min (the pressure and velocities are computed in the post-processed mesh). 253
Figure 5.25 – Relative energy dissipation for the optimized topologies of a vertical inlet Tesla pump for different rotation / flow rate ratios, considering the cases of 0.25 L/min, 0.5 L/min and 0.75 L/min. 255
Figure 5.26 – Pressure head (H) and isentropic efficiency (η_s) of a vertical inlet Tesla pump for different rotation / flow rate ratios, considering the cases of 0.25 L/min, 0.5 L/min and 0.75 L/min. 256
Figure 5.27 – Comparison between the one- and two-channel Tesla pumps for 0.5 L/min. 257
Figure 5.28 – Convergence curve for the objective function value (100% vorticity) of a one-channel Tesla pump for 500 rpm and 0.5 L/min (the circles indicate the beginning of a new step of iterations, by changing parameters and restarting the IPOPT algorithm; the squares indicate change in the rotation of the disks). 258

Figure 5.29 – Topology optimization result of the one-channel Tesla pump optimized for 100% vorticity for 500 rpm and 0.5 L/min (the pressure and velocities are computed in the post-processed mesh). 259
Figure 5.30 – Topology optimization for 100% vorticity for 500 rpm and 0.5 L/min, considering the objective function without the porous medium effect term. 260
Figure 5.31 – Topology optimization result of a one-channel Tesla pump optimized for 50% vorticity and 50% of relative energy dissipation for 500 rpm and 0.5 L/min (the pressure and velocities are computed in the post-processed mesh). 261
Figure 5.32 – Mesh smoothing being applied to an optimized topology. 262
Figure 5.33 – Comparison of pressure head (H) and isentropic efficiency (η_s) between a straight and an optimized horizontal inlet Tesla pump. . 263
Figure 5.34 – Comparison of pressure head (H) and isentropic efficiency (η_s) between a straight and an optimized vertical inlet one-channel Tesla pump. 263
Figure 5.35 – Comparison of pressure head (H) and isentropic efficiency (η_s) between a straight and an optimized vertical inlet two-channel Tesla pump. 263
Figure 5.36 – Design domain for two-outlet channel design. 267
Figure 5.37 – Mesh used in the two-outlet channel design. 267
Figure 5.38 – Non-Newtonian viscosity in the optimized two-outlet channel designs for the non-Newtonian fluid flow at 0.05 L/min (20 rpm) before post-processing (i.e., still including the material model) (in logarithmic scale). The contours of the optimized topologies are delimited by thin dark lines. 268
Figure 5.39 – Effect of the flow rate in the non-Newtonian and Newtonian two-outlet channel designs. 269
Figure 5.40 – Non-Newtonian viscosities in the optimized two-outlet channel designs (in logarithmic scale). 271
Figure 5.41 – Convergence curves for the non-Newtonian and Newtonian two-outlet channel designs (0.05 L/min, 20 rpm). 271

Figure 5.42 – Optimized topologies, 3D representations, pressures and velocities for the non-Newtonian and Newtonian two-outlet channel designs (0.05 L/min, 20 rpm). 272
Figure 5.43 – Design domain for the Tesla blood pump design. 274
Figure 5.44 – Mesh used in the Tesla blood pump design. 274
Figure 5.45 – Reference straight-channel Tesla pump for comparing with the optimized results. 274
Figure 5.46 – Total hemolysis index ($I_{H,T}$) and relative energy dissipation (Φ_{rel}) for the topology optimization considering the effect of the flow rate and rotation. 275
Figure 5.47 – Convergence curve for the optimized topology for w_H = 0.5, 1 L/min and 1500 rpm. 276
Figure 5.48 – Topology optimization results for different rotations (n_0) (for 1 L/min and w_H = 0.5). 278
Figure 5.49 – Topology optimization results for different flow rates (Q) (for 1500 rpm and w_H = 0.5). 280
Figure 5.50 – Topology optimization results for different w_H values (for 1 L/min and 1500 rpm). 281
Figure 5.51 – Optimized topology, 3D representation, pressure and velocity for w_H = 0.5, 1 L/min and 1500 rpm. 282
Figure 5.52 – Hemolysis index for the optimized topology for w_H = 0.5, 1 L/min and 1500 rpm. 282
Figure 5.53 – Non-Newtonian viscosity the optimized topology for w_H = 0.5, 1 L/min and 1500 rpm. 283
Figure 5.54 – Topology optimization results for the Tesla blood pump under different weights in the multi-objective function for the PAS index. 286
Figure 5.55 – Topology optimization results for the Tesla blood pump under different weights in the multi-objective function for the hemolysis index. 287
Figure 5.56 – Optimized topology for the combined case ($w_{PAS} = 0.1$ and $w_H = 0.5$) for the Tesla blood pump. 287
Figure 5.57 – Straight disks reference topology for the Tesla blood pump. 287
Figure 5.58 – Convergence curve of the topology optimization of the Tesla blood pump for the combined case ($w_{PAS} = 0.1$ and $w_H = 0.5$). 288

Figure 5.59 – Optimized topology, pressure, velocity, dynamic viscosity, PAS index, and hemolysis index for the optimized Tesla blood pump for two different cases. 290
Figure 5.60 – Velocities on the outlet of the optimized Tesla pump rotor (1 L/min and 2000 rpm, $w_H = 0.9$). 291
Figure 5.61 – Representation of the 2D model from the middle of the outlet of the rotor (the optimized Tesla pump rotor is shown in a *section view*). 291
Figure 5.62 – Domain for the design of the volute. 293
Figure 5.63 – Mesh for the design of the volute. 293
Figure 5.64 – Topology optimization results for the volute under different weights in the multi-objective function for the PAS index. 297
Figure 5.65 – Topology optimization results for the volute under different weights in the multi-objective function for the hemolysis index. 298
Figure 5.66 – Contours of the optimized topologies for $w_H = 0.9$ and $w_{PAS} = 0.5$. 298
Figure 5.67 – Optimized topology for the combined case ($w_{PAS} = 0.3$ and $w_H = 0.3$) for the volute. 299
Figure 5.68 – Contours of the optimized topologies for $w_\Phi = 1$, "$w_H = 0.5$ and $w_{PAS} = 0.9$", $w_H = 0.5$ and $w_{PAS} = 0.9$. 299
Figure 5.69 – Convergence curve of the topology optimization of the volute for $w_\Phi = 1$. 300
Figure 5.70 – Optimized topology, pressure, velocity, PAS index, hemolysis index and dynamic viscosity for the optimized volute for $w_\Phi = 1$. 301
Figure 5.71 – Types of design that may be considered for bladed rotor topology optimization. 303
Figure 5.72 – Example of the 2D design of blades for a hybrid Tesla pump rotor (*side*-type design for 4 blades). 303
Figure 5.73 – Domain for the design of the bladed pump (*side*-type design). . . . 305
Figure 5.74 – Mesh for the design of the bladed pump (*side*-type design). 305
Figure 5.75 – Topology optimization results for the bladed pump (*side*-type design) under different weights in the multi-objective function for the PAS index. 308

Figure 5.76 – Topology optimization results for the bladed pump (*side*-type design) under different weights in the multi-objective function for the hemolysis index. 309
Figure 5.77 – Optimized topology for the combined case ($w_{PAS} = 0.3$ and $w_H = 0.5$) for the bladed pump (*side*-type design). 310
Figure 5.78 – Contours of the optimized topologies for $w_H = 0.5$, $w_{PAS} = 0.5$, $w_H = 0.75$ and "$w_{PAS} = 0.3$ and $w_H = 0.5$". 310
Figure 5.79 – Convergence curve of the topology optimization of the bladed pump (*side*-type design) for $w_{PAS} = 0.85$. 311
Figure 5.80 – Optimized topology, pressure, velocity, PAS index, hemolysis index and dynamic viscosity for the optimized bladed pump (*side*-type design) for $w_{PAS} = 0.85$. The type of plot of the PAS index was changed to logarithmic in order to allow a better visualization of the results. 312
Figure 5.81 – Interpretation of the optimized blades (*side*-type design). 313
Figure 5.82 – Domain for the design of the bladed pump (*full-inlet*-type design). 313
Figure 5.83 – Mesh for the design of the bladed pump (*full-inlet*-type design). . . 314
Figure 5.84 – Initial guess for the design of the bladed pump (*full-inlet*-type design). The geometric center of the initial guess is positioned at 36°. 314
Figure 5.85 – Contours of the optimized topologies for the bladed rotor (*full-inlet*-type design). 316
Figure 5.86 – Optimized topologies for the bladed pump (*full-inlet*-type design). . 317
Figure 5.87 – Convergence curve of the topology optimization of the bladed pump (*full-inlet*-type design) for $\beta = 20°$ considering blood damage (exemplified for $w_{PAS} = 0.9$). 318
Figure 5.88 – Optimized topology, pressure, velocity, PAS index, hemolysis index and dynamic viscosity for the optimized bladed pump (*full-inlet*-type design) for $w_{PAS} = 0.9$. 319
Figure 5.89 – Interpretation of the optimized blades (*full-inlet*-type design). . . . 320
Figure 5.90 – Interpretation of the optimized blades (*full-inlet*-type design), highlighting the flow between a pair of blades, which resembles the optimized topologies from Section 5.1.7.1. 320

Figure 5.91 – Design domain for the rotating nozzle. 322
Figure 5.92 – Mesh used in the design of the rotating nozzle. 323
Figure 5.93 – Topology optimization results for the rotating nozzle under different wall rotations, for laminar and turbulent flows. 325
Figure 5.94 – Laminar and turbulent flow optimized topologies operating under the flow configurations of each other. 326
Figure 5.95 – Convergence curve of the topology optimization of the rotating nozzle for laminar (50 rpm wall rotation) and turbulent flows (5000 rpm wall rotation). 327
Figure 5.96 – Optimized topologies and variables for optimized rotating nozzles. 328
Figure 5.97 – Design domain for the hydrocyclone-type device. 329
Figure 5.98 – Topology optimization results for the hydrocyclone-type device under different inlet rotations. 331
Figure 5.99 – Convergence curve of the topology optimization of the hydrocyclone-type device (1000 rpm inlet rotation). 331
Figure 5.100–Optimized topologies and variables for the optimized hydrocyclone-type device (1000 rpm inlet rotation). 332
Figure 5.101–Design domain for the Tesla pump. 332
Figure 5.102–Mesh used in the design of the Tesla pump. 333
Figure 5.103–Straight disks reference design for the Tesla pump. 333
Figure 5.104–Optimized topology for the Tesla pump. 334
Figure 5.105–Convergence curve of the topology optimization of the Tesla pump. 334
Figure 5.106–Optimized topology and variables for the optimized Tesla pump. . 335
Figure 5.107–Optimized Tesla pump rotor with $r_{shaft} = 2.5$ mm (2000 rpm, 1 L/min, optimized considering $w_H = 0.9$). 336
Figure 5.108–Boundary conditions for the simulations of the designed prototypes. 338
Figure 5.109–Mesh for the simulations of the designed prototypes (exemplified for the optimized rotor). 338
Figure 5.110–Functions computed in the simulations for 1.0 L/min and 2000 rpm (the percentages correspond to the relative difference fractions with respect to the values for the straight rotor). 340
Figure 5.111–Intermediary flow rates around the rotor. 342
Figure 5.112–Simulation results for the straight rotor (1 L/min, 2000 rpm). 343

Figure 5.113–Simulation results for the optimized rotor (1 L/min, 2000 rpm). . . 344
Figure 5.114–Simulation results for the optimized rotor (no disk spacers) (1 L/min, 2000 rpm). 344
Figure 5.115–Simulation results for the optimized rotor (with blades) (1 L/min, 2000 rpm). 345
Figure 5.116–Experimental pump curves (expressed as $\Delta p \times Q$). 346
Figure 5.116–[Continued] Experimental pump curves (expressed as $\Delta p \times Q$). . 347
Figure 5.117–Comparison of experimental results with simulations for the optimized rotor at 2500 rpm. 348
Figure 5.118–Comparison of experimental results with simulations for the rotors at 2500 rpm, given by the pump curve expressed as $\Delta p \times Q$. . . . 349
Figure 5.119–Functions computed in the simulations for 0.1 L/min and 2500 rpm (the percentages correspond to the relative difference fractions with respect to the values for the straight rotor). 350
Figure A.1 – Computational domain for a vertical inlet Tesla pump with two disks. 404
Figure A.2 – Comparison of simulation results for the vertical inlet Tesla pump with two disks. 405
Figure B.1 – Representation of the linear averaging around a vertex “0” on the closed contour, considering $n_{\mathrm{cf}} = 1$. 408
Figure B.2 – Illustration of an example of mesh smoothing by contour filtering (for a nodal design variable). 409
Figure C.1 – Laminar and turbulent velocity profiles for the same *2D flow rate* (area below the curves). 411
Figure E.1 – Design domain considered for the hydrocyclone-type device. . . . 413
Figure E.2 – Mesh considered in the design of the hydrocyclone-type device. . 414
Figure E.3 – Topology optimization results for the hydrocyclone-type device for $w_{PAS} = 0.5$, considering different $\kappa_{PAS,\max}$ values. 415
Figure E.4 – Contours of the optimized topologies from Fig. E.3. 416
Figure E.5 – Topology optimization results for the hydrocyclone-type device for different w_{PAS} values ($\kappa_{PAS,\max} = 10^3$ s^{-1}). 417
Figure E.6 – Contours of the optimized topologies from Fig. E.5. 417
Figure E.7 – Topology optimization results for the hydrocyclone-type device for different w_H values. 418

Figure E.8 – Contours of the optimized topologies from Fig. E.7. 418
Figure E.9 – Topology optimization results for the hydrocyclone-type device considering w_{PAS} and w_H. 419
Figure E.10 – Contours of the optimized topologies from Fig. E.9. 419
Figure E.11 – Convergence curve of the topology optimization of the hydrocyclone-type device ($w_{PAS} = 0.5$, $\kappa_{PAS,\max} = 10^3$ s^{-1}). 420
Figure E.12 – Optimized topology, pressure, velocity, dynamic viscosity, PAS index and hemolysis index for the optimized hydrocyclone-type device ($w_{PAS} = 0.5$, $\kappa_{PAS,\max} = 10^3$ s^{-1}). 421
Figure E.13 – Design domain considered for the bypass graft. 422
Figure E.14 – Mesh considered in the design of the bypass graft. 422
Figure E.15 – Optimized topologies for the bypass graft. 423
Figure E.16 – Optimized topology, pressure, velocity, PAS index, hemolysis index and dynamic viscosity for the optimized bypass grafts. 425
Figure F.1 – Schematic illustration of the compensation of the simulated (static) pressure for comparing with the experiments. 426

LIST OF TABLES

Table 1.1 – Approximated typical operating conditions for a VAD. 60
Table 2.1 – Dimensionless parameters for analysis in Tesla-type devices. . . . 125
Table 2.2 – Definitions of the hemolysis index correlated to experiments. 130
Table 4.1 – Example of a Newtonian blood analogue. 227
Table 5.1 – Parameters used for the topology optimization of the nozzle. 234
Table 5.2 – Reference parameters for the optimization schemes (steps) for the nozzle. 235
Table 5.3 – Values of the objective function and pressure head for the optimized topologies of the nozzle after post-processing. 235
Table 5.4 – Parameters used for the topology optimization of the hydrocyclone-type device. 238
Table 5.5 – Reference parameters for the optimization schemes (steps) for the hydrocyclone-type device. 239
Table 5.6 – Values of the objective function and pressure head for the optimized topologies of the hydrocyclone-type device after post-processing. . 239
Table 5.7 – Parameters used for the topology optimization of a horizontal inlet Tesla pump. 244
Table 5.8 – Operational parameters of the optimized topology of the horizontal inlet Tesla pump for 0.5 L/min and 500 rpm. 248
Table 5.9 – Parameters used for the topology optimization of a vertical inlet Tesla pump. 249
Table 5.10 – Operational parameters of the optimized topology of a one-channel Tesla pump for 500 rpm and 0.5 L/min. 251
Table 5.11 – Operational parameters of the optimized topology of a two-channel Tesla pump for 500 rpm and 0.5 L/min. 253
Table 5.12 – Operational parameters of the optimized topology of a one-channel Tesla pump optimized for 100% vorticity for 500 rpm and 0.5 L/min. 260
Table 5.13 – Operational parameters of the optimized topology of a one-channel Tesla pump optimized for 50% vorticity and 50% of relative energy dissipation for 500 rpm and 0.5 L/min. 262

Table 5.14 – Operational parameters of the smoothened optimized topologies of vertical inlet Tesla pump for 500 rpm and 0.5 L/min for comparison with straight disks solutions. 264
Table 5.15 – Parameters used for the topology optimization of the two-outlet channel. 268
Table 5.16 – Reference parameters for the optimization schemes (steps) for the non-Newtonian and Newtonian two-outlet channel designs. 270
Table 5.17 – Optimization parameters for each optimized topology* ($q = 1$). . . . 276
Table 5.18 – Parameters considered for the topology optimization of the Tesla blood pump. 284
Table 5.19 – Relative comparison of the optimized topologies for the Tesla blood pump with the reference design (Fig. 5.57). 286
Table 5.20 – Average velocities on the outlet of the optimized Tesla pump rotor (1 L/min and 2000 rpm, $w_H = 0.9$), from Fig. 5.60. 292
Table 5.21 – Parameters used for the topology optimization of the volute. 294
Table 5.22 – Relative comparison of the optimized topologies for the volute with the optimized topology for $w_\Phi = 1$. 300
Table 5.23 – Parameters used for the topology optimization of the bladed pump (*side*-type design). 306
Table 5.24 – Relative comparison of the optimized topologies for the bladed pump (*side*-type design) with the optimized topology for $w_\Phi = 1$. 311
Table 5.25 – Parameters used for the topology optimization of the bladed pump (*full-inlet*-type design). 315
Table 5.26 – Comparison of the optimized topologies for the bladed pump (*full-inlet*-type design). 317
Table 5.27 – Relative comparison of the optimized topologies for the bladed pump (*full-inlet*-type design) with the optimized topology for $\beta = 20°$ and $w_\Phi = 1$ (“min. rel. energy diss.”). 317
Table 5.28 – Parameters used for the topology optimization of the rotating nozzle. 324
Table 5.29 – Parameters used for the topology optimization of the hydrocyclone-type device. 330
Table 5.30 – Parameters used for the topology optimization of the Tesla pump. . 333

Table 5.31 – Computed values for the reference and optimized topologies for the Tesla pump device. 334
Table 5.32 – Topology optimization results for the volute under different weights in the multi-objective function for the hemolysis index. 336
Table 5.33 – Prototype designs. 337
Table E.1 – Parameters considered for the topology optimization of the hydrocyclone-type device. 414
Table E.2 – Parameters considered for the topology optimization of the bypass graft. 423
Table E.3 – Computed values in the optimized topologies for the bypass design. 424

LIST OF ABBREVIATIONS AND ACRONYMS

AD	Automatic Differentiation
B	Bubble shape functions
BEP	Best Efficiency Point
BESO	Bi-directional Evolutionary Structural Optimization
BiVAD	Bi-Ventricular Assist Device
BTD	Bridge To Destination
BTT	Bridge To Therapy
C	Differentiability Class
CAD	Computer Aided Design
CBC	Coin-or Branch and Cut
CD	Continuous velocity/Discontinuous pressure (element)
CFD	Computational Fluid Dynamics
CG	Continuous Galerkin
CHF	Congestive Heart Failure
COIN-OR	COmputational INfrastructure for Operations Research
CR	Crouzeix-Raviart (disposition of nodes)
CSG	Constructive Solid Geometry
CVD	CardioVascular Disease
DAV	"*Dispositivo de Assistência Ventricular*" (VAD, Ventricular Assist Device)
dijitso	distributed just-in-time shared library building (from FEniCS)
DC	Direct Current
DG	Discontinuous Galerkin
DNS	Direct Numeric Simulation
DOLFIN	Dynamic Object-oriented Library for FINite element computation (from FEniCS)

DoE	Design of Experiments
dP	discontinuous Polynomial
EPUSP	Polytechnic School of the University of São Paulo ("*Escola Politécnica da Universidade de São Paulo*")
FAPESP	São Paulo Research Foundation ("*Fundação de Amparo à Pesquisa do Estado de São Paulo*")
FEM	Finite Element Method
FEniCS	Finite Element Computational Software
FFC	FEniCS Form Compiler (from FEniCS)
FIAT	FInite element Automatic Tabulator (from FEniCS)
FMUSP	Faculty of Medicine of the University of São Paulo ("*Faculdade de Medicina da Universidade de São Paulo*")
FSI	Fluid-Structure Interaction
FVM	Finite Volume Method
GT	Geometry Trimming
HF	Heart Failure
IBM	International Business Machines Corporation
InCor	Heart Institute of the *Hospital das Clínicas* of FMUSP ("*Instituto do Coração do Hospital das Clínicas da FMUSP*")
IPOPT	Interior-Point OPTimizer
ILP	Integer Linear Programming
JIT	Just-In-Time (compilation)
KKT	Karush-Kuhn-Tucker (condition)
LA	Left Atrium
LBB	Ladyžhenskaya-Babuška-Brezzi (condition)
LBM	Lattice-Boltzmann Method
LES	Large Eddy Simulation
LSFEM	Least-Squares Finite Element Method

LU	Lower-Upper (decomposition)
LV	Left Ventriculum
LVAD	Left-Ventricular Assist Device
MAP	Mean Arterial Pressure
mgNIH	Normalized miligram Index of Hemolysis
MIH	Modified Index of Hemolysis
MMGS	MiliMeters-Grams-Seconds
mshr	mesh generation (from FEniCS)
MSOL	Multiphysics Systems Optimization Laboratory ("*Laboratório de Otimização de Sistemas Multifísicos*" – Research laboratory in Poli-USP, in which the author of this work participates)
MUMPS	MUltifrontal Massively Parallel sparse direct Solver
NDF	Fluids & dynamics research group ("*Núcleo de Dinâmica e Fluidos"*)
NIH	Normalized Index of Hemolysis
NURBS	Non-Uniform Rational Basis Spline
OpenFOAM	Open-source Field Operation And Manipulation
P	Polynomial (Lagrange interpolation)
PAS	Platelet Activation State
PDE	Partial Differential Equation
PETSc	Portable, Extensible Toolkit for Scientific computation
PIV	Particle Image Velocimetry
Poli-USP	Polytechnic School of the University of São Paulo ("*Escola Politécnica da Universidade de São Paulo*")
RA	Right Atrium
RANS	Reynolds-Averaged Navier-Stokes (models/equations)
RBC	Red Blood Cell
RCGI	Research Centre for Greenhouse Gas Innovation (previously called "Research Centre for Gas Innovation", before October, 8th, 2021)

ROL	Rapid Optimization Library
RSM	Response Surface Methodology
RV	Right Ventriculum
RVAD	Right-Ventricular Assist Device
SI	International System of Units (“*Système International d’unités*”)
SILP	Sequential Integer Linear Programming
SIMPLE	Semi-Implicit Method for Pressure-Linked Equations
SIMPLER	SIMPLE Revised
SLIP	Sequential Linear Integer Programming
SNES	Scalable Nonlinear Equations Solvers
SRF	Single Rotating Frame
SST	Shear Stress Transport
SUPG	Streamline Upwind Petrov Galerkin (stabilization)
TAH	Total Artificial Heart
TOBS	Topology Optimization of Binary Structures
TOM	Topology Optimization Method
UFL	Unified Form Language (from FEniCS)
UMFPACK	Unsymmetric MultiFrontal PACKage
UVH	Uni-Ventricular Heart
USP	University of São Paulo (“*Universidade de São Paulo*”)
USNCCM	U.S. National Congress on Computational Mechanics (international conference)
VAD	Ventricular Assist Device (DAV, “*Dispositivo de Assistência Ventricular*”)
WA2018	Wray-Agarwal 2018 (turbulence model)
WCCM	World Congress in Computational Mechanics (international conference)

LIST OF SYMBOLS

Pressure-velocity state variables

$\boldsymbol{u}$	State vector.
p	(Static) pressure.
$\boldsymbol{v}$	(Relative) velocity.
v_i	Components of the (relative) velocity (in the 2D flow model, $i = x, y$; in the 2D swirl flow model, $i = r, \theta, z$).
p_0	A (static) pressure level.
T_{K}	Absolute temperature (in Kelvin).
$\boldsymbol{v}_{\mathrm{abs}}$	Absolute velocity.
$v_{\mathrm{abs},i}$	Components of the absolute velocity components (in the 2D flow model, $i = x, y$; in the 2D swirl flow model, $i = r, \theta, z$).

Weak form

R_m	Weak form (*Residual*) of the momentum (Navier-Stokes) equations.
R_c	Weak form (*Residual*) of the continuity equation.
R_{SA}	Weak form (*Residual*) of the Spalart-Allmaras equation.
R_w	Weak form (*Residual*) of the wall distance equation (modified Eikonal equation).
R_{WA2018}	Weak form (*Residual*) of the Wray-Agarwal (WA2018) equation.
F	Weak form of the complete fluid flow problem.
$\boldsymbol{w}_v$	Test function for the velocity.
$w_{v,i}$	Components of the test function for the velocity (in the 2D flow model, $i = x, y$; in the 2D swirl flow model, $i = r, \theta, z$).

w_p	Test function for the pressure.
$w_{\tilde{\nu}_\mathrm{T}}$	Test function for $\tilde{\nu}_\mathrm{T}$ (Spalart-Allmaras model).
w_G	Test function for G (reciprocal distance of the wall distance computation from the modified Eikonal equation).
w_{R_T}	Test function for R_T (Wray-Agarwal (WA2018) model).
$\boldsymbol{v}\vert_{\mathrm{projected,linear}}$	Relative velocity projected in a linear function space.
$w_{\mathrm{proj,v}}$	Test function for the projection of the relative velocity.
$(\boldsymbol{v}\bullet\nabla)\tau_{\mathrm{m,total}}\vert_{\mathrm{approximated}}$	Convective derivative of the shear stress magnitude approximated in a linear function space.
$w_{\mathrm{a,cd},\tau}$	Test function for the approximation of the convective derivative of the shear stress magnitude.

Boundary conditions

R_vasc	Vascular resistance.
Δp_circ	Variation of pressure in the systemic or pulmonary circulation (depending if the analysis is of LVAD or RVAD).
σ	Normal stress.
σ_0	Reference value for the normal stress.

Fluid properties

μ	Dynamic viscosity of the fluid.
ρ	Density of the fluid.
ν	Kinematic viscosity of the fluid.
c_v	Specific heat at constant volume of the fluid.
c_p	Specific heat at constant pressure of the fluid.
k_sh	Ratio of specific heats of the fluid.

M_{molar}	Molar mass.
R_{U}	Ideal (*Universal*) gas constant (8.31451 J/(mol K)).

Non-Newtonian fluid

τ_{m}	Viscous shear stress magnitude (*viscous scalar shear stress*).
$\dot{\gamma}_{\mathrm{m}}$	Viscous shear rate magnitude (*viscous scalar shear rate*).
$\tau_{\mathrm{m,total}}$	Total shear stress magnitude (*total scalar shear stress*).
$\dot{\gamma}_{\mathrm{m,total}}$	Total shear rate magnitude (*total scalar shear rate*).
λ	Time constant (*characteristic time*) of the Carreau-Yasuda model.
n	Exponential factor of the Carreau-Yasuda model.
a	Yasuda coefficient, of the Carreau-Yasuda model (except in Appendix D, where it is the name of a generic variable).
μ_0	Maximum (*low shear rate*) dynamic viscosity of the Carreau-Yasuda model.
μ_∞	Minimum (*Newtonian*) dynamic viscosity of the Carreau-Yasuda model.

Turbulence

μ_{T}	Turbulent dynamic viscosity.
ν_{T}	Turbulent kinematic viscosity.
I_T	Turbulence intensity.
ℓ_T	Turbulence length scale.
$\tilde{\nu}_{\mathrm{T}}$	Auxiliary turbulent viscosity of the Spalart-Allmaras model.
$\tilde{\nu}_{\mathrm{T,mat}}$	Auxiliary turbulent viscosity in relation to the value on walls (Spalart-Allmaras model).
$\tilde{\nu}_{\mathrm{T,wall}}$	Auxiliary turbulent viscosity on the wall (Spalart-Allmaras model).

$\tilde{\nu}_{\mathrm{T},in}$ Auxiliary turbulent viscosity on the inlet (Spalart-Allmaras model).

$\lambda_{\tilde{\nu}_\mathrm{T}}$ Adjustable parameter for the intensity of the attenuation of turbulence inside the solid material (Spalart-Allmaras model).

c_{b1}, c_{b2}, c_{v1}, f_Ω, c_{w1}, c_{w2}, c_{w3}, σ, χ, f_{v2}, $\tilde{S}$, S, Ω_m, $\boldsymbol{\Omega}$, f_{v1}, f_{v2}, f_w, c_{w3}, g, r_i, c_{w2}, $\tilde{S}_r$ Additional variables used in the Spalart-Allmaras model.

κ_{vk} von Kármán constant.

n_v Number of velocity components.

ℓ_w Wall distance.

G Reciprocal wall distance (modified Eikonal equation).

ℓ_ref Reference value for the wall distance (modified Eikonal equation).

G_0 Reciprocal of the reference value for the wall distance (modified Eikonal equation).

σ_w Relaxation factor for the wall distance computation (modified Eikonal equation).

R_T Undamped eddy (turbulent) viscosity of the Wray-Agarwal (WA2018) model.

λ_{R_T} Adjustable parameter for the intensity of the attenuation of turbulence inside the solid material (Spalart-Allmaras model).

f_μ, C_1, S, f_1, $C_{1,k\text{-}\omega}$, $C_{2,k\text{-}\omega}$, $C_{1,k\text{-}\varepsilon}$, $C_{2,k\text{-}\varepsilon}$, C_m, $\boldsymbol{W}$, χ, c_w, η, σ_R, $\sigma_{k\text{-}\omega}$, $\sigma_{k\text{-}\varepsilon}$, arg_1, C_μ, k_T, ω_T Additional variables used in the Wray-Agarwal (WA2018) model.

Other variables

$\boldsymbol{r}$ Radial position of the fluid with respect to the rotation axis.

$\boldsymbol{s}$ Position of the fluid.

$\boldsymbol{a}$ A generic vector-valued variable.

x, y Coordinates in the 2D model. x may refer to a generic variable or coordinate when this other meaning is explicitly stated.

r, θ, z	Cylindrical coordinates.
r, z	Coordinates in the 2D swirl flow model.
$\boldsymbol{e}_x, \boldsymbol{e}_y, \boldsymbol{e}_z$	Unit vectors in Cartesian coordinates.
$\boldsymbol{e}_x, \boldsymbol{e}_y$	Unit vectors in the 2D model.
$\boldsymbol{e}_r, \boldsymbol{e}_\theta, \boldsymbol{e}_z$	Unit vectors in cylindrical coordinates / 2D swirl flow model.
$\boldsymbol{T}$	Stress tensor.
$\boldsymbol{\epsilon}$	Deformation (strain) tensor.
$\boldsymbol{I}$	Identity matrix.
$\boldsymbol{\tau}$	Shear stress tensor.
$\boldsymbol{T}_R$	Reynolds (turbulent) stress tensor.
$\boldsymbol{\epsilon}_R$	Reynolds (turbulent) deformation (strain) tensor.
$\boldsymbol{\epsilon}_{\text{total}}$	Total deformation (strain) tensor.
$\boldsymbol{\tau}_{\text{total}}$	Total shear stress tensor.
$\rho \boldsymbol{f}$	Body force per unit volume acting on the fluid.
$\boldsymbol{\omega}$	Rotation vector of the fluid flow device, which is the same of the reference frame.
ω_0	Rotation of the fluid flow device, which is the same of the reference frame (rad/s).
n_0	Rotation of the fluid flow device, which is the same of the reference frame (rpm).
$\boldsymbol{\omega}_{\text{in}}$	Inlet rotation vector of the fluid flow device.
ω_{in}	Inlet rotation of the fluid flow device (rad/s).
n_{in}	Inlet rotation of the fluid flow device (rpm).
$\boldsymbol{\omega}_{\text{mat}}$	Rotation vector of the solid material being optimized.

ω_{mat}	Rotation of the solid material being optimized (rad/s).
n_{mat}	Rotation of the solid material being optimized (rpm).
$\boldsymbol{n}$	Normal unit vector.
g	Gravitational acceleration.
$\boldsymbol{v}_{in}$	Inlet velocity.
$\boldsymbol{v}_{\mathrm{abs},in}$	Absolute inlet velocity.
$\boldsymbol{v}_{out}$	Outlet velocity.
$\boldsymbol{v}_{2D}$	Velocity in the "2D plane": $\boldsymbol{v}_{2D} = \boldsymbol{v}_{rz} = (v_r,\ v_z)$ (2D swirl flow model), $\boldsymbol{v}_{2D} = \boldsymbol{v} = (v_x,\ v_y)$ (2D).
$\boldsymbol{v}_{rz}$	Radial-axial velocity.
$\boldsymbol{v}_{2D,t}$	Tangential velocity in the "2D plane".
$v_{rz,\mathrm{mag}}$	Magnitude of the radial-axial velocity.
$\boldsymbol{v}_{rz,\mathrm{cut}}$	Radial-axial velocity for the case of an obstacle cut from the mesh.
$\boldsymbol{v}_{rz,\mathrm{material}}$	Radial-axial velocity for the case of a modeled obstacle (with a material model).
x_{cut}	Generic variable for the case of an obstacle cut from the mesh.
x_{material}	Generic variable for the case of a modeled obstacle (with a material model).
f_x	Relative difference (*difference fraction*) for a generic variable x.
Δp_ℓ	Pressure drop in the leakage flow (Δp_ℓ).
$\Delta p_{\mathrm{centrifugal}}$	Pressure contribution of the centrifugal effect.
Δp_{seal}	Pressure difference inside the labyrinth seal.
ℓ_t	Total length of a labyrinth unit.
ℓ_g	Length of the gap.

ℓ_c	Length of the chamber.
h_c	Height of the chamber.
h_s	Gap spacing/height.
n_ℓ	Quantity of labyrinths.
Q_ℓ	Leakage (volumetric) flow rate.
α_c	Contraction coefficient.
Re_ω	Reynolds number for the rotation (labyrinth seal).
Re_c	Reynolds number for the chambers (labyrinth seal).
v_ℓ	Average leakage velocity (*axial velocity in the gap*).
r_d^2	Coefficient of determination.
a_r, b_r	Linear regression coefficients.
n_{patterns}	Quantity of stacked patterns.
Q_{stacked}	Flow rate of the stacked topology (by stacking various Tesla pump *single channel* topologies).
$\boldsymbol{B}$	Vectorial blockage ratio.
B_r	Radial blockage ratio.
B_θ	Tangential blockage ratio.
$\ell_{spacer,\theta}$	Tangential extension of a spacer.
$\ell_{spacer,r}$	Radial extension of a spacer.
$n_{spacers}$	Number of spacers.
r_{spacer}	Radius in which the geometric center of the spacer is located.
$\theta_{spacer,max}$	Maximum angle coordinate of a spacer.
$\theta_{spacer,min}$	Minimum angle coordinate of a spacer.

$r_{spacer,max}$	Maximum radial coordinate of a spacer.
$r_{spacer,min}$	Minimum radial coordinate of a spacer.

Topology optimization

α	Pseudo-density (design variable for fluid topology optimization).
α_0	Initial value of the pseudo-density.
α_i	Value of α in the node i of the mesh (or in the element i, depending on the finite element modeling) ($i = 1,\ 2,\ ...,\ n_\alpha$).
α_{ub}	Upper bound of the design variable.
α_{lb}	Lower bound of the design variable.
n_α	Quantity of values of the design variable (α) that are distributed over the mesh.
$\boldsymbol{f}_r(\alpha)$	Resistance force of the porous medium.
$f_{r,v}(\alpha)$	Proportional factor of the resistance force of the porous medium.
f	Specified volume fraction. In Section 3.2, as explicitly written in the text, f represents a generic function.
V_0	Volume of the design domain.
J	Multi-objective function.
J_i	Objective function i.
w_i	Weight of the objective function i (except when it refers to a test function).
J_{ref}	Objective function used as reference for the measurement units in the initial weight multi-objective function.
n_F	Number of objective functions.
$\boldsymbol{\lambda}_{J_i}$, λ_{J_iH}, λ_{J_iPAS}, $\boldsymbol{\lambda}_H$, $\boldsymbol{\lambda}_{PAS}$	Adjoint variables.
F_H	Weak form of the hemolysis model.

F_{PAS}	Weak form of the PAS model.
$\kappa(\alpha)$	Inverse permeability.
$\boldsymbol{\kappa}(\alpha)$	Inverse permeability matrix.
$\kappa_{\min}$	Minimum inverse permeability value.
$\kappa_{\max}$	Maximum inverse permeability value.
q	Penalty parameter of the inverse permeability.
$\mathrm{Da}_{\max}$	Maximum Darcy number.
$\kappa_i(\alpha)$	Inverse permeability for the direction i.
$\kappa_{i,\min}$	Minimum inverse permeability value for the direction i.
$\kappa_{i,\max}$	Maximum inverse permeability value for the direction i.
q_i	Penalty parameter of the inverse permeability for the direction i.
$\kappa_{PAS}(\alpha)$	Additional penalization parameter for the PAS index.
$\kappa_{PAS,\min}$	Minimum additional penalization parameter value for the PAS index.
$\kappa_{PAS,\max}$	Maximum additional penalization parameter value for the PAS index.
$\gamma(\alpha)$	Wall penalization (modified Eikonal equation).
$\gamma_{\min}$	Minimum wall penalization value (modified Eikonal equation).
$\gamma_{\max}$	Maximum wall penalization value (modified Eikonal equation).
k_D	Formation permeability, of the Brinkman-Forchheimer model.
β_F	Coefficient of inertial flow resistance, of the Brinkman-Forchheimer model.
C_F	Dimensionless form-drag constant.
$\zeta(\alpha)$	Convex interpolation function between solid and fluid.

Helmholtz filter

α_f	Filtered design variable.
$\alpha_{f,new}$	New filtered design variable (with an adjustment).
r_H	Filter length parameter of the modified Helmholtz equation.
w_H	Test function for the filtered design variable in the modified Helmholtz equation.

Performance quantities

Q	(Volumetric) flow rate.
Q_{2D}	(Volumetric) flow rate per unit thickness (*2D (volumetric) flow rate*).
$\dot{m}$	(Mass) flow rate.
Δp	Variation of (static) pressure.
Δp_d	Variation of dynamic pressure.
Δp_T	Variation of total (*stagnation*) pressure.
$\overline{p}_{out}$	Average (static) outlet pressure.
$\overline{p}_{T,out}$	Average total (*stagnation*) outlet pressure.
$\overline{p}_{D,out}$	Average dynamic outlet pressure.
$\overline{p}_{in}$	Average (static) inlet pressure.
$\overline{p}_{T,in}$	Average total (*stagnation*) inlet pressure.
$\overline{p}_{D,in}$	Average dynamic inlet pressure.
Φ_{rel}	Relative energy dissipation.
Φ_{abs}	Absolute energy dissipation.
P_f	*Pump* power.
P'_f	*Turbine* power.

$\boldsymbol{F}_{\text{ext}}$	External force acting on the fluid.
$\boldsymbol{T}_{\text{ext}}$	Torque of the external force acting on the fluid .
$\boldsymbol{\xi}_{\text{abs}}$	Absolute vorticity vector.
$\boldsymbol{\xi}$	Relative vorticity vector.
$\boldsymbol{\xi}_{\kappa}$	Increase in vorticity modeled in the porous medium.
k_V	Proportionality constant for the increase in vorticity modeled in the porous medium.
$\xi_{V,\text{rel}}$	Relative vorticity in the least squares approach.
η_s	Isentropic efficiency.
H	Pressure head (except when noted otherwise, such as when representing a dimension from a design domain).
H_{rel}	Relative pressure head.
H'	Head loss.
P_{ideal}	Ideal (*pump*) power.
P_{real}	Real (actual) (*pump*) power.
Δh_s	Variation of specific enthalpy (specific work) in the ideal process.
Δp_{VAD}	Static pressure rise in the VAD.
Δp_{rotor}	Static pressure rise in the rotor of the VAD.
Δp_{volute}	Static pressure rise in the volute of the VAD.
$\Delta p_{D,\text{rotor}}$	Dynamic pressure rise in the rotor of the VAD.
$\Delta p_{D,\text{volute}}$	Dynamic pressure rise in the volute of the VAD.
$\Delta p_{T,\text{rotor}}$	Total pressure rise in the rotor of the VAD.
$\Delta p_{T,\text{volute}}$	Total pressure rise in the volute of the VAD.
$\overline{p}_{in,\text{VAD}}$	Average (static) pressure on the inlet of the VAD.

$\overline{p}_{out,\mathrm{VAD}}$	Average (static) pressure on the outlet of the VAD.
M_{ND}	Measure of Non-Discreteness.
$I_{H,T}$	(Total) hemolysis index.
I_H	Local hemolysis index.
$I_{H,\mathrm{in}}$	Local hemolysis index on the inlet.
$I_{H,\mathrm{out}}$	Local hemolysis index on the outlet.
w_{I_H}	Test function for the local hemolysis index.
$I_{H,L,T}$	(Total) linear damage index (for hemolysis).
$I_{H,L}$	Local linear damage index (for hemolysis).
$I_{H,L,\mathrm{in}}$	Local linear damage index (for hemolysis) on the inlet.
$I_{H,L,\mathrm{out}}$	Local linear damage index (for hemolysis) on the outlet.
C_H, β_s, β_t	Coefficients of the Giersiepen-Wurzinger correlation (for hemolysis index).
$I_{PAS,T}$	(Total) PAS index.
I_{PAS}	Local PAS index.
$I_{PAS,\mathrm{in}}$	Local PAS index on the inlet.
$I_{PAS,\mathrm{out}}$	Local PAS index on the outlet.
$I_{PAS,\mathrm{mat}}$	Local PAS index value imposed inside the modeled solid material.
$w_{I_{PAS}}$	Test function for the local PAS index.
C_{PAS}, α_s, α_t	Coefficients of the Giersiepen-Wurzinger correlation (for PAS index).
$C_{PAS,sl}$	Proportionality factor for the stress level effect (of the shear-induced platelet activation model).

$C_{PAS,sr}$, δ_s, δ_t	Coefficients for the stress rate effect (of the shear-induced platelet activation model).
$C_{PAS,S}$	Proportionality factor for the sensitization effect (of the shear-induced platelet activation model).
S_τ	*Shear stress history* (of the shear-induced platelet activation model).
$I_{PAS,S}$	PAS index contribution from the sensitization effect.
$I_{PAS,sl}$	PAS index contribution from the shear level effect.
$I_{PAS,sr}$	PAS index contribution from the shear rate effect.
$D_{PAS,sl}$	Mechanical dose of PAS from the stress level.
$D_{PAS,sr}$	Mechanical dose of PAS from the stress rate.
w_{S_τ}	Test function for S_τ.
$w_{D_{PAS,sl}}$	Test function for $D_{PAS,sl}$.
$w_{D_{PAS,sr}}$	Test function for $D_{PAS,sr}$.
Hb	Quantity of hemoglobin per volume of blood (g/dL).
$\Delta\mathrm{Hb}_{\mathrm{pf}}$	Variation of the quantity of free hemoglobin in the plasma per volume of blood (g/dL).
$\mathrm{Hb}_{\mathrm{pf}}$	Quantity of free hemoglobin in the plasma per volume of blood (g/dL).
$\mathrm{Hb}_{\mathrm{pf,out}}$	Quantity of free hemoglobin in the plasma per volume of blood (g/dL) on the outlet.
$\mathrm{Hb}_{\mathrm{pf,in}}$	Quantity of free hemoglobin in the plasma per volume of blood (g/dL) on the inlet.
Δr_{tg}	Variation of the rate of thrombin generation of the activated platelets.

r_{tg}	Rate of thrombin generation of the activated platelets.
$r_{\mathrm{tg,full}}$	Rate of thrombin generation of the activated platelets of fully activated platelets (i.e., the maximum thrombin generation capacity).
$r_{\mathrm{tg,out}}$	Rate of thrombin generation of the activated platelets on the outlet.
$r_{\mathrm{tg,in}}$	Rate of thrombin generation of the activated platelets on the inlet.
Ht	Hematocrit (percentage of volume occupied by RBCs in the total volume of blood).
n_{passes}	Total number of passes.
V_{flow}	Volume of blood due to the fluid flow.
Δt_{m}	Measurement time.
$V_{\mathrm{circulating}}$	Total volume of blood circulating in the fluid flow circuit.
$\Delta t_{\mathrm{exposure}}$	Exposure time.
Δt	Time interval.
C_H	Proportionality factor for the hemolysis index.
β_s	Exponent of the shear stress magnitude.
β_t	Exponent of the exposure time.
Ph	Pohlhausen parameter.
$\mathrm{Re}_{\mathrm{ext},\ell}$	Local Reynolds number in relation to the external radius.
Nd	Local viscogeometric (Nendl) parameter.
A_Q	Essential machine data parameter.
$\mathrm{Re}_{\mathrm{V},\ell}$	Local Reynolds number for the volute.
$\mathrm{Re}_{\mathrm{2D\ swirl},\ell}$	Local Reynolds number for 2D swirl flow devices.
Ma_ℓ	Local Mach number.
n_{outlets}	Number of outlets of the Tesla pump.

$e_{\min}$	Minimum spacing between two disks.
r_{int}	Internal (inlet) radius of the rotor of the pump.
r_{ext}	External (outlet) radius of the rotor of the pump.
r_{shaft}	Radius of the shaft of the pump.
d_{rotor}	Diameter (external diameter) of the rotor of the pump.
e	Thickness of the radial margin considered in the volute design (Section 5.1.6).
$n_{\mathrm{b,in}}$	Number of inlets of the 2D model for the bladed rotor.
r'_{int}	Internal (inlet) radius of the 2D model for the bladed rotor.
e_{approx}	Approximated thickness of the 2D model for the bladed rotor.
$c_{p,R}$	Static pressure recovery coefficient.
$c_{p,T,L}$	Total pressure loss coefficient.
$c_{p,U}$	Unified pressure performance coefficient.
$\ell_{\Gamma_{\Pi,i}}$	Length of the boundary i considering the porous medium.
$n_{\text{repeated zones}}$	Number of repeated zones (in pattern repetition).

Post-processing

α_{th}	Thresholded design variable.
$\alpha_{\mathrm{th,lim}}$	Threshold limit for the design variable.
α_{mesh}	Design variable obtained by comparing the post-processed mesh with the mesh used in the optimization.
α_{label}	Label for a design variable value.
$\gamma_{\mathrm{c,int}}$	Corner angle in relation to the internal (*fluid*) part of the mesh.
$\gamma_{\mathrm{c,ext}}$	Corner angle in relation to the external (*solid*) part of the mesh.

$\gamma_{\mathrm{ic,int,min}}$, $\gamma_{\mathrm{ic,int,max}}$	Minimum and maximum values (respectively) of the angle bounds that define an internal corner (in mesh smoothing by generation of contours).
$\gamma_{\mathrm{ec,int,min}}$, $\gamma_{\mathrm{ec,int,max}}$	Minimum and maximum values (respectively) of the angle bounds that define an external corner (in mesh smoothing by generation of contours).
$\boldsymbol{s}_0$	Previous coordinates of a vertex (in mesh smoothing by contour filtering).
$\boldsymbol{s}_{0,\mathrm{new}}$	New coordinates of a vertex (in mesh smoothing by contour filtering).
$w_{cf,i}$	*Smoothing* weight of each vertex (in mesh smoothing by contour filtering).
n_{cf}	Number of vertices that are considered around the vertex of the contour (in mesh smoothing by contour filtering).
r_{cf}	Averaging radius of contour filtering (in mesh smoothing by contour filtering).
$\boldsymbol{s}_i$	Coordinates of a vertex labeled i (in mesh smoothing by contour filtering).

Experimental setup

L_{mH}	Inductance given in mH.

Numerical implementation

$c_{\mathrm{eq},i}$	Definition of the equality constraint i.
$c_{\mathrm{ineq},i}$	Definition of the inequality constraint i.
n_{eq}	Number of equality constraints.
n_{ineq}	Number of inequality constraints.
μ_{IPOPT}	Logarithmic barrier parameter (*homotopy parameter*).

$\boldsymbol{s}_{\text{bound}}$	Set of slack variables for bound constraints in IPOPT.
$s_{\text{bound},i}$	Slack variable for the bound constraint i in IPOPT.
$c_{\text{bound},i}$	Definition of the bound constraint i.
$\Delta\alpha$	Design variable step.
$\delta_{\text{eq,i}}$	Small bound for the definition of the equality constraints converted to inequality constraints.
$\beta_{\text{flip limit}}$	Factor that limits the *number of flips/jumps* of α from one discrete value to another.
$\varepsilon_{\text{relax}}$	Constraint relaxation parameter.
$c_{\text{ref},i}$	Reference value for constraint i.
n_{elements}	Number of elements in the mesh.
n_{nodes}	Number of nodes/vertices in the mesh.
V_{element}	Volume of each element of the mesh.
V_{average}	Average element volume for the design variable interpolation.
$V_{\substack{\text{neighbor elements} \\ \text{of the node}}}$	Summed volume of the neighbor elements touching a node/vertex in the mesh.
A_{element}	Area of each element of the mesh.
$A_{\substack{\text{neighbor elements} \\ \text{of the node}}}$	Summed area of the neighbor elements touching a node/vertex in the mesh.
w_{L^2}	Test function for $\frac{dJ}{d\alpha}\big\vert_{L^2}$.
$\frac{dJ}{d\alpha}\big\vert_{L^2}$	Sensitivity computed through the L^2 inner product.
$\frac{dJ}{d\alpha}\big\vert_{\text{corrected}}$	Corrected sensitivity.
$\varepsilon_{\text{axis}}$	Small value for numerical adjustment for $r = 0$.
$\varepsilon_{\text{adjustment}}$	Sufficiently small value not recognized as zero by FEniCS.

`DOLFIN_EPS`	Smallest representable number in FEniCS.
Δp_{comp}	Compensated variation of (static) pressure.
Δp_{sim}	Variation of (static) pressure from the simulation.
R_{tube}	Internal radius of the tubes used in the experiments.
$\Delta h_{\mathrm{probes}}$	Variation of height between the pressure measurement probes.

Numerical results

L	Characteristic dimension in Section 5.1.1.
H, R, h_1, h_2, r_{zone}, e_{out}, R_{int}, R_{ext}, h_1, h'_1, h_2, h'_2, h_3, h'_3, h_4, h'_4, r_o, h_o, r_1, h, b, y_{rotor}, x_{rotor}, θ_1, $\Delta\theta$, β	Design/computational domain dimensions (in the context of specifying the dimensions of each design domain).
h	Height (except when noted otherwise, such as when representing a dimension from a design domain (Section 5.1.6)).
h_{in}	Height of the inlet.
h_{out}	Height of the outlet.

Domains, boundaries, operators and definitions

$\mathcal{O}(a)$	Order of magnitude (i.e., in the *big O notation*) of the variable a.
δ_{BL}	Thickness of the boundary layer.
Π	Computational domain in a generic model.
Γ_{Π}	Boundary of the computational domain in a generic model.
Ω	Computational domain in 2D / 2D swirl flow model.
Γ	Boundary of the computational domain in 2D / 2D swirl flow model.
Π_α	Design domain in a generic model.
Γ_{Π_α}	Boundary of the design domain in a generic model.
Ω_α	Design domain in 2D / 2D swirl flow model.

Γ_α	Boundary of the design domain in 2D / 2D swirl flow model.
$\Gamma_{\Pi,\mathrm{in}}$	Inlet boundary of the computational domain in a generic model.
$\Gamma_{\Pi,\mathrm{out}}$	Outlet boundary of the computational domain in a generic model.
$\Gamma_{\Pi,\mathrm{disks/shaft}}$	Disks/shaft boundary of the computational domain in a generic model.
$\Gamma_{\Pi,\mathrm{wall}}$	Wall boundary of the computational domain in a generic model.
$\Gamma_{\Pi,\mathrm{sym}}$	Symmetry axis boundary of the computational domain in a generic model (valid for the 2D swirl flow model).
Γ_{in}	Inlet boundary of the design domain in 2D / 2D swirl flow model.
Γ_{out}	Outlet boundary of the design domain in 2D / 2D swirl flow model.
$\Gamma_{\mathrm{disks/shaft}}$	Disks/shaft boundary of the design domain in 2D swirl flow model.
Γ_{wall}	Wall boundary of the design domain in 2D / 2D swirl flow model.
Γ_{sym}	Symmetry axis boundary of the design domain in 2D swirl flow model.
a_s	Example scalar field.
$\overline{()}$	Average value weighted by the length.
$\widetilde{()}$	Average value weighted by the volumetric flow rate.
$\left\|\left\|()\right\|\right\|_1$	One-norm (ℓ_1 norm).
$\bullet$	Inner product.
$\wedge$	Cross product.
$\frac{d()}{dt}$	(Total) derivative.
$\frac{\partial()}{\partial t}$	Partial derivative.
$\nabla(), \mathtt{grad}$	Gradient operator.
$\nabla\bullet(), \mathtt{div}$	Divergent operator.

$\nabla\wedge(), \texttt{curl}$	Curl operator.
$\frac{D()}{Dt} = \frac{\partial()}{\partial t} + \boldsymbol{v} \bullet \nabla()$	Material derivative in the relative reference frame.
$\frac{\partial()}{\partial \boldsymbol{n}} = (\nabla() \bullet \boldsymbol{n})\boldsymbol{n}$	Gradient normal to boundary.

CONTENTS

1	**INTRODUCTION**	**54**
1.1	REVIEW OF THE STATE OF THE ART	54
1.1.1	**Ventricular assist devices**	55
1.1.1.1	Operation of VADs	58
1.1.1.2	Common operating conditions of VADs	59
1.1.1.3	Blood damage in VADs	60
1.1.1.4	CFD analysis and optimization in VADs	62
1.1.2	**2D swirl flow devices**	65
1.1.2.1	Tesla pump	66
1.1.3	**Tesla pump as a VAD**	72
1.1.4	**Casing/volute design**	77
1.1.5	**Optimization methods**	81
1.1.6	**Fluid flow topology optimization**	82
1.1.7	**Summary of the state of the art**	86
1.2	MOTIVATION	87
1.3	OBJECTIVES	87
1.4	SCIENTIFIC CONTRIBUTION	88
1.5	OUTLINE OF THE THESIS	89
2	**THEORETICAL FOUNDATION**	**91**
2.1	FORMULATION AND MODELING FOR FLUID FLOW	91
2.1.1	**Equilibrium equations (laminar flow)**	92
2.1.2	**Non-Newtonian fluid modeling**	94
2.1.2.1	Modeling of blood flow	96
2.1.3	**Turbulence modeling**	100
2.1.3.1	Spalart-Allmaras turbulence model	102
2.1.3.2	Wray-Agarwal turbulence model	103
2.1.4	**Boundary conditions**	106
2.1.4.1	Boundary conditions for the velocity-pressure formulation	106
2.1.4.2	Additional boundary conditions for the turbulence model	110
2.1.5	**Boundary value problem**	111

2.2 FINITE ELEMENT METHOD . . . 112
2.2.1 **Weak formulation** . . . 112
2.2.2 **Finite element modeling** . . . 114
2.3 PERFORMANCE AND CHARACTERIZATION QUANTITIES . . . 117
2.3.1 **Energy dissipation** . . . 118
2.3.2 **Fluid power** . . . 120
2.3.3 **Vorticity** . . . 120
2.3.4 **Pressure head** . . . 122
2.3.5 **Isentropic efficiency** . . . 123
2.3.6 **Pressure coefficients** . . . 123
2.3.7 **Static pressure rise** . . . 124
2.3.8 **Specific dimensionless characterization parameters** . . . 125
2.4 BLOOD DAMAGE MODELING . . . 126
2.4.1 **Hemolysis modeling** . . . 128
2.4.1.1 Numerical prediction of the hemolysis index . . . 130
2.4.1.1.1 *Asymptotically consistent damage index model* . . . 133
2.4.1.1.2 *Simplified analysis for the asymptotically consistent damage index model* . . . 135
2.4.2 **Thrombosis modeling** . . . 137
2.4.2.1 Numerical prediction of the PAS index . . . 138
2.4.2.1.1 *Mechanical dose shear-induced PAS model* . . . 139
2.5 FORMULATION OF THE TOPOLOGY OPTIMIZATION PROBLEM . 144
2.5.1 **Material model** . . . 145
2.5.1.1 Brinkman model . . . 145
2.5.1.2 Extended material model for the 2D swirl flow model . . . 147
2.5.1.3 Brinkman-Forchheimer model . . . 148
2.5.1.4 Material model for the non-Newtonian viscosity . . . 150
2.5.1.5 Material model for the PAS index . . . 152
2.5.1.6 Material model for the wall distance . . . 152
2.5.2 **Measure of non-discreteness** . . . 153
2.5.3 **Topology optimization problem** . . . 153
2.5.4 **Multi-objective function** . . . 154
2.5.4.1 Initial weight multi-objective function . . . 156
2.5.4.2 Logarithmic multi-objective function . . . 156

2.5.5 **Sensitivity analysis of the multi-objective function** 157
2.5.6 **Pattern repetition** 159
2.5.7 **Regularization** 160
2.5.7.1 Helmholtz pseudo-density filter 161
2.5.8 **Post-processing of the optimized topologies** 164
2.5.8.1 Thresholding 164
2.5.8.2 Mesh smoothing 166
2.5.8.2.1 *Mesh smoothing by generation of contours* 169
2.5.8.2.2 *Mesh smoothing by point cloud* 172

3 NUMERICAL IMPLEMENTATION 176
3.1 IMPLEMENTATION OF THE FINITE ELEMENT AND TOPOLOGY OPTIMIZATION METHODS 177
3.1.1 **Optimization algorithms** 181
3.1.1.1 IPOPT algorithm 182
3.1.1.2 TOBS algorithm 183
3.1.2 **Implementation of the adjoint model** 186
3.2 NUMERICAL CONSIDERATIONS 188
3.3 INTERFACING FEniCS WITH OpenFOAM® FOR THE EVALUATION OF TURBULENCE AND HIGH-SPEED FLOWS 194
3.3.1 **Implementation of the computation of sensitivities while interfacing with OpenFOAM®** 197
3.3.2 **Correspondence of boundary conditions in FEniCS and OpenFOAM®** 200
3.4 IMPLEMENTATION OF CYCLIC BOUNDARY CONDITIONS 202
3.5 IMPLEMENTATION OF THE 3D PUMP SIMULATIONS 203
3.5.1 **Relation to experimental measurements** 206

4 EXPERIMENTAL SETUP 207
4.1 GENERAL DESIGN CONSIDERATIONS 207
4.1.1 **Driving system** 207
4.1.2 **Bearings** 208
4.1.3 **Leakage** 209

4.1.3.1 Seal . . . 213
4.1.4 **Inlet channels** . . . 216
4.1.5 **Disk spacers** . . . 217
4.1.6 **Stagnated fluid below the rotor** . . . 218
4.1.7 **Clearances above and below the rotor** . . . 220
4.2 FABRICATION OF THE PROTOTYPE . . . 221
4.3 EXPERIMENTAL APPARATUS . . . 223
4.4 BLOOD ANALOGUE . . . 226

5 RESULTS AND ANALYSES . . . 228
5.1 NUMERICAL RESULTS . . . 228
5.1.1 **Newtonian 2D swirl flow design** . . . 232
5.1.1.1 Nozzle . . . 233
5.1.1.2 Hydrocyclone-type device . . . 237
5.1.2 **Newtonian Tesla pump design** . . . 242
5.1.2.1 Horizontal inlet Tesla pump . . . 243
5.1.2.2 Vertical inlet Tesla pump . . . 248
5.1.2.2.1 *Optimizing for relative energy dissipation* . . . 249
5.1.2.2.2 *Effect of rotation / flow rate* . . . 254
5.1.2.2.3 *Optimizing for vorticity* . . . 257
5.1.2.2.4 *Optimizing for vorticity and relative energy dissipation* . . . 260
5.1.2.3 Comparing performance with straight disks . . . 262
5.1.3 **Non-Newtonian 2D swirl flow design** . . . 266
5.1.3.1 Two-outlet channel . . . 266
5.1.4 **Tesla blood pump design considering hemolysis** . . . 273
5.1.4.1 Design domain and mesh . . . 273
5.1.4.2 Topology optimization results . . . 274
5.1.4.3 Simulation of the optimized result for w_H = 0.5, 1 L/min and 1500 rpm . . . 281
5.1.5 **Tesla blood pump design considering thrombosis** . . . 284
5.1.5.1 Design domain and mesh . . . 284
5.1.5.2 Topology optimization results . . . 285
5.1.5.3 Simulations of optimized results . . . 288
5.1.6 **Volute design considering blood damage** . . . 291

5.1.6.1 Design domain and mesh . . . 292
5.1.6.2 Topology optimization results . . . 296
5.1.6.3 Simulation of the optimized result for $w_\Phi = 1$ . . . 300
5.1.7 **Bladed pump design considering blood damage** . . . 302
5.1.7.1 *Side*-type design . . . 304
5.1.7.1.1 *Design domain and mesh* . . . 304
5.1.7.1.2 *Topology optimization results* . . . 307
5.1.7.1.3 *Simulation of the optimized result for* $w_{PAS} = 0.85$ . . . 311
5.1.7.2 *Full-inlet*-type design . . . 313
5.1.7.2.1 *Design domain and mesh* . . . 313
5.1.7.2.2 *Topology optimization results* . . . 315
5.1.7.2.3 *Simulation of the optimized result for* $\beta = 20°$ *considering blood damage* . . . 318
5.1.8 **Turbulent 2D swirl flow design (WA2018 model)** . . . 321
5.1.8.1 Rotating nozzle . . . 322
5.1.8.2 Hydrocyclone-type device . . . 328
5.1.8.3 Tesla-type pump device . . . 332
5.1.9 **Tesla VAD design considering rotor and volute** . . . 336
5.1.9.1 Prototype designs . . . 337
5.1.9.2 Simulations of the designed prototypes . . . 338
5.2 EXPERIMENTAL RESULTS . . . 346
5.2.1 **Comparison of the experiments with simulations for blood and a blood analogue** . . . 348
5.2.2 **Comparison of the experiments with simulations for the different types of rotor** . . . 348

6 CONCLUSIONS AND FUTURE WORK . . . 351
6.1 FUTURE WORK . . . 353

REFERENCES . . . 356

APPENDIX A – VERIFICATION OF THE SIMULATION IMPLEMENTED IN FEniCS . . . 404

APPENDIX B – MESH SMOOTHING BY CONTOUR FILTERING . 407

APPENDIX C – COMPUTATION OF FLUID FLOW VELOCITY PROFILES 410

APPENDIX D – RELATIVE REFERENCE FRAME IN THE 2D SWIRL FLOW MODEL 412

APPENDIX E – OTHER NUMERICAL RESULTS FOR THROMBOSIS 413

APPENDIX F – ADJUSTMENT FOR COMPARING WITH THE EXPERIMENTAL RESULTS 426

APPENDIX G – TECHNICAL DRAWINGS 428

1 INTRODUCTION

There is currently a high demand for heart transplants, which is not satisfied (COLVIN-ADAMS *et al.*, 2015; ABTO, 2015, 2016, 2017, 2018). This lack of heart transplants is mainly worked around by the use of small-scale blood pumps, which are the main part of Ventricular Assist Devices (VADs). From the various possibilities of VAD designs, the Tesla pump is able to reduce blood damage in relation to bladed pumps. The operation of a Tesla pump is based on viscous friction rather than in the variation of linear momentum (bladed pumps). The potential reduction of blood damage makes the Tesla pump an interesting possibility for optimization – in particular, for topology optimization. Moreso, a Tesla pump is part of a more generic class of fluid flow devices, called *2D swirl flow devices*. Therefore, in order to optimize a Tesla VAD, a novel formulation for topology optimization needs to be developed, based on 2D swirl flow, novel material models, and blood damage models. In this chapter, the review of the state of the art of VADs, 2D swirl flow devices, Tesla pump, volute and fluid topology optimization is presented. Then, the motivation, objectives and scientific contribution are outlined.

1.1 REVIEW OF THE STATE OF THE ART

Around the world, it is estimated that CVDs (CardioVascular Diseases) resulted in about 31% of all global deaths in 2016, which corresponds to about 17.9 million people (W.H.O., 2017). A similar ratio is also observed in Brazil during the same year (28.5% of all deaths in Brazil – 362,091 deaths) (SBC, 2020; IBGE, 2016), and has been approximately the same throughout the previous years (LIMA *et al.*, 2013). Studies also point that Heart Failure (HF) is one of the main causes of hospitalization (BOCCHI, 2013). Particularly in the U.S., studies say that the number of individuals with HF should increase 46% by 2030 (MARTONIK, 2017). CVDs and HFs are closely related to cardiac insufficiency, in which the heart is unable to maintain the required blood flow to the rest of the body. These are cases in which the patient may require heart transplantation. However, the number of hearts available for transplantation is not enough to account for the whole demand (COLVIN-ADAMS *et al.*, 2015). Particularly in Brazil, in 2018, only 21.25% of the annual demand of heart transplants was satisfied (380 heart transplants)

(ABTO, 2018), and this ratio is approximately the same in the previous years (ABTO, 2015, 2016, 2017, 2018). Therefore, there is a high demand for heart transplants which is not currently satisfied (COLVIN-ADAMS *et al.*, 2015; ABTO, 2015, 2016, 2017, 2018), and it should increase even more, due to the expected increase in HF in the next years (MARTONIK, 2017).

With the aim of working around this situation, cardiac assist devices – artificial hearts (TAHs, Total Artificial Hearts) and VADs (Ventricular Assist Devices) – are being increasingly used to aid failing hearts and to alleviate suffering (BEHBAHANI *et al.*, 2009). In this work, the use of VADs is detailed.

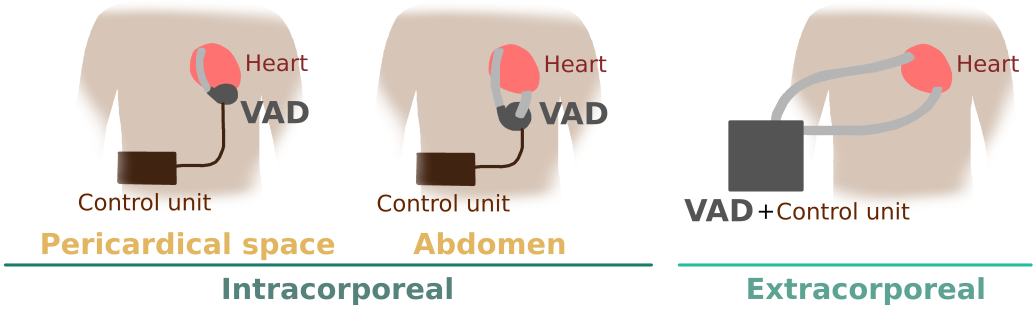
1.1.1 **Ventricular assist devices**

VADs (Ventricular Assist Devices) are devices that substitute or temporarily assist the heart and blood circulation of patients with weakened hearts (NIST, 2016), such as from cardiovascular diseases or from recovery from surgery/transplant. The main part of these devices is a small-scale blood pump, which reduces the work load over the heart while maintaining an adequate blood pressure (NOSÉ *et al.*, 2000). Initially, the use of VADs was considered to be temporary (BTT, Bridge To Therapy) (MILLER *et al.*, 2007; SLAUGHTER *et al.*, 2013), but it has already been extended as permanent (*long-term*) clinical solutions (BTD, Bridge To Destination) (BEHBAHANI *et al.*, 2009; NONAKA *et al.*, 2001; ANDRADE *et al.*, 2005), such as in cases of patients with Congestive Heart Failure (CHF) or valvular disease (SHERIFF *et al.*, 2013). It is expected that this extended use significantly grows in 2017-2025 (ACUTE MARKET REPORTS, 2017).

There are 3 types of VADs (BEHBAHANI *et al.*, 2009): that can assist both ventricles (BiVAD) or only one – left (LVAD) or right (RVAD). It can also be mentioned that paired VADs (one VAD for each ventricle) have also been used to substitute the entire heart (BEHBAHANI *et al.*, 2009). VADs can be implanted internally in the abdomen (such as HeartMate II®), internally in the pericardial space (such as Medtronic/HeartWare HVAD®) or even extracorporeally (such as CentriMag) (BEHBAHANI *et al.*, 2009) (see Fig. 1.1). The VAD is connected to the heart ventricle and the corresponding aorta through tubes and is managed by a control unit that supplies energy for the blood pump operate. According to Patlolla *et al.* (2009), the survival rate for intracorporeal VADs is

higher when compared to extracorporeal VADs.

Figure 1.1 – Types of VAD implantation.



Source: Author.

The first blood pump was developed in 1934 by Michael DeBakey for transfusion (ANDRADE *et al.*, 2005), but the first successful implantation of a VAD only happened in 1966 (DEBAKEY, 2000). From there, efforts have been taken in order to improve the efficiency of heart pumps and to reduce their size. According to Behbahani *et al.* (2009), since 1990, new technologies increased the efficiency of VADs, and companies started developing VADs. Particularly, studies show increasing efficiencies in commercial VADs (AARONSON *et al.*, 2012), being able to reach survival rates comparable to heart transplantation. Although VADs have saved or extended the lives of patients with heart diseases (FRASER *et al.*, 2011; LAHPOR, 2009), there are risks inherent to the use of VADs, which vary depending on the device, and are due to the unphysiological conditions that are induced in the circulatory system, possibly leading to complications such as inflammation, infection, thromboembolism, thrombosis, heart attacks, impairments of kidney and liver functions etc. (FRASER *et al.*, 2011). The technological improvements in VADs throughout the years have been helping to reduce these negative effects. There are essentially three generations of VADs (OLSEN, 1999; OLSEN, 2000; BEHBAHANI *et al.*, 2009): the first, which consists of pulsatile (positive-displacement) pumps; the second, which consists of rotary pumps of continuous and nonpulsatile flow with contact bearings and/or seals; and the third, which is equal to the second, but with magnetic suspension bearings, which increase the durability and reduce the hemolysis level.

According to Allen *et al.* (1997) and Ündar (2004), there is better compatibility of the human body towards pulsatile flow, while nonpulsatile flow can cause alterations in biochemical functions, such as in maintaining homeostasis, and organ specific blood flow, such as in kidneys. Further aspects have been analyzed by Siess and Reul

(2000). However, in terms of bioengineering, the engineering complexity of pulsatile flow devices is higher, because there is significant stress over the constantly moving flexible diaphragm (ALLEN *et al.*, 1997), which demands more energy and may degenerate the blood contacting surface, causing thrombosis, calcification, decrease in compliance, and even failure of the device. Nonpulsatile flow devices consist of only one rigid moving part in order to operate as a complete circulatory system (HORNE *et al.*, 2015) and do not need flexible components, valves and seams (ALLEN *et al.*, 1997). Therefore, their durability and reliability are superior and they are more compact (smaller) than pulsatile flow devices (ALLEN *et al.*, 1997; CHENG *et al.*, 2014). Horne *et al.* (2015) also highlights the ease of implant and transportability of nonpulsatile flow devices. For Uni-Ventricular Hearts (UVHs), which are the result of congenital cardiac malformations that lead to a single (or almost a single) ventricular chamber to be functional (KHAIRY *et al.*, 2007), nonpulsatile flow devices have been shown to be superior than pulsatile flow devices (HORNE *et al.*, 2015): one argument is that the systemic venous flow is continuous to the lungs, making nonpulsatile flow devices more adequate for this application. In the case of using a VAD, the weakened heart is still present in the circulation and pumping, which means that there is pulsatility inherently coming from it. Thus, a nonpulsatile VAD would act so as to increase the continuous flow component, admist the pulsatile component that is generated by the native heart (SHU *et al.*, 2009). This residual pulsatility should induce flow separation (destabilization) during deceleration/diastole within the outlet diffuser, due to the inertial effect, and restabilization of the flow during acceleration/systole (SHU *et al.*, 2009). Also, even when the VAD is nonpulsatile, the residual pulsatility leads to hysteresis, creating a closed loop in the pump curve (SONG *et al.*, 2004c; SONG *et al.*, 2004b) – pressure head (H) $\times$ flow rate (Q) curve. This means that the flow inside VADs is intrinsically transient. However, since transient analyses demand higher computational costs, they are much less studied than steady state analyses in VADs (FRASER *et al.*, 2011). Another complication is the inlet velocity profile, which should depend on the interaction of the VAD with the native heart and aorta (FRASER *et al.*, 2011). Since the flow in nonpulsatile VADs is usually modeled as steady state, the optimization is also usually performed in steady state (FRASER *et al.*, 2011).

1.1.1.1 Operation of VADs

There are essentially three types of rotary blood pumps (REUL; AKDIS, 2000): radial/centrifugal (fluid flow direction predominantly radial), axial (fluid flow direction predominantly axial) and diagonal (mixed fluid flow direction). According to Behbahani *et al.* (2009), centrifugal pumps can produce higher pressures at lower rotational speeds, whereas axial pumps demand higher speeds to build up the pressure for the required flow rate. The main advantages of axial pumps is that they are smaller and require less power to operate (BEHBAHANI *et al.*, 2009). However, since higher speeds may lead to higher shear stresses, the probability of blood damage should be smaller for centrifugal pumps. Diagonal pumps tend to have the advantages of centrifugal and axial pumps, such as producing higher pressures (centrifugal pump) and higher flow rates (axial pump) (REUL; AKDIS, 2000). Various types of pumps have been studied and applied to VADs. Fig. 1.2 shows some blood pump models that have been used and/or developed: rotary diagonal (Spiral Pump® , VentrAssist®), rotary centrifugal (Gyro® C1E3, HeartMate III® , CorAide® , DuraHeart®), rotary axial (Hemopump® , Jarvik 2000® , DeBakey/NASA® , HeartMate II®), and pulsatile (HeartMate® , DAV-InCor, Jarvik-7® TAH, AbioCor®) (ANDRADE *et al.*, 2005).

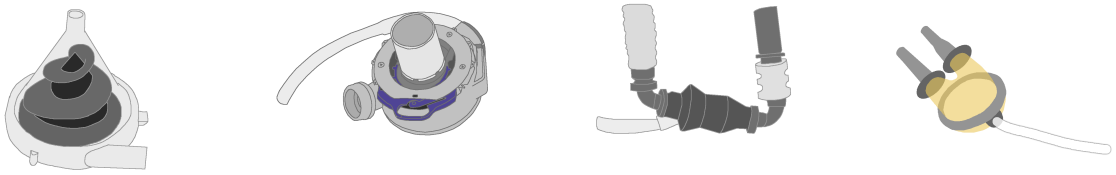
Figure 1.2 – Some blood pump models for VADs.

(a) Rotary diagonal blood pump (Spiral Pump®).

(b) Rotary centrifugal pump (HeartMate III®).

(c) Rotary axial pump (HeartMate II®).

(d) Pulsatile pump (DAV-InCor).



Source: Author (based on (a) Dinkhuysen *et al.* (2007), (b) Abbott (2018), (c) Thoratec (2018), (d) InCor (2018)).

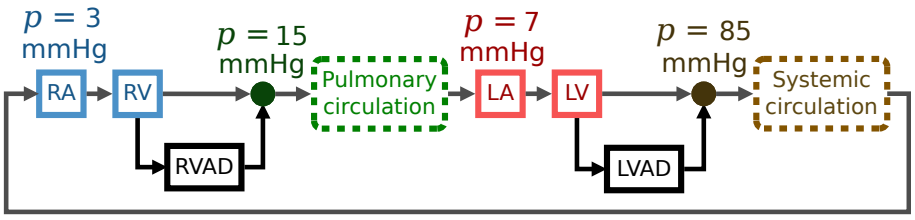
According to Martonik (2017), there are 4 key parameters (called “4P”) that should be monitored during the operation of a VAD: Pump flow (flow rate in L/min), Pump speed (rotation in rpm), Pulse index (dimensionless parameter given by the difference between the peak systolic blood flow rate and the minimum diastolic blood flow rate, divided by the mean flow rate during a cardiac cycle (BARIĆ, 2014)) and

Power (power consumption in W). The pump speed and power are the consequences of the required pump flow and pulse index.

1.1.1.2 Common operating conditions of VADs

The operating conditions are based on the pressure head and the flow rate, which would represent the necessary pumping capacity of blood in the human body. The pressure head would be closely related to the variation of total (*stagnation*) pressure, but the static part (static pressure) may also be used for characterization. The static pressure is the one that is normally measured in blood flow devices, since measuring the total pressure would require the use of an intrusive device, in order to probe the flowing blood, such as a Pitot tube. The pressures and flow rates required for a VAD would correspond to values that are similar to those required by a human heart. The flow rate would correspond to the cardiac output of the human heart (SALVI, 2012), that is approximately 5 L/min (STERN *et al.*, 2001; LEVINE *et al.*, 2014), but may also increase to 20∼30 L/min during extreme exercise (STERN *et al.*, 2001). Since the human heart normally operates at about 85 bpm (beats/min) (i.e., 706 ms/beat) (STERN *et al.*, 2001), the blood pressure varies according to the cardiac contraction (diastole-systole), which is typically 120/80 mmHg (STERN *et al.*, 2001). In the case of nonpulsatile devices, the blood pressure to be considered is a mean value. Some mean values are shown in Fig. 1.3. According to Martonik (2017) and Chmielinski and Koons (2017), the mean pressure in arteries (MAP, Mean Arterial Pressure) should be between 60 mmHg (8 kPa) and 90 mmHg (12 kPa) in order to maintain sufficient pump flow. Therefore, some reference values for the necessary pumping capacity of VADs, also considering some commercial VAD values for reference, are approximately: about 15 mmHg (2 kPa) for RVAD application, and about 75 mmHg (10 kPa) for LVAD application. In the case of LVADs for pediatric use, Throckmorton *et al.* (2003) consider 2∼5 L/min and 70∼95 mmHg for 2 to 12 years old; and Throckmorton *et al.* (2004) consider 0.5∼3 L/min and 50∼95 mmHg for 1 to 10 years old.

Figure 1.3 – Typical blood (static) pressure values in the human body. The LVAD and RVAD positions are also illustrated (a BiVAD would correspond to both LVAD and RVAD positions) (BONOW *et al.*, 2012; GREYSON, 2010). ("RA" stands for Right Atrium, "RV" stands for Right Ventriculum, "LA" stands for Left Atrium, "LV" stands for Left Ventriculum).



Source: Author.

The size is an important factor if the device is aimed for intracorporeal implantation (such as HeartMate III®, HeartMate II® and DAV-InCor (see Fig. 1.2)), but is not an issue if the device is extracorporeal (such as Spiral Pump®, CentriFlux BR-100 and Rotaflow (see Figs. 1.2 and 1.15)).

The materials used for fabricating the device should be biocompatible (WAGNER *et al.*, 2000; SIN *et al.*, 2009), since they would be in contact with blood flow, and, if the implantation is intracorporeal, they would be in contact with other human body tissues. This can normally be achieved through the use of biomaterials or as a special surface that induces the formation of a *blood* biosurface (such as in HeartMate III®).

Therefore, the approximated typical operating conditions for a VAD are summarized in Table 1.1, showing approximated values and ranges for the flow rate and pressure rise in the VAD.

Table 1.1 – Approximated typical operating conditions for a VAD.

Approximated operating conditions	
Flow rate	0.5∼5 L/min
Static pressure rise (LVAD application)	≈ 75 mmHg (10 kPa)
Static pressure rise (RVAD application)	≈ 15 mmHg (2 kPa)

1.1.1.3 Blood damage in VADs

According to Behbahani *et al.* (2009), a blood pump for VADs should operate in a large range of flow rates and pressure heads (i.e., the performance should be suitable and vary minimally with the operating condition) (FRASER *et al.*, 2011), minimize blood damage (i.e., have a good hematological compatibility) and should be sufficiently small for easy implantation in children and adults. Typical isentropic efficiencies for blood pumps are in the range of 20∼30% (FRASER *et al.*, 2011). Blood damage that occurs

in blood pumps consists of hemolysis and thrombosis (BEHBAHANI *et al.*, 2009), which are nowadays the main limiters of the usage time of VADs (SASTRY *et al.*, 2006).

Hemolysis is the premature damage of Red Blood Cells (RBCs), in which the membranes of the RBCs suffer lysis (*breakdown*), releasing their hemoglobin content into the plasma. Also, an excess of hemoglobin being free in the plasma is considered to be toxic and may lead to renal failure (GARON; FARINAS, 2004; DEUEL *et al.*, 2016; GRAW *et al.*, 2022). The main causes of hemolysis are high shear stresses and the exposure times to these stress levels (i.e., even if the shear stress is high, if the exposure time is a few milliseconds, the resulting hemolysis should be minimum) (BEHBAHANI *et al.*, 2009; GHATTAS *et al.*, 1995; GARON; FARINAS, 2004). Contributions from other effects such as osmosis, chemical and thermal processes can be neglected (APEL *et al.*, 2001). In VADs, the stress conditions may happen due to the mechanical interaction of the blood flow with the device (GARON; FARINAS, 2004). According to Behbahani *et al.* (2009), although modern atraumatic designs can avoid RBC lysis, even minor hemolysis can raise the hemoglobin level of the blood, deteriorating the patient's condition and possibly leading to kidney dysfunction and multiple organ failure. In normal conditions, the characteristic shear stresses in a human vein/artery are in the range of 0.1$\sim$20 Pa (LEE *et al.*, 2004). However, blood pumps normally induce shear stresses in the range of 1$\sim$1000 Pa (LEE *et al.*, 2004), which may mean a higher risk of hemolysis. According to Behbahani *et al.* (2009), the total characteristic time of an RBC inside a VAD is in the order of 500 ms.

Thrombosis is the formation of blood clotting (*thrombus*), by aggregating platelets and RBCs in vessels (PACKHAM, 1994), and is normally initiated by the body in order to prevent bleeding, but may be caused by abnormal conditions in the blood circulation, obstructing healthy vessels. The three main factors that lead to clotting, also called *Virchow's triad*, are, as initially defined: flow (alterations in the blood flow), surface (abnormalities of the vascular wall), and blood (alterations in the constitution of blood) (BEHBAHANI *et al.*, 2009; BAGOT; ARYA, 2008). This way, thrombosis can be caused by high shear stresses, recirculation/stagnation, and blood contacting surfaces with low hemocompatibility (BEHBAHANI *et al.*, 2009; DING *et al.*, 2015). If blood clotting is formed on the surface of a VAD, it can compromise its function and, if it detaches itself from the surface it was formed, it may negatively affect the blood vessels of the whole body. According to Behbahani *et al.* (2009), thrombosis is one of the primary causes of

death for patients with VADs.

Kusters *et al.* (2017) analyzed the effect of pump heating (0.5℃) in hemolysis, showing that, for this case, no relationship between them can be perceived. This finding can be seen in relation to a maximum temperature rise from the normal human body temperature, that is around 37℃ (BOMMADEVARA; ZHU, 2002). According to Poder *et al.* (2015), at temperatures lower than 43$\sim$46℃, hemolysis caused by blood heating seems to be negligible. This would mean that the temperature should not increase more than 6$\sim$9℃ for the safe operation of a blood pump. The temperature rise may also be caused by parts other than the rotor, such as by the volute, contact bearings and shaft seal (GANUSHCHAK *et al.*, 2006). Blood heating and damage are closely related to the efficiency of the pump (TAKAMI *et al.*, 1997), which would mean that a higher efficiency should be able to reduce pump heating.

According to Behbahani *et al.* (2009), blood has various non-Newtonian fluid properties due to its heterogeneous composition (plasma, red blood cells, white blood cells and platelets): shear-thinning (*pseudoplasticity*, viscosity decreasing when under shear stress, due to the orientation and disaggregation of red blood cells), viscoelasticity (viscous and elastic behaviors when under deformation), and thixotropy (viscosity decreasing through time). Due to the high shear rates that can be found in blood pumps, the blood viscosity has been normally assumed as constant (Newtonian fluid) (FRASER *et al.*, 2011). However, according to heart pump simulations performed by Al-Azawy *et al.* (2017), the non-Newtonian characteristics of blood should induce larger recirculation regions and smaller thrombosis than an equivalent Newtonian fluid. Moreover, the predicted levels of shear stresses on the walls should not vary significantly (AL-AZAWY *et al.*, 2017). Since the compressibility of blood is small, according to Hinghofer-Szalkay and Greenleaf (1987), blood may be assumed as incompressible, with a density (ρ) of 1056 kg/m^3.

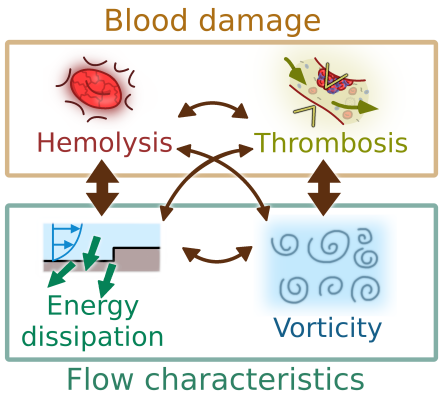
1.1.1.4 CFD analysis and optimization in VADs

According to Behbahani *et al.* (2009), the use of CFD (Computational Fluid Dynamics) in the field of heart pump development started in the 1990s, and is nowadays used for the design of medical devices that involve blood flow, such as blood pumps (WIEGMANN *et al.*, 2018), oxygenators (WU *et al.*, 2013), and artificial heart

valves (YOGANATHAN *et al.*, 2005). Also, CFD provides information to predict hydraulic efficiency, flow patterns, hemolysis, stagnation zones, local shear stress levels and exposure times of RBCs to shear stresses (BEHBAHANI *et al.*, 2009; FRASER *et al.*, 2011; YU, 2015; WIEGMANN *et al.*, 2018; SONG *et al.*, 2003). Through comparative studies, it was reported that blood damage predicted by CFD shows good agreement with experimental hemolysis (SONG *et al.*, 2004d; SONG *et al.*, 2004a; MITOH *et al.*, 2003; TASKIN *et al.*, 2012).

The applicability of optimization to design blood pumps using CFD has been first outlined by Antaki *et al.* (1995), who applied shape optimization for some non-pump cases. Some major challenges for the design were outlined as: (1) the development of more accurate models for modeling the governing physics of blood flow; (2) the development of CFD models for blood-related phenomena; and (3) the development of optimization algorithms capable of changing the shape of the device. Nowadays, the first challenge can be considered in two ways: by modeling each RBC in the fluid flow (higher computational cost), or by modeling an average RBC influence in the fluid flow through non-Newtonian fluid models (lower computational cost) (see Section 2.1.2.1). The second challenge is related to modeling blood damage in CFD, through hemolysis and thrombosis models (see Section 2.4). The third challenge is related to the optimization algorithms (see Section 1.1.5). Antaki *et al.* (1995) considers three objective functions for optimization: shear stress, magnitude of vorticity and viscous energy dissipation. The shear stress is closely related to the main cause of hemolysis (BEHBAHANI *et al.*, 2009). Vorticity indicates recirculation of bubbles in the flow (ANTAKI *et al.*, 1995). Viscous energy dissipation should indicate efficiency and a viscous heating measure (ANTAKI *et al.*, 1995). Energy dissipation and hemolysis have been shown to be related (BLUESTEIN; MOCKROS, 1969; NAKAHARA; YOSHIDA, 1986). In particular, Bluestein and Mockros (1969) fit a straight line between energy dissipation and hemolysis rate in a log-log plot for blood flow under some different conditions and flow rate ranges. Since vorticity may imply flow recirculation (BEHBAHANI *et al.*, 2009), it is related to energy dissipation and thrombosis. Since thrombosis can be caused by high shear stresses (BEHBAHANI *et al.*, 2009), it is related to hemolysis and, therefore, energy dissipation. These relationships can be visualized in Fig. 1.4.

Figure 1.4 – Representation of the relationship between energy dissipation, vorticity, hemolysis and thrombosis.



Source: Author.

According to Fraser *et al.* (2011), depending on the specific device, VADs normally operate between low and transitional Reynolds numbers. Although there has been some development on transitional flow models throughout the years (MENTER *et al.*, 2006; LANGTRY *et al.*, 2006; AUPOIX *et al.*, 2011; FÜRST *et al.*, 2013), since traditional turbulence models have been historically developed and stablished for high Reynolds numbers (i.e., for usual engineering requirements), the modeling of the flow in VADs is normally performed by assuming laminar or fully turbulent flow. The inlets of pumps may feature turbulent flow, with Reynolds numbers of about 6,600∼7,000 (FRASER *et al.*, 2011), which are above the transition Reynolds number in pipes (2,300). However, the interior of the pumps seems to be under laminar flow, with Reynolds numbers of about 77,000∼155,000 (FRASER *et al.*, 2011), which are below the transition Reynolds number in pumps (which is in the order of 10^6) (SABERSKY *et al.*, 1971; WU, 2007). This means that the laminar flow assumption seems to be justifiable (SMITH *et al.*, 2004; ZHANG *et al.*, 2006; ZHANG *et al.*, 2007; CHUA *et al.*, 2007). This assumption has been experimentally tested by Burgreen *et al.* (2004) and Zhang *et al.* (2007), showing a reported error of about 10% in the pressure rise (about 13 mmHg) with respect to the experiments. Turbulence models have also been used for comparison (FRASER *et al.*, 2011) and, depending on the pump and the turbulence model, the error in the pressure rise reduced or increased in relation to experiments. According to Kameneva *et al.* (2004), turbulent flow generates turbulent stresses that exponentially increase hemolysis. Pinotti (2000) related turbulent eddies with mechanical hemolysis, delimiting the size of eddies that interact with RBCs for hemolysis to be dependent/independent

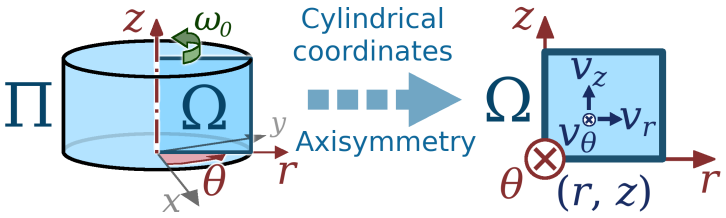
from the exposure time. According to Wu (2007), in general, as the Reynolds number increases, the efficiency should also slowly increase.

1.1.2 **2D swirl flow devices**

The Tesla pump is part of a more generic class of fluid flow devices, being referred to as a *2D swirl flow device*. 2D swirl flow devices are fluid flow devices based on the 2D swirl concept (*2D swirl flow model*). The 2D swirl flow model (*2D axisymmetric flow model with a swirl*) is a specific type of model that assumes a 2D mesh and axisymmetry. This way, the coordinates are cylindrical and there are all three velocity components (see Fig. 1.5). The additional velocity component (v_θ) points towards the outside of the 2D plane, and may be described as the swirl component of the flow. An advantage of the 2D swirl flow model is that using a 2D mesh means that the computational cost towards a 3D model is significantly reduced.

Particularly, the 2D swirl flow model shows good agreement with experiments and 3D simulations (REY, 2004; KO, 2005; SUSAN-RESIGA *et al.*, 2006). However, it may neglect some inlet/outlet geometries, some specific flow oscillations (KO, 2005) and the presence of auxiliary non-axisymmetric structures needed for the mechanical assembly of the fluid flow device, such as spacers/pins needed to separate disks from one to another or needed to attach disks to a shaft, for example.

Figure 1.5 – Representation of the 2D swirl flow model.

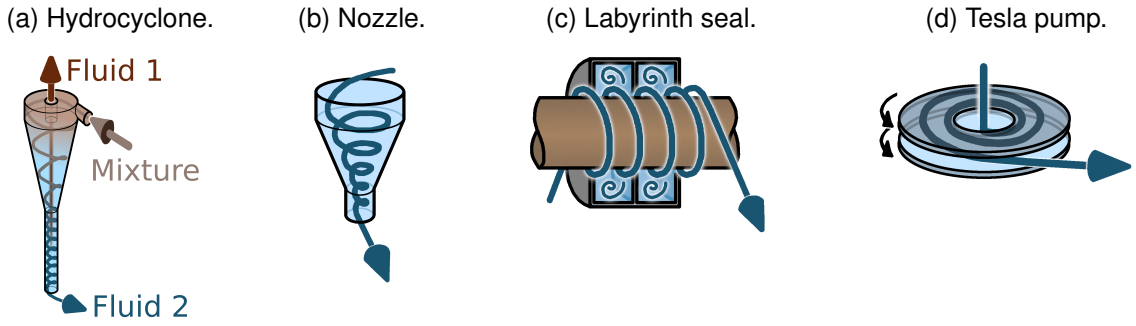


Source: Author.

Some examples of fluid flow devices that can be modeled by the 2D swirl flow model are hydrocyclones (KO, 2005; MOTIN, 2015; PALADINO *et al.*, 2007; OSEI *et al.*, 2016), swirling nozzles/diffusers (AMINI, 2016; HALLGREN *et al.*, 2007; ESLAMIAN *et al.*, 2012), some labyrinth seals (ZHANG *et al.*, 2016b; BELLAOUAR *et al.*, 2013) and some pumps and turbines (TESLA, 1913a; TESLA, 1913b; FORD, 2018) (see Fig. 1.6).

A particularly well-known example, which is one of the aims of this work, is the Tesla pump (TESLA, 1913a; REY, 2004), which is described in the next section.

Figure 1.6 – Some examples of 2D swirl flow devices.



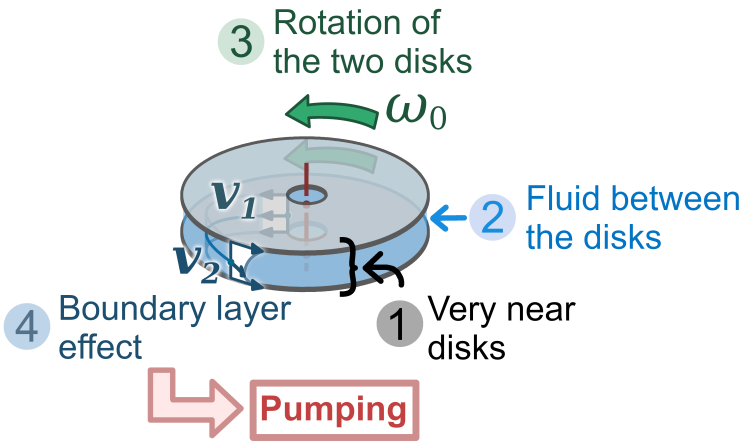
Source: Author.

1.1.2.1 Tesla pump

A Tesla pump is a centrifugal pump without blades (TESLA, 1913a) composed of parallel rotating disks spaced along a shaft (rotor), with the fluid axially entering the rotor and radially leaving it (SASTRY *et al.*, 2006). It is also referred as: *multiple disk centrifugal pump* (MILLER *et al.*, 1990), *boundary layer pump* (GILLIAM, 2012), *bladeless pump* (GRANDE III; DRAPER, 2005), *disc pump* (DISCFLO, 2000), *viscous flow pump* (similarly to Lemma *et al.* (2008)), *friction pump* (LOGAN Jr, 2003), and *shear-force pump* (HASINGER; KEHRT, 1963).

The basic working principle of a Tesla pump is the Tesla principle – also called *Tesla shear principle* or *Tesla effect* by Maloney and Buckberg (1999) – and is closely related to the formation of the boundary layer (viscosity + Coandă effect) and is simplifiedly represented in Fig. 1.7, in which the pumping effect appears due to the imposed rotation over the two near disks with fluid between them. This pumping effect is due to the shear forces that appear from the effect of viscosity on the velocity difference between the fluid and the rotating disk surface, leading to the formation of a spiral movement of fluid. If the rotation (i.e., velocity difference) is increased, the shear force should also increase. Furthermore, if the fluid flow is increased, a drop in pressure head is expected (HASINGER; KEHRT, 1963). More specifically, the type of boundary layer involved in the Tesla principle is sometimes referred as *Ekman layer* (SCHULER *et al.*, 1990).

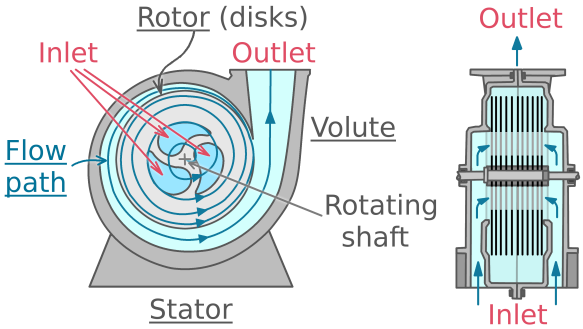
Figure 1.7 – Tesla principle exemplified for a two-disk Tesla pump ($\boldsymbol{v}_1$ and $\boldsymbol{v}_2$ are the velocities of fluid on the inlet and on the outlet, respectively).



Source: Author (based on Breiter and Pohlhausen (1962), Yu (2015) and Lennemann (1974)).

The spiral movement of the fluid inside a Tesla pump is illustrated in Fig. 1.8, which also shows the main components of a Tesla pump.

Figure 1.8 – Spiral movement of fluid inside a Tesla pump and main components, according to the geometry initially proposed by Tesla (1913a).



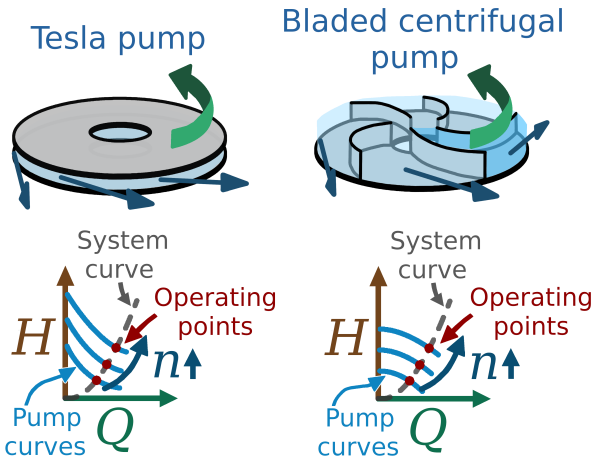
Source: Author (based on Alonso *et al.* (2019)).

In a bladed pump (*bladed centrifugal pump*), the fluid is mainly pumped by the variation of linear momentum on the blades (*lift forces*), leading to a discontinuous slightly pulsatile flow (in batches between each pair of blades). On the other hand, in a Tesla pump, the fluid is mainly pumped by the effect of the viscosity (*Tesla principle*), leading to a comparatively smoother flow (i.e., with a smooth change in linear momentum) and a continuous and nonpulsatile flow. This causes the pump curves to become quite different (see Fig. 1.9), with the Tesla pump featuring an inverse relationship between pressure head (H) and flow rate (Q) (MALONEY; BUCKBERG, 1999; DODSWORTH; GROULX, 2015), while the bladed pump has a slower transition. Therefore, a Tesla pump may need higher rotations or higher sizes in order to operate at the same operating point as

a bladed pump.

Some advantages of the use of a Tesla pump in relation to a bladed pump are (MEDVITZ *et al.*, 2011): smaller turbulent stresses, absent cavitation conditions (since, for bladed pumps, the blades have a pressure difference on both sides, which may generate local vacuum from the movement of the blades and cause cavitation), no blade to blade leakage flow, more uniform forces (since there is no blade force when the flow exits the rotor) and simpler manufacturing and assembly. Also, the effect of vibration in the efficiency is quite small (DODSWORTH; GROULX, 2015). According to Dodsworth (2016), Tesla pumps are less sensitive to vibration-induced cavitation in relation to conventional pumps, and work well with viscous fluids, which is advantageous to cooling applications (DODSWORTH, 2016) and volatile work fluids, such as liquid fuels (DODSWORTH, 2016). According to Hasinger and Kehrt (1963), since there is no flow separation as in bladed pumps, the noise level should be small.

Figure 1.9 – Illustration of the flow in a Tesla pump compared to the flow in a bladed centrifugal pump (H is the pressure head, Q is the flow rate, and n is the rotation of the rotor in rpm).

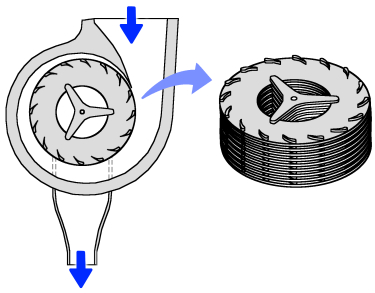


Source: Author.

The Tesla principle can be essentially applied to pumps or turbines, and has a wide range of applications, such as steam and gas (RAJE *et al.*, 2015; TESLA, 1921), fluids with particulates (RAJE *et al.*, 2015), fluids with low and high viscosities (RAJE *et al.*, 2015), compressors (RICE, 1991), energy generation (CAREY, 2010; LAMPART *et al.*, 2009), fans (ENGIN *et al.*, 2009), lab-on-a-chip (HABHAB *et al.*, 2016), air for warming therapy (KHODAK, 2009) etc. The Tesla wind turbine designed by Fuller (2010) is reproduced in Fig. 1.10. For simplicity, any fluid flow device, such as pumps and turbines, that is based on the Tesla principle is referred as *Tesla-type device* in this

work.

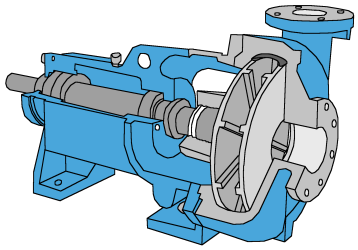
Figure 1.10 – Tesla wind turbine proposed by Fuller (2010).



Source: Author (based on Fuller (2010)).

Tesla pumps produced by companies such as Discflo Corporation and MXQ are used industrially (DISCFLO, 2000; MXQ, 2000) in mainly hard-to-pump applications (PACELLO; HANAS, 2000) (see Fig. 1.11), such as for pumping highly viscous fluids, abrasive fluids, slurries with high solid content, fluids entrained with air/gas and delicate and shear sensitive fluids. Some examples of such fluids would be paper stock, food, beverages, wastewater, residues from chemical processes etc. Despite the lower efficiency of Tesla pumps, according to Pacello and Hanas (2000), the use of a Tesla pump can reduce the incidence of pump and seal failure, reduce wear from abrasion/cavitation and prevent damage to delicate and shear sensitive fluids. In particular, some Tesla pump design configurations have been considered for abrasive fluid pumping in Figueira Júnior *et al.* (2021), in order to show that it is feasible to use a Tesla pump in mineral pumping.

Figure 1.11 – Discflo (2000)'s Tesla pump (for hard-to-pump applications).



Source: Author (based on Discflo (2000)).

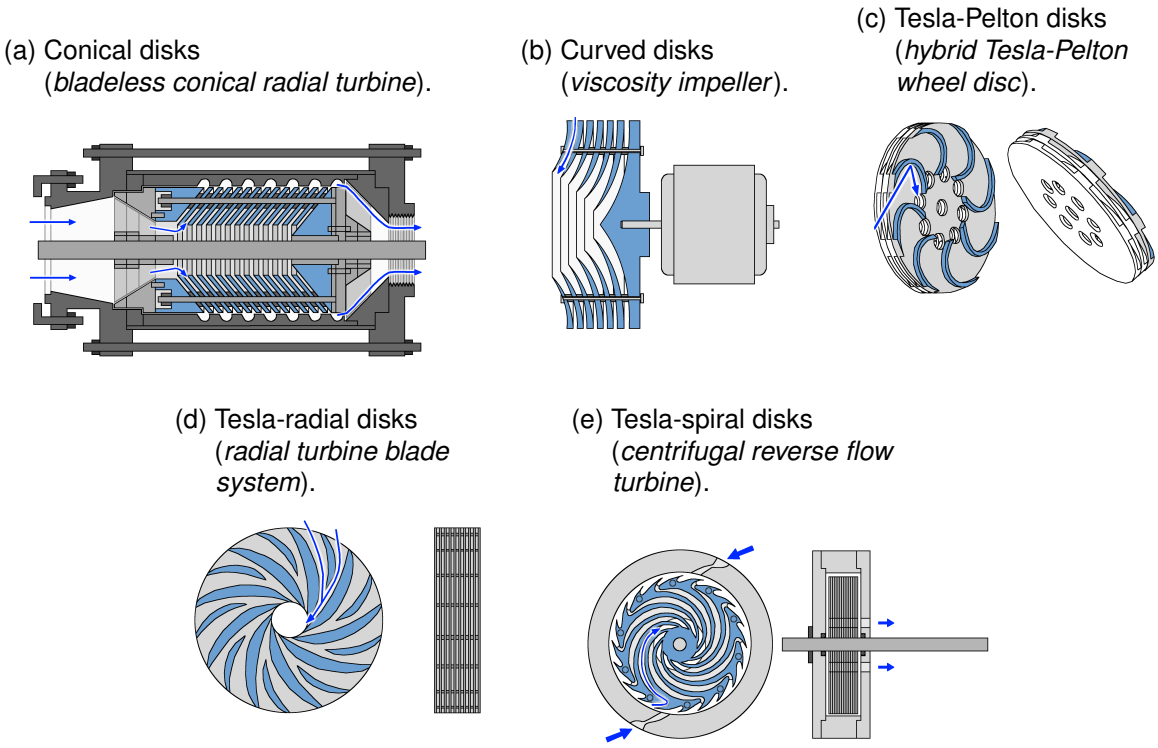
The performance of Tesla-type devices depends on (RAJE *et al.*, 2015): the number of disks (higher quantity would mean more torque being delivered) (BORATE; MISAL, 2012), the disk size (higher sizes mean that the fluid flows through a longer path and can deliver more torque), the spacing between disks (BORATE; MISAL, 2012),

the Reynolds number (since the boundary layer thickness depends on the Reynolds number) and the velocity of the fluid.

According to Yu (2015), the head losses that happen in a Tesla pump are due to 4 main factors: (1) steep change of the flow direction near the pump inlet; (2) viscous energy dissipation between the disks, which should be relatively small in laminar flow; (3) turbulent spiral flow formed on the radial outlet of the disks, which can be reduced by reducing disk spacing and radius (YU, 2015); and (4) transition from laminar to turbulent flow in the Tesla pump "chamber" (where the disks are) and the volute. A disadvantage can be seen when the fluid contains large suspensions, where they may block the gap between the Tesla pump disks (FOSTER, 2006). There is also a tendency of gas bubbles becoming entrapped between the Tesla pump disks (FOSTER, 2006).

Various alternative rotor (disk) designs of Tesla-type devices have been developed, such as with a spiral surface roughness (BORATE; MISAL, 2012) (that is capable of increasing the efficiency), conical disks (GRANDE III; DRAPER, 2005), curved disks (YU, 2015; EFFENBERGER, 1983) and even *hybrid* forms, such as when using blades between the disks of the Tesla-type device (COUTO; BATISTA, 2011; JOSHI *et al.*, 2016; O'HEAREN, 2003) or even spiral slots (SAITOH, 2011). Some of these alternative designs can be seen in Fig. 1.12, in which the designs that are axisymmetric consist of conical (Fig. 1.12a) or curved disks (Fig. 1.12b).

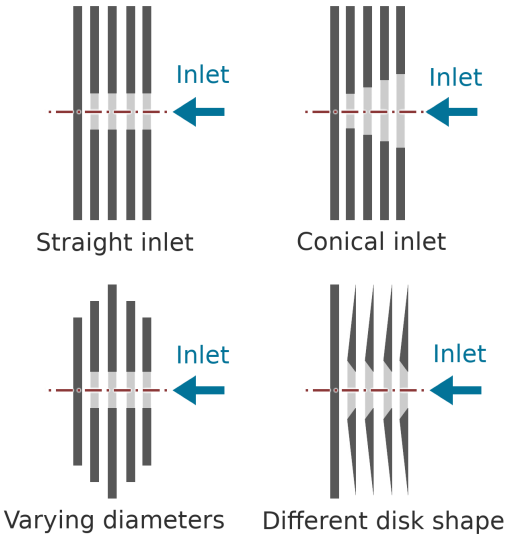
Figure 1.12 – Alternative designs for Tesla-type devices.



Source: Author (based on (a) Grande III and Draper (2005), (b) Effenberger (1983), (c) Couto and Batista (2011), (d) O'Hearen (2003), (e) Saitoh (2011)).

Fig. 1.13 shows some possible axisymmetric designs for Tesla-type devices: the traditional one (straight disks and inlet); conical inlet (according to Medvitz *et al.* (2011), the efficiency becomes slightly higher); varying diameters (FOSTER, 2006); and a different disk shape (FOSTER, 2006). There are also some other variations presented in Wilson (2006). According to Foster (2006), the disk thickness near the outlet should be small in order not to induce the formation of a turbulent (wake) region.

Figure 1.13 – Some axisymmetric designs of Tesla-type devices compared to the traditional (*straight inlet*) design.



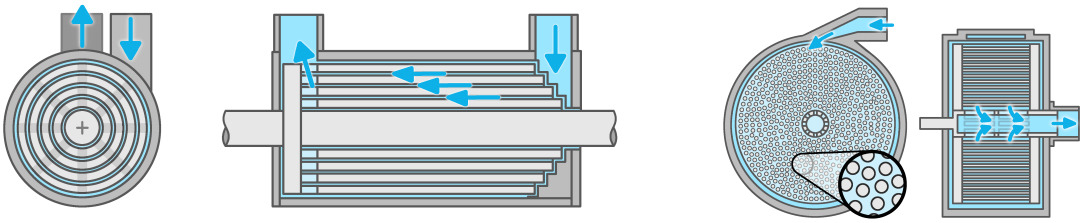
Source: Author.

It is also possible to apply the Tesla principle not only in the radial direction, but in the axial direction. Some examples are shown in Fig. 1.14: concentric tubes (FORD, 2018) and parallel filaments (JIAN SHI, 2016). The parallel filaments design can be described as a hybrid device, including the Tesla principle and a linear momentum variation effect.

Figure 1.14 – Axial designs from the Tesla principle.

(a) Concentric tubes (*Tubular adhesion turbine or pump*).

(b) Parallel filaments (*Filamentous turbine*).



Source: Author (based on (a) Ford (2018), (b) Jian Shi (2016)).

1.1.3 **Tesla pump as a VAD**

The application of a Tesla pump to VADs (YU, 2015) is of great interest, because its flow is continuous and nonpulsatile, leading to a reduction in blood damage – hemolysis and thrombosis (IZRAELEV *et al.*, 2009), which are the main limiting factors to the time of usage of VADs (SASTRY *et al.*, 2006). According to Yu (2015), in comparison to

bladed pumps, the average shear stress induced by the flow, which is the main cause of hemolysis, is small. Also, the movement of blades may provoke hemolysis. Therefore, there is the possibility of significantly reducing the occurrence of hemolysis by using a Tesla pump. Since Tesla pumps are said to be less prone to hemolysis and thrombosis than bladed pumps, this work aims to improve this solution even further.

Some authors report that the efficiency of a Tesla pump is relatively small (less than 20% (YU, 2015; FOSTER, 2006)), but others (HASINGER; KEHRT, 1963) report that efficiencies up to 60% should be possible. In the case of a Tesla turbine, Shimeles (2014) reports a maximum efficiency of about 48% in his Tesla turbine model in Ansys® Fluent. A low efficiency should generate heat transfer to the blood and arises the possibility of becoming a problem to the blood and the patient's health (YU, 2015). Therefore, there is a need to improve this efficiency.

The low efficiency mentioned in the previous paragraph is not verified when operating in laminar flow with a large number of disks and optimum small flow rates for each pair of disks, in which, it would be possible to get to efficiencies as high as 95% (analytical result) (RICE, 1991; CHOON *et al.*, 2011; YU, 2015; LOGAN Jr, 2003). Crawford and Rice (1974) claim that a Tesla pump can be designed with high efficiency for fluids with any viscosity and density. According to Logan Jr (2003), while the pumping efficiency of the fluid between the disks can be very high, the inherent losses on the inlet and outlet of the rotor may considerably reduce the efficiency. From published information concerning actual Tesla-type pumps, the efficiency did not exceed 60% (LOGAN Jr, 2003).

The idea of using a Tesla device as a blood pump was first examined by Dorman *et al.* (1966 apud MOODY, 2016) and from then it has been studied by various other scientists (HASINGER; KEHRT, 1963; RICE, 1991; IZRAELEV *et al.*, 2009). Miller *et al.* (1993) experimentally analyzed the operation of a Tesla pump for a blood analogue at a range of physiological conditions, which showed good agreement of pressure levels and flow rates of natural hearts and various VADs. Also, the experiments showed that the necessary rotation speeds for Tesla blood pumps were smaller than other pumps, leading to lower shear forces on the flow, which should decrease hemolysis. Miller *et al.* (1993) also analyzed the the effect of using a pulsatile rotation in a Tesla pump: by reducing rotation during diastole, the need for valves as a mechanism to control flow direction was also reduced. Miller *et al.* (1995) performed a preliminary flow visualization

study of a Tesla pump through Particle Image Velocimetry (PIV), showing that no eddies or flow stagnation were formed in the tested flow rates with rotations between 500 and 2000 rpm. The flow pattern for pulsatile flow resulted the same as in the corresponding continuous flow, with only the velocity magnitude varying according to the pulsation. Miller and Rainer (1999) experimentally analyzed the performance of Tesla pumps for blood flow considering different quantities of disks and disk spacings. Manning and Miller (1999) analyzed the effect of the interface between the shaft and a mechanical seal (i.e., not using magnetic suspension), for shaft seals made of Teflon or nylon, and shafts coated with stainless steel or Melonite. The study was performed with a gas (air), showing significant heat generation, but the authors claim that the use of a liquid (such as water or blood) should act as a coolant, which may reduce the temperature rise, and mean that heat thermal effects such as heat initiated hemolysis may not be an issue for the case of pumping blood.

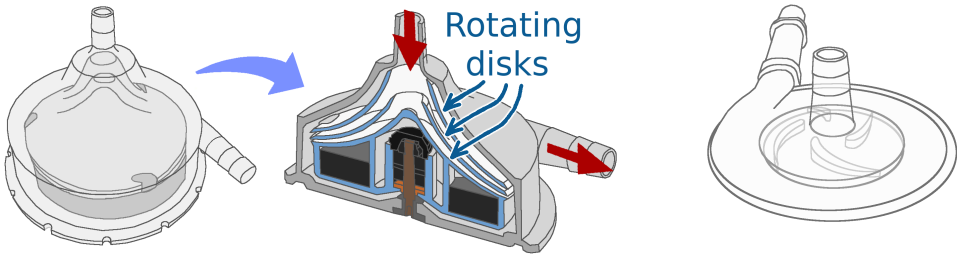
The effect of turbulence in the performance of a Tesla pump has been hinted by Naz *et al.* (2017), that performed simulations considering turbulence. However, there was no comparison of whether laminar or turbulent flow is better for the performance of a Tesla pump or not. In the case of a Tesla turbine, simulations performed by Rey (2004) with incompressible fluid showed a 40% increase in the efficiency when operating under turbulent flow. Similar results were obtained for compressible fluid (air) by Siddiqui *et al.* (2014) and Peshlakai (2012). In fact, Peshlakai (2012) even comments that turbulence in the flow should be essential for achieving high power and high efficiency, and also that, even though the efficiency slightly reduces as turbulence increases in the flow, the power output maintains a steady linear increase. In the case of a Tesla pump for VADs, since turbulent stresses should also lead to increasing hemolysis, there should be a trade-off between turbulence and hemolysis.

There are patents that consider the use of a Tesla pump as a VAD, with straight disks (GILL *et al.*, 2009) and curved disks (KLETSCHKA; RAFFERTY, 1975; RAFFERTY; KLETSCHKA, 1972; RAFFERTY; KLETSCHKA, 1976). Fig. 1.15 shows some commercial extracorporeal Tesla pumps for blood flow. The first one (Fig. 1.15a) is CentriFlux BR-100 (Braile® Biomédica), which is similar to BPX-80 BIO-Pump Plus (Medtronic®), composed of three rotating disks. The second one (Fig. 1.15b) is a Rotaflow pump (Maquet®), which is similar to Safira CentriFlux (Braile® Biomédica), and can be roughly said to be a hybrid Tesla pump due to the small outlet disk spacing

– the overall geometry is a slightly conical disk below the blades and a conical shape over the blades, gradually reducing the disk spacing with the radius. Another “rough” hybrid Tesla pump would be Affinity CP (Medtronic®), which features a single rotating conical disk. CentriFlux BR-100 and Affinity CP use a mechanically-coupled rotating shaft, while Rotaflow uses a magnetic driving system, but maintaining a small contact bearing sphere. As opposed to the contact bearing approach, the bladed centrifugal pump CentriMag, which is not a Tesla pump, uses magnetic bearings.

Figure 1.15 – Some commercial extracorporeal Tesla pump models.

(a) CentriFlux BR-100. (b) Rotaflow.



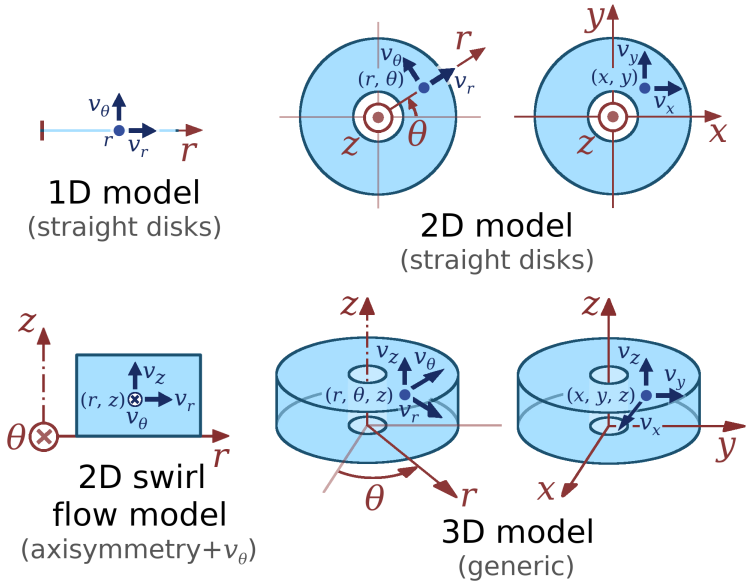
Source: Author (based on (a) Braile Biomédica (2017), (b) Maquet (2018)).

Couto *et al.* (2006) analytically estimates the necessary number of disks required for a Tesla device in order to perform a desired function. Choon *et al.* (2011) performed parametric optimization in 3D, in relation to the number of disks, spacing between disks, diameter of the disks and size of the volute, reaching an efficiency of 10.7% with a torque of 0.0330 Nm. Dodsworth and Groulx (2015) performed an experimental parametric analysis of the disk spacing with water, concluding that smaller disk spacings lead to higher efficiencies. According to Borate and Misal (2012), machining spiral surface roughness on the disks can increase efficiency. By using a hybrid Tesla device with Tesla-Pelton disks (COUTO; BATISTA, 2011) (see Fig. 1.12c), the Pelton-like blades imbued on the disk should increase the torque transmission. According to Foster (2006), the outlet thickness of the disks should be small so as not to form a wake-like region when the fluid exits the disks.

The possible ways to model the flow in a Tesla pump rotor can be seen in Fig. 1.16. In the case of modeling the flow between straight disks, it is possible to simplify it to a 1D model (PUZYREWSKI; TESCH, 2010; BASSETT, 1975) or a 2D model (SCHOSSER *et al.*, 2014; SCHOSSER *et al.*, 2017; BEANS, 1966) viewing an averaged fluid flow from above the disks (in Cartesian or cylindrical coordinates).

The 3D model may be expressed in Cartesian or cylindrical coordinates. Rey (2004) analyzed the applicability of the 2D swirl flow and 3D models in CFD (Computational Fluid Dynamics), concluding that the difference between the results is small, which shows that the application of the 2D swirl flow model to the analysis of a Tesla pump is valid. Shimeles (2014) also arrived at a similar conclusion. In this work, the Tesla pump rotor is modeled by the 2D swirl flow model.

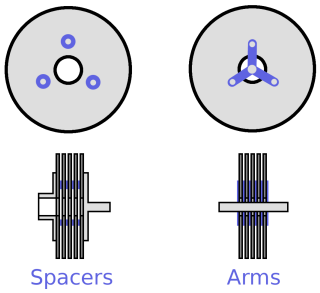
Figure 1.16 – Possible ways to model a Tesla pump rotor.



Source: Author.

It can be highlighted that, although the 2D swirl flow model is adequate for modeling the Tesla pump rotor, since a Tesla pump rotor may be composed of more than two disks, there is a mechanical need for circumferentially-spaced *spacers* to separate the disks (LETOURNEAU, 1981; FOSTER, 2006; DODSWORTH, 2016; MOODY, 2016; HOLLAND, 2015; POLISETTI *et al.*, 2017), or *arms* to connect the disks to the rotating shaft (TESLA, 1913a; TESLA, 1913b; KRISHNAN, 2015; RYKE; IGARASHI, 2015; LI *et al.*, 2017) (see Fig. 1.17). It is also possible to consider both configurations at the same time (LETOURNEAU, 1981; RYKE; IGARASHI, 2015). Note that the commercial Tesla blood pump CentriFlux BR-100 considers circumferentially-spaced spacers. Other pumps that consider these spacers are from the hard-to-pump applications (PACELLO; HANAS, 2000), such as from Discflo Corporation and MXQ (see Fig. 1.11). Since the 2D swirl flow model features axisymmetry, the presence and the effect of such structures are neglected.

Figure 1.17 – *Spacers* or *arms* positioned on Tesla pump rotor disks.

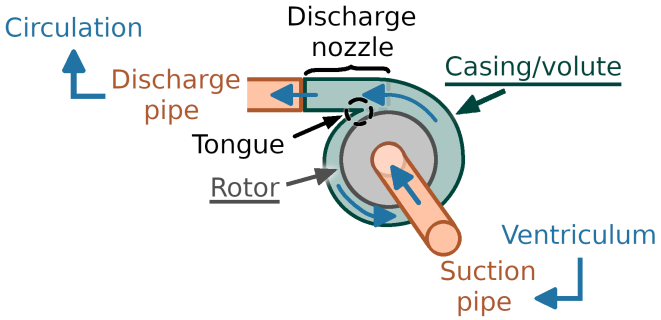


Source: Author.

1.1.4 **Casing/volute design**

In this work, the casing/volute is optimized with the same tooling that is devised and implemented for the Tesla pump rotor. However, although the Tesla pump rotor can be designed with the use of the 2D swirl flow model, the casing is not modelable the same way. The casing of a VAD is illustrated in Fig. 1.18. It has the objective to convert the fluid kinetic energy from the rotor into (static) pressure, while also redirecting the flow towards the discharge pipe. Since the casing highly influences the efficiency of the pump, the head loss in it should be minimum (LOBANOFF; ROSS, 1910), as well as the eddy formation (SAHU, 2000).

Figure 1.18 – Simplified configuration of the rotor and the volute in a VAD, showing the terminology that is used for some parts of the volute – *tongue* and *discharge nozzle*.



Source: Author.

The casing of a pump is defined as the housing of the rotor, which may be connected or not to the rotating shaft. There are essentially three types of casing design for centrifugal pumps (SAHU, 2000) (see Fig. 1.19): *volute-type* casing, which features a flow path around the rotor until the discharge pipe; *diffuser ring* casing, which features a diffuser ring (guide blades/vanes – since these additional blades are static, this type

of casing is also called *turbine casing*); and *vortex casing* (also called *whirlpool casing*), which features a vortex chamber (whirlpool chamber) around the rotor. These three types may lead to improvement in the pump efficiency and may be used combined or isolated.

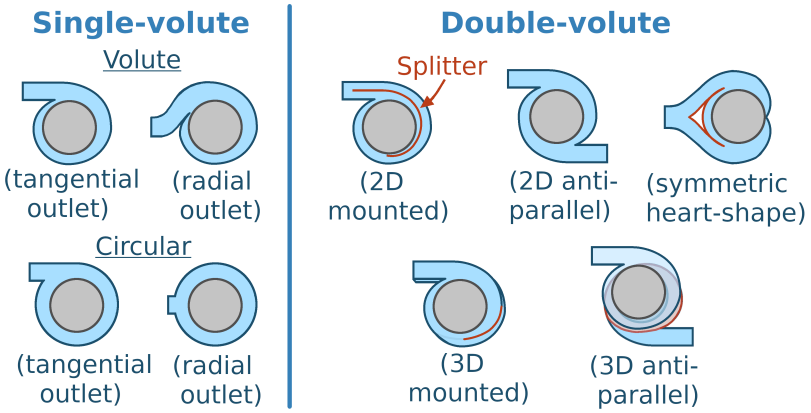
Figure 1.19 – Types of casing design for centrifugal pumps (the rotor is represented illustratively by a gray circle and is represented with, illustratively, different external diameters for each type of casing).



Source: Author.

In this work, only the volute-type casing is considered. The volute-type casing is the most used because of the simplicity of its construction. Various types of volute-type casing are shown in Fig. 1.20.

Figure 1.20 – Types of volute-type casing.



Source: Author.

The simplest and first developed type of volute is the single-volute (LOBANOFF; ROSS, 1910), with only one channel. There are essentially two main shapes that are used (see Fig. 1.20), which are the volute (spiral) and circular shapes. The discharge nozzle/outlet may be positioned tangentially (SATOH *et al.*, 2005; MATSUI *et al.*, 2006; YANG *et al.*, 2011; LOBANOFF; ROSS, 1910) or radially (MAJIDI; SIEKMANN, 2000; BANSAL, 2005; GÜLICH, 2014; ASUAJE *et al.*, 2005) in relation to the rotor. According to Lobanoff and Ross (1910), the circular shape is more adequate for low pressure heads and/or low rotations, featuring higher efficiencies than the volute shape under

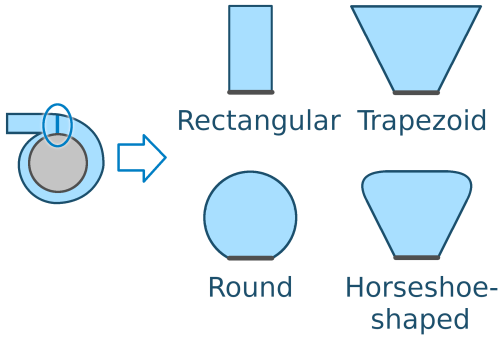
these conditions. This happens because the velocities and pressure in the circular shape are uniform at lower velocities, while, in the volute shape, they are only uniform at the BEP (Best Efficiency Point) (LOBANOFF; ROSS, 1910). Therefore, circular volutes are normally used when it is needed to pump large volumes of liquid instead of when a higher pressure head is needed (MC NALLY INSTITUTE, 2019). Lobanoff and Ross (1910) do not recommend using the circular shape when operating with multiple stages. For the volute shape, Tuzson (2000) recommends that the diameter of the base circle of the volute curve is 10% higher than the diameter of the rotor.

The volute may feature more than one channel (see Fig. 1.20). By including a splitter (dividing rib) inside the single-volute, the original volute becomes two mounted volutes (double-volute, also referred as *dual-volute*) inside the same 2D plane (*2D mounted*). Other double-volute configurations may be in a 3D configuration (*3D mounted*) or in a combination of both 2D and 3D configurations (LOBANOFF; ROSS, 1910; RODRIGUES, 2011). This causes a reduction in radial thrust and it is possible to achieve higher efficiencies (LOBANOFF; ROSS, 1910). It is also possible to include more splitters, as in triple-volutes and quad-volutes, but the manufacturing cost should increase more than the flow characteristics are improved (LOBANOFF; ROSS, 1910). Other variations for the double-volute are also shown in Fig. 1.20: 2D anti-parallel (without splitter) (LIU *et al.*, 2015; REY, 2004; SHIMELES, 2014), symmetric heart-shape (with an arrow-like splitter) (FLATHERS *et al.*, 1996) and 3D anti-parallel (with a circular splitter) (JIAO *et al.*, 2009; KUSZTELAN *et al.*, 2011). While using a double-volute, Becker *et al.* (1981) includes a small splitter near the end of the volute, claiming that it enhances the flow characteristics. The tongue (*cutwater*) (shown in Fig. 1.18) (LOBANOFF; ROSS, 1910) has been optimized through parametric optimization by Chen *et al.* (2017). Mohite (2013) mentions that an adjustable tongue may be used for operating under conditions other than the design conditions.

The volute may feature different cross sections (LOBANOFF; ROSS, 1910; YANG *et al.*, 2011; CFTURBO, 2019), such as rectangular (adequate for low speeds), trapezoid (which features less intense secondary flow than the rectangular cross section), round, and horseshoe-shaped (see Fig. 1.21). According to the simulation results by Yang *et al.* (2011), the round cross section is the most efficient, while the least efficient are the rectangular and trapezoid cross sections. Further analysing the round cross section, Lee *et al.* (2017) varied its aspect ratio, changing it to an ellipse, and observed that, if

the ellipse is stretched in the radial direction, the efficiency slightly decreases due to more significant secondary flow development in the volute (no significant difference in efficiency was observed for the circle and the ellipse stretched in the axial direction). Since the cross section cannot be visualized in a simplified 2D model for the flow path, if a 2D model is used for the optimization, an adequate cross section would need to be selected when fabricating it (such as from Fig. 1.21).

Figure 1.21 – Some types of volute cross sections.



Source: Author.

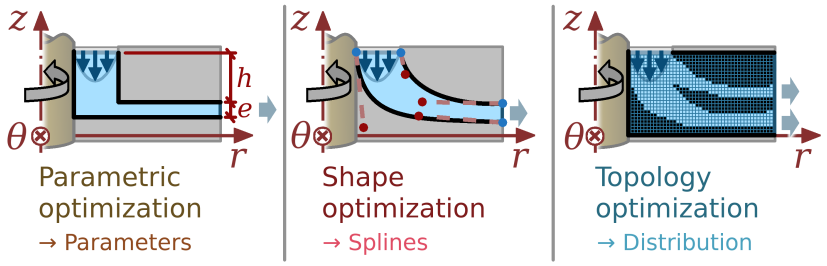
Heinrich and Schwarze (2016) perform shape optimization of the cross sections of the 3D model of a volute, reducing the total pressure loss by 12%. Heinrich (2016) points out three main characteristics for the design: location of the inlet of the volute shape in relation to the rotor outlet, radial location of the discharge nozzle, and format of the cross sections. According to Heinrich (2016), if the first two of the pointed out characteristics are well selected, the influence of the format of the cross section does not have a significant effect on efficiency. Considering this statement, it can be said that a 2D model should be able to capture the main characteristics that influence volute efficiency.

Baloni *et al.* (2015) performs parametric optimization of the volute of a blower through the Taguchi method. Kim *et al.* (2012) applies RSM (Response Surface Methodology) to optimize the volute, aiming to increase the pressure head. Shim *et al.* (2016) employs parametric optimization for the splitter of a double-volute, considering the k-ω turbulence model, and three objective functions: hydraulic efficiency at the design flow rate, and radial thrust coefficient at 70% and 120% of the design flow rate.

1.1.5 Optimization methods

According to Logan Jr (2003), most of the Tesla devices are designed using intuition and simple calculations (*1D model*) or empirical experiences (*trial and error*) and *rules of thumb*. This shows the need of applying a systematic process (*optimization*) to reach an optimal design for a given application of a Tesla device. There are essentially three distinct optimization methods in Engineering (see Fig. 1.22): parametric optimization, which aims to optimize a closed set of parameters of the design; shape optimization, which aims to optimize the contour, by using, for example, a closed set of splines (or NURBS), level-set functions or the direct movement of boundary nodes; and topology optimization, which aims to optimize the distribution of a variable in the design domain. All deterministic optimization methods are based on the computation of sensitivities (derivatives) with respect to the design variables. The way the sensitivities are considered characterizes each optimization method and directly corresponds to how the optimization proceeds: parametric optimization is based on parametric (*pointwise*) sensitivities, shape optimization is based on shape (*boundary*) sensitivities (present only on the shape (*boundary*)), and topology optimization is based on the distributed (*domain*) sensitivities (distributed over a predefined design domain).

Figure 1.22 – Examples of optimization methods applied to the design of a Tesla pump rotor in the 2D swirl flow model.



Source: Author.

The possibility of using optimization methods in blood pump design was initially presented by Antaki *et al.* (1995), and the main advantage is that they can guarantee an improvement of performance. Optimization in equipments which operate under the Tesla principle has already been performed parametrically, for quantity, spacing and size of the disks (CHOON *et al.*, 2011).

From the optimization methods presented in Fig. 1.22, the most generic is the

topology optimization method, because it can create any type of shape from an initial design domain, being even able to create boundaries that did not initially exist in the initial guess of the shape, which is not possible in shape optimization. Furthermore, it normally has the advantage of not requiring the finite element mesh to be redrawn during each optimization step, which require a special treatment in parametric and shape optimizations. The topology optimization method was initially applied to structural problems (BENDSØE; KIKUCHI, 1988) and has been extended to the area of fluids by Borrvall and Petersson (2003).

1.1.6 **Fluid flow topology optimization**

Fluid flow topology optimization (*fluid topology optimization*) is the topology optimization method considered for fluid flow. It consists of distributing fluid and solid over a given design domain. The way the topology optimization method performs this distribution may be realized by various approaches, such as: the pseudo-density approach (ROZVANY *et al.*, 1992; ROZVANY, 2001), extended to fluid problems by Borrvall and Petersson (2003); the level-set approach (OSHER; SETHIAN, 1988; DUAN *et al.*, 2016; ZHOU; LI, 2008); or topological derivatives (SOKOLOWSKI; ZOCHOWSKI, 1999; SÁ *et al.*, 2016). The pseudo-density approach optimizes the distribution of a variable (pseudo-density) inside the design domain, defining the positions in which there is solid or fluid. The level-set approach consists of optimizing an initially sinuous 3D surface in which one of its contour levels corresponds to the optimized contours between solid and fluid. Topological derivatives consist of optimizing through perturbations around the solid portions of the design domain, which means that they change how the sensitivities are computed, how the topology optimization progresses, and operate with the design variable binarily. The pseudo-density approach is used in this work, since, according to Deng *et al.* (2013b), it provides a rapid and robust convergence, a weak dependence in relation to the initial distribution of the design variable and it can deal with multiple constraints.

From the initial work by Borrvall and Petersson (2003), the topology optimization method has been applied to various different fluid flow physics: Stokes flows (BORRVALL; PETERSSON, 2003), Darcy-Stokes flows (GUEST; PRÉVOST, 2006; WIKER *et al.*, 2007), Navier-Stokes flows (EVGRAFOV, 2004; GERSBORG-HANSEN

et al., 2005; OLESEN *et al.*, 2006), slightly compressible flows (EVGRAFOV, 2006), compressible flows (SÁ *et al.*, 2021; OKUBO *et al.*, 2022), non-Newtonian flows (PINGEN; MAUTE, 2010; HYUN *et al.*, 2014; ZHANG; LIU, 2015; ROMERO; SILVA, 2017; ALONSO *et al.*, 2020), turbulent flows (PAPOUTSIS-KIACHAGIAS *et al.*, 2011; YOON, 2016; DILGEN *et al.*, 2018; YOON, 2020; SÁ *et al.*, 2021), thermal-fluid flows (KOGA *et al.*, 2013; YAJI *et al.*, 2016; SATO *et al.*, 2018; RAMALINGOM *et al.*, 2018), unsteady flows (NØRGAARD *et al.*, 2016; CHEN *et al.*, 2017) etc. The topology optimization method has also been extended to design fluid devices, such as valves (SONG *et al.*, 2009), mixers (ANDREASEN *et al.*, 2009), rectifiers (JENSEN *et al.*, 2012), and centrifugal bladed pumps/turbines (ROMERO; SILVA, 2014, 2017). In the design of centrifugal bladed pumps/turbines, Romero and Silva (2014, 2017) modeled the fluid flow in a rotating reference frame, optimizing the fluid motion over the impeller of centrifugal pumps, in which Coriolis and centrifugal effects are present. Sá (2016) and Sá *et al.* (2018) performed experiments to evaluate the topology optimization designs obtained through this formulation.

In particular, the use of a 2D swirl flow model in topology optimization was considered in Alonso *et al.* (2018), and was further analyzed for Newtonian laminar pump design in Alonso *et al.* (2019), which also considers a material model for topology optimization that includes a different intensity for the *swirl* effect.

The material model that performs the transition between liquid and solid may be given by a porous medium with permeability controlled by the topology optimization. The model that has first been considered in this approach for topology optimization is the Brinkman model (based on Darcy's Law) (DARCY, 1856; BRINKMAN, 1947) in Borrvall and Petersson (2003). Another possible model includes an additional inertial effect (Forchheimer term (FORCHHEIMER, 1901)) that is present in porous materials, leading to the *Brinkman-Forchheimer model* (or *Forchheimer model*) (HUANG; AYOUB, 2006; ALIMOHAMADI *et al.*, 2014; PHILIPPI; JIN, 2015; ALONSO; SILVA, 2021; ALONSO; SILVA, 2022b). The effect of body forces, such as gravity force, and Coriolis and centrifugal inertial forces, has been previously analyzed by Deng *et al.* (2013a, 2013b). Since not all fluids feature Newtonian properties (linear properties), and can exhibit non-Newtonian effects (nonlinear effects), the optimized topologies may vary. This is shown in Pingen and Maute (2010) for 2D channel design considering blood flow according to the Carreau-Yasuda model. Non-Newtonian fluid design has also been

analyzed by Romero and Silva (2017) for bladed blood pump design (modified Cross model), by Zhang and Liu (2015) for arterial by-pass grafts (modified Cross model), and by Alonso *et al.* (2020) for 2D swirl flow (Carreau-Yasuda model). Particularly, some works consider additional penalizations in the non-Newtonian viscosity inside the modeled solid material: Pingen and Maute (2010) consider an additional penalization for enforcing the *Newtonian* value of blood viscosity inside the modeled solid material, whereas Hyun *et al.* (2014) and Alonso *et al.* (2020) consider the additional penalization to enforce the *low-shear rate* value of blood viscosity inside the modeled solid material.

Previously, works on topology optimization aimed to minimize hemolysis by indirectly minimizing the energy dissipation (ZHANG; LIU, 2015) or a simplified version close to the real hemolysis index – from Montevecchi *et al.* (1995) (ROMERO; SILVA, 2017). In terms of thrombosis, it had only been considered indirectly through vorticity (ROMERO; SILVA, 2017). However, recent works (ALONSO; SILVA, 2021) considered the computation of the real hemolysis and thrombosis indices, which require the solution of differential equations.

There is a relatively recent field called *Adaptive Topology Optimization* (EVGRAFOV, 2015; DUAN *et al.*, 2015; GUPTA *et al.*, 2020), in which the finite element mesh for the simulation can be adaptively refined/coarsened according to the current topology in order to try to better simulate the fluid flow behavior and/or define the optimized boundaries better. This scheme may be considered as a multi-resolution scheme when the design variable is given for a different discretization than the fluid flow simulation.

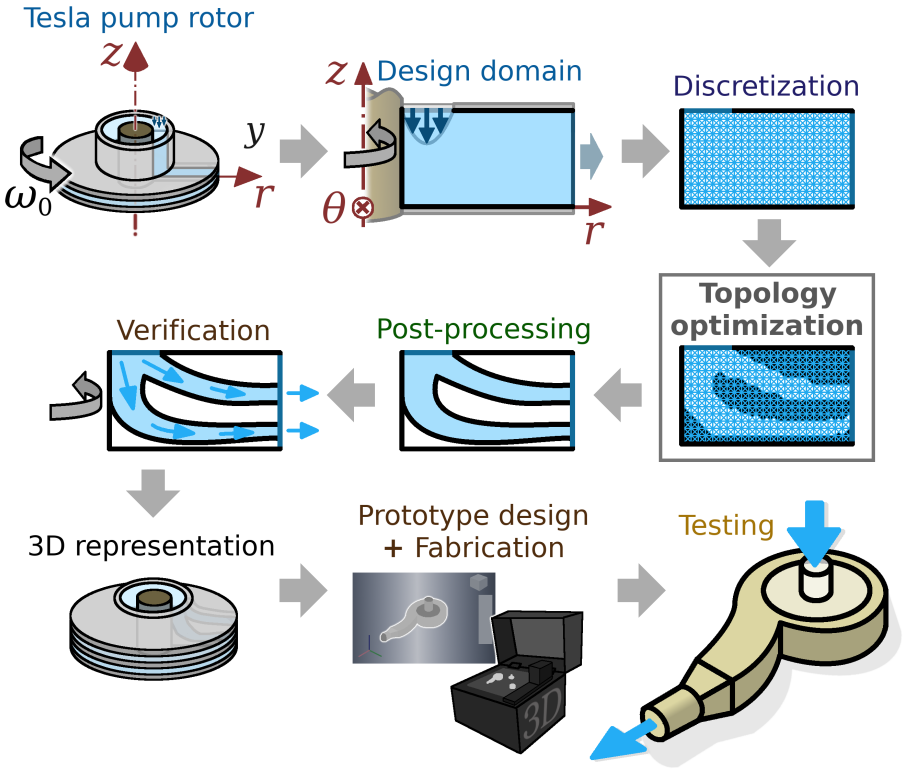
The pseudo-density approach for topology optimization normally relies on the relaxation of the binary values for solid (0) and fluid (1), by enabling a continuous transition between these two values (Section 2.5.1.1). This is performed for better numerical conditioning. However, there are researches that rely on some adaptations/filterings or linearizations in order to stably allow applying topology optimization to binary values, as in the BESO (Bi-directional Evolutionary Structural Optimization) (HUANG; XIE, 2007) and TOBS (Topology Optimization of Binary Structures) (SIVAPURAM; PICELLI, 2018; SIVAPURAM *et al.*, 2018; PICELLI *et al.*, 2020b) methods, which rely on integer optimizers (ILP, Integer Linear Programming). Therefore, a discrete solution is imposed in the optimizer level, which enforces a binary variables solution through a linearization, making it possible to achieve clearly defined topologies during topology optimization

rather than in its end. Particularly, the TOBS algorithm has been first considered for structural topology optimization (SIVAPURAM; PICELLI, 2018; SIVAPURAM *et al.*, 2018; PICELLI *et al.*, 2020b), but has also been considered for fluid flow optimization (SOUZA *et al.*, 2021), and for FSI applications (PICELLI *et al.*, 2020a). It can also be mentioned that, since TOBS considers discrete design variable configurations during topology optimization, the dependency of the material model penalization in the optimization process is lessened with respect to the optimization performed for continuous values (due intermediate design variable values not appearing). From the TOBS algorithm, there is also the TOBS-GT (Topology Optimization of Binary Structures - Geometry Trimming) approach (PICELLI *et al.*, 2021), which may be roughly described as a *multi-resolution* scheme, since it relies on TOBS being applied to a fixed mesh for the design variable, but the simulations being performed in post-processed meshes with smoothed contours. The main advantage of TOBS-GT would involve having explicitly defined boundaries during topology optimization, allowing the direct application of wall functions, which are normally required for two-equation turbulence models such as the k-ϵ and k-ω models.

The topology optimization problem may have more than one solution (*local minima*), as in a *bifurcation problem* (FARRELL *et al.*, 2016; PAPADOPOULOS *et al.*, 2020), depending on the parameters of the optimization and how they are varied (BORRVALL; PETERSSON, 2003).

The sequence of a design approach using topology optimization is shown in Fig. 1.23. It starts with the definition of the design domain for the fluid flow device (in this case, the Tesla pump rotor), together with the corresponding boundary conditions. Then, the domain is discretized, in the form of a mesh. After this, the topology optimization method is defined for given objective functions and constraints that are specific to the problem. By performing the topology optimization algorithm, the optimized topology is obtained. The optimized topology is then post-processed and verified through simulations. In the end, the corresponding prototype is designed, fabricated and tested.

Figure 1.23 – Sequence of a design approach using topology optimization.



Source: Author.

1.1.7 **Summary of the state of the art**

From the last sections, the technological gap previous to this work could be noticed in the topology optimization of 2D swirl flow devices. For clarity, some of the main points are highlighted below:

- The 2D swirl flow model was not previously considered for topology optimization. This means that it needs to be included in the topology optimization formulation (ALONSO *et al.*, 2018);
- The material model in fluid topology optimization has been previously considered as the Brinkman model (BORRVALL; PETERSSON, 2003), and as the Brinkman-Forchheimer model (PHILIPPI; JIN, 2015; ALONSO; SILVA, 2022b). For 2D swirl flow, specific adjustments may be introduced in the fluid topology optimization material model (ALONSO *et al.*, 2019);
- Non-Newtonian fluid flow has been previously considered only for 2D flow (PINGEN; MAUTE, 2010; HYUN *et al.*, 2014). This means that it was yet to be considered in 2D swirl flow topology optimization (ALONSO *et al.*, 2020);

- Blood damage models were not previously considered in topology optimization. Previously, the minimization of blood damage was considered indirectly, as a shear stress power (for hemolysis) (ANTAKI *et al.*, 1995; ROMERO; SILVA, 2017), and as vorticity (for thrombosis) (ROMERO; SILVA, 2017). This means that a direct minimization was yet to be included in the topology optimization formulation (ALONSO; SILVA, 2021);
- Turbulent flow has been previously considered for 2D flow (YOON, 2016; DILGEN *et al.*, 2018; YOON, 2020), but still not for 2D swirl flow. For 2D swirl flow, it was yet to be considered in 2D swirl flow topology optimization (ALONSO *et al.*, 2021; ALONSO *et al.*, 2022).

1.2 MOTIVATION

Among the possible types of VADs, the Tesla pump is a highly relevant option for pumping blood, mostly due to its possibility, in relation to bladed pumps, of reducing blood damage. This makes the Tesla pump an interesting possibility for optimization – in particular, for topology optimization. For this aim, a novel formulation for topology optimization needs to be developed, based on 2D swirl flow, novel material models, Non-Newtonian fluid, blood damage models, and laminar/turbulent flows. Furthermore, a turbulence model that is more adequate for topology optimization should also be incorporated in the topology optimization formulation – i.e., the Wray-Agarwal turbulence model (WA2018), due to its compactness and dependency with less topology optimization parameters than other models.

1.3 OBJECTIVES

The objectives of this work are to:

- Devise a novel topology optimization methodology for optimizing 2D swirl flow devices (more generic class of devices which includes the Tesla pump), by considering non-Newtonian fluid (blood), and laminar/turbulent flows;
- Include the minimization of hemolysis and thrombosis in topology optimization through blood damage models;

- Formulate a topology optimization approach for considering the Wray-Agarwal turbulence model (WA2018);
- Design Tesla VAD prototypes based on the 2D swirl concept (rotor and volute);
- Fabricate the optimized Tesla VAD prototypes through additive manufacturing and experimentally evaluate them.

1.4 SCIENTIFIC CONTRIBUTION

The scientific contributions of this work are:

- Topology optimization methodology for optimizing 2D swirl flow devices (more generic class of devices which includes the Tesla pump), by considering non-Newtonian fluid (blood), and laminar/turbulent flows;
- Topology optimization formulation including the minimization of hemolysis and thrombosis through blood damage models;
- Topology optimization formulation considering the Wray-Agarwal turbulence model (WA2018);
- Design of the rotor and volute of VADs based on the 2D swirl concept;
- Fabrication of the optimized Tesla VADs through additive manufacturing and experimental evaluation of the prototypes.

Currently, nine related journal articles have been published, while one has been accepted for publication:

- “Topology optimization applied to the design of 2D swirl flow devices” (ALONSO *et al.*, 2018);
- “Topology optimization based on a two-dimensional swirl flow model of Tesla-type pump devices” (ALONSO *et al.*, 2019);
- “Non-Newtonian laminar 2D swirl flow design by the topology optimization method” (ALONSO *et al.*, 2020);
- “Topology optimization for blood flow considering a hemolysis model” (ALONSO; SILVA, 2021);

- “Flexible framework for fluid topology optimization with OpenFOAM® and finite element-based high-level discrete adjoint method (FEniCS/dolfin-adjoint)” (ALONSO *et al.*, 2021);
- “Topology optimization applied to the design of Tesla-type turbine devices” (ALONSO; SILVA, 2022b);
- “Topology optimization method based on the Wray-Agarwal turbulence model” (ALONSO *et al.*, 2022);
- “Topology optimization of turbulent fluid flow via the TOBS method and a geometry trimming procedure” (PICELLI *et al.*, 2021);
- “Topology optimisation for rotor-stator fluid flow devices” (MOSCATELLI *et al.*, 2022);
- “Blood flow topology optimization considering a thrombosis model” (ALONSO; SILVA, 2022a, accepted).

The author had related works presented in the international conferences WCCM (World Congress in Computational Mechanics) and USNCCM (U.S. National Congress on Computational Mechanics). They are listed as follows:

- “Topology Optimization Applied to the Design of a Tesla Pump” (WCCMXIII, 2018);
- “Design of non-Newtonian 2D swirl flow devices by using the Topology Optimization Method” (USNCCM15, 2019);
- “Topology optimization design considering 2D swirl turbulent flow” (WCCM14, 2021);
- “Topology optimization design of blood flow devices considering a hemolysis model” (USNCCM16, 2021).

Furthermore, the source code of the *FEniCS TopOpt Foam* library (ALONSO *et al.*, 2021) is made available in a git repository [1].

1.5 OUTLINE OF THE THESIS

The thesis is organized as follows:

[1] https://github.com/diego-hayashi/fenics_topopt_foam

- In Chapter 2 (“THEORETICAL FOUNDATION”), the fluid flow modeling is formulated, from the equilibrium equations for 2D fluid flow, the non-Newtonian fluid model, and the boundary conditions; the Finite Element Method (FEM) is then briefly derived and defined; performance and characterization quantities related to the design of the Tesla pump device are defined; the blood damage modeling for hemolysis and thrombosis is presented; and the topology optimization method is presented, alongside pattern repetition, regularization and post-processing.
- In Chapter 3 (“NUMERICAL IMPLEMENTATION”), the implementation of the topology optimization method is described, some numerical considerations necessary for the numerical implementation are also presented, and an interfacing with the OpenFOAM® software for the computation of turbulence is presented.
- In Chapter 4 (“EXPERIMENTAL SETUP”), the design and fabrication of the experimental apparatus and prototypes are described.
- In Chapter 5 (“RESULTS AND ANALYSES”), the numerical and experimental results are presented, by considering the articles that have already been published, and some further results.
- In Chapter 6 (“CONCLUSIONS AND FUTURE WORK”), some conclusions are inferred and some ideas for future work are presented.

2 THEORETICAL FOUNDATION

The fluid flow in a Tesla pump rotor can be interpreted as an axisymmetric flow comprising rotation around an axis. Therefore, it may be modeled by a 2D swirl flow model. The 2D swirl flow model is a simplification of the complete 3D model by considering axisymmetry, and consists of a 2D domain with three velocity components (i.e., including a swirl velocity component besides the 2D plane velocity components). From this simplification, the simulations should be computationally less expensive than a complete 3D model (ALONSO *et al.*, 2018; ALONSO *et al.*, 2019). The fluid flow in the volute can be interpreted as a 2D flow exiting the rotor, towards an outlet. For this interpretation, it is necessary to assume that the effect of the boundary layer outside the 2D plane is negligible. This way, the volute may be modeled by a 2D flow. Throughout this work, the greek letter Π refers to the corresponding 3D domains, whilst the greek letter Ω refers to the 2D / 2D swirl flow domains. From the explanation in Section 1.1.1, the Tesla pump rotor is modeled considering steady state in this work. Since the flow exiting the Tesla pump rotor can be assumed to be axisymmetric, the inlet flow to the volute can be assumed to be approximately uniform and the transient condition would not necessarily need to be considered. Note that, in the case of a bladed pump, since the fluid is pumped in batches, such analysis should be more important.

Therefore, the fluid flow is modeled for incompressible non-Newtonian fluid (blood), steady state regime, and a rotating reference frame. The extension to turbulent flow is also presented. In the following sections, the formulation and modeling of the fluid flow for the numerical implementation are presented.

2.1 FORMULATION AND MODELING FOR FLUID FLOW

There are two main approaches to model fluid flow, which are the hydrodynamic and kinetic approaches. The hydrodynamic approach is based on the hydrodynamic description of fluid flow, which is a macroscale description from the continuum equations for fluid flow (i.e., the continuity and Navier-Stokes equations) (NØRGAARD, 2017). The kinetic approach is based on the kinetic description of fluid flow, which is a mesoscale description from the kinetic theory, considering that the fluid particles are distributed statistically (it is essentially composed of the Lattice-Boltzmann Method (LBM)) (SHAN

et al., 2006; NØRGAARD, 2017; PERUMAL; DASS, 2015). Both approaches are valid for modeling fluid flow and have been applied to the simulation and optimization of fluid flow devices (EVGRAFOV, 2004; YAJI *et al.*, 2016).

In this work, the fluid flow is modeled by the hydrodynamic approach, mainly through FEM. The Partial Differential Equations (PDEs) (*strong form*) used for modeling the fluid flow are presented next, initially for laminar flow. Then, this formulation is extended to turbulent flow.

2.1.1 **Equilibrium equations (laminar flow)**

The fluid flow is presented in this section for for laminar incompressible flow under steady state conditions. By considering a rotating reference frame, the continuity and Navier-Stokes (linear momentum) equations are presented as follows (MUNSON *et al.*, 2009; WHITE, 2011; ROMERO; SILVA, 2014; REDDY; GARTLING, 2010)

$$\nabla \bullet \boldsymbol{v} = 0 \tag{2.1}$$

$$\rho \nabla \boldsymbol{v} \bullet \boldsymbol{v} = \nabla \bullet \boldsymbol{T} + \rho \boldsymbol{f} - 2\rho(\boldsymbol{\omega} \wedge \boldsymbol{v}) - \rho \boldsymbol{\omega} \wedge (\boldsymbol{\omega} \wedge \boldsymbol{r}) \tag{2.2}$$

where $\boldsymbol{v}$ is the velocity relative to the reference frame, $\boldsymbol{r}$ is the radial position in the fluid with respect to the rotation axis, ρ is the density of the fluid, $\rho \boldsymbol{f}$ is the body force per unit volume acting on the fluid, $\boldsymbol{\omega}$ is the rotation of the reference frame, $-2\rho(\boldsymbol{\omega} \wedge \boldsymbol{v})$ is the Coriolis force, $-\rho \boldsymbol{\omega} \wedge (\boldsymbol{\omega} \wedge \boldsymbol{r})$ is the centrifugal inertial force, " $\bullet$ " is used to denote the inner product as defined in Gurtin (1981), " $\wedge$ " is used to denote cross product, and $\boldsymbol{T}$ is the stress tensor given by

$$\boldsymbol{T} = 2\mu \boldsymbol{\epsilon} - p\boldsymbol{I}, \quad \boldsymbol{\epsilon} = \frac{1}{2}(\nabla \boldsymbol{v} + \nabla \boldsymbol{v}^T) \tag{2.3}$$

where $\boldsymbol{\epsilon}$ is the deformation (strain) tensor, p is the pressure, μ is the dynamic viscosity (*viscosity coefficient*) of the fluid, and $\boldsymbol{I}$ is the identity matrix.

It can be mentioned that, specifically for 2D swirl flow, eqs. (2.1) and (2.2) can be equivalently considered in the absolute reference frame, except (possibly) by numerical convergence. This is due to the axisymmetry assumption, which implies that the derivatives in relation to θ are zero (i.e., $\frac{\partial(\ )}{\partial \theta} = 0$). With this assumption, the reference frame transformation reduces itself to simply a conversion between absolute and relative

velocities (see Appendix D). It can be highlighted that other cases, such as the 2D bladed pump (ROMERO; SILVA, 2014), do not portray this correspondence, since an additional tangential acceleration effect (θ direction) appears, which depicts the transient movement of the mesh (in the 2D swirl flow case, the mesh does not change position when under rotation).

In the case of the rotor, the rotation of the reference frame is the rotation of the disks ($\boldsymbol{\omega} = \omega_0 \boldsymbol{e_z}$). In the case of the volute, since the volute is not under rotation, $\boldsymbol{\omega} = \mathbf{0}$. If the body force per unit volume acting on the fluid ($\rho \boldsymbol{f}$) is the gravity force, then $\rho \boldsymbol{f} = \rho \boldsymbol{g} = -\rho g \boldsymbol{e_z}$ (where the gravitational acceleration is given by $g \approx 9.8$ m/s^2). However, since normally the forces involved in flow pumps are much higher than the gravitational force, it is normally assumed that $\boldsymbol{f} = \mathbf{0}$.

Eqs. (2.1) and (2.2) are deduced by considering a rotating reference frame with a rotation of $\boldsymbol{\omega} = \omega_0 \boldsymbol{e}_z$. In this case, the velocity and acceleration on the stationary (absolute) reference frame need to be converted as (WHITE, 2011)

$$\boldsymbol{v}_{\text{abs}} = \boldsymbol{v}_{\text{ref}} + \boldsymbol{v} + \boldsymbol{\omega} \wedge \boldsymbol{r} \tag{2.4}$$

$$\boldsymbol{a}_{\text{abs}} = \boldsymbol{a}_{\text{ref}} + \boldsymbol{a} + 2\boldsymbol{\omega} \wedge \boldsymbol{v} + \boldsymbol{\omega} \wedge (\boldsymbol{\omega} \wedge \boldsymbol{r}) + \dot{\boldsymbol{\omega}} \wedge \boldsymbol{r} \tag{2.5}$$

where $\boldsymbol{\omega}$ is the rotational speed of the reference system, $\boldsymbol{v}_{\text{abs}}$ and $\boldsymbol{a}_{\text{abs}}$ are the absolute velocity and acceleration, $\boldsymbol{v}$ and $\boldsymbol{a}$ are the relative velocity and acceleration, and $\boldsymbol{v}_{\text{ref}}$ and $\boldsymbol{a}_{\text{ref}}$ are the velocity and acceleration of the origin of the rotating reference frame (in this case, the origin is at the center of rotation, therefore $\boldsymbol{v}_{\text{ref}} = \mathbf{0}$ and $\boldsymbol{a}_{\text{ref}} = \mathbf{0}$). In the case of steady state flow, the rotational acceleration is zero ($\dot{\boldsymbol{\omega}} = \mathbf{0}$). By considering eq. (2.4), it can be proven that $(\nabla \boldsymbol{v}_{\text{abs}} + \nabla \boldsymbol{v}_{\text{abs}}{}^T) = (\nabla \boldsymbol{v} + \nabla \boldsymbol{v}^T)$ (term that is used in eq. (2.3)). Eq. (2.5) is also shown in Appendix D.

In cylindrical coordinates, the position and velocity are given as follows:

$$\begin{aligned} \boldsymbol{s} &= (r,\ \theta,\ z) = r\boldsymbol{e}_r(\theta) + z\boldsymbol{e}_z \\ \boldsymbol{v} &= (v_r,\ v_\theta,\ v_z) = v_r\boldsymbol{e}_r(\theta) + v_\theta\boldsymbol{e}_\theta + v_z\boldsymbol{e}_z \end{aligned} \tag{2.6}$$

Since, in a 2D swirl flow model, there are all the 3D velocity components and no dependence in relation to the θ coordinate (see Fig. 1.5),

$$\begin{aligned} \boldsymbol{s} &= (r,\ 0,\ z) = r\boldsymbol{e}_r + z\boldsymbol{e}_z \\ \boldsymbol{v} &= (v_r,\ v_\theta,\ v_z) = v_r\boldsymbol{e}_r + v_\theta\boldsymbol{e}_\theta + v_z\boldsymbol{e}_z \end{aligned} \tag{2.7}$$

Notice that, in 2D swirl flow, from eq. (2.7), it is equivalent to use $\boldsymbol{s}$ (position of the fluid) in $\boldsymbol{\omega}\wedge\boldsymbol{r}$ (from eq. (2.2)) instead of $\boldsymbol{r}$ ($\boldsymbol{r} = (r,\ 0, 0) = r\boldsymbol{e}_r$). In the case of a 2D domain with center of rotation on $(0,\ 0)$, $\boldsymbol{r} = \boldsymbol{s}$.

Also, the differential operators (∇, $\nabla\wedge$, $\nabla\bullet$) should be used in their cylindrical coordinates' versions (LAI *et al.*, 2009), and, since axisymmetry is implied, the derivatives in relation to θ are zero (i.e., $\frac{\partial(\ )}{\partial\theta} = 0$).

For the sake of completeness, the 2D model implies that

$$\begin{aligned}\boldsymbol{s} &= (x,\ y) = x\boldsymbol{e}_x + y\boldsymbol{e}_y \\ \boldsymbol{v} &= (v_x,\ v_y) = v_x\boldsymbol{e}_x + v_y\boldsymbol{e}_y\end{aligned} \tag{2.8}$$

In topology optimization, an additional body force may be included in order to emulate a solid material inside the fluid domain. This force is defined and explained in Section 2.5. Since the solid material may be modeled by a porous medium with a small permeability (see Section 2.5), this additional body force is a *resistance force of the porous medium* ($\boldsymbol{f}_r(\alpha)$). By including this porous medium effect, eqs. (2.1) and (2.2) become:

$$\nabla\bullet\boldsymbol{v} = 0 \tag{2.9}$$

$$\rho\nabla\boldsymbol{v}\bullet\boldsymbol{v} = \nabla\bullet\boldsymbol{T} + \rho\boldsymbol{f} - 2\rho(\boldsymbol{\omega}\wedge\boldsymbol{v}) - \rho\boldsymbol{\omega}\wedge(\boldsymbol{\omega}\wedge\boldsymbol{r}) + \boldsymbol{f}_r(\alpha) \tag{2.10}$$

Eqs. (2.9) and (2.10) are presented in Alonso *et al.* (2018) for the 2D swirl flow model for Newtonian fluid with the definitions of the differential operators (gradient and divergent) substituted.

2.1.2 **Non-Newtonian fluid modeling**

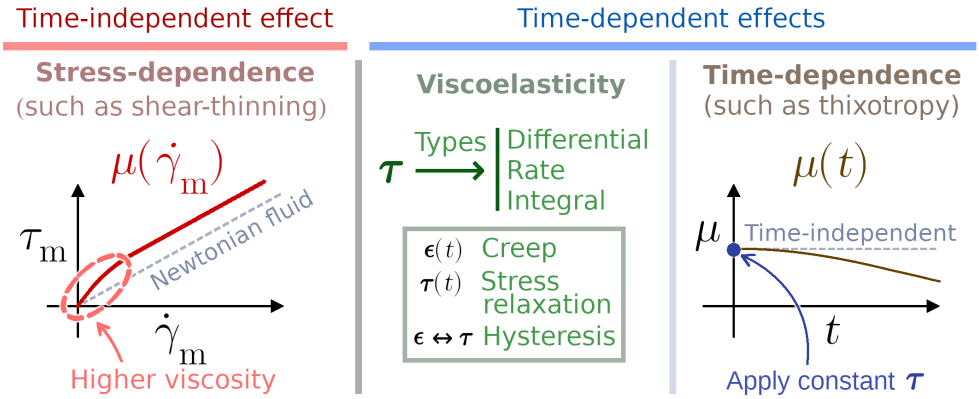
Non-Newtonian fluids are fluids in which the relationship between viscous shear rate and viscous shear stress is nonlinear, as opposed to the linear behavior of Newtonian fluids (according to Newton's Law of Viscosity). As such, the simulation results and, therefore, the optimized topologies may vary when considering a fluid with a nonlinear behavior. This can be noticed in the topology optimization performed by Pingen and Maute (2010) for 2D channel design (blood flow according to the Carreau-Yasuda

model). Topology optimization has also been considered for non-Newtonian fluid for designing bladed blood pumps (modified Cross model) (ROMERO; SILVA, 2017), arterial by-pass grafts (modified Cross model) (ZHANG; LIU, 2015; HYUN *et al.*, 2014; KIAN, 2017), roller-type blood viscous micropumps (power-law model) (ZHANG *et al.*, 2016a), aneurysm implants (JIANG *et al.*, 2017), and viscoelastic rectifiers (viscoelastic Oldroyd-B model) (JENSEN, 2013).

A generic non-Newtonian fluid can feature three types of characteristics (as shown in Fig. 2.1):

- Stress-dependence: The viscosity changes when the fluid is under different stress levels. It can be given as: shear-thinning (*pseudoplastic* behavior, in which the viscosity is higher at lower viscous shear rates, such as in blood (CHO; KENSEY, 1991), activated sludge (GARAKANI *et al.*, 2011) and ketchup (BAYOD *et al.*, 2008)), shear-thickening (*dilatant* behavior, in which the viscosity is lower at lower viscous shear rates, such as in the mixture of corn starch and water) or Bingham plastic/pseudoplastic (such as in concrete (FERRARIS; DE LARRARD, 1998));
- Viscoelasticity: The fluid exhibits viscous and solid elastic behaviors when under deformation, in such a way that the shear stress is expressed in a time-dependent form (*differential* (depending on the time derivatives of $\boldsymbol{\epsilon}$), *rate* (depending on the time derivatives of $\boldsymbol{\tau}$ and $\boldsymbol{\epsilon}$) or *integral* (depending on past events)) (QUARTERONI *et al.*, 2000) (such as in a Bogers fluid (JENSEN, 2013)). Therefore, viscoelasticity is able to model creep, stress relaxation and hysteresis;
- Time-dependence: The viscosity changes with time when under a given load. It can be given as: thixotropy (viscosity decreasing with time) or rheopecty (viscosity increasing with time) (such as in colloidal and particle suspensions) (MCARDLE *et al.*, 2012; BARNES, 1997).

Figure 2.1 – Possible behaviors of non-Newtonian fluids.



Source: Author.

In particular, the non-Newtonian fluid in a VAD (Ventricular Assist Device) is blood, having a rheology that has been extensively analyzed (CHO; KENSEY, 1991; QUARTERONI *et al.*, 2000), and features applications in the design of medical devices (SLAUGHTER *et al.*, 2010; ZHANG; LIU, 2015), and has even been used in topology optimization by various authors (PINGEN; MAUTE, 2010; ROMERO; SILVA, 2017; ZHANG; LIU, 2015; HYUN *et al.*, 2014; KIAN, 2017; ZHANG *et al.*, 2016a). The modeling of blood flow is described in the next section.

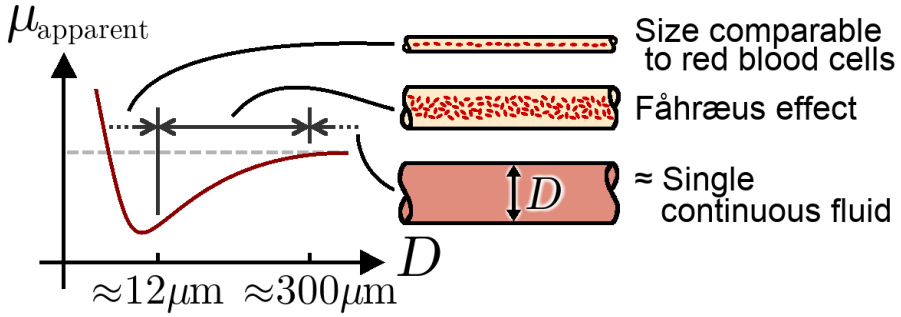
2.1.2.1 Modeling of blood flow

Blood is a biochemical suspension of different particles in an aqueous solution, being composed of plasma, RBCs (Red Blood Cells, erythrocytes, white blood cells (leukocytes), platelets (thrombocytes), lipoproteins, ions etc (BEHBAHANI *et al.*, 2009; QUARTERONI *et al.*, 2000; ANAND; RAJAGOPAL, 2017). As mentioned in Section 1.1.1, blood may be assumed as incompressible, with a density (ρ) of 1056 kg/m^3 (HINGHOFER-SZALKAY; GREENLEAF, 1987). According to Quarteroni *et al.* (2000) and Vlachopoulos *et al.* (2011), RBCs have the largest influence in blood rheology, since their volume concentration, which is about 45% (BEHBAHANI *et al.*, 2009; CHO; KENSEY, 1991), is much higher than the volume concentration of white blood cells and thrombocytes, which are about 1% (BEHBAHANI *et al.*, 2009). The plasma, which has a volume concentration of about 55% (BEHBAHANI *et al.*, 2009), should behave as a Newtonian fluid except when air-plasma interfaces are formed, which may lead to the formation of a denatured protein layer at the interface (VLACHOPOULOS *et al.*,

2011; WAYLAND, 1967). RBCs are deformable and their physicochemical properties vary through time (QUARTERONI *et al.*, 2000), which gives rise to the following characteristics (rheological behavior) of blood flow (BEHBAHANI *et al.*, 2009): shear-thinning (*pseudoplasticity*), viscoelasticity, and thixotropy, which are shown in Fig. 2.1. According to Quarteroni *et al.* (2000), the shear-thinning effect in blood is due to the formation of macroaggregates (called *rouleaux*) at low strain rates. At higher strain rates, these aggregates should separate, increasing the importance of the RBC deformation in shear-thinning. Viscoelasticity in blood is due to the fact that younger RBCs can deform and aggregate more than older RBCs (VLACHOPOULOS *et al.*, 2011). Thixotropy is due to time changes in structural arrangements at the microscopic level (ANAND; RAJAGOPAL, 2017; THURSTON, 1979; MCMILLAN *et al.*, 1986).

There are limits to which blood can be considered to be a single continuous fluid. Near walls, there is a thin layer composed of plasma, without any RBCs. Considering the case of blood flowing inside a tube, when the diameter is less than 300 μm (0.3 mm) (VLACHOPOULOS *et al.*, 2011), this separation becomes significant (Fåhræus effect), clearly leading to a two-phase flow of only plasma near the walls and plasma with RBCs near the core (SECOMB, 2016). This decreases the apparent viscosity (Fåhræus-Lindqvist effect) (QUARTERONI *et al.*, 2000). When the diameter of the tube is comparable to the size of RBCs (such as about 12 μm or smaller (QUARTERONI *et al.*, 2000; VLACHOPOULOS *et al.*, 2011; REINKE *et al.*, 1987; CHEBBI, 2015)), blood separates into the flow of one fluid (plasma) and deformable cells (RBCs) (FEDOSOV *et al.*, 2014), leading to complicating factors (REINKE *et al.*, 1987) such as microcirculation effects (QUARTERONI *et al.*, 2000; WAYLAND, 1967). Fig. 2.2 illustrates the limit of the continuum hypothesis for blood flow inside tubes of different diameters, in terms of the change in apparent viscosity.

Figure 2.2 – Limit of the continuum hypothesis for blood flow inside tubes of different diameters.



Source: Author.

In blood flow, the *Virchow's triad* (as mentioned in Section 1.1.1.3), gives the conditions for the formation of clotting (thrombus). When clotting happens, biochemical changes lead to the formation of a new material obstructing the blood flow, which features a viscosity that is much higher than the blood viscosity (ANAND; RAJAGOPAL, 2017). Therefore, the modeling of such phenomenon rests on time-dependent equations based on reaction, diffusion, convection, and spatial distribution of enzymes (ANAND; RAJAGOPAL, 2017).

The study performed by Gijsen *et al.* (1999) showed that the main contributor to the blood behavior should be the shear-thinning effect (which is time-independent). There are various models that can be used in order to account for the non-Newtonian shear-thinning effect (CHO; KENSEY, 1991; BIRD *et al.*, 1987), such as the power-law model, the Casson model, the modified Cross model (also called *Bird-Carreau law* (QUARTERONI *et al.*, 2000)), and the Carreau-Yasuda model (also called *Bird-Carreau-Yasuda model* in OpenFOAM®). According to Hyun *et al.* (2014), the power-law model is less suitable for describing shear-thinning than the Carreau-Yasuda model. In fact, Leondes (2000) mentions that the power law model should be valid only for a small interval of viscous shear rates (between 1 and 100 s^{-1}) – that is, it would only be adequate for the region in which the non-Newtonian fluid behavior starts becoming more pronounced. Also, the power-law model does not converge to the Newtonian viscosity for larger viscous shear rates.

Gijsen *et al.* (1999) mentions that the Casson and Carreau-Yasuda models should be able to accurately predict velocity distributions. However, the U-tube viscosimeter experiments performed by Pratumwal *et al.* (2017) indicate that the Carreau-Yasuda model fits better the experimental results than the Casson model. In fact, according to Leondes (2000), the Casson model is not correct for low viscous shear rates (below 1 s^{-1}), since it does not consider the effect of the dynamic viscosity achieving a maximum value. In order to account for such effect, the *modified Casson model* (*Quemada model*) (LEONDES, 2000) was developed, leading it to a behavior that resembles the Carreau-Yasuda and modified Cross models. According to Abraham *et al.* (2005), the modified Cross model is equivalent to the Carreau-Yasuda model by choosing the parameters accordingly. Since the Carreau-Yasuda model seems to represent well the rheological properties of blood and also offers high flexibility for adjusting experimental curves, it is the shear-thinning model selected for this work. The Carreau-Yasuda model is given by

(CHO; KENSEY, 1991; BIRD *et al.*, 1987)

$$\mu(\dot{\gamma}_{\mathrm{m}}) = \mu_{\infty} + (\mu_0 - \mu_{\infty})[1 + (\lambda\dot{\gamma}_{\mathrm{m}})^a]^{\frac{n-1}{a}} \tag{2.11}$$

where $\dot{\gamma}_{\mathrm{m}}$ is the viscous shear rate magnitude (also called *viscous scalar shear rate*) (ABRAHAM *et al.*, 2005), λ is a time constant (*characteristic time*), n is an exponential factor, a is the Yasuda coefficient, μ_0 is the maximum (*low shear rate*) dynamic viscosity and μ_{∞} is the minimum (*Newtonian*) dynamic viscosity.

The viscous shear rate magnitude ($\dot{\gamma}_{\mathrm{m}}$) is a generalization of the expression of the simple 2D shear flow (i.e., Newton's law of viscosity), which is given by $\tau_{xy} = \mu\frac{\partial v_x}{\partial y} = \mu\dot{\gamma}_{xy}$. Thus, the viscous shear stress magnitude (*viscous scalar shear stress*, τ_{m}) and the viscous shear rate magnitude (*viscous scalar shear rate*, $\dot{\gamma}_{\mathrm{m}}$) are given by (LAI *et al.*, 2009; TESCH, 2013; ARORA *et al.*, 2004)

$$\begin{aligned} \tau_{\mathrm{m}} &= \mu\dot{\gamma}_{\mathrm{m}} \\ \dot{\gamma}_{\mathrm{m}} &= \sqrt{2\boldsymbol{\epsilon}\bullet\boldsymbol{\epsilon}} \end{aligned} \tag{2.12}$$

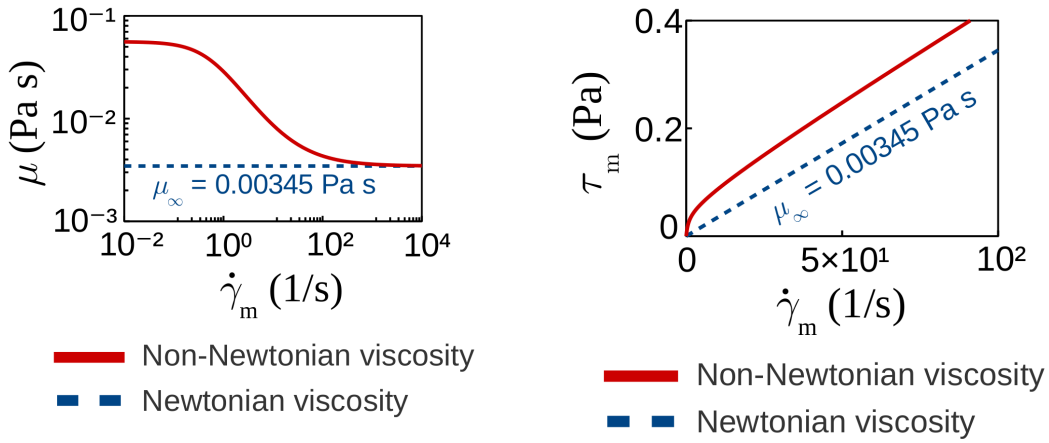
where $\boldsymbol{\epsilon} = \frac{1}{2}(\nabla\boldsymbol{v} + \nabla\boldsymbol{v}^T)$ is the viscous stress deformation tensor and " $\bullet$ " is the inner product as defined in Gurtin (1981).

According to Cho and Kensey (1991) and Pingen and Maute (2010), for blood, the constants in the Carreau-Yasuda model are $\lambda = 1.902$ s, $n = 0.22$, $a = 1.5$, $\mu_0 = 0.056$ Pa s and $\mu_{\infty} = 0.00345$ Pa s. The variation of the dynamic viscosity (μ) in function of the viscous shear rate magnitude ($\dot{\gamma}_{\mathrm{m}}$) and the rheological diagram are illustrated in Fig. 2.3. The corresponding Newtonian fluid model is shown in dashed lines, with a constant viscosity of $\mu = \mu_{\infty} = 0.00345$ Pa s.

Figure 2.3 – Carreau-Yasuda model for blood flow.

(a) Variation of the non-Newtonian viscosity (μ) with the viscous shear rate magnitude ($\dot{\gamma}_{\mathrm{m}}$).

(b) Rheological diagram.



Source: Author (ALONSO *et al.*, 2020).

As shown by Bappoo *et al.* (2017), the Carreau-Yasuda model fails in taking into account the Fåhræus-Lindqvist effect (described in Section 2.1.2.1), therefore it should not adequate for modeling tubes with a diameter less than 300 μm (0.3 mm). According to Abraham *et al.* (2005), the Newtonian assumption should be valid when the viscous shear rates are high. Also, from Boyd *et al.* (2007) and Vlachopoulos *et al.* (2011), it should be valid for tubes with large diameters when compared to the RBC size.

According to Vlachopoulos *et al.* (2011), the viscosity increases for higher hematocrits (Ht, percentage of volume occupied by RBCs in the total volume of blood), and the non-Newtonian properties are apparent for hematocrits higher than 10%. This dependency is shown by Walburn and Schneck (1976) and Yeow *et al.* (2002) in the form of adjustments to the shear-thinning models for blood. Since, for a healthy person, $\mathrm{Ht} = 45\%$ (ARORA *et al.*, 2006b; NAM *et al.*, 2011; BEHBAHANI *et al.*, 2009; CHO; KENSEY, 1991), the non-Newtonian behavior should not be ignored in human blood flow.

2.1.3 **Turbulence modeling**

When considering higher speed fluid flows (i.e., higher Reynolds numbers), it is possible that the fluid flow behavior changes to a turbulent behavior. A turbulent behavior is characterized for being chaotic, diffusive, dissipative and intermittent (SAAD,

2007), and is present in most flows in nature. In fact, as mentioned in Section 1.1.1.4, both laminar and turbulent flows may be considered for modeling VADs. For modeling the turbulent behavior, there are essentially three approaches: DNS (Direct Numeric Simulation) (ORSZAG, 1970), LES (Large Eddy Simulation) (SMAGORINSKY, 1963; DEARDORFF, 1970), and RANS (Reynolds-Averaged Navier-Stokes) (REYNOLDS, 1895). The first approach (DNS) implies considering the Navier-Stokes equations with a mesh resolution that is capable of considering the smallest scale vortices, as well as a sufficiently small time step, which pose a high computational cost, while the second approach (LES) poses a somewhat smaller computational cost due to it filtering smaller scale vortices. However, the RANS approach poses a lower computational cost in relation to DNS and LES, due to it considering statistical time-averaging, which leads to the possibility of considering a coarser mesh in RANS with respect to DNS/LES (CELIK, 2003).

In terms of turbulence modeling, eqs. (2.9) and (2.14) are changed to consider $(\boldsymbol{T} + \boldsymbol{T}_R)$ (i.e., including the Reynolds (turbulent) stress tensor) instead of $\boldsymbol{T}$, and the state variables definition become that of statistical time-averages. The resulting equations become:

$$\nabla \bullet \boldsymbol{v} = 0 \tag{2.13}$$

$$\rho \nabla \boldsymbol{v} \bullet \boldsymbol{v} = \nabla \bullet (\boldsymbol{T} + \boldsymbol{T}_R) + \rho \boldsymbol{f} - 2\rho(\boldsymbol{\omega} \wedge \boldsymbol{v}) - \rho \boldsymbol{\omega} \wedge (\boldsymbol{\omega} \wedge \boldsymbol{r}) + \boldsymbol{f}_r(\alpha) \tag{2.14}$$

where $\boldsymbol{T}_R$ is the Reynolds (turbulent) stress tensor given by:

$$\boldsymbol{T}_R = \mu_{\mathrm{T}}(\nabla \boldsymbol{v} + \nabla \boldsymbol{v}^T) \tag{2.15}$$

where μ_{T} is the turbulent dynamic viscosity (i.e., the flow parameter which accounts for the statistical time-averaged effect of turbulence in the stress tensor). It can be mentioned that eq. (2.15) actually has one more term (*isotropic turbulence term*). However, this term is non-existent in one-equation turbulence models, and, even when it does exist, it is sometimes neglected due to its small magnitude, such as in the default OpenFOAM® implementations for the k-ε and k-ω models.

In the following sections, two one-equation turbulence models are presented: the Spalart-Allmaras model and the Wray-Agarwal model (WA2018).

2.1.3.1 Spalart-Allmaras turbulence model

The Spalart-Allmaras model (SPALART; ALLMARAS, 1994; BUENO-OROVIO *et al.*, 2012; WILCOX, 2006) is a single-equation turbulence RANS model, which is said to be adequate for mild boundary layer separations (ANSYS, 2006). Particularly, according to Bardina *et al.* (1997), the Spalart-Allmaras model does not require a finer mesh resolution near walls in wall-bounded flows as two-equation turbulence models (such as the k-ε and k-ω models), and shows good convergence for simpler flows. Also, it is said to show improvements in the prediction of fluid flows under adverse pressure gradients (when the pressure increases towards the outlet) when compared to the standard k-ε and k-ω models (BARDINA *et al.*, 1997). There are various modifications that have been proposed in the Spalart-Allmaras model along the years (NASA, 2019). In this work, the modifications that are considered are based in the OpenFOAM® (OPENFOAM FOUNDATION, 2020) implementation. An additional term based on Yoon (2016), Dilgen *et al.* (2018), and Papoutsis-Kiachagias and Giannakoglou (2016) is included in order to take the effect of the modeled solid material (of topology optimization) into account. This way, the Spalart-Allmaras model is given by (OPENFOAM FOUNDATION, 2020; ALONSO *et al.*, 2021):

$$\mu_{\mathrm{T}} = \rho f_{v1} \tilde{\nu}_{\mathrm{T}} \tag{2.16}$$

$$\begin{aligned} \rho \boldsymbol{v} \bullet \nabla \tilde{\nu}_{\mathrm{T}} = & \underbrace{c_{b1} \rho \tilde{S} \tilde{\nu}_{\mathrm{T}}}_{\text{Production}} + \underbrace{\left[-c_{w1} f_w \rho \left(\frac{\tilde{\nu}_{\mathrm{T}}}{\ell_w} \right)^2 \right]}_{\text{Destruction}} + \underbrace{\frac{1}{\sigma} \nabla \bullet (\rho(\nu + \tilde{\nu}_{\mathrm{T}}) \nabla \tilde{\nu}_{\mathrm{T}})}_{\text{Diffusion (conservative)}} \\ & + \underbrace{\frac{c_{b2}}{\sigma} \rho \nabla \tilde{\nu}_{\mathrm{T}} \bullet \nabla \tilde{\nu}_{\mathrm{T}}}_{\text{Diffusion (non-conservative)}} + \underbrace{\left[-\lambda_{\tilde{\nu}_{\mathrm{T}}} f_{r,v}(\alpha) \tilde{\nu}_{\mathrm{T,mat}} \right]}_{\substack{\text{Attenuation of turbulence} \\ \text{in the porous medium}}} \end{aligned} \tag{2.17}$$

where $\tilde{\nu}_{\mathrm{T}}$ is the auxiliary turbulent viscosity of the Spalart-Allmaras model, $f_{r,v}(\alpha)$ is the proportional factor of the resistance force of the porous medium ($\boldsymbol{f}_r(\alpha) = f_{r,v}(\alpha)\boldsymbol{v}_{\mathrm{mat}}$), $\tilde{\nu}_{\mathrm{T,mat}} = \tilde{\nu}_{\mathrm{T}} - \tilde{\nu}_{\mathrm{T,wall}}$ is the auxiliary turbulent viscosity in relation to its *wall value* ($\tilde{\nu}_{\mathrm{T,wall}}$, which is assumed as equal to 0 m^2/s), and $\lambda_{\tilde{\nu}_{\mathrm{T}}}$ is an adjustable parameter for the intensity of the attenuation of turbulence inside the solid material (it can be chosen, for

example, as $\lambda_{\tilde{\nu}_\mathrm{T}} = 1$). The other terms of eq. (2.17) are specified as follows:

$$
\begin{gathered}
c_{b1} = 0.1355,\ c_{b2} = 0.6220,\ c_{v1} = 7.1,\ \sigma = \frac{2}{3},\ f_\Omega = 0.3 \\
c_{w1} = \frac{c_{b1}}{\kappa_{vk}^2} + \frac{1 + c_{b2}}{\sigma},\ c_{w2} = 0.3,\ c_{w3} = 2,\ \chi = \frac{\tilde{\nu}_\mathrm{T}}{\nu},\ \tilde{S} = \max\left[S + \frac{\tilde{\nu}_\mathrm{T}}{\kappa_{vk}^2 \ell_w^2} f_{v2},\ f_\Omega \Omega_\mathrm{m}\right] \\
S = \Omega_\mathrm{m},\ \Omega_\mathrm{m} = \sqrt{2\boldsymbol{\Omega}\bullet\boldsymbol{\Omega}},\ \boldsymbol{\Omega} = \frac{1}{2}(\nabla \boldsymbol{v} - \nabla \boldsymbol{v}^T),\ f_{v1} = \frac{\chi^3}{\chi^3 + c_{v1}^3},\ f_{v2} = 1 - \frac{\chi}{1 + \chi f_{v1}} \\
f_w = g\left(\frac{1 + c_{w3}^6}{g^6 + c_{w3}^6}\right)^{1/6},\ g = r_i + c_{w2}(r_i^6 - r_i),\ r_i = \min\left[\frac{\tilde{\nu}_\mathrm{T}}{\tilde{S}_r \kappa_{vk}^2 \ell_w^2}, 10\right],\ \tilde{S}_r = \max\left[\tilde{S}, 10^{-6}\right]
\end{gathered}
\tag{2.18}
$$

where $\kappa_{vk} = 0.41$ is the von Kármán constant, ℓ_w is the wall distance, and $\nu = \frac{\mu}{\rho}$ is the kinematic viscosity.

In fluid topology optimization, the walls change according to the distribution of the pseudo-density (α), which means that the wall distance (ℓ_w) also changes accordingly. Thus, in order to consider such changes in the simulation and in the adjoint model, it is necessary to consider the solution of, for example, a modified Eikonal equation (YOON, 2016) or a stabilized Eikonal equation (SÁ *et al.*, 2021). By considering the modified Eikonal equation from Yoon (2016),

$$
\ell_w = \frac{1}{G} - \frac{1}{G_0},\ G_0 = \frac{1}{\ell_\mathrm{ref}} \tag{2.19}
$$

$$
\underbrace{\nabla G \bullet \nabla G}_{\substack{\text{From the original} \\ \text{Eikonal equation}}} + \underbrace{\sigma_w G(\nabla^2 G)}_{\substack{\text{Elliptic diffusion} \\ \text{for alleviating} \\ \text{non-linearities}}} = \underbrace{(1 + 2\sigma_w)}_{\substack{\text{For satisfying} \\ \text{inverse linear} \\ \text{behavior}}} \underbrace{G^4}_{\substack{\text{From the original} \\ \text{Eikonal equation}}} + \underbrace{\gamma(\alpha)(G - G_0)}_{\substack{\text{Porous medium} \\ \text{penalization}}} \tag{2.20}
$$

where G is the reciprocal wall distance, ℓ_ref is a reference value for the wall distance (which leads ℓ_w to emphasize objects that are larger than it, and can be chosen, for example, as the maximum size of the elements of the mesh (largest of the maximum distances between two vertices of an element)), $\gamma(\alpha)$ is the wall penalization, which varies according to the pseudo-density (α) in order to consider the presence of a wall changing during the topology optimization (Section 2.5.1.6), and σ_w is a relaxation factor for the wall distance computation.

2.1.3.2 Wray-Agarwal turbulence model

The Wray-Agarwal turbulence model is a single-equation turbulence RANS model which consists of a combination of the advantages of the near-wall modeling from the

k-ω model with the freestream modeling from the k-ε model (WRAY; AGARWAL, 2015), being also partly based on the SST k-ω model (WRAY; AGARWAL, 2015). Wray and Agarwal (2015) show that the Wray-Agarwal turbulence model leads to more accurate boundary layer separation predictions than the Spalart-Allmaras model, and that it is also competitive with the SST k-ω model for wall-bounded flows. Throughout the years, several evaluations, improvements and variations have been developed (HAN *et al.*, 2015; WRAY; AGARWAL, 2016; ZHANG *et al.*, 2016; HAN *et al.*, 2017; HAN *et al.*, 2018). Particularly in this work, the 2018 version (referred in Han *et al.* (2018) as WA2018) is considered. The main advantage of the 2018 version is that it does not rely on the computation of the wall distance. Not needing to compute the wall distance is advantageous in a topology optimization point of view, because the wall distance computation requires an additional penalization term (YOON, 2016) in order to account for the modeled solid material, which needs to be calibrated (i.e., adequately chosen) for obtaining the optimized topology. An additional term to account for the attenuation of turbulence in the porous medium is included in this work by re-deducing the Wray-Agarwal model equations while including the attenuation of turbulence in the k-ω model equations (in a similar fashion as Yoon (2016), Papoutsis-Kiachagias and Giannakoglou (2016), and Dilgen *et al.* (2018)). Therefore, the Wray-Agarwal model (WA2018) (HAN *et al.*, 2018) modified for topology optimization becomes (ALONSO *et al.*, 2022):

$$\mu_{\mathrm{T}} = \rho f_{\mu} R_{\mathrm{T}} \tag{2.21}$$

$$\begin{aligned} \rho \boldsymbol{v} \bullet \nabla R_{\mathrm{T}} = & \underbrace{\nabla \bullet \left[(\sigma_R \rho R_{\mathrm{T}} + \mu) \nabla R_{\mathrm{T}} \right]}_{\substack{\text{Turbulence transport by} \\ \text{viscous and turbulent stresses}}} \underbrace{+ \rho C_1 R_{\mathrm{T}} S}_{\text{Turbulence production}} \underbrace{+ f_1 C_{1,k\text{-}\omega} \rho \frac{R_{\mathrm{T}}}{S} \nabla R_{\mathrm{T}} \bullet \nabla S}_{\substack{\text{Near-wall (“}k\text{-}\omega\text{”)} \\ \text{turbulence destruction}}} \\ & \underbrace{- \rho (1 - f_1) \min \left[C_{2,k\text{-}\varepsilon} R_{\mathrm{T}}^2 \left(\frac{\nabla S \bullet \nabla S}{S^2} \right), \, C_m \nabla R_{\mathrm{T}} \bullet \nabla R_{\mathrm{T}} \right]}_{\text{Freestream (“}k\text{-}\varepsilon\text{”) turbulence destruction}} \underbrace{- \lambda_{R_{\mathrm{T}}} f_{r,v}(\alpha) R_{\mathrm{T}}}_{\substack{\text{Turbulence attenuation} \\ \text{in the porous medium}}} \end{aligned} \tag{2.22}$$

where R_{T} is the undamped eddy (turbulent) viscosity, and $\lambda_{R_{\mathrm{T}}}$ is an adjustable parameter for the intensity of the attenuation of turbulence inside the modeled solid material. The

other terms of eq. (2.22) are specified as follows (HAN *et al.*, 2018):

$$
\begin{aligned}
&\boldsymbol{S} = \frac{1}{2}(\nabla \boldsymbol{v} + \nabla \boldsymbol{v}^T),\ S = \sqrt{2\boldsymbol{S}\bullet\boldsymbol{S}},\ \boldsymbol{W} = \frac{1}{2}(\nabla \boldsymbol{v} - \nabla \boldsymbol{v}^T),\ W = \sqrt{2\boldsymbol{W}\bullet\boldsymbol{W}} \\
&f_\mu = \frac{\chi^3}{\chi^3 + c_w^3},\ \chi = \frac{R_\mathrm{T}}{\nu},\ c_w = 8.54,\ \eta = S \max\left[1,\ \left|\frac{W}{S}\right|\right],\ C_m = 8.0 \\
&\sigma_R = f_1(\sigma_{k\text{-}\omega} - \sigma_{k\text{-}\varepsilon}) + \sigma_{k\text{-}\varepsilon},\ \sigma_{k\text{-}\varepsilon} = 1.0,\ \sigma_{k\text{-}\omega} = 0.72 \\
&f_1 = \tanh(arg_1^4),\ arg_1 = \frac{\nu + R_\mathrm{T}}{2}\frac{\eta^2}{C_\mu\, k_T|_{\text{log-layer}}\, \omega_T|_{\text{log-layer}}} \\
&k_T|_{\text{log-layer}} = \frac{\nu_\mathrm{T} S}{\sqrt{C_\mu}},\ \omega_T|_{\text{log-layer}} = \frac{S}{\sqrt{C_\mu}},\ C_\mu = 0.09 \\
&C_1 = f_1(C_{1,k\text{-}\omega} - C_{1,k\text{-}\varepsilon}) + C_{1,k\text{-}\varepsilon},\ C_{2,k\text{-}\omega} = \frac{C_{1,k\text{-}\omega}}{\kappa_{vk}^2} + \sigma_{k\text{-}\omega},\ C_{2,k\text{-}\varepsilon} = \frac{C_{1,k\text{-}\varepsilon}}{\kappa_{vk}^2} + \sigma_{k\text{-}\varepsilon} \\
&C_{1,k\text{-}\omega} = 0.0829,\ C_{1,k\text{-}\varepsilon} = 0.1284
\end{aligned}
\tag{2.23}
$$

where $\kappa_{vk} = 0.41$ is the von Kármán constant, and $\nu = \frac{\mu}{\rho}$ is the kinematic viscosity.

It can be noticed that the term that accounts for the attenuation of turbulence in the porous medium in eq. (2.22) assumes that, inside a modeled solid material, $R_\mathrm{T} = 0$ m^2/s.

With respect to the additional parameter λ_{R_T}, it may be noticed that it is similar to the penalization parameters included in other turbulence models for topology optimization (YOON, 2016; DILGEN *et al.*, 2018; YOON, 2020). Although some references assume all additional penalization parameters as being equal to 1, this may not always be the best choice, since the topology optimization may behave better for a higher or a lower value. In fact, in the present work, the optimized topologies from the Appendices consider values that are higher than 1. Also, in the case of two-equation models, such as the k-ω model, it is unknown if the same coefficient should really be used for the k and ω equations. Experimentally, the turbulence coefficients of these equations are different, which means that these two equations should be probably penalized differently. This effect may be “shadowed” by highly penalizing both equations, but the problem should still remain and may possibly affect the topology optimization iterations. For the case of the Spalart-Allmaras model, it may be mentioned that the penalization parameter is chosen differently than 1 in Yoon (2016), and that the additional penalization parameter of the modified Eikonal equation has to be calibrated for the given problem and is normally not set as equal to 1 (YOON, 2016). In some problems, it may be better to consider a “stronger” modeled solid material wall, while it may be better to relax it in other cases. Moreso, depending on the distribution of the design variable, it may be necessary to

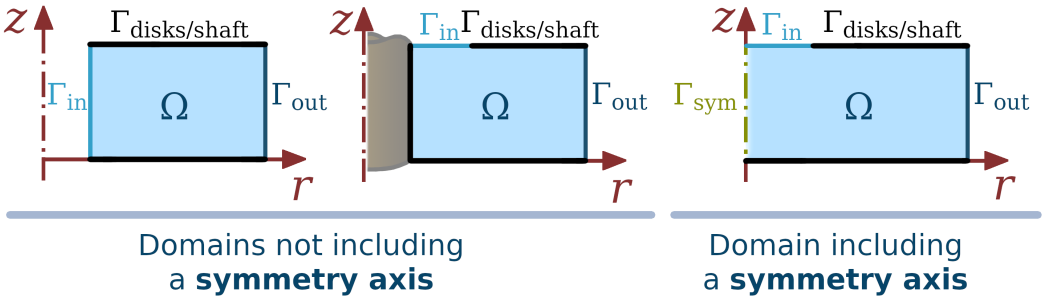
increase the *relaxation term* that is shown in Yoon (2016), to favor convergence.

2.1.4 **Boundary conditions**

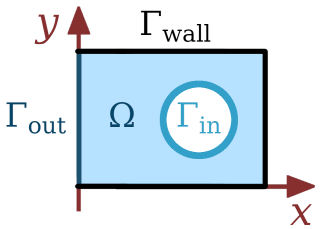
There are five types of boundaries considered in this work: inlet ($\Gamma_{\Pi,\text{in}}$), outlet ($\Gamma_{\Pi,\text{out}}$), static walls ($\Gamma_{\Pi,\text{wall}}$), disks/shaft ($\Gamma_{\Pi,\text{disks/shaft}}$), and symmetry axis ($\Gamma_{\Pi,\text{sym}}$). The Π subscript represents the fact that a *generic domain* is being considered. These boundaries are shown in Fig. 2.4 without the Π subscript, because they are illustrated in 2D/2D swirl flow cases (Γ_{in}, Γ_{out}, Γ_{wall}, $\Gamma_{\text{disks/shaft}}$). Note that, since the coupled system of equations is being considered for the finite element method, this means that a single boundary condition should be chosen for the velocity-pressure formulation on each boundary (instead of one boundary condition for pressure and one boundary condition for velocity).

Figure 2.4 – Types of boundaries in the computational domains.

(a) Tesla pump rotor design in the 2D swirl flow model.



(b) Volute design in the 2D model.



Source: Author.

2.1.4.1 Boundary conditions for the velocity-pressure formulation

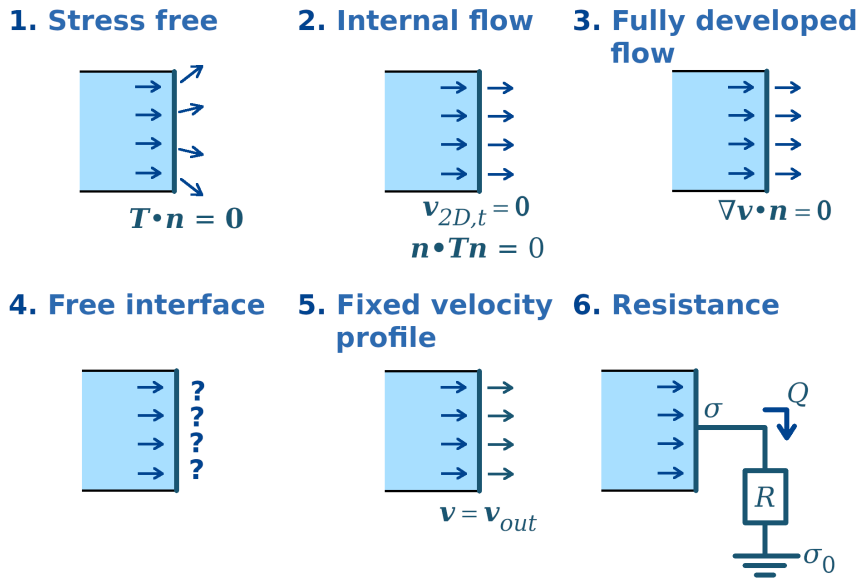
On the **inlet** ($\Gamma_{\Pi,\text{in}}$), the boundary condition is a **fixed velocity profile**, which may be in the form of, for example, a parabolic velocity profile (for the rotor) or a rotating

velocity profile (for the volute). It is given by the Dirichlet boundary condition:

$$\boldsymbol{v} = \boldsymbol{v}_{in} \text{ on } \Gamma_{\Pi,\text{in}} \tag{2.24}$$

On the **outlet** ($\Gamma_{\Pi,\text{out}}$), there are six main approaches that can be used: stress free, internal flow, fully developed flow, free interface, fixed velocity profile, and resistance. They are illustrated in Fig. 2.5 and described as follows.

Figure 2.5 – Some approaches for defining the boundary conditions for the outlet.



Source: Author.

1. Stress free (*traction free*) (QUARTERONI; ROZZA, 2003; DENG *et al.*, 2013b; HASUND, 2017; ALONSO *et al.*, 2018; ALONSO *et al.*, 2019): The outlet is assumed as being open to the atmosphere. According to Elman *et al.* (2005), this means that the pressure is weakly imposed as zero on the outlet. The stress free boundary condition is given by the Neumann boundary condition:

$$\boldsymbol{T}\bullet\boldsymbol{n} = \boldsymbol{0} \text{ on } \Gamma_{\Pi,\text{out}} \tag{2.25}$$

In fact, by substituting eq. (2.3) in eq. (2.25), it can be noticed that this boundary condition imposes that the shear stress on the outlet section ($(2\mu\boldsymbol{\epsilon})\bullet\boldsymbol{n}$) be equal to the pressure ($(2\mu\boldsymbol{\epsilon})\bullet\boldsymbol{n} = p\boldsymbol{n}$).

Furthermore, when the pressure level matters (such as for compressible flow), eq. (2.25) can be changed to impose a different pressure level (instead of zero), leading to a *fixed stress* boundary condition given by

$$\boldsymbol{T}\bullet\boldsymbol{n} = (-p_0\boldsymbol{I})\bullet\boldsymbol{n} \text{ on } \Gamma_{\Pi,\text{out}} \tag{2.26}$$

where p_0 is a given pressure level at the outlet. Notice that eq. (2.26) means that the pressure is weakly imposed on the outlet boundary as p_0, and also notice that $(2\mu\boldsymbol{\epsilon})\bullet\boldsymbol{n} = (p - p_0)\boldsymbol{n}$.

2. Internal flow (BARTH; CAREY, 2007; OTHMER, 2008; ALONSO *et al.*, 2018): In this case, two conditions are imposed on the outlet boundary. The first condition is that the velocity in the "2D plane" ($\boldsymbol{v}_{2D}$) is perpendicular to the outlet (Dirichlet boundary condition) (i.e., the tangential components of the velocity in the "2D plane" are zero ($\boldsymbol{v}_{2D,t} = \boldsymbol{0}$)). In the case of the 2D swirl flow model, the velocity in the "2D plane" is the radial-axial velocity ($\boldsymbol{v}_{2D} = \boldsymbol{v}_{rz} = (v_r,\ v_z)$); in the case of the 2D model, it is the velocity itself ($\boldsymbol{v}_{2D} = \boldsymbol{v} = (v_x,\ v_y)$). The second condition is that the normal stress is zero on the outlet boundary ($\boldsymbol{n}\bullet\boldsymbol{T}\boldsymbol{n} = 0$) (Neumann boundary condition). This last imposition means a weak imposition of pressure with a zero value on the boundary (BARTH; CAREY, 2007; ALONSO *et al.*, 2018). If the pressure on the outlet was strongly imposed (i.e., as a Dirichlet boundary condition), it is possible that it would, as opposed to the weak imposition of the pressure value (Neumann boundary condition), lead to sharp spikes of negative pressure right before the outlet, which would characterize an ill-posed boundary condition. The boundary conditions for this internal flow boundary condition are given as follows:

$$\boldsymbol{v}_{2D,t} = \boldsymbol{0} \text{ and } \boldsymbol{n}\bullet\boldsymbol{T}\boldsymbol{n} = 0 \text{ on } \Gamma_{\Pi,\text{out}} \tag{2.27}$$

3. Fully developed flow: It consists of assuming that the gradient of the flow that is normal to the interface is zero. The main limitation is that it requires that the flow is already fully developed before reaching the outlet, which is not always possible. The fully developed flow boundary condition is given by the Neumann boundary condition:

$$\nabla\boldsymbol{v}\bullet\boldsymbol{n} = \boldsymbol{0} \text{ on } \Gamma_{\Pi,\text{out}} \tag{2.28}$$

4. Free interface: In this case, nothing is imposed on the boundary terms of the weak form of the Navier-Stokes equations (equation (2.42)). The main problem of this approach is that the outlet lacks a boundary condition, which may leave the fluid flow problem ill-posed.

5. Fixed velocity profile (BORRVALL; PETERSSON, 2003; GUEST; PRÉVOST, 2006; DILGEN *et al.*, 2018): Since it corresponds a Dirichlet boundary condition on all velocity

components, the velocity boundary condition implies that the test function for velocity is zero ($\boldsymbol{w}_v = \mathbf{0}$). Therefore, there is no implication over the test function for pressure (w_p) and the reference pressure level should not have a defined value from the boundary conditions. Then, the reference pressure level would be determined from the initial guess of the problem. Since, in incompressible fluid flow problems, what matters is the variation of pressure, this should not be a problem. According to Hasund (2017), the fixed velocity profile can be used only if the outlet velocity profile can be determined beforehand, since the velocity profile should be a consequence of the fluid flow inside the computational domain. Therefore, imposing the outlet velocity profile may be excessively strong as a boundary condition. The fixed velocity profile is given by the Dirichlet boundary condition:

$$\boldsymbol{v} = \boldsymbol{v}_{out} \text{ on } \Gamma_{\Pi,\text{out}} \tag{2.29}$$

6. Resistance: According to Moon *et al.* (2014), the stress free boundary condition is normally used for its simplicity, but, when applied to blood flow, it would mean, for example, that the vessel is cut and exposed to atmospheric air conditions (i.e., as if it was "bleeding"). Thus, it neglects wave reflection from downstream vessels, due to the flow pulsatility and elasticity of blood vessels (MOON *et al.*, 2014). In order to consider the presence of a vessel outside the computational domain (and, therefore, wave reflection), impedance boundary conditions can be used, leading to more accurate simulations (MOON *et al.*, 2014). In the case of steady state fluid flow, the impedance boundary condition is simplified to the resistance boundary condition (VIGNON-CLEMENTEL *et al.*, 2006; ALVAREZ, 2016).

The vascular resistance of the systemic circulation (for LVAD) or the pulmonary circulation (for RVAD) can be estimated as:

$$R_{\text{vasc}} \approx \frac{\Delta p_{\text{circ}}}{Q} \tag{2.30}$$

where R_{vasc} is the vascular resistance, Δp_{circ} is the variation of pressure in the systemic or pulmonary circulation (depending if the analysis is of LVAD or RVAD), and Q is the flow rate.

According to Vignon-Clementel *et al.* (2006), the resistance value can be related to the normal stress, as a Neumann boundary condition, by substituting p from the equation below in the boundary term of the weak form of the Navier-Stokes equations

(eq. (2.42)):

$$\underbrace{-p + \boldsymbol{n}\bullet\boldsymbol{\tau}\boldsymbol{n}}_{\text{Normal stress } (\sigma)} - \underbrace{\sigma_0}_{\substack{\text{Reference value} \\ \text{for the normal stress}}} = R_{\text{vasc}} \underbrace{\int_{\Gamma_{\Pi,\text{in}}} \boldsymbol{v}\bullet\boldsymbol{n} d\Gamma_{\Pi,\text{in}}}_{\text{Flow rate } (Q)} \tag{2.31}$$

where $\boldsymbol{\tau} = 2\mu\boldsymbol{\epsilon}$ (see equation (2.3)) and σ_0 is assumed as 0. In some cases, $\boldsymbol{n}\bullet\boldsymbol{\tau}\boldsymbol{n}$ is negligible, leading to $\sigma \approx p$. Equation (2.31) can also be presented as follows, considering $\sigma_0 = 0$:

$$\underbrace{\boldsymbol{n}\bullet\boldsymbol{T}\boldsymbol{n}}_{\text{Normal stress } (\sigma)} = R_{\text{vasc}} Q \tag{2.32}$$

For simplicity, and also because it is numerically more stable (i.e., convergence is normally easier), the **outlet** ($\Gamma_{\Pi,\text{out}}$) is normally assumed with a **stress free** (*traction free*) boundary condition.

On **static walls** ($\Gamma_{\Pi,\text{wall}}$), the **no-slip condition** is imposed for the absolute velocity. It is given by the Dirichlet boundary condition:

$$\boldsymbol{v}_{\text{abs}} = \mathbf{0} \text{ on } \Gamma_{\Pi,\text{wall}} \tag{2.33}$$

where $\boldsymbol{v}_{\text{abs}}$ is given in eq. (2.4).

On **disks/shaft** ($\Gamma_{\Pi,\text{disks/shaft}}$), the **no-slip condition** is imposed for the rotating velocity. Since the reference frame is assumed to be rotating, it is given by the Dirichlet boundary condition for the relative velocity:

$$\boldsymbol{v} = \mathbf{0} \text{ on } \Gamma_{\Pi,\text{disks/shaft}} \tag{2.34}$$

On the **symmetry axis** ($\Gamma_{\Pi,\text{sym}}$), the boundary condition is given by zero radial velocity and zero derivatives in relation to the r coordinate:

$$v_r = 0 \text{ and } \frac{\partial v_r}{\partial r} = \frac{\partial v_\theta}{\partial r} = \frac{\partial v_z}{\partial r} = \frac{\partial p}{\partial r} = 0 \text{ on } \Gamma_{\Pi,\text{sym}} \tag{2.35}$$

2.1.4.2 Additional boundary conditions for the turbulence model

Additional boundary conditions are required according to the turbulence model being considered. The Spalart-Allmaras model is set for an imposed inlet turbulence

($\tilde{\nu}_{\mathrm{T},in}$), while the walls feature a constant value (set as $\tilde{\nu}_{\mathrm{T,wall}} = 0$ m^2/s) and the outlet considers a developed auxiliary turbulent viscosity (through zero normal flux):

$$\begin{aligned}
\tilde{\nu}_{\mathrm{T}} &= \tilde{\nu}_{\mathrm{T},in} \text{ on } \Gamma_{\mathrm{\Pi,in}} \\
\nabla\tilde{\nu}_{\mathrm{T}}\bullet\boldsymbol{n} &= 0 \text{ on } \Gamma_{\mathrm{\Pi,out}} \\
\tilde{\nu}_{\mathrm{T}} &= \tilde{\nu}_{\mathrm{T,wall}} \text{ on } \Gamma_{\mathrm{\Pi,wall}} \\
\tilde{\nu}_{\mathrm{T}} &= \tilde{\nu}_{\mathrm{T,wall}} \text{ on } \Gamma_{\mathrm{\Pi,disks/shaft}} \\
\frac{\partial\tilde{\nu}_{\mathrm{T}}}{\partial r} &= 0 \text{ on } \Gamma_{\mathrm{\Pi,sym}}
\end{aligned} \tag{2.36}$$

where the inlet values for the turbulent variable ($\tilde{\nu}_{\mathrm{T},in}$) may be given from the turbulence intensity (I_T) and the turbulence length scale (ℓ_T), as:

$$\tilde{\nu}_{\mathrm{T},in} = \sqrt{\frac{n_v}{2}} I_T \ell_T |\boldsymbol{v}_{\mathrm{abs},in}| \tag{2.37}$$

where $|\boldsymbol{v}_{\mathrm{abs},in}|$ is the absolute value of the velocity on the inlet, and n_v is the number of velocity components (for 2D, $n_v = 2$; for 2D axisymmetry and 3D, $n_v = 3$). It can be mentioned that eq. (2.37) may also be considered from a mean inlet velocity value ($\overline{|\boldsymbol{v}_{\mathrm{abs},in}|}$) instead of local inlet velocity values ($|\boldsymbol{v}_{\mathrm{abs},in}|$). The mean inlet velocity value would then be computed as:

$$\overline{|\boldsymbol{v}_{\mathrm{abs},in}|} = \frac{\int_{\Gamma_{\mathrm{\Pi,in}}} |\boldsymbol{v}_{\mathrm{abs},in}| d\Gamma_{\mathrm{\Pi,in}}}{\int_{\Gamma_{\mathrm{\Pi,in}}} d\Gamma_{\mathrm{\Pi,in}}} \tag{2.38}$$

The modified Eikonal equation is set for the following boundary conditions:

$$\begin{aligned}
\nabla G\bullet\boldsymbol{n} &= 0 \text{ on } \Gamma_{\mathrm{\Pi,in}} \\
\nabla G\bullet\boldsymbol{n} &= 0 \text{ on } \Gamma_{\mathrm{\Pi,out}} \\
G &= G_0 \text{ on } \Gamma_{\mathrm{\Pi,wall}} \\
G &= G_0 \text{ on } \Gamma_{\mathrm{\Pi,disks/shaft}} \\
\frac{\partial G}{\partial r} &= 0 \text{ on } \Gamma_{\mathrm{\Pi,sym}}
\end{aligned} \tag{2.39}$$

For the Wray-Agarwal model (WA2018), the boundary conditions are analogous to those presented in eqs. (2.36) and (2.37), but considered for R_{T} instead of $\tilde{\nu}_{\mathrm{T}}$.

2.1.5 **Boundary value problem**

By considering a generic case in which the 2D swirl flow domain may include a symmetry axis or not (i.e., not include or include a shaft), the boundary value problem

can be stated as follows, for laminar flow.

$$\begin{aligned}
\nabla \bullet \boldsymbol{v} &= 0 && \text{in } \Omega \\
\rho \nabla \boldsymbol{v} \bullet \boldsymbol{v} &= \nabla \bullet \boldsymbol{T} + \rho \boldsymbol{f} - 2\rho(\boldsymbol{\omega} \wedge \boldsymbol{v}) - \rho \boldsymbol{\omega} \wedge (\boldsymbol{\omega} \wedge \boldsymbol{r}) + \boldsymbol{f}_r(\alpha) && \text{in } \Omega \\
\boldsymbol{v} &= \boldsymbol{v}_{in} && \text{on } \Gamma_{\Pi,\text{in}} \\
\boldsymbol{v}_{\text{abs}} &= \boldsymbol{0} && \text{on } \Gamma_{\Pi,\text{wall}} \\
\boldsymbol{v} &= \boldsymbol{0} && \text{on } \Gamma_{\Pi,\text{disks/shaft}} \\
v_r = 0 \text{ and } \frac{\partial v_r}{\partial r} &= \frac{\partial v_\theta}{\partial r} = \frac{\partial v_z}{\partial r} = \frac{\partial p}{\partial r} = 0 && \text{on } \Gamma_{\Pi,\text{sym}} \\
\boldsymbol{T} \bullet \boldsymbol{n} &= 0 && \text{on } \Gamma_{\Pi,\text{out}}
\end{aligned} \tag{2.40}$$

When considering turbulence, $\boldsymbol{T}$ is substituted by $(\boldsymbol{T} + \boldsymbol{T}_R)$, and the additional differential equations from Section 2.1.3 need to be considered in eq. (2.40), as well as the boundary conditions presented in Section 2.1.4.2.

2.2 FINITE ELEMENT METHOD

In order to employ the Finite Element Method (FEM), it is necessary to define the weak form of the differential equations and the finite element modeling, which are described as follows.

2.2.1 **Weak formulation**

The weak form of the problem, first presented for the laminar flow case, is the strong form (differential equations) (eqs. (2.9) and (2.10)) solved approximately, in an integral form with weights (weighted-residual and Galerkin methods) with a reduced order of derivatives (by applying Gauss's divergence theorem). The reduced order reduces the continuity requirements of the state variables (i.e., lower order elements may be used) and also leads the Neumann boundary conditions to become transparent (i.e., easy to manipulate). Thus, the mixed (velocity-pressure) formulation is obtained as follows: eqs. (2.9) and (2.10) should be multiplied by test functions for pressure (w_p) and velocity (in 2D flow, $\boldsymbol{w}_v = (w_{v,x},\ w_{v,y})$; in 2D swirl flow, $\boldsymbol{w}_v = (w_{v,r},\ w_{v,\theta},\ w_{v,z})$), and integrated over the whole 3D domain ($\int_\Pi [\ \ ] d\Pi$), which is given by $d\Pi = d\Omega$ in 2D flow, and $d\Pi = 2\pi r d\Omega$ in 2D swirl flow. By also applying Gauss's divergence theorem in order to keep only first derivatives in the equations, contour terms appear ($\int_{\Gamma_\Pi} d\Gamma_\Pi$), which

are given by $d\Gamma_\Pi = d\Gamma$ in 2D flow, and $d\Gamma_\Pi = 2\pi r d\Gamma$ in 2D swirl flow. Thus, the following forms are obtained:

$$R_c = \int_\Pi [\nabla \bullet \boldsymbol{v}] w_p d\Pi \tag{2.41}$$

$$\begin{aligned} R_m = &\int_\Pi \left[\rho \nabla \boldsymbol{v} \bullet \boldsymbol{v} - \rho \boldsymbol{f} + 2\rho(\boldsymbol{\omega} \wedge \boldsymbol{v}) + \rho \boldsymbol{\omega} \wedge (\boldsymbol{\omega} \wedge \boldsymbol{r})\right] \bullet \boldsymbol{w}_v d\Pi + \int_\Pi \boldsymbol{T} \bullet (\nabla \boldsymbol{w}_v) d\Pi \\ &- \oint_{\Gamma_\Pi} (\boldsymbol{T} \bullet \boldsymbol{w}_v) \bullet \boldsymbol{n} d\Gamma_\Pi - \int_\Pi \boldsymbol{f}_r(\alpha) \bullet \boldsymbol{w}_v d\Pi \end{aligned} \tag{2.42}$$

where c stands for *continuity equation*, m stands for *linear momentum equation* (i.e., the Navier-Stokes equations), and $\boldsymbol{n}$ is the normal unit vector (in the 2D flow, $\boldsymbol{n} = (n_x,\ n_y)$; in 2D swirl flow, $\boldsymbol{n} = (n_r,\ 0,\ n_z)$). It can be noticed that, in the case of 2D swirl flow, the equations may be divided by 2π, since it is a constant multiplier.

Since the two test functions (w_p and $\boldsymbol{w}_v$) are independent from each other, eqs. (2.41) and (2.42) can be summed in order to form a single equation for the weak form, as

$$F = R_c + R_m = 0 \tag{2.43}$$

When considering turbulence, $\boldsymbol{T}$ is substituted by $(\boldsymbol{T} + \boldsymbol{T}_R)$, and the weak forms obtained from the strong forms (differential equations) from Section 2.1.3 become:

$$\begin{aligned} R_{SA} = &\int_\Pi \left[\rho \boldsymbol{v} \bullet \nabla \tilde{\nu}_\mathrm{T} - c_{b1} \rho \tilde{S} \tilde{\nu}_\mathrm{T} + c_{w1} f_w \rho \left(\frac{\tilde{\nu}_\mathrm{T}}{\ell_w}\right)^2 - \frac{c_{b2}}{\sigma} \rho \nabla \tilde{\nu}_\mathrm{T} \bullet \nabla \tilde{\nu}_\mathrm{T}\right] w_{\tilde{\nu}_\mathrm{T}} d\Pi \\ &+ \int_\Pi \frac{1}{\sigma} (\rho(\nu + \tilde{\nu}_\mathrm{T}) \nabla \tilde{\nu}_\mathrm{T}) \bullet \nabla w_{\tilde{\nu}_\mathrm{T}} d\Pi - \oint_{\Gamma_\Pi} \frac{1}{\sigma} \boldsymbol{n} \bullet (\rho(\nu + \tilde{\nu}_\mathrm{T}) \nabla \tilde{\nu}_\mathrm{T} w_{\tilde{\nu}_\mathrm{T}}) d\Gamma_\Pi \\ &- \int_\Pi \left[-\lambda_{\tilde{\nu}_\mathrm{T}} \kappa(\alpha) \tilde{\nu}_{\mathrm{T,mat}}\right] w_{\tilde{\nu}_\mathrm{T}} d\Pi \end{aligned} \tag{2.44}$$

$$\begin{aligned} R_w = &\int_\Pi \left[\nabla G \bullet \nabla G - (1 + 2\sigma_w) G^4\right] w_G d\Pi - \int_\Pi \left[(\nabla G) \bullet \nabla (\sigma_w G w_G)\right] d\Pi \\ &+ \oint_{\Gamma_\Pi} \boldsymbol{n} \bullet [(\nabla G)(\sigma_w G w_G)] d\Gamma_\Pi - \int_\Pi \left[\gamma(\alpha)(G\ -\ G_0)\right] w_G d\Pi \end{aligned} \tag{2.45}$$

$$\begin{aligned} R_{\mathrm{WA2018}} = &\int_\Pi \left[\rho \boldsymbol{v} \bullet \nabla R_\mathrm{T}\right] w_{R_\mathrm{T}} d\Pi + \int_\Pi \left[(\sigma_R \rho R_\mathrm{T} + \mu) \nabla R_\mathrm{T}\right] \bullet \nabla w_{R_\mathrm{T}} d\Pi \\ &- \oint_{\Gamma_\Pi} \boldsymbol{n} \bullet \left[(\sigma_R \rho R_\mathrm{T} + \mu) \nabla R_\mathrm{T}\right] w_{R_\mathrm{T}} d\Gamma_\Pi - \int_\Pi \rho C_1 R_\mathrm{T} S w_{R_\mathrm{T}} d\Pi \\ &- \int_\Pi f_1 C_{1,k\text{-}\omega} \rho \frac{R_\mathrm{T}}{S} \nabla R_\mathrm{T} \bullet \nabla S w_{R_\mathrm{T}} d\Pi \\ &+ \int_\Pi \rho(1 - f_1) \min\left[C_{2,k\text{-}\varepsilon} R_\mathrm{T}^2 \left(\frac{\nabla S \bullet \nabla S}{S^2}\right),\ C_m \nabla R_\mathrm{T} \bullet \nabla R_\mathrm{T}\right] w_{R_\mathrm{T}} d\Pi \\ &+ \int_\Pi \lambda_{R_\mathrm{T}} \kappa(\alpha) R_\mathrm{T} w_{R_\mathrm{T}} d\Pi \end{aligned} \tag{2.46}$$

where the subscripts SA, w and $\mathrm{WA2018}$ refer to the *Spalart-Allmaras* equation, the *wall distance* equation (modified Eikonal equation) and the Wray-Agarwal model (WA2018) equation, respectively. The test functions of the additional state variables ($\tilde{\nu}_\mathrm{T}$, G and R_T) are given by $w_{\tilde{\nu}_\mathrm{T}}$, w_G and w_{R_T}, respectively. Then, for the Spalart-Allmaras model, eq. (2.44) (Spalart-Allmaras model) may be included in eq. (2.43) in the same way R_c and R_m were included (i.e., summing), while eq. (2.45) (modified Eikonal equation) may also be included in the same way or may be included to be solved before $F = 0$, as $R_w = 0$, due to it not depending on any other state variable. For the Wray-Agarwal model, eq. (2.46) is included in eq. (2.43) in the same way that was described for the Spalart-Allmaras model.

2.2.2 **Finite element modeling**

For fluid flow, the coupling between the discretizations of the pressure and the velocity may result in instabilities and non-physical oscillations in the pressure (LANGTANGEN; LOGG, 2016; REDDY; GARTLING, 2010). This can be avoided by choosing a finite element that obeys the LBB (Ladyžhenskaya-Babuška-Brezzi) condition (GIRAULT; RAVIART, 2012; GUZMÁN *et al.*, 2013; BREZZI; FORTIN, 1991). Some examples of finite elements that are LBB-stable are Taylor-Hood elements, MINI elements and Crouzeix-Raviart elements (BARRENECHEA; WACHTEL, 2020; ARNOLD *et al.*, 1984; LAMICHHANE, 2014). When the element does not satisfy the LBB condition, it may be necessary to include stabilization, leading to *stabilized elements*. Another interesting type of element is the CD element, which, although not being LBB-stable (TERREL, 2010), can possibly lead to reasonable results even without any stabilization (LOGG *et al.*, 2012). The lowest order versions of these elements are represented in Fig. 2.6. The Taylor-Hood element's lowest degree version is given by a linear interpolation for pressure (*piecewise linear*, P_1, "CG1") and a quadratic interpolation for velocity (P_2, "CG2"). CD elements (Continuous velocity/Discontinuous pressure) feature the pressure interpolation with one degree less than in Taylor-Hood elements, which means that their lowest order degree version uses a discrete interpolation (*element-wise*, dP_0, "DG0") (BREZZI; FORTIN, 1991). MINI elements change the velocity interpolation by enriching a lower degree element (*piecewise linear*, P_1, "CG1") with bubble shape functions (B_3) (ARNOLD *et al.*, 1984; LOGG *et al.*, 2012). Crouzeix-Raviart elements consider a linear

interpolation for the velocity, but in a different nodal positioning (CR_1) (CROUZEIX; RAVIART, 1973). The last element (*stabilized*) relies on a linear interpolation for the velocity (*piecewise linear*, P_1), which demands, for stability, that a stabilization method be included in the finite element equations (REDDY; GARTLING, 2010), such as pressure (LOGG *et al.*, 2012; ELHANAFY *et al.*, 2017; LANGTANGEN *et al.*, 2002) or SUPG (Streamline Upwind Petrov Galerkin) (FRANCA, 1992) stabilizations.

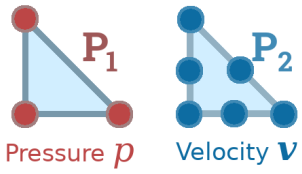
The most commonly used finite element is the Taylor-Hood element (LOGG *et al.*, 2012), which is considered to be very stable and provides 3rd order spatial accuracy for velocities (VARCHANIS *et al.*, 2019). It also results in smaller error than the other types of finite elements (LOGG *et al.*, 2012). However, due to the quadratic interpolation of the velocity, it can be quite computationally demanding. Since CD elements do not reduce the interpolation degree of the velocity, the reduction in computational cost is relatively not much. MINI elements show relatively accurate results (LANGTANGEN; LOGG, 2016). Since Crouzeix-Raviart elements do not feature nodes on the edges of the finite elements, they are non-conforming (SHI; WANG, 2014; SHI, 2002); also, Crouzeix-Raviart elements show poor accuracy in simulations (LANGTANGEN; LOGG, 2016). Stabilized elements include stabilization parameters which may have to be calibrated for the problem that is being solved.

It is also possible to "dodge" the need of satisfying the LBB condition by using the Least-Squares Method (PONTAZA; REDDY, 2006) instead of the Galerkin formulation used in this work. However, it introduces an additional computational cost, since a *derived variable* (*vorticity vector*, $\nabla \wedge \boldsymbol{v} = \boldsymbol{\xi}$) needs to be included as a new state variable in order to avoid higher order derivatives in the formulation. Another method for stability of the velocity-pressure formulation is the penalized approach (Scott-Vogelius) (SCOTT; VOGELIUS, 1985; COUSINS *et al.*, 2013; LANGTANGEN; LOGG, 2016), which changes the format and solution method of the equations and iteratively solves for only one state variable (velocity). This single variable requires higher order interpolation ($\geqslant P_4$) (LANGTANGEN; LOGG, 2016), which increases the computational cost. One more method is the Discontinuous Galerkin formulation, in which the velocity and pressure interpolations are discrete ("DG"). However, it is a nonconforming method, requires that the fluid flow equations be adequately rewritten for modeling the element-element interfacing, and may suffer difficulties that may require the use of stabilization (LI, 2006). This formulation is similar to FVM (Finite Volume Method), since it would

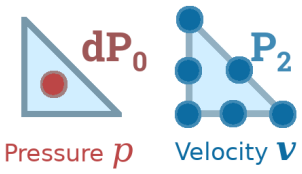
enforce flow continuity between the elements instead of the global continuity (as in the other FEM methods) during the iterations of the simulation.

Figure 2.6 – Some LBB-stable finite elements (lowest-order versions).

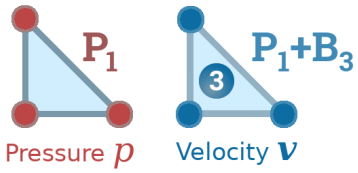
(a) Taylor-Hood element.



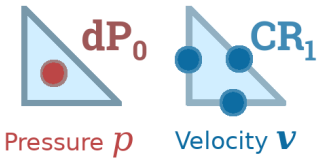
(b) CD element.



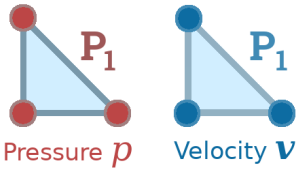
(c) MINI element.



(d) Crouzeix-Raviart element.



(e) Stabilized element.

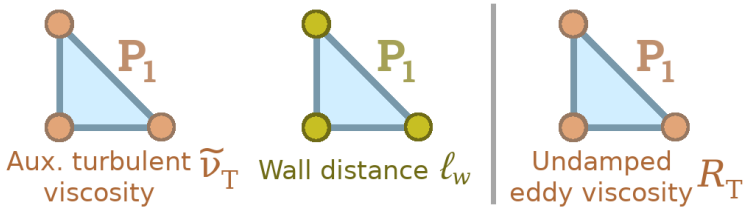


Source: Author.

Although the LBB condition has been shown to be valid for Stokes/Navier-Stokes flow (GIRAULT; RAVIART, 2012; GUZMÁN *et al.*, 2013; BREZZI; FORTIN, 1991), it still lacks a general proof for any constitutive equation and formulation (REDDY; GARTLING, 2010), such as a generic non-Newtonian fluid model. The work done by Galvin (2013) verifies the convergence rates for a non-Newtonian fluid modeled by the Cross model, which is similar to the Carreau-Yasuda model used in this work, using Taylor-Hood elements. In this work, Taylor-Hood and MINI elements are considered.

For the turbulence models, the additional state variables are included through linear interpolation (*piecewise linear*, P_1, “CG1”) (see Fig. 2.7).

Figure 2.7 – Finite element interpolation for the turbulent variables. The interpolation of the reciprocal wall distance (G) is indicated as ℓ_w, for the figure to be more generic – i.e., ℓ_w may be computed from other wall distance equations (YOON, 2016; SÁ *et al.*, 2021).



Source: Author.

2.3 PERFORMANCE AND CHARACTERIZATION QUANTITIES

In order to evaluate the performance of the fluid flow device and, more specifically, of a VAD, some performance quantities need to be defined together with how they are computed. The quantities that are defined in this section are:

- Energy dissipation, which is an indirect measure of the pressure head;
- Fluid power, which measures the necessary amount of power to pump the fluid;
- Vorticity, which measures the vortex formation (recirculation) in the fluid flow;
- Pressure head, which measures the transferred energy to the fluid flow;
- Isentropic efficiency, in order to measure the closeness to ideal operating conditions;
- Pressure coefficients, in order to dimensionlessly characterize the pressure increment of the fluid flow device;
- Static pressure rise, since blood flow requirements are normally expressed with the required static pressure rise.

Also, some specific dimensionless characterization parameters for the Tesla pump rotor, and the volute are presented. Some basic definitions required for the definitions of the performance quantities in this section are given as:

- (Volumetric) flow rate (Q):

$$Q = \int_{\Gamma_{\Pi,\mathrm{out}}} (\boldsymbol{v}_{\mathrm{abs}} \bullet \boldsymbol{n}) d\Gamma_{\Pi,\mathrm{out}} = -\int_{\Gamma_{\Pi,\mathrm{in}}} (\boldsymbol{v}_{\mathrm{abs}} \bullet \boldsymbol{n}) d\Gamma_{\Pi,\mathrm{in}} \tag{2.47}$$

- Variation of (static) pressure (Δp):

$$\Delta p = \overline{p}_{out} - \overline{p}_{in} = \frac{\int_{\Gamma_{\Pi,\text{out}}} p d\Gamma_{\Pi,\text{out}}}{\int_{\Gamma_{\Pi,\text{out}}} d\Gamma_{\Pi,\text{out}}} - \frac{\int_{\Gamma_{\Pi,\text{in}}} p d\Gamma_{\Pi,\text{in}}}{\int_{\Gamma_{\Pi,\text{in}}} d\Gamma_{\Pi,\text{in}}} \tag{2.48}$$

where $\overline{p}_{out}$ and $\overline{p}_{in}$ are the average pressures on the outlet and inlet, respectively.

It can be noticed that eq. (2.47) can be defined with the relative velocity $\boldsymbol{v}$, because $\boldsymbol{v}_{\text{abs}} \bullet \boldsymbol{n} = \boldsymbol{v} \bullet \boldsymbol{n}$ when the inlet/outlet surfaces are tangent to the rotating motion. This is the case for the 2D swirl flow model, because v_θ is always perpendicular to the the rz coordinate plane, and also for the 2D/3D pump model (ROMERO; SILVA, 2014; OKUBO *et al.*, 2021). It can be highlighted that $\boldsymbol{v} \bullet \boldsymbol{n} > 0$ on the outlet, and $\boldsymbol{v} \bullet \boldsymbol{n} < 0$ on the inlet.

Similar to eq. (2.48), the following equations may be defined for the dynamic and total (*stagnation*) pressures

- Variation of dynamic pressure (Δp_d):

$$\Delta p_d = \overline{p}_{d,out} - \overline{p}_{d,in} = \frac{\int_{\Gamma_{\Pi,\text{out}}} \left(\frac{\rho |\boldsymbol{v}_{\text{abs}}|^2}{2} \right) d\Gamma_{\Pi,\text{out}}}{\int_{\Gamma_{\Pi,\text{out}}} d\Gamma_{\Pi,\text{out}}} - \frac{\int_{\Gamma_{\Pi,\text{in}}} \left(\frac{\rho |\boldsymbol{v}_{\text{abs}}|^2}{2} \right) d\Gamma_{\Pi,\text{in}}}{\int_{\Gamma_{\Pi,\text{in}}} d\Gamma_{\Pi,\text{in}}} \tag{2.49}$$

- Variation of total (*stagnation*) pressure (Δp_T):

$$\Delta p_T = \overline{p}_{T,out} - \overline{p}_{T,in} = \frac{\int_{\Gamma_{\Pi,\text{out}}} \left(p + \frac{\rho |\boldsymbol{v}_{\text{abs}}|^2}{2} \right) d\Gamma_{\Pi,\text{out}}}{\int_{\Gamma_{\Pi,\text{out}}} d\Gamma_{\Pi,\text{out}}} - \frac{\int_{\Gamma_{\Pi,\text{in}}} \left(p + \frac{\rho |\boldsymbol{v}_{\text{abs}}|^2}{2} \right) d\Gamma_{\Pi,\text{in}}}{\int_{\Gamma_{\Pi,\text{in}}} d\Gamma_{\Pi,\text{in}}} \tag{2.50}$$

The variation of (static) pressure may be computed for the Tesla blood pump rotor, because it is normally evaluated for blood pumps. The total (*stagnation*) pressure may also be computed for the Tesla blood pump rotor, because the volute (which converts dynamic pressure into static pressure) is designed separately in this work.

2.3.1 **Energy dissipation**

The energy dissipation represents the amount of energy (in the form of power) that is dissipated in the fluid flow, and that may be derived from the Energy equation (1st Law of Thermodynamics) (WHITE, 2011; INCROPERA *et al.*, 2011; BIRD *et al.*, 2002). It was first used in fluid topology optimization by Borrvall and Petersson (2003) and has then been used in numerous other articles (EVGRAFOV, 2004; LIU *et al.*, 2011; ROMERO; SILVA, 2014; LIN *et al.*, 2015; ALONSO *et al.*, 2019). The energy dissipation in a rotating reference frame can be defined considering inertial effects, as defined in

Alonso *et al.* (2019), which is based on the energy dissipation defined in Borrvall and Petersson (2003). By also considering zero external body forces,

$$\Phi_{\mathrm{rel}} = \underbrace{\int_{\Pi} \left[\frac{1}{2}\mu(\nabla \boldsymbol{v} + \nabla \boldsymbol{v}^T)\bullet(\nabla \boldsymbol{v} + \nabla \boldsymbol{v}^T) \right] d\Pi}_{\text{Viscous effect}} \\ \underbrace{- \int_{\Pi} \boldsymbol{f}_r(\alpha)\bullet\boldsymbol{v} d\Pi}_{\text{Porous medium effect}} + \underbrace{\int_{\Pi} (2\rho(\boldsymbol{\omega}\wedge\boldsymbol{v}) + \rho\boldsymbol{\omega}\wedge(\boldsymbol{\omega}\wedge\boldsymbol{r}))\bullet\boldsymbol{v} d\Pi}_{\text{Inertial effect}} \tag{2.51}$$

Note that, when using the 2D swirl flow model, since $\boldsymbol{\omega} = \omega_0 \boldsymbol{e}_z$ and from eq. (2.7), the Coriolis term $(2\rho(\boldsymbol{\omega}\wedge\boldsymbol{v})\bullet\boldsymbol{v})$ is equal to zero. Also, when considering turbulence, μ from eq. (2.51) is substituted by $(\mu + \mu_{\mathrm{T}})$. When there is no reference frame rotation ($\omega = \mathbf{0}$), eq. (2.51) becomes the absolute energy dissipation: $\Phi_{\mathrm{rel}} = \Phi_{\mathrm{abs}}$.

It can be mentioned that, in the original formulation from Borrvall and Petersson (2003), which considered Stokes flow, the energy dissipation is equal to the functional that, when minimized, results in the solution of the Stokes equations for fluid flow. The only difference between the Stokes equations and the Navier-Stokes equations is that the convective term $(\rho\nabla\boldsymbol{v}\bullet\boldsymbol{v})$ is neglected – due to considering an extremely low Reynolds number ($\mathrm{Re} \ll 1$). Therefore, when energy dissipation is used as an objective function in topology optimization, it may enforce the formation of an optimized topology that can accommodate a “non-convective flow” from the inlet towards the outlet. Also, when considering the inertial effects in the formulation of the energy dissipation, the “convective flow” due to the reference frame should also be accommodated in the optimized topology.

The minimization of the relative energy dissipation from eq. (2.51) is closely related to the maximization of the pressure head, which would mean, for the case of a pump, a higher capability of pumping the fluid. This relationship can be derived from the Navier-Stokes equations multiplied (inner product) by the velocity vector ($\boldsymbol{v}$). Particularly, from the derivation performed in Alonso and Silva (2022b), a relative pressure head term (computed for relative velocity values) appears, which corresponds to the power balance considered in Okubo *et al.* (2021). Also, as mentioned in Section 1.1.1, energy dissipation and hemolysis are related (BLUESTEIN; MOCKROS, 1969; NAKAHARA; YOSHIDA, 1986).

2.3.2 **Fluid power**

The fluid power is the amount of power that is transferred between the fluid flow and the fluid device. It may be represented in two forms: as the power transferred from the fluid device to the fluid flow (*pump* power, P_f), and as the power transferred from the fluid flow to the fluid device (*turbine* power, $P'_f = -P_f$). Its expression may be derived from the integral form of the angular momentum equation (MUNSON *et al.*, 2009) as

$$\frac{\partial}{\partial t}\int_{\Pi}(\boldsymbol{r}\wedge\boldsymbol{v}_{\text{abs}})\rho d\Pi + \int_{\Gamma_\Pi}(\boldsymbol{r}\wedge\boldsymbol{v}_{\text{abs}})\rho\boldsymbol{v}_{\text{abs}}\bullet\boldsymbol{n}d\Gamma_\Pi = \boldsymbol{r}\wedge\boldsymbol{F}_{\text{ext}}|_\Pi \tag{2.52}$$

where $\boldsymbol{v}_{\text{abs}} = \boldsymbol{v} + \boldsymbol{\omega}\wedge\boldsymbol{r}$ (absolute velocity, from eq. (2.4)) and $\boldsymbol{F}_{\text{ext}}$ is the external force acting on the fluid. In eq. (2.52), the right side of the equation is given by

$$\boldsymbol{r}\wedge\boldsymbol{F}_{\text{ext}}|_\Pi = \boldsymbol{T}_{\text{ext}} - \int_\Pi \boldsymbol{r}\wedge(\rho\boldsymbol{f})d\Pi - \int_\Pi \boldsymbol{r}\wedge\boldsymbol{f}_r(\alpha)d\Pi \tag{2.53}$$

where $\boldsymbol{T}_{\text{ext}}$ is the torque. The resistance force of the porous medium ($\boldsymbol{f}_r(\alpha)$) is included in a similar way as the body forces $\rho\boldsymbol{f}$.

Therefore, by substituting eq. (2.53) in eq. (2.52), and assuming steady state flow and zero external body forces,

$$\boldsymbol{T}_{\text{ext}} = \int_{\Gamma_\Pi}(\boldsymbol{r}\wedge\boldsymbol{v}_{\text{abs}})\rho\boldsymbol{v}_{\text{abs}}\bullet\boldsymbol{n}d\Gamma_\Pi + \int_\Pi \boldsymbol{r}\wedge\boldsymbol{f}_r(\alpha)d\Pi \tag{2.54}$$

Since $P_f = \boldsymbol{\omega}\bullet\boldsymbol{T}_{\text{ext}}$, the power is given by (ALONSO; SILVA, 2022b)

$$P_f = \underbrace{\int_{\Gamma_\Pi}\boldsymbol{\omega}\bullet(\boldsymbol{r}\wedge\boldsymbol{v}_{\text{abs}})\rho\boldsymbol{v}_{\text{abs}}\bullet\boldsymbol{n}d\Gamma_\Pi}_{\text{Fluid flow effect}} + \underbrace{\int_\Pi \boldsymbol{\omega}\bullet[\boldsymbol{r}\wedge\boldsymbol{f}_r(\alpha)]d\Pi}_{\text{Porous medium effect}} \tag{2.55}$$

where eq. (2.55) includes the resistance force of the porous medium, which is analogous to the material model term of the energy dissipation (eq. (2.51)).

2.3.3 **Vorticity**

The vorticity is a measure of the formation of vortices in the fluid flow from the local rotating motion of the fluid. The vortices that are formed inside the fluid flow may negatively contribute to the performance of a flow machine, leading to head losses, nonuniformities in the fluid flow, and may even lead to a reversion in the fluid flow path. The vorticity vector is defined as (MUNSON *et al.*, 2009):

$$\boldsymbol{\xi}_{\text{abs}} = \nabla\wedge\boldsymbol{v}_{\text{abs}} \tag{2.56}$$

From the vorticity transport equation (LAI *et al.*, 2009), the material derivative of the vorticity of eq. (2.58) ($\frac{D\boldsymbol{\xi}_{\text{abs}}}{Dt}$) can be divided into two terms: vortex stretching ($(\boldsymbol{\xi}_{\text{abs}}\bullet\nabla)\boldsymbol{v}_{\text{abs}}$) and viscous diffusion of vorticity ($\frac{\mu}{\rho}\nabla^2\boldsymbol{\xi}_{\text{abs}}$). In a 2D model, since the vorticity vector is entirely in the z direction, the vortex stretching term is zero, which implies that any formed vortex is dissipated only by viscosity. However, in a 2D swirl flow model, since the three velocity components are present (in the directions r, θ and z), with only tangential (θ direction) derivatives neglected, the vortices can be dissipated by viscosity, and also be axisymmetrically stretched.

By substituting $\boldsymbol{v}_{\text{abs}} = \boldsymbol{v} + \boldsymbol{\omega}\wedge\boldsymbol{r}$ (eq. (2.4)),

$$\boldsymbol{\xi}_{\text{abs}} = \underbrace{\nabla \wedge \boldsymbol{v}}_{\text{Relative vorticity vector}} + \underbrace{\nabla \wedge (\boldsymbol{\omega}\wedge\boldsymbol{r})}_{\text{Rotation effect}} \tag{2.57}$$

Since the rotation is an inherent aspect of flow machines, the part of the vorticity vector that is of more interest in this work is the relative vorticity vector, which is then given by

$$\boldsymbol{\xi} = \nabla \wedge \boldsymbol{v} \tag{2.58}$$

A porous medium effect term may be included in the vorticity vector in order to reduce the generation of grayscale results (ALONSO *et al.*, 2019), resulting in:

$$\boldsymbol{\xi} = \nabla \wedge \boldsymbol{v} + \boldsymbol{\xi}_{\kappa} \tag{2.59}$$

where $\boldsymbol{\xi}_{\kappa}$ is a compensation of vorticity in the porous medium.

If the influence of the porous medium is considered to be directly proportional to the curl of the deceleration caused by the porous medium,

$$\boldsymbol{\xi}_{\kappa} = k_V \nabla \wedge \left(\frac{\boldsymbol{f}_r(\alpha)}{\rho}\right) \tag{2.60}$$

where k_V is a proportionality constant.

Therefore,

$$\boldsymbol{\xi} = \nabla \wedge \boldsymbol{v} + \frac{k_V}{\rho}\nabla \wedge (\boldsymbol{f}_r(\alpha)) \tag{2.61}$$

In order to evaluate a single scalar value for the vorticity, the vorticity vector may be evaluated in a least squares approach (ROMERO; SILVA, 2014)

$$\xi_{V,\text{rel}} = \int_{\Pi} |\boldsymbol{\xi}|^2 d\Pi = \int_{\Pi} \left| \underbrace{\nabla \wedge \boldsymbol{v}}_{\text{Fluid flow effect}} \underbrace{+\frac{k_V}{\rho}\nabla \wedge (\boldsymbol{f}_r(\alpha))}_{\text{Porous medium compensation}} \right|^2 d\Pi \tag{2.62}$$

2.3.4 **Pressure head**

The pressure head is a measure of the fluid energy that is effectively transferred along the fluid flow path inside the flow machine. In other words, it would represent the maximum height of fluid that can be balanced by the energy provided by the pump to the fluid. It may be represented in two forms: as the gain of energy of the fluid flow (*pump* pressure head, H), and as the loss of energy of the fluid flow (*turbine* pressure head, $H' = -H$). It is given from the integral form of the energy equation (1st Law of Thermodynamics) (MUNSON *et al.*, 2009) by simplifying for an incompressible steady state flow with negligible heat transfer.

$$H = \frac{1}{Q}\left[\int_{\Gamma_{\Pi,\text{out}}}\left(\frac{p}{\rho g}+\frac{|\boldsymbol{v}_{\text{abs}}|^2}{2g}+h\right)\boldsymbol{v}_{\text{abs}}\bullet\boldsymbol{n}d\Gamma_{\Pi,\text{out}}+\int_{\Gamma_{\Pi,\text{in}}}\left(\frac{p}{\rho g}+\frac{|\boldsymbol{v}_{\text{abs}}|^2}{2g}+h\right)\boldsymbol{v}_{\text{abs}}\bullet\boldsymbol{n}d\Gamma_{\Pi,\text{in}}\right] \tag{2.63}$$

where Q is the (volumetric) flow rate (from eq. (2.47)), and h is the height. It can be pointed out that $\boldsymbol{v}_{\text{abs}}\bullet\boldsymbol{n} > 0$ on the outlet, and $\boldsymbol{v}_{\text{abs}}\bullet\boldsymbol{n} < 0$ on the inlet.

By also considering zero external body forces (in particular, zero gravitational force), h_{in} and h_{out}, which come from h in eq. (2.63), are neglected,

$$H = \frac{1}{Q}\left[\int_{\Gamma_{\Pi,\text{out}}}\left(\frac{p}{\rho g}+\frac{|\boldsymbol{v}_{\text{abs}}|^2}{2g}\right)\boldsymbol{v}_{\text{abs}}\bullet\boldsymbol{n}d\Gamma_{\Pi,\text{out}}+\int_{\Gamma_{\Pi,\text{in}}}\left(\frac{p}{\rho g}+\frac{|\boldsymbol{v}_{\text{abs}}|^2}{2g}\right)\boldsymbol{v}_{\text{abs}}\bullet\boldsymbol{n}d\Gamma_{\Pi,\text{in}}\right] \tag{2.64}$$

As can be seen in eq. (2.64), the pressure head can be described as a variation of total (*stagnation*) pressure (eq. (2.50)) weighted by the flow rate between the outlet and inlet. Since both terms of eq. (2.64) are multiplied by $\boldsymbol{v}_{\text{abs}}\bullet\boldsymbol{n}$ and by considering $\boldsymbol{v}\bullet\boldsymbol{n}$ instead of $\boldsymbol{v}_{\text{abs}}\bullet\boldsymbol{n}$, which is different than zero only on inlets/outlets and is valid for the 2D swirl flow model and the 2D/3D pump model, eq. (2.64) may be expressed as

$$H = \frac{1}{Q}\left[\oint_{\Gamma_\Pi}\left(\frac{p}{\rho g}+\frac{|\boldsymbol{v}_{\text{abs}}|^2}{2g}\right)\boldsymbol{v}\bullet\boldsymbol{n}d\Gamma_\Pi\right] \tag{2.65}$$

It may be pointed out that $\boldsymbol{v}\bullet\boldsymbol{n}$ should be used in eq. (2.65), and not $\boldsymbol{v}_{\text{abs}}\bullet\boldsymbol{n}$, because only $\boldsymbol{v}\bullet\boldsymbol{n}$ is zero on the rotating walls of 2D (ROMERO; SILVA, 2014) and 3D pump models (OKUBO *et al.*, 2021).

For the operation as a pump, the pressure head (H) must be higher than zero, which means that the rotor is capable of pumping the fluid ($H > 0$). Thus, this defines a breakpoint for the fluid flow device to operate as a pump, which depends on the flow rate and rotation for a given fluid flow device topology.

2.3.5 **Isentropic efficiency**

The isentropic efficiency is a measure of how near the real (actual) performance of the fluid flow device is in relation to ideal operating conditions. For pump devices, from the definitions of the pressure head (H, eq. (2.64)) and the power transferred to the fluid (P_f, eq. (2.55)), the isentropic efficiency is defined as (SONNTAG; BORGNAKKE, 2013; REY, 2004)

$$\eta_s = \frac{P_{ideal}}{P_{real}} = \frac{\Delta h_s}{P_f/\dot{m}} = \frac{gH}{P_f/\dot{m}} \tag{2.66}$$

where $\dot{m}$ is the mass flow rate, and $\Delta h_s = gH$ is the variation of specific enthalpy (specific work) in the ideal process (SONNTAG; BORGNAKKE, 2013), for incompressible fluid. It can be mentioned that the fraction shown in eq. (2.66) is inverted for turbine devices (i.e., for turbines, $\eta_s = \frac{P_{real}}{P_{ideal}} = \frac{P_f/\dot{m}}{gH}$).

2.3.6 **Pressure coefficients**

The rise in the static pressure in relation to the conversion of kinetic energy into enthalpy can be characterized in terms of dimensionless coefficients. The static pressure recovery ($c_{p,R}$) and total pressure loss ($c_{p,T,L}$) coefficients can be given as (GAO *et al.*, 2017; AYDER *et al.*, 1993; EYNON; WHITFIELD, 2000; BALONI *et al.*, 2012; BALONI *et al.*, 2015)

$$c_{p,R} = \frac{\overline{p}_{out} - \overline{p}_{in}}{\overline{p}_{T,in} - \overline{p}_{in}} = \frac{\overline{p}_{out} - \overline{p}_{in}}{\overline{p}_{D,in}} \tag{2.67}$$

$$c_{p,T,L} = \frac{-(\overline{p}_{T,out} - \overline{p}_{T,in})}{\overline{p}_{T,in} - \overline{p}_{in}} = \frac{\overline{p}_{T,in} - \overline{p}_{T,out}}{\overline{p}_{D,in}} \tag{2.68}$$

where $\overline{p}_i$ is the average (static) pressure, $\overline{p}_{D,i}$ is the average dynamic pressure, $\overline{p}_{T,i}$ is the average total (*stagnation*) pressure, in refers to the inlet of the fluid device, out refers to the outlet of the fluid device. When there is a porous medium in the computational domain, such as in topology optimization, the pressure on porous medium interfaces needs to be disconsidered. Thus, the average pressures of eqs. (2.67) and (2.68) need to be decreased by the effect of the pseudo-density (α) values. However, that influence is not linear, as can be seen in eq. (2.129). Therefore, the influence of the penalty

parameter (q) needs to be considered. The pressure values averaged by the length of the boundary and considering the porous medium become:

$$\begin{aligned}
\overline{p}_i &= \frac{1}{\ell_{\Gamma_{\Pi,i}}} \int_{\Gamma_{\Pi,i}} [p] \left[\alpha \left(\frac{1+q}{\alpha+q}\right)\right] d\Gamma_{\Pi,i} \\
\overline{p}_{D,i} &= \frac{1}{\ell_{\Gamma_{\Pi,i}}} \int_{\Gamma_{\Pi,i}} \left[\frac{\rho|\boldsymbol{v}_{\text{abs}}|^2}{2}\right] \left[\alpha \left(\frac{1+q}{\alpha+q}\right)\right] d\Gamma_{\Pi,i} \\
\overline{p}_{T,i} &= \overline{p}_i + \overline{p}_{D,i}
\end{aligned} \tag{2.69}$$

where $\ell_{\Gamma_{\Pi,i}} = \int_{\Gamma_{\Pi,i}} \left[\alpha \left(\frac{1+q}{\alpha+q}\right)\right] d\Gamma_{\Pi,i}$ is the length of the boundary i considering the porous medium.

From eqs. (2.67) and (2.68), a unified pressure performance coefficient can be defined as (GAO *et al.*, 2017)

$$c_{p,U} = \frac{c_{p,R}}{c_{p,T,L}} \tag{2.70}$$

2.3.7 **Static pressure rise**

The static pressure rise is closely related to the requirements for the design of a VAD, since blood flow requirements are normally expressed with the required static pressure rise. The static pressure rise in a VAD (Δp_{VAD}) is given by

$$\Delta p_{\text{VAD}} = \overline{p}_{out,\text{VAD}} - \overline{p}_{in,\text{VAD}} = \Delta p_{\text{rotor}} + \Delta p_{\text{volute}} \tag{2.71}$$

where $\overline{p}_{in,\text{VAD}}$ is the average (static) pressure on the inlet, $\overline{p}_{out,\text{VAD}}$ is the average (static) pressure on the outlet, Δp_{rotor} is the (static) pressure rise in the rotor, and Δp_{volute} is the pressure rise in the volute.

By considering the static pressure recovery coefficient $c_{p,R}$ of the volute (eq. (2.67)), the required (static) pressure in relation to rotor pressures becomes

$$\Delta p_{\text{VAD}} = \Delta p_{\text{rotor}} + (c_{p,R} \Delta p_{D,\text{volute}}) = \Delta p_{\text{rotor}} + (c_{p,R} \Delta p_{D,\text{rotor}}) \tag{2.72}$$

where $\Delta p_{D,\text{volute}}$ is the dynamic pressure rise in the volute, and $\Delta p_{D,\text{rotor}}$ is the dynamic pressure rise in the rotor.

Therefore, if all the inlet dynamic pressure in the volute could be approximately converted to static pressure, $c_{p,R} \approx 1$, which is unlikely to happen due to energy dissipation related to redirecting the fluid flow. In fact, notice that $c_{p,R} = 1$ is impossible, otherwise the outlet fluid would be static. For such hypothetical case,

$$\Delta p_{\text{VAD}} \approx \Delta p_{T,\text{rotor}} \tag{2.73}$$

where $\Delta p_{T,\mathrm{rotor}}$ is the total pressure variation in the rotor.

2.3.8 **Specific dimensionless characterization parameters**

There are some dimensionless parameters that are specific to the analysis of Tesla-type devices. Some selected parameters are presented in Table 2.1 (ALONSO *et al.*, 2019). Their original definitions are adapted in order to enable their analyses in topology optimization results.

Table 2.1 – Dimensionless parameters for analysis in Tesla-type devices.

Dimensionless parameter	Equation *
Boundary layer characterization	
Pohlhausen parameter (based on Rey (2004) and Breiter and Pohlhausen (1962)) → Represents the spacing between the disks.	$\mathrm{Ph} = e_{\min}\sqrt{\frac{\omega_0}{\nu}}$
Flow regime characterization	
Local Reynolds number in relation to the external radius (based on Rey (2004)) → Represents the flow regime for each point of the fluid in relation to the external diameter of the disks. It may also be expressed in terms of the external radius (r_{ext} instead of $2r_{ext}$)	$\mathrm{Re}_{\mathrm{ext},\ell} = \frac{\lvert\boldsymbol{v}_{\mathrm{abs}}\rvert\,(2r_{ext})}{\nu}$
Local viscogeometric (Nendl) parameter (based on Rey (2004)) → Reynolds number (in relation to the spacing of the disks) combined with a geometric parameter.	$\mathrm{Nd}_{\mathrm{ext},\ell} = \frac{\lvert\boldsymbol{v}_{\mathrm{abs}}\rvert {e_{\min}}^2}{\nu r_{ext}}$
Flow rate characterization	
Essential machine data parameter (based on Foo *et al.* (2010)) → Represents the flow rate in relation to the viscosity.	$\mathrm{A}_Q = \frac{Q e_{\min}}{n_{\mathrm{outlets}}\nu r_{int}^2}$

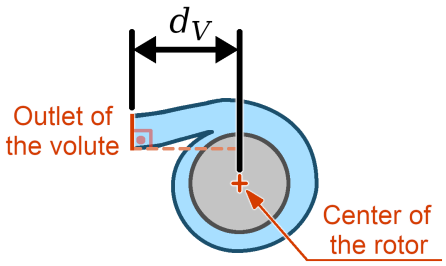
* Legend:
ω_0 : Angular velocity of the fluid flow device.
$\nu = \frac{\mu}{\rho}$: Kinematic viscosity.
$e_{\min}$: Minimum spacing between two disks.
r_{int} : Internal (inlet) radius of the rotor of the pump.
r_{ext} : External (outlet) radius of the rotor of the pump.
$\boldsymbol{v}_{\mathrm{abs}}$: Absolute velocity of the fluid.
Q : Volumetric flow rate (eq. (2.47)).
n_{outlets} : Number of outlets of the Tesla pump.

For simplicity and easy extension to arbitrary fluid flow device topologies, the Reynolds number for the volute may be defined as:

$$\mathrm{Re}_{\mathrm{V},\ell} = \frac{\lvert\boldsymbol{v}_{\mathrm{abs}}\rvert\, d_{\mathrm{V}}}{\nu} \tag{2.74}$$

where d_{V} is the distance from the line that defines the outlet of the volute to the center of the rotor (shown in Fig. 2.8).

Figure 2.8 – Characteristic dimension selected for the Reynolds number of the volute.



Source: Author.

Additionally, it is possible to consider a local inlet Reynolds number, by substituting $\boldsymbol{v}_{\text{abs}}$ by $\boldsymbol{v}_{\text{abs},in}$ in Table 2.1 and eq. (2.74).

2.4 BLOOD DAMAGE MODELING

Although the relationships represented in Fig. 1.4 have been shown to exist, it is not guaranteed that these relationships should be linear when comparing different fluid flow device shapes/topologies. Therefore, it may be necessary to perform the evaluation of hemolysis and thrombosis through hemolysis and thrombosis models, respectively. This evaluation is treated as a “post-processing” operation, since the fluid flow simulation has already been performed.

One aspect that is present in all hemolysis and thrombosis models is the shear stress magnitude (*viscous scalar shear stress*) (mentioned in eq. (2.12)), which has an important role in hemolysis and thrombosis. There are two main approaches for the computation in the evaluation of hemolysis (ARORA *et al.*, 2004): stress-based and strain-based. The first approach for computing the shear stress magnitude over the RBCs is the stress-based approach, which assumes that the RBCs deform immediately when under any shear stress. The shear stress magnitude is based on the total shear stress, which can be given considering the most generic case (i.e., considering the presence of turbulence) (ALEMU; BLUESTEIN, 2007; SOARES *et al.*, 2013; WU *et al.*, 2005)

$$\boldsymbol{\tau}_{\text{total}} = \boldsymbol{\tau} + \boldsymbol{T}_R \tag{2.75}$$

where $\boldsymbol{\tau}_{\text{total}}$ is the total shear stress tensor, $\boldsymbol{\tau} = \mu(\nabla\boldsymbol{v} + \nabla\boldsymbol{v}^T)$ is the shear stress tensor, and $\boldsymbol{T}_R$ is the Reynolds (turbulent) stress tensor.

Then, the total shear stress magnitude ($\tau_{\mathrm{m,total}}$) may be computed through different methods and values. One common approach is by directly using the (instantaneous) shear stress, as in eq. (2.12). By considering eqs. (2.12) and (2.75), the total shear stress magnitude ($\tau_{\mathrm{m,total}}$) and total shear rate magnitude ($\dot{\gamma}_{\mathrm{m,total}}$) may be given as (TESCH, 2013; ARORA *et al.*, 2004)

$$\begin{aligned} \tau_{\mathrm{m,total}} &= \sqrt{2\boldsymbol{\tau}_{\mathrm{total}}\bullet\boldsymbol{\tau}_{\mathrm{total}}} \\ \dot{\gamma}_{\mathrm{m,total}} &= \sqrt{2\boldsymbol{\epsilon}_{\mathrm{total}}\bullet\boldsymbol{\epsilon}_{\mathrm{total}}} \end{aligned} \tag{2.76}$$

where $\boldsymbol{\epsilon}_{\mathrm{total}} = \boldsymbol{\epsilon} + \boldsymbol{\epsilon}_R$ is the total deformation (strain) tensor, $\boldsymbol{\epsilon}_R = \frac{\boldsymbol{T}_R}{2\mu}$ is the Reynolds (turbulent) deformation (strain) tensor.

Other approaches that are also used for computing the total shear stress magnitude ($\tau_{\mathrm{m,total}}$) assume it to be equal to, for example, a *von Mises stress*-like equation (BLUDSZUWEIT, 1995; TASKIN *et al.*, 2012; FRASER *et al.*, 2010; FRASER *et al.*, 2011), a *Tresca stress*-like equation (PINOTTI; ROSA, 1995; GARON; FARINAS, 2004) or the second stress invariant (PAULI *et al.*, 2013; NAM *et al.*, 2011).

The second approach for computing the shear stress magnitude is the strain-based approach, which consists of considering the biophysical aspects of an RBC (shape distortion and relaxation of the viscoelastic membrane of the RBC) (ARORA *et al.*, 2004; BARTHES-BIESEL; RALLISON, 1981) in determining the strain rate acting over the blood flow (and, therefore, the shear stress magnitude over the RBCs) (PAULI *et al.*, 2013). This approach considers the deformation of RBCs being modeled as fluid droplets (ARORA *et al.*, 2004; ARORA *et al.*, 2006b), meaning that the shapes of the RBCs are modelled as ellipsoids represented by morphology tensors which may be evaluated by an Eulerian approach. The main drawback of this method may be that it requires the solution of an additional tensorial equation, which may represent a high computational cost.

Since the stress-based approach assumes that the RBCs deform immediately, which is unrealistic under physiological conditions (PAULI *et al.*, 2013), and since the residence time (interval of time in which the RBCs are inside the device, which affects the shape distortion of the RBCs) is normally small for blood pumps, the stress-based approach should overpredict blood damage (PAULI *et al.*, 2013).

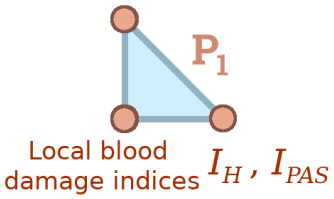
Under homogeneous steady shear flow (i.e., under a spatially constant total shear rate), both approaches are equivalent (PAULI *et al.*, 2013). However, under transient

or steady inhomogeneous flows (i.e., under a total shear rate that varies spatially), the hemolysis predictions of both models may significantly differ (PAULI *et al.*, 2013), due to the assumption of immediate deformation of RBCs in the stress-based approach.

In this work, the shear stress magnitude for hemolysis and thrombosis is computed through the shear stress approach based on instantaneous shear stresses (eq. (2.76)) due to the aforementioned proximity of results, and the lower computational cost (since it is not required to solve an additional tensorial differential equation).

For the finite element modeling, the local values of the blood damage indices and the auxiliary variables used in their calculations, which are presented in the following sections, are assumed with linear interpolation (P_1) (see Fig. 2.9).

Figure 2.9 – Finite element interpolation for the blood damage indices (also used for the auxiliary variables used in their computations).



Source: Author.

2.4.1 **Hemolysis modeling**

Hemolysis may be evaluated by the hemolysis index. The hemolysis index (also called *blood damage index* in Grigioni *et al.* (2004)) is based on the quantity of hemoglobin (internal protein of RBCs responsible for transporting oxygen to the tissues) in the plasma, being given by (FRASER *et al.*, 2010; TASKIN *et al.*, 2012)

$$I_{H,T} = \frac{\Delta \mathrm{Hb}_{\mathrm{pf}}}{\mathrm{Hb}} = \frac{\mathrm{Hb}_{\mathrm{pf,out}} - \mathrm{Hb}_{\mathrm{pf,in}}}{\mathrm{Hb}} \tag{2.77}$$

where $I_{H,T}$ is the hemolysis index (referred here as the *total hemolysis index*), $\Delta \mathrm{Hb}_{\mathrm{pf}} = \mathrm{Hb}_{\mathrm{pf,out}} - \mathrm{Hb}_{\mathrm{pf,in}}$ is the variation of the quantity of free hemoglobin in the plasma per volume of blood (*plasma free hemoglobin*) (g/dL) and Hb is the quantity of hemoglobin per volume of blood (g/dL). For a healthy person, $\mathrm{Hb} = 1500$ g/dL (ARORA *et al.*, 2006b).

While eq. (2.77) is essentially the difference between the outlet and the inlet hemoglobin, it is also possible to define the *local hemolysis index*, which is distributed over the entire computational domain, as

$$I_H = \frac{\mathrm{Hb}_{\mathrm{pf}}}{\mathrm{Hb}} \tag{2.78}$$

where I_H is the local hemolysis index and $\mathrm{Hb}_{\mathrm{pf}}$ is the quantity of free hemoglobin in the plasma per volume of blood (g/dL). It may also be mentioned that the local index values may represent a potential damage map rather than the damage itself, which depends on the fluid flow over the "damaging" regions.

The hemolysis index is sometimes weighted (*corrected*) by the percentage of volume not occupied by RBCs in the total volume of blood (*plasma volume*) (ASTM F1841-97, 1997; GARON; FARINAS, 2004). This weighting is known to numerically underestimate the hemolysis (DE WACHTER; VERDONCK, 2002; GARON; FARINAS, 2004), and consists of multiplying eq. (2.77) by $(1-\mathrm{Ht})$, where $(1-\mathrm{Ht})$ is the percentage of volume not occupied by RBCs in the total volume of blood, and Ht is the hematocrit (percentage of volume occupied by RBCs in the total volume of blood) (BILLETT, 1990). For a healthy person, $\mathrm{Ht} = 45\%$ (ARORA *et al.*, 2006b; NAM *et al.*, 2011; BEHBAHANI *et al.*, 2009; CHO; KENSEY, 1991).

Since the local hemolysis index (I_H) varies with respect to each point of the flow, the value averaged by the flow rate can be used to define the total hemolysis index ($I_{H,T}$) (NAM *et al.*, 2011),

$$I_{H,T} = \Delta\widetilde{I_H} = \widetilde{I_{H,\mathrm{out}}} - \widetilde{I_{H,\mathrm{in}}} = \frac{\int_{\Gamma_{\Pi,\mathrm{out}}} I_H(\boldsymbol{v}_{\mathrm{abs}}\bullet\boldsymbol{n})d\Gamma_{\Pi,\mathrm{out}}}{\int_{\Gamma_{\Pi,\mathrm{out}}}(\boldsymbol{v}_{\mathrm{abs}}\bullet\boldsymbol{n})d\Gamma_{\Pi,\mathrm{out}}} - \frac{\int_{\Gamma_{\Pi,\mathrm{in}}} I_H(\boldsymbol{v}_{\mathrm{abs}}\bullet\boldsymbol{n})d\Gamma_{\Pi,\mathrm{in}}}{\int_{\Gamma_{\Pi,\mathrm{in}}}(\boldsymbol{v}_{\mathrm{abs}}\bullet\boldsymbol{n})d\Gamma_{\Pi,\mathrm{in}}} \quad (2.79)$$

where " $\widetilde{\ }$ " represents the average value weighted by the volumetric flow rate.

Since $(\boldsymbol{v}_{\mathrm{abs}}\bullet\boldsymbol{n})$ is different than zero only on inlets and outlets, and the flow rate that enters the fluid device is the same that exits it ($(\boldsymbol{v}_{\mathrm{abs}}\bullet\boldsymbol{n})|_{\mathrm{in}} = -(\boldsymbol{v}_{\mathrm{abs}}\bullet\boldsymbol{n})|_{\mathrm{out}}$) (i.e., the continuity equation (eq. (2.41)) is being respected), eq. (2.79) can also be written as:

$$I_{H,T} = \Delta\widetilde{I_H} = \widetilde{I_{H,\mathrm{out}}} - \widetilde{I_{H,\mathrm{in}}} = \frac{\oint_{\Gamma_\Pi} I_H(\boldsymbol{v}_{\mathrm{abs}}\bullet\boldsymbol{n})d\Gamma_\Pi}{Q} \quad (2.80)$$

where Q is the volumetric flow rate (eq. (2.47)).

There are some definitions for the hemolysis index that are directly correlated to measurements from experiments used to evaluate hemolysis, which are given in Table 2.2.

Table 2.2 – Definitions of the hemolysis index correlated to experiments.

Type of hemolysis index definition	Equation *
Normalized (total) hemolysis index → Total hemolysis index normalized for a single fluid pass (TASKIN *et al.*, 2012), considering that there are multiple passes of blood in the device for each experimental measure, which means that the variation of the quantity of free hemoglobin in the plasma per volume of blood is used as a total value of all these passes (i.e., $\Delta\mathrm{Hb}_{\mathrm{pf,total}} = \sum_{i=0}^{n_{\mathrm{passes}}} \Delta\mathrm{Hb}_{pf,i}$).	$I_{H,T',\mathrm{normalized}} = \frac{\frac{\Delta\mathrm{Hb}_{\mathrm{pf,total}}}{\mathrm{Hb}}}{n_{\mathrm{passes}}}$
Corrected and normalized (total) hemolysis value → Total hemolysis value (not dimensionless), normalized for a single fluid pass, and corrected for the plasma volume (based on the hematocrit (ASTM F1841-97, 1997; GARON; FARINAS, 2004)). If given in g/dL, it is called NIH (Normalized Index of Hemolysis) (ASTM F1841-97, 1997), and, if given in mg/dL, it is called mgNIH (Normalized miligram Index of Hemolysis) (ASTM F1841-97, 1997).	$I_{H,T',\substack{\mathrm{normalized}\\ \mathrm{and\ corrected}\\ \mathrm{value}}} = \frac{\Delta\mathrm{Hb}_{\mathrm{pf,total}}}{n_{\mathrm{passes}}}(1-\mathrm{Ht})$
Corrected and normalized (total) hemolysis index → Total hemolysis index, normalized for a single fluid pass, and corrected for the plasma volume (based on the hematocrit). It is the hemolysis index that is recommended by ASTM F1841-97 (1997) to express the degree of hemolysis caused by a blood pump in a recirculating system, being referred to as MIH (Modified Index of Hemolysis).	$I_{H,T',\substack{\mathrm{normalized}\\ \mathrm{and\ corrected}}} = \frac{\frac{\Delta\mathrm{Hb}_{\mathrm{pf,total}}}{\mathrm{Hb}}}{n_{\mathrm{passes}}}(1-\mathrm{Ht})$

* Legend:
$n_{\mathrm{passes}} = \frac{V_{\mathrm{flow}}}{V_{\mathrm{circulating}}}$: Total number of passes.
$V_{\mathrm{flow}} = Q\Delta t_{\mathrm{m}}$: Volume of blood due to the fluid flow.
Δt_{m} : Measurement time.
Q : Volumetric flow rate (eq. (2.47)).
$V_{\mathrm{circulating}}$: Total volume of blood circulating in the fluid flow circuit used in the experiments.

2.4.1.1 Numerical prediction of the hemolysis index

The numerical prediction models for the hemolysis index are developed based on the following requirements (GOUBERGRITS, 2006; GRIGIONI *et al.*, 2005): (1) the principle of causality (i.e., blood damage does not reduce and is always increased: $\frac{DI_H}{Dt} > 0$) (GRIGIONI *et al.*, 2004); (2) under constant uniform shear stress conditions, it should match the Giersiepen-Wurzinger correlation, which has been experimentally verified for this case (STEINES *et al.*, 1999); (3) the load history for time-dependent loading should be taken into account (according to the *damage accumulation hypothesis*, which considers that blood damage is accumulated with time – i.e., considers that the RBCs are progressively destroyed).

There are essentially two approaches for evaluating hemolysis in blood flow, which are: the *power-law approach* (based on the Giersiepen-Wurzinger correlation

(GIERSIEPEN *et al.*, 1990)), and the *threshold approach* (GOUBERGRITS, 2006). Since the *threshold approach* (GOUBERGRITS, 2006; LU *et al.*, 2001) is an "all or nothing approach", which assumes that there is a critical shear stress magnitude value (*hemolytic threshold*) before which hemolysis is 0%, and above which hemolysis is 100%, it is not adequate for estimating hemolysis. According to Lu *et al.* (2001)'s experimental results, the hemolytic threshold would correspond to 800 Pa. The *power-law approach* is based on the Giersiepen-Wurzinger correlation (GIERSIEPEN *et al.*, 1990) and serves as the basis for all other hemolysis models. Its original application assumes a constant uniform shear stress, which is clearly not valid for various fluid flow problems, including VADs (FRASER *et al.*, 2010). The Giersiepen-Wurzinger correlation has been originally developed for total scalar shear stresses ($\tau_{\mathrm{m,total}}$) smaller than 255 Pa, and for exposure times ($\Delta t_{\mathrm{exposure}}$) smaller than 700 ms (GIERSIEPEN *et al.*, 1990; TASKIN *et al.*, 2012). This original application of the correlation is known to overestimate the hemolysis index (DE WACHTER; VERDONCK, 2002) and is given by (GIERSIEPEN *et al.*, 1990; BLUDSZUWEIT, 1995; TASKIN *et al.*, 2012; FRASER *et al.*, 2010; ZHANG *et al.*, 2011)

$$I_{H,T} = \Delta\widetilde{I_H} = C_H \tau_{\mathrm{m,total}}^{\beta_s} \Delta t_{\mathrm{exposure}}^{\beta_t} \tag{2.81}$$

where $\tau_{\mathrm{m,total}}$ is the shear stress magnitude, $\Delta t_{\mathrm{exposure}}$ is the exposure time (i.e., the time interval in which $\tau_{\mathrm{m,total}}$ is active), C_H is the proportionality factor for the hemolysis index, β_s is the exponent of the shear stress magnitude, and β_t is the exponent of the exposure time.

The coefficients of the Giersiepen-Wurzinger correlation are determined from regression of experimental data (TASKIN *et al.*, 2012). According to Zhang *et al.* (2011), the coefficients that were originally determined in Giersiepen *et al.* (1990) are overestimated because of the use of a mechanical seal in the experiments, and, therefore, presents a new set of coefficients. The new set of coefficients consists of $C_H = 1.228 \times 10^{-5}$ $\mathrm{Pa}^{-\beta_s}\mathrm{s}^{-\beta_t}$, $\beta_s = 1.9918$, and $\beta_t = 0.6606$ (ZHANG *et al.*, 2011).

In order to numerically predict the hemolysis index under more generic conditions, differential equations based on the Giersiepen-Wurzinger correlation have been developed. These equations may be solved by either of two approaches (TASKIN *et al.*, 2012; FRASER *et al.*, 2010): the Lagrangian approach, in which the integration follows the pathlines, and the Eulerian approach, in which the integration is performed in the

entire computational domain. According to Pauli *et al.* (2013), the advantage of the Lagrangian approach is that it is easier to compute the residence time (interval of time in which the RBCs are inside the device). However, near zero velocities and recirculation regions pose a computational problem for computing the pathlines necessary for the Lagrangian approach, and, due to the choice of pathlines, the entire flow field is not necessarily considered (FRASER *et al.*, 2010). Also, Taskin *et al.* (2012) reported higher correlation coefficients between the Eulerian approach and experiments (for a bladed blood pump) than the Lagrangian approach. Therefore, the Eulerian approach seems to be more interesting for computing the hemolysis index (FRASER *et al.*, 2010).

Various hemolysis models have been developed, which are mainly the *linear damage index* model (GARON; FARINAS, 2004), the *asymptotically consistent damage index* model (FARINAS *et al.*, 2006), and the *mechanical dose infinitesimal damage index* model (GRIGIONI *et al.*, 2005). There are other models, such as: *linear damage accumulation* (MITOH *et al.*, 2003; YANO *et al.*, 2003), which is restricted to the Lagrangian approach for each RBC pathline (i.e., cannot be represented in an Eulerian form), *power law damage accumulation* (SONG *et al.*, 2003), which fails to reproduce the total damage under uniform shear stress (from the Giersiepen-Wurzinger correlation) (GRIGIONI *et al.*, 2004; GRIGIONI *et al.*, 2005) and portrays some undesirable dependency with respect to the time step (TASKIN *et al.*, 2012), *power law damage accumulation based on damage curve* (YELESWARAPU *et al.*, 1995), and *infinitesimal damage index* (GRIGIONI *et al.*, 2004; SHERIFF *et al.*, 2013), which depends on the residence time of the RBCs (interval of time in which the RBCs are inside the device, which affects the shape distortion of RBCs).

While the *linear damage index* and *asymptotically consistent damage index* models require solving a single differential equation for obtaining the hemolysis index, the *mechanical dose infinitesimal damage index* model requires solving two equations – one for a *mechanical dose* of hemolysis, and another for the *hemolysis index*. In particular, the *asymptotically consistent damage index* model is the *linear damage index* model with a correction for only nondestroyed RBCs to undergo hemolysis, which means that it is more suitable for evaluating hemolysis. Since both *asymptotically consistent damage index* and *mechanical dose infinitesimal damage index* models should be acceptable for evaluating hemolysis (although the second one being more generic), and the *asymptotically consistent damage index* model requires solving a single differential

equation, which is linear, the model selected in this work is the *asymptotically consistent damage index* model.

2.4.1.1.1 *Asymptotically consistent damage index model*

Since the *asymptotically consistent damage index* model consists of the *linear damage index* model with a correction, the *linear damage index* model is first briefly described. The *linear damage index* model assumes that the Giersiepen-Wurzinger correlation is valid for any fluid volume and completely describes the damage evolution of the blood flow (GARON; FARINAS, 2004; FARINAS *et al.*, 2006; TASKIN *et al.*, 2012; NAM *et al.*, 2011). In this case, the original equation of the Giersiepen-Wurzinger correlation (eq. (2.81)) is adapted to the differential form as follows (GARON; FARINAS, 2004; FRASER *et al.*, 2010), for each pathline,

$$\begin{aligned} \Delta I_H &= C_H \tau_{\mathrm{m,total}}^{\beta_s} \Delta t^{\beta_t} \\ \frac{(\Delta I_H)^{\frac{1}{\beta_t}}}{\Delta t} &= C_H^{\frac{1}{\beta_t}} \tau_{\mathrm{m,total}}^{\frac{\beta_s}{\beta_t}} \end{aligned} \tag{2.82}$$

where Δt is here the time interval in the pathline of a single RBC.

Then, it is assumed that $(\Delta I_H)^{\frac{1}{\beta_t}} \approx \Delta(I_H^{\frac{1}{\beta_t}})$, which is particularly true when $I_{H,\mathrm{in}} = 0$ in $\Delta I_H = I_{H,\mathrm{out}} - I_{H,\mathrm{in}}$ (notice that this assumption is not needed in the *mechanical dose infinitesimal damage index* model). By also considering a *linear damage index* (given by $I_{H,L} = I_H^{\frac{1}{\beta_t}}$), an infinitesimal time step ($\Delta t \to 0^+$) and $\tau_{\mathrm{m,total}}$ being time-independent, the following equation is obtained:

$$\frac{D I_{H,L}}{Dt} = C_H^{\frac{1}{\beta_t}} \tau_{\mathrm{m,total}}^{\frac{\beta_s}{\beta_t}} \tag{2.83}$$

where the value of the local hemolysis index (I_H) is then recovered by considering $I_H = I_{H,L}^{\beta_t}$. According to Nam *et al.* (2011), an additional diffusion term can also be included in eq. (2.83), but this term should not be significant in typical fluid flow devices.

According to Farinas *et al.* (2006), when the *linear damage index* model is under large shear stresses and/or exposure time, it may “generate” a hemolysis index larger than 1. This overestimates the hemolysis, since it would mean that already lysed RBCs continue being lysed (FARINAS *et al.*, 2006). In such case, it is needed to add a saturation effect to the hemolysis index computed by the *linear damage index* model. This saturation effect limits the maximum hemolysis index to 1 (i.e., 100% RBC

destruction), removing nonphysical results from the validity range (FARINAS *et al.*, 2006). Therefore, eq. (2.83) becomes (FARINAS *et al.*, 2006; NAM *et al.*, 2011):

$$\frac{DI_{H,L}}{Dt} = C_H^{\frac{1}{\beta_t}} \tau_{\mathrm{m,total}}^{\frac{\beta_s}{\beta_t}} \underbrace{(1 - I_{H,L})}_{\substack{\text{Correction term} \\ \text{for nondestroyed} \\ \text{RBCs}}} \tag{2.84}$$

From the definition of the material derivative, considering a relative reference frame,

$$\frac{\partial I_{H,L}}{\partial t} + (\boldsymbol{v} \bullet \nabla) I_{H,L} = C_H^{\frac{1}{\beta_t}} \tau_{\mathrm{m,total}}^{\frac{\beta_s}{\beta_t}} (1 - I_{H,L}) \tag{2.85}$$

The weak form can be obtained by multiplying eq. (2.85) by the test function for the linear damage index ($w_{I_{H,L}}$), which would correspond to the weighted-residual and Galerkin methods. By also considering steady state flow,

$$\int_\Pi \left[(\boldsymbol{v} \bullet \nabla) I_{H,L} - C_H^{\frac{1}{\beta_t}} \tau_{\mathrm{m,total}}^{\frac{\beta_s}{\beta_t}} (1 - I_{H,L}) \right] w_{I_{H,L}} d\Pi = 0 \tag{2.86}$$

This approach is also referred to as the FEM (Finite Element Method) approach. However, in the performed tests, this formulation resulted unstable for the solution of $I_{H,L}$ (i.e., the values resulted in a *checkerboard*-like distribution of extremely high positive and extremely low negative values). This is probably because, when the total shear stress magnitude ($\tau_{\mathrm{m,total}}$) is small and the fluid velocity ($\boldsymbol{v}$) is also small, there is a *singularity* in eq. (2.86) (i.e., "$0 \approx 0$"). Therefore, an alternative approach is considered. This alternative approach is based on the LSFEM (Least-Squares Finite Element Method) formulation, as used in Nam *et al.* (2011) and Pauli *et al.* (2013). The LSFEM approach considers the minimization of $\int_\Pi R^2 d\Pi$, where R is the residual of the differential equation. The minimization implies that the variational of $\int_\Pi R^2 d\Pi$ be zero, which means that $\int_\Pi 2R\delta R d\Pi = 0$ (or, when dividing by 2, $\int_\Pi R\delta R d\Pi = 0$), where δR represents the variational of R. Therefore,

$$\int_\Pi \left[(\boldsymbol{v} \bullet \nabla) I_{H,L} - C_H^{\frac{1}{\beta_t}} \tau_{\mathrm{m,total}}^{\frac{\beta_s}{\beta_t}} (1 - I_{H,L}) \right] \left[(\boldsymbol{v} \bullet \nabla) w_{I_{H,L}} + C_H^{\frac{1}{\beta_t}} \tau_{\mathrm{m,total}}^{\frac{\beta_s}{\beta_t}} w_{I_{H,L}} \right] d\Pi = 0 \tag{2.87}$$

In order to "soften" the *singularity* that may still be present near small shear stress magnitudes ($\tau_{\mathrm{m,total}}$) and small fluid velocities ($\boldsymbol{v}$) (i.e., "$0 \approx 0$"), eq. (2.87) is divided by $C_H^{\frac{1}{\beta_t}} \tau_{\mathrm{m,total}}^{\frac{\beta_s}{\beta_t}}$, resulting in:

$$\int_\Pi \left[\frac{(\boldsymbol{v} \bullet \nabla)}{C_H^{\frac{1}{\beta_t}} \tau_{\mathrm{m,total}}^{\frac{\beta_s}{\beta_t}}} I_{H,L} - (1 - I_{H,L}) \right] \left[(\boldsymbol{v} \bullet \nabla) w_{I_{H,L}} + C_H^{\frac{1}{\beta_t}} \tau_{\mathrm{m,total}}^{\frac{\beta_s}{\beta_t}} w_{I_{H,L}} \right] d\Pi = 0 \tag{2.88}$$

The formulation given by eq. (2.88) should be enough for evaluating the hemolysis index, and it also did not achieve negative values (*negative concentration problem*), as had been previously reported by Nam *et al.* (2011) in the formulation given by eq. (2.87). Therefore, there should be no need to consider a quadratic variable transformation, which is proposed in Nam *et al.* (2011) and requires the use of a non-linear solver (i.e., solving by using an iterative method, such as the Newton-Raphson method), with inherent convergence issues (NAM *et al.*, 2011)

Since no boundary term appears in eq. (2.88), the only boundary condition that is imposed is a Dirichlet boundary condition on the inlet, which may consist of, for example, zero inlet hemolysis ($I_H = 0 \implies I_{H,L} = 0$).

2.4.1.1.2 *Simplified analysis for the asymptotically consistent damage index model*

It is also possible to perform a simplified analysis in eq. (2.84) (FARINAS *et al.*, 2006), but with the disadvantage of not giving the *local information* of the hemolysis index (i.e., the sources of RBC damage inside the device) (GARON; FARINAS, 2004; FARINAS *et al.*, 2006). In this case, by assuming steady state flow in eq. (2.84),

$$(\boldsymbol{v}\bullet\nabla)I_{H,L} = C_H^{\frac{1}{\beta_t}} \tau_{\mathrm{m,total}}^{\frac{\beta_s}{\beta_t}} (1 - I_{H,L}) \tag{2.89}$$

By separating the variables and integrating in the whole computational domain (Π),

$$\int_\Pi \frac{(\boldsymbol{v}\bullet\nabla)I_{H,L}}{(1 - I_{H,L})} d\Pi = \int_\Pi C_H^{\frac{1}{\beta_t}} \tau_{\mathrm{m,total}}^{\frac{\beta_s}{\beta_t}} d\Pi \tag{2.90}$$

From the power rule for derivatives, $\frac{\nabla I_{H,L}}{1-I_{H,L}} = -\nabla[\ln(1 - I_{H,L})]$. Therefore,

$$-\int_\Pi \boldsymbol{v}\bullet\nabla[\ln(1 - I_{H,L})] d\Pi = \int_\Pi C_H^{\frac{1}{\beta_t}} \tau_{\mathrm{m,total}}^{\frac{\beta_s}{\beta_t}} d\Pi \tag{2.91}$$

From the product rule for derivatives, for a given scalar field "a_s", $(\boldsymbol{v}\bullet\nabla)a_s = \boldsymbol{v}\bullet\nabla a_s = \nabla\bullet(\boldsymbol{v}a_s) - (\nabla\bullet\boldsymbol{v})a_s$. Thus, by applying this relation to eq. (2.91) and also considering an incompressible fluid (i.e., the continuity equation (eq. (2.1))),

$$-\int_\Pi \nabla\bullet(\boldsymbol{v}\ln(1 - I_{H,L})) d\Pi = \int_\Pi C_H^{\frac{1}{\beta_t}} \tau_{\mathrm{m,total}}^{\frac{\beta_s}{\beta_t}} d\Pi \tag{2.92}$$

By applying Gauss' divergence theorem,

$$-\int_{\Gamma_\Pi} \boldsymbol{n}\bullet(\boldsymbol{v}\ln(1 - I_{H,L})) d\Gamma_\Pi = \int_\Pi C_H^{\frac{1}{\beta_t}} \tau_{\mathrm{m,total}}^{\frac{\beta_s}{\beta_t}} d\Pi \tag{2.93}$$

By assuming that $\int_{\Gamma_\Pi} \boldsymbol{n}\bullet(\boldsymbol{v}\ln(1-I_{H,L}))d\Gamma_\Pi \approx Q\widetilde{\Delta\ln(1-I_{H,L})}$, and also considering $I_{H,L,T} = \Delta\widetilde{I_{H,L}} = \widetilde{I_{H,L,\text{out}}} - \widetilde{I_{H,L,\text{in}}}$, where $\widetilde{I_{H,L,\text{in}}}$ is a constant value specified by a Dirichlet boundary condition and $I_{H,L,T}$ is the total linear damage index,

$$-Q\widetilde{\ln(1-I_{H,L,\text{out}})} = \int_\Pi C_H^{\frac{1}{\beta_t}} \tau_{\text{m,total}}^{\frac{\beta_s}{\beta_t}} d\Pi - Q\widetilde{\ln(1-I_{H,L,\text{in}})} \tag{2.94}$$

$$-\widetilde{\ln(1-I_{H,L,\text{out}})} = \frac{1}{Q}\int_\Pi C_H^{\frac{1}{\beta_t}} \tau_{\text{m,total}}^{\frac{\beta_s}{\beta_t}} d\Pi - \widetilde{\ln(1-I_{H,L,\text{in}})} \tag{2.95}$$

By assuming that $\widetilde{\ln(1-I_{H,L,\text{out}})} = \ln(1-\widetilde{I_{H,L,\text{out}}})$ and $\widetilde{\ln(1-I_{H,L,\text{in}})} = \ln(1-\widetilde{I_{H,L,\text{in}}})$, which are not particularly true,

$$\widetilde{I_{H,L,\text{out}}} = 1 - e^{-\frac{1}{Q}\int_\Pi C_H^{\frac{1}{\beta_t}} \tau_{\text{m,total}}^{\frac{\beta_s}{\beta_t}} d\Pi + \ln(1-\widetilde{I_{H,L,\text{in}}})} \tag{2.96}$$

By substituting $I_H = I_{H,L}^{\beta_t}$ in eq. (2.96),

$$\widetilde{I_{H,\text{out}}} = \left[1 - e^{-\frac{1}{Q}\int_\Pi C_H^{\frac{1}{\beta_t}} \tau_{\text{m,total}}^{\frac{\beta_s}{\beta_t}} d\Pi + \ln(1-\widetilde{I_{H,\text{in}}}^{\frac{1}{\beta_t}})}\right]^{\beta_t} \tag{2.97}$$

If, additionally, $I_{H,\text{in}} = 0$,

$$I_{H,T} = \left[1 - e^{-\frac{1}{Q}\int_\Pi C_H^{\frac{1}{\beta_t}} \tau_{\text{m,total}}^{\frac{\beta_s}{\beta_t}} d\Pi}\right]^{\beta_t} \tag{2.98}$$

The same reasoning can be applied to the *linear damage index* model (eq. (2.83)), which would result in:

$$\widetilde{I_{H,\text{out}}} = \left[\frac{1}{Q}\int_\Pi C_H^{\frac{1}{\beta_t}} \tau_{\text{m,total}}^{\frac{\beta_s}{\beta_t}} d\Pi + \widetilde{I_{H,\text{in}}}^{\frac{1}{\beta_t}}\right]^{\beta_t} \tag{2.99}$$

If, additionally, $I_{H,\text{in}} = 0$,

$$I_{H,T} = \left[\frac{1}{Q}\int_\Pi C_H^{\frac{1}{\beta_t}} \tau_{\text{m,total}}^{\frac{\beta_s}{\beta_t}} d\Pi\right]^{\beta_t} \tag{2.100}$$

As can be noticed, the equations obtained from the simplified models (eqs. (2.98) and (2.100)) consider assumptions that may not be valid. Notice that eq. (2.100) is different from the one presented in Montevecchi *et al.* (1995) ($I_{H,T} = \frac{\int_\Pi \tau_{\text{m,total}}^{\beta_s} d\Pi}{Q}$), which is essentially the integration of eq. (2.81) in the entire computational domain while ignoring the time dependency factor.

2.4.2 **Thrombosis modeling**

The mechanism of thrombosis is directly related to platelet activation and aggregation. In fact, in VADs, platelets activate and aggregate, forming blood clotting (*thrombus*), due to mechanically induced high shear stress levels (SHERIFF *et al.*, 2013), requiring patients to take anti-coagulation medications, which may also lead to bleeding (FRASER *et al.*, 2010).

Platelet activation is closely related to the initiation of the formation of blood clotting (*thrombus*) (YUN *et al.*, 2016). Since minimizing platelet activation minimizes the risk of thrombosis and lowers the dose of anti-coagulation medications (FRASER *et al.*, 2010), it is an important aspect that should be taken into account in the design of blood flow devices. However, because of the previous lack of validated models for platelet activation (SOARES *et al.*, 2013), VADs are historically designed to account for only minimizing hemolysis, which corresponds to stress levels that are 10 times higher (i.e., one order of magnitude higher) than platelet activation (SHERIFF *et al.*, 2013; TRAVIS *et al.*, 2001; SOARES *et al.*, 2013).

In high speed VADs, the shear stresses acting in VADs can reach up to 800 Pa and extremely high shear stresses may act for short time intervals (in the order of ms) (SOARES *et al.*, 2013; KINI *et al.*, 2001; CHENG *et al.*, 2004). These brief durations of high shear stress levels may be sufficient to activate platelets and/or sensitize them (SHERIFF *et al.*, 2010). According to Soares *et al.* (2013), this sensitization means that the previously stressed platelets should not return to their pre-exposure condition, and should activate at higher shear stresses (SHERIFF *et al.*, 2010; SOARES *et al.*, 2013). According to Soares *et al.* (2013), the entire shear stress history must be taken into account in order to capture this effect.

Another factor contributing to thrombosis is platelet aggregation (CHOPARD *et al.*, 2017). However, according to Fraser *et al.* (2010), the models for platelet aggregation are complex and computationally high demanding, being therefore unsuitable for evaluating platelet aggregation in real fluid devices. Note that this means that the currently available platelet aggregation models are also unsuitable for topology optimization, since this computation would need to be repeated at each topology optimization iteration. Therefore, only platelet activation is considered in this work for evaluating thrombosis.

In order to measure the level of platelet activation, the PAS (Platelet Activation

State) index is normally used. The PAS index quantifies the contribution of platelet activation to the generation of thrombin, which is the protein responsible for activating platelets (BRASS, 2003; MONROE *et al.*, 2002; CONSOLO *et al.*, 2016). It is given by a dimensionless continuous measure in the interval [0, 1], and is experimentally measured by a PAS assay (SHERIFF *et al.*, 2014; CONSOLO *et al.*, 2016; NOBILI *et al.*, 2008; RAZ *et al.*, 2007). From the PAS assay, the PAS index may be expressed as

$$I_{PAS,T} = \frac{\Delta r_{\mathrm{tg}}}{r_{\mathrm{tg,full}}} = \frac{r_{\mathrm{tg,out}} - r_{\mathrm{tg,in}}}{r_{\mathrm{tg,full}}} \tag{2.101}$$

where $I_{PAS,T}$ is the PAS index (referred here as the *total PAS index*), $\Delta r_{\mathrm{tg}} = r_{\mathrm{tg,out}} - r_{\mathrm{tg,in}}$ is the variation of the rate of thrombin generation of the activated platelets, and $r_{\mathrm{tg,full}}$ is the rate of thrombin generation of fully activated platelets (i.e., the maximum thrombin generation capacity).

The *local PAS index*, which is distributed over the entire computational domain, would then be defined as

$$I_{PAS} = \frac{r_{\mathrm{tg}}}{r_{\mathrm{tg,full}}} \tag{2.102}$$

where I_{PAS} is the local PAS index and r_{tg} is the rate of thrombin generation of the activated platelets.

As in eq. (2.79), the total PAS index ($I_{PAS,T}$) may be given as a function of the local PAS index (I_{PAS}),

$$\begin{aligned} I_{PAS,T} =& \widetilde{\Delta I_{PAS}} = \widetilde{I_{PAS,\mathrm{out}}} - \widetilde{I_{PAS,\mathrm{in}}} = \\ & \frac{\int_{\Gamma_{\Pi,\mathrm{out}}} I_{PAS}(\boldsymbol{v}_{\mathrm{abs}} \bullet \boldsymbol{n}) d\Gamma_{\Pi,\mathrm{out}}}{\int_{\Gamma_{\Pi,\mathrm{out}}} (\boldsymbol{v}_{\mathrm{abs}} \bullet \boldsymbol{n}) d\Gamma_{\Pi,\mathrm{out}}} - \frac{\int_{\Gamma_{\Pi,\mathrm{in}}} I_{PAS}(\boldsymbol{v}_{\mathrm{abs}} \bullet \boldsymbol{n}) d\Gamma_{\Pi,\mathrm{in}}}{\int_{\Gamma_{\Pi,\mathrm{in}}} (\boldsymbol{v}_{\mathrm{abs}} \bullet \boldsymbol{n}) d\Gamma_{\Pi,\mathrm{in}}} \end{aligned} \tag{2.103}$$

The same simplification of eq. (2.80) is also possible:

$$I_{PAS,T} = \widetilde{\Delta I_{PAS}} = \widetilde{I_{PAS,\mathrm{out}}} - \widetilde{I_{PAS,\mathrm{in}}} = \frac{\oint_{\Gamma_\Pi} I_{PAS}(\boldsymbol{v}_{\mathrm{abs}} \bullet \boldsymbol{n}) d\Gamma_\Pi}{Q} \tag{2.104}$$

2.4.2.1 Numerical prediction of the PAS index

Some numerical prediction models for the PAS index are based on the same formulation used for the numerical prediction of the hemolysis index (Section 2.4.1.1). For example, the Giersiepen-Wurzinger correlation (eq. (2.81)) can be used by changing the coefficients from $C_H = 1.228 \times 10^{-5}\mathrm{Pa}^{-\beta_s}\mathrm{s}^{-\beta_t}$ to $C_{PAS} = 1.47 \times 10^{-6}\mathrm{Pa}^{-\alpha_s}\mathrm{s}^{-\alpha_t}$, from $\beta_s = 1.9918$ to $\alpha_s = 1.0400$ and from $\beta_t = 0.6606$ to $\alpha_t = 1.3000$ (GIERSIEPEN *et al.*,

1990; SHERIFF *et al.*, 2013). Some models that can be converted from hemolysis index models to PAS index models are: *linear damage index* (GIERSIEPEN *et al.*, 1990; SHERIFF *et al.*, 2013), *asymptotically consistent damage index* (GIERSIEPEN *et al.*, 1990; SHERIFF *et al.*, 2013), *mechanical dose infinitesimal damage index* (HELLUMS, 1994; NOBILI *et al.*, 2008), *infinitesimal damage index* (SHERIFF *et al.*, 2013), and *power law damage accumulation* (ALEMU; BLUESTEIN, 2007; SHERIFF *et al.*, 2013).

In this work, a formulation which is not simply a reuse of a hemolysis model with different coefficients is considered. The model is the *shear-induced platelet activation* model (SOARES *et al.*, 2013), which is able not only to capture the effect of the shear stress, but to capture the sensitization effect of platelets, in which the necessary shear stress levels for platelets to activate increases if the platelets are exposed to high shear stress levels during some interval of time. However, the original formulation of this model is highly non-linear, which leads to numerical convergence issues when solving with the finite element method (Eulerian approach). In order to solve this problem, the original model is reformulated based on the mechanical dose definition from Hellums (1994), reducing the non-linearity of the model (*mechanical dose shear-induced PAS* model).

2.4.2.1.1 *Mechanical dose shear-induced PAS model*

The *mechanical dose shear-induced PAS* model is a *mechanical dose*-based version of the *shear-induced platelet activation* model (SOARES *et al.*, 2013). As in the original *shear-induced platelet activation* model (SOARES *et al.*, 2013), this model is based on three effects (sensitization, stress level and stress rate), and also a correction for non-activated platelets. An additional term is included in order to penalize the PAS index inside the modeled solid material. The terms are described as follows (ALONSO; SILVA, 2022a):

1. Sensitization effect: The sensitization effect depends on the current level of activation (PAS index, I_{PAS}) and explicitly on the total shear stress accumulation of the entire history up to time "t" ($\int_0^t \tau_{\mathrm{m,total}} dt$). The form of this term has been experimentally determined (trial and error approach) (SOARES *et al.*, 2013) based on experimental data from Sheriff *et al.* (2010), which shows that platelets that were exposed to high shear stresses showed significantly higher rates of activation than platelets that were

not exposed to these high shear stresses (SHERIFF *et al.*, 2010; SHERIFF *et al.*, 2013). It may be given for each pathline from:

$$S_\tau = \int_0^t \tau_{\mathrm{m,total}} dt \tag{2.105}$$

$$\Delta I_{PAS,S} = C_{PAS,S} I_{PAS} S_\tau \Delta t \tag{2.106}$$

where $I_{PAS,S}$ is the PAS index contribution from the sensitization effect, S_τ is the *shear stress history*, and $C_{PAS,S}$ is the proportionality factor for the sensitization effect. According to Soares *et al.* (2013), $C_{PAS,S} = 1.5701 \times 10^{-7}\mathrm{Pa}^{-1}\mathrm{s}^{-2}$.

The corresponding differential forms become:

$$\frac{DS_\tau}{Dt} = \tau_{\mathrm{m,total}} \tag{2.107}$$

$$\frac{DI_{PAS,S}}{Dt} = C_{PAS,S} I_{PAS} S_\tau \tag{2.108}$$

2. Stress level effect: The stress level effect is based on the Giersiepen-Wurzinger correlation (eq. (2.81)). For the case of platelet activation, eq. (2.81) adapted for each pathline becomes:

$$\Delta I_{PAS,sl} = C_{PAS,sl} \tau_{\mathrm{m,total}}^{\alpha_s} \Delta t^{\alpha_t} \tag{2.109}$$

where $I_{PAS,sl}$ is the PAS index contribution from the shear level effect, α_s is the shear stress level exponent, and α_t is the stress level exposure time exponent. According to Soares *et al.* (2013), $C_{PAS,sl} = 1.4854 \times 10^{-7}\mathrm{Pa}^{-\alpha_s}\mathrm{s}^{-1}$, $\alpha_s = 1.4854$, and $\alpha_t = 1.4401$.

The original formulation of the *shear-induced platelet activation* model (SOARES *et al.*, 2013) assumes an infinitesimal time step ($\Delta t \rightarrow 0^+$), $\tau_{\mathrm{m,total}}$ being time-independent in eq. (2.109), and considers the power rule for derivatives, $\frac{D(I_{PAS}^{\frac{1}{\alpha_t}})}{Dt} = \frac{1}{\alpha_t} {I_{PAS}}^{\frac{1}{\alpha_t}-1} \frac{DI_{PAS}}{Dt}$. Therefore,

$$\frac{DI_{PAS,sl}}{Dt} = C_{PAS,sl}^{\frac{1}{\alpha_t}} \alpha_t \tau_{\mathrm{m,total}}^{\frac{\alpha_s}{\alpha_t}} {I_{PAS}}^{\frac{\alpha_t - 1}{\alpha_t}} \tag{2.110}$$

Note that there is a clear non-linearity present in eq. (2.110) due to the exponent of I_{PAS}. In order to avoid it, the mechanical dose approach (HELLUMS, 1994; NOBILI *et al.*, 2008) is considered. In the mechanical dose approach, a *mechanical dose of*

PAS from the stress level is defined as $\Delta D_{PAS,sl} = \tau_{\mathrm{m,total}}^{\frac{\alpha_s}{\alpha_t}} \Delta t$, which, from eq. (2.109), leads to

$$\Delta I_{PAS,sl} = C_{PAS,sl} \Delta D_{PAS,sl}^{\alpha_t} \tag{2.111}$$

By assuming an infinitesimal time step ($\Delta t \rightarrow 0^+$) and $\tau_{\mathrm{m,total}}$ being time-independent, the differential forms from eq. (2.111) become:

$$\frac{D D_{PAS,sl}}{Dt} = \tau_{\mathrm{m,total}}^{\frac{\alpha_s}{\alpha_t}} \tag{2.112}$$

$$\frac{D I_{PAS,sl}}{Dt} = C_{PAS,sl} \alpha_t D_{PAS,sl}^{\alpha_t - 1} \frac{D D_{PAS,sl}}{Dt} \tag{2.113}$$

3. Stress rate effect: The stress rate effect considers a formulation that is analogous to the Giersiepen-Wurzinger correlation. The resulting formulation was found by Soares *et al.* (2013) to correlate well to previous experimental data:

$$\Delta I_{PAS,sr} = C_{PAS,sr} |\dot{\tau}_{\mathrm{m,total}}|^{\delta_s} \Delta t^{\delta_t} \tag{2.114}$$

where $I_{PAS,sr}$ is the PAS index contribution from the shear rate effect, δ_s is the shear stress rate exponent, δ_t is the stress rate exposure time exponent, and $\dot{\tau}_{\mathrm{m,total}} = \frac{D\tau_{\mathrm{m,total}}}{Dt}$. It can be mentioned that Hansen *et al.* (2015) considers $\dot{\tau}_{\mathrm{m,total}}$ to be small and, therefore, neglects it. According to Soares *et al.* (2013), $C_{PAS,sr} = 1.3889 \times 10^{-4} \mathrm{Pa}^{-\delta_s} \mathrm{s}^{\delta_s - 1}$, $\delta_s = 0.5720$, and $\delta_t = 0.5125$.

The original formulation of the *shear-induced platelet activation* model (SOARES *et al.*, 2013) assumes $\ddot{\tau}_{\mathrm{m,total}} = \frac{D^2 \tau_{\mathrm{m,total}}}{Dt^2} = 0$, leading to

$$\frac{D I_{PAS,sr}}{Dt} = C_{PAS,sr}^{\frac{1}{\delta_t}} \delta_t \left| \frac{D\tau_{\mathrm{m,total}}}{Dt} \right|^{\frac{\delta_s}{\delta_t}} {I_{PAS}}^{\frac{\delta_t - 1}{\delta_t}} \tag{2.115}$$

As can be noticed, there is a clear non-linearity present in eq. (2.115) due to the exponent of I_{PAS}. In order to avoid it, the mechanical dose approach (HELLUMS, 1994; NOBILI *et al.*, 2008) is considered. In the mechanical dose approach, a *mechanical dose of PAS from the stress rate* is defined as $\Delta D_{PAS,sr} = \tau_{\mathrm{m,total}}^{\frac{\delta_s}{\delta_t}} \Delta t$, which, from eq. (2.114), leads to

$$\Delta I_{PAS,sr} = C_{PAS,sr} \Delta D_{PAS,sr}^{\delta_t} \tag{2.116}$$

By assuming $\ddot{\tau}_{\mathrm{m,total}} = \frac{D^2\tau_{\mathrm{m,total}}}{Dt^2} = 0$, the differential forms from eq. (2.116) become:

$$\frac{DD_{PAS,sr}}{Dt} = \left|\frac{D\tau_{\mathrm{m,total}}}{Dt}\right|^{\frac{\delta_s}{\delta_t}} \tag{2.117}$$

$$\frac{DI_{PAS,sr}}{Dt} = C_{PAS,sr}\delta_t D_{PAS,sr}^{\delta_t - 1}\frac{DD_{PAS,sr}}{Dt} \tag{2.118}$$

4. Correction term for non-activated platelets: The original formulation of the *shear-induced platelet activation* model (SOARES *et al.*, 2013) also considers a *correction term for non-activated platelets*, which is analogous to the corresponding one in the *asymptotically consistent damage index* model (FARINAS *et al.*, 2006), and consists of multiplying all the effects by $(1 - I_{PAS})$. Soares *et al.* (2013) also suggests that other saturation terms, such as a sigmoidal function (*Gompertz function*), may be used instead of the linear correction $(1 - I_{PAS})$. When considering the mechanical dose approach (HELLUMS, 1994; NOBILI *et al.*, 2008), this correction is not required for bounding I_{PAS} between 0 and 1; however, this correction may be useful for the sensitization effect, which means that it is included in this work.

5. Solid material penalization: An additional term is included in order to penalize the PAS index inside the modeled solid material. This term is given as:

$$+\kappa_{PAS}(\alpha)(I_{PAS} - I_{PAS,\mathrm{mat}}) \tag{2.119}$$

where $\kappa_{PAS}(\alpha)$ is an additional penalization parameter for the PAS index (Section 2.5.1.5), and $I_{PAS,\mathrm{mat}}$ is the value of the PAS index being imposed inside the modeled solid material. $I_{PAS,\mathrm{mat}}$ can be set, for example, as $I_{PAS,\mathrm{mat}} = 10^{-14}$ (a small value).

It can be highlighted that the hemolysis model formulation (Section 2.4.1.1) did not require an additional penalization term, because it depends essentially on the value of the total shear stress magnitude, which does not induce high values inside the modeled solid material. However, the PAS formulation depends on the *shear stress history*, which may significantly increase the platelet activation that occurs inside the modeled solid material. This high value inside the solid material can hinder the topology optimization process.

The complete differential form is obtained by combining the presented five effects (sensitization, stress level, stress rate, correction term for non-activated platelets, and

solid material penalization). By also unfolding the material derivative terms in the relative reference frame ($\frac{D()}{Dt} = \frac{\partial()}{\partial t} + (\boldsymbol{v}\bullet\nabla)()$) and assuming steady state flow, the *mechanical dose shear-induced PAS* model in the differential form becomes a set of 3 linear differential equations and 1 non-linear differential equation:

$$(\boldsymbol{v}\bullet\nabla)S_\tau = \tau_{\mathrm{m,total}} \tag{2.120}$$

$$(\boldsymbol{v}\bullet\nabla)D_{PAS,sl} = \tau_{\mathrm{m,total}}^{\frac{\alpha_s}{\alpha_t}} \tag{2.121}$$

$$(\boldsymbol{v}\bullet\nabla)D_{PAS,sr} = \left|(\boldsymbol{v}\bullet\nabla)\tau_{\mathrm{m,total}}\right|^{\frac{\delta_s}{\delta_t}} \tag{2.122}$$

$$\begin{aligned}(\boldsymbol{v}\bullet\nabla)I_{PAS} = \Bigg[& \underbrace{C_{PAS,S}I_{PAS}S_\tau}_{\text{Sensitization effect}} + \underbrace{C_{PAS,sl}\alpha_t D_{PAS,sl}^{\alpha_t-1}(\boldsymbol{v}\bullet\nabla)D_{PAS,sl}}_{\text{Stress level effect}} \\ & + \underbrace{C_{PAS,sr}\delta_t D_{PAS,sr}^{\delta_t-1}(\boldsymbol{v}\bullet\nabla)D_{PAS,sr}}_{\text{Stress rate effect}} \Bigg] \underbrace{(1-I_{PAS})}_{\substack{\text{Correction term}\\ \text{for non-activated}\\ \text{platelets}}} \\ & \underbrace{+\kappa_{PAS}(\alpha)(I_{PAS}-I_{PAS,\mathrm{mat}})}_{\text{Solid material penalization}}\end{aligned} \tag{2.123}$$

The weak form, as in the case of the *asymptotically consistent damage index* model for the hemolysis index (Section 2.4.1.1.1), can be defined from LSFEM for the same stability reason, and an additional division can be included as in the equations:

$$\int_\Pi \left[\frac{(\boldsymbol{v}\bullet\nabla)S_\tau}{\tau_{\mathrm{m,total}}} - 1\right]\left[(\boldsymbol{v}\bullet\nabla)w_{S_\tau}\right] d\Pi = 0 \tag{2.124}$$

$$\int_\Pi \left[\frac{(\boldsymbol{v}\bullet\nabla)D_{PAS,sl}}{\tau_{\mathrm{m,total}}^{\frac{\alpha_s}{\alpha_t}}} - 1\right]\left[(\boldsymbol{v}\bullet\nabla)w_{D_{PAS,sl}}\right] d\Pi = 0 \tag{2.125}$$

$$\int_\Pi \left[\frac{(\boldsymbol{v}\bullet\nabla)D_{PAS,sr}}{\left|(\boldsymbol{v}\bullet\nabla)\tau_{\mathrm{m,total}}\right|^{\frac{\delta_s}{\delta_t}}} - 1\right]\left[(\boldsymbol{v}\bullet\nabla)w_{D_{PAS,sr}}\right] d\Pi = 0 \tag{2.126}$$

$$
\begin{aligned}
&\left\{ \frac{(\boldsymbol{v} \bullet \nabla) I_{PAS}}{S_\tau} - \left[C_{PAS,S} I_{PAS} + \frac{C_{PAS,sl} \alpha_t D_{PAS,sl}^{\alpha_t - 1} (\boldsymbol{v} \bullet \nabla) D_{PAS,sl}}{S_\tau} \right.\right. \\
&\left.\left. + \frac{C_{PAS,sr} \delta_t D_{PAS,sr}^{\delta_t - 1} (\boldsymbol{v} \bullet \nabla) D_{PAS,sr}}{S_\tau} \right] (1 - I_{PAS}) - \kappa_{PAS}(\alpha)(I_{PAS} - I_{PAS,\mathrm{mat}}) \right\} \\
&\left\{ (\boldsymbol{v} \bullet \nabla) w_{I_{PAS}} - \left[C_{PAS,S} w_{I_{PAS}} S_\tau (1 - I_{PAS}) + \left(C_{PAS,S} I_{PAS} S_\tau \right.\right.\right. \\
&\left.\left.\left. + C_{PAS,sl} \alpha_t D_{PAS,sl}^{\alpha_t - 1} (\boldsymbol{v} \bullet \nabla) D_{PAS,sl} + C_{PAS,sr} \delta_t D_{PAS,sr}^{\delta_t - 1} (\boldsymbol{v} \bullet \nabla) D_{PAS,sr} \right) (-w_{I_{PAS}}) \right] \right. \\
&\left. - \kappa_{PAS}(\alpha) w_{I_{PAS}} \right\} d\Pi = 0
\end{aligned}
\tag{2.127}
$$

where w_{S_τ}, $w_{D_{PAS,sl}}$, $w_{D_{PAS,sr}}$ and $w_{I_{PAS}}$ are the test functions.

Since no boundary terms appear in eqs. (2.124), (2.125), (2.126) and (2.127), the only boundary conditions that are imposed are Dirichlet boundary conditions on the inlet, which may consist of, for example, zero inlet thrombosis ($S_\tau = 0$, $D_{PAS,sl} = 0$, $D_{PAS,sr} = 0$, $I_{PAS} = 0$).

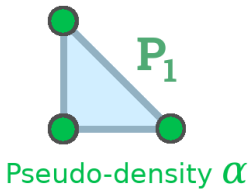
Notice that $(\boldsymbol{v} \bullet \nabla) D_{PAS,sl}$ and $(\boldsymbol{v} \bullet \nabla) D_{PAS,sr}$ in eq. (2.123) can be substituted from eqs. (2.121) and (2.122), but the resulting system of equations would achieve a worse numerical conditioning (as has been observed in some tests). It has been observed that the numerical conditioning is much better when using the formulation presented in eq. (2.123).

Since eqs. (2.124), (2.125), (2.126) and (2.127) are independent, they may be solved independently and, therefore, sequentially.

2.5 FORMULATION OF THE TOPOLOGY OPTIMIZATION PROBLEM

The formulation of the topology optimization problem is described as follows. The design variable is the pseudo-density, which, in this work, is assumed with a linear interpolation (*piecewise linear*, P_1, “CG1”) (see Fig. 2.10). It can be mentioned that a discrete interpolation (*element-wise*, dP_0, “DG0”) can also be used in topology optimization (BORRVALL; PETERSSON, 2003); however, as explained in Section 2.5.7.1, if the Helmholtz pseudo-density filter is used, the pseudo-density has to be using at least linear interpolation (P_1).

Figure 2.10 – Finite element interpolation for the pseudo-density.



Source: Author.

2.5.1 **Material model**

The material model in topology optimization represents the influence of the design variable in the topology optimization process. In fluid topology optimization, the material model is used to model the presence of a solid material. A commonly used approach is by considering a porous medium (BORRVALL; PETERSSON, 2003), whose permeability is varied in order to allow or block fluid flow.

2.5.1.1 Brinkman model

The resistance force of the porous medium ($\boldsymbol{f}_r(\alpha)$) may be defined according to Darcy's Law (Brinkman model) (BORRVALL; PETERSSON, 2003; DARCY, 1856; BRINKMAN, 1947). The Brinkman model considers that the porous medium generates a resistance force directly proportional to the relative velocity between the fluid flow and the porous medium (VAFAI, 2005), which is given by:

$$\boldsymbol{f}_r(\alpha) = -\kappa(\alpha)\boldsymbol{v}_{\text{mat}} \tag{2.128}$$

where $\boldsymbol{f}_r(\alpha)$ is the resistance force of the porous medium, $\kappa(\alpha)$ is the inverse permeability (*absorption coefficient*), $\boldsymbol{v}_{\text{mat}}$ is the velocity of the fluid in relation to the porous material (in a rotating reference frame, $\boldsymbol{v}_{\text{mat}} = \boldsymbol{v} - \boldsymbol{v}_{\text{material}}$, where $\boldsymbol{v}_{\text{material}} = \boldsymbol{\omega}_{\text{mat}} \wedge \boldsymbol{r}$ is the relative velocity of the porous medium, $\boldsymbol{\omega}_{\text{mat}} = \omega_{\text{mat}}\boldsymbol{e_z}$ is the rotation of the porous medium in relation to the reference frame), and α is the pseudo-density, which attains values between 0 (solid) and 1 (fluid) in order to represent the porous medium. Since the pseudo-density (α) is used to vary the permeability of the fluid flow, it is used as the design variable of topology optimization.

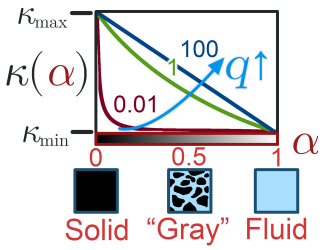
The main objective in topology optimization is to obtain a sufficiently discrete distribution of the design variable (pseudo-density) inside the design domain, which

means that, for better numerical conditioning, the subtle transition between the *binary* values $\alpha = 0$ (for solid) and $\alpha = 1$ (for fluid) can be *relaxed*. This *relaxation* allows the presence of an intermediate porous medium, which is normally referred as a *gray* material – with pseudo-density values between 0 and 1 (*real* values). Borrvall and Petersson (2003) considers the following convex interpolation function for the inverse permeability $\kappa(\alpha)$:

$$\kappa(\alpha) = \kappa_{\max} + (\kappa_{\min} - \kappa_{\max})\alpha\frac{1+q}{\alpha+q} \tag{2.129}$$

where the inverse permeability ($\kappa(\alpha)$) is bounded by maximum ($\kappa_{\max}$) and minimum ($\kappa_{\min}$) values, and has its convexity (*relaxation*) guided by the penalization parameter $q > 0$ (large values of q lead to *less relaxed* material models). The inverse permeability of eq. (2.129) is illustrated in Fig. 2.11.

Figure 2.11 – Illustration of Borrvall and Petersson (2003)'s inverse permeability material model.



Source: Author.

As can be seen in Fig. 2.11, when $\alpha = 0$, there is solid ($\kappa(\alpha = 0) = \kappa_{\max}$), and when $\alpha = 1$, there is fluid ($\kappa(\alpha = 1) = \kappa_{\min}$). For intermediary values (*gray*), the resistance force is determined by the penalty parameter (q). The value for $\kappa_{\min}$ may be selected as 0 or as a sufficiently small value if needed for numerical stability (BORRVALL; PETERSSON, 2003). The value for $\kappa_{\max}$ has to be selected according to the fluid flow problem, since a low value can cause the fluid to penetrate in solid regions and a too high value can stagnate the design in the topology optimization process. The value of q can be low, *relaxing* more the transition between solid and fluid (i.e., allowing some of the intermediary values of α to exert lower inverse permeability values, which allows an increased presence of fluid during topology optimization), or high, with a more direct transition. Thus, in order to obtain discrete solutions, it should be useful to start with lower values of q and then increase them during the topology optimization process. Furthermore, it is possible to optionally define $\kappa_{\max}$ in function

of a dimensionless number (the maximum Darcy number, $\mathrm{Da}_{\max}$), which is given as (OLESEN *et al.*, 2006):

$$\mathrm{Da}_{\max} = \frac{\mu}{\kappa_{\max} L^2} \tag{2.130}$$

where L is a characteristic dimension. Since this work considers various different numerical examples, for clarity, $\kappa_{\max}$ is expressed as the value $\frac{1}{\mathrm{Da}_{\max} L^2}$, by indicating its value in function of μ.

2.5.1.2 Extended material model for the 2D swirl flow model

Alonso *et al.* (2019) proposes a modification to eq. (2.128) in the 2D swirl flow model, by considering that the tangential velocity behaves differently than the other velocity components (because the 2D swirl flow model is axisymmetric), and thus the inverse permeability may be weaker in the tangential direction in relation to the radial and axial directions. The resistance force of the porous medium (eq. (2.128)) becomes:

$$\boldsymbol{f}_r(\alpha) = -\boldsymbol{\kappa}(\alpha)\boldsymbol{v}_{\mathrm{mat}} = -(\kappa_r(\alpha) v_{\mathrm{mat},r}\ ,\ \kappa_\theta(\alpha) v_{\mathrm{mat},\theta}\ ,\ \kappa_z(\alpha) v_{\mathrm{mat},z}) \tag{2.131}$$

where $\boldsymbol{\kappa}(\alpha) = \begin{bmatrix} \kappa_r(\alpha) & 0 & 0 \\ 0 & \kappa_\theta(\alpha) & 0 \\ 0 & 0 & \kappa_z(\alpha) \end{bmatrix}$ is an absorption (*inverse permeability*) matrix. Alonso *et al.* (2019) suggests that, for the design of a Tesla pump in a rotating reference frame, one possible choice for the parameters would be $\kappa_r(\alpha) = \kappa_z(\alpha)$, while $\kappa_\theta(\alpha)$ assumes smaller $\kappa_{\max}$ and/or q (i.e., more relaxed). This should enforce the formation of a channel connecting the inlet and the outlet in relation to the rotation effect, which may try to add material on larger radii in order to accelerate the fluid flow tangentially (ALONSO *et al.*, 2019).

By considering the extended material model, eq. (2.129) becomes

$$\kappa_r(\alpha) = \kappa_{r,\max} + (\kappa_{r,\min} - \kappa_{r,\max})\alpha \frac{1+q_r}{\alpha+q_r} \tag{2.132a}$$

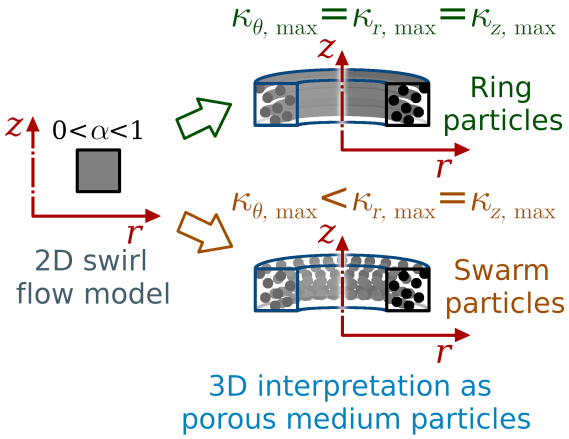
$$\kappa_\theta(\alpha) = \kappa_{\theta,\max} + (\kappa_{\theta,\min} - \kappa_{\theta,\max})\alpha \frac{1+q_\theta}{\alpha+q_\theta} \tag{2.132b}$$

$$\kappa_z(\alpha) = \kappa_{z,\max} + (\kappa_{z,\min} - \kappa_{z,\max})\alpha \frac{1+q_z}{\alpha+q_z} \tag{2.132c}$$

where $\kappa_{i,\min}$ and $\kappa_{i,\max}$ ($i = r, \theta$ or z) are, respectively, the minimum and the maximum values of $\kappa_i(\alpha)$. The parameter q_i is the penalty parameter.

Fig. 2.12 shows a comparison of the approaches considering $\kappa_{\theta,\max} = \kappa_{r,\max} = \kappa_{z,\max}$, and $\kappa_{\theta,\max} < \kappa_{r,\max} = \kappa_{z,\max}$. As can be seen, in the first approach, the uniform porosity *zone*/*element* (in $0 < \alpha < 1$) can be interpreted as ring particles. In the second approach, the particles would be organized differently in each cross-section, maintaining the same difficulty for the fluid to flow in the rz direction, but with "more porosity" (i.e., easier to flow) in the tangential (*swirl*) direction.

Figure 2.12 – 3D interpretation of the porosity of the 2D swirl flow model as porous medium particles.



Source: Author.

2.5.1.3 Brinkman-Forchheimer model

The material model from eq. (2.128) can be extended in order to include not only the Darcy term (DARCY, 1856; BRINKMAN, 1947) (*Brinkman model*) of the original formulation, but also the Forchheimer term (FORCHHEIMER, 1901). This type of augmentation in the material model has been first considered by Philippi and Jin (2015) in fluid topology optimization, and is referred to as the *complete porosity formulation*. In relation to the name *Brinkman model* (BRINKMAN, 1947), which refers to the case where only the Darcy term is considered, some references refer to the augmented formulation as the *Brinkman-Forchheimer model* (or *Forchheimer model*) (HUANG; AYOUB, 2006; ALIMOHAMADI *et al.*, 2014).

According to Geertsma (1974), when modeling a porous medium, the Darcy's law (linear law) is only valid to model porous material for low velocities (sufficiently low Reynolds numbers) and for single-phase flow (KUNDU *et al.*, 2016; DARCY, 1856; WANG *et al.*, 2015). The more generic equation is given by Forchheimer's law (quadratic law) and is given by including the Forchheimer correction (*non-Darcy flow behavior*) to

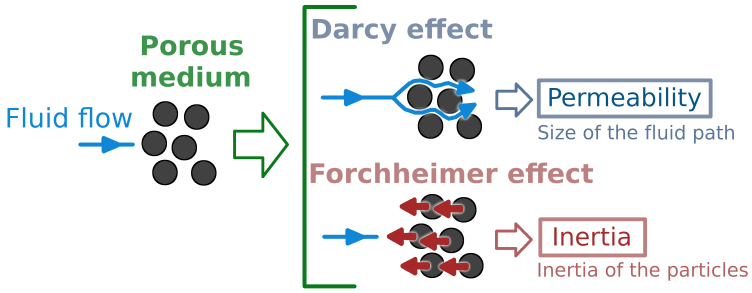
Darcy's law. The original formulation of Forchheimer's law is given by the pressure drop in a porous medium (FORCHHEIMER, 1901 apud GEERTSMA, 1974) (BEAR, 2018; JOSEPH *et al.*, 1982; VAFAI, 2005)

$$-\nabla p = \underbrace{\frac{\mu}{k_D}\boldsymbol{v}_{\text{mat}}}_{\text{Darcy term}} + \underbrace{\beta_F \rho |\boldsymbol{v}_{\text{mat}}| \boldsymbol{v}_{\text{mat}}}_{\text{Forchheimer term}} \tag{2.133}$$

where μ is the dynamic viscosity, ρ is the density, k_D is the formation permeability, p is the pressure, $\boldsymbol{v}_{\text{mat}}$ is the velocity of the fluid in relation to the porous medium, β_F is the coefficient of inertial flow resistance, and $|\boldsymbol{v}_{\text{mat}}| = \sqrt{\boldsymbol{v}_{\text{mat}} \bullet \boldsymbol{v}_{\text{mat}}}$.

The influence of each term of equation (2.133) is represented in Fig. 2.13: the Darcy term gives the reduction of the size of the fluid path due to the porous medium, while the Forchheimer term gives the fluid deceleration due to the inertia of the particles of the porous medium. According to Lasseux and Valdés-Parada (2017), the effect of the Forchheimer term is not significant for low Reynolds numbers.

Figure 2.13 – Darcy and Forchheimer effects in a porous medium.



Source: Author (ALONSO; SILVA, 2022b).

According to Cimolin and Discacciati (2013), $\beta_F = \frac{C_F}{\sqrt{k_D}}$, where C_F is the dimensionless form-drag constant (BEAR, 2018), also called Forchheimer constant (ALIMOHAMADI *et al.*, 2014). Therefore, by representing the porous medium of eq. (2.133) as a resistance force as shown in eq. (2.128), and considering $\frac{\mu}{k_D} \equiv \kappa(\alpha)$ and $\frac{\rho}{\sqrt{\mu}} C_F \equiv k_{\text{inertia}}$ (ALONSO; SILVA, 2022b)

$$\boldsymbol{f}_r = \underbrace{-\kappa(\alpha)\boldsymbol{v}_{\text{mat}}}_{\text{Darcy term}} \underbrace{-k_{\text{inertia}}\sqrt{\kappa(\alpha)}|\boldsymbol{v}_{\text{mat}}|\boldsymbol{v}_{\text{mat}}}_{\text{Forchheimer term}} \tag{2.134}$$

where $k_{\text{inertia}} = \frac{\rho}{\sqrt{\mu}} C_F$ is the inertial resistance factor. If $\kappa(\alpha)$ is given by the extended material model ($\boldsymbol{\kappa}(\alpha)$) (from Section 2.5.1.2), then $\sqrt{\kappa(\alpha)}$ is calculated for each term of

$\boldsymbol{\kappa}(\alpha)$, as "$\sqrt{\boldsymbol{\kappa}(\alpha)}$" $= \begin{bmatrix} \sqrt{\kappa_r(\alpha)} & 0 & 0 \\ 0 & \sqrt{\kappa_\theta(\alpha)} & 0 \\ 0 & 0 & \sqrt{\kappa_z(\alpha)} \end{bmatrix}$.

The Forchheimer constant C_F varies according to the type of porous medium (JOSEPH *et al.*, 1982; BEAVERS; SPARROW, 1969; SHWARTZ; PROBSTEIN, 1969). If the diameter of the porous medium "particles" is much smaller than the microscopic scale (PHILIPPI; JIN, 2015), C_F can be assumed as a *universal* constant (WARD, 1964) given by $C_F = 0.55$ (PHILIPPI; JIN, 2015). Since, in topology optimization, the porous material is used to model a solid wall and not a specific type of porous material, C_F is assumed as 0.55 in this work.

According to Varsakelis and Papalexandris (2017), eqs. (2.9) and (2.10) considering eq. (2.134) consist of a well-posed problem. The other approach for modeling the Forchheimer equation is given by the semi-empirical approach (Carman-Kozeny equation) (TOSCO *et al.*, 2013; AMIGO *et al.*, 2018; WHITAKER, 1996), which considers a dependency on microscopic and macroscopic particles characteristics of the porous medium, and distances the porosity modeling from the modeling of solid material used in this work.

Outside the topology optimization field, the Brinkman-Forchheimer model has been applied to fluid flow simulations for blood in porous medium (ALIMOHAMADI *et al.*, 2014; BHARGAVA *et al.*, 2007). However, for this same application, the Brinkman model (KUMAR *et al.*, 2016; CHEEMA *et al.*, 2014; GAUR; GUPTA, 2014) has also been applied.

2.5.1.4 Material model for the non-Newtonian viscosity

When $\alpha = 0$ (solid), it is expected that the velocity of the fluid be minimum, and, therefore, it is expected that the viscous shear rate magnitude ($\dot{\gamma}_{\mathrm{m}}$) be near zero. In this case, eq. (2.11) results in $\mu(\dot{\gamma}_{\mathrm{m}}) \approx \mu_0$ (i.e., the non-Newtonian viscosity assumes its higher non-Newtonian value). Since even small fluid velocities can lead the viscous shear rate magnitude ($\dot{\gamma}_{\mathrm{m}}$) not to approach zero inside the solid material, a penalization scheme may be used in order to improve this behavior of having $\mu(\dot{\gamma}_{\mathrm{m}}) \approx \mu_0$ inside the solid material. The penalization scheme consists of changing the non-Newtonian viscosity to the following equation:

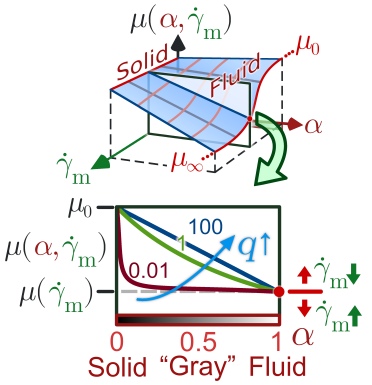
$$\mu(\alpha, \dot{\gamma}_{\mathrm{m}}) = \mu_0 + (\mu(\dot{\gamma}_{\mathrm{m}}) - \mu_0)\alpha\frac{1+q}{\alpha+q} \tag{2.135}$$

where the dynamic viscosity in the solid is μ_0 and the dynamic viscosity in the fluid is $\mu(\dot{\gamma}_{\mathrm{m}})$ (eq. (2.11)). The penalization parameter $q > 0$ is the same of eq. (2.129).

This approach is similar to what has been proposed by Pingen and Maute (2010), but with the "solid material viscosity" being the *highest* viscosity (μ_0) and not the *lowest* viscosity (μ_∞), which was used by Pingen and Maute (2010). Also, Pingen and Maute (2010)'s penalization was used to counter a coupling issue that happened between the non-Newtonian viscosity and the inverse permeability of the Lattice-Boltzmann Method (LBM), which is the kinetic approach for modeling fluid flow, while this work relies on the hydrodynamic approach for modeling fluid flow (i.e., the continuity and Navier-Stokes equations) and aims to improve the consistency of the non-Newtonian viscosity with the expected/desired values inside a modeled solid material. A non-Newtonian penalization approach proposed by Hyun *et al.* (2014) in the context of 2D flow topology optimization says that using the non-Newtonian penalization would avoid numerical instability due to the non-linearity of eq. (2.11).

Fig. 2.14 illustrates the material model presented in eq. (2.135). The upper part of the figure portrays a 3D plot of the material model for the non-Newtonian viscosity: when $\alpha = 0$ (solid), the non-Newtonian viscosity is given by $\mu(\alpha, \dot{\gamma}_{\mathrm{m}}) \approx \mu_0$; when $\alpha = 1$ (fluid), the non-Newtonian viscosity is given by $\mu(\alpha, \dot{\gamma}_{\mathrm{m}}) = \mu(\dot{\gamma}_{\mathrm{m}})$ (i.e., eq. (2.11)). Therefore, the material model is the surface connecting the curves of $\alpha = 0$ (solid) and $\alpha = 1$ (fluid). The upper part of the figure shows the material model with an almost straight line (high penalization parameter value (q)), and the "slice" shown in the lower part of the figure shows some possible values of the penalization parameter (q). As indicated in the lower part of the figure, the "lower limit" of the viscosity ($\mu(\dot{\gamma}_{\mathrm{m}})$) has a dependency on the viscous shear rate magnitude ($\dot{\gamma}_{\mathrm{m}}$): a lower viscous shear rate magnitude implies a higher "lower limit" for the viscosity, and a higher viscous shear rate magnitude implies a lower "lower limit" for the viscosity.

Figure 2.14 – Material model for the non-Newtonian viscosity.



Source: Author (ALONSO *et al.*, 2020).

The main consequence of the use of eq. (2.135) is that the non-Newtonian viscosity becomes higher and uniform inside a modeled solid material – see the Appendix 2 from Alonso *et al.* (2020). From performed tests, the computed pressure and velocities are mostly affected during the topology optimization iterations, while there are still *gray* regions in the topology. The effect of the non-Newtonian penalization in the pressure and velocities becomes small in the final optimized topology (assuming that $\kappa_{\max}$ from eq. (2.129) is high enough so as to block fluid flow). Throughout this work, the penalization shown in eq. (2.135) is referred to as *non-Newtonian penalization*.

2.5.1.5 Material model for the PAS index

The material model for the solid material penalization of the PAS index (Section 2.4.2.1) is given as:

$$\kappa_{PAS}(\alpha) = \kappa_{PAS,\max} + (\kappa_{PAS,\min} - \kappa_{PAS,\max})\alpha\frac{1+q}{\alpha+q} \tag{2.136}$$

where $\kappa_{PAS,\max}$ and $\kappa_{PAS,\min}$ are, respectively, the maximum and minimum values of the additional penalization parameter $\kappa_{PAS}(\alpha)$. The penalization parameter $q > 0$ is the same of eq. (2.129). $\kappa_{PAS,\min}$ is set as zero, in order for only the modeled solid material to include the additional penalization.

2.5.1.6 Material model for the wall distance

The material model for the solid material penalization of the wall distance (Section 2.1.3.1) is given as:

$$\gamma(\alpha) = \gamma_{\max} + (\gamma_{\min} - \gamma_{\max})\alpha\frac{1+q}{\alpha+q} \tag{2.137}$$

where $\gamma_{\max}$ and $\gamma_{\min}$ are, respectively, the maximum and minimum values of the wall penalization $\gamma(\alpha)$. The penalization parameter $q > 0$ is the same of eq. (2.129). $\gamma_{\min}$ is set as zero, in order for only the modeled solid material to include the wall penalization.

2.5.2 **Measure of non-discreteness**

In order to evaluate the discreteness of the optimized topology, the measure of non-discreteness (SIGMUND, 2007) may be used. It is a quantity related to the performance of the topology optimization that has been performed. The measure of non-discreteness of the optimized topology refers to how near the final values of the design variable (α) are in relation to the bounds (i.e., to $\alpha = 0$ (solid) and $\alpha = 1$ (fluid)):

$$M_{ND} = \frac{\int_{\Pi} 4\alpha(1-\alpha) d\Pi}{\int_{\Pi} d\Pi} \tag{2.138}$$

where M_{ND} = 0% in the case of a fully discrete topology ($\alpha = 0$ or $\alpha = 1$), and M_{ND} = 100% in the case of a fully gray topology ($\alpha = 0.5$).

2.5.3 **Topology optimization problem**

The topology optimization problem is formulated as shown below.

$$\begin{aligned} &\textbf{min}_{\alpha}\ J(\boldsymbol{u}(\alpha), \alpha) \\ &\textbf{such that} \\ &\quad \text{Fluid volume constraint: } \int_{\Pi_\alpha} \alpha d\Pi_\alpha \leqslant f V_0 \\ &\quad \text{Box constraint of } \alpha\text{: } 0 \leqslant \alpha \leqslant 1 \end{aligned} \tag{2.139}$$

where Π_α is the design domain; f is the specified volume fraction; $V_0 = \int_{\Pi_\alpha} d\Pi_\alpha$ is the volume of the design domain; $J(\boldsymbol{u}(\alpha), \alpha)$ is the multi-objective function; and $\boldsymbol{u}(\alpha) = (p(\alpha), \boldsymbol{v}(\alpha))$ (for laminar flow) is the state vector given by the boundary value problem (eq. (2.40)), which features an indirect dependency with respect to the design variable α. When considering turbulent flow, the additional state variables from the solution of turbulence are also included in the state vector: $\tilde{\nu}_{\mathrm{T}}(\alpha)$ and $G(\alpha)$, for the Spalart-Allmaras model, and $R_{\mathrm{T}}(\alpha)$, for the Wray-Agarwal model (WA2018). The volume constraint is normally used in topology optimization in order to limit the solution space

and better condition the topology optimization problem, because an excessively wide solution space in some problems may possibly lead the topology optimization to worse local minima or hinder the topology optimization process in relation to a constrained solution. The box constraint of the design variable (α) is used in order to restrict the values of the design variable (α) in the optimization to the possible ones (between 0 and 1).

The multi-objective function, in the case of considering the total hemolysis index ($I_{H,T}$) and the total PAS index ($I_{PAS,T}$) may also be expressed as $J(p(\alpha), \boldsymbol{v}(\alpha), \alpha, I_H(p(\alpha), \boldsymbol{v}(\alpha), \alpha), I_{PAS}(p(\alpha), \boldsymbol{v}(\alpha), \alpha))$ (for laminar flow) in order to explicitly show the dependency of the objective function with the solution of the blood damage weak forms (eqs. (2.88), (2.124), (2.125), (2.126) and (2.127)). The multi-objective function is defined in the next section.

2.5.4 **Multi-objective function**

When defining the topology optimization problem, it may be necessary to consider more than one objective, such as improving the performance and reducing blood damage. The objectives considered in this work are selected from Sections 2.3 and 2.4:

- Minimization of the relative energy dissipation (Φ_{rel}, eq. (2.51)), meaning the reduction of energy dissipation in the fluid flow, and the maximization of pressure head;
- Minimization of fluid power (P_f, eq. (2.55)), meaning the reduction of the necessary amount of power to pump the fluid;
- Minimization of vorticity ($\xi_{V,\mathrm{rel}}$, eq. (2.62)), meaning the reduction of the formation of vortices (recirculation) in the fluid flow;
- Minimization of the total hemolysis index ($I_{H,T}$, eq. (2.79)), directly meaning the reduction of hemolysis in the fluid flow;
- Minimization of the total PAS index ($I_{PAS,T}$, eq. (2.103)), directly meaning the reduction of thrombosis in the fluid flow.

It can be noticed that not all performance quantities presented in Section 2.3 are considered as objective functions. Particularly, the pressure head (H, eq. (2.64))

is not directly included, because it is indirectly considered through the relative energy dissipation objective function. Also, the pressure coefficients and static pressure rise represent effects of the flow machine operation which may also be improved through the relative energy dissipation objective function. The isentropic efficiency is not considered here as an objective function, because one problem of directly using only the isentropic efficiency as the objective function (or the ratio $\frac{P_f}{H}$) is that extremely small power and extremely small pressure heads can also lead to "high" isentropic efficiencies, which means that additional constraints would need be included in the topology optimization problem. In order not to further increase the complexity or the computational cost, a multi-objective function is used in this work, but the approach considering isentropic efficiency may be evaluated in a future research.

The necessary objective functions are then weighted into a single function (multi-objective function). This is a way for combining various objectives in a single function for optimization (*multi-objective optimization*). Normally, such approach would enable drawing a *Pareto front* (SATO *et al.*, 2017); however, when the objective functions are not fully independent (not simple trade-offs), such thing becomes harder (i.e., improving one function may possibly improve, instead of worsening, the other one), and also not all optimized topologies for all weights may be feasible (i.e., sufficiently discrete, without any artificial structure generated only by the overprioritization of one objective at the expense of the others etc.) – There are also cases in which overprioritizing one objective may possibly worsen the objective itself. Therefore, in this work, some specific cases of the weights of the multi-objective function are evaluated, as well as how the optimized topology varies when changing some of the parameters of the simulation and/or the optimization.

Two approaches are considered for writing the multi-objective function, which are the initial weight approach, and the logarithmic approach. When considering a single objective function, the objective function value is directly considered in the optimization (i.e., the multi-objective function is not used). For example, when $w_\Phi = 1$ (i.e., only Φ_{rel} in the multi-objective function), J is changed to $J = \Phi_{\mathsf{rel}}$.

2.5.4.1 Initial weight multi-objective function

Since the measurement units of each objective function may be different, the magnitudes and sensitivities may significantly vary from one objective function to another. Thus, in order to reduce such disparity and avoid a possible predominance of one objective function over the others during the optimization process, an initial weight multi-objective function may be defined as

$$J(\alpha) = \sum_{i=0}^{n_F} w_i \underbrace{\left| \frac{J_{\text{ref}}(\alpha_0)}{J_i(\alpha_0)} \right|}_{\text{Initial weight}} J_i(\alpha) \tag{2.140}$$

where n_F is the number of objective functions, w_i are the weights such that $\sum_{i=0}^{n_F} w_i = 1$, $\left| \frac{J_{\text{ref}}(\alpha_0)}{J_i(\alpha_0)} \right|$ is the *initial weight*, α_0 is the initial distribution of the design variable, J_i is the objective function i, and J_{ref} is a reference objective function (i.e., the objective function chosen as reference for the measurement units). The initial values (at α_0) refer to the objective function values in the beginning of each optimization step (sequence of iterations). The reference objective function (J_{ref}) is defined for consistency in the measurement units of $J(\alpha)$. However, it should also end up influencing the choice of the weights (w_i). Note that the initial weight objective function is different from using an adaptive weight factor setting scheme (ZHU *et al.*, 2014; ZHU *et al.*, 2015), since the ratio between the objective functions is not adaptive (i.e., they are not updated for each iteration of the optimization).

It can be noticed that eq. (2.140) shows the objectives functions as $J_i(\alpha)$, without making explicit the other dependencies (such as $p(\alpha)$, $\boldsymbol{v}(\alpha)$, $I_H(p(\alpha), \boldsymbol{v}(\alpha), \alpha)$, and $I_{PAS}(p(\alpha), \boldsymbol{v}(\alpha), \alpha)$), treating them as *reduced functionals* (i.e., depending only in the design variable). Nonetheless, the sensitivities (*derivatives*) of these objective functions need to be analyzed from each dependency explicitly, which is shown in Section 2.5.5.

2.5.4.2 Logarithmic multi-objective function

In order to leverage the influence of each objective function in topology optimization, the multi-objective function may be considered in a logarithmic approach. When considering the logarithmic approach, the objective function becomes independent from the measurement unit. This can be viewed from the logarithm product rule, since $\ln([\text{constant}]J_i) = \ln([\text{constant}]) + \ln(J_i)$, meaning that the conversion between measurement units (represented by "[constant]") of an objective function J_i becomes a

summed constant ("$\ln([\text{constant}])$"), which does not influence the optimization procedure. In order to take negative objective function values into account, the logarithm of the value is substituted by the logarithm of the absolute value and then multiplied by the corresponding sign. The logarithmic multi-objective function is then given as

$$J = f_{\text{scal}} \sum_{i=0}^{n_F} w_i \text{sgn}(J_i(\alpha)) \ln|J_i(\alpha)| \tag{2.141}$$

where "$\ln$" is the natural logarithm, "sgn" is the sign, w_i are the weights such that $\sum_{i=0}^{n_F} w_i = 1$, and f_{scal} is a scaling factor for the multi-objective function. It may be mentioned that the relative energy dissipation (Φ_{rel}) may achieve negative values, which is the reason for considering the sign of the objective function ($\text{sgn}(J_i(\alpha_0))$). It can be highlighted that eq. (2.141) cannot take *exactly-zero*-valued objective function values into account, which is not a problem in the numerical examples of this work, but may be optionally numerically worked around by changing "$\ln|\square|$" and "$\frac{1}{|\square|}$" by "$\ln(|\square|+\varepsilon_{\text{adjustment}})$" and "$\frac{1}{|\square|+\varepsilon_{\text{adjustment}}}$", respectively, where $\varepsilon_{\text{adjustment}}$ is a sufficiently small value (such as 10^{-14}).

The main advantage of the logarithmic multi-objective function with respect to the initial weight multi-objective function is that it does not depend on a reference value for the objective functions ($J_i(\alpha_0)$) for computing the *initial weights*. Nonetheless, both multi-objective functions are valid, although the implementation of the logarithmic approach in dolfin-adjoint is not as straight-forward as the initial weight approach, requiring the implementation of a Python function that overloads the NumPy logarithm operator and manually defines the resulting sensitivity of this operator.

2.5.5 **Sensitivity analysis of the multi-objective function**

The sensitivity of the initial weight multi-objective function (eq. (2.140)) is given by

$$\frac{dJ}{d\alpha} = \sum_{i=0}^{n_F} w_i \left| \frac{J_{\text{ref}}(\alpha_0)}{J_i(\alpha_0)} \right| \frac{dJ_i}{d\alpha} \tag{2.142}$$

For the logarithmic multi-objective function (eq. (2.141)), the sensitivity becomes

$$\frac{dJ}{d\alpha} = f_{\text{scal}} \sum_{i=0}^{n_F} w_i \text{sgn}(J_i) \frac{1}{|J_i|} \frac{d|J_i|}{d\alpha} \tag{2.143}$$

In this work, the sensitivity is given by the adjoint method. Therefore, if the dependencies of the objective function are α, and $\boldsymbol{u}$,

$$\left(\frac{dJ_i}{d\alpha}\right)^* = \left(\frac{\partial J_i}{\partial \alpha}\right)^* - \left(\frac{\partial F}{\partial \alpha}\right)^* \boldsymbol{\lambda}_{J_i} \tag{2.144}$$

$$\left(\frac{\partial F}{\partial \boldsymbol{u}}\right)^* \boldsymbol{\lambda}_{J_i} = \left(\frac{\partial J_i}{\partial \boldsymbol{u}}\right)^* \text{(adjoint equation)} \tag{2.145}$$

where $\boldsymbol{u} = (p, \boldsymbol{v})$ is the state vector (if laminar flow is considered), J_i is an objective function, the weak form of the fluid flow simulation is given by from $F = 0$ (eq. (2.43)), " * " represents conjugate transpose, and $\boldsymbol{\lambda}_{J_i}$ is the adjoint variable (Lagrange multiplier for the weak form) of the objective function J_i.

For the case of the objective function also depending on $I_H(p(\alpha), \boldsymbol{v}(\alpha), \alpha)$ and $I_{PAS}(p(\alpha), \boldsymbol{v}(\alpha), \alpha)$ (for the laminar flow case), the new dependencies need to be "cascaded", resulting in

$$\begin{aligned}\frac{dJ_i}{d\alpha}^* =& \frac{\partial J_i}{\partial \alpha}^* - \frac{\partial F}{\partial \alpha}^* \boldsymbol{\lambda}_{J_i} - \left(\frac{\partial F_{PAS}}{\partial \alpha}^* - \frac{\partial F}{\partial \alpha}^* \boldsymbol{\lambda}_{PAS}\right) \lambda_{J_i PAS} \\ & - \left(\frac{\partial F_H}{\partial \alpha}^* - \frac{\partial F}{\partial \alpha}^* \boldsymbol{\lambda}_H\right) \lambda_{J_i H}\end{aligned} \tag{2.146}$$

$$\left(\frac{\partial F}{\partial \boldsymbol{u}}\right)^* \boldsymbol{\lambda}_{J_i} = \frac{\partial J_i}{\partial \boldsymbol{u}}^* \tag{2.147}$$

$$\left(\frac{\partial F}{\partial \boldsymbol{u}}\right)^* \boldsymbol{\lambda}_{PAS} = \frac{\partial F_{PAS}}{\partial \boldsymbol{u}}^* \tag{2.148}$$

$$\left(\frac{\partial F_{PAS}}{\partial I_{PAS}}\right)^* \lambda_{J_i PAS} = \frac{\partial J_i}{\partial I_{PAS}}^* \tag{2.149}$$

$$\left(\frac{\partial F}{\partial \boldsymbol{u}}\right)^* \boldsymbol{\lambda}_H = \frac{\partial F_H}{\partial \boldsymbol{u}}^* \tag{2.150}$$

$$\left(\frac{\partial F_H}{\partial I_H}\right)^* \lambda_{J_i H} = \frac{\partial J_i}{\partial I_H}^* \tag{2.151}$$

where $F_{I_H} = 0$ is the weak form of the hemolysis model (eq. (2.88)), $F_{PAS} = 0$ corresponds to eq. (2.127) from the PAS model, and $\lambda_{J_i H}$, $\lambda_{J_i PAS}$, $\boldsymbol{\lambda}_H$, and $\boldsymbol{\lambda}_{PAS}$ are additional adjoint variables. It can also be mentioned that a similar "cascading" approach needs to be repeated for S_τ, $D_{PAS,sl}$ and $D_{PAS,sr}$ (eqs. (2.124), (2.125) and (2.126)). If

more differential equations need to be solved in order to compute the objective function, they should be included in a similar fashion as shown in eqs. (2.146) to (2.151).

In the case of using the FEniCS platform with dolfin-adjoint, it is not necessary to derive the adjoint equations by hand, since this may be automated (see Section 3.1.2). The main advantages are that the "cascading" procedure is automated and, when considering a non-Newtonian viscosity (such as the one shown in eq. (2.11) or eq. (2.135)), it would become difficult and laborious to derive the continuous adjoint model by hand. In the case of a non-Newtonian fluid, the continuous adjoint model is derived in Alonso *et al.* (2020), by considering automatic differentiation only for the sensitivity of the non-Newtonian viscosity.

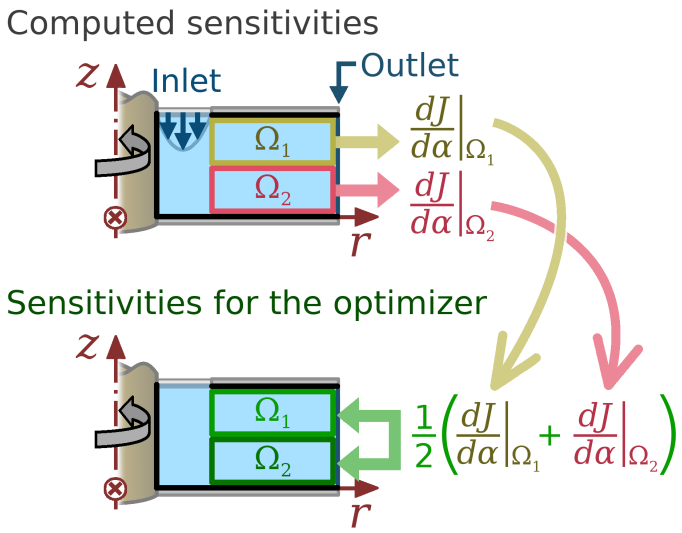
2.5.6 **Pattern repetition**

When using the relative energy dissipation (Φ_{rel}, eq. (2.51)) as the objective function, it is possible that the optimization algorithm finds that the formation of a single channel is an "easier" local minimum. In order to verify this assumption, the formation of more than one channel can be "forced" through a pattern repetition scheme (ALMEIDA *et al.*, 2010). The pattern repetition scheme consists of computing the sensitivity of the multi-objective function in the whole design domain and then performing an average between the sensitivities of the repeated zones. The averaged sensitivity between the repeated zones is then used in the optimizer. This procedure can be summarized in the following equation:

$$\left.\frac{dJ}{d\alpha}\right|_{\Omega_i,\text{new}} = \frac{1}{n_{\text{repeated zones}}} \sum_{j=0}^{n_{\text{repeated zones}}-1} \left.\frac{dJ}{d\alpha}\right|_{\Omega_j} \tag{2.152}$$

where $\left.\frac{dJ}{d\alpha}\right|_{\Omega_i,\text{new}}$ is the *new* sensitivity (including the pattern repetition scheme), Ω_i and Ω_j are subdomains that are included in the pattern repetition ($i, j \in [0,\ n_{\text{repeated zones}}]$), $n_{\text{repeated zones}}$ is the number of repeated zones. Outside the subdomains that are included in the pattern repetition, $\left.\frac{dJ}{d\alpha}\right|_{\text{new}} = \frac{dJ}{d\alpha}$. In order for this scheme to work, the nodes of the mesh should match exactly between the repeated zones. Fig. 2.15 illustrates the application of pattern repetition in the case of two repeated zones (Ω_1 and Ω_2).

Figure 2.15 – Example of pattern repetition for two repeated zones.



Source: Author.

The presented pattern repetition scheme can be interpreted as a *projection* in topology optimization, since it restricts the solution space of topology optimization to the solutions that obey this pattern repetition.

2.5.7 **Regularization**

The fact that the optimized topology is represented by a discrete material distribution ($\alpha = 0$ or $\alpha = 1$) can cause numerical instabilities due to the lack of smoothness in the finite element equations (KAWAMOTO *et al.*, 2013), possibly culminating in mesh dependency or local minima – in the case of structural topology optimization, it may even lead to checkerboard patterns (SIGMUND; PETERSSON, 1998). One way to better condition the optimization problem and avoid such problem is by “blurring” the effect of the variables. Image processing-based filtering techniques have been proposed for achieving this effect (BENDSØE; SIGMUND, 2003; SIGMUND, 2007), which are: density (*pseudo-density*) filters (applied to the design variable) and sensitivity filters (applied to the objective functions’ sensitivities).

Filters in topology optimization were originally implemented as operations in the same function space and array of values, which means that each calculated value included some values that were just filtered (SIGMUND, 2001; BENDSØE; SIGMUND, 2003). Nowadays, this approach has been changed to projection techniques, which separate the function spaces of the filtered variables (*solution space*) in relation to

the original variables (SIGMUND, 2007). In such case, only the previous values of the variables can influence the filtered values. Filters may be implemented algebraically (*algebraic filters*) (BENDSØE; SIGMUND, 2003; SVANBERG; SVARD, 2013) or by the solution of a Partial Differential Equation (PDE) (*PDE-based filters*) (LAZAROV; SIGMUND, 2010; KAWAMOTO *et al.*, 2013). The advantage of a PDE-based filter is that it does not require information about neighbor cells, which may be difficult to obtain in the case of fine meshes, design domains with complex shapes, or when using parallel computing (in which the mesh is decomposed in various partitions) (LAZAROV; SIGMUND, 2010).

Projection techniques are not limited to filters, and are characterized by projecting the design variable onto a solution space which imposes constraints to the possible topologies. They can serve as: a way to induce more discrete optimized topologies (such as Lazarov and Sigmund (2010)'s sigmoidal projection), a way to impose a minimum length scale for the structure or holes (GUEST *et al.*, 2004; ALMEIDA *et al.*, 2009), a way to impose manufacturing constraints (VATANABE *et al.*, 2016) etc.

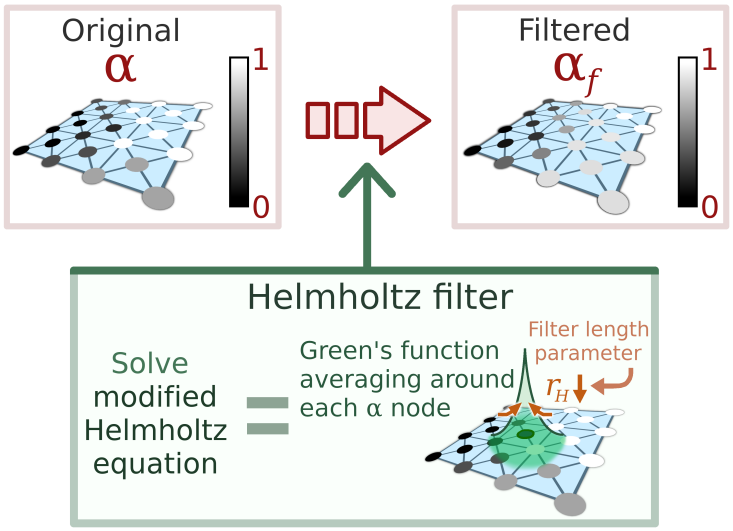
In the implementation of a filter/projection, the design variable present in the equations should be changed to the filtered/projected design variable, which means that each function $f(\alpha)$ should become $f(\alpha_f(\alpha))$. Thus, the sensitivity of each function with respect to the design variable becomes, from the chain rule for derivatives, $\frac{\partial f(\alpha_f)}{\partial \alpha} = \frac{\partial f(\alpha_f)}{\partial \alpha_f}\frac{\partial \alpha_f}{\partial \alpha}$, where $\frac{\partial \alpha_f}{\partial \alpha}$ is the sensitivity of the filter/projection, and $\frac{\partial f(\alpha_f)}{\partial \alpha_f}$ is the *original* sensitivity. It is possible to include more than one filter/projection – In such case, the chain rule is applied in order to account for the sensitivities of all filters/projections.

The Helmholtz pseudo-density filter is described in the following sections.

2.5.7.1 Helmholtz pseudo-density filter

The Helmholtz filter is a PDE-based pseudo-density filter proposed by Lazarov and Sigmund (2010). It is represented schematically in Fig. 2.16, in which α represents the original distribution of the design variable and α_f represents the filtered distribution of the design variable. In the following description, the positions in which there are design variable values defined (from the finite element interpolation) are referred as "α nodes".

Figure 2.16 – Schematic illustration of the application of a Helmholtz filter.



Source: Author.

In Fig. 2.16, each α node is weighted with its surrounding nodes with a Green's function, that is always positive and whose integral is equal to 1 ("100%") (LAZAROV; SIGMUND, 2010). It approaches a Dirac's delta function in the case of smaller filter length parameters (r_H) ($\alpha_f \xrightarrow{r_H \to 0^+} \alpha$). The action of applying this type of averaging over all α nodes is equivalent to solving a modified Helmholtz equation with homogeneous Neumann boundary conditions, represented by the following boundary value problem (LAZAROV; SIGMUND, 2010; ZAUDERER, 1989)

$$\begin{aligned} -r_H^2 \nabla^2 \alpha_f + \alpha_f &= \alpha \quad \text{in } \Pi \\ \frac{\partial \alpha_f}{\partial \boldsymbol{n}} &= \mathbf{0} \quad \text{on } \Gamma_\Pi \setminus \Gamma_{\Pi,\text{sym}} \end{aligned} \tag{2.153}$$

where α is the design variable, α_f is the filtered design variable, r_H is the filter length parameter, $\boldsymbol{n}$ is the normal unit vector to the boundaries of the mesh, Π is the computational domain, and $\Gamma_\Pi \setminus \Gamma_{\Pi,\text{sym}}$ is the boundary of the computational domain (excluding the $\Gamma_{\Pi,\text{sym}}$ boundary, from Section 2.1.4).

The weak form (variational formulation) of the above PDE is given by multiplying it by a test function w_H and integrating in the whole domain. Therefore,

$$\int_\Pi (-r_H^2 \nabla^2 \alpha_f + \alpha_f - \alpha) w_H d\Pi = 0 \tag{2.154}$$

In order to avoid the presence of second order terms in eq. (2.154), the term $\int_\Pi r_H^2 (\nabla^2 \alpha_f) w_H d\Pi$ is unfolded in first order derivatives. First, the Laplacian $\nabla^2 \alpha_f$ is

unfolded as $\nabla\bullet(\nabla\alpha_f)$, and then, from the product rule,

$$\begin{aligned}\nabla\bullet(\nabla\alpha_f w_H) &= \nabla\bullet(\nabla\alpha_f)w_H + (\nabla\alpha_f)\bullet\nabla w_H \\ \implies \nabla\bullet(\nabla\alpha_f)w_H &= \nabla\bullet(\nabla\alpha_f w_H) - (\nabla\alpha_f)\bullet\nabla w_H\end{aligned} \tag{2.155}$$

By using Gauss's divergence theorem,

$$\int_\Pi \nabla\bullet(\nabla\alpha_f w_H)d\Pi = \int_{\Gamma_\Pi} \boldsymbol{n}\bullet(\nabla\alpha_f w_H)d\Gamma_\Pi \tag{2.156}$$

Therefore, eq. (2.154) becomes

$$-r_H^2 \oint_{\Gamma_\Pi} \boldsymbol{n}\bullet(\nabla\alpha_f w_H)d\Gamma_\Pi + r_H^2 \int_\Pi (\nabla\alpha_f)\bullet\nabla w_H d\Pi + \int_\Pi \alpha_f w_H d\Pi - \int_\Pi \alpha w_H d\Pi = 0 \tag{2.157}$$

where $\frac{\partial\alpha_f}{\partial\boldsymbol{n}} = \mathbf{0}$ should be directly substituted in the boundary term of this equation for $\Gamma_\Pi \setminus \Gamma_{\Pi,\mathrm{sym}}$. For $\Gamma_{\Pi,\mathrm{sym}}$, $\frac{\partial\alpha_f}{\partial r} = 0$ should be substituted. Since the effect of the Helmholtz filter at smaller radii is small (due to the fact that the fluid volume is smaller at smaller radii), it is possible, as an approximation, to assume all boundary terms of eq. (2.157) to be set as $\frac{\partial\alpha_f}{\partial\boldsymbol{n}} = \mathbf{0}$ (including $\Gamma_{\Pi,\mathrm{sym}}$).

When using a Helmholtz filter, eq. (2.157) is solved right before computing the weak form, the objective functions, constraints and their sensitivities, and α_f is used instead of α when computing them (i.e., the fluid equations are solved in the filtered variable α_f). It can be highlighted that, since eq. (2.157) includes a gradient of the filtered design variable ($\nabla\alpha_f$), the design variable needs to be at least of class C^1 (i.e., (at least) the first derivative needs to be continuous), which means that the interpolation of the design variable should be at least linear (P_1) in order to use the Helmholtz pseudo-density filter. One suggestion for choosing the value for the filter length parameter (r_H) is by choosing from multiples of the minimum/maximum size of an element in the mesh (the referred minimum/maximum sizes are the smallest/largest of the maximum distances between any two vertices of the elements).

When the design domain is smaller than the computational domain, the design variable value can still be filtered (α_f) inside the whole computational domain (Ω). However, its value outside the design domain ($\Omega \setminus \Omega_\alpha$) can be optionally enforced as the previous value (α). Therefore, the variable $\alpha_{f,\mathrm{new}}$ may be used in the equations, being given in function of the position ($\boldsymbol{s}$):

$$\alpha_{f,\mathrm{new}}(\boldsymbol{s}) = \begin{cases}\alpha_f, \text{ if } \boldsymbol{s} \in \Omega_\alpha \\ \alpha, \quad \text{if } \boldsymbol{s} \in \Omega \setminus \Omega_\alpha\end{cases} \tag{2.158}$$

2.5.8 **Post-processing of the optimized topologies**

The post-processing of the optimized topologies consists of any operation performed in the topologies after the topology optimization algorithm has converged. In fluid topology optimization, the presence of the solid material is modeled by means of a porous medium. This effect of the porous medium (in the fluid flow and computed quantities) may be removed by a post-processing technique and the final simulation can be performed with the Navier-Stokes equations without the effect of the porous medium. It also enables optimized topologies achieved with different optimization parameters to be compared. Since, in fluid flow topology optimization, the post-processing includes the recognition of the boundaries between fluid and solid, these techniques may be referred to as *contour recognition* schemes, or even *surface-capture* schemes. In the context of topology optimization for the pseudo-density approach, the optimized topology is a continuously distributed variable in the design domain, which means that the *contour recognition* schemes may possibly include "guessing" ("interpreting") how the optimized boundaries should be. The *contour recognition* schemes include, essentially, three cases: *thresholding* (directly removing the *solid* values from the mesh), *mesh smoothing* (mapping and smoothing the boundaries of the optimized topologies) and *topology interpretation* (manual adjustment of curves on to the optimized topology). Apart from *topology interpretation*, which relies on manual adjustments, the *thresholding* and *mesh smoothing* techniques may be automated by algorithms and are described in the following sections. Depending on the optimized topology being post-processed, it may be interesting to apply morphological operators (of image processing) or even the Helmholtz pseudo-density filter in order to "clean" small structures from the mesh before applying *thresholding* or *mesh smoothing*.

2.5.8.1 Thresholding

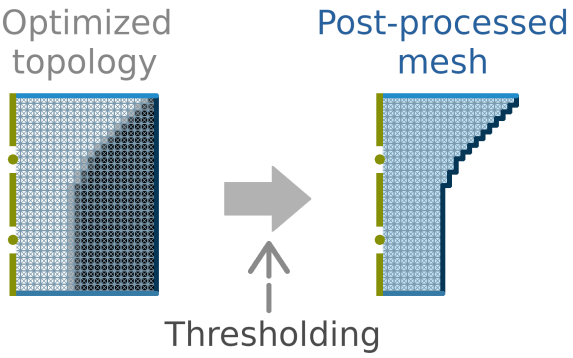
The simplest type of post-processing of the optimized topologies is thresholding, which consists of removing the *solid* values from the mesh. The values of the design variable (pseudo-density) are first post-processed by a threshold (step) function:

$$\alpha_{\mathrm{th}} = \begin{cases} 1 \text{ (fluid), if } \alpha \geqslant \alpha_{\mathrm{th,lim}} \\ 0 \text{ (solid), if } \alpha < \alpha_{\mathrm{th,lim}} \end{cases} \tag{2.159}$$

where $\alpha_{\mathrm{th,lim}}$ is the threshold limit for the design variable ($0 \leqslant \alpha_{\mathrm{th,lim}} \leqslant 1$). One example is using, for example, $\alpha_{\mathrm{th,lim}}$ as 0.5 or 0.6.

From the application of the threshold function, the design variable achieves a binary distribution (α_{th}, *thresholded design variable*), which is then cut in order to remove the solid material ($\alpha = 0$) from the computational domain (see Fig. 2.17). This is shown in Algorithm 2.1.

Figure 2.17 – Illustration of the thresholding technique applied to an optimized topology.



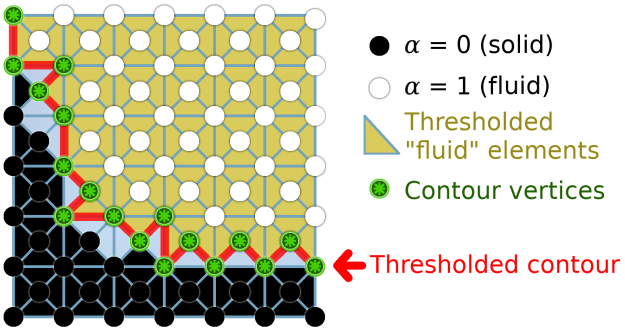
Source: Author.

Algorithm 2.1 Pseudocode of mesh thresholding.

1: **Input parameters:** Mesh, optimized topology (i.e., the optimized α), and the threshold limit ($\alpha_{\mathrm{th,lim}}$).
2: **Result:** Thresholded mesh.
3: **1** Apply thresholding in the design variable values (eq. (2.159)) of the center of each element.
4: **2** Cut the mesh in order to remove the solid material ($\alpha = 0$) from the computational domain (in FEniCS, this is done with the functions `SubDomain` and `SubMesh`).

For reference in the following section, Fig. 2.18 shows a “rough” thresholded mesh (normally, the “roughness” would be much less pronounced because of the different values in the transition between solid and fluid – i.e., the *gray* values in the transition) from a given distribution of the design variable (α).

Figure 2.18 – Illustration of an example of thresholding (for a nodal design variable).



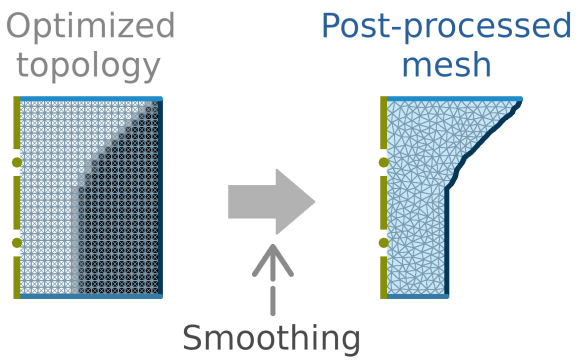
Source: Author.

From Fig. 2.18, it can be noticed that, depending on the discretization used in topology optimization, the resulting mesh may contain some additional “roughness” on the new mesh boundaries (*jagged mesh* effect), which may slightly worsen the values of the computed performance quantities. In order to try to reduce this effect, a *mesh smoothing* technique may be applied.

2.5.8.2 Mesh smoothing

Mesh smoothing is a technique performed in order to reduce the additional “roughness” effect that may appear when using the thresholding technique (see Fig. 2.19). There may be various ways to implement a mesh smoothing technique, such as by *generation of contours*, *contour filtering* and *point cloud*. Among them, the *generation of contours* and *point cloud* techniques are described in the following sections. The first technique to be implemented was the *generation of contours* technique, which is considered in some numerical results of Section 5.1.2, while the *point cloud* technique is used in the numerical results of Section 5.1.4. Since the *contour filtering* technique ended up not being used in this work, it is included separately as Appendix B.

Figure 2.19 – Illustration of a smoothing technique applied to an optimized topology.



Source: Author.

Even after applying a mesh smoothing technique, the resulting mesh may result slightly *jagged*. In such case, an additional procedure may be applied onto the contours that were obtained by mesh smoothing, before generating the mesh with FEniCS, such as:

- Savitzky-Golay filter approach: One possibility, which has been first considered in Picelli *et al.* (2021), is by considering the Savitzky-Golay filter (SAVITZKY; GOLAY, 1964), which is a low-pass filter capable of smoothing noisy data. It operates by considering a least-square fit with a high-order polynomial inside a set of points (*window*) around each value – an example is using a 2nd order polynomial, with a *window* of size 9. This way, this filter can be applied onto each mesh coordinate (x, y, z, and r), leading to smoother contours. However, some care should be taken in the selection of its parameters, since they tend to filter imperfections, being possible to "over-filter", leading to a different smoothened mesh than wanted. The Savitzky-Golay filter is already implemented in the SciPy library ("`scipy.signal.savgol_filter`"). When considering the Savitzky-Golay filter, depending on the choice of its parameters, the resulting boundaries can result highly smooth, as it would be in *body-fitted meshes*. The contours given from the Savitzky-Golay filter can be further improved by successively adding intermediary vertices (additional vertices in the middle distance between each vertex pair of the contours) to the point list of the contours, and applying the Savitzky-Golay filter again (*intermediary-vertex procedure*).

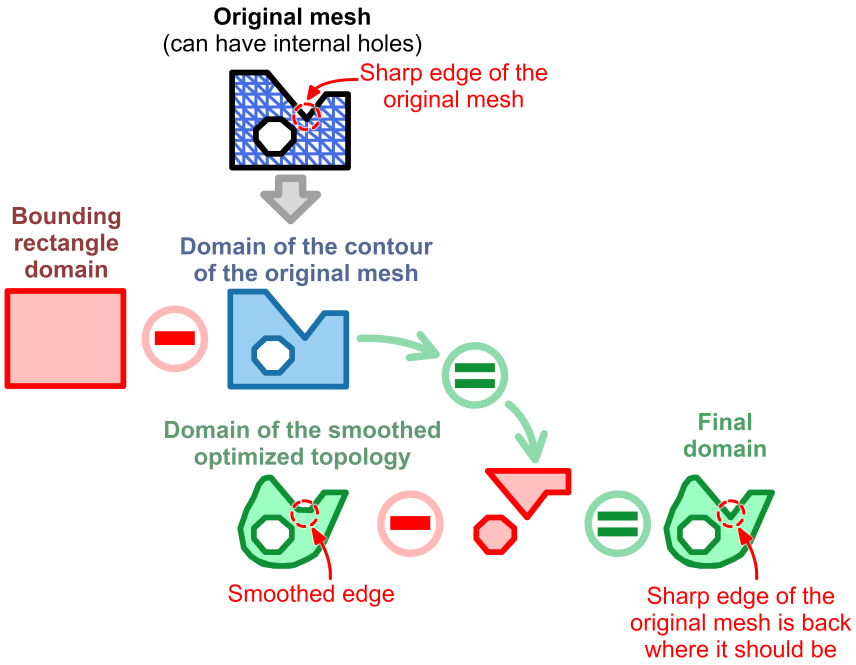
- Chaikin's corner cutting algorithm approach: An alternative approach is by considering Chaikin's corner cutting algorithm (JOY, 1999; BITYUKOV; DENISKIN, 2016).

In such case, as suggested in this work, the algorithm is adjusted for smoothing closed boundaries, and is run successively. Due to the increase in resolution of the boundaries during the execution of this algorithm (i.e., the quantity of boundary vertices is doubled), some of the vertices are ignored (half of the vertices, in a zig-zag-like fashion). This is important, since Chaikin's corner cutting algorithm is able to better smooth optimized topology contours when the vertices are more spaced. With respect to the Savitzky-Golay filter approach, the Chaikin's corner cutting algorithm approach (successively run some times) does not suffer from the appearance of "undesired" edges when trying to perform a high smoothing, which may appear in the case of the Savitzky-Golay filter approach when a large *window* size is selected.

One observation is that, depending on the mesh smoothing technique, since sharp edges are smoothened, if one wants to keep some specific sharp edges in the final mesh, such as when the sharp edges are part of the mesh contour, these sharp edges can be reincluded by generating a domain with the desired sharp edges, subtracting it from a rectangle that bounds the whole domain, and then subtracting the resulting shape from the domain of the smoothened optimized topology, through CSG (Constructive Solid Geometry) (in FEniCS, this can be done in the mshr module). This procedure is illustrated in Fig. 2.20. It can be noticed that this procedure only works for internal edges, as the one shown in Fig. 2.20. When considering circular interfaces that include boundary conditions, the placement of vertices may be critical for the simulation. One main example is a circular interface, which needs to be kept circular in order for the boundary conditions to be imposed correctly. A first approach is considering a CSG approach (similar to the one considered for the sharp edges (Fig. 2.20)), which is the one considered in the post-processing for the volute design (Section 5.1.6), due to the fact that the model includes a non-optimizable circle around the circular boundary. A more generic approach for circular-shaped boundaries would be considering that the intermediary vertex placement from the *intermediary-vertex procedure* (mentioned previously in this section) may be changed near the boundaries for computing the intermediary vertices from polar coordinates (i.e., radial and angular coordinates) with respect to the center of the circle, which guarantees that the radial coordinate will be kept the same in the intermediary vertices. This procedure is considered in the

post-processing for the bladed pump design (Section 5.1.7).

Figure 2.20 – Example of the procedure to reinclude a sharp edge of the original mesh after smoothing, through CSG.



Source: Author.

2.5.8.2.1 *Mesh smoothing by generation of contours*

The mesh smoothing technique by generation of contours is based on the one presented in Ma *et al.* (2006) and Varela (2012), and consists of first identifying the contours from the optimized topology (i.e., α) and then adjusting the contour vertices in order to avoid the presence of overly sharp corners. Since the original algorithm was developed for a mesh composed of rectangular elements and an element-wise (dP_0) design variable, it is here adapted for a mesh composed of triangular elements and a design variable with linear interpolation (P_1). If the interpolation of the design variable is not linear, it needs to be converted to a linear interpolation in order to apply the technique described in this section, because of the assumption that every node with a design variable value corresponds to a vertex of the mesh.

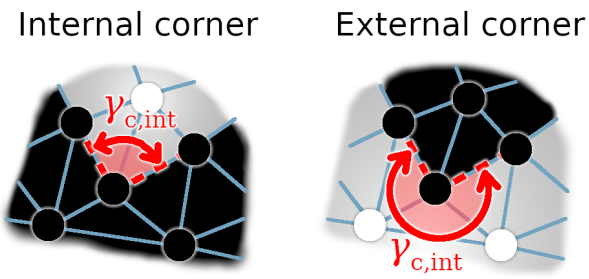
The mesh smoothing technique by generation of contours relies on identifying sequences of subsequent internal and external corners and substituting them for intermediate vertices between these corners. The definition of the corner angle in relation to the internal (*fluid*) part of the mesh $\gamma_{\mathrm{c,int}}$ is shown in Fig. 2.21 (note that it is also possible to define this same angle in relation to the external (*solid*) part of the mesh,

which can be related to $\gamma_{\mathrm{c,int}}$ as $\gamma_{\mathrm{c,ext}} = 360° - \gamma_{\mathrm{c,int}}$). The corners are identified by bounds around the angle between neighbors of a solid ($\alpha = 0$) vertex, as:

$$\begin{aligned}
&\gamma_{\mathrm{ic,int,min}} \leqslant \gamma_{\mathrm{c,int}} \leqslant \gamma_{\mathrm{ic,int,max}} && \Longrightarrow \text{ Internal corner vertex} \\
&\gamma_{\mathrm{ec,int,min}} \leqslant \gamma_{\mathrm{c,int}} \leqslant \gamma_{\mathrm{ec,int,max}} && \Longrightarrow \text{ External corner vertex} \\
&\gamma_{\mathrm{ic,int,max}} < \gamma_{\mathrm{c,int}} < \gamma_{\mathrm{ec,int,min}} && \Longrightarrow \text{ Vertex to directly include in the smoothened contour} \\
&\gamma_{\mathrm{ec,int,max}} < \gamma_{\mathrm{c,int}} < \gamma_{\mathrm{ic,int,min}} && \Longrightarrow \text{ Vertex to directly include in the smoothened contour}
\end{aligned} \tag{2.160}$$

where $\gamma_{\mathrm{ic,int,min}}$ and $\gamma_{\mathrm{ic,int,max}}$ are the angle bounds that define an internal corner, and $\gamma_{\mathrm{ec,int,min}}$ and $\gamma_{\mathrm{ec,int,max}}$ are the angle bounds that define an external corner. These angles may need to be adjusted as necessary for a given optimized topology. Some possible angles are, for example, $\gamma_{\mathrm{ic,int,min}} = 0°$ and $\gamma_{\mathrm{ic,int,max}} = 90°$ for defining an internal corner, and $\gamma_{\mathrm{ec,int,min}} = 205°$ and $\gamma_{\mathrm{ec,int,max}} = 360°$ for defining an external corner.

Figure 2.21 – Internal and external corners with $\gamma_{\mathrm{c,int}}$ indicated for each case.



Source: Author.

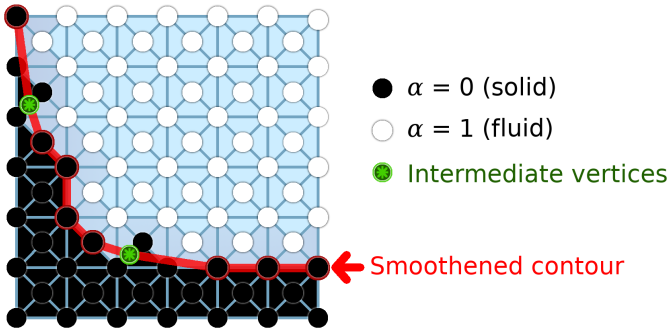
The mesh smoothing technique by generation of contours is detailed in Algorithm 2.2 and illustrated in Fig. 2.22.

Algorithm 2.2 Pseudocode of mesh smoothing by generation of contours.

Input parameters: Mesh, optimized topology (i.e., the optimized α), the threshold limit ($\alpha_{\text{th,lim}}$), $\gamma_{\text{ic,int,max}}$, $\gamma_{\text{ic,int,min}}$, $\gamma_{\text{ec,int,max}}$, and $\gamma_{\text{ec,int,min}}$.
Result: Smoothened mesh obtained by generation of contours.
1 Apply thresholding in the design variable values (eq. (2.159)).
2 Identify the boundary vertices of the design variable in the mesh.
3 Create labels (α_{label}) **for** each vertex of the mesh:
    3.1 If $\alpha = 1.0$ (fluid):
        3.1.1 If it is a boundary vertex: $\alpha_{\text{label}} =$ "`internal`"; **continue**.
        3.1.2 Else: $\alpha_{\text{label}} =$ "`lateral`"; **continue**.
    3.2 Else: ($\alpha = 0.0$ (solid))
        3.2.1 If there is at least one neighbor vertex that is $\alpha = 1.0$ (fluid):
            3.2.1.1 If it is a vertex completely surrounded by $\alpha = 1.0$ (fluid) vertices: $\alpha_{\text{label}} =$ "`internal`"; **continue**.
            3.2.1.2 If it is a boundary vertex: $\alpha_{\text{label}} =$ "`lateral`"; **continue**.
            3.2.1.3 Compute the corner angle ($\gamma_{\text{c,int}}$) in relation to the $\alpha = 0.0$ (solid) vertex (see Fig. 2.21).
            3.2.1.4 If $\gamma_{\text{ic,int,min}} \leqslant \gamma_{\text{c,int}} \leqslant \gamma_{\text{ic,int,max}}$: $\alpha_{\text{label}} =$ "`internal corner`"; **continue**.
            3.2.1.5 Elif $\gamma_{\text{ec,int,min}} \leqslant \gamma_{\text{c,int}} \leqslant \gamma_{\text{ec,int,max}}$: $\alpha_{\text{label}} =$ "`external corner`"; **continue**.
            3.2.1.6 Else: $\alpha_{\text{label}} =$ "`lateral`"; **continue**.
        3.2.2 $\alpha_{\text{label}} =$ "`external`".
4 Between the internal corners ($\alpha_{\text{label}} =$ "`internal corner`") and external corners ($\alpha_{\text{label}} =$ "`internal corner`") that are neighbors, create vertices with intermediate coordinates (i.e., the average of the corner vertices' coordinates) (*intermediate vertices*) and label them as lateral ($\alpha_{\text{label}} =$ "`lateral`").
5 Group all vertices labeled lateral ($\alpha_{\text{label}} =$ "`lateral`") in a separated list (*lateral list*).
6 From the *lateral list*, create lists of closed contours, marking **if** theses vertices have neighbor vertices with internal ($\alpha_{\text{label}} =$ "`internal`") or external ($\alpha_{\text{label}} =$ "`external`") labels.
7 Generate the mesh from the lists of closed contours (in FEniCS, this can be done by creating `Polygon`'s (from the mshr module) for each closed contour and summing/subtracting them (CSG (Constructive Solid Geometry) operations), and then generating a non-structured mesh with a given mesh discretization/resolution (`generate_mesh`). Note that, for mshr, the closed contours have to be given in the counterclockwise order.)

* Obs. "**continue**" indicates to continue in the next iteration of the closest loop (as it is in the "`continue`" statement in C and Python).

Figure 2.22 – Illustration of an example of mesh smoothing by generation of contours (for a nodal design variable).



Source: Author.

Adjustments may also be included in the algorithm, such as eliminating too small closed contours (that include, for example, less than 5 vertices) and eliminating isolated edges that may possibly arise in the process of determining the intermediate vertices, depending on the optimized topology.

2.5.8.2.2 *Mesh smoothing by point cloud*

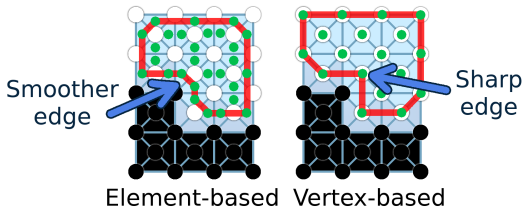
Unlike the mesh smoothing techniques presented in the previous sections, the mesh smoothing by point cloud relies on polygon recognition and extraction over the whole *cloud* of nodal values of the design variable (α). The implementation uses the *Polylidar* Python library (CASTAGNO; ATKINS, 2020), which is implemented underneath in C++ and is able to efficiently recognize and extract polygons from 2D and 3D point clouds. The implementation that is described in this section is extended from the original implementation by Souza (2021), by considering a different selection of nodes that are included in the point cloud (such as by including boundary nodes) and different adjustments to the algorithm.

Before applying polygon recognition/extraction, it is necessary to define which points will be inside the point cloud. This choice can be *element-based* or *vertex-based* (see Fig. 2.23a). As can be seen, the *element-based* approach can smoothen some sharp edges better than the *vertex-based* approach. Therefore, the *element-based* approach is chosen. Fig. 2.23b shows three possible approaches to treat the presence of a boundary of the original mesh (before smoothing). When there is a boundary in the original mesh, there is normally a boundary condition being applied on it. Therefore, it is interesting to keep all boundary coordinates that correspond to *fluid* in the same

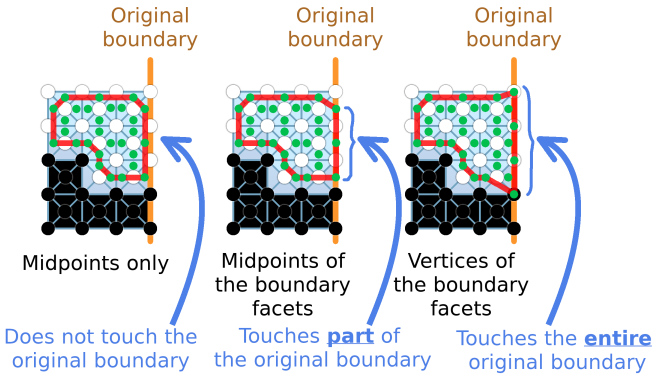
positions as before smoothing. For this, the approach *vertices of the boundary facets*, in which the vertices of the boundary facets are included, is chosen.

Figure 2.23 – Possible choices to define the point cloud (the points of the point cloud are represented in green color, while the recognized contour is represented in red color. The other symbols are the same as Fig. 2.24).

(a) *Element-based* and *vertex-based* approaches for defining the point cloud.



(b) Possible treatments for the boundaries of the original mesh.



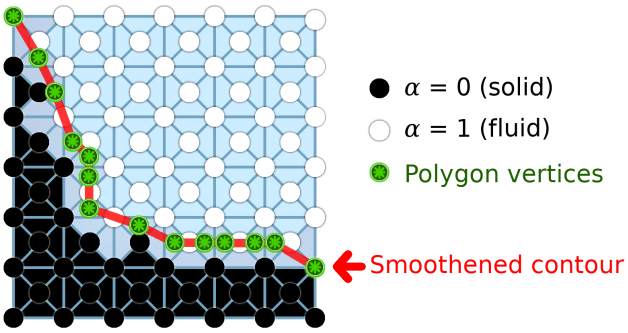
Source: Author.

The mesh smoothing technique by point cloud is detailed in Algorithm 2.3 and is illustrated in Fig. 2.24.

Algorithm 2.3 Pseudocode of mesh smoothing by point cloud.

1: **Input parameters:** Mesh, optimized topology (i.e., the optimized α), the threshold limit ($\alpha_{\text{th,lim}}$), and Polylidar parameters.
2: **Result:** Smoothened mesh obtained by point cloud.
3: **1** Apply thresholding in the design variable values (eq. (2.159)).
4: **2** Obtain all boundary facets of the original boundary of the mesh that correspond to $\alpha = 1$ (fluid).
5: **3** Create a list for storing the boundary vertices (vertices of the boundary facets).
6: **4 For** all boundary facets:
7: **4.1 If** the center of the cell connected to the boundary facet corresponds to $\alpha = 1$ (fluid), include all vertices of the boundary facet in the list.
8: **5** Remove repeated boundary vertices from the list.
9: **6** Extract the center coordinates that correspond to $\alpha = 1$ (fluid) and include in the point cloud.
10: **7** Include the boundary vertices in the point cloud.
11: **8** Use the Polylidar parameters and the point cloud to perform the polygon recognition and extraction (`extractPlanesAndPolygons`).
12: **10** From the extracted polygons, generate the mesh (in FEniCS, this can be done by creating `Polygon`'s (from the mshr module) for each Polylidar polygon and summing/subtracting them (CSG (Constructive Solid Geometry) operations), and then generating a non-structured mesh with a given mesh discretization/resolution (`generate_mesh`).)

Figure 2.24 – Illustration of an example of mesh smoothing by point cloud (for a nodal design variable).



Source: Author.

The *Polylidar parameters* referred in Algorithm 2.3 are the ones for 2D meshes: the maximum circumradius of a triangle in the point cloud (in Polylidar, "`alpha`"), and/or the maximum length of any edge in a triangle in the point cloud (in Polylidar, "`lmax`") (CASTAGNO; ATKINS, 2020). One suggestion is using the *maximum length* as 2 times the maximum edge length of the elements of the mesh (in FEniCS, it can be obtained by projecting "`l_max = MaxCellEdgeLength(mesh)`" on to a linear interpolation function space (P_1) and then extracting the maximum value ("`l_max.vector().max()`")). The minimum triangle size can also be set (in Polylidar, "`minTriangles`"), for example, as 8. It can be noticed that this technique can be extended to 3D. One drawback of the mesh

smoothing by point cloud is that the polygon recognition by the Polylidar Python library may have recognition problems when there are various specifically aligned nodes in the point cloud. One way to workaround this problem is by including a small random fluctuation (such as in the order of 10^{-14}) in all vertices of the contour (except the boundary vertices of the original mesh, in order not to change the positions where the boundary conditions are applied). In the case one wants to keep some sharp corners, which may be present in the original mesh, one possibility is by subtracting an additional term from the `Polygon`'s of the step 10 from Algorithm 2.3: This additional term would consist of a shape composed of the subtraction of a combination of `Polygon`'s that represent the original computational domain (CSG), from a rectangle that bounds the whole mesh.

3 NUMERICAL IMPLEMENTATION

The software platform used for the numerical implementation of the simulation and the optimization should provide sufficient flexibility and control over the implementation itself. Since commercial software does not provide the source code and normally this flexibility, open source software is preferred. Some open source softwares for different numerical methods are: FEniCS/Firedrake (finite element method) (LOGG *et al.*, 2012; RATHGEBER *et al.*, 2016), OpenFOAM® (finite volume method) (WELLER *et al.*, 1998; CHEN *et al.*, 2014) and Devito (finite differences method) (KUKREJA *et al.*, 2016). It is also possible to create an implementation *from scratch*, by using a programming language, such as Python, Matlab® , C, C++, Fortran etc. The FEniCS (Finite Element Computational Software) software (LOGG *et al.*, 2012) is chosen, because it allows the implementation of the weak form in a high-level representation, not needing to derive the finite element matrices by hand (i.e., they are automatically generated as low-level C++ code), and allows the implementation to be performed in the Python programming language, which has a simple and flexible syntax that allows faster programming and debugging. The cost of the flexibility of the Python programming language rests in a decreased computational performance when compared to lower-level programming languages such as C, C++ and Fortran, although Python's computational performance has been improving over the last decades. The performance of a Python code may be improved by using the Python libraries designed for scientific computation, since they are internally implemented in C/C++ (such as SciPy, NumPy and FEniCS itself), or by using some lower-level Python syntax (Cython) or acceleration (Numba library) in the functions that require more computational effort (such as in Firedrake).

The computed values, with the exception of the convergence curves, are computed in the post-processed meshes. The plots/images in this thesis are made by using either ParaView (AYACHIT, 2015), Matplotlib (HUNTER, 2007), LibreOffice (THE DOCUMENT FOUNDATION, 2022), GIMP (THE GIMP DEVELOPMENT TEAM, 2022), Dia (DIA DEVELOPMENT TEAM, 2022) or Autodesk® Inventor® .

The 3D model of the prototype was made in the CAD software Autodesk® Inventor® , through an academic license. The meshes from Chapter 5.1.9 were generated by using Gmsh (GEUZAINE; REMACLE, 2009) from the CAD model, and converted by using the *meshio* library (SCHLÖMER, 2021).

3.1 IMPLEMENTATION OF THE FINITE ELEMENT AND TOPOLOGY OPTIMIZATION METHODS

The FEniCS software is composed of 6 modules: DOLFIN (Dynamic Object-oriented Library for FINite element computation), which is the PDE (Partial Differential Equation) solving interface; mshr (mesh generation), which is used for mesh generation; UFL (Unified Form Language), which is the high-level representation used for PDEs and may consider, if necessary, automatic differentiation; FFC (FEniCS Form Compiler), which compiles PDEs written in UFL to low-level C++ code; FIAT (FInite element Automatic Tabulator), which implements the finite element basis functions; and dijitso (distributed just-in-time shared library building), which performs JIT (Just-In-Time) compilation for FFC.

Since the system of equations that results from the Navier-Stokes equations is nonlinear, the iterative Newton-Raphson method (also called *Newton's method* and *Newton-Kantorovich's method*) is used. The selected linear solver for the linearized problems at each iteration is MUMPS (MUltifrontal Massively Parallel sparse direct Solver) (AMESTOY *et al.*, 2001), which is adequate for large sparse matricial equations. For the hemolysis and thrombosis models (Sections 2.4.1 and 2.4.2), the linear differential equations are directly solved by using a linear solver, which is selected in this work as an LU solver (UMFPACK (DAVIS, 2004)). The iterative Newton-Raphson method is used for solving the non-linear equation of the thrombosis model (Section 2.4.2).

In order to implement the topology optimization method, the sensitivities (derivatives) are calculated with the adjoint method, through the dolfin-adjoint library (FARRELL *et al.*, 2013; MITUSCH *et al.*, 2019) interfaced with FEniCS. The dolfin-adjoint library provides interfaces to optimization solvers, such as IPOPT (Interior-Point OPTimizer) (WÄCHTER; BIEGLER, 2006), SciPy solvers and ROL (Rapid Optimization Library) (KOURI *et al.*, 2017) solvers. The IPOPT solver is composed of an interior point method, which means that its main advantage is that it imposes a logarithmic barrier term to enforce the solution to be searched only in the feasible space (i.e., satisfying the constraints). The difference of IPOPT and other interior point methods is that it augments it by using a line-search filter method, avoiding having to determine the exact value of the penalty parameter of the logarithmic barrier. On the other hand, the usual implementation of the optimization solvers (such as in IPOPT and SciPy) assume the use of the

Euclidean inner product (ℓ_2 inner product), which is not correct when considering that the state variables reside in a function space (*primal space*) that is different than the function space of the adjoint variables (*dual space*). In practical terms, this problem is caused by the fact that the design variable is distributed in a continuous space (*primal space*) and not in a discretized space, meaning that the sensitivities of the topology that is being optimized should be computed without the discretization effect (i.e., the effect of the size of the element). In order to connect the two different spaces (*primal* and *dual* spaces), the mathematically correct approach is to apply a Riesz map operation (considering, for example, L^2 or H^1 inner products), which is supported by ROL solvers. In practical terms, the effects of applying the Riesz map are that: (1) When increasing the discretization of uniform meshes, the computational time of solving the adjoint system reaches a maximum value (i.e., not applying the Riesz map means that the computational time should continue to increase at higher discretizations); (2) Under highly non-uniform discretizations, applying the Riesz map gives the correct sensitivity (mesh-independency), while not applying it clearly shows mesh-dependency (SCHWEDES *et al.*, 2017). Since the ROL library does not have support for the IPOPT algorithm, IPOPT is used by considering uniformly discretized meshes (with all elements with the same area (in 2D and 2D swirl meshes), and the same volume (in 3D meshes)), which gives results that are consistent to when the Riesz map is applied, even at the cost of a slightly higher computational time when under higher discretizations. It can be highlighted that the sensitivity computed without considering the Riesz map is able to lead to an optimized topology, possibly to another local minimum, and in a possibly slower fashion. When using non-uniform meshes, and the solver does not explicitly support Riesz map, the sensitivities may be optionally *corrected* as an element volume averaging, which is similar to considering the L^2 inner product followed a multiplication by an average element volume given for the design variable interpolation. It can be pointed out that this type of correction (adjustment) is done in order to make the sensitivity that is distributed over the mesh “look like” as if the mesh was uniform, while also keeping the same measurement unit as the *original* sensitivity. The volume averaging, which may also be described as a *mass matrix* averaging (SCHWEDES *et al.*, 2017), may be given as follows:

- For an element-wise design variable:

$$\left.\frac{dJ}{d\alpha}\right|_{\text{corrected}} = \frac{1}{V_{\text{element}}}\frac{dJ}{d\alpha}\underbrace{\left[\frac{\sum\limits_{n_{\text{elements}}} V_{\text{element}}}{n_{\text{elements}}}\right]}_{\text{Average element volume}} \tag{3.1}$$

- For a nodal design variable:

$$\left.\frac{dJ}{d\alpha}\right|_{\text{corrected}} = \frac{1}{V_{\substack{\text{neighbor elements}\\ \text{of the node}}}}\frac{dJ}{d\alpha}\underbrace{\left[\frac{\sum\limits_{n_{\text{nodes}}} V_{\substack{\text{neighbor elements}\\ \text{of the node}}}}{n_{\text{nodes}}}\right]}_{\text{Average neighbor elements' volume}} \tag{3.2}$$

where V_{element} is the volume of each element of the mesh, n_{elements} is the number of elements in the mesh, $V_{\substack{\text{neighbor elements}\\ \text{of the node}}}$ is the summed volume of the neighbor elements touching a node/vertex in the mesh, and n_{nodes} is the number of nodes/vertices in the mesh. It can be noticed that $\sum\limits_{n_{\text{elements}}} V_{\text{element}} = \int_{\Pi} d\Pi$ (total volume of the computational domain). In the case of a 2D mesh, the volume computations (V_{element}, $V_{\substack{\text{neighbor elements}\\ \text{of the node}}}$) are substituted by their area counterparts (A_{element}, $A_{\substack{\text{neighbor elements}\\ \text{of the node}}}$). In the case of 2D swirl flow, there are two approaches: (1) Compute the area of the elements of the mesh; or (2) Compute the *axisymmetric volume* of the element in the mesh (volume of the element computed by considering axisymmetry – i.e., a *ring-shaped* element volume). The first approach would correspond to the normal application of the Riesz map to a 2D mesh, while the second approach would correspond to a Riesz map adapted for the *axisymmetric volume*. It can be highlighted that the second approach should be considered even in uniformly discretized meshes, because the *axisymmetric volume* varies according to the radial coordinate of each element. The best approach for a 2D swirl mesh seems to be the second one, because it considers the *axisymmetric nature* of the 2D swirl flow model, leading the sensitivities to become similar to a corresponding 3D problem. As an example of application, during the topology optimization of a 2D swirl nozzle (Section 5.1.1.1), the *gray* material shown near the symmetry axis in part of the convergence curve in Fig. 5.6, depending on the problem setup (flow and material model setups) may take a large quantity of optimization iterations to vanish, while, with the *axisymmetric volume* correction, it vanishes faster. In a FEniCS/dolfin-adjoint implementation, the implementation of the element area/volume averaging can be performed as: for the sensitivity of the constraints of the optimization,

the "`UFLInequalityConstraint`"/"`UFLEqualityConstraint`" objects (from dolfin-adjoint) can be overloaded to include this averaging; and, for the sensitivity of the objective function, the averaging can be included inside the "`derivative_cb_post`" callback of the "`ReducedFunctional`" object (from dolfin-adjoint).

It is also possible to consider an integral approach for eqs. (3.1) and (3.2), which is given by first computing the sensitivity for the L^2 inner product:

$$\int_{\Pi} \left.\frac{dJ}{d\alpha}\right|_{L^2} w_{L^2} d\Pi = \frac{dJ}{d\alpha} \tag{3.3}$$

where w_{L^2} is the test function for $\left.\frac{dJ}{d\alpha}\right|_{L^2}$, and $\left.\frac{dJ}{d\alpha}\right|_{L^2}$ is the sensitivity computed through the L^2 inner product.

Then, the resulting value is multiplied by the average element volume for the design variable interpolation, which is given by:

$$\left.\frac{dJ}{d\alpha}\right|_{\text{corrected}} = V_{\text{average}} \left.\frac{dJ}{d\alpha}\right|_{L^2} \tag{3.4}$$

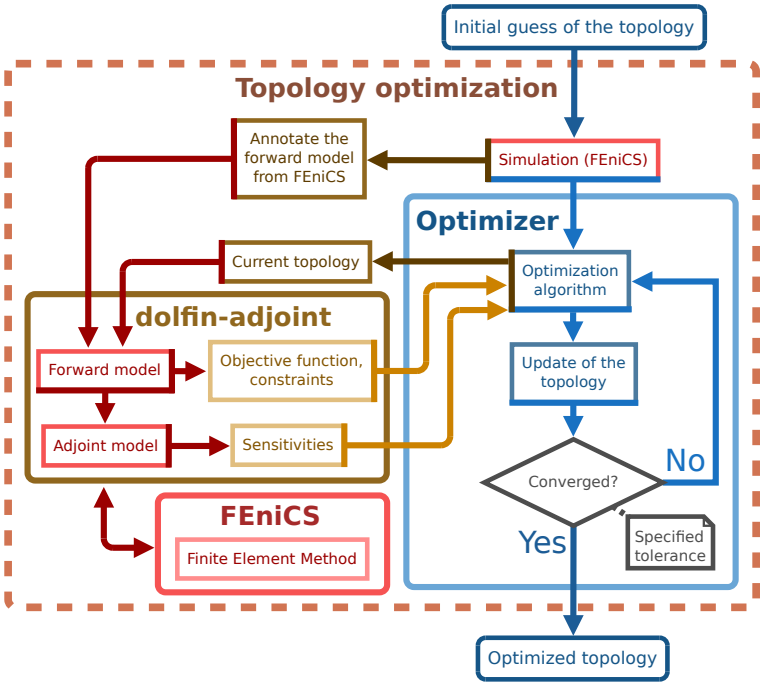
where V_{average} is the average element volume for the design variable interpolation, given as $V_{\text{average}} = \frac{\sum^{n_{\text{elements}}} V_{\text{element}}}{n_{\text{elements}}}$ (for an element-wise design variable) and as $V_{\text{average}} = \frac{\sum^{n_{\text{elements}}} V_{\text{element}}}{n_{\text{nodes}}}$ (for a nodal design variable).

The advantage of computing from the *volume averaging* approach (eqs. (3.1) and (3.2)) instead of the "L^2 integral" approach (eqs. (3.3) and eqs. (3.4)), is that it consists of an *element-wise* multiplication in the discretized sensitivity values, whereas the "L^2 integral" approach requires the solution of a linear system. Nonetheless, the "L^2 integral" approach can be more easily considered in parallelism when considering the implementation in FEniCS, because it does not depend on local mesh information (such as element volumes, vertices, and neighbors), which is normally not available in all processors and is required in the *volume averaging* approach.

The flowchart in Fig. 3.1 shows the interconnection of the software packages used to implement the topology optimization method. The topology optimization starts with an initial guess of the topology (distribution of the design variable), which is then used for the simulation (*forward model*) by using the finite element method in FEniCS. This initial simulation is used for *annotating* (*storing*) the forward model for the automatic derivation of the adjoint model. Then, the optimization loop from the optimizer (*optimization solver*) is started, by interacting with dolfin-adjoint for the computation

of the objective function, constraints and sensitivities from the adjoint method (*adjoint model*). In each loop, the design variable is updated, defining a new topology. The topology optimization loop continues until a specified tolerance for a given optimality error is reached (convergence criterion).

Figure 3.1 – Flowchart of the implementation of the topology optimization method.



Source: Author.

FEniCS and dolfin-adjoint use Automatic Differentiation (AD, also called *algorithmic differentiation* and *computational differentiation*) (LOGG *et al.*, 2012; FARRELL *et al.*, 2013), which means that the derivatives are computed numerically by repeating the chain rule for all basic functions/operations. This approach is more interesting than symbolic differentiation (or differentiation *by hand*) and numerical differentiation (finite differences), since it does not require the programmer to organize the equations of the derivatives in a computationally efficient way and neither incurs in the round-off errors that are intrinsic of finite differences (GRIEWANK, 2000).

3.1.1 **Optimization algorithms**

The formulation of the algorithms of the optimization solvers (*optimizers*) that are considered in this work are briefly described as follows. For easiness of the descriptions, a topology optimization problem that is more generic than eq. (2.139) is considered,

being given as:

$$\begin{aligned}
&\textbf{min}_{\alpha}\ J(\alpha)\\
&\textbf{such that}\\
&\quad \text{Equality constraints: } c_{\mathrm{eq},i}(\alpha)=0,\ i=1,\ 2\ ...\ n_{\mathrm{eq}}\\
&\quad \text{Inequality constraints: } c_{\mathrm{ineq},i}(\alpha)\leqslant 0,\ i=1,\ 2\ ...\ n_{\mathrm{ineq}}\\
&\quad \text{Box constraint of } \alpha\text{: } \alpha_{lb}\ \leqslant\ \alpha\ \leqslant\ \alpha_{ub}
\end{aligned} \tag{3.5}$$

where $J(\alpha)$ is the objective/multi-objective function, $c_{\mathrm{eq},i}(\alpha)$ is the definition of the equality constraint i, $c_{\mathrm{ineq},i}(\alpha)$ is the definition of the inequality constraint i, n_{eq} is the number of equality constraints, n_{ineq} is the number of inequality constraints, α_{ub} is the upper bound of the design variable, and α_{lb} is the lower bound of the design variable. It can be pointed out that, for the optimizer, eq. (3.5) consists of a multivariable optimization problem, in which the number of variables is given by the quantity of values of the design variable (α) that are distributed over the mesh, obtained by considering the finite element modeling (n_{α}) (as described in the beginning of Section 2.5).

3.1.1.1 IPOPT algorithm

The IPOPT (Interior-Point OPTimizer) algorithm (WÄCHTER; BIEGLER, 2006) is composed of an interior point method, and is briefly described in the beginning of Section 3.1. IPOPT converts the inequality constraint (i.e., the volume constraint that is being used in this work) into a logarithmic barrier term and gradually reduces the barrier parameter to zero during the optimization. The convergence criterion consists of attaining a specified tolerance for the optimality error in the IPOPT barrier problem. The optimality error of the IPOPT barrier problem corresponds to the maximum norm of each optimality (KKT, Karush-Kuhn-Tucker) condition (WÄCHTER; BIEGLER, 2006). Essentially, the optimization problem from eq. (3.5) is successively solved by IPOPT as the following barrier formulation:

$$\begin{aligned}
&\textbf{min}_{\alpha,\boldsymbol{s}_{\mathrm{bound}}}\ J(\alpha)-\mu_{\mathrm{IPOPT}}\sum_{i=1}^{2n_{\alpha}+n_{\mathrm{ineq}}}\ln(c_{\mathrm{bound},i}(\alpha,\boldsymbol{s}_{\mathrm{bound}}))\\
&\textbf{such that}\\
&\quad \text{Equality constraints: } c_{\mathrm{eq},i}(\alpha,\boldsymbol{s}_{\mathrm{bound}})=0,\ i=1,\ 2\ ...\ (n_{\mathrm{eq}}+n_{\mathrm{ineq}})
\end{aligned} \tag{3.6}$$

where μ_{IPOPT} is the logarithmic barrier parameter (*homotopy parameter*), which is gradually reduced to zero during the optimization. The *box constraint of* α is treated as $2n_\alpha$ bound constraints by IPOPT (represented as $c_{\mathrm{bound},i}(\alpha, \boldsymbol{s}_{\mathrm{bound}}) = \alpha_i - \alpha_{lb} \geqslant 0$ and $c_{\mathrm{bound},n_\alpha+i}(\alpha, \boldsymbol{s}_{\mathrm{bound}}) = \alpha_{ub} - \alpha_i \geqslant 0$, where α_i is the value of α in the node i of the mesh (or in the element i, depending on the finite element modeling)). The inequality constraints are converted by IPOPT to equality and bound constraints by including auxiliary variables (*slack variables*, $s_{\mathrm{bound},i}$, represented as part of a set ($\boldsymbol{s}_{\mathrm{bound}}$)), which means that $c_{\mathrm{ineq},i}(\alpha) \leqslant 0$ becomes: the bound constraint $c_{\mathrm{bound},2n_\alpha+i}(\alpha, \boldsymbol{s}_{\mathrm{bound}}) = -s_{\mathrm{bound},i} \geqslant 0$, and the equality constraint $c_{\mathrm{eq},n_{\mathrm{eq}}+i}(\alpha, \boldsymbol{s}_{\mathrm{bound}}) = c_{\mathrm{ineq},i}(\alpha) - s_{\mathrm{bound},i} = 0$. The solution of the IPOPT barrier problem (eq. (3.6)) is performed by a damped Newton-Raphson method augmented with a line-search filter method (WÄCHTER; BIEGLER, 2006).

3.1.1.2 TOBS algorithm

The TOBS (Topology Optimization of Binary Structures) algorithm (SIVAPURAM; PICELLI, 2018; SIVAPURAM *et al.*, 2018) can be described as a combination of features from SILP (Sequential Integer Linear Programming) (also sometimes called SLIP (Sequential Linear Integer Programming)) (SVANBERG; WERME, 2007) and BESO (HUANG; XIE, 2007), for topology optimization. It consists of a binary variables' formulation which is given by sequentially solving linearized integer variable problems (considering $\alpha_{lb} = 0$ and $\alpha_{ub} = 1$). Essentially, the optimization problem from eq. (3.5) is successively solved in TOBS as the following linearized formulation for the variation of the design variable (*design variable step*, $\Delta\alpha$):

$$
\begin{aligned}
&\textbf{min}_{\Delta\alpha} \quad \left.\frac{dJ}{d\alpha}\right|_{\alpha=\alpha} \Delta\alpha \\
&\textbf{such that} \\
&\quad \text{Inequality constraints: } \left.\frac{dc_{\mathrm{ineq},i}}{d\alpha}\right|_{\alpha=\alpha} \Delta\alpha \leqslant \Delta c_{\mathrm{ineq},i}(\alpha),\ i = 1,\ 2\ \ldots\ (n_{\mathrm{ineq}} + 2n_{\mathrm{eq}}) \\
&\quad \text{Truncation error constraint: } \|\Delta\alpha\|_1 \leqslant \beta_{\text{flip limit}} n_\alpha \\
&\quad \text{Allowed values of } \Delta\alpha\text{: } \Delta\alpha \in \{\alpha_{lb} - \alpha, \alpha_{ub} - \alpha\}
\end{aligned}
\tag{3.7}
$$

where α is the value of the design variable in the beginning of the iteration of the optimization, $\left.\frac{dJ}{d\alpha}\right|_{\alpha=\alpha}$ and $\left.\frac{dc_{\mathrm{ineq},i}}{d\alpha}\right|_{\alpha=\alpha}$ are the sensitivities of the objective/multi-objective function and the inequality constraints, respectively, computed at α, $\beta_{\text{flip limit}}$ is a factor

that limits the *number of flips/jumps* of α from one discrete value to another (0 or 1), n_α is the quantity of values of the design variable (α) that are distributed over the mesh, $\|\Delta\alpha\|_1$ is the one-norm (ℓ_1 norm) of $\Delta\alpha$, and the next value of the design variable is given as $\alpha + \Delta\alpha$. It can be noticed that equality constraints ($c_{\mathrm{eq},i}(\alpha)$) that are computed with floating point numbers are numerically extremely hard (if not impossible) to be exactly satisfied, which may lead to linearized problems with *impossible* integer solutions. In such case, the equality constraints should be substituted in eq. (3.5) by inequality constraints with a given variation around the bounds (i.e., $c_{\mathrm{eq},i}(\alpha) - \delta_{\mathrm{eq,i}} \leqslant 0$ and $-(c_{\mathrm{eq},i}(\alpha) + \delta_{\mathrm{eq,i}}) \leqslant 0$, where $\delta_{\mathrm{eq,i}}$ is a small bound for the definition of the equality constraints converted to inequality constraints). Therefore, the number of inequality constraints becomes $n_{\mathrm{ineq}} + 2n_{\mathrm{eq}}$.

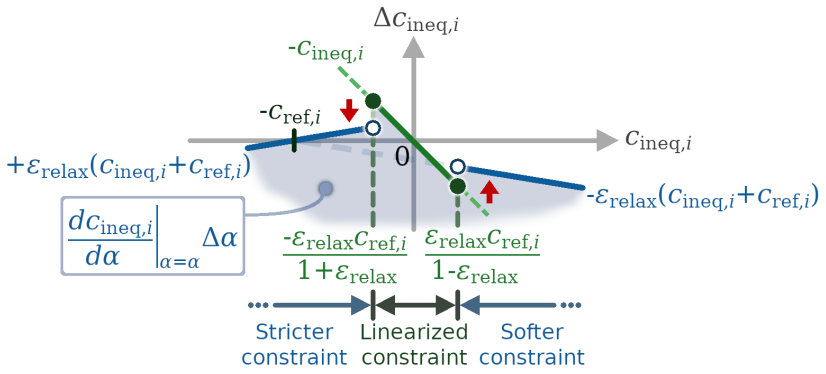
The truncation error constraint is included in order to keep the truncation error of the linearization small (SIVAPURAM; PICELLI, 2018). The linearized inequality constraint bound ($\Delta c_{\mathrm{ineq},i}(\alpha)$) is relaxed in order to guarantee that the integer solution of the linearized problem is feasible (SIVAPURAM; PICELLI, 2018). This relaxation essentially changes the value of $\Delta c_{\mathrm{ineq},i}(\alpha)$ when $c_{\mathrm{ineq},i}$ is "far" (based on a reference value ($c_{\mathrm{ref},i}$)). Then, the relaxation presented in Sivapuram and Picelli (2018) becomes:

$$\Delta c_{\mathrm{ineq},i}(\alpha) = \begin{cases} -\varepsilon_{\mathrm{relax}}(c_{\mathrm{ineq},i}(\alpha) + c_{\mathrm{ref},i}), & \text{if } c_{\mathrm{ineq},i}(\alpha) > \frac{\varepsilon_{\mathrm{relax}} c_{\mathrm{ref},i}}{1-\varepsilon_{\mathrm{relax}}} \\ -c_{\mathrm{ineq},i}(\alpha), & \text{if } \frac{-\varepsilon_{\mathrm{relax}} c_{\mathrm{ref},i}}{1+\varepsilon_{\mathrm{relax}}} \leqslant c_{\mathrm{ineq},i}(\alpha) \leqslant \frac{\varepsilon_{\mathrm{relax}} c_{\mathrm{ref},i}}{1-\varepsilon_{\mathrm{relax}}} \\ \varepsilon_{\mathrm{relax}}(c_{\mathrm{ineq},i}(\alpha) + c_{\mathrm{ref},i}), & \text{if } c_{\mathrm{ineq},i}(\alpha) < \frac{-\varepsilon_{\mathrm{relax}} c_{\mathrm{ref},i}}{1+\varepsilon_{\mathrm{relax}}} \end{cases} \tag{3.8}$$

where $0 < \varepsilon_{\mathrm{relax}} < 1$ is a constraint relaxation parameter, and $c_{\mathrm{ref},i} \neq 0$ is a reference value for constraint i. The reference value $c_{\mathrm{ref},i}$ is a representative value for the magnitude of the values that are achievable in the constraint, in order to define the size of the linearized interval. The reference value $c_{\mathrm{ref},i}$ cannot be set as 0, otherwise eq. (3.8) becomes $\Delta c_{\mathrm{ineq},i}(\alpha) = -\varepsilon_{\mathrm{relax}}|c_{\mathrm{ineq},i}(\alpha)|$, meaning that the linearized interval disappeared from the formulation. When considering a volume constraint, $c_{\mathrm{ref},i}$ is normally set as the imposed limiting volume (SIVAPURAM; PICELLI, 2018; SOUZA *et al.*, 2021), which corresponds, in the case of eq. (2.139), to $c_{\mathrm{ref},i} = fV_0$. This is also the case considered in this work. Eq. (3.8) is illustrated in Fig. 3.2: when $c_{\mathrm{ineq},i}(\alpha) > \frac{\varepsilon_{\mathrm{relax}} c_{\mathrm{ref},i}}{1-\varepsilon_{\mathrm{relax}}}$, the constraint bound is *softened*, widening the solution space; when $\frac{-\varepsilon_{\mathrm{relax}} c_{\mathrm{ref},i}}{1+\varepsilon_{\mathrm{relax}}} < c_{\mathrm{ineq},i}(\alpha) < \frac{\varepsilon_{\mathrm{relax}} c_{\mathrm{ref},i}}{1-\varepsilon_{\mathrm{relax}}}$, the linearized value is used for the constraint bound; and when $c_{\mathrm{ineq},i}(\alpha) < \frac{-\varepsilon_{\mathrm{relax}} c_{\mathrm{ref},i}}{1+\varepsilon_{\mathrm{relax}}}$, the constraint bound is *stricter*, decreasing the solution space to enforce a feasible or

near-feasible value. The red colored arrows represent the change in the solution space from the linearized constraint when considering the relaxation. The solution space is represented in blue color, and represents the possible values for $\frac{dc_{\text{ineq},i}}{d\alpha}\Big|_{\alpha=\alpha} \Delta\alpha$ (from eq. (3.7)).

Figure 3.2 – Relaxation of the linearized inequality constraint bound ($\Delta c_{\text{ineq},i}(\alpha)$).



Source: Author (ALONSO *et al.*, 2022).

The convergence criterion can be analyzed from successive objective function values (HUANG; XIE, 2007) or when there are no more changes in the topology ($\Delta\alpha = 0$). The solution of the TOBS linearized problem (eq. (3.7)) is performed by an integer programming optimizer, such as the commercial software CPLEX® (from IBM), or the open source software CBC (Coin-or Branch and Cut) (from the COIN-OR project). In particular, this work considers the use of CPLEX® , because it is currently faster than CBC (Coin-or Branch and Cut) and provides an academic license. In order to allow more flexibility in the implementation, the author of this work ported the original Matlab® implementation of the TOBS algorithm to Python, and developed an interface for dolfin-adjoint, which is based on the IPOPT interface currently available in dolfin-adjoint.

In the integer programming optimizer, the solution is obtained from the branch and bound method (LAND; DOIG, 1960; VANDERBEI, 2014), which essentially performs some operations recursively until an integer solution is obtained: (1) Solve the linear problem for obtaining a non-integer variable solution (such as from the Simplex method); (2) Separate into two different computations (recursion, *branch*) for each variable value, where one computation considers an additional integer upper bound ($\leqslant$) and the other considers an additional integer lower bound ($\geqslant$) around the non-integer variable value from step (1) – If the non-integer variable solution from step (2) is worse, then the given *branch* is discarded. In Sivapuram and Picelli (2020)'s work, a comparison of the rise

in computational cost of the integer programming optimizer and the simulation was performed with respect to the mesh resolution, showing that it increased much faster for the simulation (exponentially) than for the integer programming optimizer (linearly).

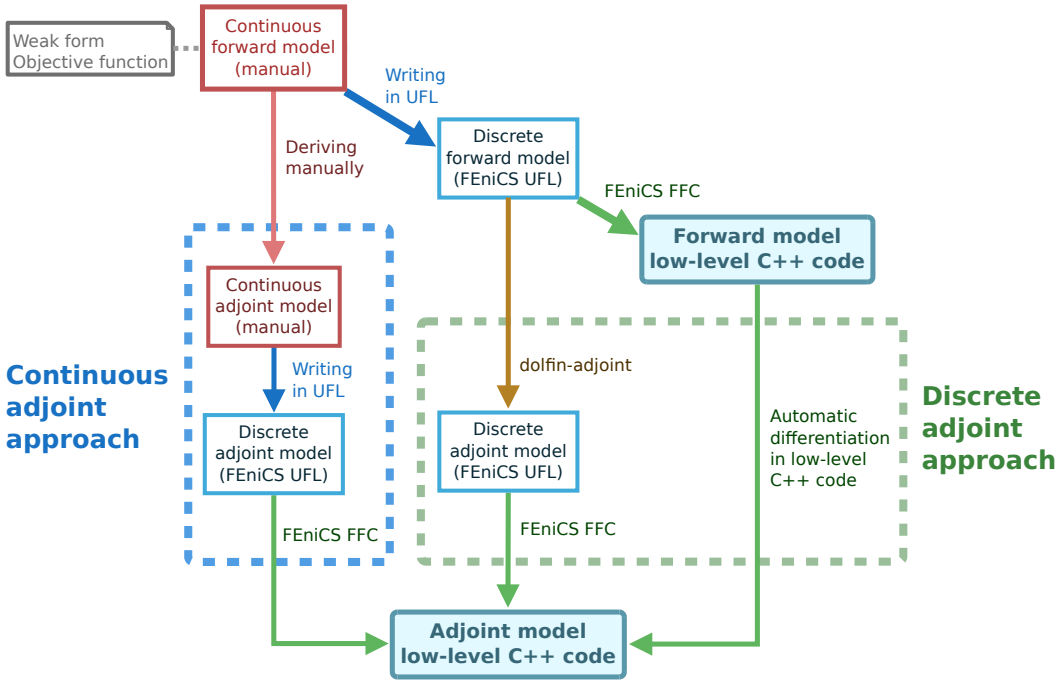
It can be mentioned that the numerical implementation of the TOBS algorithm includes additional normalizations (from the source code from Sivapuram and Picelli (2018)), which are: $\frac{dJ}{d\alpha}\Big|_{\alpha=\alpha} \Delta\alpha$ is divided by $\max\left[\frac{dJ}{d\alpha}\Big|_{\alpha=\alpha}\right]$, while $\frac{dc_{\mathrm{ineq},i}}{d\alpha}\Big|_{\alpha=\alpha} \Delta\alpha \leqslant \Delta c_{\mathrm{ineq},i}(\alpha)$ is divided by $\max\left[\frac{dc_{\mathrm{ineq},i}}{d\alpha}\Big|_{\alpha=\alpha}\right]$.

Also, when the design variable distribution is not respecting the constraints by a large margin, which may possibly happen in the initial guess of the design variable distribution, some specific considerations have to be made: if the optimizer is able to find an optimal solution (even while the constraints are not fully satisfied), this solution is accepted for the topology optimization step; if the optimizer is able to find a non-optimal solution, an under-relaxation is applied in the limits of the inequality and truncation error constraints (from eq. (3.8)) (such as multiplying them by 0.3); if the optimizer is unable to find any solution, a relaxation is applied in the limits of the truncation error constraint (multiplying them, for example, by 4) until an integer solution to the linearized optimization problem (eq. (3.8)) exists.

3.1.2 **Implementation of the adjoint model**

There are essentially two approaches for implementing the adjoint model (NADARAJAH; JAMESON, 2000; FUNKE, 2013): the *continuous adjoint* approach and the *discrete adjoint* approach. The *continuous adjoint* approach consists of directly specifying the adjoint equations to be solved, while the *discrete adjoint* approach consists of using the discretized equations (*discrete forward model* or the *forward model low-level code*) in order to solve the adjoint model. These approaches are illustrated in Fig. 3.3, considering the FEniCS platform and its high-level abstraction for defining functionals (FEniCS UFL).

Figure 3.3 – Flowchart showing the approaches for deriving the adjoint model (based on Farrell *et al.* (2013) and Funke (2013)).



Source: Author.

The forward model is solved as shown in the upper part of Fig. 3.3, where the continuous forward model equations (weak form and objective function) are first manually specified. Then, these equations are written in FEniCS's high-level abstraction language (UFL), which corresponds to the *discrete forward model*, which already contains information about the function spaces (i.e., the finite element modeling) being used. The *forward model low-level C++ code*, which corresponds to the matricial equations to be solved, is then generated by FEniCS FFC.

The *continuous adjoint* approach is implemented by deriving the adjoint equations manually (*by hand*) (or symbolically, by using, for example, the SymPy library (MEURER *et al.*, 2017)). The manual derivation of the continuous adjoint model is specific to each problem, may be laborious (FUNKE, 2013), and, even when it is symbolically derived, the adjoint equations may be presented in a format that is not computationally efficient. In this last case, the equations would require further manipulation in order to get to a computationally efficient format. One advantage of the *continuous adjoint* approach is that it is possible to discretize the forward and adjoint models differently, which may be useful in some cases (FANG *et al.*, 2006).

The *discrete adjoint* approach may be implemented by considering automatic differentiation. In this case, there are essentially two different ways to implement it: as

a low-level automatic differentiation, or as a high-level automatic differentiation. Traditionally, the *discrete adjoint* approach has been implemented as a low-level automatic differentiation, which is directly applied onto the *forward model low-level C++ code*. The main problem of this implementation is that it may be computationally inefficient, since the low-level C++ code would have to be automatically differentiated at each iteration of the optimization. Also, this implementation incurs in discretization errors two times (from the *forward model low-level C++ code* and the *adjoint model low-level C++ code*).

The *discrete adjoint* approach implemented as high-level automatic differentiation consists of using an automated method. The automated method consists of using the scheme provided by the dolfin-adjoint library (FARRELL *et al.*, 2013) in order to automatically derive an efficient discrete adjoint model from the discrete forward model specified in FEniCS UFL. The scheme used to obtain the discrete adjoint model consists of manipulating the dependencies / assemblies of the matricial equations of the forward model and applying automatic differentiation wherever required. As in the continuous adjoint model, it is also possible to discretize the forward and adjoint models differently, but that requires *overloading* a specific internal function of the solver object in the dolfin-adjoint library, regarding the *forward simulation* (which is called "`_forward_solve`", and is located inside the "`SolveBlock`" class), to perform a simulation in another mesh and to project the result back to the mesh of the adjoint model. One advantage of the *discrete adjoint* approach implemented as high-level automatic differentiation is that, as in the *continuous adjoint* approach, it incurs in discretization errors a single time (that is, only when generating the *adjoint model low-level C++ code*).

The sensitivities computed by each approach can be different, because the adjoint model is derived at different stages of the forward model (see Fig. 3.3). Since the dolfin-adjoint library provides an automated way to derive the adjoint model, tools to verify the adjoint model, and is also computationally efficient (FARRELL *et al.*, 2013), it is the approach that is used in this work.

3.2 NUMERICAL CONSIDERATIONS

The implementation in the FEniCS platform is direct from the description provided of the equations and numerical implementation/considerations, because FEniCS uses a high-level description for the variational formulation (UFL), automating the generation

of the matrix equations. In the case of 2D swirl flow, since the coordinate system is cylindrical, the differential operators ("`grad`", "`curl`", "`div`") must be programmed by hand by using the "`Dx(var,component_num)`" or "`var.dx(component_num)`" functions, because the operators provided by FEniCS assume Cartesian coordinates. Since these differential operators ("`grad`", "`curl`", "`div`") in cylindrical coordinates include divisions by the radial coordinate (r), which may numerically pose a problem when the computational domain includes a symmetry axis ($r = 0$), it would be necessary to adapt the finite element equations (eqs. (2.42) and (2.41), in Section 2.2.1), the computation of the performance quantities (Section 2.3) and the blood flow modeling (Section 2.4). One solution would be by multiplying these equations by r and developing them until eliminating any dependency with $\frac{1}{r}$; however, that may not be simple when considering a non-Newtonian fluid from eq. (2.11) or eq. (2.135). Therefore, there are two other solutions: change $\frac{1}{r}$ to $\frac{1}{r+\varepsilon_{\text{axis}}}$, or create the mesh with a minimum radius of $r = \varepsilon_{\text{axis}}$ (one can use, for example, $\varepsilon_{\text{axis}} = 10^{-11}$). In this work, it is chosen to change the finite element mesh, which avoids having to change the definitions of the differential operators.

In the implemented code, when computing the equations, the MMGS (MiliMeters-Grams-Seconds) unit system is used instead of the SI unit system. This is done in order to have a better numerical conditioning for calculating the weak form, functionals and sensitivities, and also improving the convergence rate. This way, small computed values are forced to stay farther (higher) from the numerical precision used in the numerical integration by FEniCS FFC (10^{-14}), and also farther (higher) from the smallest representable number in FEniCS, which is given by `DOLFIN_EPS` $= 3 \times 10^{-16}$. Comparing the units of the weak forms of the continuity and Navier-Stokes equations, since $\boldsymbol{w}_v$ has the same measurement unit as $\boldsymbol{v}$, and w_p has the same measurement unit as p, the units of the weak forms are kg m^2/s^3 ($= 10^9$ g mm^2/s^3). Therefore, the equations of the weak forms become multiplied by 10^9 in MMGS. The computed values of velocity and pressure, from the measurement units, change to: $[\boldsymbol{v}]$ = m/s $= 10^3$ mm/s and $[p]$ = Pa = kg/(m s^2) = g/(mm s^2). Therefore, computing the weak forms and state variables with these higher magnitudes (for example) should improve the precision of the computations, in the case small values are computed (in the SI unit system). In terms of observed results, the MMGS (MiliMeters-Grams-Seconds) unit system enabled simulating with higher Reynolds numbers under steady state (for example, those in Section 5.1.2), and the sensitivities could be computed with more precision (otherwise,

the sensitivities would get somewhat blurred).

In some cases, in order to facilitate the convergence of the simulation, a continuation scheme is performed in order to generate a better initial guess for the simulation. In this work, this continuation scheme may be performed in the viscosity (μ), starting from a higher viscosity and then gradually reducing its value until reaching the *real* viscosity of the fluid; in the volumetric flow rate (Q), slowly increasing it; or in the rotation (ω_0), slowly increasing it. When a continuation scheme is not needed, the initial guess for the velocity is selected as $\boldsymbol{v}_{\text{abs}} = \mathbf{0}$ (zero absolute velocity) for the 2D swirl flow cases, while it is chosen as $\boldsymbol{v} = \mathbf{0}$ for the 2D cases (zero relative velocity).

No numerical instabilities (oscillations) that would justify the inclusion of an additional numerical stabilization were noticed, even in the higher rotations that were used. Although stabilization methods may improve the accuracy of some numerical results, they may result in nonphysical results depending on the selected stabilization parameters (OLSHANSKII *et al.*, 2009). Therefore, no stabilization methods were used. One interesting stabilization method is briefly described as follows (grad-div stabilization), since Linke *et al.* (2011) mentions that, for grad-div stabilization, a large choice for the stabilization parameter for Taylor-Hood elements would not worsen the solution and would not lead to over-stabilization, converging to the Scott-Vogelius elements' solution instead. Grad-div stabilization can improve global mass conservation and convergence rate of the iterative method used to solve the weak form (OLSHANSKII; REUSKEN, 2004; CASE *et al.*, 2011; JENKINS *et al.*, 2012; AXELSSON *et al.*, 2015). It is based on the continuity equation for incompressible flow (eq. (2.1)), which is a *divergent-free* relationship, and is given by adding $-\gamma\nabla(\nabla\bullet\boldsymbol{v})$ to the right side of eq. (2.2) or eq. (2.10), where γ is a stabilization parameter (LINKE *et al.*, 2011) (OLSHANSKII; REUSKEN, 2004). When deriving the weak form (i.e., applying the gradient theorem (REDDY, 2013) to this term), the boundary term (on Γ_{Π}) due to this additional term is neglected (LINKE *et al.*, 2011), leaving only the term $+\int_{\Pi}\gamma(\nabla\bullet\boldsymbol{v})(\nabla\bullet\boldsymbol{w}_v)d\Pi$. However, when performing simulations with the 2D swirl flow model here, it has been observed that a high value for γ decouples the *swirl* motion from the radial-axial motion. In other words, the radial-axial motion keeps the same pressure-velocity distribution independently of the rotation for large γ. Therefore, grad-div stabilization is not suitable for applying to 2D swirl flow.

The calculation of the shear stress magnitude ($\dot{\gamma}_{\text{m}}$) of the equation for the Carreau-Yasuda model (eq. (2.11)), defined in eq. (2.12), is adapted for the numerical implemen-

tation as shown below

$$\dot{\gamma}_{\mathrm{m}} = \sqrt{2\boldsymbol{\epsilon}\bullet\boldsymbol{\epsilon} + \varepsilon_{\mathrm{adjustment}}} \tag{3.9}$$

where $\varepsilon_{\mathrm{adjustment}}$ is a sufficiently small value not recognized as zero by FEniCS (selected as 10^{-14} s^{-2} – i.e., the same value of the numerical precision used in the numerical integration by FEniCS FFC). As can be seen in Fig. 2.3, this value for $\varepsilon_{\mathrm{adjustment}}$ is not significant to influence the non-Newtonian behavior of blood. This term is included because of the algorithm of automatic differentiation, since, considering a function f (representing $2\boldsymbol{\epsilon}\bullet\boldsymbol{\epsilon}$) and the quotient rule for derivatives, the derivative of the square root of f is given by $(\sqrt{f})' = (f^{1/2})' = \frac{1}{2}\frac{f'}{f^{1/2}}$. In the initial guess, f is exactly equal to zero, which makes makes the derivative $(f^{1/2})'$ undetermined. When f' is also zero, which is the case, it would be possible to apply L'Hôpital's rule, but the automatic differentiation algorithm is unable to compute it when the denominator is *exactly equal* to zero. In order to compensate this fact, the sufficiently small value $\varepsilon_{\mathrm{adjustment}}$, which, from its order of magnitude, can be viewed as a *numerical error*, is included as shown in eq. (3.9). It is also possible to achieve a similar effect by assuming an initial guess (of the finite element method) for the velocity, in which $\dot{\gamma}_{\mathrm{m}}$ is different than zero (obtained, for example, from a simulation for the corresponding Newtonian fluid, or by adding a small random number to the initial guess). The described adjustment of summing $\varepsilon_{\mathrm{adjustment}}$ is also considered whenever necessary in the other equations of this work.

Since there is a term with a square root in eq. (2.134) of the Brinkman-Forchheimer model, some care should be taken in two aspects: (1) the numerical error of the term inside the square root ($\kappa(\alpha)$) when it is near zero (for example, it may possibly drop to a value such as -10^{-16}, which corresponds to a numerical error); (2) the derivative of $\sqrt{\kappa(\alpha)}$ includes a term of the format $\frac{1}{\sqrt{\kappa(\alpha)}}$, which may possibly become a division by zero (although in such case this term is multiplied by a zero term and the result should be zero). In order to avoid any of these problems, the value of $\kappa(\alpha)$, which should always be positive, may be manually thresholded to positive values before computing the equations in each iteration of the topology optimization and the derivative of this term may be adjusted in order to avoid division by zero – In dolfin-adjoint, this may be implemented by manually programming the adjoint of the square root operator – i.e., by creating an *overloaded function*.

For the hemolysis and thrombosis models (Sections 2.4.1 and 2.4.2), boundary

conditions of zero damage on the inlet can be changed to sufficiently small values (10^{-14}) for better numerical conditioning. When considering a mesh with edges/corners, for computing hemolysis and thrombosis, there may appear a high negative value only in some edge/corner nodes of the mesh. In order to avoid this case, all variables from the hemolysis and thrombosis models are post-processed for removing these *unphysical* values – In dolfin-adjoint, this may be implemented by manually programming it as a new operator (i.e., by creating an *overloaded function*). Furthermore, the divisions by stress terms in the hemolysis and thrombosis equations may be incremented with small values (10^{-14}). The concept of summing a small value in order to avoid division by zero is also used in some excerpts of the source code of the open source software OpenFOAM® (OPENFOAM FOUNDATION, 2020; WELLER *et al.*, 1998; CHEN *et al.*, 2014).

During the computation of eq. (2.45) through the Newton-Raphson, if, by any chance, the reciprocal wall distance (G) assumes a negative value, even if only due to numerical precision, this would result in a numerical error in eq. (2.45). Thus, in order to guarantee that such situation would never be achieved, the reciprocal wall distance (G) is enforced to be always positive in every Newton-Raphson iteration.

In the Wray-Agarwal model (WA2018), in eq. (2.23), there is the hyperbolic tangent term ($\tanh(arg_1^4)$), whose derivative would include the term $\frac{1}{\cosh(arg_1^4)}$. When arg_1^4 is sufficiently high, $\frac{1}{\cosh(arg_1^4)}$ approaches zero. However, even though $\frac{1}{\cosh(arg_1^4)}$ exists, the computation of the term $\cosh(arg_1^4)$ may result in a numerical overflow in FEniCS. Thus, the numerical value of arg_1^4 is constrained in order to avoid this issue, with a "`ufl.Min`" operator limiting a maximum value of 100, which results in $\frac{1}{\cosh(arg_1^4)} \approx 7.44 \times 10^{-44} \approx 0$.

In FEniCS, the integration is performed by default through Gauss quadrature. If not specified, FEniCS FFC tries to automatically assess the degree of the integrand, and chooses a quadrature degree that matches the exact quadrature rule for the integrations. However, when considering a non-Newtonian fluid (eqs. (2.11) and (2.135)) or the Brinkman-Forchheimer model (eq. (2.134)) or even some 3D models, the determined quadrature degree may become excessively high (higher than 99), which may give an overflow error and requires it to be reduced to a smaller value, such as 20 or even 5, for example. Although reducing the quadrature degree in the solution of the weak form may give coherent results, it may not be adequate when projecting some equation into a function space in FEniCS, since the "quality" (correspondence with expected values)

of the projection drastically reduces under lower quadrature degrees.

In the hemolysis and thrombosis models (Sections 2.4.1 and 2.4.2), another adjustment that may be performed is the use of the relative velocity ($\boldsymbol{v}$) projected in the same linear function space used in the hemolysis and thrombosis models. For reference, the projection may be computed from the weak form:

$$\int_{\Pi} \boldsymbol{v}|_{\text{projected,linear}}\, w_{\text{proj,v}} d\Pi - \int_{\Pi} \boldsymbol{v} w_{\text{proj,v}} d\Pi = 0 \tag{3.10}$$

where $\boldsymbol{v}|_{\text{projected,linear}}$ is the relative velocity projected in a linear function space, and $w_{\text{proj,v}}$ is the test function for the projection of the relative velocity. Eq. (3.10) may be solved with an LU solver (UMFPACK (DAVIS, 2004)) without any boundary conditions, or considering the velocity boundary conditions of the fluid flow simulation.

One more adjustment that may be performed is the approximated computation of the convective derivative $(\boldsymbol{v}\bullet\nabla)\tau_{\text{m,total}}$ (in the thrombosis model), which is required depending on the interpolation degree of the velocity (i.e., it is not required only when the interpolation degree is $\geqslant 2$, such as in Taylor-Hood elements). This approximate computation is based on a similar idea presented in Mortensen *et al.* (2011), and is briefly deduced below:

$$\int_{\Pi} (\boldsymbol{v}\bullet\nabla)\tau_{\text{m,total}}|_{\text{approximated}}\, w_{\text{a,cd},\tau} d\Pi - \int_{\Pi} (\boldsymbol{v}\bullet\nabla)\tau_{\text{m,total}} w_{\text{a,cd},\tau} d\Pi = 0 \tag{3.11}$$

where $(\boldsymbol{v}\bullet\nabla)\tau_{\text{m,total}}|_{\text{approximated}}$ is the convective derivative of the shear stress magnitude approximated in a linear function space, and $w_{\text{a,cd},\tau}$ is the test function for the approximation of the convective derivative of the shear stress magnitude.

By applying the product rule for derivatives,

$$\begin{aligned} \nabla\bullet(\boldsymbol{v}\tau_{\text{m,total}} w_{\text{a,cd},\tau}) &= (\nabla\bullet\boldsymbol{v})\tau_{\text{m,total}} w_{\text{a,cd},\tau} + \tau_{\text{m,total}}(\boldsymbol{v}\bullet\nabla w_{\text{a,cd},\tau}) \\ &\quad + (\boldsymbol{v}\bullet\nabla\tau_{\text{m,total}}) w_{\text{a,cd},\tau} \\ \implies (\boldsymbol{v}\bullet\nabla\tau_{\text{m,total}}) w_{\text{a,cd},\tau} &= \nabla\bullet(\boldsymbol{v}\tau_{\text{m,total}} w_{\text{a,cd},\tau}) - (\nabla\bullet\boldsymbol{v})\tau_{\text{m,total}} w_{\text{a,cd},\tau} \\ &\quad - \tau_{\text{m,total}}(\boldsymbol{v}\bullet\nabla w_{\text{a,cd},\tau}) \end{aligned} \tag{3.12}$$

Therefore, by substituting eq. (3.12) in eq. (3.11) and also applying Gauss' divergence theorem,

$$\begin{aligned} &\int_{\Pi} (\boldsymbol{v}\bullet\nabla)\tau_{\text{m,total}}|_{\text{approximated}}\, w_{\text{a,cd},\tau} d\Pi - \oint_{\Gamma_\Pi} (\boldsymbol{v}\tau_{\text{m,total}} w_{\text{a,cd},\tau})\bullet\boldsymbol{n} d\Gamma_\Pi \\ &+ \int_{\Pi} (\nabla\bullet\boldsymbol{v})\tau_{\text{m,total}} w_{\text{a,cd},\tau} d\Pi + \int_{\Pi} \tau_{\text{m,total}}(\boldsymbol{v}\bullet\nabla w_{\text{a,cd},\tau}) d\Pi = 0 \end{aligned} \tag{3.13}$$

By considering the continuity equation (eq. (2.41)), and also neglecting the boundary term (as an approximation, which is similar to some approximations performed by Mortensen *et al.* (2011)),

$$\int_{\Pi} (\boldsymbol{v}\bullet\nabla)\tau_{\mathrm{m,total}}\big|_{\mathrm{approximated}}\, w_{\mathrm{a,cd},\tau} d\Pi + \int_{\Pi} \tau_{\mathrm{m,total}}(\boldsymbol{v}\bullet\nabla w_{\mathrm{a,cd},\tau}) d\Pi = 0 \tag{3.14}$$

Eq. (3.14) is then solved with an LU solver (UMFPACK (DAVIS, 2004)) without any boundary conditions, similarly to Mortensen *et al.* (2011).

OpenFOAM® provides two types of solver for the velocity, which are the segregated solver (in which the velocity components are solved separately) and the vector-coupled matrix solver (in which the velocity components are solved at the same time in a matricial form). The vector-coupled matrix solver applied to 2D swirl flow showed better convergence (i.e., faster) than the segregated solver. In this work, the vector-coupled matrix solver is considered only in cases where the computational domain does not border the symmetry axis, due to an issue in the simulation results from OpenFOAM® 7.0 when including the symmetry axis with the vector-coupled matrix solver.

3.3 INTERFACING FEniCS WITH OpenFOAM® FOR THE EVALUATION OF TURBULENCE AND HIGH-SPEED FLOWS

Although FEniCS is a nice platform for programming and prototyping in the weak form of the finite element method (due to the easiness of use of UFL and due to the user interface being in Python), and also allows automatic derivation of the adjoint model (dolfin-adjoint), the implementation may not be as computationally efficient as in some other platforms. It is possible to improve the computational efficiency by considering parallelism / algebraic multigrid / block subsystems / preconditioners / etc. (LOGG *et al.*, 2012), but these adjustments can sometimes be problem-specific, and need to be implemented *by hand*.

On the other hand, OpenFOAM® is more prepared regarding computational efficiency, different discretization methods and approximations, more specifically regarding 3D simulations (due to the element-wise finite volumes), turbulent and compressible flows. OpenFOAM® (Open-source Field Operation And Manipulation) (WELLER *et al.*, 1998; CHEN *et al.*, 2014) is an open source CFD software written in C++, in which the syntax for specifying the finite volume equations is, as in the case of FEniCS

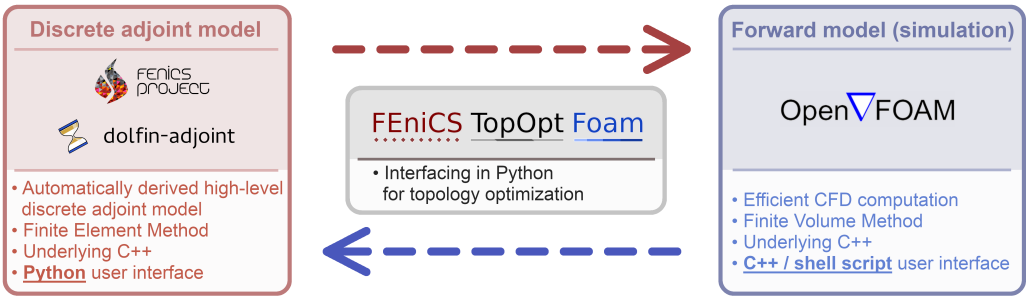
UFL, close to the representation of the equations themselves. There are historically three main versions of OpenFOAM® : *OpenFOAM® by The OpenFOAM® Foundation* (“openfoam.org”), *OpenFOAM® by ESI Group* (“openfoam.com”), and *FOAM-Extend by Wikki Ltd.*. In this work, the version that is considered is the “OpenFOAM® by The OpenFOAM® Foundation”. Since OpenFOAM® operates in the lowest degree of finite volumes (*element-wise*), the simulation should become less computationally expensive than when using the traditional Taylor-Hood elements or MINI elements of Section 2.2.2 for the same discretization (although the numerical accuracy should be lower due to the lower interpolation degree). Also, the finite volume method is based on the local conservation of fluxes (i.e., between finite volumes), which is different from the finite element method (i.e., based on the global conservation of fluxes – except, perhaps, only for Discontinuous Galerkin finite elements (Section 2.2.2)). The main drawback regarding the use of OpenFOAM® in topology optimization is the derivation of the adjoint model. The derivation of the adjoint model in OpenFOAM® has already been performed in three ways: by manually deriving and implementing the adjoint equations in a SIMPLE-like scheme (which may be a high demanding task for the programmer, especially when considering turbulent/compressible/non-Newtonian models) (*continuous adjoint* approach) (PAPOUTSIS-KIACHAGIAS *et al.*, 2015); by using C++ generic automatic differentiation tools (such as CoDiPack (SAGEBAUM *et al.*, 2018) and Adept (ADEPT, 2021), which are normally considered to be non-intuitive and show reduced performance) (*discrete adjoint* approach) in a SIMPLE-like scheme (TOWARA; NAUMANN, 2013); and by applying finite differences (which may imply some additional computational cost) (*discrete adjoint* approach) (HE *et al.*, 2018; HE *et al.*, 2020). Note that there is no high-level automatic differentiation approach such as that provided by FEniCS/dolfin-adjoint available in OpenFOAM® . More recently, aiming topology optimization, two approaches have been presented: using FEniCS/dolfin-adjoint automatic derivation (ALONSO *et al.*, 2021), and finite differences through a grouping algorithm (OKUBO *et al.*, 2022). Here, the approach presented by Alonso *et al.* (2021) is considered.

OpenFOAM® is considered in this work for performing turbulent or simply high-speed flow simulation. Turbulent simulations in FEniCS have already been previously performed by Mortensen *et al.* (2011) and Valen-Sendstad *et al.* (2013), and the source code is even available in internet in Mortensen (2011) and Mortensen (2013). However, the latest version (MORTENSEN, 2016) removed the turbulence module due to the

work required for it to be adapted to newer FEniCS versions. It can be mentioned that this implementation does not support the automatic derivation of the adjoint model from dolfin-adjoint, and neither the 2D swirl flow model. Therefore, some of the solution schemes from Mortensen *et al.* (2011) (such as wall functions, projections of variables at each iteration of the simulation, segregated solution of the equations, Picard solver approach, and pseudo-transient continuation) were reimplemented in order to account for dolfin-adjoint and the 2D swirl flow model. However, the convergence of the solution of the turbulent problem turned out to be harder in the implementation performed in FEniCS than when using OpenFOAM® . Therefore, OpenFOAM® is used in this work instead of FEniCS in order to perform turbulent flow simulation. Moreso, FEniCS may also suffer convergence difficulties in laminar flows with higher flow velocities, thus making OpenFOAM® a possibility for considering these cases.

Therefore, the aim would be for the simulation to be efficiently performed in OpenFOAM® while the adjoint model would be automatically derived and solved in FEniCS (by using dolfin-adjoint). Since no previous work has yet performed this type of interfacing between OpenFOAM® and FEniCS, a library was implemented in order to perform this interfacing. Since dolfin-adjoint is a Python-only library, OpenFOAM® 's C++ and shell script functionalities should be made accessible in Python. The interfacing between FEniCS/dolfin-adjoint and OpenFOAM® , for topology optimization, is represented in Fig. 3.4, through a library developed in this work (*FEniCS TopOpt Foam*). The details about the framework using *FEniCS TopOpt Foam* are described in Alonso *et al.* (2021), and the *FEniCS TopOpt Foam* library is made available in a git repository[1].

Figure 3.4 – Interfacing between the adjoint model and the forward model with *FEniCS TopOpt Foam*, outlining the main differences/similarities between FEniCS/dolfin-adjoint and OpenFOAM® .



Source: Author.

The topology optimization flowchart of Fig. 3.1 remains the same, but with

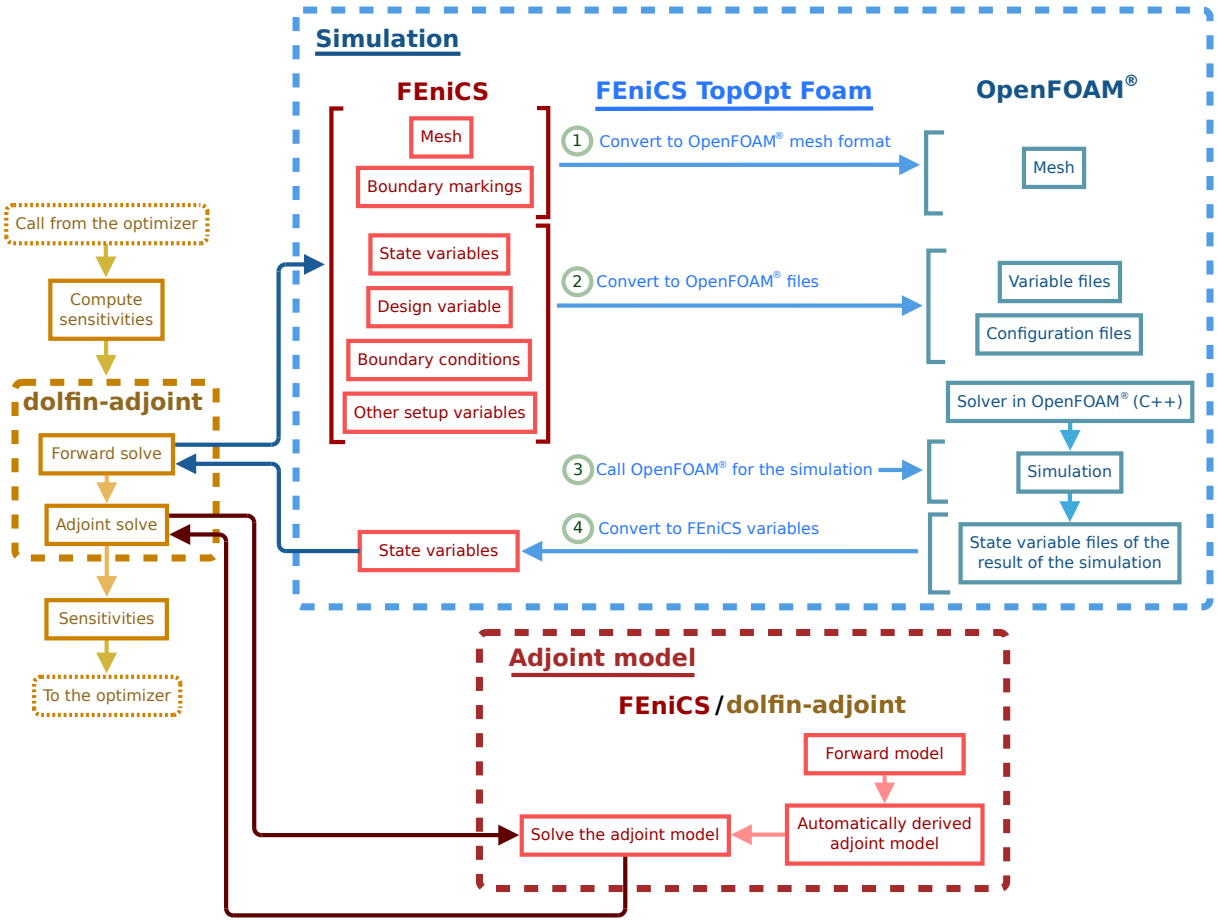
[1] https://github.com/diego-hayashi/fenics_topopt_foam

OpenFOAM® being called for performing the simulation instead of FEniCS. In terms of implementation, when using the *FEniCS TopOpt Foam* library, two simulation models should be programmed: one in FEniCS, which is used to automatically derive the adjoint model (dolfin-adjoint), and one in OpenFOAM® , for the simulation.

3.3.1 Implementation of the computation of sensitivities while interfacing with OpenFOAM®

The objective function is computed directly with FEniCS after the simulation with OpenFOAM® is performed, while the computation of the sensitivities uses the simulation result for later solving the adjoint model equations. A diagram illustrating the computation of the sensitivities is given in Fig. 3.5.

Figure 3.5 – Diagram illustrating the computation of the sensitivities when using OpenFOAM® and the *FEniCS TopOpt Foam* library for the fluid flow simulation.

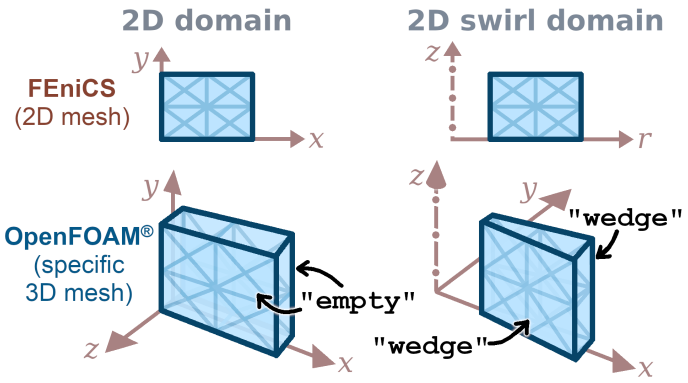


Source: Author (ALONSO *et al.*, 2021).

The diagram of Fig. 3.5 starts with a call from the optimizer for dolfin-adjoint to compute the sensitivities. The first step is computing the forward model (i.e., the

simulation). It starts by passing the mesh (FEniCS "`Mesh`"), together with a boundary marking (FEniCS "`MeshFunction`") (i.e., names of each group of facets – edges (2D / 2D swirl) or faces (3D) – of the boundary), to *FEniCS TopOpt Foam* to convert to the OpenFOAM® mesh format. It should be mentioned that OpenFOAM® operates only in 3D meshes/coordinates, but allows simulating for 2D and 2D swirl flows if the mesh has a specific construction (i.e., one-element uniform thickness (for 2D), and one-element "wedge" thickness (i.e., thickness linearly varying from zero radius, for a sufficiently small wedge angle)) and specific boundary conditions ("`empty`" for the parallel faces with respect to the 2D plane (of the 2D mesh), and "`wedge`" for the parallel faces with respect to the 2D plane (of the 2D swirl mesh)) (see Fig. 3.6). Since, in OpenFOAM® , the boundary conditions are applied on the external faces of the 3D mesh, the symmetry axis boundary condition (from the 2D swirl flow model) is implicitly considered when applying the "`wedge`" boundary conditions in OpenFOAM® . A similar scheme of using a 3D mesh for 2D/2D swirl simulation is also used in Ansys® CFX. If the mesh is the same during all iterations of the topology optimization, this conversion can be performed a single time.

Figure 3.6 – Representation of 2D and 2D swirl computational domains in FEniCS and OpenFOAM® (the specific boundary conditions "`wedge`" are presented separately, because they are imposed separately on each *almost parallel* face with respect to the 2D plane in OpenFOAM®).



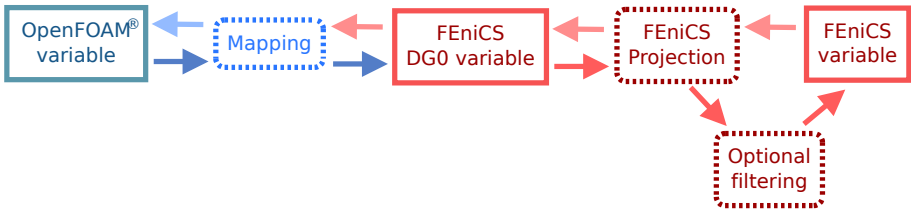
Source: Author (ALONSO *et al.*, 2021).

Then, the state variables (FEniCS "`Function`" 's), the design variable (FEniCS "`Function`"), the boundary conditions (specified as required by OpenFOAM®) and other setup variables are converted by *FEniCS TopOpt Foam* to variable and configuration files, which, in OpenFOAM® , are in the subfolders "`0`" (initial guess for the simulation), "`constant`" (mesh and properties) and "`system`" (solver parameters). With the OpenFOAM® files prepared, a specific solver for OpenFOAM® , which corresponds to

the simulation defined in FEniCS, is selected for being used. In case the simulation includes the design variable, the *default* OpenFOAM® solvers cannot be used without an adjustment that includes the design variable in it (i.e., a *new* solver has to be programmed). Then, the OpenFOAM® simulation is performed. After the simulation, the state variable files of the result of the OpenFOAM® simulation are converted to the state variables in FEniCS. With the simulation result, dolfin-adjoint is then used to compute the adjoint model that is automatically generated from the forward model specified in FEniCS.

The conversion from the OpenFOAM® files to the FEniCS variables (see Fig. 3.7) is performed by first mapping the internal values of the OpenFOAM® variables to element-wise variables in FEniCS (dP_0, "DG0"). Then, the element-wise variables are projected (FEniCS "`project`") into the interpolation that is being used in the adjoint model. The isolated state variables are then joined together in a single state vector by using a "`FunctionAssigner`" in FEniCS. In the case of turbulent variables, it may be needed to guarantee that their conversion to FEniCS is strictly positive and non-zero (compensating any numerical error in this aspect), because some turbulence models rely on some specific square-roots/divisions, and some other specific square-roots/divisions may arise due to the automatic derivation performed by FEniCS. After this imposition, a small-radius Helmholtz filter (LAZAROV; SIGMUND, 2010) may be applied to the turbulent variables in order to slightly filter some consequent sharp transitions which may hinder post-processing operations in FEniCS (one possible choice for the Helmholtz filter radius is $1/10^{th}$ of the minimum size of an element in the mesh (i.e., the smallest of the maximum distances between any two vertices of the elements)). An additional step is imposing the original Dirichlet boundary conditions (FEniCS "`DirichletBC`") onto the state vector, because the converted values from OpenFOAM® correspond only to the internal values of each cell and not to the external facets, which may generate numerical error on the boundaries.

Figure 3.7 – Diagram illustrating the conversion of variables between OpenFOAM® and FEniCS.



Source: Author (ALONSO *et al.*, 2021).

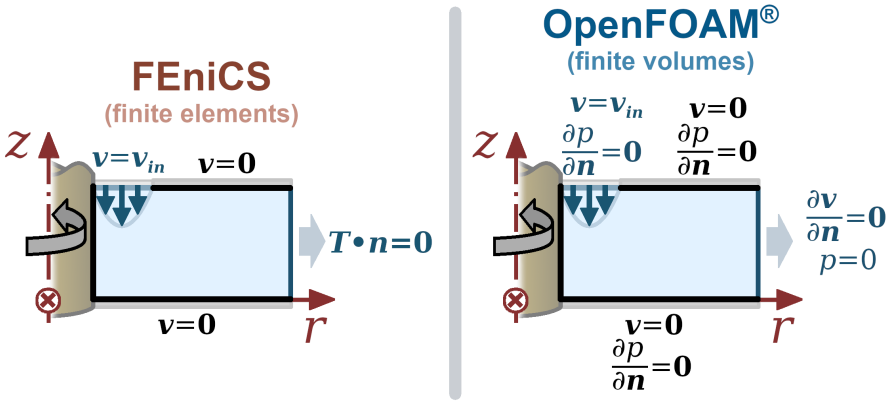
The interfacing of the simulation with dolfin-adjoint requires *overloading* a specific internal function of the solver object in the dolfin-adjoint library, regarding the *forward simulation* (which is called "`_forward_solve`", and is located inside the "`SolveBlock`" class, or the "`GenericSolveBlock`" class, depending on the version).

In terms of a parallel computation of the simulation and optimization, both OpenFOAM® and FEniCS provide independent implementations of parallelism out-of-the-box, which means that both softwares may partition the mesh differently according to their needs and what is set up by the user, and also independently call MPI operations. In the current version of *FEniCS TopOpt Foam*, it is possible to consider both parallelisms independently, which means that FEniCS may be set to run in parallel, such as from "`mpiexec -n 2 python my_code.py`" (for 2 processes), whilst OpenFOAM® may be set up to run in parallel from *FEniCS TopOpt Foam* functions independently. Sensitivity analyses using *FEniCS TopOpt Foam* are available in Alonso *et al.* (2021, 2022).

3.3.2 Correspondence of boundary conditions in FEniCS and OpenFOAM®

The boundary conditions that are possible to impose in OpenFOAM® may be different from those that are imposed in FEniCS due to the different solution methods and systems of equations (of finite volumes and finite elements, respectively). Therefore, the boundary conditions should be chosen to be with a close resemblance for corresponding simulation results. Although other variations are possible, one possibility for velocity and pressure is shown in Fig. 3.8.

Figure 3.8 – An example of boundary conditions in FEniCS and OpenFOAM® for the pressure-velocity formulation.



Source: Author.

Although in finite elements (FEniCS), no boundary conditions need to be explicitly imposed for the pressure, and for the outlet velocity (because of the stress free boundary condition), OpenFOAM® (finite volumes) requires all boundary conditions to be explicitly imposed. On the walls, the normal gradient of the pressure is set to zero ($\frac{\partial p}{\partial \boldsymbol{n}} = \mathbf{0}$) in OpenFOAM® (Neumann boundary condition). This boundary condition is originated from Prandtl's boundary layer equations (SCHLICHTING, 1979), where, inside the boundary layer, $\frac{1}{\rho}\frac{\partial p}{\partial \boldsymbol{n}} = \mathcal{O}(\delta_{\mathrm{BL}}) \approx \mathbf{0}$, where δ_{BL} is the thickness of the boundary layer, $\mathcal{O}(\delta_{\mathrm{BL}})$ represents the order of magnitude (i.e., in the *big O notation*) of δ_{BL}, and the fluid is assumed to be attached to the wall. Particularly when the fluid is incompressible, $\frac{\partial p}{\partial \boldsymbol{n}} \approx \mathbf{0}$. Therefore, setting the normal gradient of the pressure to zero is an approximation. In reality, $\frac{\partial p}{\partial \boldsymbol{n}}$ is non-zero (REMPFER, 2006), but the *correct* boundary condition would lead to a mathematically ill-posed problem (REMPFER, 2006). According to Rempfer (2006), due to the approximation, the "pressure" value used in finite volumes numerical methods – such as the SIMPLE algorithm (PATANKAR, 1980; OPENFOAM WIKI, 2014) – would, in reality, correspond to an *artificial pressure* value, which should attain a systematic deviation from the *correct* pressure value, and may or may not be corrected during the execution of the numerical method.

The normal gradient of the pressure is set to zero ($\frac{\partial p}{\partial \boldsymbol{n}} = \mathbf{0}$) on the inlet in OpenFOAM® (Neumann boundary condition), and the velocity profile is specified (Dirichlet boundary condition).

The outlet boundary condition in OpenFOAM® is given by imposing a zero normal gradient for the velocity ($\frac{\partial \boldsymbol{v}}{\partial \boldsymbol{n}} = \mathbf{0}$) (Neumann boundary condition) and a fixed pressure

value ($p = 0$) (Dirichlet boundary condition). In FEniCS, the boundary condition is *stress free*: $\boldsymbol{T}\bullet\boldsymbol{n} = \mathbf{0}$ (from eq. (2.25)), which corresponds to the weak imposition of a fixed zero pressure value ($p = 0$). From the substitution of eq. (2.3) in eq. (2.25) and considering $p \approx 0$,

$$(2\mu\boldsymbol{\epsilon})\bullet\boldsymbol{n} = \mu(\nabla\boldsymbol{v} + \nabla\boldsymbol{v}^T)\bullet\boldsymbol{n} \approx \mathbf{0} \tag{3.15}$$

Therefore,

$$(\nabla\boldsymbol{v} + \nabla\boldsymbol{v}^T)\bullet\boldsymbol{n} \approx \mathbf{0} \tag{3.16}$$

Since $\nabla\boldsymbol{v}\bullet\boldsymbol{n} = \frac{\partial\boldsymbol{v}}{\partial\boldsymbol{n}}$,

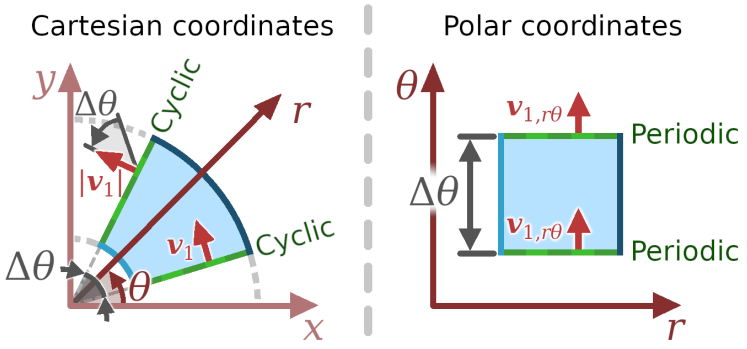
$$\frac{\partial\boldsymbol{v}}{\partial\boldsymbol{n}} \approx -\nabla\boldsymbol{v}^T\bullet\boldsymbol{n} \tag{3.17}$$

Since $\nabla\boldsymbol{v}$ is not symmetric, $\nabla\boldsymbol{v}^T\bullet\boldsymbol{n}$ of eq. (3.17) cannot be further simplified. Therefore, the zero normal gradient imposed for the velocity in OpenFOAM® does not correspond to the formulation from eq. (3.17), and the relation between both boundary conditions can be said to be approximated. Other outlet boundary conditions (Section 2.1.4) can also be used with FEniCS, but are normally less numerically stable than the stress free boundary condition.

3.4 IMPLEMENTATION OF CYCLIC BOUNDARY CONDITIONS

In Section 5.1.7.2, cyclic boundary conditions are considered for a 2D bladed pump model. This special type of boundary condition consists of periodic boundary conditions for the scalar fields (such as the pressure and the design variable itself), but requires *periodic boundary conditions* considering an angular difference in the directions of vector fields (such as the velocity) (see Fig. 3.9).

Figure 3.9 – Representation of a computational domain with cyclic boundary conditions.



Source: Author.

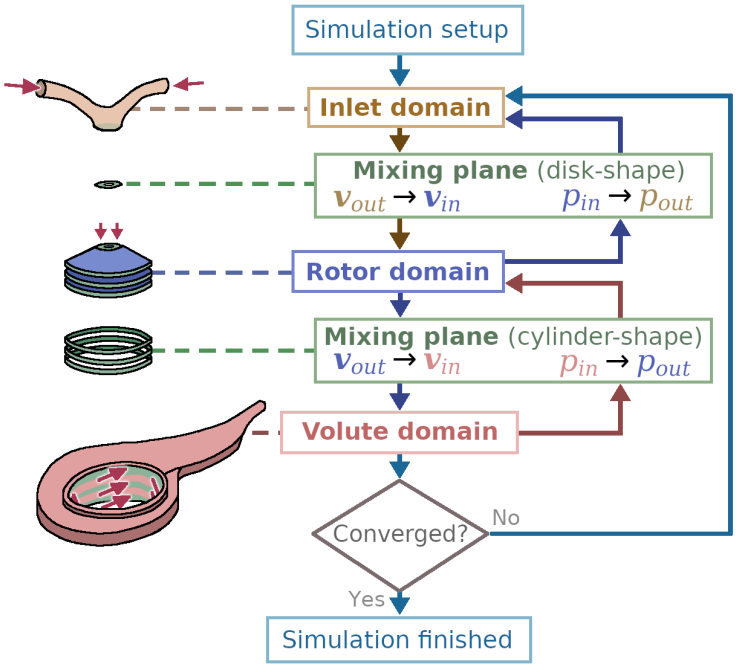
Since periodic boundary conditions in FEniCS are implemented from mapping degrees of freedom and reducing the size of the finite elements systems, this means that, implementation-wise, if the Cartesian coordinate system is used, it is not possible to impose an angular difference in the direction of the velocity. Although the matrix systems of equations could also be considered in their form without periodicity, and then manually edited to consider the cyclic boundary conditions, the imposition would not be as strong as when it is imposed with the mapping of degrees of freedom used by FEniCS in periodic boundary conditions. Thus, the natural way to impose cyclic boundary conditions in FEniCS would be by considering a coordinate system which turns cyclic boundary conditions into periodic boundary conditions: i.e., polar coordinates (for 2D) and cylindrical coordinates (for 3D). This also means that the integration domains should be used as $d\Pi = rd\Omega$ and $d\Gamma_{\Pi} = rd\Gamma$, while the coordinates become $(r,\ \theta)$ for 2D, and $(r,\ \theta,\ z)$ for 3D. The differential operators should also be adjusted accordingly (LAI *et al.*, 2009). If one wants to consider OpenFOAM® for the simulation in this case, OpenFOAM® provides built-in cyclic boundary conditions. Therefore, a mapping operation has been implemented between the *cyclic* ($(r,\ \theta)$, $(r,\ \theta,\ z)$) mesh in FEniCS, and the *Cartesian* ($(x,\ y)$, $(x,\ y,\ z)$) mesh in OpenFOAM® .

3.5 IMPLEMENTATION OF THE 3D PUMP SIMULATIONS

In Section 5.1.9, a 3D model is considered for simulating the designed prototype. The simulation is based on the mixing plane approach. Here, the mixing plane approach consists of circumferentially averaging the state variables that exit the inlet zone and enter the rotor, and the state variables that exit the rotor and enter the volute, meaning that it approximates the contribution of the continuous rotating movement of the rotor domain. Inside the rotor domain, the fluid flow equations are solved in the rotating reference frame. This consists of an approximation of the contribution of the movement of the mesh that would be present in a transient simulation. From the deduction in Appendix D (eq. (D.5)), the rotor domain should be imposed at least where there are structures (blades) that are perpendicular to the fluid flow, which result in $\frac{\partial \boldsymbol{v}}{\partial \theta} \neq \boldsymbol{0}$. Therefore, since the shaft is axisymmetric, it can be partially left in the outside of the rotor domain. When considering three domains (inlet, rotor and volute domains), the fluid flow equations should be solved iteratively as shown in Fig. 3.10. First, the

simulation is solved for the inlet domain. The outlet boundary condition is considered as a fixed stress boundary condition. Then, circumferential averaging is performed for the exiting velocity values, and the resulting averaged values are considered for the inlet boundary condition of the rotor domain. The rotor domain is solved in a relative (rotational) reference frame. After solving for the rotor domain, circumferential averaging is performed for the inlet pressure values, which are then considered as the reference pressure of the fixed stress outlet boundary condition of the inlet domain. Then, the same procedure is performed for the mixing plane between the rotor and the volute domains. This iterative loop is repeated until convergence is reached, which means the convergence of both simulations, as well as the mixing plane values.

Figure 3.10 – Mixing plane approach for the pressure and the velocity in the simulation of the designed prototypes.

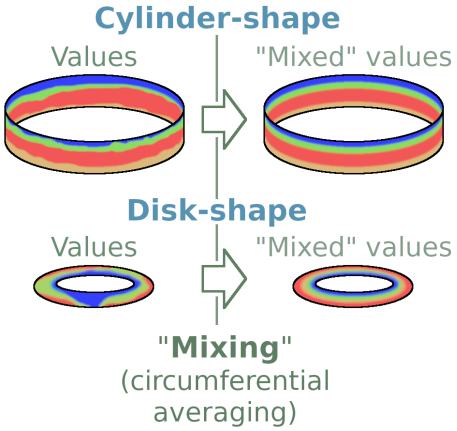


Source: Author.

The circumferential averaging, also called pitchwise averaging (RODRIGUES; MARTA, 2015), consists of computing the averages for each circumference in the z direction (cylinder-shape), or for each circumference in the radial direction (disk-shape). This is illustrated in Fig. 3.11. The basic types of circumferential averaging are: area-weighted or flow rate-weighted (ANSYS, 2021). In this work, as recommended in the source code of *FOAM-Extend*, area-based averaging is considered for the radial velocity (v_r) in order to guarantee mass/volume conservation, while the tangential (v_θ) and axial

(v_z) components are weighted by the flow rate, which, for the cylinder-shape mixing plane, correspond to the conservation of linear momentum for the θ and z directions on the interface, because the radius of the interface is constant. Pressure is computed considering area-based weighting. The OpenFOAM® version considered in this work ("openfoam.org") does not have a built-in mixing plane feature, although the *FOAM-Extend* version has it (BEAUDOIN *et al.*, 2014). With respect to the *FOAM-Extend* version, its code base seems to have significantly drifted apart from newer versions of "openfoam.org", and it seems to demand that the mixing plane interface is composed of structured quadrilaterals. Furthermore, the *FOAM-Extend* version still does not have the desired averaging scheme for the velocity (even though it recommends it). Thus, an implementation is made for performing the necessary circumferential averaging. For ease of implementation, although at the cost of some numerical precision and computational time, the interfacing was implemented by using the *FEniCS TopOpt Foam* library. In order to allow more flexibility for the generation of the mesh for the mixing plane interface (i.e., not restricting to only structured quadrilateral interfaces), an auxiliary structured grid is constructed for performing the averaging, and then the averaged values are interpolated back to the interface of the mesh.

Figure 3.11 – Circumferential averaging examples, for cylinder-shape and disk-shape mixing planes.



Source: Author.

In order to guarantee conservation of flow rate in the simulations, especially for cases where there may be fluid coming from the volute to the part below the rotor (due to the washout hole), OpenFOAM® 's "`matchedFlowRateOutletVelocity`" boundary condition, which includes some adjustments in order to enforce mass/volume conservation, is considered. Also, the flow rate entering the volute is manually adjusted

in order to exactly match the flow rate entering the inlet-rotor domain.

3.5.1 **Relation to experimental measurements**

For the simulation of the complete design from a 3D model, the simulation model is presented in Section 5.1.9, while the corresponding experimental setup is presented in Chapter 4. There are some characteristics of the experimental setup that are not considered in the simulations. However, some of these effects in the variation of (static) pressure (Δp) can be partially compensated through an analytical take on them, which is considered only for comparing the simulated and experimental values. From Appendix F, the variation of (static) pressure from the simulations is compensated as follows, only when comparing to the experimental results:

$$\Delta p_{\mathrm{comp}} = \Delta p_{\mathrm{sim}} + \frac{3}{4}\rho \left(\frac{Q}{\pi R_{\mathrm{tube}}^2} \right)^2 - \rho g \Delta h_{\mathrm{probes}} \tag{3.18}$$

where Δp_{comp} is the compensated variation of (static) pressure, Δp_{sim} is the variation of (static) pressure from the simulation, Q is the flow rate, R_{tube} is the internal radius of the tubes used in the experiments, g is the gravitational acceleration, and $\Delta h_{\mathrm{probes}}$ is the variation of height between the pressure measurement probes (20 mm).

4 EXPERIMENTAL SETUP

The experimental setup depends on the designs of the prototype and the experimental apparatus, as well as on other related aspects. They are described alongside the related design considerations.

4.1 GENERAL DESIGN CONSIDERATIONS

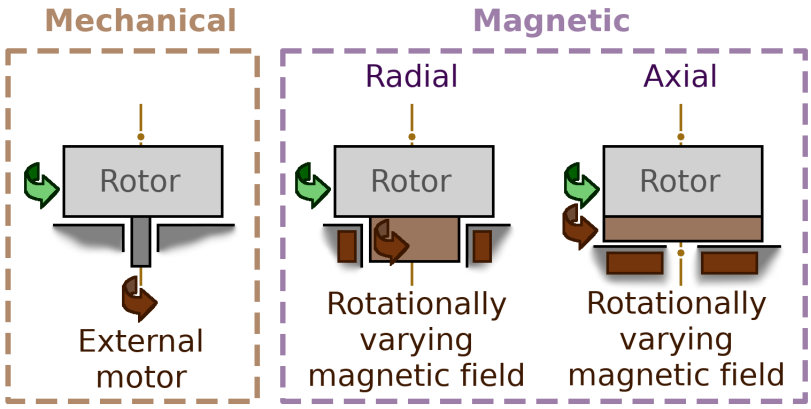
In order to design the prototype and the experimental apparatus, it is necessary to perform some design choices. The corresponding design considerations are outlined as follows.

4.1.1 **Driving system**

The VAD pump design initially started with mechanical driving systems (i.e., mechanically coupling the motor and rotor shafts). However, most recent VAD pump designs consider the use of magnetic drives (i.e., the third generation VADs, mentioned in Section 1.1.1), which may act over the pump rotor radially (HOSHI *et al.*, 2005; BUMRUNGPETCH, 2016; SÁ, 2016), such as CentriMag, or axially (HILTON; TANSLEY, 2008; SÁ *et al.*, 2018; SÁ, 2019), such as Rotaflow. These driving systems can be viewed in Fig. 4.1. Combined magnetic driving systems – with both (radial and axial) constructions – should also be possible if needed to impose a higher driving torque (JACK *et al.*, 1999). Between radial and axial magnetic drives, an axial magnetic drive requires more magnet material (windings, magnets) in order to induce the same amount of torque as radial magnet drives (MAGNETIC INNOVATIONS, 2021). Also, depending on the length of the lower part of the rotor in the radial magnetic drive case, in order to avoid fluid stagnation, it may be interesting to include an additional channel connecting the lower and upper parts of the rotor (*washout hole*) (BUMRUNGPETCH, 2016). The varying magnetic fields indicated in Fig. 4.1 can be induced not only by specific motor windings (SÁ, 2016), but also by the rotation of magnets from an external motor (BUMRUNGPETCH, 2016). In the case of the radial magnetic drive, it is also possible to consider an upper shaft (instead of the “lower shaft” shown in Fig. 4.1) to attach the magnets (WAMPLER, 1997). Although the use of magnetic drives is much better

for blood flow, due to it reducing shear stresses, completely eliminating leakage and avoiding unnecessary mechanical friction (which may induce wear, heating and even release small particles in the blood flow), the design of a magnetic drive is much more complex than simply mechanically attaching a shaft from the motor to the rotor. Thus, although the use of a magnetic drive would be the best choice for blood flow, in order to ease the design and construction for the experiments of this work, a mechanical driving system is considered.

Figure 4.1 – Possible driving systems (for simplicity, the driving magnets are depicted as rectangles in darker brown color).



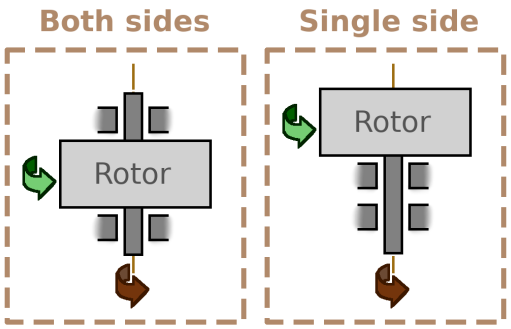
Source: Author.

4.1.2 **Bearings**

Traditionally, pumps are designed through mechanical bearings, such as contact (sliding, roller, ball etc.) and non-contact (hydrodynamic, magnetic etc.). The third generation of VADs, mentioned in Section 1.1.1, mainly makes use of magnetic bearings (i.e., magnetic levitation/suspension) (SÁ, 2019), but there may be some exceptions, such as Rotaflow, which features a single small bearing sphere. Particularly, the designs considered by Hilton and Tansley (2008) and Sá *et al.* (2018) use two contact bearings in conjunction to magnetic drives. In terms of magnetic bearings, Hilton and Tansley (2008) consider an axial magnetic drive with the use of a slightly slanted configuration below the rotor, which may ease alignment and even increase the torque provided by the axial magnetic drive to the rotor (in fact, this configuration has been adopted in the commercial pump Rotaflow). Furthermore, when the pump rotor is under rotation, the fluid (blood) may create a fluid layer near the upper and lower walls, which would then create a *hydrodynamic bearing*-like interface that may also contribute to maintaining the

axial distance between the rotor and the volute. Since a mechanical driving system is being considered in the experiments of this work, a contact bearing configuration is also considered. When considering a contact bearing configuration for a mechanical driving system, when the shaft of the motor is different from the shaft of the rotor, there may be essentially two options: the rotor may be supported from both sides, or the rotor may be supported from a single side (HOLLAND, 2015) (Fig. 4.2). Using two bearings aims to reduce vibration and misalignment. When considering the rotor being supported from a single side, if the shaft being considered is long, bending may need to be evaluated through a resistance of materials approach. In this work, in order to facilitate assembly and use, the rotor is chosen to be supported from a single side.

Figure 4.2 – Possible bearing configurations.



Source: Author.

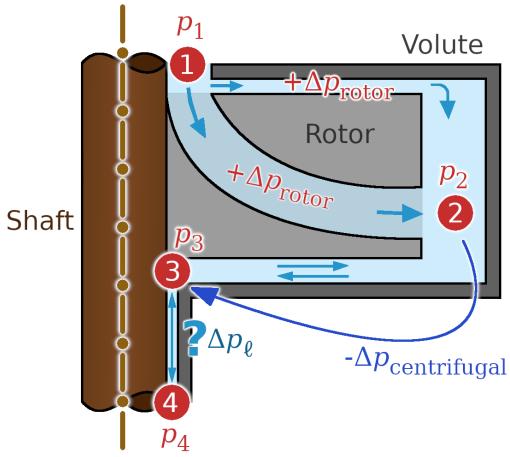
4.1.3 **Leakage**

When considering the use of a magnetic drive, since the the drive does not require the use of a shaft extending from the inside to the outside of the pump, there is no leakage. This condition should be ideal for blood flow, since the blood flow quantity would not be reduced while passing through the VAD. However, when considering the use of a mechanical drive, leakage has to be taken into account (SAHU, 2000), and a seal has to be considered in order to deal with it. The pressure drop in the leakage flow (Δp_ℓ) can be roughly estimated as shown in Fig. 4.3 (PFLEIDERER; PETERMANN, 1979; GÜLICH, 2014; CHILDS, 2019). From Fig. 4.3, the pressure at point “3” (p_3) may be given as a function of the other pressure values, as:

$$p_3 = p_1 + \Delta p_{\text{rotor}} - \Delta p_{\text{centrifugal}} = p_4 + \Delta p_\ell \tag{4.1}$$

where the pressure contribution of the centrifugal effect is approximated by $\Delta p_{\text{centrifugal}} = \rho\omega_0^2 \frac{(r_{ext}^2 - r_{shaft}^2)}{2}$ (PFLEIDERER; PETERMANN, 1979).

Figure 4.3 – Approximated analysis for the pressures in the case the motor is mechanically coupled through the shaft in the lower side of the figure.



Source: Author.

Therefore,

$$\Delta p_\ell = (p_1 - p_4) + \Delta p_{\text{rotor}} - \rho\omega_0^2 \frac{(r_{ext}^2 - r_{shaft}^2)}{2} \tag{4.2}$$

By considering the density of blood ($\rho = 1056$ kg/m^3) (HINGHOFER-SZALKAY; GREENLEAF, 1987), $r_{ext} = 15$ mm, $r_{shaft} = 2.5$ mm and $\omega_0 = 209.44$ rad/s (2000 rpm),

$$\Delta p_\ell = (p_1 - p_4) + \Delta p_{\text{rotor}} - 5.1\text{kPa} \tag{4.3}$$

From Section 5.1.5, Δp_{rotor} can reach a value of about 410 Pa for 1 L/min and 2000 rpm. Also, p_4 can be assumed as being the relative pressure value 0 kPa, representing the atmospheric pressure level. Therefore,

$$\Delta p_\ell = p_1 - 4.7\text{kPa} \tag{4.4}$$

If, additionally, p_1 is also considered to be at the atmospheric pressure level (relative value, 0 kPa), $\Delta p_\ell = -4.7$kPa, which is negative. This negative pressure value means that the pressure at point “3” in Fig. 4.3 is lower than the atmospheric pressure, possibly indicating a tendency of air being suctioned to the inside the pump. This would possibly consist of an unfavorable condition. Although this is an approximated estimation, and there are other effects (viscosity) that have not been considered, it should be interesting to consider a way to avoid this potential issue. In order to workaround

it without changing operating conditions (variation of pressure and flow rate) some possibilities would be:

1. The use of a magnetic drive, which poses zero risk of leakage but is more complex to design.

2. *Flooding* the pump inlet, which would mean including a column of fluid (of height h) before the inlet, increasing the value of p_1 to $\rho g h$. This would, however, mean that, in order to compensate 4.7 kPa, a 46 cm column of fluid would be required.

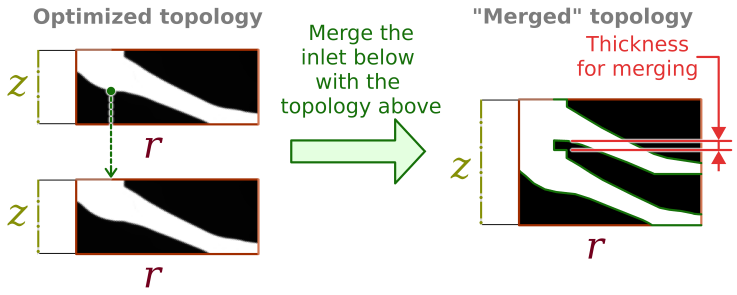
3. Including blades, in a *hybrid* approach for the design. This would, however, mean that the resulting device would not be a "true" Tesla pump anymore.

4. Considering *pattern repetition* (Section 2.5.6) in the design, which enforces more disks in the optimization, since the inclusion of more disks increases the pressure rise in the rotor ($\Delta p_{\mathrm{rotor}}$). The main limitation of the considered approach is that it does not allow the appearance of inclined disk optimized topologies without including disks with high thicknesses.

5. *Pattern stacking* approximation, in which the optimized topology for a single channel is stacked a multiple amount of times (Fig. 4.4), increasing the number of disks and, therefore, $\Delta p_{\mathrm{rotor}}$. In such case, in order to match the approximation, each single-channel topology would need to be designed for a flow rate of $Q = Q_{\mathrm{stacked}}/n_{\mathrm{patterns}}$, where n_{patterns} is the desired quantity of stacked patterns, and Q_{stacked} is the flow rate of the stacked topology.

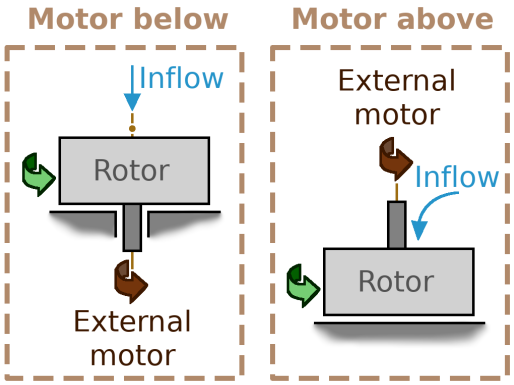
6. Changing the position of the motor. Instead of leaving the shaft of the motor below the rotor, which suffers from the issue presented in eq. (4.4), this negative pressure situation can be avoided by considering the shaft of the motor in the same side of the inlet (see Fig. 4.5). In such case, by following the same notation from Fig. 4.3, eq. (4.1) is changed to $\Delta p_\ell = p_1 - p_4$, meaning that, if p_1 is given as 0 kPa, $\Delta p_\ell = 0$ kPa. When considering that there is some pressure drop due to the flow inside the tube, it can be pointed out that this can be compensated by a small column of fluid before the inlet ($p_1 = \rho g h$), thus solving the issue.

Figure 4.4 – Illustration of the *pattern stacking* approximation.



Source: Author.

Figure 4.5 – Side of the shaft of the external motor.



Source: Author.

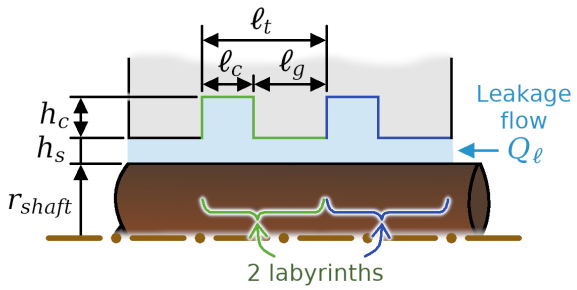
From the presented possibilities, since a mechanical drive was selected in this work, the first possibility (magnetic drive) is not valid for this case. The second possibility (*flooding* the pump inlet) requires the inclusion of a column of fluid, which can be quite high depending on the inlet rotation, thus ruling it out of the possibilities. The third possibility (blades) suggests the inclusion of blades, which is an aspect that will also be evaluated in the experiments. The fourth possibility (*pattern repetition*) imposes some limitations in the inclination of the disks, which may not be suitable for this case, since the optimized topologies feature inclined disks (Section 5.1.5). The fifth possibility (*pattern stacking*) is an interesting possibility. However, it may be more interesting to consider the same topology as it was optimized, in this work. Furthermore, the inclusion of more disks in a Tesla pump may be compared to the inclusion of more blades in a bladed pump, increasing not only the power transmitted to the fluid but also the resulting blood damage. The last possibility (changing the position of the motor) is the one selected in this work, due to it enabling the use of a mechanical drive whilst naturally avoiding the negative pressure issue.

4.1.3.1 Seal

With a positive pressure drop in the leakage flow (Δp_ℓ), a seal needs to be considered in order to reduce leakage from the mechanical coupling as much as possible. Some possibilities would be the use of rotary seals (*retainers*), o'rings, gaskets or labyrinth seals (LOBANOFF; ROSS, 1910; PFLEIDERER; PETERMANN, 1979; PFLEIDERER; PETERMANN, 1991; MACKAY, 2004; MAYER, 2013; GÜLICH, 2014). At a first glance, the best choice would probably be the labyrinth seal, because it does not contact the shaft and, thus, does not suffer from wear. It is even used in its axial form in the original Tesla turbine design (TESLA, 1913b). However, from the given dimensions of the prototype, it would be hard to make an effective labyrinth seal that does not demand an excessive length, which can even be higher than 5 cm. Therefore, in this work, the labyrinth seal design is augmented by including rubber gaskets, as will be explained in the following analysis.

For the labyrinth seal design, the approach presented in Pfleiderer and Petermann (1979) is considered for computing the resulting leakage, in an approximated manner. The configuration of the labyrinth seal is given as shown in Fig. 4.6 for 2 labyrinths ($n_\ell = 2$), where ℓ_t is the total length of a labyrinth unit, ℓ_g is the length of the gap, ℓ_c is the length of the chamber, h_c is the height of the chamber, h_s is the gap spacing/height, r_{shaft} is the radius of the shaft, and Q_ℓ is the leakage (volumetric) flow rate.

Figure 4.6 – Labyrinth seal design for 2 labyrinths.



Source: Author.

The equation that corresponds to the leakage flow (i.e., Q_ℓ) is given from some considerations: (1) conservation of volume (volumetric flow rate) between the flow through the cross sections of the gap and the chamber; (2) Bernoulli equation (i.e., steady state flow, incompressibility, negligible viscous dissipation, and single stream-

line); (3) negligible effect of the gravity acceleration inside the seal; (4) experimental coefficients; (4) gap (h_s) sufficiently small with respect to the radius of the shaft (r_{shaft}) (PFLEIDERER; PETERMANN, 1979). The resulting equation is shown below (PFLEIDERER; PETERMANN, 1979):

$$Q_\ell = \mu_Q (2\pi r_{shaft} h_s) \sqrt{\frac{2\Delta p_{\text{seal}}}{\rho}} \tag{4.5}$$

where Δp_{seal} is the pressure difference inside the labyrinth seal, while the corresponding average leakage velocity (*axial velocity in the gap*) is $v_\ell = \mu_Q \sqrt{\frac{2\Delta p_{\text{seal}}}{\rho}}$, and μ_Q is the flow coefficient, which is given as follows, by also considering that all labyrinth units are equal:

$$\mu_Q = \frac{1}{\sqrt{\frac{n_\ell}{\alpha_c^2} + \lambda_r \frac{n_\ell \ell_g}{2h_s}}} \tag{4.6}$$

where α_c is the contraction coefficient, and λ_r is the resistance coefficient. Both coefficients depend on the computation of two Reynolds numbers related to the labyrinth seal:

- Reynolds number for the rotation:

$$\text{Re}_\omega = \frac{2h_s(\omega_0 r_{shaft})}{\nu} \tag{4.7}$$

- Reynolds number for the chambers:

$$\text{Re}_c = \frac{2h_s v_\ell}{\nu} \tag{4.8}$$

where $\nu = \frac{\mu}{\rho}$ is approximated, in this work, by the Newtonian viscosity of blood ($\mu \approx \mu_\infty$).

Particularly, when $\text{Re}_c < 2,000$, which is the case in this work, and the shaft rotation does not present any eccentricity, the resistance coefficient (λ_r) may be computed as (GÜLICH, 2014):

$$\lambda_r = \frac{96}{\text{Re}_c} \left[1 + 0.2 \left(\frac{\text{Re}_\omega}{2000} \right)^{1.03} \right] \tag{4.9}$$

The contraction coefficient (α_c) may be estimated from experimental data that correlates it to Re_c (PFLEIDERER; PETERMANN, 1979). However, the ranges of experimental data presented by Pfleiderer and Petermann (1979) do not comprise the Re_c values computed in this work. Therefore, in order to get at least a “really rough” estimate (or, at the very least, a “faint idea”) of the leakage, the presented data in Pfleiderer and Petermann (1979) is extrapolated. This extrapolation is performed by

considering $\frac{\ell_t}{\ell_g} = 0.5$. By plotting the values for α_c and Re_c for $\frac{\ell_c}{\ell_g} = 0.5$ and considering a bi-logarithmic plot, all experimental points ended up coincidentally aligned (straight line). Therefore, the contraction coefficient (α_c) for $\frac{\ell_t}{\ell_g} = 0.5$ may be given through linear regression, with a coefficient of determination of "$r_d^2 = 0.98$", as:

$$\alpha_c = 10^{a_r \log_{10}(\mathrm{Re}_c) + b_r} \tag{4.10}$$

where the linear regression coefficients between $\log_{10}(\alpha_c)$ and $\log_{10}(\mathrm{Re}_c)$ are $a_r = 0.158928$ and $b_r = -0.513639$.

Then, from the previous equations and considering an initial guess for μ_Q (such as $\mu_Q = 0.5$), the value of the leakage flow rate (Q_ℓ) can be computed iteratively through the method of successive approximations (*fixed-point iteration*).

For the geometric dimensions, Pfleiderer and Petermann (1979) recommend the use of the following aspect ratios: $\frac{\ell_t}{h_s} = 15 \sim 25$, $\frac{h_c}{h_s} = 3 \sim 10$ and $\frac{\ell_c}{\ell_t} = 0.5 \sim 1.0$. By considering $\ell_c = 4$ mm, $\ell_g = 4$ mm, $h_s = 0.5$ mm, and $h_c = 1.5$ mm, the aspect ratios become $\frac{\ell_t}{h_s} = 16$, $\frac{h_c}{h_s} = 3$ and $\frac{\ell_c}{\ell_t} = 0.5$. The other geometric parameters are given as $r_{shaft} = 2.5$ mm and $n_\ell = 2$ labyrinths.

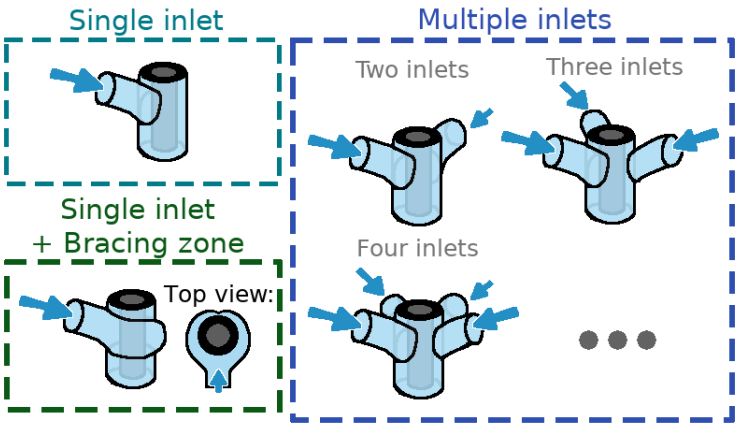
For the considered fluid, $\rho = 1056$kg/m^3 and $\mu_\infty = 0.00345$ Pa s. By assuming $\omega_0 = 209.44$ rad/s (2000 rpm), and, for example, 5 cm of fluid column on the inlet ($\Delta p_{\mathrm{seal}} = 517.44$ Pa), the leakage flow rate becomes Q_ℓ = 0.0918 L/min = 91.8 mL/min = 30.6 drops/s (1 drop = 0.05 mL). Therefore, the leakage flow for the presented conditions seems to be relatively high, and would correspond, in fact, to about 10% of an inlet flow of 1 L/min. In order to further reduce this value, the alternatives would be, for example, to increase the size of the labyrinths (ℓ_c, ℓ_g) while adjusting the number of labyrinths (n_ℓ), or reduce the gap spacing/height (h_s). The first alternative means that the length of the labyrinth would have to be increased from 2 cm to about 5 cm to be able to reduce to a leakage flow rate in the order of about 2 drops/s. However, increasing this size may pose issues with respect to the length of the shaft, which means that this is not a feasible solution. The second alternative considers reducing the gap spacing/height (h_s), because reducing it even for a bit may significantly reduce leakage. The second alternative is the one considered in this work, given by substituting the first two "teeth" that are positioned farther from the rotor by rubber gaskets. This pair of rubber gaskets may also contribute to aligning the shaft and, if fluid passes through the rubber gaskets, then they may function as hydrodynamic bearings. Since contact between the shaft and

the rubber is partly allowed, this final setup faintly resembles a friction-based seal, and an abradable labyrinth seal (BURCHAM, 1978), which allows partial contact in order to reduce the gap spacing/height, at the cost of some friction. Some adjustments were made in order to fit the designed labyrinth seal in the experimental apparatus.

4.1.4 **Inlet channels**

From Section 4.1.3, it has been decided to place the motor shaft in the same side of the inlet of the pump. This means that, because of the presence of the shaft, it is not possible to have an axial inlet – i.e., the inlet would have to be necessarily radial or diagonal. In such case, some possibilities for the design of the inlet are presented in Fig. 4.7. The “bracing zone” is hinted in Wu *et al.* (2010), and a variation is present in Timms (2005). It may be highlighted that the flow entering the rotor from more inlets should better resemble the axisymmetry condition of the 2D swirl flow model used in the topology optimization. In this work, two inlets are considered, in order to try to partially keep some axisymmetry for the inlet flow in the rotor. More inlets could have been considered, but there were space restrictions in the design that would not allow it (otherwise, there would be no space to have screws for the rubber gaskets). Particularly, it can be mentioned that this is similar to the procedure used in Tesla turbines in order to achieve rotating inlet velocities, in which some common approaches are, for example, considering one or more tubes directed at a circular volute (TESLA, 1913b; BEANS, 1966; LEAMAN, 1950; REY, 2004; KRISHNAN, 2015), or a single inlet split into a “cylindrical flow” (SUSAN-RESIGA *et al.*, 2006).

Figure 4.7 – Some possibilities for the design of the inlet around the shaft.



Source: Author.

4.1.5 **Disk spacers**

In the construction of the Tesla pump rotor prototype, when not considering a *hybrid* design (with blades), it is necessary to include circumferentially spaced *spacers* to separate the disks, or *arms* to connect the disks to the rotating shaft, as shown in Fig. 1.17. In this work, since the spacing between disks is small, in order to help keeping the right spacing between disks more easily, the presence of *spacers* was considered. However, with respect to Fig. 1.17, it was decided to consider a different shape than circular spacers. It may also be mentioned that the commercial pump CentriFlux BR-100 (Fig. 1.15a) uses three radially spaced clippers, located at the outer radius. In this work, the choice was to consider an aerodynamically better shape (i.e., *airfoil-like*-shaped spacers) positioned tangent to the outer radius of the rotor, which is, in fact, a similar choice with respect to the Tesla wind turbine from Fig. 1.10. This choice aims to reduce the flow separating effect that may happen behind circular spacers.

The blockage ratio (DODSWORTH, 2016) may be defined in order to quantity the *amount of obstruction* of the fluid flow path caused by the spacers. It may be highlighted that this is a simplistic take on the problem, since it does not take into account how much the shape of the spacers affect the fluid flow behind them (i.e., flow separation is not taken into account). Nonetheless, the blockage ratio can work as a measure of how much flow is being blocked by the spacers. In this work, the original concept from Dodsworth (2016) is extended in order to be able to take non-circular spacers into account. Considering Fig. 4.8, a vectorial blockage ratio can be defined as:

$$\boldsymbol{B} = (B_r, B_\theta) \tag{4.11}$$

where B_r is the radial blockage ratio (i.e., blockage caused in a radial straight line), and B_θ is the tangential blockage ratio (i.e., blockage caused in a long spiral). Both are given as shown below:

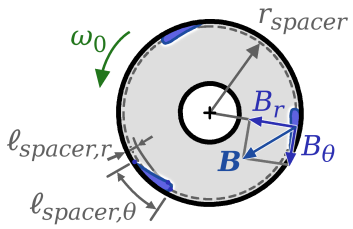
$$B_r = \frac{n_{spacers}\ell_{spacer,\theta}}{2\pi r_{spacer}} \tag{4.12}$$

$$B_\theta = \frac{\ell_{spacer,r}}{r_{spacer}} \tag{4.13}$$

where $\ell_{spacer,\theta}$ is the tangential extension of a spacer (maximum tangential length, $\ell_{spacer,\theta} = (\theta_{spacer,max} - \theta_{spacer,min})r_{spacer}$) of each spacer, $\ell_{spacer,r}$ is the radial extension

of a spacer (maximum radial length, $\ell_{spacer,r} = r_{spacer,max} - r_{spacer,min}$) of each spacer, $n_{spacers}$ is the number of spacers, and r_{spacer} is the radius in which the geometric center of the spacer is located.

Figure 4.8 – Blockage ratio and the dimensions used to compute it.



Source: Author.

In this work, $n_{spacers} = 3$, $\ell_{spacer,\theta} \approx$ 6.68 mm, , $\ell_{spacer,r} \approx$ 1.3 mm, and $r_{spacer} \approx$ 14.2 mm. Therefore, $\boldsymbol{B} = (0.225, 0.092)$ ($\boldsymbol{B} = 0.243\underline{/22.2°}$). Since Dodsworth (2016) considered circular spacers and obtained a blockage ratio of $\boldsymbol{B} = (0.285, 0.07)$ ($\boldsymbol{B} = 0.293\underline{/13.8°}$), the obtained values in this work seem to be acceptable, indicating a small influence of the spacers.

4.1.6 **Stagnated fluid below the rotor**

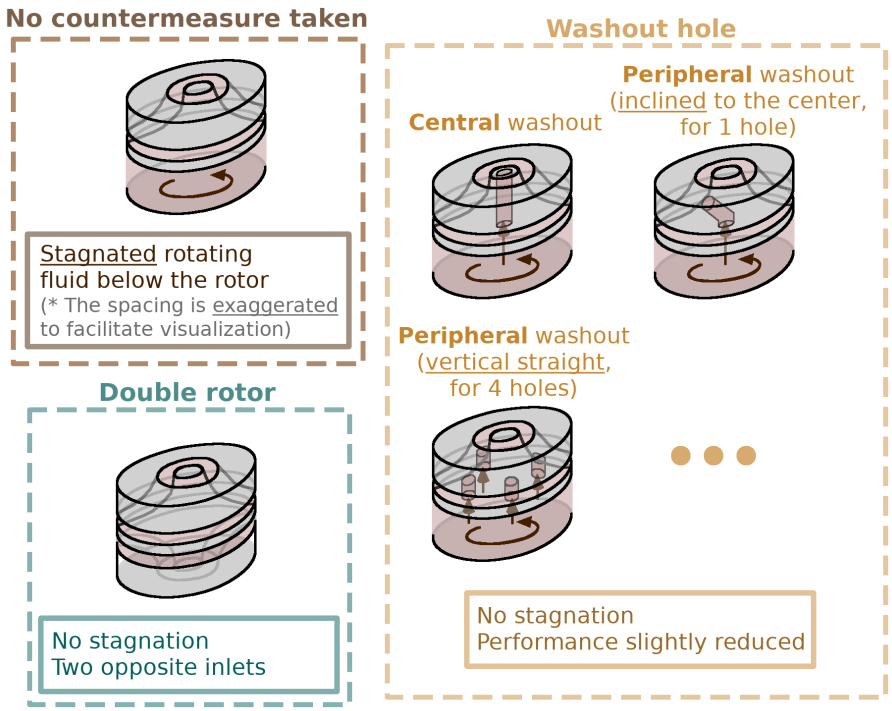
Below the rotor (i.e., in the clearance gap between the rotor and the volute), there may be stagnated fluid, which should increase thrombosis. Throughout the years, some countermeasures have been developed for it, and are present in various current commercial blood pumps, such as CentriMag and Rotaflow. The main possible countermeasure is based on the inclusion of one or more *washout holes*. These holes serve so as to induce the pumped flow (with higher pressure) to partially leak to the region below the blood pump (with lower pressure) and then be sent back to circulation (with higher pressure), which should eliminate stagnation. In the overall, this countermeasure tends to slightly reduce the pressure head and the efficiency of the pump, while greatly improving thrombosis and slightly improving hemolysis throughout the device (BUMRUNGPETCH, 2016). The flow that passes through these holes is regarded as *washout flow* and even *leakage flow* (CHAN; WONG, 2006), due to its negative impact in the performance of the rotor. There are mainly two types of washout holes: *central* and *peripheral*. The *central* (*balancing*) washout holes (WAKISAKA *et al.*,

1997; TSUKIYA *et al.*, 2002; TASKIN *et al.*, 2010) are those that have been considered in CentriMag (SCHIBILSKY *et al.*, 2020) through a small central hole, in the newly developed MT-Mag (SCHIBILSKY *et al.*, 2020) through a small central hole, and in Rotaflow through a larger central hole, with arms for connecting the rotor to the bearing sphere. Another type of washout hole is of the *peripheral* type, which implies including one or more *peripheral* holes. The *peripheral* washout holes may be positioned vertically straight (IKEDA *et al.*, 1996; NISHIDA *et al.*, 1998), or inclined to the middle of the rotor (TSUKAMOTO *et al.*, 2000; MARUYAMA *et al.*, 2005; BUMRUNGPETCH, 2016). Particularly, Bumrungpetch (2016) showed that considering a single inclined washout hole should have better hemodynamic behavior than considering none, or two inclined washout holes.

Another type of solution to the stagnated flow, which does not lead to loss of pressure head or efficiency, is the *double* rotor countermeasure. The *double* rotor countermeasure requires the use of two opposing inlet flows, and may be considered by directly manufacturing two opposing rotors “glued” together (SIN *et al.*, 2006; TIMMS, 2005), with the blades adequately positioned for the direction of the rotation. This way, the previous stagnating zone becomes non-existent, eliminating the problem. It can also be highlighted that this type of configuration can also be used for BiVAD configurations (SIN *et al.*, 2006), where there can be two types of rotor of different diameters: one designed for LVAD operation and the other designed for RVAD operation. The disadvantages of this approach would be the need to fabricate a *double* rotor, as well as a *double* volute for the two inlets.

The presented countermeasures are illustrated in Fig. 4.9. In this work, the washout hole countermeasure is selected for a more compact design. Among the possible types of washout holes, it is not possible to consider a *central* washout hole, due to the presence of a central shaft. Therefore, in this work, the washout hole is based on one of the *peripheral* configurations shown in Fig. 4.9, more specifically on the inclined configuration.

Figure 4.9 – Some possibilities for the fluid below the rotor (the spacing is exaggerated to facilitate visualization).

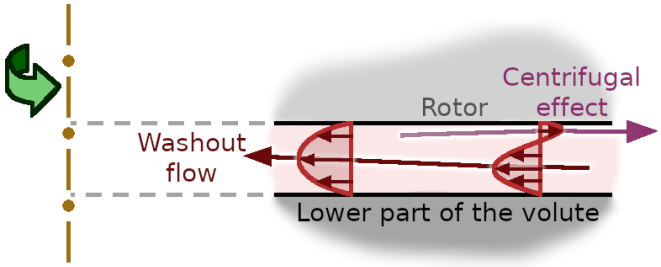


Source: Author.

4.1.7 Clearances above and below the rotor

There are clearances above and below the rotor (with respect to the volute), in which the fluid flow profile may feature a reverse flow, as shown in Fig. 4.10 for the clearance below the rotor (CHAN *et al.*, 2000; CHAN; WONG, 2006). According to Anderson *et al.* (2000), reducing the clearances seems to lead to less scalar shear stress, which may lead to less hemolysis and thrombosis. Therefore, the clearance in this work is made to be as small as possible, but given design, manufacturing, assembly and operation constraints and limitations.

Figure 4.10 – Typical flow in the clearance below the rotor.

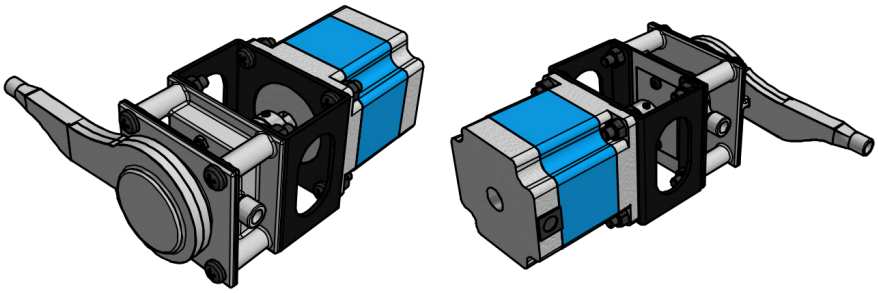


Source: Author (based on Chan and Wong (2006)).

4.2 FABRICATION OF THE PROTOTYPE

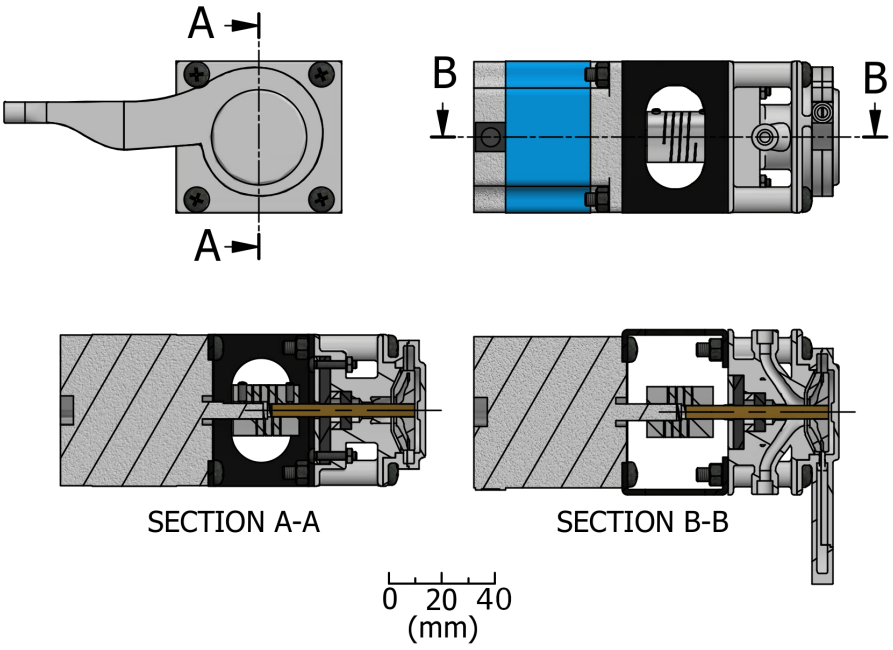
The 3D model of the prototype can be visualized in Figs. 4.11 and 4.12. The two inlets and the outlet feature a short length for gluing the inlet and outlet tubes.

Figure 4.11 – 3D views of the prototype.



Source: Author.

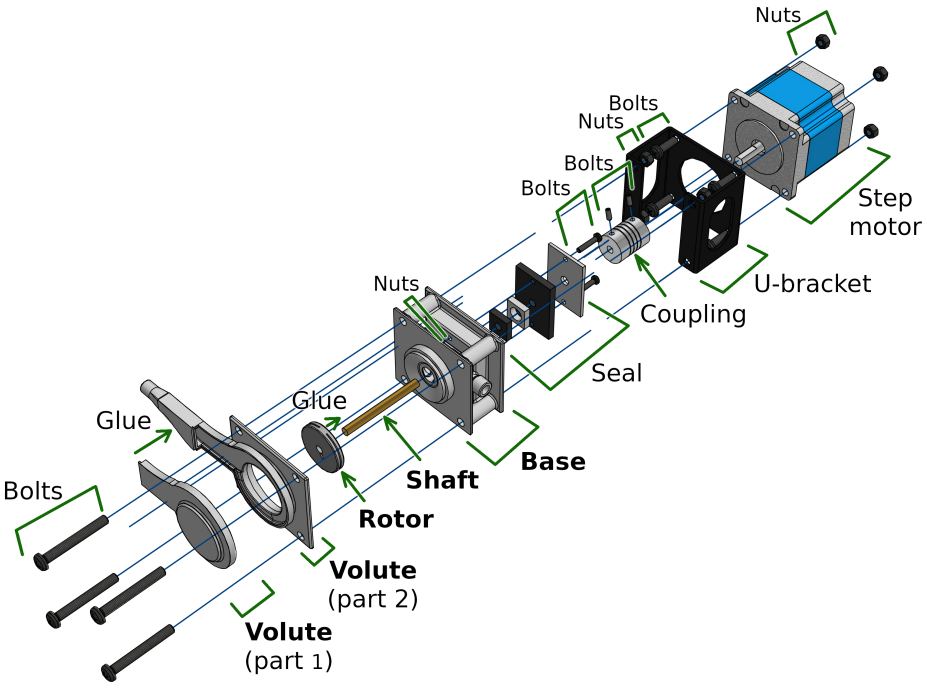
Figure 4.12 – Projected/section views of the prototype.



Source: Author.

An exploded view is shown in Fig. 4.13, showing the components and assembly of the prototype.

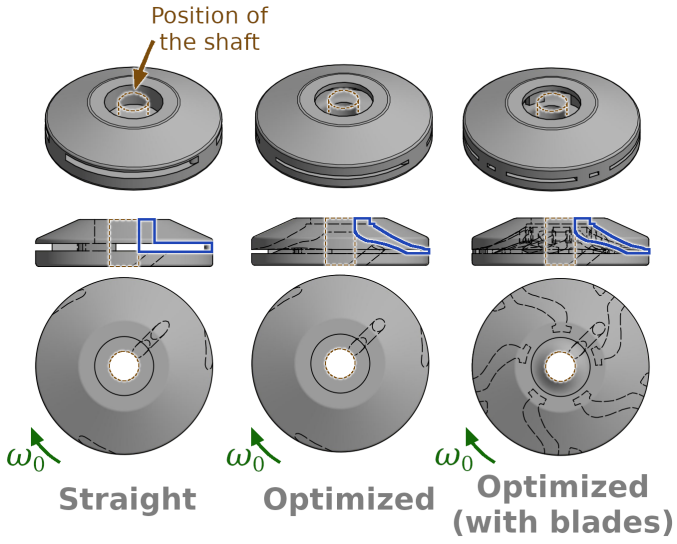
Figure 4.13 – Exploded view of the prototype, showing its components and assembly.



Source: Author.

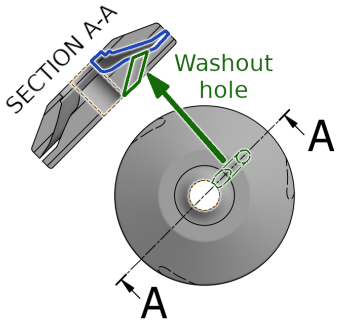
The considered rotors are shown in Fig. 4.14. The design of these rotors is explained in Section 5.1.9, together with the design of the volute. For ease of visualization, the washout hole described in Section 4.1.6 is indicated in a specific cross-section in Fig. 4.15.

Figure 4.14 – Rotors considered in the experiments, where the brown dashed lines indicate the position where the central shaft is attached. The rotation viewed from above the rotors is clockwise.



Source: Author.

Figure 4.15 – Washout hole in the rotor (inclined hole with diameter equal to 2 mm), illustrated from the rotor cross-section that crosses it.



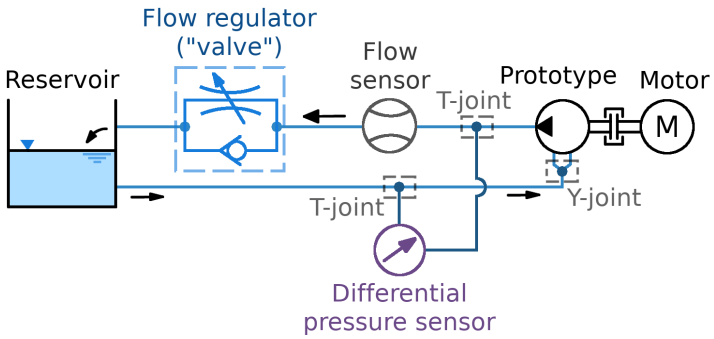
Source: Author.

The prototypes are fabricated mainly through additive manufacturing, from the polymer 3D printer Stratasys® Objet30 (USP MULTI, 2022, "*EMU-G3 - Prototipagem Rápida e Impressoras 3D - Impressora 3D Polyjet*"). Some other parts – such as the U-bracket (black-colored), the coupling, the bolts, the nuts and the brass shaft – were either bought or machined. Silicone glue and/or superglue were used to attach some of the printed parts together. Technical drawings of the prototype are available in Appendix G.

4.3 EXPERIMENTAL APPARATUS

The experimental apparatus is schematized in Fig. 4.16, and is used for the measurement of flow rate and pressure.

Figure 4.16 – Schematic view of the fluid flow circuit.



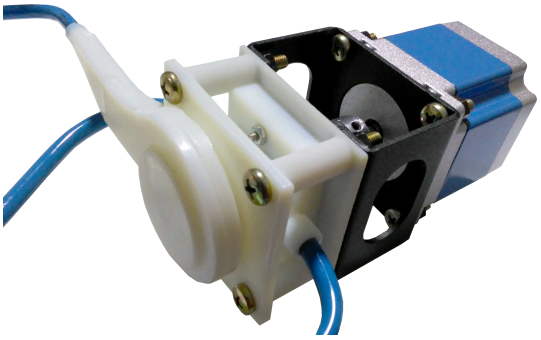
Source: Author.

The flow sensor is yf-s402 (Hall effect sensor), which is capable of measuring flow rates below 6 L/min, until around 0.05 L/min, which has been experimentally verified

for water. The differential pressure sensor is mpx5010dp (piezoresistive sensor), which is capable of measuring pressures between 0 and 10 kPa. The flow regulator serves as a valve, for imposing resistance to the fluid flow. The motor is selected as a step motor (SM1.8-D12-CS), which does not require rotation feedback, thus simplifying the control logic while also supplying a consistent rotation. Another aspect is that it does not need a current limiter or, at least, the same caution towards the current value as DC motors, since it is unable to *pull* more current than what the step motor driver supplies/chops. Nonetheless, a DC motor could also have been used, but with sufficient torque, proper rotation feedback (encoder) and caution against the consumed current. The internal diameter of the tubes of the fluid circuit is given as 4 mm (external diameter of 6 mm), resembling the internal diameter of a coronary artery (DODGE JR *et al.*, 1992; DOUGLAS *et al.*, 1988) and also making it easier for attaching the sensors and other components to the fluid flow circuit (same diameters). Particularly, the flow regulator, T-joints and Y-joint are components which are typical to pneumatic/hydraulic circuits. The measurement of flow rate is taken as the average of the pulses of the flow sensor for every 1 s, while the pressure measurement is taken as an average of the measurements for every 1 s. Before starting the measurements, the flow and pressure sensors were calibrated: the calibration of the pressure sensor is performed from a column of water, assuming that 10 kPa = 1 m$\mathrm{H_2O}$ (meter of water column); and the calibration of the flow sensor is performed through measuring the volume of water that is pumped after a given time interval (such as 1 minute).

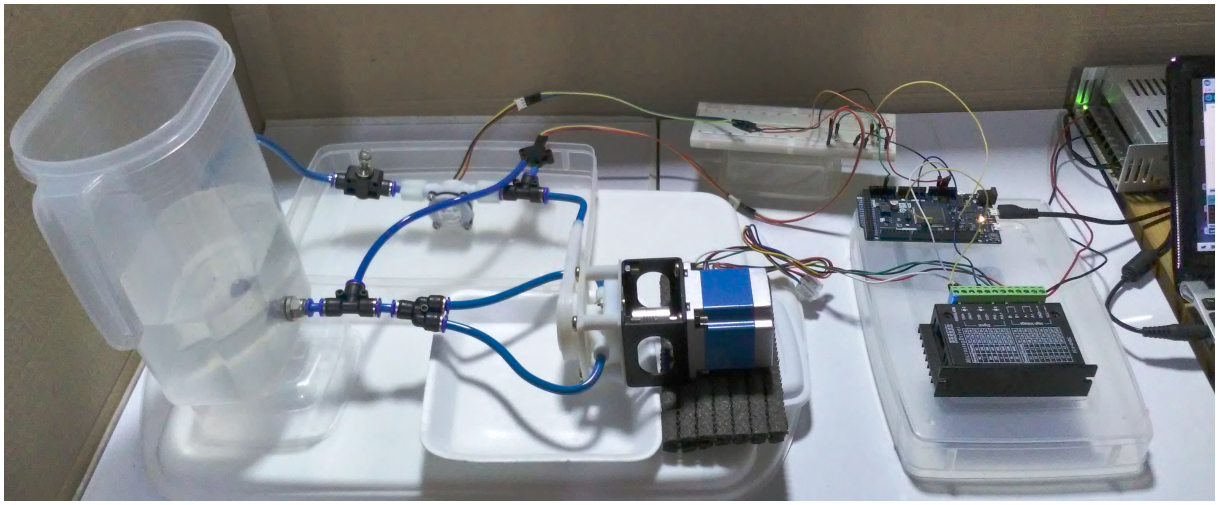
The fabricated prototype is shown in Fig. 4.17, and the experimental apparatus is shown in Fig. 4.18. In order to help removing air bubbles from when filling the pump with fluid, the outlet of the reservoir is positioned slightly higher than the pump inlet (20 mm higher), with the outlet tube being slightly slanted, and then the rotor is accelerated multiple times until no air bubbles are present. After filling up the pump with the fluid, the air that is accumulated in the pressure measurement probes is removed by unplugging and plugging them again in the fluid flow circuit.

Figure 4.17 – Fabricated prototype.



Source: Author.

Figure 4.18 – Photo showing the experimental setup.



Source: Author.

The control and measurements were performed from an Arduino Due connected to a step motor driver (TB6600/TB67S109AFTG) and to the flow and pressure sensors. The step motor configuration was set for a bipolar series connection. Although this connection does not provide the highest speed and torque, such as the bipolar parallel connection (TANG, 2020; EARL, 2021), it was employed because it was sufficient for the performed experiments, and also provides less heating and demands less current. Microstepping was also considered for a smoother rotating movement, from a 1/32 step setup. The power source was set for 32 V, from an adjustable power supply unit, in order for the motor to be able to reach a rotation of 3200 rpm. The voltage value (32 V) was set lower than the maximum recommended value by Geckodrive, which is based on heating measurements, and consists of using a voltage up to $32\sqrt{L_{\mathrm{mH}}}$ (where L_{mH} is the inductance in mH) (MECHMATE FORUM, 2009), resulting in a maximum voltage

of 67 V, for the 4.4 mH inductance of the considered step motor (SM1.8-D12-CS) in bipolar series connection.

With respect to the experimental setup, the use of a step motor turned out to be a rather convenient choice, both in provided torque and rotation control. However, the noise due to the step motor operation falls in the audible range, turning into a high pitched noise at high rotations. In order to reduce the noise, one option would be to design an acoustic isolation mechanism, and another option would be to use a DC motor (+ rotation sensor), which is much more silent. In terms of other sources of noise, there would be the vibration of the table when under low rotations (resonance). However, using a piece of rubber carpet below the step motor solved this issue and no significant vibration was noticed. Note that the step motor operating under higher rotations does not feature any significant vibration, meaning that the piece of rubber carpet would be unnecessary in this case. Removing all air bubbles from the fluid flow circuit before the experiments took a long time. The presence of air bubbles could easily be noticed from the characteristic “bubbly” sound, and also by lower variations of pressure, lower flow rates and leakage. After the air bubbles were removed from the fluid flow circuit, the leakage flow turned out small or almost inexistent when the rotor was rotating. The step motor featured some heating, which can be optionally reduced by including a fan near it.

4.4 BLOOD ANALOGUE

Since performing experiments with blood is costly, involves safety and ethical issues, and there are various issues inherent to blood, which may involve oxygenation, temperature and nutrients of RBCs (CAMPO-DEAÑO *et al.*, 2013), blood analogues have been developed throughout the years. The correspondence of properties with respect to blood is not perfect, where there may be some inherent difference in properties depending on the composition. There are essentially two types of blood analogue, with various possibilities in their composition: Newtonian and non-Newtonian. The Newtonian analogues aim to attain the *Newtonian viscosity* of blood – i.e, the viscosity of blood at higher shear stresses (μ_∞). Some solutions that are commonly used to model this effect are glycerin and water mixtures (CHANDRAN; KHALIGHI, 1984; MILLER *et al.*, 1993; MOODY, 2016; GANUSHCHAK *et al.*, 2006; BAZAN; ORTIZ, 2016). The non-Newtonian analogues require adding other components that can lead to a similar

behavior with the shear-thinning effect of blood. Some of these components are xanthan gum, polyacrylamide and carboxymethylcellulose (BROOKSHIER; TARBELL, 1993; BRINDISE *et al.*, 2018). Particularly, xanthan gum (PHILLIPS; WILLIAMS, 2000) seems to be well suited for the non-Newtonian analogue, although it is still more elastic than blood, which may produce inconsistent wall shear stresses to those of blood (MANN; TARBELL, 1990; WYATT; LIBERATORE, 2009). Also, in comparison to polyacrylamide solutions, xanthan gum does not produce abnormal wall shear stress waveforms in physiological flows (MANN; TARBELL, 1990). It is also possible to consider particles to emulate the RBCs in the blood analogue composition (SADEK *et al.*, 2021). Table 4.1 shows a possible Newtonian blood analogues, without particulates. As can also be noticed in Table 4.1, there is some inherent degree of mismatch between the properties of blood with respect to the blood analogue. Particularly, some other components that may be used to improve the non-Newtonian analogue may be HA (hyaluronic acid), NaI (sodium iodate), NaSCN (sodium thiocyanate) etc. (CAMPO-DEAÑO *et al.*, 2013; NAJJARI *et al.*, 2016; BRINDISE *et al.*, 2018). However, most of these additional components may have restrictions for their use, which should make their use less practical. In this work, the Newtonian analogue from Table 4.1 is considered in the experiments.

Table 4.1 – Example of a Newtonian blood analogue.

	Blood	Newtonian blood analogue (NAJJARI *et al.*, 2016)		
Composition		%w*	%v**	For 1 L of water*[3]
- Glycerol:		40%	34.6%	529.1 mL
- Deionized/distilled water:		60%	65.4%	1 L
Density (ρ) (kg/m^3)				
ρ (kg/m^3)	1056*[4]	1090		
Newtonian dynamic viscosity (μ_∞) (Pa s)				
μ_∞ (Pa s)	0.00345	0.004142		

* Weight percentages.
** Volume percentages.
*[3] Considering densities of: glycerol: 1.26 g/cm^3 (NIH, 2021); water: 1 g/cm^3.
*[4] (HINGHOFER-SZALKAY; GREENLEAF, 1987).

5 RESULTS AND ANALYSES

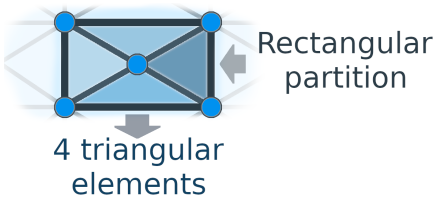
The results are separated in two parts: numerical and experimental, which are presented in sections 5.1 and 5.2, respectively. The letter n is used to represent rotation in rpm, and the greek letter ω is used to represent rotation in rad/s. The plots of the optimized topologies consider the values of the design variable (α) in the center of each finite element.

5.1 NUMERICAL RESULTS

The numerical results consist of the optimized/simulated results. Some simulations have been performed in order to check the finite element implementation for laminar flow in FEniCS with another software (OpenFOAM®) (Appendix A).

In some of the numerical results, continuation schemes (i.e., schemes in which one or more parameters are progressively varied) are performed in the optimization parameters in order to better condition the optimization, with a maximum number of allowed optimization iterations defined for each continuation step (for example, in the range of 10 to 800). In the beginning of each continuation step, the IPOPT algorithm is restarted. The convergence criterion for the simulation using MUMPS is based on residuals: absolute tolerance of 10^{-10} (except in Section 5.1.1, where 10^{-7} is used), and relative tolerance of 10^{-9} (except in Section 5.1.1, where 10^{-7} is used). For the optimization, the convergence criterion is based on a desired relative tolerance of 10^{-10} for the optimality error of the IPOPT barrier problem, that essentially corresponds to the maximum norm of each KKT condition (WÄCHTER; BIEGLER, 2006). In the inverse permeability of the material model (Section 2.5.1), $\kappa_{\min}$ is chosen as 0 kg/(m^3/s) in all numerical results. External body forces are not considered in the numerical examples, which means that $\rho \boldsymbol{f} = \boldsymbol{0}$. The inlet velocity profiles are computed as shown in Appendix C, for laminar and turbulent flows. When structured meshes are used, they are composed of rectangular partitions composed of 4 triangles each (Fig. 5.1).

Figure 5.1 – *Crossed triangular elements* (triangular elements distributed in rectangular partitions).

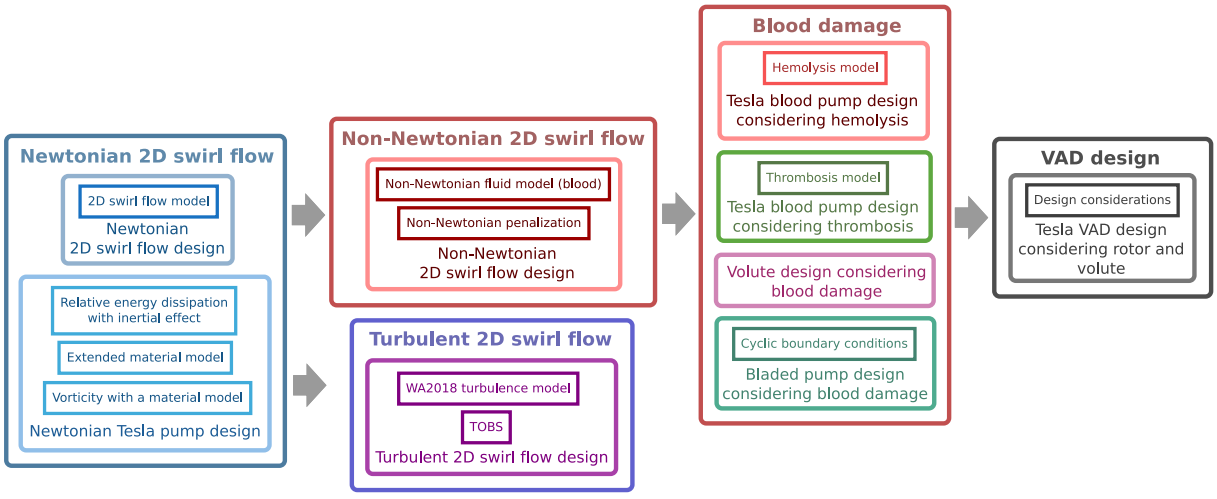


Source: Author.

When considering a multi-objective function, for simplicity, in figures and tables, the values for w_Φ are not written in all cases, but may be calculated, for example, as $w_\Phi = 1 - w_{PAS} - w_H$ when not specified (in the case the multi-objective function is composed of Φ_{rel}, I_H and I_{PAS}). Also, for example, if w_{PAS} is not specified, $w_{PAS} = 0$, and, if w_H is not specified, $w_H = 0$. The sensitivity correction from eq. (3.2) is not considered only in the numerical results until Section 5.1.4, where the classical approach – *Euclidean inner product* (ℓ_2 inner product) – is considered.

The research is presented progressively in the following sections and appendices, including a new aspect into consideration in each step of the research, and most of the numerical results have already been published. Fig. 5.2 highlights some of these aspects, while also characterizing the results in five research fronts for topology optimization: *Newtonian 2D swirl flow*, *Non-Newtonian 2D swirl flow*, *Turbulent 2D swirl flow*, *Blood damage* and *VAD design*. The formatting of the figures of each section may differ due to them pertaining to different articles. They are briefly described as follows:

Figure 5.2 – Research fronts being considered for topology optimization and further results.



Source: Author.

- **Newtonian 2D swirl flow design** (Section 5.1.1): Topology optimization applied

to 2D swirl flow devices for Newtonian fluid (ALONSO *et al.*, 2018);

- **Newtonian Tesla pump design** (Section 5.1.2): Topology optimization applied to Tesla-type pump devices, considering the extended material model (Section 2.5.1.2), relative energy dissipation including the inertial effect (eq. (2.51)), and a vorticity objective function including the effect of the material model (eq. (2.62)) (Section 2.5.1.2) (ALONSO *et al.*, 2019);
- **Non-Newtonian 2D swirl flow design** (Section 5.1.3): Topology optimization applied to 2D swirl flow devices for non-Newtonian fluid considering non-Newtonian penalization (Section 2.5.1.4) (ALONSO *et al.*, 2020);
- **Tesla blood pump design considering hemolysis** (Section 5.1.4): Topology optimization applied to Tesla-type pump devices, considering the Brinkman-Forchheimer model (Section 2.5.1.3), blood (non-Newtonian fluid), and a hemolysis model (Section 2.4.1) in topology optimization (ALONSO; SILVA, 2021);
- **Tesla blood pump design considering thrombosis** (Section 5.1.5): Topology optimization applied to blood flow devices, considering the Brinkman-Forchheimer model (Section 2.5.1.3), blood (non-Newtonian fluid), a hemolysis model (Section 2.4.1) and a thrombosis model (Section 2.4.2) in topology optimization (ALONSO; SILVA, 2022a);
- **Volute design considering blood damage** (Section 5.1.6): The topology optimization framework developed in previous works is used for optimizing the volute of an optimized Tesla pump rotor, by considering blood damage;
- **Bladed pump design considering blood damage** (Section 5.1.7): The topology optimization framework developed in previous works is used for optimizing blades, aiming for a *hybrid* Tesla pump design, and by considering blood damage;
- **Turbulent 2D swirl flow design (WA2018 model)** (Section 5.1.8): Topology optimization for turbulent flow (Wray-Agarwal model, WA2018), considering TOBS (ALONSO *et al.*, 2022);
- **Tesla VAD design considering rotor and volute** (Section 5.1.9): The design of a complete Tesla VAD pump is presented alongside simulations, by using OpenFOAM® .

Before considering *FEniCS TopOpt Foam* for 2D swirl turbulent flow in Alonso *et al.* (2022), it was initially shown for laminar flow, the Spalart-Allmaras model and the IPOPT algorithm (Section 3.1.1.1), in Alonso *et al.* (2021), for 2D, 2D axisymmetric and 3D domains.

Topology optimization has also been considered to design Tesla-type turbine devices, which involve the opposite operating behavior of pumps (ALONSO; SILVA, 2022b). It has been proved to be more challenging for exploring the effects in 2D swirl flow, while also including the Brinkman-Forchheimer model (Section 2.5.1.3), a power objective function considering the effect of the material model (eq. (2.55)), and MINI elements – which are less computationally expensive than Taylor-Hood elements (Section 2.2.2).

Most of the topology optimization results were processed in a computer with an Intel® Core™ i9-7900X CPU (10 cores, 20 threads, 13.75 MB L3 Cache, 3.30 GHz) and 32 GB RAM (and some in an Intel® Core™ i7-920 CPU – 2 cores, 4 threads, 8 MB Intel® Smart Cache, 2.67 GHz – and 8 GB RAM), with more than one topology optimization being performed simultaneously (ten, at most), and mostly without relying on parallelism, with the exception of some results, which relied on parallelism in the OpenFOAM® level, and the simulations from Section 5.1.9, which were processed in a computer with an AMD Ryzen™ 9 5950X CPU (16 cores, 32 threads, 64 MB L3 Cache, 3.4 GHz $\sim$ 4.9 GHz) and 64 GB RAM, and a cluster (NDF, 2022, *Mintrop cluster*), by relying on both FEniCS and OpenFOAM® parallelisms. The fact that more than one topology optimization was being processed simultaneously has possibly hindered the resulting computational time. Nonetheless, the laminar 2D swirl nozzle results (Section 5.1.1) took less than 5 hours, as well as the turbulent 2D swirl nozzle results (Section 5.1.8). The Tesla blood pump design considering hemolysis (Section 5.1.4), for w_H = 0.5, 1 L/min and 1500 rpm, took about 2.5 days, mostly due to the high amount of computed optimization iterations.

5.1.1 **Newtonian 2D swirl flow design**

In this section, the topology optimization method is applied to 2D swirl flow devices for Newtonian fluid, in order to evaluate the application of the 2D swirl flow model in topology optimization (ALONSO *et al.*, 2018).

In the numerical results of this section, the fluid is considered as water (Newtonian fluid), with a dynamic viscosity (μ) of 0.001 Pa s, and a density (ρ) of 1000.0 kg/m^3. The Taylor-Hood element is considered for the finite element method (see Section 2.2.2). The material model for topology optimization is given by the Brinkman model (Section 2.5.1.1). The IPOPT algorithm (Section 3.1.1.1) is used for the optimization in this section. The objective function is the relative energy dissipation (eq. (2.51)), but, as opposed to the numerical results in other sections, without including the *inertial effect* term. The *inertial effect* term is used starting from the next section (Section 5.1.2).

Two numerical examples are presented for analyzing different aspects of the 2D swirl flow model: nozzle (effect of the wall rotation) (Section 5.1.1.1) and hydrocyclone-type device (effect of the inlet rotation) (Section 5.1.1.2). For these two examples, the outlet boundary condition is chosen as *internal flow* (see Section 2.1.4). Other examples are presented in Alonso *et al.* (2018), for a two-outlet channel (effect of the flow rate and inlet rotation), and a two-way channel (effect of the aspect ratio), in which the outlet boundary is considered as *stress free* ($\boldsymbol{T}\bullet\boldsymbol{n} = \boldsymbol{0}$) (see Section 2.1.4).

The Reynolds number for the 2D swirl flow devices is chosen as:

$$\mathrm{Re}_{\text{2D swirl},\ell} = \frac{|\boldsymbol{v}_{\mathrm{abs}}|\, L}{\nu} \tag{5.1}$$

where $\boldsymbol{v}_{\mathrm{abs}}$ is the absolute fluid velocity, L is a characteristic dimension and ν is the kinematic viscosity. The characteristic dimension (L) is considered as: the diameter of the design domain, for the nozzle; and the height of the design domain, for the hydrocyclone-type device.

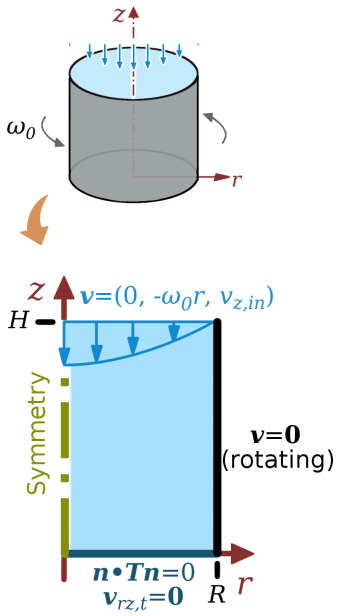
The specified fluid volume fraction (f) is chosen as 30%. The initial guess for the design variable is mainly chosen as a uniform distribution consisting of $\alpha = f - 1\%$ (*initial volume fraction initial guess*), where f is the specified volume fraction and 1% is a margin set in order to guarantee that the initial guess is not violating the volume constraint (because of the numerical accuracy of the calculations). Some of the numerical examples use a previously converged topology as the initial guess to better

condition the topology optimization. The initial guess is explicitly indicated for all of the following numerical examples, and has been assessed not to significantly influence the optimized topologies (such as for *all fluid*, *all solid*, *all gray* (volume fraction) and *random* initial guesses). The post-processing is performed by thresholding (Section 2.5.8.1).

5.1.1.1 Nozzle

The first numerical example is the design of a nozzle, which is a device that is used to control the characteristics of a fluid flow entering or leaving another fluid flow device. In this case, the flow enters without rotation, while the nozzle walls rotate around the symmetry axis with the same rotation as the reference frame (ω_0). The design domain is selected as in Fig. 5.3, and the solid material distribution is optimized on the rotating walls of the nozzle.

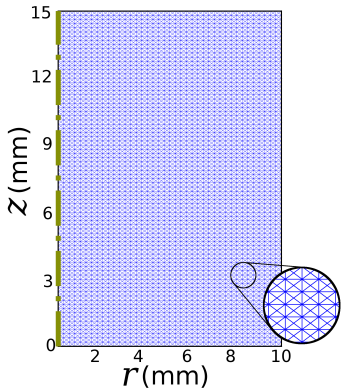
Figure 5.3 – Design domain for the nozzle.



Source: Author (ALONSO *et al.*, 2018) (edited).

The mesh is composed of 40 radial and 80 axial rectangular partitions of crossed triangular elements, which totals 6,521 nodes and 12,800 elements (see Fig. 5.4). The input parameters and dimensions of the design domain are shown in Table 5.1.

Figure 5.4 – Mesh used in the design of the nozzle.



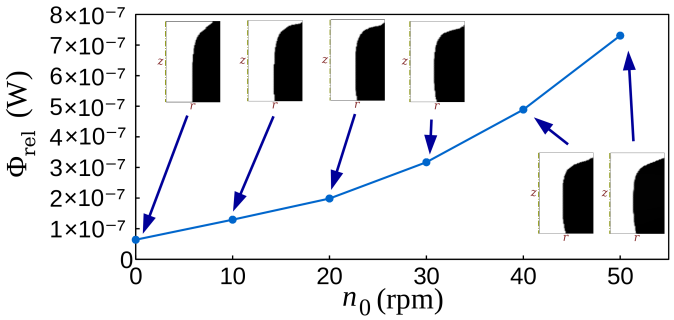
Source: Author (ALONSO *et al.*, 2018).

Table 5.1 – Parameters used for the topology optimization of the nozzle.

Input parameters	
Inlet flow rate (Q)	0.05 L/min
Wall rotation	$\omega_0 \neq 0$ rad/s (rotating)
Inlet velocity profile	Parabolic
Dimensions	
H	15 mm
R	10 mm

A series of optimizations is performed for a sequence of wall rotations in order to analyze the influence of the wall rotation in the optimized topology. Fig. 5.5 shows the value of the objective function (relative energy dissipation) in relation to the wall rotation and the corresponding optimized topologies. The objective function value corresponds to the post-processed topology (Section 2.5.8.1). The maximum Reynolds number is evaluated as 1040 (for 50 rpm, $\max(|\boldsymbol{v}_{\text{abs}}|) = 0.052$ m/s, $L = 20$ mm, $\nu = 10^{-6}$ m^2/s). In the case of the simulation of a rotating pipe with a constant diameter, the Reynolds number may be defined with an average axial velocity (NAGIB *et al.*, 1969). According to Nagib *et al.* (1969), the Reynolds number of a rotating pipe should be below about 1000 for laminar flow. In the case of the optimized topologies of the nozzle, since the diameter is not constant and the maximum absolute velocity value is used for computing the maximum Reynolds number, the fluid flow should be laminar for all optimized topologies for the nozzle.

Figure 5.5 – Effect of the wall rotation in the design of the nozzle.



Source: Author (ALONSO *et al.*, 2018).

In Fig. 5.5, it can be seen that, for 0 rpm, there is a solid region blocking part of the inlet. This solid region is similar to Borrvall and Petersson (2003)'s optimized topologies for diffuser/nozzle.

The optimization schemes are shown in Table 5.2. Table 5.3 shows the values of the objective function and pressure head for the optimized topologies shown in Fig. 5.5. From Table 5.3, it can be noticed that the pressure head is negative, meaning that the device is passive. It can also be noticed that there is a slight increase in pressure head from 10 rpm to 20 rpm, which is due to the larger inlet zone, and from 30 rpm to 40 rpm, which is due to the fact that the change in diameter became slightly smoother for 40 rpm (see Fig. 5.5).

Table 5.2 – Reference parameters for the optimization schemes (steps) for the nozzle.

Rotation (n_0) (rpm)	$\kappa_{\max}$ ($\times 10^3$kg/(m^{3}s))	q
0	20.0 $\sim$ 50.0	1.0 $\sim$ 10.0
10	25.0	1000.0
20	30.0	1000.0
30	80.0	1000.0
40	100.0	1000.0
50	50.0 $\sim$ 150.0	1000.0

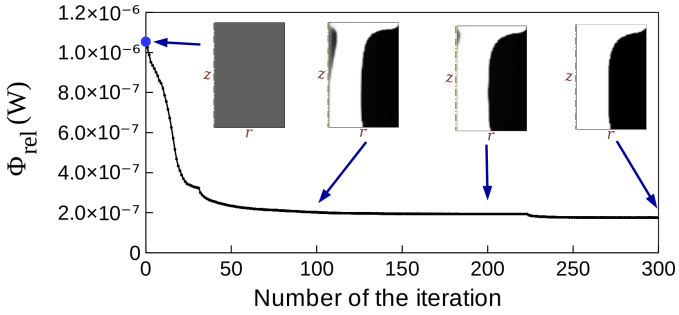
In Fig. 5.5, it can be inferred that the wall rotation has the effect of enforcing a less smooth change in diameter, and the increase of rotation seems to prioritize an initial area with larger diameter.

Table 5.3 – Values of the objective function and pressure head for the optimized topologies of the nozzle after post-processing.

Rotation (n_0) (rpm)	0	10	20	30	40	50
Relative energy dissipation (Φ_{rel}) ($\times 10^{-7}$W)	0.64	1.29	1.99	3.17	4.89	7.31
Pressure head (H) ($\times 10^{-5}$m)	-0.79	-1.19	-1.14	-1.19	-1.18	-1.29

Fig. 5.6 shows the convergence curve for the optimized nozzle for 20 rpm wall rotation (maximum Reynolds number of 420) (i.e., for the 3rd point of Fig. 5.5). The convergence values of the relative energy dissipation (objective function) are shown.

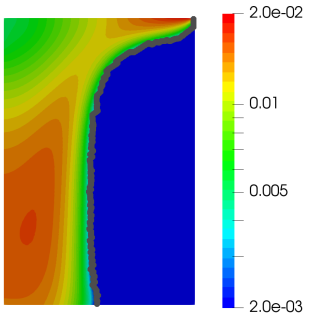
Figure 5.6 – Convergence curve for the nozzle optimized for 20 rpm wall rotation.



Source: Author (ALONSO *et al.*, 2018).

In order to assert the effectiveness of the material model to block the fluid flow, the relative velocity field is plotted in Fig. 5.7 for a Reynolds number of 420 (20 rpm wall rotation). As expected, the velocity is extremely small in the solid region of the optimized topology, showing that the material model is effective to block the fluid flow.

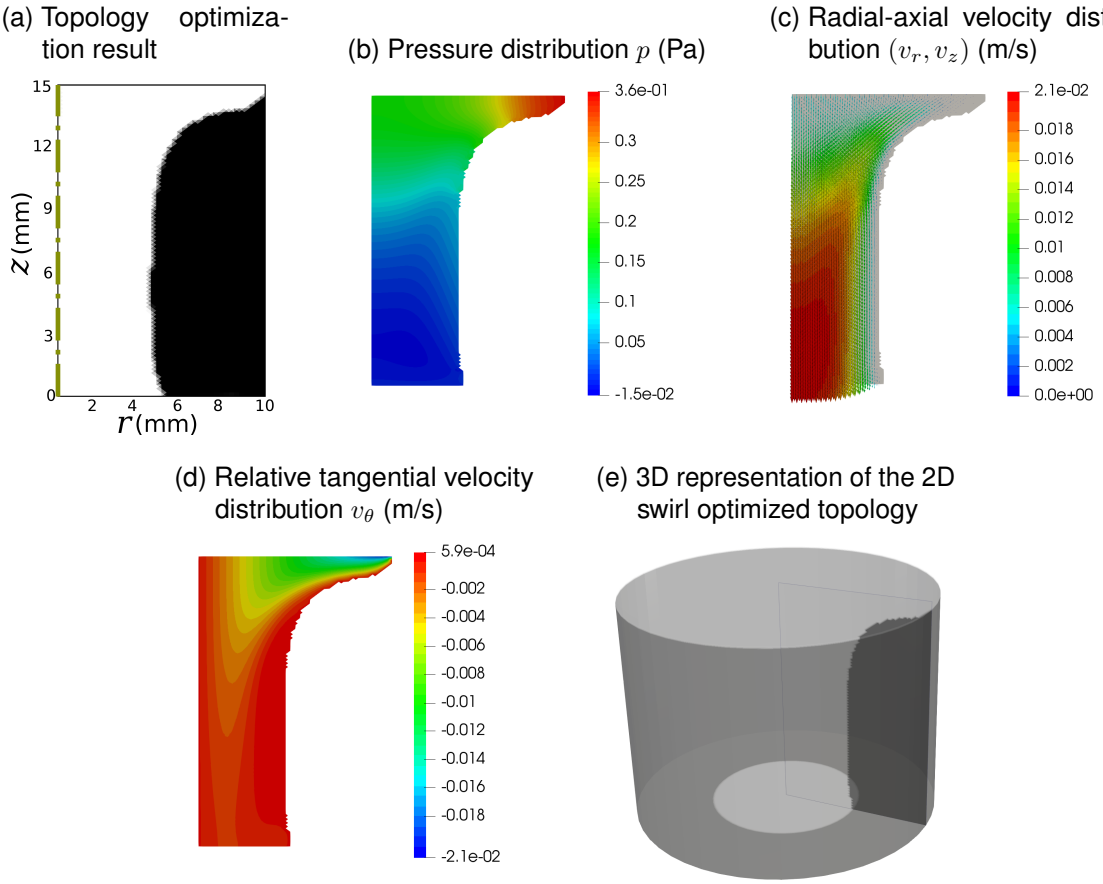
Figure 5.7 – Plot of the relative velocity field ($|\boldsymbol{v}| = \sqrt{v_r^2 + v_\theta^2 + v_z^2}$ (m/s)) in logarithmic scale for 20 rpm wall rotation (maximum Reynolds number of 420) (the boundary line of the optimized topology is indicated with a gray thick line).



Source: Author (ALONSO *et al.*, 2018).

Fig. 5.8 shows the topology optimization result for 20 rpm wall rotation (maximum Reynolds number of 420), the pressure and velocity distributions for the post-processed result and a 3D representation of the optimized topology. The topology optimization result is highly discrete, with a Measure of non-discreteness (M_{ND}) of 1.98%.

Figure 5.8 – Topology optimization result of the nozzle for 20 rpm wall rotation (the pressure and velocities are computed in the post-processed result).



Source: Author (ALONSO *et al.*, 2018).

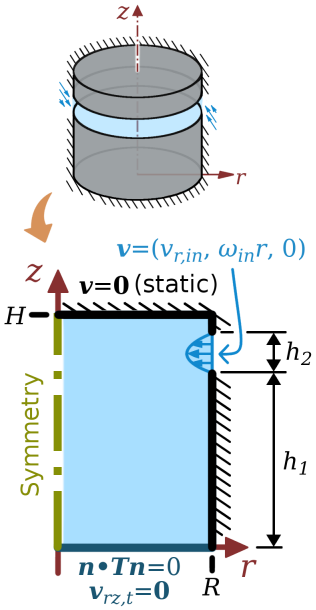
The relative tangential velocity (Fig. 5.8d) portrays the effect of the acceleration of the inlet fluid due to the rotating walls: the fluid enters without any rotation ($v_{\mathrm{abs},\theta} = 0$, which means $v_\theta = -\omega_0 r$), and then is tangentially accelerated (i.e., the tangential velocity is increased, achieving values closer to the tangential velocity on the walls ($v_{\mathrm{abs},\theta} = \omega_0 r$, which means $v_\theta = 0$)). In Fig. 5.8b, it can be noticed that the pressure is reduced after the nozzle cross sectional area is reduced, but has a slight increase to near 0 Pa when getting near the outlet.

5.1.1.2 Hydrocyclone-type device

The second example is the design of a hydrocyclone-type device, which differs from a real hydrocyclone device, because, instead of considering a two-phase flow, it considers a single-phase flow. This flow enters the fluid flow device with a given rotation (ω_{in}) from a single inlet towards a single outlet (in the case of a real hydrocyclone device, there are two outlets). The design domain is selected as in Fig. 5.9, and the solid

material distribution is optimized on the static walls ($\omega_0 = 0$ rad/s) of the hydrocyclone-type device.

Figure 5.9 – Design domain for the hydrocyclone-type device.



Source: Author (ALONSO *et al.*, 2018).

The mesh is composed of 40 radial and 80 axial rectangular partitions of crossed triangular elements, which totals 6,521 nodes and 12,800 elements (see Fig. 5.4). The input parameters and dimensions of the design domain are shown in Table 5.4.

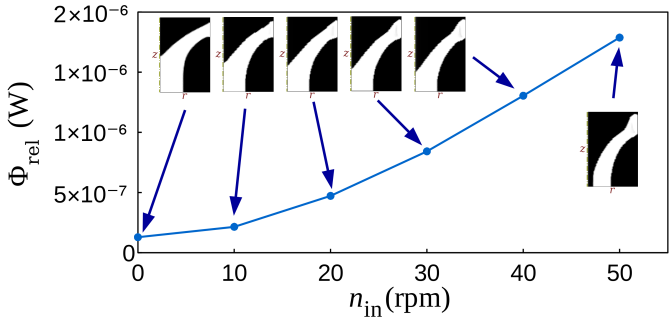
Table 5.4 – Parameters used for the topology optimization of the hydrocyclone-type device.

Input parameters	
Inlet flow rate (Q)	0.03 L/min
Wall rotation	$\omega_0 = 0$ rad/s (static)
Inlet velocity profile	Parabolic
Dimensions	
H	15 mm
R	10 mm
h_1	11 mm
h_2	3 mm

A series of optimizations is performed for a sequence of inlet rotations in order to analyze the influence of the inlet rotation in the optimized topology. In this case, the first topology ($n_{\text{in}} = 0$ rpm) assumes the *initial volume fraction initial guess* (see the beginning of Section 5.1.1), while the subsequent rotations use the optimized topology of the immediately previous rotation as the initial guess. Fig. 5.10 shows the value

of the objective function (relative energy dissipation) in relation to the inlet rotation and the corresponding optimized topologies. The objective function value corresponds to the post-processed topology (Section 2.5.8.1). The maximum Reynolds number is evaluated as 795, which shows that the flow must still be laminar in all results (for 50 rpm, $\max(|\boldsymbol{v}_{\text{abs}}|) = 0.053$ m/s, $L = 15$ mm, $\nu = 10^{-6}$ m^2/s). The initial guesses for the optimizations under rotation are the optimized topologies for each immediately lower rotation shown in Fig. 5.10. The optimization schemes are shown in Table 5.5.

Figure 5.10 – Effect of the inlet rotation in the design of the hydrocyclone-type device.



Source: Author (ALONSO *et al.*, 2018).

Table 5.5 – Reference parameters for the optimization schemes (steps) for the hydrocyclone-type device.

Rotation (n_0) (rpm)	$\kappa_{\max}$ ($\times 10^3$kg/(m^{3}s))	q
0	8.0 $\sim$ 25.0	0.1 $\sim$ 1.0
10	250.0	10.0
20 $\sim$ 40	200.0	10.0
50	300.0	10.0

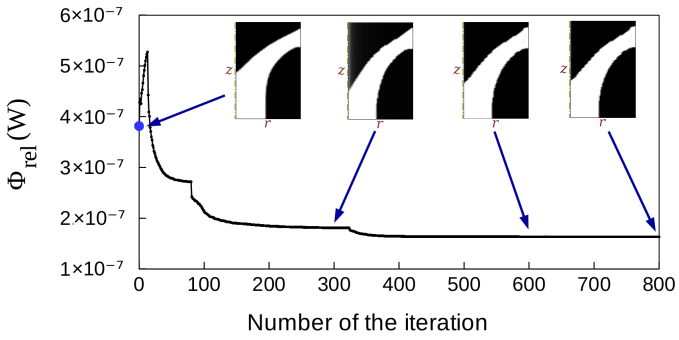
In Fig. 5.10, it can be seen that the rotation features the effect of pulling the channel up to about 45° in relation to the inlet. Also, near the inlet, in the results in which there is inlet rotation, a ring shape (considering the axisymmetry of the 2D swirl flow model) starts to be formed. Table 5.6 shows the values of the objective function and pressure head for the optimized topologies shown in Fig. 5.10. From Table 5.6, it can be noticed that the pressure head is negative, meaning that the device is passive.

Table 5.6 – Values of the objective function and pressure head for the optimized topologies of the hydrocyclone-type device after post-processing.

Rotation (n_{in}) (rpm)	0	10	20	30	40	50
Relative energy dissipation (Φ_{rel}) ($\times 10^{-6}$W)	0.13	0.21	0.47	0.84	1.30	1.80
Pressure head (H) ($\times 10^{-4}$m)	-0.26	-0.40	-0.85	-1.52	-2.36	-3.24

Fig. 5.11 shows the convergence curve for the optimized hydrocyclone-type device for 10 rpm inlet rotation (maximum Reynolds number of 285) (i.e., for the 2nd point of Fig. 5.10). The convergence values of the relative energy dissipation (objective function) are shown.

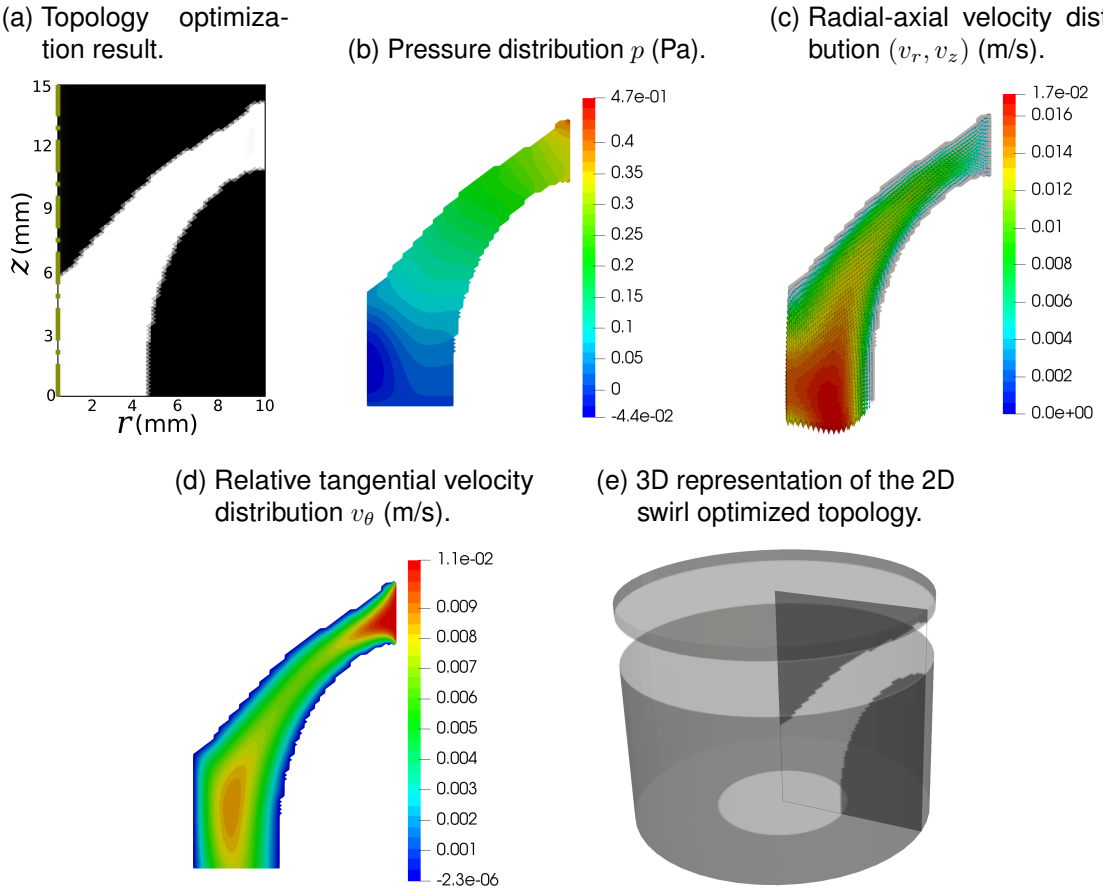
Figure 5.11 – Convergence curve for the hydrocyclone-type device optimized for 10 rpm inlet rotation.



Source: Author (ALONSO *et al.*, 2018).

Fig. 5.12 shows the topology optimization result for 10 rpm inlet rotation (maximum Reynolds number of 285), the pressure and velocity distributions for the post-processed result and the 3D representation of the optimized topology. The topology optimization result is highly discrete, with a Measure of non-discreteness (M_{ND}) of 2.56%.

Figure 5.12 – Topology optimization result of the hydrocyclone-type device for 10 rpm inlet rotation (the pressure and velocities are computed in the post-processed result).



Source: Author (ALONSO *et al.*, 2018).

In Figs. 5.12c and 5.12d, it can be noticed that, due to the inlet rotation, the outlet flow velocity is concentrated near the wall.

5.1.2 **Newtonian Tesla pump design**

In this section, the topology optimization method is applied to Tesla-type pump devices, considering the extended material model (Section 2.5.1.2), relative energy dissipation including the inertial effect (eq. (2.51)), and a vorticity objective function including the effect of the material model (eq. (2.62)) (ALONSO *et al.*, 2019).

In the numerical results of this section, the fluid is considered to be the same of Section 5.1.1: water (Newtonian fluid), with a dynamic viscosity (μ) of 0.001 Pa s, and a density (ρ) of 1000.0 kg/m^3. The Taylor-Hood element is considered for the finite element method (see Section 2.2.2). The material model for topology optimization is given by the Brinkman model (Section 2.5.1.1) and the extended material model (Section 2.5.1.2). The material being optimized is assumed with the same rotation as the reference frame, which means that $\boldsymbol{v}_{\mathrm{mat}} = \boldsymbol{v}$. The IPOPT algorithm (Section 3.1.1.1) is used for the optimization in this section.

In the following numerical results, the design of a Tesla pump rotor is analyzed for a horizontal inlet and a vertical inlet, where the vertical inlet consideres two cases: with and without pattern repetition (corresponding to *one channel* and *two channels*, respectively), which is described in Section 2.5.6. First, the horizontal inlet Tesla pump is optimized for relative energy dissipation considering various rotations (Section 5.1.2.1). The effect of the extended material model (Section 2.5.1.2) is also evaluated. Then, the vertical inlet Tesla pump is optimized for relative energy dissipation considering various rotations and flow rates (Section 5.1.2.2). Further results are presented in Alonso *et al.* (2019), such as for different aspect ratios, which shows that higher aspect ratios (i.e., longer channels) lead to higher pressure heads and isentropic efficiencies; and also for the presence of a shaft, whose absence showed a quite small effect due to the smaller volume of fluid near the symmetry axis. The vorticity objective function is also analyzed for the vertical inlet Tesla pump. Finally, a comparison with some traditional straight disk Tesla pumps is considered (Section 5.1.2.3). The multi-objective function is considered through the initial weight approach (Section 2.5.4.1). When considering the Helmholtz filter, eq. (2.158) is not considered.

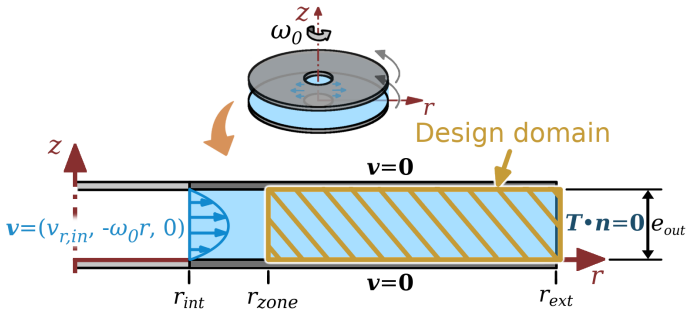
The Reynolds number ($\mathrm{Re}_{\mathrm{ext},\ell}$) is considered from the external radius (r_{ext}), from Table 2.1. The post-processing is performed by thresholding (Section 2.5.8.1), except in the comparison of performance with straight disks (Section 5.1.2.3), in which mesh

smoothing is performed by generation of contours (Section 2.5.8.2.1).

5.1.2.1 Horizontal inlet Tesla pump

The first design configuration is the horizontal inlet Tesla pump, which is essentially composed of two rotating horizontal flat interfaces, a horizontal inlet and a horizontal outlet. As can be noticed, it does not consider the effect of the change in direction that is present near the inlet of pumps. In order to keep the entire inlet section without any partial *fluid flow blocking* during the topology optimization, the inlet zone is considered outside the design domain (see Fig. 5.13).

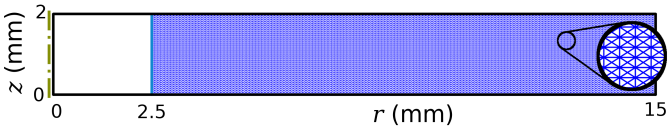
Figure 5.13 – Model for the optimization of a horizontal inlet Tesla pump, considering an inlet zone outside the design domain.



Source: Author (ALONSO *et al.*, 2019).

The mesh is composed of 160 radial and 40 axial rectangular partitions of crossed triangular elements, which totals 13,001 nodes and 25,600 elements (see Fig. 5.14). The input parameters and dimensions of the design domain are shown in Table 5.7.

Figure 5.14 – Mesh for the optimization of a horizontal inlet Tesla pump.



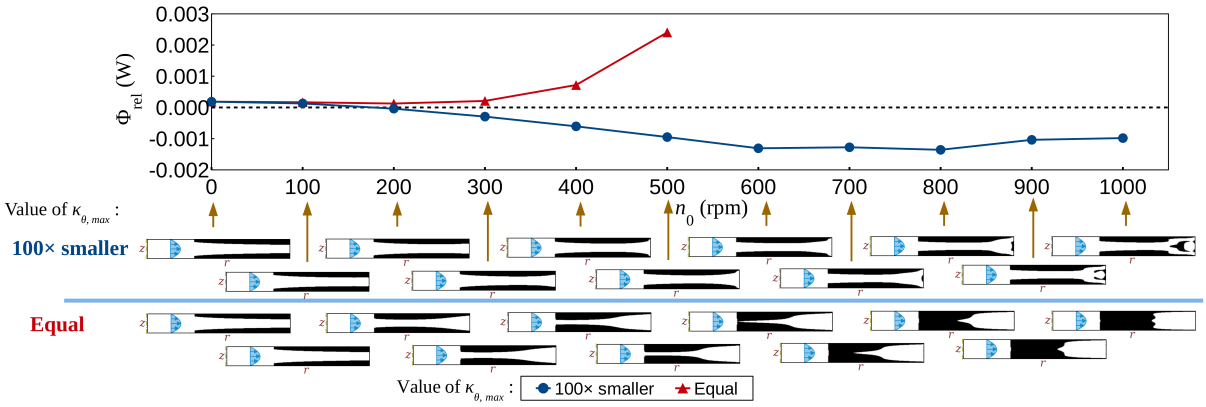
Source: Author (ALONSO *et al.*, 2019).

Table 5.7 – Parameters used for the topology optimization of a horizontal inlet Tesla pump.

Input parameters	
Inlet velocity profile	Parabolic
Flow rate	0.5 L/min
Dimensions	
r_{int}	2.5 mm
r_{zone}	5.0 mm
r_{ext}	15 mm
e_{out}	2 mm

The effect of the rotation in the optimization of the horizontal inlet Tesla pump is analyzed for 0.5 L/min, with a specified volume fraction of $f = 50\%$ and an initial guess of the design variable as $\alpha = f - 1\% = 0.49$, which represents 49% of the volume occupied by fluid. The objective function is the relative energy dissipation, whose values are shown in Fig. 5.15 for rotations varying from 0 rpm to 1000 rpm. Two cases are presented in order to show the effect of the extended material model (Section 2.5.1.2). The two cases presented are considering: $\kappa_{\theta,\max}$ being 100 times lower than $\kappa_{r,\max} = \kappa_{z,\max}$ (i.e., $\kappa_{\theta,\max} = \kappa_{r,\max}/100$); and $\kappa_{\theta,\max}$ being equal to $\kappa_{r,\max} = \kappa_{z,\max}$ (i.e., $\kappa_{\theta,\max} = \kappa_{r,\max}$). For these cases, $\kappa_{r,\max} = \kappa_{z,\max}$ is chosen as 2.5×10^3 kg/(m^3 s). In some cases, it is necessary to multiply these values by 2 or 3 in order to help the convergence to discrete topologies. In all of these cases, $q_r = q_\theta = q_z = 100$ or 1000, and $\kappa_{r,\min} = \kappa_{\theta,\min} = \kappa_{z,\min} = 0$ kg/(m^3 s).

Figure 5.15 – Relative energy dissipation (Φ_{rel}) for the optimized topologies of a horizontal inlet Tesla pump for different rotations and different $\kappa_{\theta,\max}$ values in relation to $\kappa_{r,\max} = \kappa_{z,\max}$.



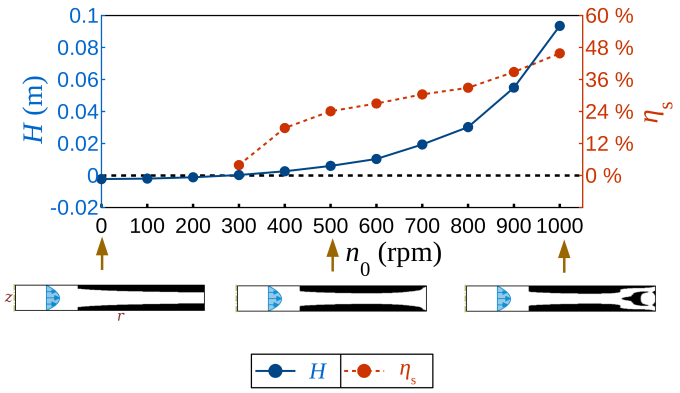
Source: Author (ALONSO *et al.*, 2019).

As can be seen in Fig. 5.15, the topologies change when increasing the rotation in the optimization. For $\kappa_{\theta,\max}$ equal to $\kappa_{r,\max} = \kappa_{z,\max}$, the optimized topologies tend to

reduce the inlet section, until it blocks it at about 600 rpm. This effect can be viewed as a consequence of increasing the rotation of the design domain, since, in order to reduce the velocity difference between the solid material and fluid flow (which is given by $\boldsymbol{v}_{\mathrm{mat}} = \boldsymbol{v}$), the porous medium effect term of the relative energy dissipation (eq. (2.51)) (given, in this case, by $\boldsymbol{\kappa}(\alpha)\boldsymbol{v} \bullet \boldsymbol{v}$) should prioritize accelerating the fluid tangentially (θ direction), which is done by including solid material near the inlet. For $\kappa_{\theta,\max}$ smaller than $\kappa_{r,\max} = \kappa_{z,\max}$, the optimized topology decreases the spacing between disks near the inlet and increases it back near the outlet. From 700 rpm onwards, an intermediary solid structure starts to be formed, splitting the previously single channel, in such a way that it resembles Borrvall and Petersson (2003)'s double pipe example.

As can be seen in Fig. 5.15, for the relative energy dissipation in relation to the rotation, the relative energy dissipation is higher for $\kappa_{\theta,\max}$ equal to $\kappa_{r,\max} = \kappa_{z,\max}$. This shows that, if the influence of the tangential velocity $v_{mat,\theta}$ in the inverse permeability matrix ($\boldsymbol{\kappa}(\alpha)$) is reduced by reducing the value of $\kappa_{\theta,\max}$, it is possible to achieve better results for the optimized topologies. In Fig. 5.15, it can be noticed that there are negative relative energy dissipation values. These negative relative energy dissipation values mean that more energy is being provided to the fluid flow than it is being dissipated (i.e., the fluid is being pumped). This effect is mainly due to the centrifugal term of the inertial effect of the relative energy dissipation ($(\rho\boldsymbol{\omega}\wedge(\boldsymbol{\omega}\wedge\boldsymbol{r}))\bullet\boldsymbol{v}$, in eq. (2.51)). The pressure head (eq. (2.64)) and isentropic efficiency (eq. (2.66)) for the topologies of Fig. 5.15 can be seen in Fig. 5.16.

Figure 5.16 – Pressure head (H) and isentropic efficiency (η_s) for the optimized topologies of a horizontal inlet Tesla pump with $\kappa_{\theta,\max}$ 100 times lower than $\kappa_{r,\max} = \kappa_{z,\max}$ for different rotations.



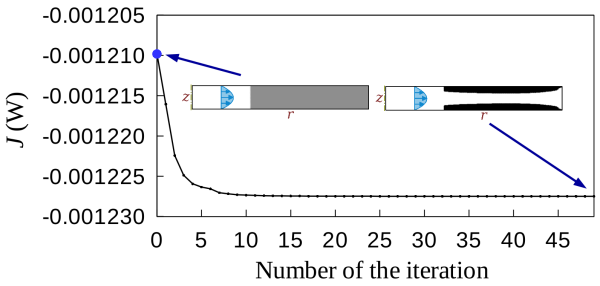
Source: Author (ALONSO *et al.*, 2019).

As shown in Fig. 5.16, the pressure head is positive from a rotation of about 300

rpm, which shows that the optimized Tesla pump rotor is capable of pumping fluid from this rotation onwards.

Fig. 5.17 shows the convergence curve for the 500 rpm optimized topology, and Fig. 5.18 shows the topology optimization result, the pressure and velocity distributions for the post-processed result and the 3D representation of the optimized topology.

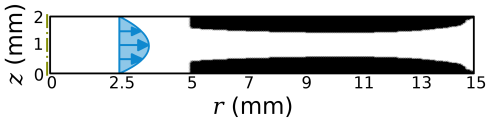
Figure 5.17 – Convergence curve for the objective function value of a horizontal inlet Tesla pump for 0.5 L/min and 500 rpm.



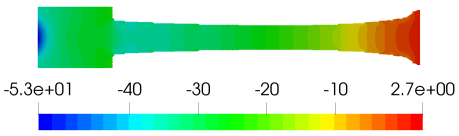
Source: Author (ALONSO *et al.*, 2019).

Figure 5.18 – Topology optimization result of the horizontal inlet Tesla pump for 500 rpm and 0.5 L/min (the pressure and velocities are computed in the post-processed mesh).

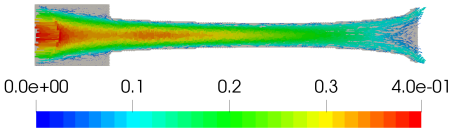
(a) Topology optimization result.



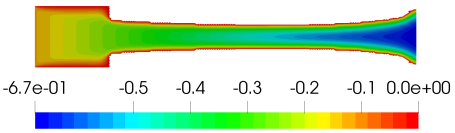
(b) Pressure distribution p (Pa).



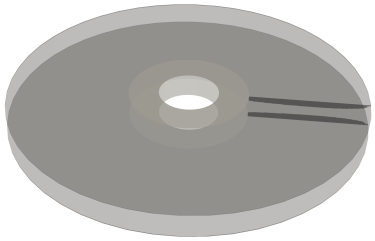
(c) Radial-axial velocity distribution (v_r, v_z) (m/s).



(d) Relative tangential velocity distribution v_θ (m/s).



(e) 3D representation of the 2D swirl optimized topology.



Source: Author (ALONSO *et al.*, 2019).

It can be seen in Fig. 5.18b that the pressure increases from about the middle of the design domain, which is due to the *nozzle-diffuser*-like shape and coupled rotation

effect. Fig. 5.18c shows that the flow near the outlet is concentrated around the upper and lower surfaces, leaving the middle zone between them with smaller flow. Also, the relative tangential velocity (Fig. 5.18d) is nearly zero near the rotating interfaces, decreasing when distancing farther from them. This can be viewed as a consequence of the Tesla principle, in which the boundary layer is formed with the capacity to "drag" the fluid, showing that the effect of the rotation of a Tesla pump is limited to a small zone near the interface and that it may be possible to improve the pumping of fluid with smaller spacings.

Since the radial-axial velocity is nearly zero in the middle of the outlet zone (Fig. 5.18c), the lower $\kappa_{\theta,\max}$ value causes the part of the relative energy dissipation (eq. (2.51)) that is due to the porous medium effect term (given, in this case, by $\boldsymbol{\kappa}(\alpha)\boldsymbol{v}\bullet\boldsymbol{v}$) to be minimal, and the topology optimization algorithm can lead to the formation of a solid structure. This effect starts to be relevant only at higher rotations (above 700 rpm), as shown in Fig. 5.15.

The magnitude of the negative values of the relative tangential velocity near the middle of the outlet boundary (in Fig. 5.18d) causes the corresponding term in the relative energy dissipation ($\kappa_{\theta,\max} v_\theta^2$) to increase. Thus, the topology optimization algorithm should have a tendency to create a solid structure in the middle of the domain in order to reduce the "v_θ^2" term. This effect can be quite intense depending on the value of $\kappa_{\theta,\max}$, since it can easily lead the fluid flow to be blocked as seen in Fig. 5.15 for $\kappa_{\theta,\max}$ equal to $\kappa_{r,\max} = \kappa_{z,\max}$. Therefore, it makes sense to use a $\kappa_{\theta,max}$ smaller than $\kappa_{r,\max} = \kappa_{z,\max}$ for the design of a Tesla pump rotor.

For reference, the operational parameters of the optimized topology of Fig. 5.18 are shown numerically in Table 5.8.

Table 5.8 – Operational parameters of the optimized topology of the horizontal inlet Tesla pump for 0.5 L/min and 500 rpm.

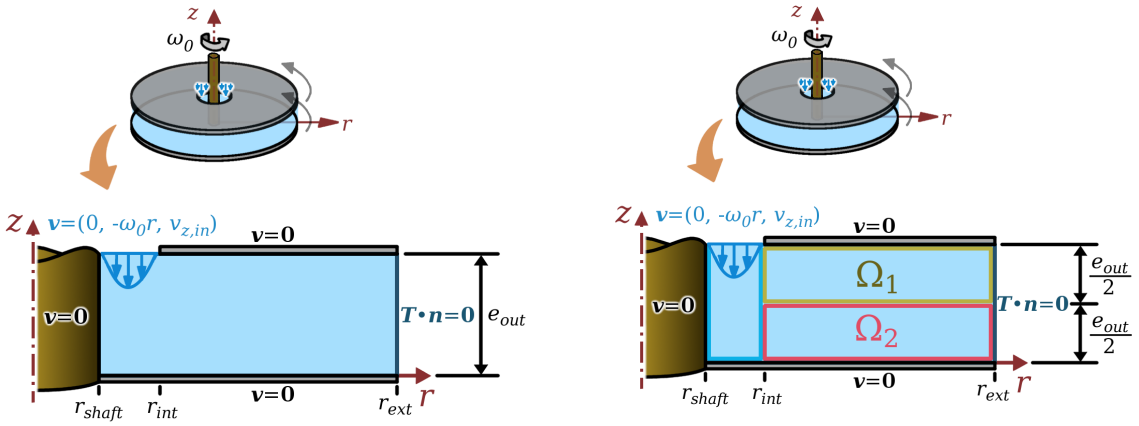
Basic parameters		
Flow rate (Q) (L/min)		0.5
Pressure head (H) (m)		6.01×10^{-3}
Fluid volume (V) (m^3)		7.21×10^{-7}
Dimensionless parameters		
Boundary layer	Ph	5.82
Flow regime	$\max(\mathrm{Re}_{\mathrm{ext},\ell})$	1.19×10^{4}
	$\max(\mathrm{Nd}_{\mathrm{ext},\ell})$	3.40×10^{1}
Flow rate	A_Q	2.68×10^{2}
Efficiency	η_s	24.1%
Functions of interest		
Relative energy dissipation (Φ_{rel}) (W)		-9.50×10^{-4}
Vorticity ($\xi_{V,\mathrm{rel}}$) (m^3/s^2)		3.46×10^{-1}

5.1.2.2 Vertical inlet Tesla pump

The second design configuration is the vertical inlet Tesla pump, which is considered with and without pattern repetition (corresponding to *one channel* and *two channels*, respectively) (see Fig. 5.19).

Figure 5.19 – Models for the optimization of a vertical inlet Tesla pump.

(a) One-channel Tesla pump. (b) Two-channel Tesla pump.



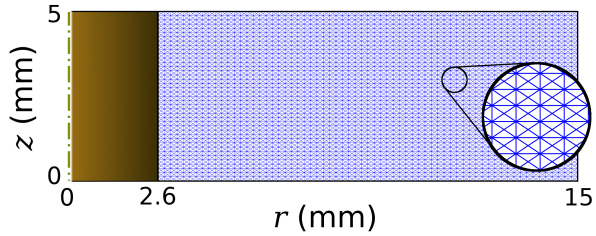
Source: Author (ALONSO *et al.*, 2019).

The one-channel Tesla pump model (Fig. 5.19a) consists of two rotating horizontal flat interfaces, a rotating shaft interface, a vertical inlet and a horizontal outlet. The two-channel Tesla pump model (Fig. 5.19b) consists of a pattern repetition (ALMEIDA *et al.*, 2010), in order to force the formation of a disk in the middle of the design domain. Therefore, the design domain is divided in three zones, as shown in Fig. 5.19b, in which

Ω_1 and Ω_2 are the zones with the same imposed pattern. The pattern repetition scheme is described in Section 2.5.6.

The mesh is the same for one and two channels, consisting of 5,387 nodes and 10,560 elements (see 5.20). The parameters used for the design domains of Fig. 5.19 are shown in Table 5.9. The specified volume fraction in the topology optimization is $f = 30\%$.

Figure 5.20 – Mesh for the optimization of a vertical inlet Tesla pump.



Source: Author (ALONSO *et al.*, 2019).

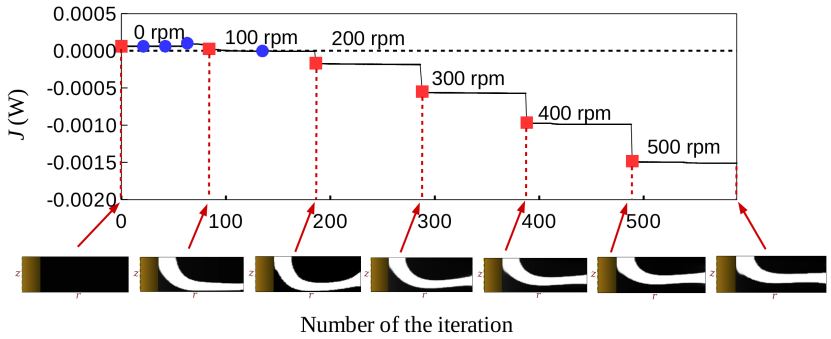
Table 5.9 – Parameters used for the topology optimization of a vertical inlet Tesla pump.

Input parameters	
Inlet velocity profile	Parabolic
Dimensions	
r_{shaft}	2.6 mm
r_{int}	5 mm
e_{out}	5 mm
r_{ext}	15 mm

5.1.2.2.1 *Optimizing for relative energy dissipation*

The one-channel Tesla pump is optimized for a rotation of 500 rpm and 0.5 L/min, considering relative energy dissipation as the objective function. The initial guess consists of an entirely solid domain ($\alpha = 0$), which is possible since $\kappa_{\max}$ assumes a finite value. Due to some convergence difficulties encountered when trying to optimize directly for a rotation of 500 rpm, a rotation updating scheme is used. The topology is gradually converged by subsequently increasing the rotation, from 0 rpm to 500 rpm, by restarting the IPOPT algorithm for each rotation. The convergence curve for the objective function value is shown in Fig. 5.21, showing the intermediary topologies until the rotation 500 rpm is reached, after 593 iterations.

Figure 5.21 – Convergence curve for the objective function value (relative energy dissipation) of a one-channel Tesla pump for 500 rpm and 0.5 L/min (the circles indicate the beginning of a new step of iterations, by changing parameters and restarting the IPOPT algorithm; the squares indicate change in the rotation of the disks).



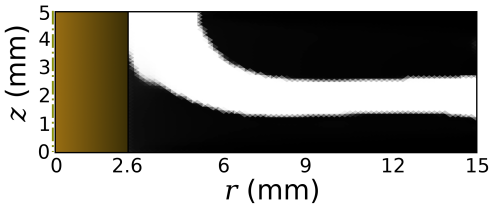
Source: Author (ALONSO *et al.*, 2019).

The final optimized topology (for 500 rpm) is considerably different from the one obtained for 0 rpm. For higher rotations, as the radial velocity increases, the curvature of the channel also increases. This is coherent with the objective function (relative energy dissipation), given that the higher curvature is located near the inlet, where the velocities are lower and the velocity gradients can be higher (i.e., near the inlet, the viscous term of the relative energy dissipation ($\frac{1}{2}\mu(\nabla\boldsymbol{v}+\nabla\boldsymbol{v}^T)\bullet(\nabla\boldsymbol{v}+\nabla\boldsymbol{v}^T)$ from eq. (2.51)) has a lower cost than the porous medium effect term (given, in this case, as $\boldsymbol{\kappa}(\alpha)\boldsymbol{v}\bullet\boldsymbol{v}$)). The sudden decreases in relative energy dissipation when the rotation changes its value are mainly due to the increase in the pumping effect of the centrifugal term of the relative energy dissipation ($(\rho\boldsymbol{\omega}\wedge(\boldsymbol{\omega}\wedge\boldsymbol{r}))\bullet\boldsymbol{v}$ in eq. (2.51)), which is negative.

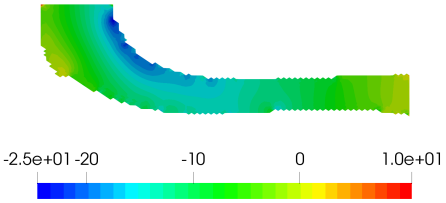
Fig. 5.22 shows the topology optimization result, the corresponding post-processed mesh, the pressure and velocity distributions for the post-processed mesh, and the 3D representation of the optimized topology. Observing Fig. 5.22c, it is possible to notice that the velocities near the outlet are higher near the disks, which is caused by the viscous effect of the boundary layer. Again, this is consistent with the Tesla principle.

Figure 5.22 – Topology optimization result of the one-channel Tesla pump for 500 rpm and 0.5 L/min (the pressure and velocities are computed in the post-processed mesh).

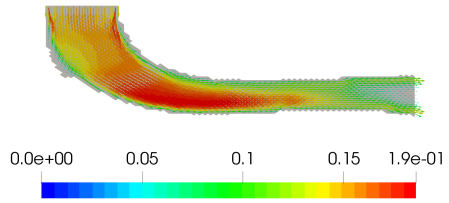
(a) Topology optimization result.



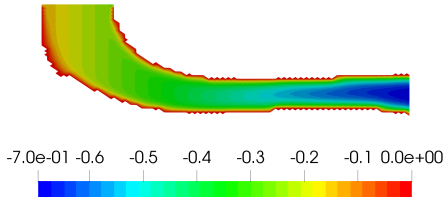
(b) Pressure distribution p (Pa).



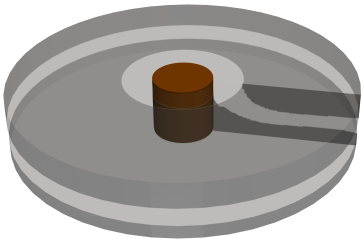
(c) Radial-axial velocity distribution (v_r, v_z) (m/s).



(d) Relative tangential velocity distribution v_θ (m/s).



(e) 3D representation of the 2D swirl optimized topology.



Source: Author (ALONSO *et al.*, 2019).

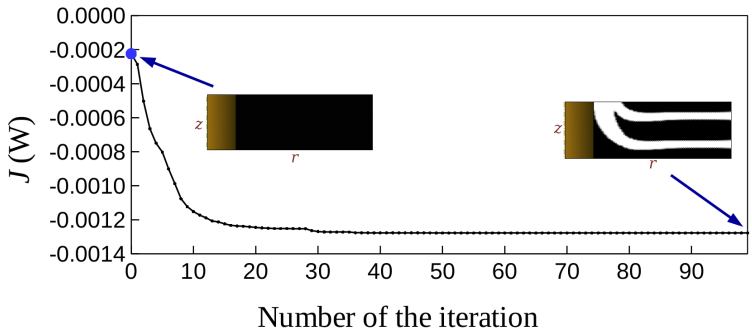
Table 5.10 shows the operational parameters of the optimized topology of Fig. 5.22.

Table 5.10 – Operational parameters of the optimized topology of a one-channel Tesla pump for 500 rpm and 0.5 L/min.

Basic parameters		
Flow rate (Q) (L/min)		0.5
Pressure head (H) (m)		6.68×10^{-3}
Fluid volume (V) (m^3)		9.32×10^{-7}
Dimensionless parameters		
Boundary layer	Ph	1.01×10^{1}
Flow regime	$\max(\mathrm{Re}_{\mathrm{ext},\ell})$	1.19×10^{4}
	$\max(\mathrm{Nd}_{\mathrm{ext},\ell})$	1.03×10^{2}
Flow rate	A_Q	4.67×10^{2}
Efficiency	η_s	27.9%
Functions of interest		
Relative energy dissipation (Φ_{rel}) (W)		-9.90×10^{-4}
Vorticity ($\xi_{V,\mathrm{rel}}$) (m^3/s^2)		2.80×10^{-1}

The two-channel Tesla pump is also optimized for a rotation of 500 rpm and 0.5 L/min, considering relative energy dissipation as the objective function. The initial guess consists of an entirely solid domain ($\alpha = 0$). The convergence curve for the objective function value is shown in Fig. 5.23, with 100 iterations.

Figure 5.23 – Convergence curve for the objective function value (relative energy dissipation) of a two-channel Tesla pump for 500 rpm and 0.5 L/min.



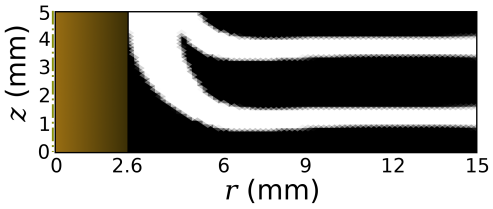
Source: Author (ALONSO *et al.*, 2019).

As can be seen in the topologies of Fig. 5.23, the two channels are equal in the region where the pattern repetition sensitivity method is used. The two-channel Tesla pump model is very similar to the one-channel Tesla pump model, with the difference that the sensitivity method forces the flow to separate into two zones. The downward path to the bottom channel is larger than the path to the upper channel; however, the mass flow at the end of both of them is almost the same. This can be explained by the fact that the fluid goes through a large path until the bottom channel entrance and then undergoes a reduction in the path width, increasing the fluid velocity.

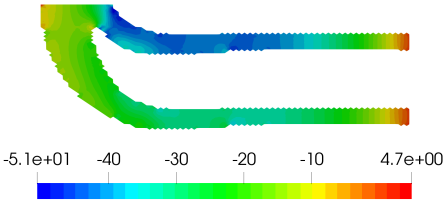
Fig. 5.24 shows the topology optimization result, the corresponding post-processed mesh, the pressure and velocity distributions for the post-processed mesh and the 3D representation of the optimized topology.

Figure 5.24 – Topology optimization result of a two-channel Tesla pump for 500 rpm and 0.5 L/min (the pressure and velocities are computed in the post-processed mesh).

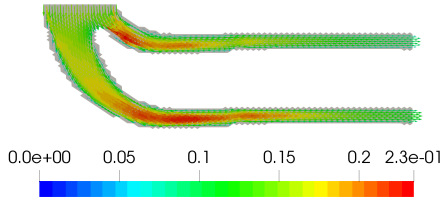
(a) Topology optimization result.



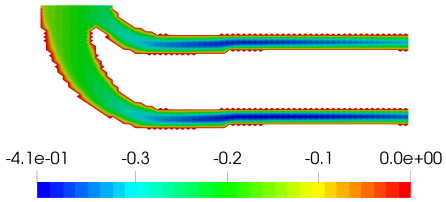
(b) Pressure distribution p (Pa).



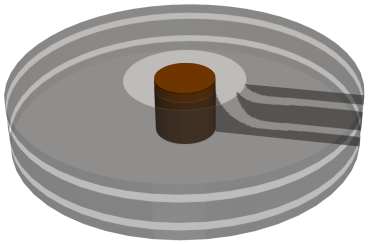
(c) Radial-axial velocity distribution (v_r, v_z) (m/s).



(d) Relative tangential velocity distribution v_θ (m/s).



(e) 3D representation of the 2D swirl optimized topology.



Source: Author (ALONSO *et al.*, 2019).

Table 5.11 shows the operational parameters of the optimized topology of Fig. 5.24.

Table 5.11 – Operational parameters of the optimized topology of a two-channel Tesla pump for 500 rpm and 0.5 L/min.

Basic parameters		
Flow rate (Q) (L/min)		0.5
Pressure head (H) (m)		1.68×10^{-2}
Fluid volume (V) (m^3)		8.88×10^{-7}
Dimensionless parameters		
Boundary layer	Ph	3.62
Flow regime	$\max(\mathrm{Re}_{\mathrm{ext},\ell})$	1.19×10^{4}
	$\max(\mathrm{Nd}_{\mathrm{ext},\ell})$	1.32×10^{1}
Flow rate	A_Q	8.33×10^{1}
Efficiency	η_s	39.5%
Functions of interest		
Relative Energy dissipation (Φ_{rel}) (W)		-2.60×10^{-4}
Vorticity ($\xi_{V,\mathrm{rel}}$) (m^3/s^2)		5.47×10^{-1}

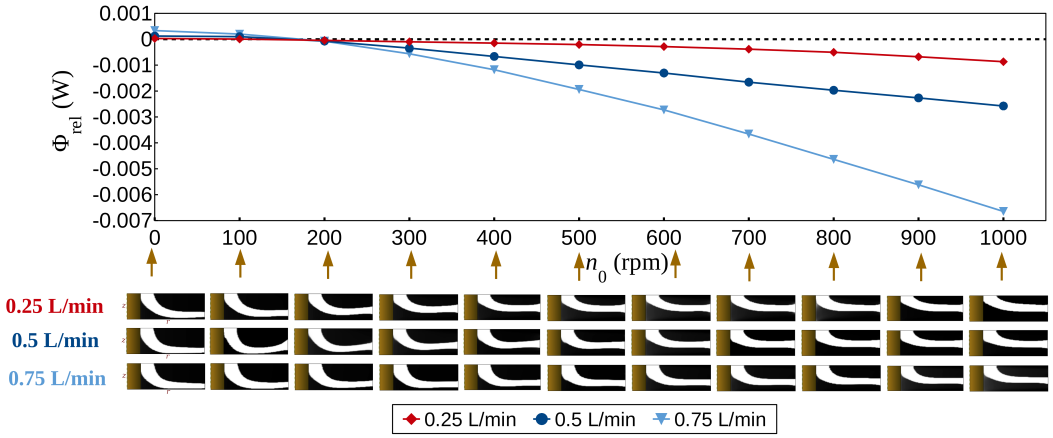
By comparing the operational parameters of the one-channel Tesla pump (Table 5.10) and the two-channel Tesla pump (Table 5.11), it can be noticed that the relative energy dissipation (Φ_{rel}) and vorticity ($\xi_{V,\mathrm{rel}}$) are higher for the two-channel case, which could mean higher viscous heating, higher pumping effect and higher formation of vortices in the flow. However, the two-channel Tesla pump is better in terms of isentropic efficiency (the difference in η_s is 11.6%) and pressure head (H is 152% higher). In terms of the dimensionless parameters, the Pohlhausen number (Ph) is about three times lower for the two-channel Tesla pump, which means that the channels are about three times thinner. Even though the Reynolds number ($\max(\mathrm{Re}_{\mathrm{ext},\ell})$) is the same, the Nendl parameter ($\max(\mathrm{Nd}_{\mathrm{ext},\ell})$) is about nine times lower because it depends on the square of the minimum channel thickness, that is three times smaller, showing that the velocities considering the geometry increase more in the case of the two-channel Tesla pump. The essential machine data parameter (A_Q) is smaller for two channels, showing that the flow rate in each channel separately is smaller.

5.1.2.2.2 *Effect of rotation / flow rate*

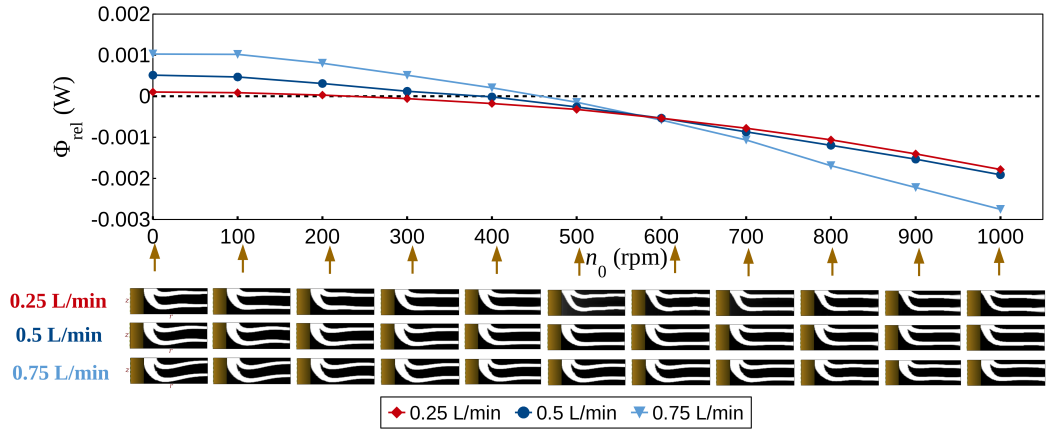
The effect of rotation / flow rate in the optimized topologies is analyzed in Fig. 5.25, for 0.25 L/min, 0.5 L/min and 0.75 L/min, from 0 rpm to 1000 rpm. The objective function is the relative energy dissipation. In some of the optimized topologies, the Helmholtz filter (LAZAROV; SIGMUND, 2010) (see Section 2.5.7.1) is used in order to regularize, with filter length parameter (r_H) of 0.05 $\sim$ 0.1 mm, which is smaller than the vertical dimension of each rectangular partition of the mesh (0.125 mm).

Figure 5.25 – Relative energy dissipation for the optimized topologies of a vertical inlet Tesla pump for different rotation / flow rate ratios, considering the cases of 0.25 L/min, 0.5 L/min and 0.75 L/min.

(a) One-channel Tesla pump.



(b) Two-channel Tesla pump.

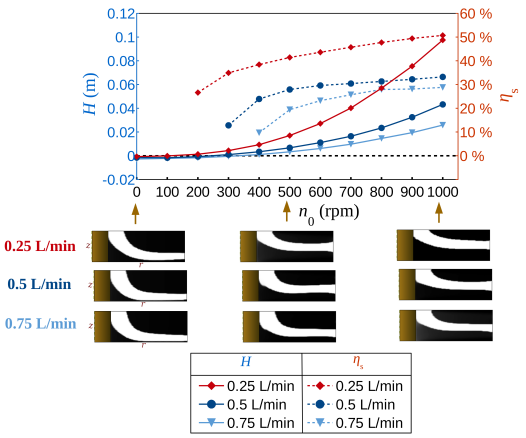


Source: Author (ALONSO *et al.*, 2019).

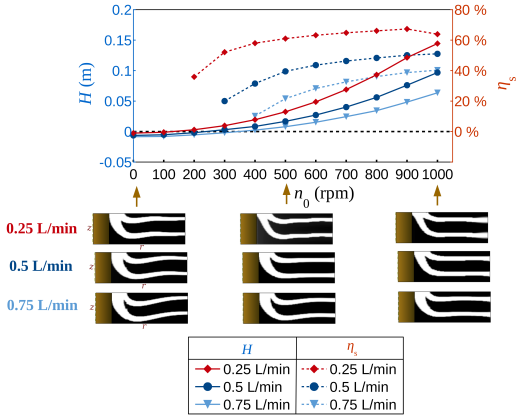
Fig. 5.25 shows that the relative energy dissipation decreases when increasing the flow rate. This is due to the increase of the pumping effect of the centrifugal term of the relative energy dissipation ($(\rho\boldsymbol{\omega}\wedge(\boldsymbol{\omega}\wedge\boldsymbol{r}))\bullet\boldsymbol{v}$ in eq. (2.51)). As can be noticed, at lower rotations – below 150 rpm (for one-channel Tesla pump) and 550 rpm (for two-channel Tesla pump) –, lower flow rates portray lower relative energy dissipations; however, lower flow rates portray higher relative energy dissipations at higher rotations. This change in behavior after the intersection of the curves is due to the fact that it is easier to pump lower flow rates at lower disk rotations, but maintaining lower flow rates at high disk rotations induce higher relative energy dissipations. The pressure head and isentropic efficiencies for the topologies of Fig. 5.25 can be seen in Fig. 5.26.

Figure 5.26 – Pressure head (H) and isentropic efficiency (η_s) of a vertical inlet Tesla pump for different rotation / flow rate ratios, considering the cases of 0.25 L/min, 0.5 L/min and 0.75 L/min.

(a) One-channel Tesla pump.



(b) Two-channel Tesla pump.



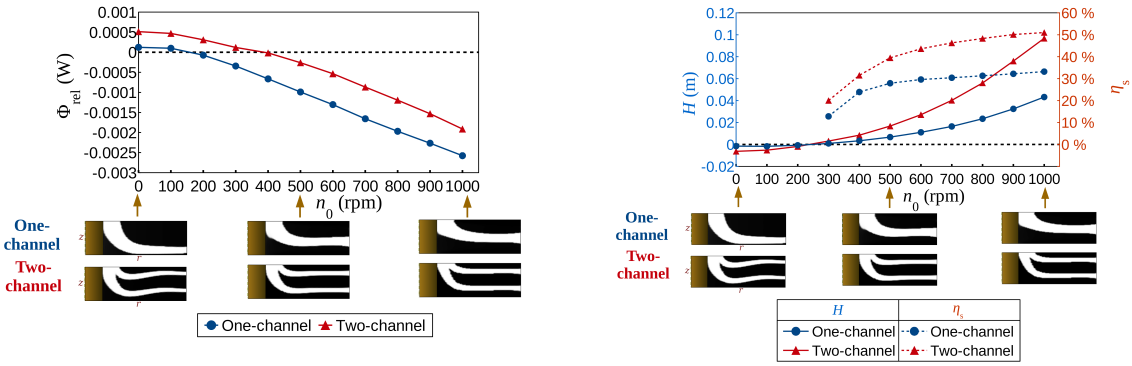
Source: Author (ALONSO *et al.*, 2019).

Figs. 5.26a and 5.26b show that lower flow rates lead to higher isentropic efficiencies and higher pressure heads. The increase in the isentropic efficiency can be related to a smaller viscous friction in the relative energy dissipation. The increase in the pressure head effect is similar to the one observed in centrifugal bladed pump curves, in which lowering the flow rate while maintaining the rotation (such as due to closing a valve near the inlet of a pump) increases the pressure head at the pump (it can be mentioned, however, that, while the mentioned behavior is the same, its variation is different (see Fig. 1.9)).

Fig. 5.27a shows the comparison of relative energy dissipation, and Fig. 5.27b shows the comparison of pressure head and isentropic efficiency for the one- and two-channel Tesla pump, for the case of a flow rate of 0.5 L/min, from 0 rpm to 1000 rpm.

Figure 5.27 – Comparison between the one- and two-channel Tesla pumps for 0.5 L/min.

(a) One-channel Tesla pump. (b) Two-channel Tesla pump.



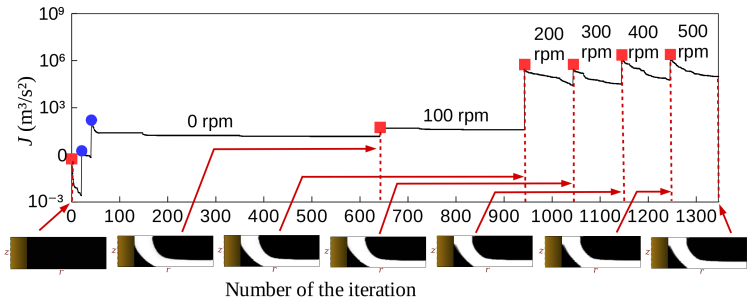
Source: Author (ALONSO *et al.*, 2019).

Fig. 5.27a shows that the relative energy dissipation is higher for two channels than for one channel. As can be seen in Fig. 5.27b, for a positive pressure head, only the optimized topologies with rotation higher than about 250 rpm can effectively operate as pumps. It can also be noticed in Figs. 5.26 and 5.27 that the two-channel design portrays a higher isentropic efficiency and generates higher pressure heads than the one-channel design from about 250 rpm.

5.1.2.2.3 *Optimizing for vorticity*

The vorticity (eq. (2.62)) is considered as the objective function for the design of a one-channel Tesla pump (Fig. 5.19a). As in Section 5.1.2.2.1, the optimization is performed for a rotation of 500 rpm and 0.5 L/min, the specified volume fraction is $f = 30\%$, the initial guess consists of an entirely solid domain ($\alpha = 0$), and a rotation updating scheme is used. The Helmholtz filter (LAZAROV; SIGMUND, 2010) (see Section 2.5.7.1) is used again with a filter length parameter (r_H) of 0.125 mm, which is equal to the vertical dimension of each rectangular partition of the mesh. The proportionality constant of the porous medium effect of the vorticity (shown in eq. (2.62)) is selected as $k_V = 1.0$. The convergence curve for the objective function value is shown in Fig. 5.28, showing the intermediary topologies until reaching the 500 rpm optimized topology in 1,347 iterations.

Figure 5.28 – Convergence curve for the objective function value (100% vorticity) of a one-channel Tesla pump for 500 rpm and 0.5 L/min (the circles indicate the beginning of a new step of iterations, by changing parameters and restarting the IPOPT algorithm; the squares indicate change in the rotation of the disks).



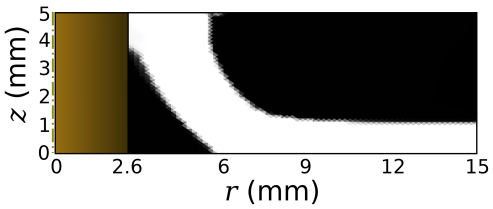
Source: Author (ALONSO *et al.*, 2019).

The vorticity effect in Fig. 5.28 is seen to lead the fluid down with a larger initial channel thickness than when compared with the relative energy dissipation case (Fig. 5.21).

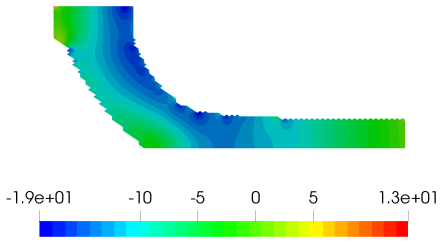
Fig. 5.29 shows the topology optimization result, the corresponding post-processed mesh, the pressure and velocity distributions for the post-processed mesh and the 3D representation of the optimized topology.

Figure 5.29 – Topology optimization result of the one-channel Tesla pump optimized for 100% vorticity for 500 rpm and 0.5 L/min (the pressure and velocities are computed in the post-processed mesh).

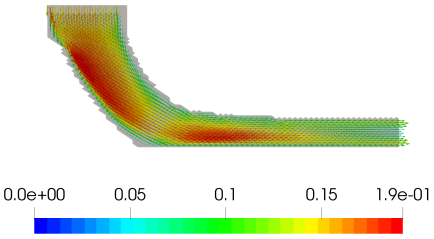
(a) Topology optimization result.



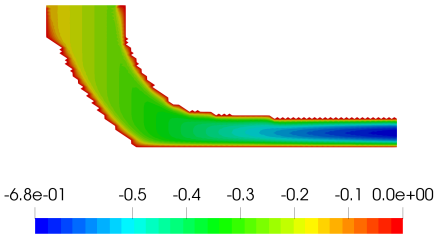
(b) Pressure distribution p (Pa).



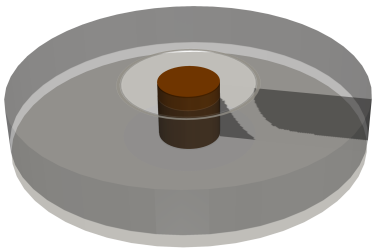
(c) Radial-axial velocity distribution (v_r, v_z) (m/s).



(d) Relative tangential velocity distribution v_θ (m/s).



(e) 3D representation of the 2D swirl optimized topology.



Source: Author (ALONSO *et al.*, 2019).

In Fig. 5.29, the final topology is highly discrete, which is due to the porous medium effect term (given, in this case, by $\frac{k_V}{\rho}\nabla \wedge (\boldsymbol{\kappa}(\alpha)\boldsymbol{v})$) and the Helmholtz filter (LAZAROV; SIGMUND, 2010).

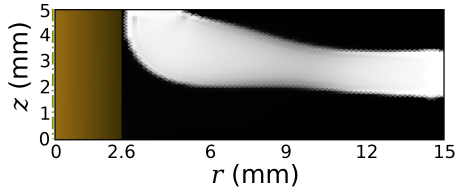
Table 5.12 shows the operational parameters of the optimized topology of Fig. 5.29.

Table 5.12 – Operational parameters of the optimized topology of a one-channel Tesla pump optimized for 100% vorticity for 500 rpm and 0.5 L/min.

Basic parameters		
Flow rate (Q) (L/min)		0.5
Pressure head (H) (m)		6.67×10^{-3}
Fluid volume (V) (m^3)		9.81×10^{-7}
Dimensionless parameters		
Boundary layer	Ph	7.24
Flow regime	$\max(\mathrm{Re}_{\mathrm{ext},\ell})$	1.19×10^{4}
	$\max(\mathrm{Nd}_{\mathrm{ext},\ell})$	5.27×10^{1}
Flow rate	A_Q	3.33×10^{2}
Efficiency	η_s	27.6%
Functions of interest		
Relative energy dissipation (Φ_{rel}) (W)		-1.01×10^{-3}
Vorticity ($\xi_{V,\mathrm{rel}}$) (m^3/s^2)		2.82×10^{-1}

If the porous medium effect term (given, in this case, by $\frac{k_V}{\rho}\nabla \wedge (\boldsymbol{\kappa}(\alpha)\boldsymbol{v})$) is not included in the vorticity calculation, the results do not form a clear (sufficiently discrete topology) topology, presenting a quite big gray region (intermediary values), as shown in Fig. 5.30, and the relative vorticity value after post-processing becomes, in this case, 7% higher than when including the porous medium effect term (3.02×10^{-1} m^3/s^2). The effect of the porous medium effect term of vorticity can be seen as analogous to the porous medium effect term of relative energy dissipation ($\boldsymbol{\kappa}(\alpha)\boldsymbol{v}\bullet\boldsymbol{v}$) (as in Borrvall and Petersson (2003)), which helps better conditioning the objective function for the topology optimization.

Figure 5.30 – Topology optimization for 100% vorticity for 500 rpm and 0.5 L/min, considering the objective function without the porous medium effect term.



Source: Author (ALONSO *et al.*, 2019).

5.1.2.2.4 *Optimizing for vorticity and relative energy dissipation*

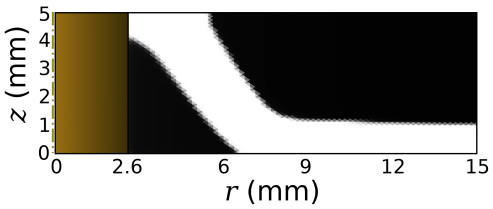
The vorticity is partially considered in the form of a multi-objective function for 50% vorticity ($w_V = 0.5$) and 50% relative energy dissipation ($w_\Phi = 0.5$) for the design of a one-channel Tesla pump (Fig. 5.19a). As in the case of Section 5.1.2.2.3, the optimization is performed for a rotation of 500 rpm and 0.5 L/min, the specified volume

fraction is $f = 30\%$, the initial guess consists of an entirely solid domain ($\alpha = 0$), a rotation updating scheme is used, and the Helmholtz filter (LAZAROV; SIGMUND, 2010) (see Section 2.5.7.1) is used with a filter length parameter (r_H) of 0.125 mm in order to improve the discreteness of the optimized topology. The proportionality constant is selected as $k_V = 1.0$ (eq. (2.62)).

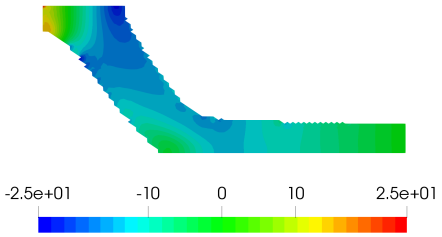
Fig. 5.31 shows the topology optimization result, the corresponding post-processed mesh, the pressure and velocity distributions for the post-processed mesh and the 3D representation of the optimized topology.

Figure 5.31 – Topology optimization result of a one-channel Tesla pump optimized for 50% vorticity and 50% of relative energy dissipation for 500 rpm and 0.5 L/min (the pressure and velocities are computed in the post-processed mesh).

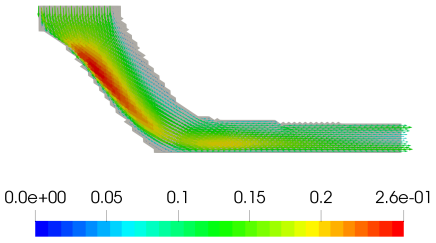
(a) Topology optimization result.



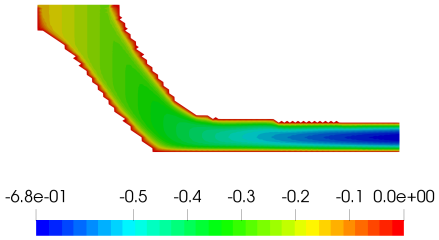
(b) Pressure distribution p (Pa).



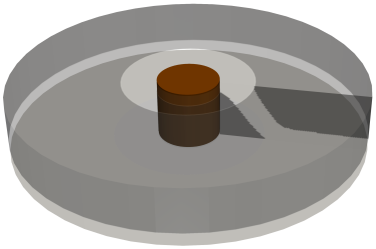
(c) Radial-axial velocity distribution (v_r, v_z) (m/s).



(d) Relative tangential velocity distribution v_θ (m/s).



(e) 3D representation of the 2D swirl optimized topology.



Source: Author (ALONSO *et al.*, 2019).

It can be noticed in Fig. 5.31 that the relative energy dissipation term caused the initial channel bending to become more straight when compared with the 100% vorticity case (Fig. 5.29).

Table 5.13 shows the operational parameters of the optimized topology of Fig. 5.31.

Table 5.13 – Operational parameters of the optimized topology of a one-channel Tesla pump optimized for 50% vorticity and 50% of relative energy dissipation for 500 rpm and 0.5 L/min.

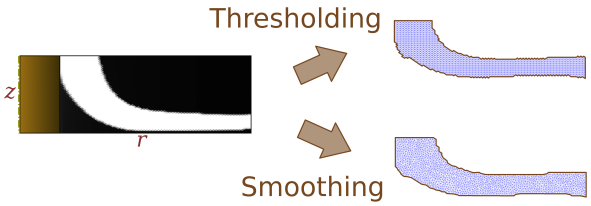
Basic parameters		
Flow rate (Q) (L/min)		0.5
Pressure head (H) (m)		6.44×10^{-3}
Fluid volume (V) (m^3)		9.49×10^{-7}
Dimensionless parameters		
Boundary layer	Ph	7.24
Flow regime	$\max(\mathrm{Re}_{\mathrm{ext},\ell})$	1.19×10^{4}
	$\max(\mathrm{Nd}_{\mathrm{ext},\ell})$	5.27×10^{1}
Flow rate	A_Q	3.33×10^{2}
Efficiency	η_s	26.6%
Functions of interest		
Relative energy dissipation (Φ_{rel}) (W)		-9.85×10^{-4}
Vorticity ($\xi_{V,\mathrm{rel}}$) (m^3/s^2)		3.08×10^{-1}

When comparing Tables 5.12 and 5.13, it can be noticed that the vorticity is smaller for the optimized topology for 100% vorticity. However, the relative energy dissipation is also smaller, which may possibly indicate that the optimization for 50% vorticity and 50% relative energy dissipation is probably a local minimum.

5.1.2.3 Comparing performance with straight disks

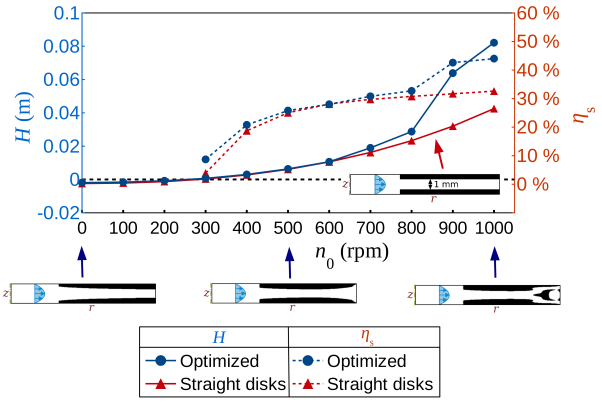
The topology optimization results for relative energy dissipation are compared with straight-channel topologies with the same volume as the one specified for each optimization ($f = 30\%$) (see Figs. 5.33, 5.34 and 5.35). In this section, smoothed post-processed meshes are used, removing sharp edges and sawtooth-like curves which may undesirably influence the calculated operational parameters (see Fig. 5.32). The mesh smoothing is performed through generation of contours (Section 2.5.8.2.1)

Figure 5.32 – Mesh smoothing being applied to an optimized topology.



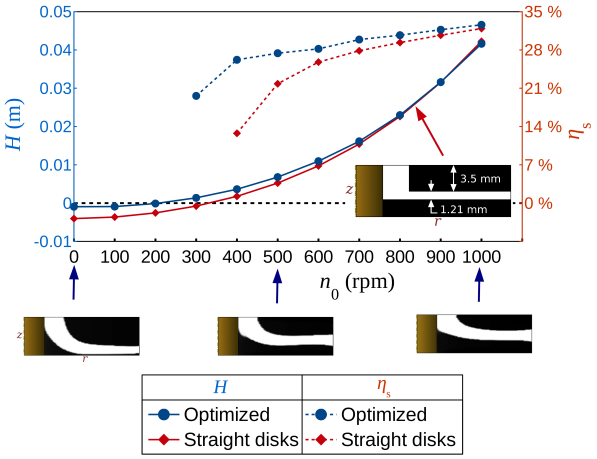
Source: Author (ALONSO *et al.*, 2019).

Figure 5.33 – Comparison of pressure head (H) and isentropic efficiency (η_s) between a straight and an optimized horizontal inlet Tesla pump.



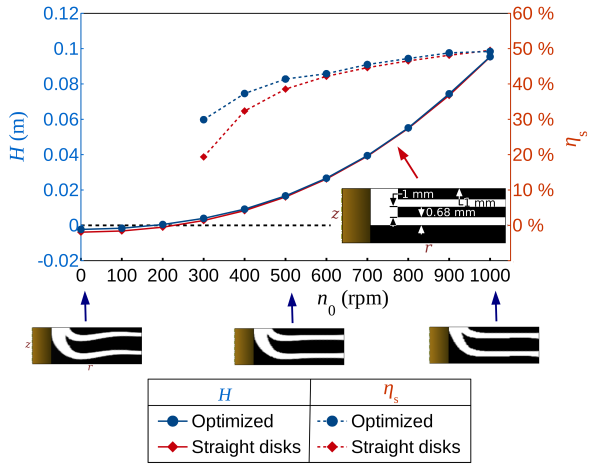
Source: Author (ALONSO *et al.*, 2019).

Figure 5.34 – Comparison of pressure head (H) and isentropic efficiency (η_s) between a straight and an optimized vertical inlet one-channel Tesla pump.



Source: Author (ALONSO *et al.*, 2019).

Figure 5.35 – Comparison of pressure head (H) and isentropic efficiency (η_s) between a straight and an optimized vertical inlet two-channel Tesla pump.



Source: Author (ALONSO *et al.*, 2019).

In Fig. 5.33, it can be noticed that the smoothened horizontal inlet optimized solution generates higher pressure heads and leads to higher isentropic efficiencies than the straight disks solution.

Figs. 5.34 and 5.35 show that the vertical inlet optimized solutions are better than the straight disks solutions with respect to pressure head and isentropic efficiency. It can be noticed that, for higher rotations, the advantage of the optimized solutions for one- and two-channels show a gradual decrease, approaching the values of the straight disk solutions. This is due to the fact that the improvement due to the smooth change of direction near the inlet portrays less effect in higher rotations.

Table 5.14 shows a comparison of the optimized topologies for the vertical inlet Tesla pump for 500 rpm and 0.5 L/min, which are similar to the values presented in Tables 5.10, 5.11 and 5.13, but are computed in the smoothened mesh.

Table 5.14 – Operational parameters of the smoothened optimized topologies of vertical inlet Tesla pump for 500 rpm and 0.5 L/min for comparison with straight disks solutions.

		One-channel				Two-channel	
		(energy dissipation)	(100% vorticity)	(50% vorticity)	(straight)	(energy dissipation)	(straight)
Basic parameters							
Flow rate (Q) (L/min)		0.5	0.5	0.5	0.5	0.5	0.5
Pressure head (H) ($\times 10^{-2}$ m)		0.68	0.68	0.65	0.52	1.67	1.60
Dimensionless parameters							
Boundary layer	Ph ($\times 10^{1}$)	1.16	0.80	0.80	0.87	0.36	0.49
Flow regime	$\max(\mathrm{Re}_{\mathrm{ext},\ell})$ ($\times 10^{4}$)	1.19	1.19	1.19	1.19	1.19	1.19
	$\max(\mathrm{Nd}_{\mathrm{ext},\ell})$ ($\times 10^{2}$)	1.35	0.64	0.64	0.76	0.13	0.24
Flow rate	A_Q ($\times 10^{2}$)	5.33	3.67	3.67	4.00	0.83	1.13
Efficiency	η_s	27.4%	28.2%	27.3%	21.8%	41.4%	38.6%
Functions of interest							
Relative energy dissipation (Φ_{rel}) ($\times 10^{-4}$ W)		-0.94	-1.04	-1.02	-0.86	-4.55	-3.38
Vorticity ($\xi_{V,\mathrm{rel}}$) ($\times 10^{-1}$ m^3/s^2)		2.54	2.60	2.83	3.41	3.60	4.32

In Table 5.14, from the values of the relative energy dissipation (Φ_{rel}), vorticity ($\xi_{V,\mathrm{rel}}$), pressure head (H) and isentropic efficiency (η_s), it can be noticed that all of the optimized topologies show better values than the corresponding straight disks: i.e., they portray smaller relative energy dissipations, smaller vorticities, higher pressure heads and higher isentropic efficiencies.

By comparing the vorticity values ($\xi_{V,\mathrm{rel}}$) of Table 5.14, it can be noticed that the

smallest vorticity is found in the one-channel Tesla pump design optimized for relative energy dissipation, which may indicate that the optimized topologies for vorticity may correspond to local minima. As expected, the vorticity for the optimized topology for 100% vorticity is smaller than the one optimized for 50% vorticity; however, the topology for 100% vorticity shows a slightly smaller relative energy dissipation (Φ_{rel}) than the one optimized for 50% vorticity. Moreover, the relative energy dissipation (Φ_{rel}) is still higher than the vorticity results, which may indicate that it has reached a local minimum. Since the mesh obtained from smoothing (as in Fig. 5.32) only removes some edges, not leading to spline-like contours, it is possible that, if completely smooth topologies are considered, the advantage of one topology in relation to the other may be over- or under-estimated in relation to the results presented in this section.

In relation to the straight disks, the Pohlhausen parameter (Ph) is higher for the optimized one-channel Tesla pump designs, which means that the optimized one-channels are thicker than the corresponding straight one-channel, but the optimized two-channel Tesla pump design shows lower Pohlhausen parameters (Ph) in relation to the straight disks, meaning that each channel of the optimized two-channel Tesla pump are thinner.

As can be noticed, all of the Reynolds numbers ($\max(\mathrm{Re}_{\mathrm{ext},\ell})$) are equal, since the maximum velocity ($|\boldsymbol{v}_{\mathrm{abs}}|$) in all of the cases turned out equal to $\omega_0 r_{ext} = 7.9 \times 10^{-1}$ m/s. The highest Nendl parameter ($\max(\mathrm{Nd}_{\mathrm{ext},\ell})$) is higher for the one-channel Tesla pump, meaning that the increase in velocity occurs in a higher disk spacing than the other topologies.

The essential machine data (A_Q) parameter shows that the flow rate effect in the disk spacings is smaller for the optimized topologies in relation to the straight disks.

In terms of isentropic efficiency (η_s), the higher efficiencies in relation to the straight one- and two-channel Tesla pumps rest on the optimized topologies for one-channel Tesla pump for 100% vorticity and two-channel Tesla pump for relative energy dissipation.

5.1.3 **Non-Newtonian 2D swirl flow design**

In this section, the topology optimization method is applied to 2D swirl flow devices for non-Newtonian fluid considering non-Newtonian penalization (ALONSO *et al.*, 2020).

In the numerical results of this section, the fluid is considered as blood (non-Newtonian fluid), with the non-Newtonian dynamic viscosity ($\mu = \mu(\dot{\gamma}_{\mathrm{m}})$) given by eq. (2.11). Since the compressibility of blood is small, as mentioned in Sections 1.1.1 and 2.1.2.1, according to Hinghofer-Szalkay and Greenleaf (1987), blood may be assumed as incompressible, with a density (ρ) of 1056 kg/m^3. The Taylor-Hood element is considered for the finite element method (see Section 2.2.2). The material model for topology optimization is given by the Brinkman model (Section 2.5.1.1). The IPOPT algorithm (Section 3.1.1.1) is used for the optimization in this section.

One numerical example is presented in this section, for a two-outlet channel (Section 5.1.3.1). Further examples can be seen in Alonso *et al.* (2020), for parallel channels and a two-way channel. The outlet boundary is considered as *stress free* ($\boldsymbol{T}\bullet\boldsymbol{n} = \boldsymbol{0}$) (see Section 2.1.4).

The Reynolds number for the 2D swirl flow devices is chosen differently than Section 5.1.1. For simplicity, it is based directly on the external diameter:

$$\mathrm{Re}_{\mathrm{ext},\ell} = \frac{\mu(\dot{\gamma}_{\mathrm{m}})\,|\boldsymbol{v}_{\mathrm{abs}}|\,(2R_{ext})}{\rho} \tag{5.2}$$

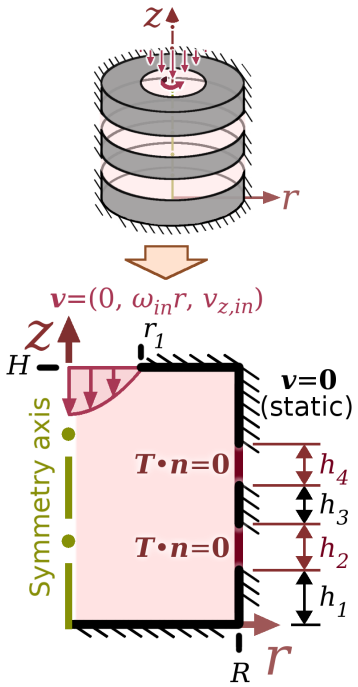
where $\mu(\dot{\gamma}_{\mathrm{m}})$ is the non-Newtonian viscosity (the dependency $\dot{\gamma}_{\mathrm{m}}$ is explicitly indicated here for clarity), which may vary in each position of the computational domain, $\boldsymbol{v}_{\mathrm{abs}}$ is the absolute velocity, which varies in each position of the computational domain, R_{ext} is the external radius of the computational domain, and ρ is the density.

The post-processing is performed by thresholding (Section 2.5.8.1).

5.1.3.1 Two-outlet channel

This example consists of the design of a two-outlet channel, which consists of a vertical inlet of rotating fluid, with two possible horizontal outlets. This example has already been treated for the 2D swirl flow model in Alonso *et al.* (2018), considering Newtonian fluid flow (water). The configuration is illustrated in Fig. 5.36. The solid material distribution is optimized on the static walls ($\omega_0 = 0$ rad/s).

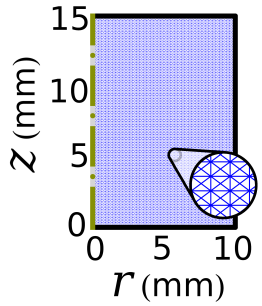
Figure 5.36 – Design domain for two-outlet channel design.



Source: Author (ALONSO *et al.*, 2020).

The mesh is composed of 40 radial and 80 axial rectangular partitions of crossed triangular elements (the same as in Fig. 5.4), totaling 6,521 nodes and 12,800 elements (see Fig. 5.37). The input parameters and dimensions of the design domain that are used are shown in Table 5.15.

Figure 5.37 – Mesh used in the two-outlet channel design.



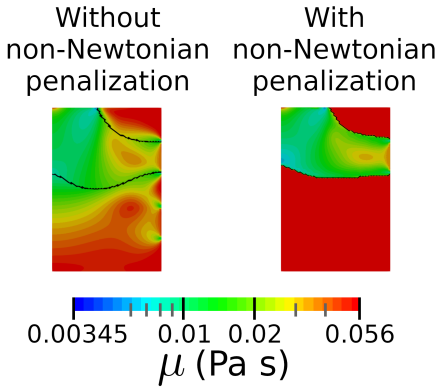
Source: Author (ALONSO *et al.*, 2020).

Table 5.15 – Parameters used for the topology optimization of the two-outlet channel.

Input parameters	
Wall rotation	$\omega_0 = 0$ rad/s (static)
Inlet rotation	$n_{in} = 20$ rpm
Inlet velocity profile	Parabolic
Dimensions	
H	15 mm
R	10 mm
r_1	4 mm
$h_1 = h_2 = h_3 = h_4$	3 mm

Fig. 5.38 shows a comparison of the non-Newtonian viscosity for the optimized two-outlet channel designs at 0.05 L/min without post-processing (i.e., still including the material model). The effect of the non-Newtonian penalization is quite apparent and the non-Newtonian viscosity, as in the other examples, is less dispersed and more consistent with its expected/desired value inside a solid material. The same effect is observed for other flow rates.

Figure 5.38 – Non-Newtonian viscosity in the optimized two-outlet channel designs for the non-Newtonian fluid flow at 0.05 L/min (20 rpm) before post-processing (i.e., still including the material model) (in logarithmic scale). The contours of the optimized topologies are delimited by thin dark lines.

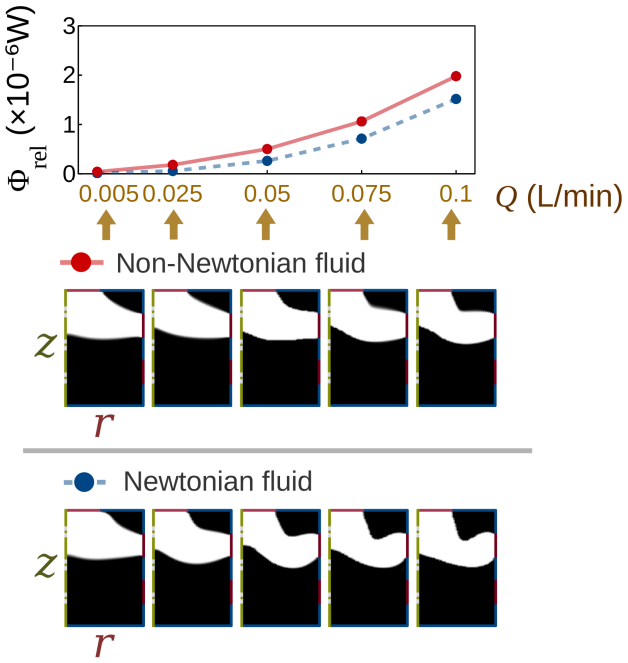


Source: Author (ALONSO *et al.*, 2020).

A series of optimizations is performed for a sequence of flow rates considering a fixed inlet rotation ($n_{in} = 20$ rpm) by considering non-Newtonian fluid (with non-Newtonian penalization) and Newtonian fluid. This is shown in Fig. 5.39, from the values of the objective function (relative energy dissipation) with respect to the flow rates for each optimized topology. As in the other examples, the objective function values correspond to the post-processed topology (Section 2.5.8.1). The highest values for the maximum local Reynolds number ($\max(\mathrm{Re}_{\mathrm{ext},\ell})$) are given at 0.1 L/min, and are

evaluated as 1.77×10^2 (non-Newtonian fluid) and 4.06×10^2 (Newtonian fluid). This significant difference in the Reynolds number is due to the predominance of the non-Newtonian effect (i.e., higher viscosity) in the optimized topologies for non-Newtonian fluid flow.

Figure 5.39 – Effect of the flow rate in the non-Newtonian and Newtonian two-outlet channel designs.



Source: Author (ALONSO *et al.*, 2020).

Fig. 5.39 shows that the optimized designs lead the fluid to exit the upper channel, which better minimizes the objective function (relative energy dissipation). By comparing the non-Newtonian with the Newtonian topologies, it can be noticed that the curvature of the channel is smoother for the non-Newtonian designs: since the Newtonian fluid has a smaller viscosity, the flow is more guided by its inertia, which means that the first part of the channel can extend longer than the last part of the channel (near the outlet); in the case of the non-Newtonian fluid, the viscosity is higher far from walls, which means that the effect of the fluid inertia is reduced in the middle of the channel, leading the topology optimization to a straighter path to the outlet.

The optimization schemes are shown in Table 5.16. It can be mentioned that lower flow rates may require higher values for $\kappa_{\max}$, since the flow may need more "strength" to form the optimized topology. Higher flow rates may also require it, in order to block the fluid flow inside the solid material. However, if $\kappa_{\max}$ is too high, it may not be possible to achieve a discrete optimized topology, which may lead to a high presence

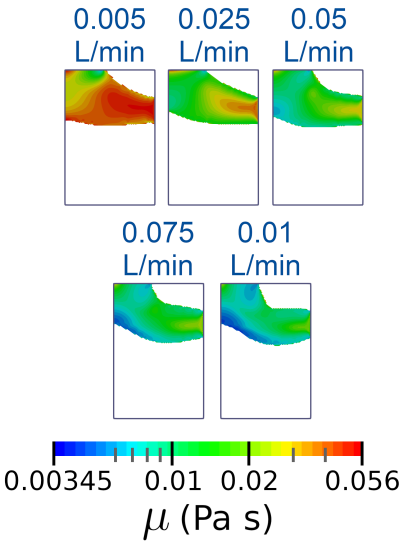
of *gray* ($0 < \alpha < 1$). This means that there is a compromise in obtaining a discrete optimized topology and blocking fluid flow inside the solid material. Also, the right choice for q may also help stabilizing a discrete optimized topology: Depending on the case, it may be necessary to *relax* the material model (smaller q), which may sometimes lead to a "better local minimum" (as in Borrvall and Petersson (2003)'s double pipe); however, in other cases, when there is no local minimum that can be achieved in this way, this can hinder the achievement of a discrete topology.

Table 5.16 – Reference parameters for the optimization schemes (steps) for the non-Newtonian and Newtonian two-outlet channel designs.

Flow rate (Q) (L/min)	$\kappa_{\max}$ ($\times 10^7 \mu_\infty$) (kg/(m^{3}s))	q
Non-Newtonian fluid		
0.005	5	1
0.025	25	0.1
0.05	0.5	10
0.075 $\sim$ 0.1	8	0.1
Newtonian fluid		
0.005 $\sim$ 0.05	0.5	1
0.075	2.5	0.1
0.1	50	0.1

The non-Newtonian viscosities in the optimized two-outlet channel designs for non-Newtonian fluid flow are plotted in Fig. 5.40. At 0.005 L/min, the non-Newtonian effect is easily noticeable, with a higher dynamic viscosity acting over most of the fluid domain. This effect is reduced at higher flow rates, though still keeping a considerable influence.

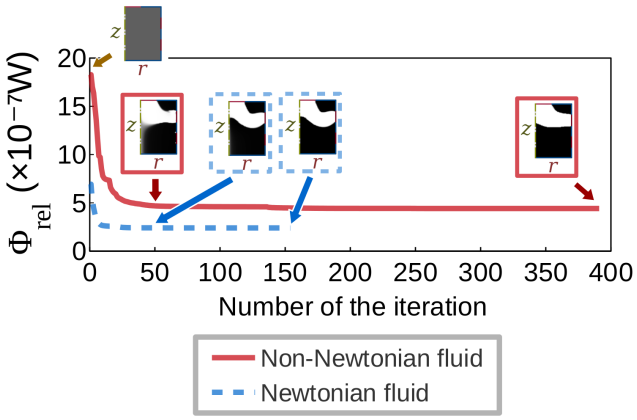
Figure 5.40 – Non-Newtonian viscosities in the optimized two-outlet channel designs (in logarithmic scale).



Source: Author (ALONSO *et al.*, 2020) (edited).

Fig. 5.41 shows the convergence curves for the non-Newtonian and Newtonian designs for 0.05 L/min and 20 rpm. The highest values for the maximum Reynolds numbers ($\max(\mathrm{Re}_{\mathrm{ext},\ell})$) for this case are 5.98 $\times$ 10^1 (non-Newtonian fluid) and 2.03 $\times$ 10^2 (Newtonian fluid).

Figure 5.41 – Convergence curves for the non-Newtonian and Newtonian two-outlet channel designs (0.05 L/min, 20 rpm).



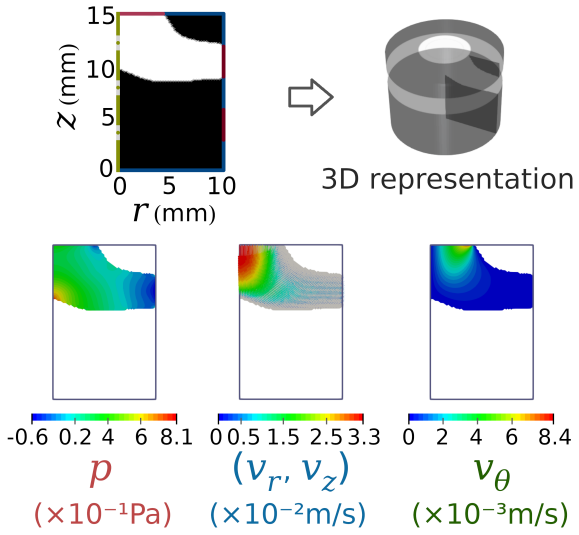
Source: Author (ALONSO *et al.*, 2020).

The simulations of the optimized topologies for the non-Newtonian and Newtonian designs for 0.05 L/min and 20 rpm are shown in Fig. 5.42. As can be noticed in the tangential velocity (v_θ) plot, the inlet rotation is “dissipated” along the channel in a “faster” manner for the non-Newtonian design than in the Newtonian design due to the increased

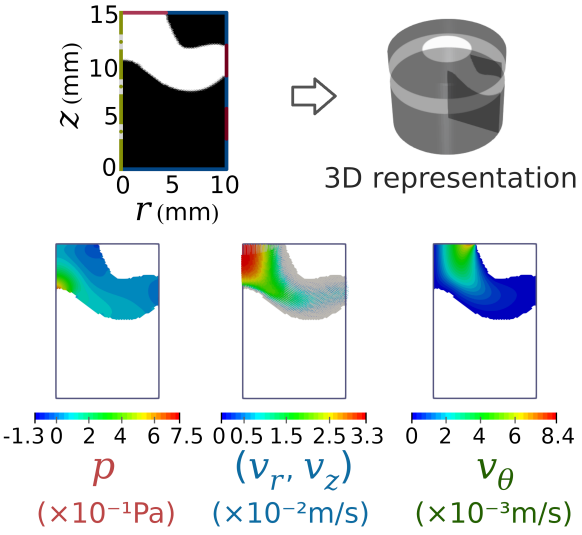
viscosity (non-Newtonian effect). Also, the decrease in pressure from the inlet towards the outlet seems to be more uniform in the non-Newtonian design.

Figure 5.42 – Optimized topologies, 3D representations, pressures and velocities for the non-Newtonian and Newtonian two-outlet channel designs (0.05 L/min, 20 rpm).

(a) Non-Newtonian two-outlet channel design.



(b) Newtonian two-outlet channel design.



Source: Author (ALONSO *et al.*, 2020).

5.1.4 **Tesla blood pump design considering hemolysis**

In this section, the topology optimization method is applied to Tesla-type pump devices, considering the Brinkman-Forchheimer model (Section 2.5.1.3), blood (non-Newtonian fluid), and a hemolysis model (Section 2.4.1) in topology optimization (ALONSO; SILVA, 2021).

In the numerical results of this section, as in Section 5.1.3, the fluid is considered as blood (non-Newtonian fluid), with the non-Newtonian dynamic viscosity ($\mu = \mu(\dot{\gamma}_{\mathrm{m}})$) given by eq. (2.11), non-Newtonian penalization (eq. (2.135)), and the density (ρ) given as 1056 kg/m^3 (HINGHOFER-SZALKAY; GREENLEAF, 1987) (Sections 1.1.1, 2.1.2.1 and 5.1.3). The Taylor-Hood element is considered for the finite element method (see Section 2.2.2), because the convergence of the simulation resulted better than MINI elements when considering non-Newtonian fluid.

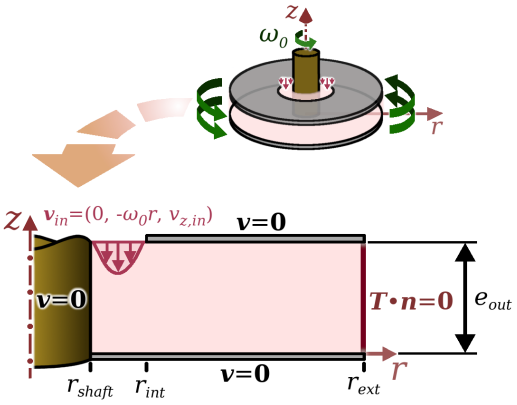
The specified fluid volume fraction (f) is chosen as 30%. The porous medium is assumed to be rotating together with the reference frame, which means that $\boldsymbol{v}_{\mathrm{mat}} = \boldsymbol{v}$. The initial guess for the pseudo-density (design variable) distribution is a uniform distribution of $\alpha = f - 1\%$, where f is the specified fluid volume fraction and 1% is a margin for the initial guess not to violate the volume constraint (because of the numerical accuracy of the calculations). The multi-objective function is considered through the initial weight approach (Section 2.5.4.1). The IPOPT algorithm (Section 3.1.1.1) is used for the optimization in this section.

The Reynolds number ($\mathrm{Re}_{\mathrm{ext},\ell}$) is considered from the external diameter ($2r_{ext}$), from Table 2.1. The post-processing is performed by smoothing by point cloud (Section 2.5.8.2.2).

5.1.4.1 Design domain and mesh

The numerical example consists of the design of a Tesla blood pump with a vertical inlet and a center shaft (Fig. 5.19a) (ALONSO *et al.*, 2019). The design domain is shown in Fig. 5.43.

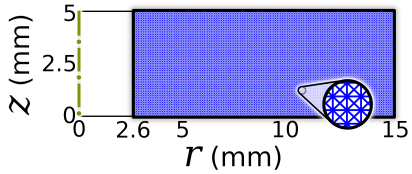
Figure 5.43 – Design domain for the Tesla blood pump design.



Source: Author (ALONSO; SILVA, 2021).

The dimensions from Fig. 5.43 are r_{shaft} = 2.6 mm, r_{int} = 5 mm, e_{out} = 5 mm, and r_{ext} = 15 mm. The inlet velocity profile is parabolic. The mesh is composed of 100 radial and 46 axial rectangular partitions of crossed triangular elements, totaling 10,277 nodes and 20,240 elements (see Fig. 5.44).

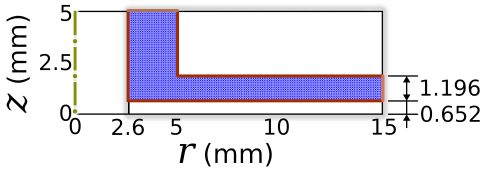
Figure 5.44 – Mesh used in the Tesla blood pump design.



Source: Author (ALONSO; SILVA, 2021).

A straight-channel Tesla pump (see Fig. 5.45) is simulated in order to compute the reference values for comparing with the optimized results in the following sections.

Figure 5.45 – Reference straight-channel Tesla pump for comparing with the optimized results.



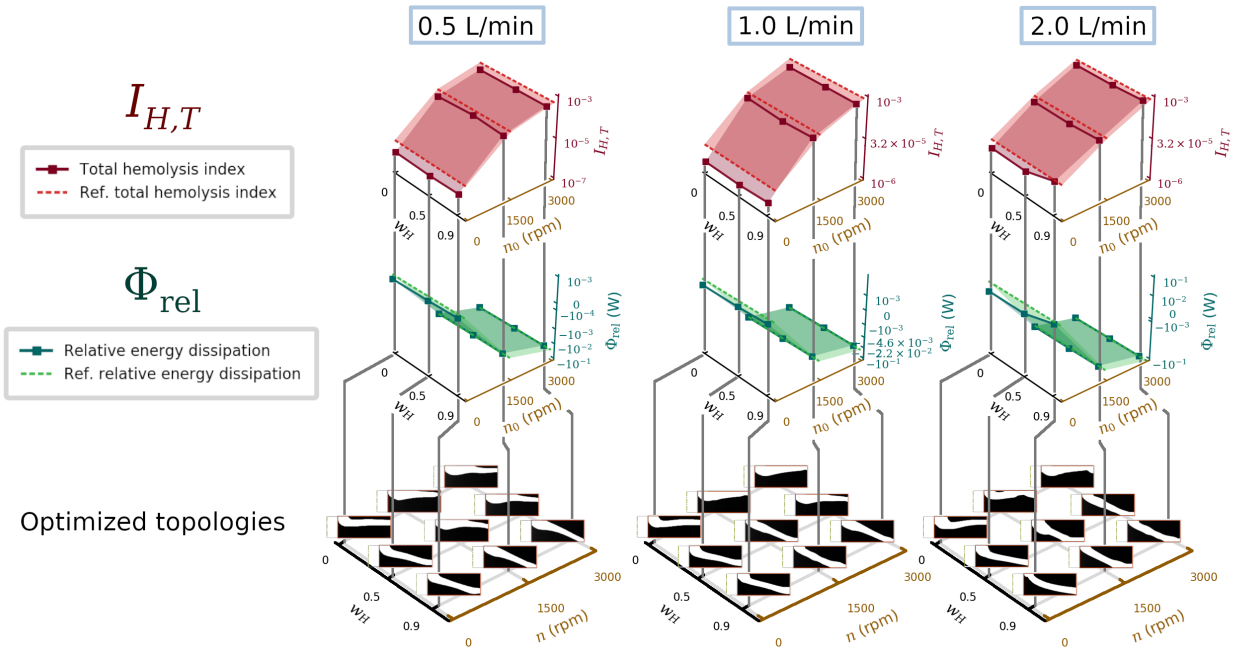
Source: Author (ALONSO; SILVA, 2021).

5.1.4.2 Topology optimization results

The effect of the hemolysis index in the multi-objective function (eq. (2.140)) is analyzed for $w_H = 0.1$, 0.5 and 0.9. The case for $w_H = 1.0$ is not evaluated, because the topology optimization is unable to form a fluid flow path in the optimized topology, with

the outlet completely blocked. This *completely blocked* outlet makes sense, because, if there is no fluid flow, the hemolysis index becomes minimal. The flow rates being considered are 0.5 L/min, 1 L/min and 2 L/min, and the rotations are 0 rpm, 1500 rpm and 3000 rpm. The optimized results for the two objective functions (total hemolysis index and relative energy dissipation) are shown in Fig. 5.46. Since the values of relative energy dissipation at 0 rpm are positive (due to the inertial term of eq. (2.51) being zero at 0 rpm), in order to plot all relative energy dissipation values in the same figure, the Matplotlib (HUNTER, 2007) *symlog* scheme is used, in which a logarithmic scale is used as "$\mathrm{sgn}(\Phi_{\mathrm{rel}})\log_{10}|\Phi_{\mathrm{rel}}|$" ("$\mathrm{sgn}(\Phi_{\mathrm{rel}})$" is the sign of Φ_{rel}), except near the zero value, around which a linear scale is used. Among the optimized results for 0 rpm, 1500 rpm and 3000 rpm, the only results in which the fluid flow device does not operate as a pump, correspond to 0 rpm, because there is only viscous dissipation inside the fluid flow device, without the fluid receiving rotational energy. This fact can also be noticed when computing the pressure head values, since the pressure head needs to be positive for the fluid flow device to pump fluid (i.e., to act as a pump).

Figure 5.46 – Total hemolysis index ($I_{H,T}$) and relative energy dissipation (Φ_{rel}) for the topology optimization considering the effect of the flow rate and rotation.



Source: Author (ALONSO; SILVA, 2021).

The optimization parameters that have been used in this work are shown in Table 5.17.

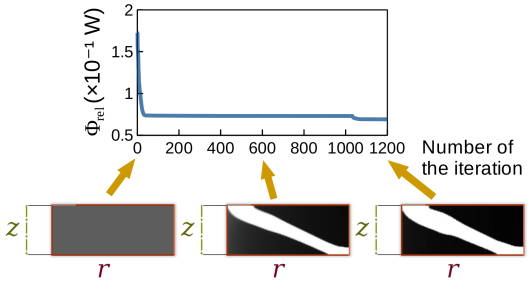
Table 5.17 – Optimization parameters for each optimized topology* ($q = 1$).

Flow rate (Q) (L/min)	Rotation (n_0) (rpm)	$\kappa_{\max}$ ($\times 10^8 \mu_\infty$) (kg/(m^{3}s))
0.5	0	5
	1500	50
	3000	100
1.0	0	5
	1500	50
	3000	80
2.0	0	5
	1500	80
	3000	100

* With the exception of the optimized results for "0.5 L/min, 0 rpm", "0.5 L/min, 1500 rpm, $w_H = 0$" and "0.5 L/min, 1500 rpm, $w_H = 0.5$", all other results consider a Helmholtz pseudo-density filter (Section 2.5.7.1) for better stabilizing the discrete optimized topologies. The filter length parameter (r_H) is set as 0.5 multiplied by the minimum element size in the mesh (i.e., the smallest of the maximum distances between any two vertices of all elements), leading to the value $r_H = 0.0564$ mm.

The convergence curve for the optimized topology for w_H = 0.5, 1 L/min and 1500 rpm is shown in Fig. 5.47. In the optimized results, the maximum Reynolds number is achieved at 3000 rpm, where, for all flow rates, $\mathrm{Re}_{\mathrm{ext},\ell} \approx 4.3 \times 10^4$. Since the transition Reynolds number in conventional pumps is in the order of 10^6 (SABERSKY *et al.*, 1971; WU, 2007), 4.3×10^4 should correspond to laminar flow.

Figure 5.47 – Convergence curve for the optimized topology for w_H = 0.5, 1 L/min and 1500 rpm.



Source: Author (ALONSO; SILVA, 2021).

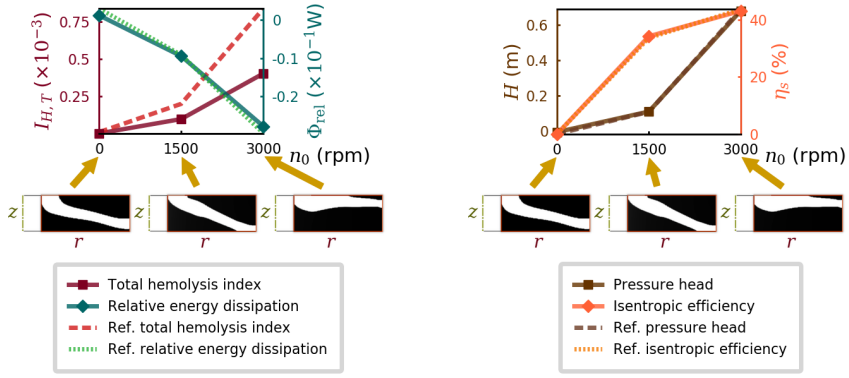
In Fig. 5.46, the reference values are shown by dashed lines, while the full lines correspond to the optimized topologies. As expected, higher rotations lead to higher total hemolysis index ($I_{H,T}$) values (i.e., higher hemolysis), and smaller relative energy dissipation values (Φ_{rel}), due to the rotational pumping motion (i.e., the inertial term in the relative energy dissipation (eq. (2.51))), which also leads to negative relative energy dissipation values (i.e., the fluid receiving more energy than dissipating it). As can be noticed from the total hemolysis index ($I_{H,T}$) plots, the optimized topologies lead to smaller hemolysis than the reference values. This can be explained by the fact that the

optimized topologies feature a “rounded” curve near the inlet, meaning that the fluid flow has a smoother change of direction in the optimized topologies than in the reference (Fig. 5.45), and which should lead to less induced stress over the RBCs. Also, the optimized topologies featuring inclined channels have smaller changes of fluid flow direction, which should also contribute to reducing the total hemolysis index. From the relative energy dissipation values (Φ_{rel}), it can be noticed that, at 0 rpm the optimized topologies lead to smaller relative energy dissipation values, but that difference is diminished at higher rotations. This difference may be better visualized in Fig. 5.48a, which shows the influence of the rotation in the topology optimization for 1 L/min and w_H = 0.5, in which the relative energy dissipation of the optimized topology achieves a higher value than the reference. Fig. 5.48a shows an improvement of about 50% of the total hemolysis index of the optimized topology with respect to the reference values. Fig. 5.48b shows the pressure head and isentropic efficiency, but no significant difference can be noticed comparing the optimized and reference values. For the variation of total/static pressure (Fig. 5.48c), the difference is also small.

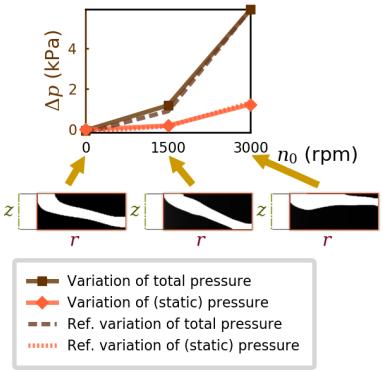
Figure 5.48 – Topology optimization results for different rotations (n_0) (for 1 L/min and w_H = 0.5).

(a) Total hemolysis index ($I_{H,T}$) and relative energy dissipation (Φ_{rel}).

(b) Pressure head (H) and isentropic efficiency (η_s).



(c) Variation of total (Δp_T) and static (Δp) pressures.



Source: Author (ALONSO; SILVA, 2021).

The optimized topologies from Fig. 5.48 show that the effect of the relative energy dissipation in the optimized topology seems to increase at higher rotations, given that the optimized topology connects to an outlet located at a higher height when the rotation is increased. This effect can also be seen in Fig. 5.46, where the optimized channel for w_H = 0.5 features an outlet located at a higher height, but, for w_H = 0.9, due to the higher effect of the total hemolysis index, the optimized topologies feature inclined channels (i.e., inclined disks). The higher position of the channels at lower w_H values (with the exception of 0 rpm) is probably due to the rotational motion of the fluid flow, which creates an inertial effect that creates a tendency for continuing the fluid motion at the same height. These *inclined disk*-like topologies slightly resemble some commercial Tesla pump devices that feature conical-shaped disks – BPX-80 BIO-Pump Plus (Medtronic®), CentriFlux BR-100 (Braile® Biomédica).

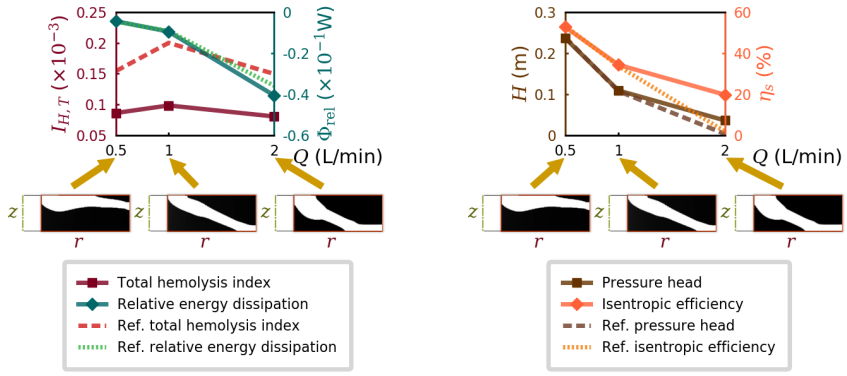
The effect of the flow rate from Fig. 5.46 is separated in Fig. 5.49, for 1500 rpm

and w_H = 0.5. As can be noticed in Fig. 5.49a, the total hemolysis index of the optimized topologies is much lower than the reference, and the relative energy dissipation is slightly smaller than the reference. One effect that can be noticed is that the total hemolysis index increases from 0.5 L/min to 1 L/min, but decreases from 1 L/min to 2 L/min. This is probably due, in the reference, to the fluid flowing close to the upper and lower surfaces for 0.5 L/min and 1 L/min, but closer to the lower surface for 2 L/min, which means that the shear stress is more concentrated below and with a higher velocity. In the case of the optimized topology, this change may be due to the change in topology, where the shear stress effect may be reduced on the straighter channel near the outlet. As can be noticed, the pressure head and isentropic efficiencies for the reference at 2 L/min in Fig. 5.49b is extremely low (around 0.003 m and 1%). This is because the minimum rotation required for the fluid flow device to act as a pump (i.e., with positive value for the pressure head) is higher for higher flow rates. It can be noticed that the pressure head and isentropic efficiency are higher for lower flow rates, which is a hint to this behavior. In the case of the reference at 2 L/min, the transition of behavior from a *dissipation channel* to a *pump-type device* is near 1500 rpm, which explains the extremely low pressure head and isentropic efficiency values at 2 L/min. This effect is more softened for the optimized topology for 2 L/min, because the new format changed the rotation of this transition of behavior to a lower value. Fig. 5.49c shows that the variation of total/static pressure is better for the optimized topologies for most cases, which should be due to the smoother change in curvature in the optimized results.

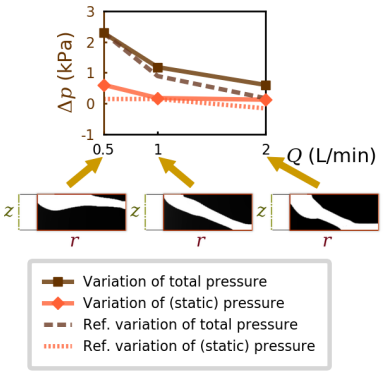
Figure 5.49 – Topology optimization results for different flow rates (Q) (for 1500 rpm and w_H = 0.5).

(a) Total hemolysis index ($I_{H,T}$) and relative energy dissipation (Φ_{rel}).

(b) Pressure head (H) and isentropic efficiency (η_s).



(c) Variation of total (Δp_T) and static (Δp) pressures.



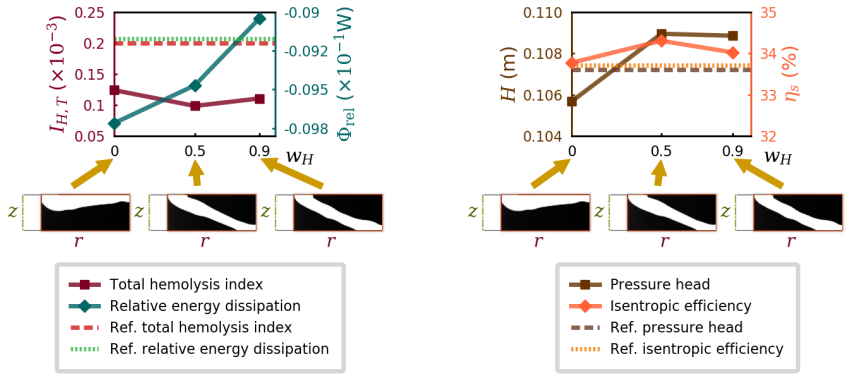
Source: Author (ALONSO; SILVA, 2021).

With respect to the composition of the multi-objective function, this effect is separated from Fig. 5.46 in Fig. 5.50, for 0.5 L/min and 1500 rpm. In this configuration, from Fig. 5.50, the values for the optimized topologies show a Pareto-like effect, in which the relative energy dissipation is worsened for higher w_H values, while the total hemolysis index improves (except from $w_H = 0.9$, where the total hemolysis index slightly worsens) due to the inclined channel/disks. In comparison to the reference values, the total hemolysis indices of the optimized topologies is always better, but the relative energy dissipation values gets worse than the reference for $w_H = 0.9$ probably due to “overprioritizing” the minimization of hemolysis in relation to the relative energy dissipation. This “overprioritization” led to a more *onstantly thicker* channel at $w_H = 0.9$, in comparison to the thinner channel at $w_H = 0.5$, which portrays a slight reduction in sectional area from the inlet to the outlet. In Fig. 5.50a, the inclined channels/disks in the optimized topologies ended up improving the pressure head value, but the isentropic

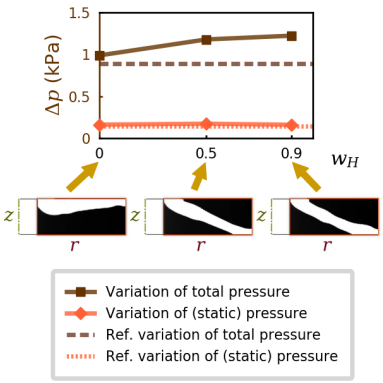
Figure 5.50 – Topology optimization results for different w_H values (for 1 L/min and 1500 rpm).

(a) Total hemolysis index ($I_{H,T}$) and relative energy dissipation (Φ_{rel}).

(b) Pressure head (H) and isentropic efficiency (η_s).



(c) Variation of total (Δp_T) and static (Δp) pressures.



Source: Author (ALONSO; SILVA, 2021).

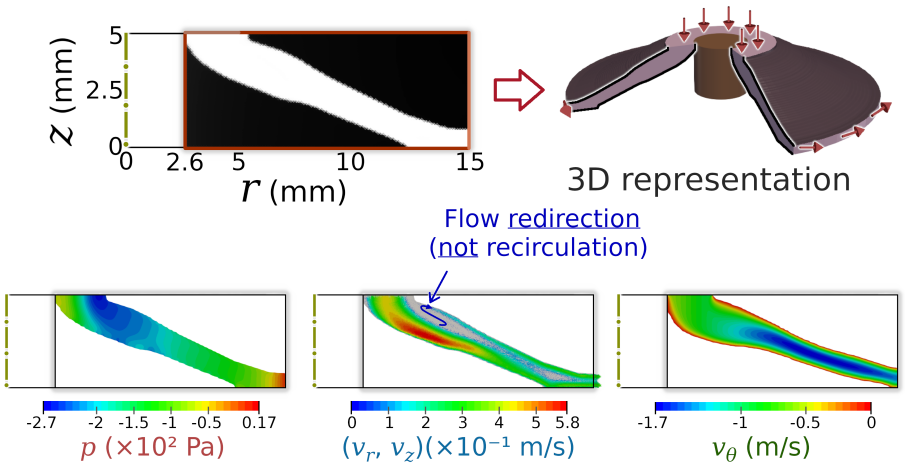
efficiency slightly drops at w_H = 0.9, which may also be caused by the same effect observed in the total hemolysis index from w_H = 0.5 to w_H = 0.9. With respect to the variation of total/static pressure (Fig. 5.50c), the optimized results are better than the reference, leading to higher variation of pressure values.

5.1.4.3 Simulation of the optimized result for w_H = 0.5, 1 L/min and 1500 rpm

The optimized topology for w_H = 0.5, 1 L/min and 1500 rpm, is simulated and is shown in Fig. 5.51. In Fig. 5.51, the 3D representation shows how the optimized topology is interpreted, with two specially shaped rotating disks. The pressure (p) plot shows that the main pressure increase occurs in the middle of the channel, which may mean that, if this length is increased (for larger Tesla pump devices), the pressure should also increase more. From the plot of the radial-axial velocity ((v_r, v_z)), two low velocity zones can be noticed. Both zones do not consist of flow recirculation, corresponding

to: (zone at higher height) A low-velocity flow redirection; (zone at lower height) Low velocity due to the presence of two separated boundary layers. The plot of the relative tangential velocity (v_θ) shows, as expected, that the higher tangential velocity is located on the rotating wall surfaces ($v_\theta = 0$, $v_{\theta,\text{abs}} = \omega_0 r$) and its value is lower where it is farther from the wall, due to the "dragging" effect from the Tesla principle.

Figure 5.51 – Optimized topology, 3D representation, pressure and velocity for w_H = 0.5, 1 L/min and 1500 rpm.

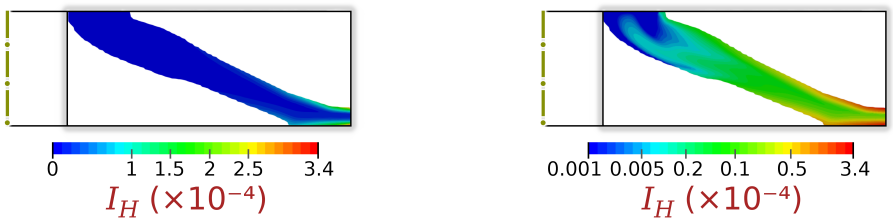


Source: Author (ALONSO; SILVA, 2021).

The local hemolysis index (I_H) is plotted in Fig. 5.52. As can be seen in Fig. 5.52a, the local hemolysis index is higher near the walls closer to the outlet, probably due to the higher shear stresses resulting from the higher fluid flow velocity and rotation. In order to better visualize the local hemolysis index distribution, Fig. 5.52b shows the same plot in logarithmic scale. As can be seen, the generation of hemolysis is small and approximately uniform in the "channel region" in the middle of the optimized topology, and highly increases near walls at higher radii due to the effect observed in Fig. 5.52a.

Figure 5.52 – Hemolysis index for the optimized topology for w_H = 0.5, 1 L/min and 1500 rpm.

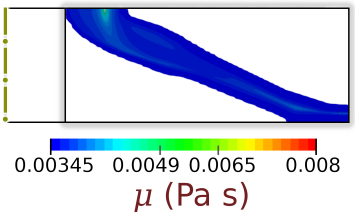
(a) Hemolysis index (normal scale). (b) Hemolysis index (logarithmic scale).



Source: Author (ALONSO; SILVA, 2021).

Since the fluid model for blood used in this work is non-Newtonian, the plot of the non-Newtonian viscosity values is shown in Fig. 5.53. As can be seen, the non-Newtonian viscosity is slightly higher at the inlet and keeps being higher near the middle of the channel section of the optimized topology. This higher viscosity means that the low-velocity redirection regions shown in Fig. 5.51 feature slightly higher viscosity values. Near walls, the non-Newtonian viscosity is smaller due to the higher shear stress.

Figure 5.53 – Non-Newtonian viscosity the optimized topology for w_H = 0.5, 1 L/min and 1500 rpm.



Source: Author (ALONSO; SILVA, 2021).

5.1.5 **Tesla blood pump design considering thrombosis**

In this section, the topology optimization method is applied to blood flow devices, considering the Brinkman-Forchheimer model (Section 2.5.1.3), blood (non-Newtonian fluid), a hemolysis model (Section 2.4.1) and a thrombosis model (Section 2.4.2) in topology optimization (ALONSO; SILVA, 2022a). The differences with respect to Section 5.1.4 are described as follows.

The multi-objective function is considered through the logarithmic approach (Section 2.5.4.2), with $f_{\text{scal}} = 10^3$. When considering the Helmholtz filter, eq. (2.158) is used. Also, the Riesz map adjustment from eq. (3.2) is considered. The post-processing is performed by smoothing by point cloud (Section 2.5.8.2.2), considering the use of the Savitzky-Golay filter (window size of 9, and degree of 2, remeshing resolution set as 128).

5.1.5.1 Design domain and mesh

The design of a Tesla-type blood pump, which has been previously considered for the hemolysis model in Alonso and Silva (2021), is considered here. The design domain and the mesh are the same from Section 5.1.4. The input parameters, geometric dimensions and material model parameters being considered in the design are shown in Table 5.18.

Table 5.18 – Parameters considered for the topology optimization of the Tesla blood pump.

Input parameters	
Inlet flow rate (Q)	1.0 L/min
Wall rotation (n_0)	2,000 rpm
Inlet velocity profile	Parabolic
Dimensions	
r_{shaft}	2.6 mm
r_{int}	5 mm
e_{out}	5 mm
r_{ext}	15 mm
Material model parameters*	
$\kappa_{\max}$ ($\times 10^9 \mu_\infty$ (kg/(m^3 s)))	8.0
q	1.0
$\kappa_{PAS,\max}$ (s^{-1})	10^2

* The optimization considers a Helmholtz pseudo-density filter (LAZAROV; SIGMUND, 2010) to better stabilize the discrete optimized topologies, with a filter length parameter of 0.0543 mm.

5.1.5.2 Topology optimization results

The topology optimization results for the PAS index are shown in Fig. 5.54. Higher w_{PAS} values than the ones shown in Fig. 5.54 are not considered, due to convergence issues. The maximum local Reynolds number in the optimized topologies is 2.9×10^4. The transition Reynolds number is in the order of 10^6 (in conventional pumps) (SABERSKY *et al.*, 1971; WU, 2007), meaning that 2.9×10^4 should correspond to laminar flow. As can be noticed in Fig. 5.54, a tendency to create an inclined channel can be seen when higher PAS index (i.e., thrombosis) weights (w_{PAS}) are considered. In Fig. 5.54a, it can be observed that the inclined channel topology is even better than the topology optimized for the relative energy dissipation ($w_\Phi = 1$). This lack of a Pareto-like behavior possibly means that the optimized topology for relative energy dissipation ($w_\Phi = 1$) is an "easier" local minimum for topology optimization, and the PAS index, even while being improved, coincidentally induced a better local minimum for the relative energy dissipation, also improving the hemolysis index, the pressure head, the isentropic efficiency and the variations of static and total pressures. In the case of $w_{PAS} = 0.4$, by comparing with $w_\Phi = 1$, the improvements would be -4.7% (relative energy dissipation), -5.4% (PAS index), -12.0% (hemolysis index), +3.0% (pressure head), +2.5% (isentropic efficiency), +16.8% (static pressure head), and +14.2% (total pressure head).

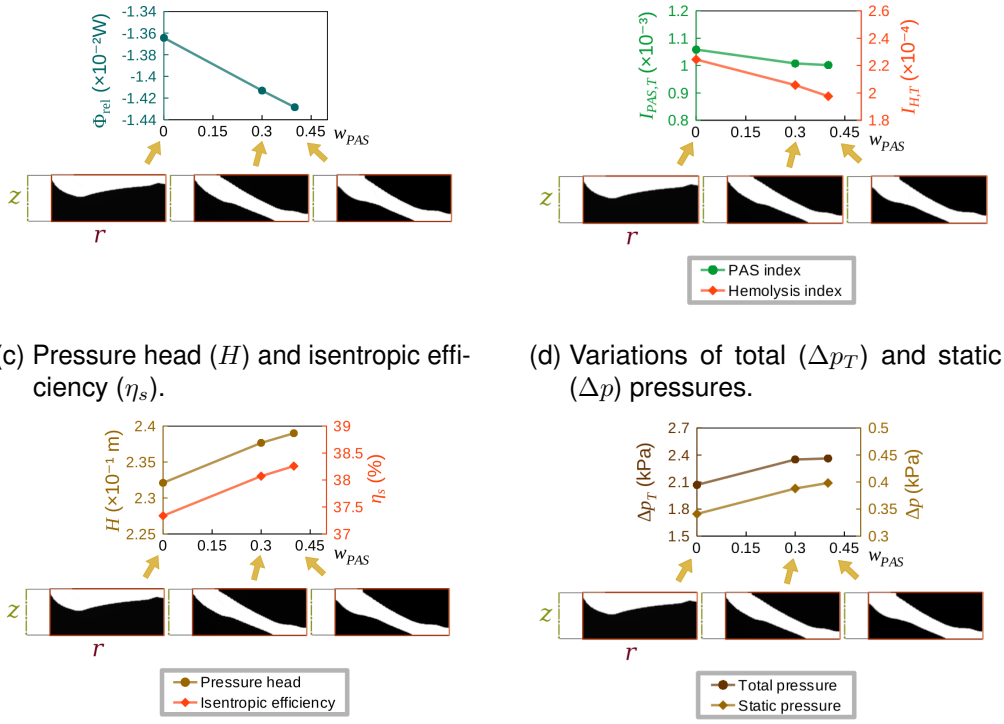
The topology optimization results for the hemolysis index are shown in Fig. 5.55. It can be noticed that the optimized topology for $w_H = 0.9$ is quite similar to the optimized topologies obtained for the PAS index (Fig. 5.54) (such as the one for $w_{PAS} = 0.4$). In fact, the small differences in the optimized topologies led the computed variables to even turn out better for $w_H = 0.9$.

For reference, an additional case combining both hemolysis and thrombosis is also considered ($w_{PAS} = 0.1$, $w_H = 0.5$). This additional case is shown in Fig. 5.56. In order to compare all of the optimized topologies, their relative values computed with respect to the reference design (Fig. 5.57) are shown in Table 5.19. As can be noticed, the worst result seems to be for $w_\Phi = 1$, which seems to indicate that the relative energy dissipation objective function induced a local minimum. This type of local minimum could possibly be avoided by taking blood damage into account in topology optimization, as can be seen from the values for the other optimized topologies. It can be noticed that the hemolysis index is significantly smaller in the optimized topologies, which is mainly due

Figure 5.54 – Topology optimization results for the Tesla blood pump under different weights in the multi-objective function for the PAS index.

(a) Relative energy dissipation (Φ_{rel}).

(b) PAS index ($I_{PAS,T}$) and hemolysis index ($I_{H,T}$).



(c) Pressure head (H) and isentropic efficiency (η_s).

(d) Variations of total (Δp_T) and static (Δp) pressures.

Source: Author (ALONSO; SILVA, 2022a).

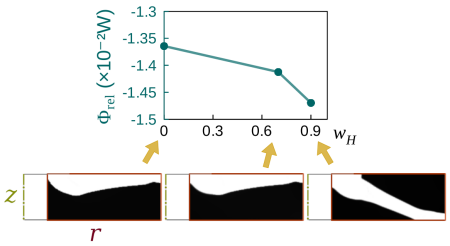
Table 5.19 – Relative comparison of the optimized topologies for the Tesla blood pump with the reference design (Fig. 5.57).

Designs	Φ_{rel}	$I_{PAS,T}$	$I_{H,T}$	H	η_s	Δp	Δp_T
$w_\Phi = 1$	+2.0%	-7.7%	-46.3%	-2.2%	-1.6%	-6.6%	+5.2%
$w_{PAS} = 0.3$	-1.5%	-12.1%	-50.8%	+0.1%	+0.3%	+6.3%	+19.5%
$w_{PAS} = 0.4$	-2.6%	-12.6%	-52.7%	+0.7%	+0.8%	+9.1%	+20.1%
$w_H = 0.7$	-1.4%	-13.3%	-48.8%	-2.3%	-1.2%	-1.9%	+7.9%
$w_H = 0.9$	-5.6%	-22.0%	-57.2%	+1.0%	+1.4%	+12.3%	+26.6%
$w_{PAS} = 0.1$ and $w_H = 0.5$	-3.8%	-13.8%	-53.0%	+0.5%	+0.9%	+10.2%	+19.6%

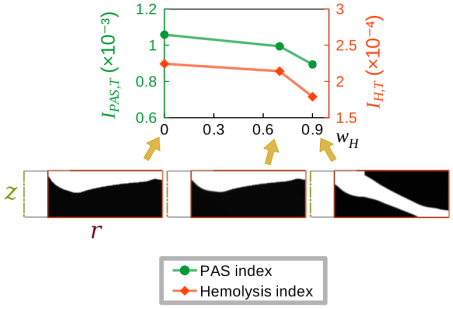
to the absence of a sharp edge that is present in the straight disks topology (Fig. 5.57). It can be noticed that the "combined" result ($w_{PAS} = 0.1$ and $w_H = 0.5$) (from Table 5.19) shows slightly better hemolysis and thrombosis with respect to $w_{PAS} = 0.4$ and $w_H = 0.7$, showing that it is possible to consider both effects in topology optimization. However, the best result that has been achieved is the one for $w_H = 0.9$, which resulted better than all other optimized topologies in all values. Thus, from Table 5.19, the "best" optimized topologies seem to be the one for $w_H = 0.9$, followed by the one for the combined case ($w_{PAS} = 0.1$ and $w_H = 0.5$).

Figure 5.55 – Topology optimization results for the Tesla blood pump under different weights in the multi-objective function for the hemolysis index.

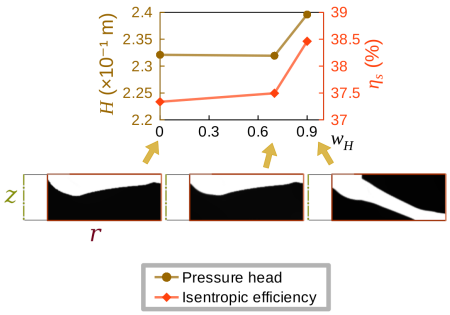
(a) Relative energy dissipation (Φ_{rel}).



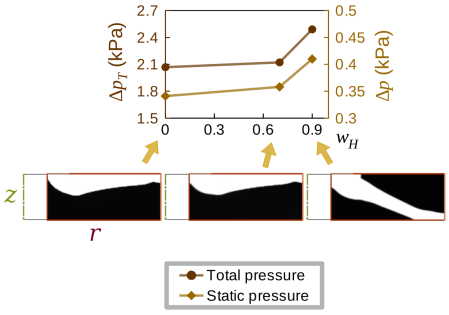
(b) PAS index ($I_{PAS,T}$) and hemolysis index ($I_{H,T}$).



(c) Pressure head (H) and isentropic efficiency (η_s).

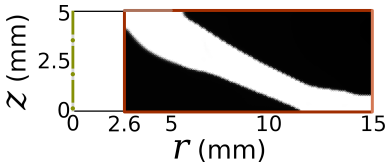


(d) Variations of total (Δp_T) and (Δp) static pressures.



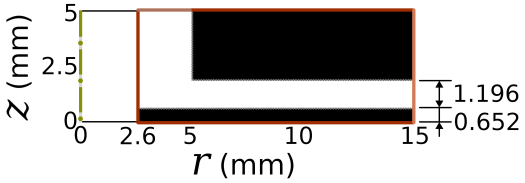
Source: Author (ALONSO; SILVA, 2022a).

Figure 5.56 – Optimized topology for the combined case ($w_{PAS} = 0.1$ and $w_H = 0.5$) for the Tesla blood pump.



Source: Author (ALONSO; SILVA, 2022a).

Figure 5.57 – Straight disks reference topology for the Tesla blood pump.

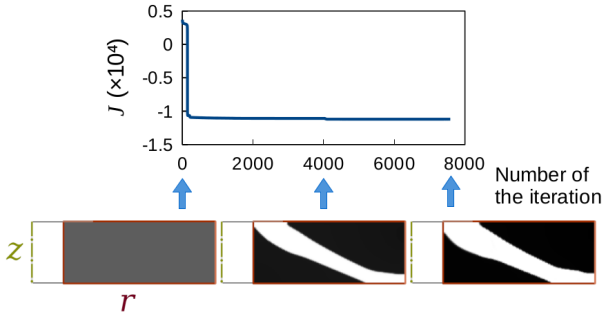


Source: Author (ALONSO; SILVA, 2022a).

In order to show an example of how the topology optimization progresses, the convergence curve of the topology optimization of the Tesla blood pump for the combined

case ($w_{PAS} = 0.1$ and $w_H = 0.5$) is shown in Fig. 5.58. The convergence curve behaves similarly for the other optimized topologies for the Tesla blood pump.

Figure 5.58 – Convergence curve of the topology optimization of the Tesla blood pump for the combined case ($w_{PAS} = 0.1$ and $w_H = 0.5$).



Source: Author (ALONSO; SILVA, 2022a).

5.1.5.3 Simulations of optimized results

The simulation results for the optimized topologies, for the combined case ($w_{PAS} = 0.1$ and $w_H = 0.5$) and for $w_H = 0.9$, are shown in Fig. 5.59. From the local hemolysis index (I_H) plots, it can be noticed that hemolysis is present at a greater intensity near the outlet. This, however, does not mean that the hemolysis near the inlet is zero (from the color scale), meaning that the hemolysis near the inlet is much smaller than near the outlet. The local PAS index (I_{PAS}) plot is more distributed along the computational domain than the hemolysis index. The pressure (p) in the middle part of the optimized topologies shows an approximately linear increase, while the radial-axial velocity (v_r, v_z) is concentrated mainly near the lower interface, although there is a smaller flow near the upper surface. The relative tangential velocity (v_θ) shows that, as the radius coordinate (r) increases, the fluid gets slower in the θ direction in the middle of the “channel”, which is consistent, since the fluid is being “dragged” near the walls. By comparing both optimized topologies, from Figs. 5.59a ($w_{PAS} = 0.1$ and $w_H = 0.5$) and 5.59b ($w_H = 0.9$), it can be noticed that the main difference is the initial curvature, which is more apparent in Fig. 5.59b ($w_H = 0.9$) than in Fig. 5.59a ($w_{PAS} = 0.1$ and $w_H = 0.5$). This seems to ease the change in flow direction (lower shear stresses), leading to lower hemolysis ($I_{H,T}$) and thrombosis ($I_{PAS,T}$) (see Table 5.19).

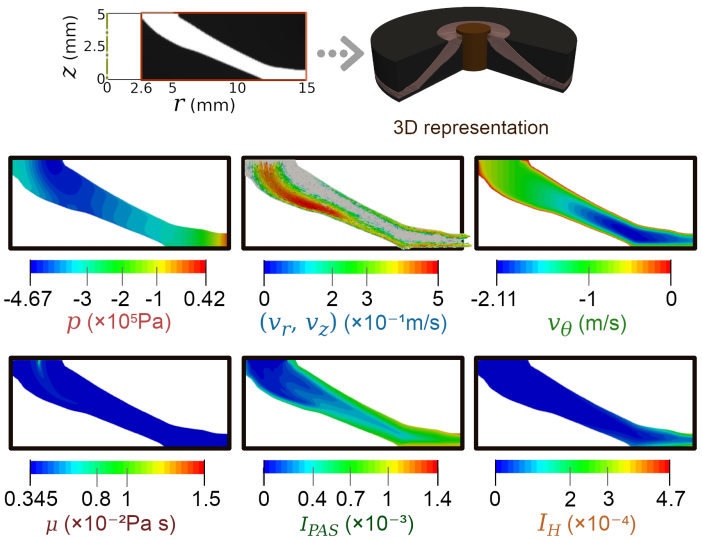
The non-Newtonian viscosity distributions are also shown in Fig. 5.59. It can be noticed that the non-Newtonian effect is more pronounced closer to the inlet and farther from the walls. This is due to the increase in shear stress when close to walls, which is

caused by the effect of the rotation and, consequently, by the *Tesla principle*.

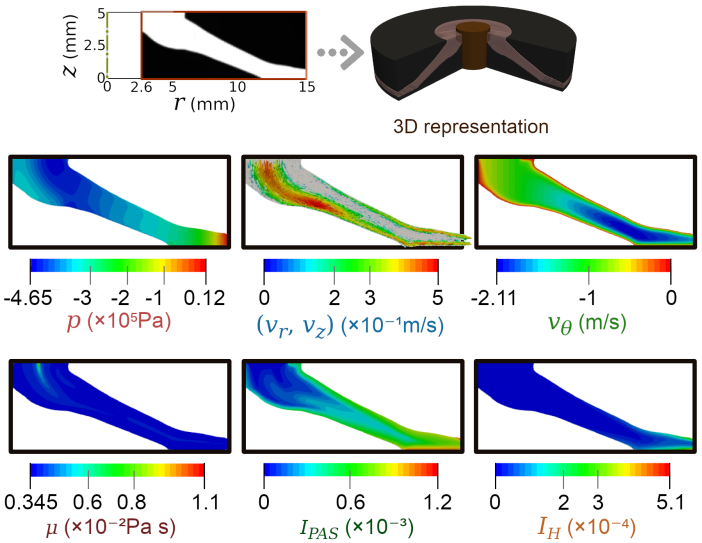
Since both hemolysis and thrombosis increase near the outlet walls, a relation between them can be perceived. This relation is given from the shear stress, which is present in their respective equations, which are eq. (2.84) and eqs. (2.120), (2.121), (2.122) and (2.123). However, as shown in Fig. 5.59, hemolysis and thrombosis still do not feature the exact same behavior, due to the different coefficients and other effects that are present in the thrombosis modeling (platelet sensitization and stress rate effects).

Figure 5.59 – Optimized topology, pressure, velocity, dynamic viscosity, PAS index, and hemolysis index for the optimized Tesla blood pump for two different cases.

(a) Optimized topology for the combined case ($w_{PAS} = 0.1$ and $w_H = 0.5$).



(b) Optimized topology for $w_H = 0.9$.

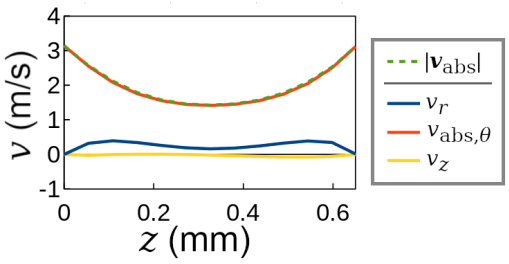


Source: Author (ALONSO; SILVA, 2022a).

5.1.6 **Volute design considering blood damage**

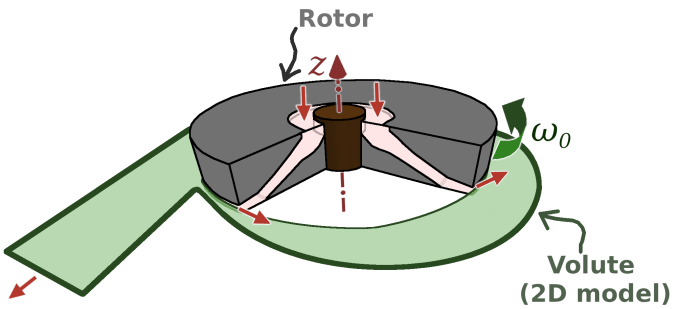
In this section, the volute is designed based on the Tesla pump rotor optimized topology for $w_H = 0.9$ for 1 L/min and 2000 rpm, which is the optimized topology from Section 5.1.5 that achieved the best results. The outlet velocities of the Tesla pump rotor (from Fig. 5.59b) are plotted as shown in Fig. 5.60. In order to design the volute through a 2D model, it is necessary to consider a single inlet velocity configuration. One possibility is considering the velocity in the middle of the outlet. The "2D plane" obtained from the middle of the outlet of the Tesla pump rotor is shown in Fig. 5.61. Although the 3D effect may have a significant effect in the values that are computed in the optimized design, due to the cross-section, such as those shown in Fig. 1.21, and the upper and lower walls, the main flow path can be optimized through a 2D model. The velocity values in the middle of the outlet, from the post-processed simulation (Fig. 5.59b) is shown in Table 5.20.

Figure 5.60 – Velocities on the outlet of the optimized Tesla pump rotor (1 L/min and 2000 rpm, $w_H = 0.9$).



Source: Author.

Figure 5.61 – Representation of the 2D model from the middle of the outlet of the rotor (the optimized Tesla pump rotor is shown in a *section view*).



Source: Author.

Table 5.20 – Average velocities on the outlet of the optimized Tesla pump rotor (1 L/min and 2000 rpm, $w_H = 0.9$), from Fig. 5.60.

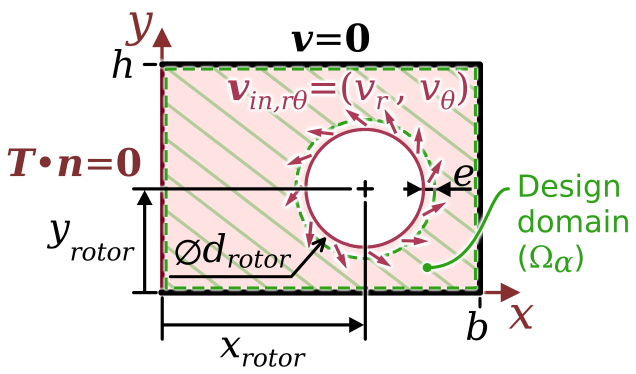
Average absolute velocity ($\|\boldsymbol{v}_{\text{abs}}\|\,|_{\text{out,middle}}$)	1.42 m/s
Average radial velocity component ($v_r|_{\text{out,middle}}$)	0.16 m/s
Average absolute tangential velocity component ($v_{\text{abs},\theta}|_{\text{out,middle}}$)	1.41 m/s
Average axial velocity component ($v_z|_{\text{out,middle}}$)	-0.019 m/s

From Table 5.20, it can be noticed that the axial velocity component ($\overline{v_z|_{\text{out}}}$) is smaller than the other components: 11.2% of $v_r|_{\text{out,middle}}$ and 1.3% of $v_{\text{abs},\theta}|_{\text{out,middle}}$. Although the small axial effect may become significant when considering a 3D simulation, it is neglected in the 2D approximation of the volute design. Also, from Table 5.20, the outlet velocity angle can be computed as $\arctan\left(\frac{v_{\text{abs},\theta}|_{\text{out,middle}}}{v_r|_{\text{out,middle}}}\right)$, which leads to an outlet angle of 83.5°.

5.1.6.1 Design domain and mesh

The design domain that is considered for the design is shown in Fig. 5.62. It consists of a rectangular domain with the fluid flow uniformly exiting a circular rotor with diameter "d_{rotor}" and entering the computational domain, which is represented in the absolute reference frame ($\omega_0 = 0$ rad/s). The outlet is left non-specified, in order to leave the outlet channel formation to topology optimization. The design domain is smaller than the computational domain, being given so as to leave a radial margin of thickness "e" outside it. This margin may be adjusted according to design requirements depending on the application (such as from the operating fluid, dimensions, manufacturing etc.). In particular, Tuzson (2000) recommends that the diameter of the base circle of the volute curve is 10% higher than the diameter of the rotor ($1.1d_{rotor}$), which would mean $e = 0.05d_{rotor}$. In this work, since the diameter of the rotor (d_{rotor}) is 30 mm, the thickness becomes $e = 0.05d_{rotor} = 1.5$ mm. In fact, this constraint may not have been necessary due to the topology optimization itself possibly being able to "naturally" create a margin close to 1.5 mm (SÁ, 2019), but it may be necessary to explicitly impose it in other design configurations, in order for the topology optimization not to include solid material too close to the rotor (ALONSO, 2017, 2018).

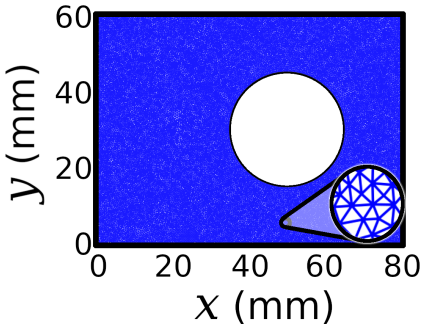
Figure 5.62 – Domain for the design of the volute.



Source: Author.

The mesh is unstructured, with a resolution of 128 (in this context, *resolution* is approximately equal to the diameter of the computational domain divided by the cell size) composed of 21,151 nodes and 41,561 elements (see Fig. 5.63). In particular, the mesh is adjusted in order to exactly match the radial margin of thickness "e", which is possible in FEniCS mshr. The input parameters, geometric dimensions and material model parameters being considered in the design are shown in Table 5.21. The specified fluid volume fraction (f) is set as 30%. The initial guess is a circular volute, in which a straight channel with a 10 mm width is set tangential to the non-optimizable circle (see the first topology of Fig. 5.69).

Figure 5.63 – Mesh for the design of the volute.



Source: Author.

Table 5.21 – Parameters used for the topology optimization of the volute.

Input parameters	
Inlet velocity	$v_r = 0.16$ m/s, $v_\theta = 1.41$ m/s
Dimensions	
h	60 mm
b	80 mm
x_{rotor}	50 mm
y_{rotor}	30 mm
d_{rotor}	30 mm
e	1.5 mm
Material model parameters*	
κ_{max} ($\times 10^8 \mu_\infty$ (kg/(m^3 s)))	1.0
q	1.0
$\kappa_{PAS,\max}$ (s^{-1})	10^4 (for w_{PAS} = 0.5) 0.1 (for w_{PAS} = 0.9) 10^2 (for "w_{PAS} = 0.3 and w_H = 0.3")

* The optimization considers a Helmholtz pseudo-density filter (Section 2.5.7.1) in order to better stabilize the discrete optimized topologies. The filter length parameter (r_H) is chosen as the value $r_H = 0.357$ mm, but is increased to $r_H = 0.536$ mm for w_H = 0.9 (in order to allow the convergence of the optimized topology), and for w_{PAS} = 0.5 (in order to allow the convergence of the optimized topology for $\kappa_{PAS,\max} = 10^4$). The choice of $\kappa_{PAS,\max}$ was adjusted in order to help the convergence of the optimized topologies.

In order to ease the convergence of the performed simulations, which suffered difficulties in FEniCS, the simulation is performed in OpenFOAM®, by considering 500 iterations of the SIMPLE algorithm for each topology optimization iteration, and using the previous simulation as the initial guess for the next simulation. The fluid flow regime is assumed as laminar, for consistency with the Tesla pump rotor design. As in the Tesla pump rotor design, the fluid is considered as blood (non-Newtonian fluid), with the non-Newtonian dynamic viscosity ($\mu = \mu(\dot{\gamma}_{\text{m}})$) given by eq. (2.11), with non-Newtonian penalization (eq. (2.135)), and with density (ρ) given as 1056 kg/m^3 (HINGHOFER-SZALKAY; GREENLEAF, 1987) (Sections 1.1.1, 2.1.2.1 and 5.1.3). Also, the Brinkman-Forchheimer model (Section 2.5.1.3) is considered. In the finite element modeling, Taylor-Hood elements are considered, also for consistency with the Tesla pump rotor design. The multi-objective function is considered through the logarithmic approach (Section 2.5.4.2), with $f_{\text{scal}} = 10^3$. The post-processing is performed by smoothing by point cloud (Section 2.5.8.2.2) considering the use of Chaikin's corner cutting algorithm (repeated 3 times, remeshing resolution set as 128). When considering the Helmholtz filter, eq. (2.158) is not considered, because the topology optimization showed better convergence to the optimized topology without it. The TOBS algorithm

(Section 3.1.1.2) is used for the optimization in this section, by considering $\varepsilon_{\text{relax}} = 0.005$ and $\beta_{\text{flip limit}} = 0.005$ for w_Φ = 1.0, and $\varepsilon_{\text{relax}} = 0.05$ and $\beta_{\text{flip limit}} = 0.05$ for the other results.

In the optimized results, the maximum computed Reynolds number, from eq. (2.74), that has been achieved is $\text{Re}_{\text{ext},\ell} \approx 2.45 \times 10^4$, which most probably consists of laminar flow, or, at most, flow transitioning from laminar to turbulent regime. If the Reynolds number is compared to the one for channels, which is based on the channel diameter/width as the characteristic length, it can be noticed, from the optimized topologies of this section, that $\text{Re}_{\text{ext},\ell}$ would become, with the characteristic length being the channel diameter/width, about 4 times smaller, resulting in $\approx 7,719$, which is higher than the transition Reynolds number in pipes (about 2,100 (MUNSON *et al.*, 2009)). Therefore, the flow in the volute may be possibly transitioning from laminar flow (from the rotor) to turbulent flow. However, since the flow exiting the volute has a tangential effect, which makes it different from pipes, it becomes even harder, without the aid of experiments, to define whether the flow really transitions inside it or not. Nonetheless, the approach that is normally followed is to assume laminar or fully turbulent flow, as mentioned in Section 1.1.1.4 (FRASER *et al.*, 2011; SABERSKY *et al.*, 1971; WU, 2007). Considering that there is a 3D effect that is not considered in the modeling, which should possibly decrease the velocities and/or turbulent effect, and that the simulation is able to effectively converge for the given flow rates and rotations without the appearance of any transient effects when considering laminar flow modeling (which would possibly mean the transition to turbulent flow), the volute design is performed considering laminar flow in this section. If the fluid flow began transitioning from laminar to turbulent flow inside the volute, this would possibly only be able to be verified through experiments. Furthermore, if the turbulence effect in the transition is still small, the laminar flow modeling may possibly be viewed as a “rough” approximation of the statistical time average effect (i.e., a “RANS model that neglects a small turbulent viscosity”). In fact, some simulations performed with the configuration of this section show that, even when a turbulence model (such as WA2018) is considered with an inlet turbulence, the turbulence ends up decreasing towards the outlet, which may indicate that, if the flow exiting the rotor is laminar, the flow in the volute may also be.

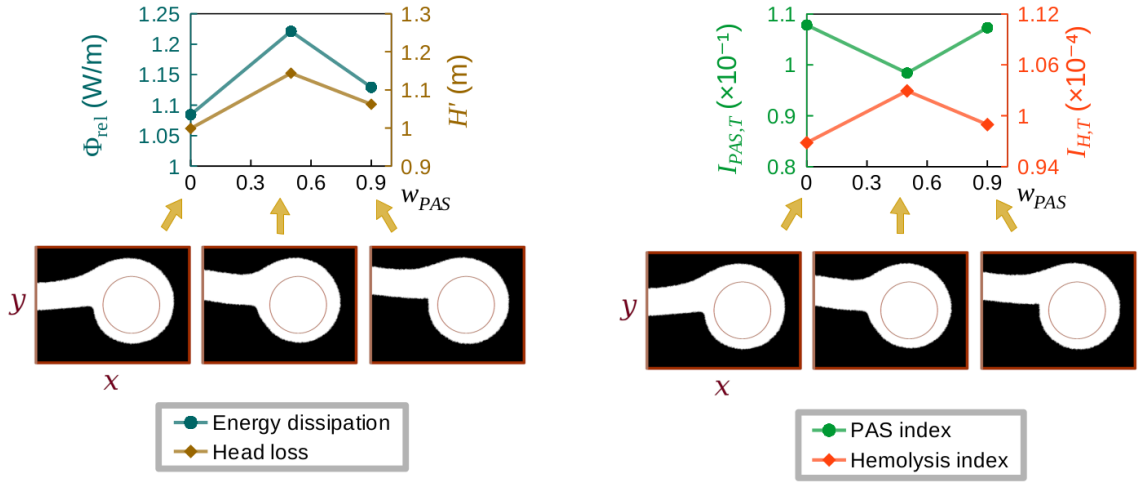
5.1.6.2 Topology optimization results

The topology optimization results for the PAS index are shown in Fig. 5.64. As can be noticed, since thrombosis was the only quantity that was improved (Fig. 5.64), this improvement can be said to be at the expense of all other quantities. Therefore, there seems to be a tradeoff between improving thrombosis, and improving the performance and the hemolysis in the volute. In essence, these improvements in thrombosis seem to be caused by: (1) drastically reducing the size of the *tongue* of the volute (see the optimized topology for $w_{PAS} = 0.5$); (2) having a slightly sharper *tongue* and a slightly larger flow path (see the optimized topology for $w_{PAS} = 0.9$). It can be mentioned that the optimized topology for $w_{PAS} = 0.9$ is most probably a local minimum, which is, in fact, the same as the optimized topology for $w_{\Phi} = 1$, but rotated and with a slightly sharper tongue.

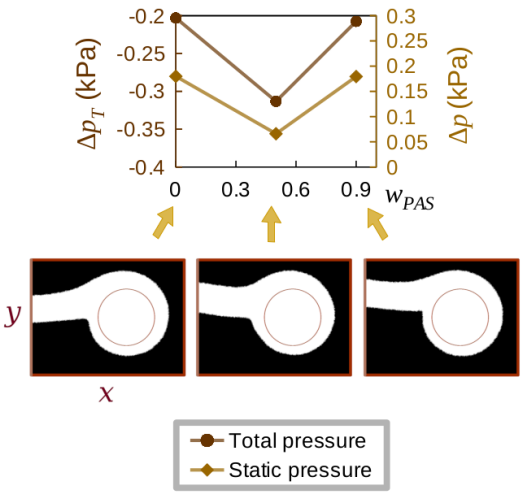
Figure 5.64 – Topology optimization results for the volute under different weights in the multi-objective function for the PAS index.

(a) Energy dissipation ($\Phi_{\text{rel}} = \Phi_{\text{abs}}$) and head loss ($H'$).

(b) PAS index (I_{PAS}) and hemolysis index (I_H).



(c) Variation of total (Δp_T) and static (Δp) pressures.



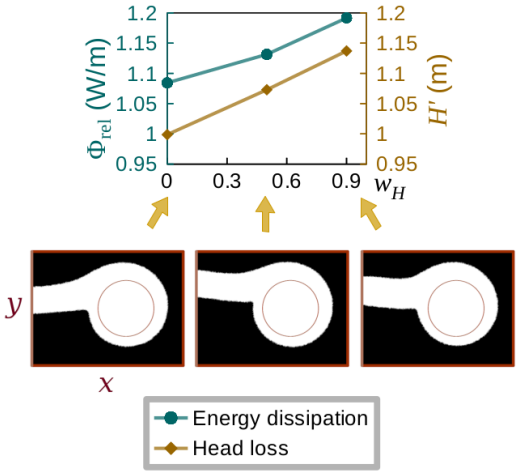
Source: Author.

The topology optimization results for the hemolysis index are shown in Fig. 5.65. As can be noticed, similarly to what has been observed for the topology optimization results for the PAS index (Fig. 5.64), there seems to be a tradeoff between hemolysis, and performance and thrombosis. By comparing the optimized topology for $w_H = 0.5$ (Fig. 5.65) with the optimized topology for $w_{PAS} = 0.9$ (Fig. 5.64), it can be noticed that they are strikingly similar, although with slight curvature and tongue differences. The optimized topology for $w_H = 0.9$ (Fig. 5.65) is similar to the optimized topology for $w_{PAS} = 0.5$ (Fig. 5.64), in which, although there is a slight curvature change in the outlet channel, the main difference is the slightly sharper tongue in the hemolysis case. This

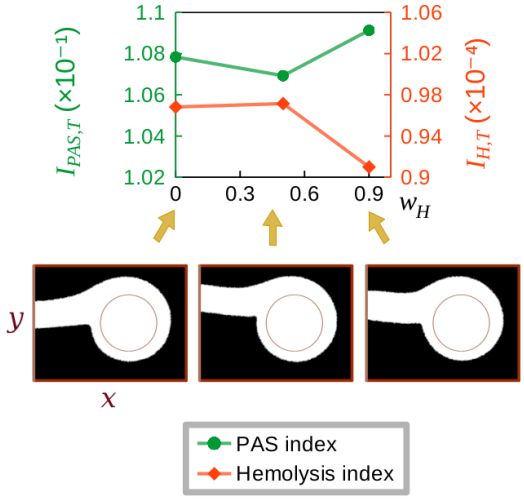
can be seen in the contours plotted in Fig. 5.66.

Figure 5.65 – Topology optimization results for the volute under different weights in the multi-objective function for the hemolysis index.

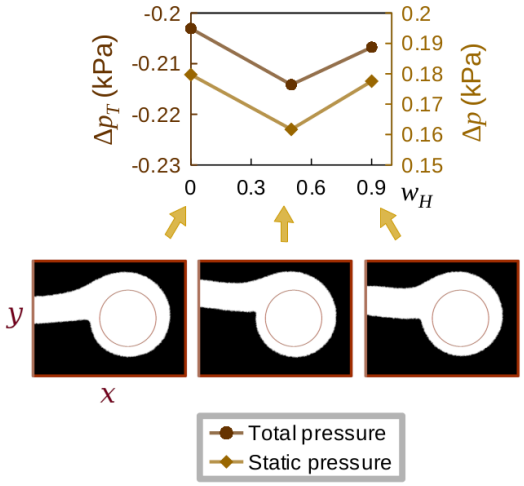
(a) Energy dissipation ($\Phi_{\text{rel}} = \Phi_{\text{abs}}$) and head loss ($H'$).



(b) PAS index (I_{PAS}) and hemolysis index (I_H).

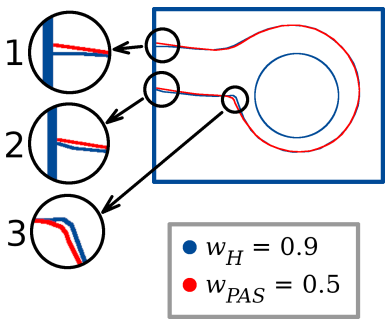


(c) Variation of total (Δp_T) and static (Δp) pressures.



Source: Author.

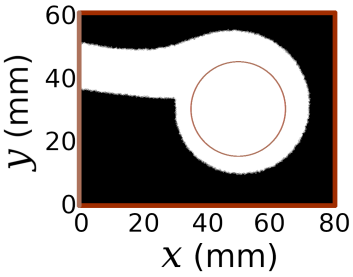
Figure 5.66 – Contours of the optimized topologies for $w_H = 0.9$ and $w_{PAS} = 0.5$.



Source: Author.

Furthermore, a combined case, considering both hemolysis and thrombosis in the multi-objective function is considered (for $w_{PAS} = 0.3$ and $w_H = 0.3$). The optimized topology is shown in Fig. 5.67, and is similar to the optimized topologies for $w_\Phi = 1$, $w_H = 0.5$ and $w_{PAS} = 0.9$, with slight curvature changes.

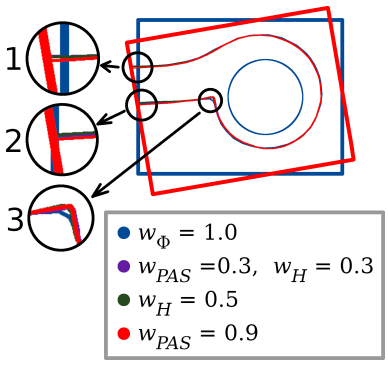
Figure 5.67 – Optimized topology for the combined case ($w_{PAS} = 0.3$ and $w_H = 0.3$) for the volute.



Source: Author.

In order to be able to better visualize the slight differences between the optimized topologies for $w_\Phi = 1$, "$w_H = 0.5$ and $w_{PAS} = 0.9$", $w_H = 0.5$, and $w_{PAS} = 0.9$, Fig. 5.68 shows the contours of these optimized topologies. As can be noticed, the contours for "$w_H = 0.5$ and $w_{PAS} = 0.9$", $w_H = 0.5$, and $w_{PAS} = 0.9$ are rotated according to the red-colored rectangle, in order to show their resemblance with the optimized topology for $w_\Phi = 1$.

Figure 5.68 – Contours of the optimized topologies for $w_\Phi = 1$, "$w_H = 0.5$ and $w_{PAS} = 0.9$", $w_H = 0.5$ and $w_{PAS} = 0.9$.



Source: Author.

The optimized topologies can be compared in Table 5.22, with respect to the optimized topology for $w_\Phi = 1$. As can be seen from Table 5.22, none of the represented optimized results are better in both hemolysis and thrombosis than the optimized result for $w_\Phi = 1$ (reference for these comparisons), and they are also worse in terms of performance (higher energy dissipation, higher head loss, and lower variations of

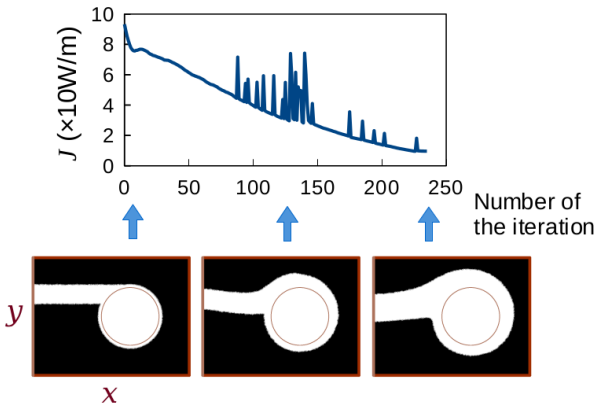
pressure). In fact, it has also been observed that the optimized topology for $w_\Phi = 1$ is a local minimum for hemolysis and thrombosis. This fact was verified by considering the optimized topology for $w_\Phi = 1$ as the initial guess for the topology optimization considering hemolysis and/or thrombosis. Therefore, the optimized topology for $w_\Phi = 1$ seems to be a good compromise for improving energy dissipation, thrombosis, hemolysis and head loss.

Table 5.22 – Relative comparison of the optimized topologies for the volute with the optimized topology for $w_\Phi = 1$.

Designs	Φ	$I_{PAS,T}$	$I_{H,T}$	H'	Δp	Δp_T
$w_{PAS} = 0.5$	+12.6%	-8.8%	+6.3%	+14.5%	-63.3%	-54.3%
$w_{PAS} = 0.9$	+4.2%	-0.5%	+2.2%	+6.4%	-0.2%	-2.2%
$w_H = 0.5$	+4.3%	-0.8%	+0.3%	+7.4%	-10.0%	-5.5%
$w_H = 0.9$	+9.9%	+1.2%	-6.0%	+13.9%	-1.2%	-1.8%
$w_{PAS} = 0.3$ and $w_H = 0.3$	+5.7%	-1.7%	+1.9%	+11.9%	-7.9%	-6.0%

The convergence curve for $w_\Phi = 1$ is shown in Fig. 5.69.

Figure 5.69 – Convergence curve of the topology optimization of the volute for $w_\Phi = 1$.



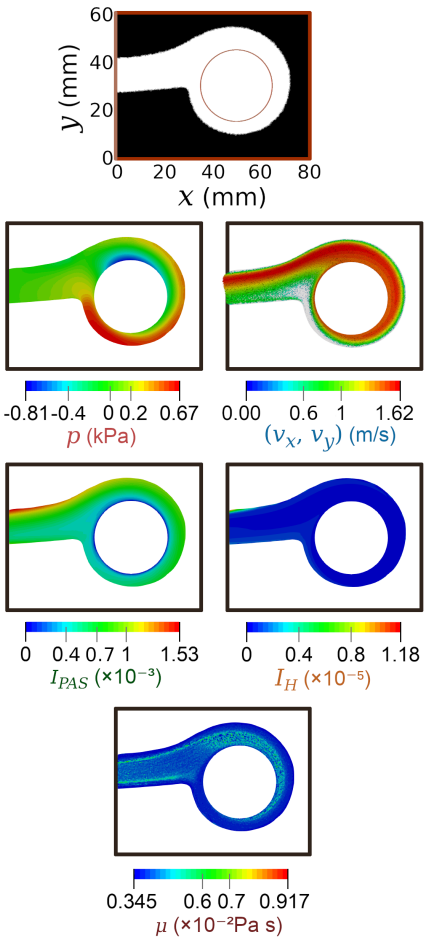
Source: Author.

5.1.6.3 Simulation of the optimized result for $w_\Phi = 1$

The simulation of the optimized result for $w_\Phi = 1$ is shown in Fig. 5.70. From it, it can be noticed that the fluid exiting the rotor accelerates mostly closer to the upper wall, while the pressure is not uniform around the rotor and ends up increasing towards the outlet. The local PAS index seems to be more apparent near the upper wall close to the outlet, where there is a small distance between the high velocity flow and the wall, while the local hemolysis index seems to be highly concentrated in a similar way. The non-Newtonian viscosity also shows its effect mainly in zones that are slightly far from

the walls. It can be noticed that the optimized topology is similar to a single-volute with a volute shape (Fig. 1.20)

Figure 5.70 – Optimized topology, pressure, velocity, PAS index, hemolysis index and dynamic viscosity for the optimized volute for $w_\Phi = 1$.



Source: Author.

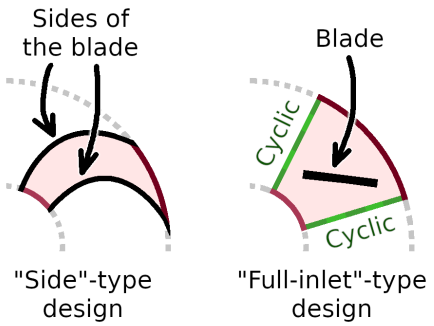
For the simulation in Fig. 5.70, the static pressure recovery coefficient ($c_{p,R}$) becomes 0.26, while the total pressure loss coefficient ($c_{p,T,L}$) becomes 0.3, leading the unified pressure performance coefficient ($c_{p,U}$) to 0.89. This means that about 26% of the dynamic pressure from the rotor was able to be converted to static pressure, while suffering 30% losses, leading to a performance of 89% for the volute to convert the dynamic pressure coming from the rotor to static pressure.

5.1.7 **Bladed pump design considering blood damage**

Among the possible Tesla pump designs, there is the possibility of incorporating blades in the Tesla pump rotor, resulting in a *hybrid* design, as mentioned in Section 1.1.2.1 (for example, the Rotaflow pump design, and the Tesla-Pelton disks from Fig. 1.12c), which would aim to combine the effect of the Tesla principle with the variation of linear momentum (blades). As such, a 2D model is used to consider the inclusion of the blades (ROMERO; SILVA, 2014; ROMERO; SILVA, 2017; SÁ *et al.*, 2017; SÁ *et al.*, 2018; SÁ *et al.*, 2021). In a generic case, it would also be possible to consider a 3D model (OKUBO *et al.*, 2021), but the computational cost would increase, and the Tesla principle effect is not guaranteed to be significant in the final optimized topology.

In this work, two types of design are considered for topology optimization, which are shown in Fig. 5.71. The first design is the *side*-type design, in which the fluid flow path between blades is designed. As can be noticed, this type of design focuses on the flow between the blades rather than considering the incoming fluid colliding with the blades. It can also be mentioned that the design of the fluid flow path resembles the rotor design configuration of the commercial Medtronic/HeartWare HVAD® , and that this design may be performed without the need of imposing cyclic boundary conditions. The second design is the *full-inlet*-type design, in which the inlet is not bounded by walls, enabling the possibility of designing blades inside the design domain. In this case, it is strictly necessary to impose cyclic boundary conditions in order to consider replicating small blades along the rotor. The entire rotor circumference is not considered as the design domain, and, instead, smaller sections of it are considered, because the optimized rotor needs to be balanced (in order to reduce vibration), which may be achieved through *cyclically* replicating the smaller designs (OKUBO *et al.*, 2021). It can also be highlighted that the values computed in the optimized topologies from both approaches (*side*-type design and *full-inlet*-type design) are not directly comparable, due to the fact that one considers the incoming fluid colliding with the blades, and the other does not.

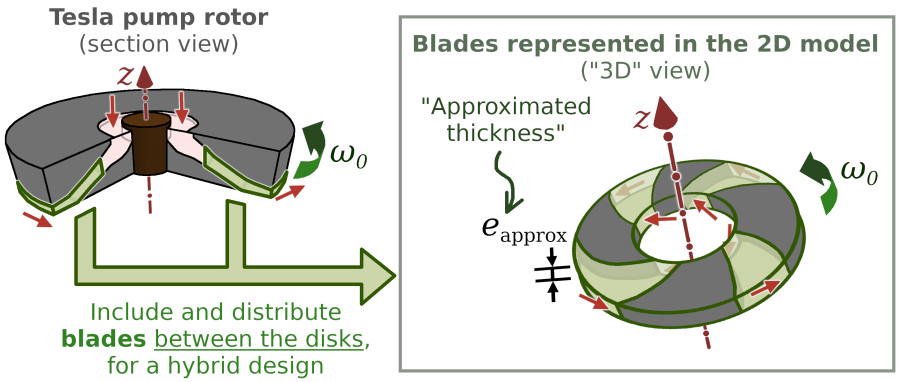
Figure 5.71 – Types of design that may be considered for bladed rotor topology optimization.



Source: Author.

In this section, the optimized topology of the Tesla pump rotor for $w_H = 0.9$ for 1 L/min and 2000 rpm, which is the optimized design from Section 5.1.5, is considered. Fig. 5.72 shows how the approximation of the blades is performed for obtaining the hybrid Tesla pump rotor, for the *side*-type design for 4 blades. In the optimized topology for the Tesla pump rotor (from the 2D swirl flow model), a part of the optimized topology is chosen in order to accomodate the blades. The internal radius of the zone (r'_{int}) is selected such as not to be excessively affected by the change in the axial velocity. In this work, from the Tesla pump rotor from Fig. 5.59b, this radius is selected as $r'_{int} = 7$ mm, which is consists of the zone that is slightly after the "bend" of the optimized topology. Then, the *thickness* of the blades in the Tesla pump rotor is approximated by a constant thickness, which is selected as $e_{approx} = 1$ mm. The approximation of the thickness is only used for computing the inlet velocities of the bladed rotor.

Figure 5.72 – Example of the 2D design of blades for a hybrid Tesla pump rotor (*side*-type design for 4 blades).



Source: Author.

In this work, the design of 5 blades is considered (i.e., 5 inlets ($n_{\mathrm{b,in}} = 5$) in the *side*-type design, and an angle of 72° (360°/5) in the *cyclic* section of the *full-inlet*-type

design). Then, the flow rate ($Q = 1$ L/min) may be used for computing the corresponding *2D flow rate* (Q_{2D}) inside the design domain, which may be given in "(m^3/s)/m" (or "(L/min)/m"), for a single inlet (considering that there are 5 inlets – $n_{\mathrm{b,in}} = 5$):

$$Q_{2D} = \frac{1}{n_{\mathrm{b,in}}} \frac{Q}{e_{approx}} = \frac{1}{5} \left(\frac{1 \text{ L/min}}{1 \text{ mm}} \right) = 0.2 \text{ (L/min)/mm} = 200 \text{ (L/min)/m} \tag{5.3}$$

Then, from eq. (5.3), the velocity profile may be computed for a constant radial velocity profile (ROMERO; SILVA, 2014). Specifically for the *side*-type design, a parabolic radial velocity profile may also be considered (SÁ *et al.*, 2018). In this work, the inlet velocity profile is considered to be radially constant in all bladed pump designs that are performed. Another assumption in this model is that the rotation of the inlet flow is considered as the same as the rotation of the rotor (2000 rpm).

After the design, the blades are included in the Tesla pump rotor by *projecting* the optimized topologies in the axial (z) direction, according to the radial (r) coordinates, in the highlighted zones shown in the left side of Fig. 5.72. It can be pointed out that the fluid flow path between both models (2D and 3D) is different, because the optimized topology of the Tesla pump rotor (2D swirl flow model) features an *inclined channel*, whereas the 2D model assumes that the channel is fully horizontal, going radially from r'_{int} to the external radius (r_{ext}). It should be possible to take the inclination effect into a special *2D model* that considers only the central line of the Tesla pump rotor while neglecting any perpendicular velocity component. However, this should lead the model to become more complex and possibly lead to convergence issues in FEniCS. Nonetheless, an implementation in OpenFOAM®, which allows easier fluid flow convergence than FEniCS, would possibly be quite complex, because OpenFOAM® does not have built-in support for custom integration domains and custom differential operators.

5.1.7.1 *Side*-type design

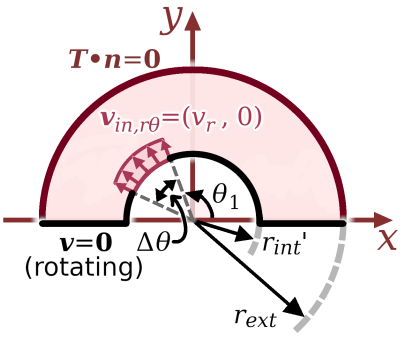
The *side*-type design consists of optimizing the fluid flow path between blades, and is considered for topology optimization in the following subsections.

5.1.7.1.1 *Design domain and mesh*

From Fig. 5.72, it may be noticed that the flow between each pair of blades is independent from one another. Thus, this design approach consists of designing

the format of the blades between a single pair of blades, and then replicate this same format a predefined amount of times around the rotation axis (ROMERO; SILVA, 2014; ROMERO; SILVA, 2017; SÁ *et al.*, 2017; SÁ *et al.*, 2018; SÁ *et al.*, 2021), achieving a format as shown in Fig. 5.72. The design domain selected in this work is shown in Fig. 5.73, for a 180° design domain. Particularly, in this work, the right-hand rule is chosen for defining the rotation of the rotor (i.e., ω_0 is set for the positive direction of the z axis). Therefore, the optimized topologies may be related to previous works which rely on the left-hand rule for the rotation (ROMERO; SILVA, 2014; ROMERO; SILVA, 2017; SÁ *et al.*, 2017; SÁ *et al.*, 2018; SÁ *et al.*, 2021) by *mirroring* them around the y axis.

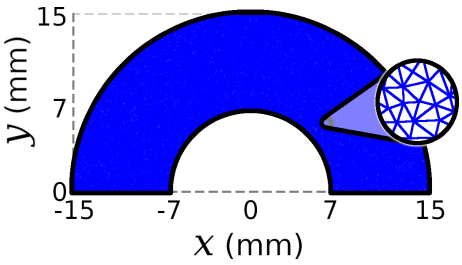
Figure 5.73 – Domain for the design of the bladed pump (*side*-type design).



Source: Author.

The mesh is unstructured, with a resolution of 128 (in this context, “resolution” is approximately equal to the diameter of the computational domain divided by the cell size) composed of 17,642 nodes and 34,554 elements (see Fig. 5.74). The input parameters, geometric dimensions and material model parameters being considered in the design are shown in Table 5.23. The specified fluid volume fraction (f) is set as 30%. The initial guess is a straight channel going directly from the inlet to the outlet (see the first topology of Fig. 5.79).

Figure 5.74 – Mesh for the design of the bladed pump (*side*-type design).



Source: Author.

Table 5.23 – Parameters used for the topology optimization of the bladed pump (*side*-type design).

Input parameters	
Inlet flow rate (Q_{2D})	0.2 (L/min)/mm = 200 (L/min)/m
Wall rotation (n_0)	2000 rpm
Inlet rotation (n_{in})	2000 rpm
Inlet velocity profile	Constant (radially)
Dimensions	
r_{ext}	15 mm
r'_{int}	7 mm
θ_1	110°
$\Delta\theta$	45°
Material model parameters*	
κ_{max} ($\times 10^9 \mu_\infty$ (kg/(m^3 s)))	2.5
q	1.0
$\kappa_{PAS,\max}$ (s^{-1})	1 (for w_{PAS} = 0.5) 0.05 (for w_{PAS} = 0.85) 10 (for "w_{PAS} = 0.3 and w_H = 0.5")

* The optimization considers a Helmholtz pseudo-density filter (Section 2.5.7.1) in order to better stabilize the discrete optimized topologies. The filter length parameter (r_H) is chosen as the value $r_H = 0.208$ mm.

In order to ease the convergence of the performed simulations, which suffered difficulties in FEniCS, the simulation is performed in OpenFOAM®, by considering 500 iterations of the SIMPLE algorithm for each topology optimization iteration, and using the previous simulation as the initial guess for the next simulation. The fluid flow regime is assumed as laminar, for consistency with the Tesla pump rotor design. As in the Tesla pump rotor design, the fluid is considered as blood (non-Newtonian fluid), with the non-Newtonian dynamic viscosity ($\mu = \mu(\dot{\gamma}_{\text{m}})$) given by eq. (2.11), with non-Newtonian penalization (eq. (2.135)), and with density (ρ) given as 1056 kg/m^3 (HINGHOFER-SZALKAY; GREENLEAF, 1987) (Sections 1.1.1, 2.1.2.1 and 5.1.3). Also, the Brinkman-Forchheimer model (Section 2.5.1.3) is considered. In the finite element modeling, Taylor-Hood elements are considered, also for consistency with the Tesla pump rotor design. The multi-objective function is considered through the logarithmic approach (Section 2.5.4.2), with $f_{\text{scal}} = 10^3$. The post-processing is performed by smoothing by point cloud (Section 2.5.8.2.2) considering the use of the Savitzky-Golay filter (window size of 9, and degree of 2, remeshing resolution set as 100). The TOBS algorithm (Section 3.1.1.2) is used for the optimization in this section, by considering $\varepsilon_{\text{relax}} = 0.05$ and $\beta_{\text{flip limit}} = 0.05$, except for $w_H = 0.75$, in which $\varepsilon_{\text{relax}} = 0.01$ and $\beta_{\text{flip limit}} = 0.01$.

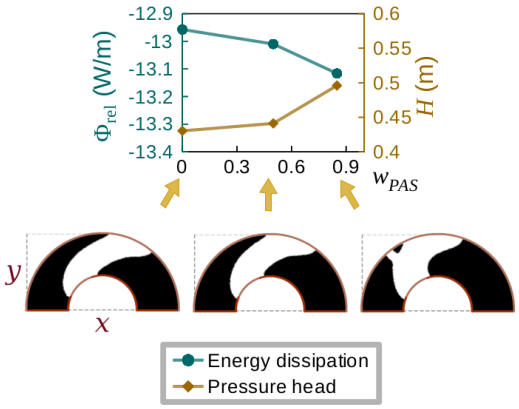
The Reynolds number ($\mathrm{Re}_{\mathrm{ext},\ell}$) is considered from Table 2.1. In the otimized results, the maximum Reynolds number computed, that has been achieved is $\mathrm{Re}_{\mathrm{ext},\ell} \approx 2.96 \times 10^4$, which is much smaller than 10^6, which corresponds to the transition Reynolds number in pumps (SABERSKY *et al.*, 1971; WU, 2007). Therefore, the flow in the bladed rotor should be laminar.

5.1.7.1.2 *Topology optimization results*

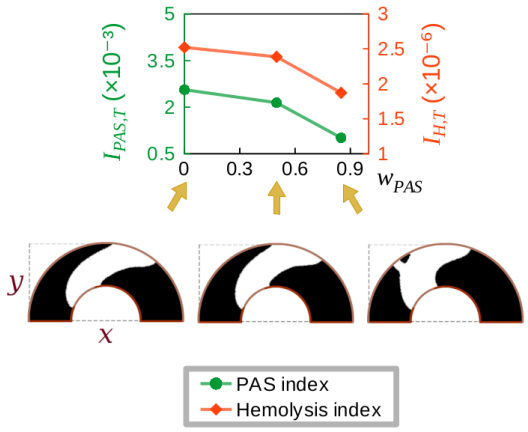
The topology optimization results for the PAS index are shown in Fig. 5.75. As can be noticed, as the w_{PAS} is increased, there is an increased tendency for the optimized topology to move closer to the inlet, with a less pronounced curve. In fact, it can be noticed that all functions computed in Fig. 5.75 improve when increasing the importance of thrombosis in topology optimization, which may mean that the optimized topology for w_{PAS} = 0 (i.e., $w_\Phi = 1.0$) should be a local minimum. In the overall, the improvement in thrombosis when including thrombosis in the multi-objective function significantly increases in the optimized topology for $w_{PAS} = 0.85$, in which there is the formation of a splitter blade. The formation of splitter blades has been previously observed in other fluids, dimensions and conditions, such as in Romero and Silva (2014), for a fictitious fluid and large dimensions, when considering vorticity in the multi-objective function, and in Romero and Silva (2017), for blood and large dimensions, when considering only energy dissipation in the objective function. It seems that, by including a splitter blade as shown in Fig. 5.75, the increase in shear stress on the walls from the inlet (until reaching the splitter blade) is “broken”, leading to a shorter path of the shear stress to the outlet and a reduction of hemolysis and thrombosis.

Figure 5.75 – Topology optimization results for the bladed pump (*side*-type design) under different weights in the multi-objective function for the PAS index.

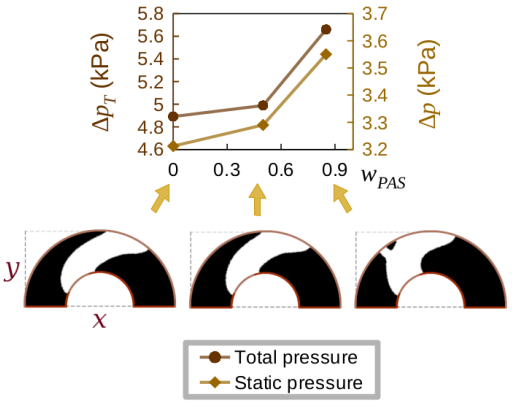
(a) Relative energy dissipation (Φ_{rel}) and head loss (H').



(b) PAS index (I_{PAS}) and hemolysis index (I_H).



(c) Variation of total (Δp_T) and static pressures (Δp).

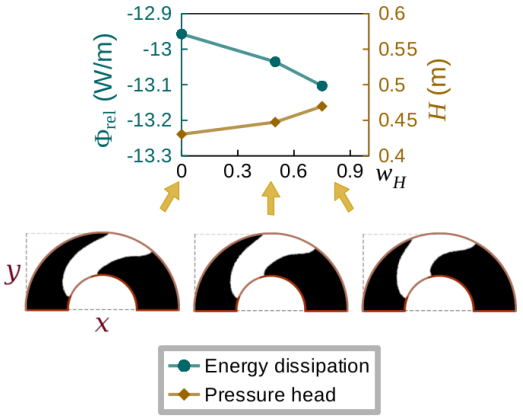


Source: Author.

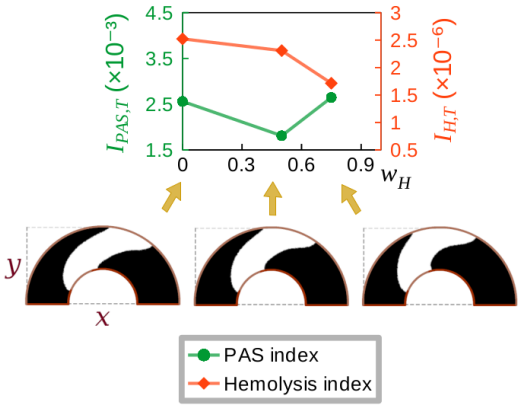
The topology optimization results for the hemolysis index are shown in Fig. 5.76. As in the topology optimization results for the PAS index (Fig. 5.75), it can be noticed that, when including hemolysis in the multi-objective function, almost all functions computed in Fig. 5.76 are improved, with the exception of the PAS index for $w_H = 0.75$. In particular, the optimized topology for $w_H = 0.5$ (Fig. 5.76) is pretty close to the optimized topology for $w_{PAS} = 0.5$ (Fig. 5.75), the difference being that $w_{PAS} = 0.5$ resulted in an optimized topology slightly tilted to the right, which is shown in Fig. 5.78.

Figure 5.76 – Topology optimization results for the bladed pump (*side*-type design) under different weights in the multi-objective function for the hemolysis index.

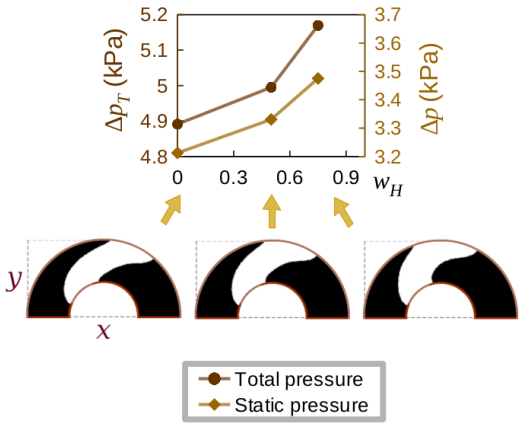
(a) Relative energy dissipation (Φ_{rel}) and head loss (H').



(b) PAS index (I_{PAS}) and hemolysis index (I_H).



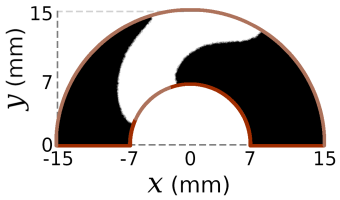
(c) Variation of total (Δp_T) and static (Δp) pressures.



Source: Author.

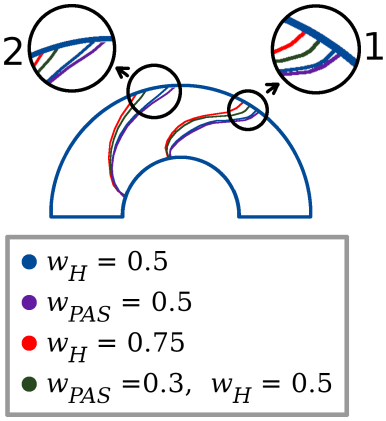
Furthermore, a combined case, considering both hemolysis and thrombosis in the multi-objective function is considered (for $w_{PAS} = 0.3$ and $w_H = 0.5$). The optimized topology is shown in Fig. 5.77 and is similar to the optimized topologies for $w_H = 0.75$ (Fig. 5.76). The contours plotted in Fig. 5.78 show the differences between the optimized topologies. From the amplified zones, it can be noticed that the optimized topology for $w_H = 0.75$ is located more to the right, and the optimized topology for "$w_{PAS} = 0.3$ and $w_H = 0.5$" more to the left.

Figure 5.77 – Optimized topology for the combined case ($w_{PAS} = 0.3$ and $w_H = 0.5$) for the bladed pump (*side*-type design).



Source: Author.

Figure 5.78 – Contours of the optimized topologies for $w_H = 0.5$, $w_{PAS} = 0.5$, $w_H = 0.75$ and "$w_{PAS} = 0.3$ and $w_H = 0.5$".



Source: Author.

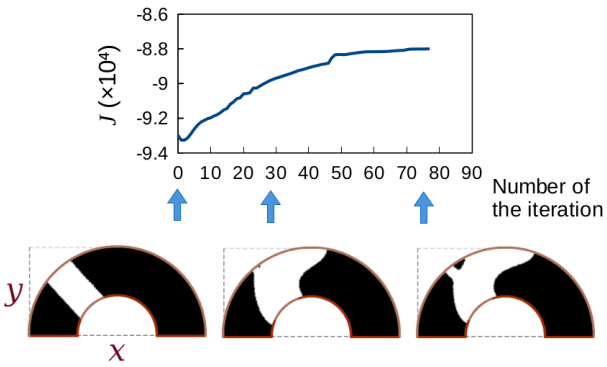
The optimized topologies can be compared in Table 5.24, with respect to the optimized topology for $w_\Phi = 1$. From Table 5.24, the best result for thrombosis was achieved for $w_{PAS} = 0.85$, while the best result for hemolysis was achieved for $w_H = 0.75$. Furthermore, the optimized topology for $w_{PAS} = 0.85$ turned out to be better than all other optimized topologies, except for the fact that the hemolysis resulted somewhat higher than for the optimized topology for $w_H = 0.75$ (Table 5.24). By comparing the values in all optimized topologies, in the overall, it seems that the optimized topology for $w_{PAS} = 0.85$ is a good compromise for improving energy dissipation, thrombosis, hemolysis and pressure head.

Table 5.24 – Relative comparison of the optimized topologies for the bladed pump (*side*-type design) with the optimized topology for $w_\Phi = 1$.

Designs	Φ_{rel}	$I_{PAS,T}$	$I_{H,T}$	H	Δp	Δp_T
$w_{PAS} = 0.5$	-0.41%	-16.3%	-5.4%	+2.5%	+2.4%	+2.0%
$w_{PAS} = 0.85$	-1.23%	-60.5%	-25.8%	+15.2%	+10.5%	+15.7%
$w_H = 0.5$	-0.60%	-29.3%	-8.5%	+4.0%	+3.7%	+2.1%
$w_H = 0.75$	-1.13%	+3.3%	-32.0%	+9.1%	+8.2%	+5.7%
$w_{PAS} = 0.3$ and $w_H = 0.5$	-1.07%	-6.8%	-10.6%	+8.3%	+7.0%	+4.1%

The convergence curve for $w_{PAS} = 0.85$ is shown in Fig. 5.79. It can be noticed that there is a rise in the objective function value, which may be possibly attributed to: the reduced number of SIMPLE iterations that have already run in the beginning of the optimization, effect of the volume constraint, effect of the material model term of the energy dissipation (or the PAS index), and the induction of a local minimum. The reduced number of SIMPLE iterations may have an impact in the computed objetive functions, worsening them while the optimized topology has still not been reached. Furthermore, in the case of the effect of the material model term, this effect is combined with the use of a Helmholtz filter, which may lead to an increase in the objective function values that are computed with the filtered design variable, and, therefore, increase the influence of the sensitivities so as to try to induce a local minimum that improves the original objective functions.

Figure 5.79 – Convergence curve of the topology optimization of the bladed pump (*side*-type design) for $w_{PAS} = 0.85$.



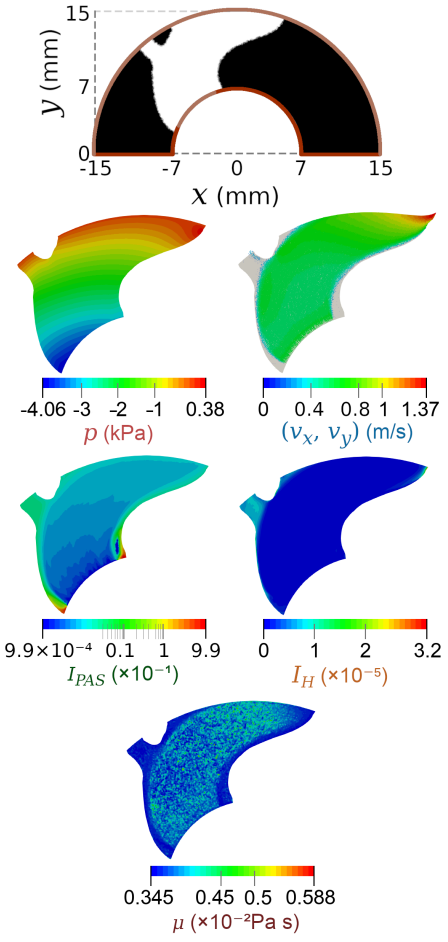
Source: Author.

5.1.7.1.3 *Simulation of the optimized result for* $w_{PAS} = 0.85$

The simulation of the optimized result for $w_{PAS} = 0.85$ is shown in Fig. 5.80. From this figure, it may be noticed that the pressure increases in an almost linear fashion,

while the velocity faces a higher increase in magnitude after the “bend” it undergoes from the inlet. It can also be noticed that the fluid flow that crosses the additional path created by the splitter blade has a smaller relative flow. In the plot of the local PAS index, it can be noticed that there are two potential higher thrombosis zones near the inlet. However, the fluid flow velocities are relatively smaller in these zones, as can be seen from the plot of the velocities, which means that their overall effect in the PAS index is small. This distance between the inlet and the walls has also been observed in Romero and Silva (2017). In the plot of the local hemolysis index, it may be noticed that hemolysis is mainly located near the outlet and the right-most blade wall, where the wall velocities are higher sue to the higher radius ($\omega_0 r_{ext}$), while the hemolysis increase is more distributed on the fluid flow path near the additional path created by the splitter blade. The plot of the non-Newtonian viscosity shows that it is higher farther from walls.

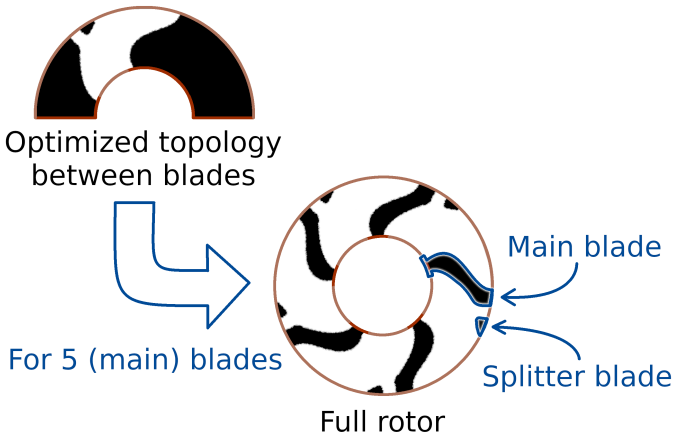
Figure 5.80 – Optimized topology, pressure, velocity, PAS index, hemolysis index and dynamic viscosity for the optimized bladed pump (*side*-type design) for $w_{PAS} = 0.85$. The type of plot of the PAS index was changed to logarithmic in order to allow a better visualization of the results.



Source: Author.

The interpretation of the optimized result is shown in Fig. 5.81, by considering 5 (main) blades.

Figure 5.81 – Interpretation of the optimized blades (*side*-type design).



Source: Author.

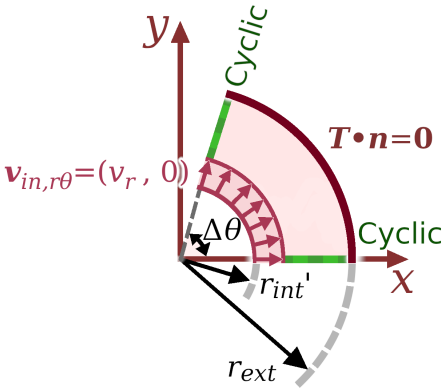
5.1.7.2 *Full-inlet*-type design

The *full-inlet*-type design consists of the case in which the inlet is not bounded by walls, which enables the possibility of designing blades inside the design domain.

5.1.7.2.1 *Design domain and mesh*

The design domain selected in this work is shown in Fig. 5.82, for a 72° design domain bounded by cyclic boundary conditions. The rotation is given from the right-hand rule (i.e., ω_0 is set for the positive direction of the z axis).

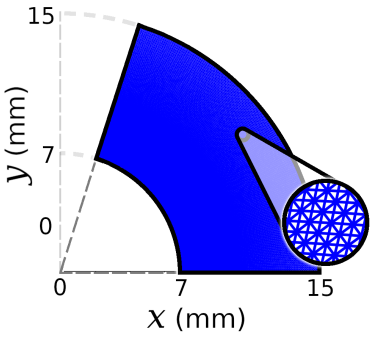
Figure 5.82 – Domain for the design of the bladed pump (*full-inlet*-type design).



Source: Author.

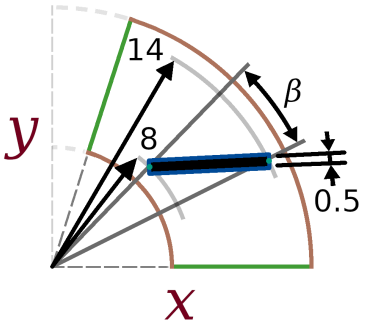
The mesh is structured, in order to facilitate the imposition of the cyclic boundary conditions, being generated with the same approach as an example presented in Logg *et al.* (2012), from an initially rectangular mesh, by deforming it and then applying a densification function. The mesh is composed of 80 radially distributed rectangular partitions of triangular elements, and 160 tangentially distributed rectangular partitions of triangular elements, totalling 25,841 nodes and 51,200 elements (see Fig. 5.83). The input parameters, geometric dimensions and material model parameters being considered in the design are shown in Table 5.25. The specified fluid volume fraction (f) is set as 85%. The initial guess is a rectangular blade (Fig. 5.84), where the β angle is its inclination.

Figure 5.83 – Mesh for the design of the bladed pump (*full-inlet*-type design).



Source: Author.

Figure 5.84 – Initial guess for the design of the bladed pump (*full-inlet*-type design). The geometric center of the initial guess is positioned at 36°.



Source: Author.

Table 5.25 – Parameters used for the topology optimization of the bladed pump (*full-inlet*-type design).

Input parameters	
Inlet flow rate (Q_{2D})	0.2 (L/min)/mm = 200 (L/min)/m
Wall rotation (n_0)	2000 rpm
Inlet rotation (n_{in})	2000 rpm
Inlet velocity profile	Constant (radially)
Dimensions	
r_{ext}	15 mm
r'_{int}	7 mm
$\Delta\theta$	72°
Material model parameters	
$\kappa_{\max}$ ($\times 10^{13}\mu_\infty$ (kg/(m^3 s)))	2.5
q	1.0
$\kappa_{PAS,\max}$ (s^{-1})	10^3

The same setup from the *side*-type design is considered (Section 5.1.7.1.1), but with some differences: the remeshing resolution is set as 64, in order for the mshr module from FEniCS to be able to generate a smooth mesh while keeping the same boundary nodes, which is required for applying the cyclic boundary condition in FEniCS, and the window size is set as 5. The TOBS algorithm (Section 3.1.1.2) is used for the optimization in this section, by considering $\varepsilon_{\text{relax}} = 0.01$ and $\beta_{\text{flip limit}} = 0.05$.

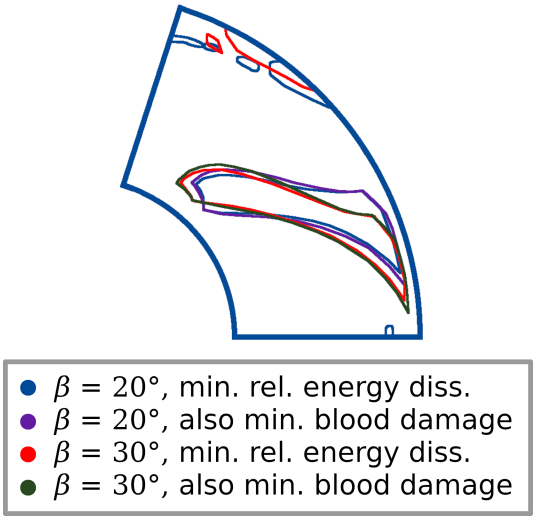
The Reynolds number ($\text{Re}_{\text{ext},\ell}$) is considered from Table 2.1. In the otimized results, the maximum Reynolds number computed, that has been achieved is $\text{Re}_{\text{ext},\ell} \approx 2.9 \times 10^4$, which is much smaller than 10^6, which corresponds to the transition Reynolds number in pumps (SABERSKY *et al.*, 1971; WU, 2007). Therefore, the flow in the bladed rotor should be laminar.

5.1.7.2.2 *Topology optimization results*

The topology optimization results are considered for two different angles (β) in the initial guess (Fig. 5.84): 20° and 30°. As an observation, inverted blades with respect to Fig. 5.84 are not considered as initial guesses, because they may suffer topology optimization convergence issues, and also trigger vortices and reflux (fluid flow going from the outlet towards the outlet). From the optimized results for 20° and 30°, it has been observed that, by including blood damage (hemolysis and/or thrombosis) in the multi-objective function, the optimized topologies, although different than the optimized topologies for $w_\Phi = 1.0$, were kept the same, independently of the weights of the blood

damage indices in the multi-objective function. This means that, for the current topology optimization and simulation setups, there are only two optimized topologies for each angle (β): for minimizing the relative energy dissipation, and for also minimizing blood damage. These optimized topologies are shown in Fig. 5.86. The contours plotted in Fig. 5.85 show the differences between the optimized topologies. Table 5.26 shows the computed values in these topologies, and Table 5.27 shows these same values, but in a relative way.

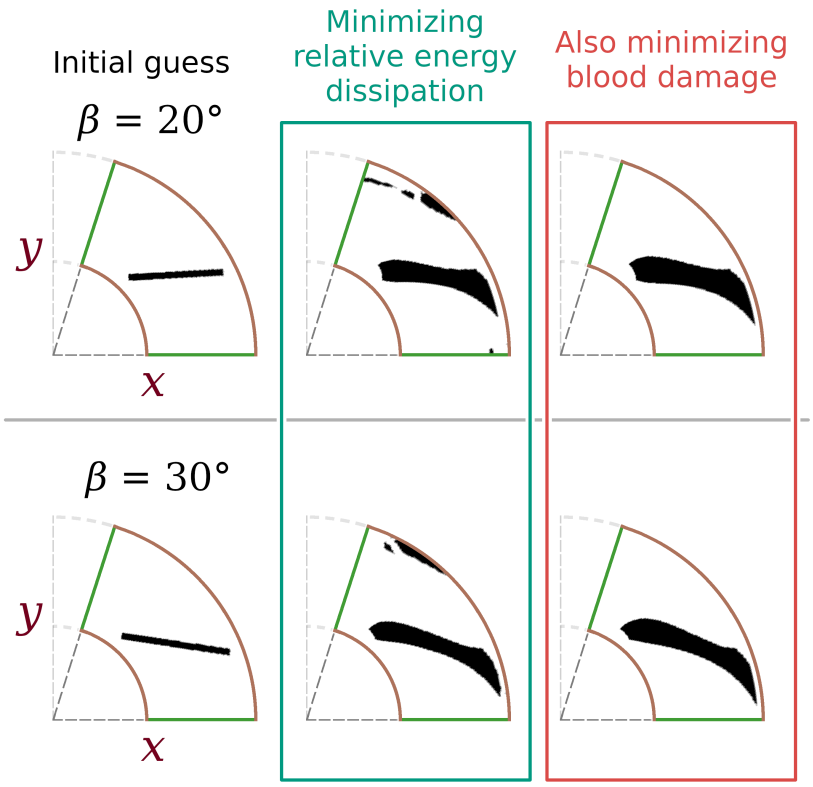
Figure 5.85 – Contours of the optimized topologies for the bladed rotor (*full-inlet*-type design).



Source: Author.

As can be noticed in Fig. 5.86, considering only relative energy dissipation in the multi-objective function, additional blades were generated, which seem to slightly improve the pressure head (see Table 5.26), but that led to a local minimum for the relative energy dissipation. With the inclusion of blood damage in the multi-objective function, these additional blades are not formed anymore, but the main (larger) blade increases its size (Fig. 5.85). As can be noticed, increasing β from 20° to 30° leads to optimized topologies that are relatively similar in terms of computed values (in the same order of magnitude), with the exception of thrombosis, which suffered from a rise of almost 3 times the values for $\beta = 20°$. This is most probably due to the flow separation tendency that may arise depending on the incidence angle on the blades. By comparing the values in all optimized topologies, in the overall, it seems that the optimized topology for $\beta = 20°$ considering blood damage ("$\beta = 20°$, also min. blood damage", in Table 5.27) seems to be a good compromise for improving energy dissipation, thrombosis, hemolysis and pressure head.

Figure 5.86 – Optimized topologies for the bladed pump (*full-inlet*-type design).



Source: Author.

Table 5.26 – Comparison of the optimized topologies for the bladed pump (*full-inlet*-type design).

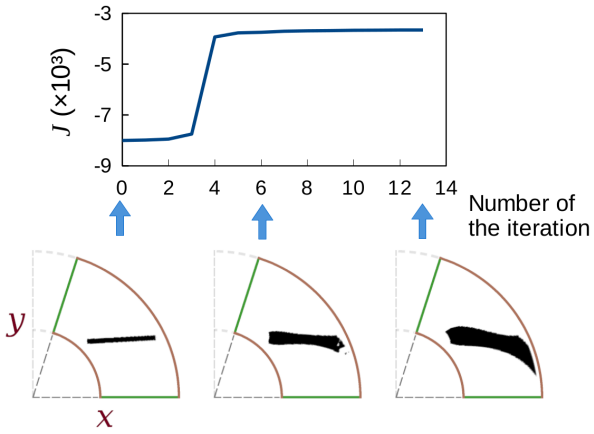
Designs	Φ_{rel} (W/m)	$I_{PAS,T}$ ($\times 10^{-2}$)	$I_{H,T}$ ($\times 10^{-6}$)	H ($\times 10^{-1}$m)	Δp (kPa)	Δp_T (kPa)
$\beta = 20°$, min. rel. energy diss.	-12.81	0.13	6.4	4.3	3.23	4.40
$\beta = 20°$, also min. blood damage	-12.97	0.12	4.4	4.2	3.27	4.37
$\beta = 30°$, min. rel. energy diss.	-12.80	4.07	4.8	4.3	3.20	4.47
$\beta = 30°$, also min. blood damage	-12.98	3.42	3.2	4.1	3.24	4.31

Table 5.27 – Relative comparison of the optimized topologies for the bladed pump (*full-inlet*-type design) with the optimized topology for $\beta = 20°$ and $w_\Phi = 1$ ("min. rel. energy diss.").

Designs	Φ_{rel}	$I_{PAS,T}$	$I_{H,T}$	H	Δp	Δp_T
$\beta = 20°$, also min. blood damage	-1.2%	-9.6%	-32.1%	-2.4%	+1.3%	-0.7%
$\beta = 30°$, min. rel. energy diss.	+0.14%	+2977.6%	-25.1%	-0.1%	-1.0%	+1.5%
$\beta = 30°$, also min. blood damage	-1.3%	+2490.5%	-50.1%	-4.6%	+0.2%	-2.0%

The convergence curve for $\beta = 20°$ considering blood damage (exemplified for $w_{PAS} = 0.9$) is shown in Fig. 5.87. It can be noticed that there is a rise in the objective function value, which may be attributed to the same factors mentioned for the *side*-type design.

Figure 5.87 – Convergence curve of the topology optimization of the bladed pump (*full-inlet*-type design) for $\beta = 20°$ considering blood damage (exemplified for $w_{PAS} = 0.9$).

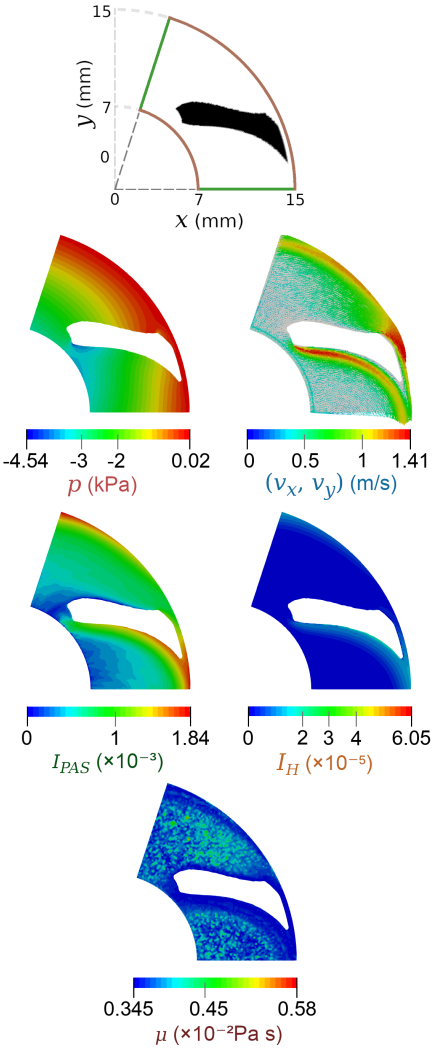


Source: Author.

5.1.7.2.3 *Simulation of the optimized result for $\beta = 20°$ considering blood damage*

The simulation of the optimized result for $\beta = 20°$ considering blood damage is shown in Fig. 5.88. It may be noticed that the edges of the post-processed mesh seem “rounder” than the distribution of the design variable, which is an aftereffect of performing the mesh smoothing procedure. From this figure, it may be noticed that the pressure radially increases in an almost linear fashion, while the velocity increases in magnitude after colliding with the front and back edges of the blade. The local PAS index plot shows that thrombosis is mostly concentrated after the back edge of the blade. In this sense, for comparison, it may be highlighted that, for the optimized topologies for $\beta = 30°$, the local PAS index is concentrated mainly *over* the blade, which may be related to flow separation, and is most probably one of the main responsible effects for the higher thrombosis for $\beta = 30°$. For the local hemolysis index, it may be noticed that it “flows” from below the blade towards the outlet, where the highest velocity gradients are located. The plot of the non-Newtonian viscosity shows that it is higher where the fluid flow velocities are smaller (mostly far from the blade).

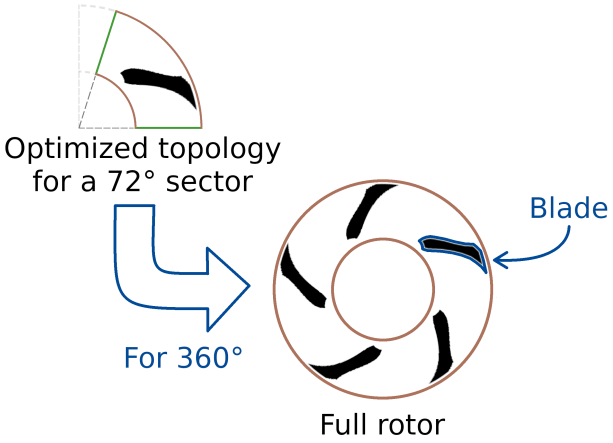
Figure 5.88 – Optimized topology, pressure, velocity, PAS index, hemolysis index and dynamic viscosity for the optimized bladed pump (*full-inlet*-type design) for $w_{PAS} = 0.9$.



Source: Author.

The interpretation of the optimized result is shown in Fig. 5.89, by considering the full rotor (360°).

Figure 5.89 – Interpretation of the optimized blades (*full-inlet*-type design).



Source: Author.

It may be mentioned that the sides of the blades of the optimized rotor for the *full-inlet*-type design bear some resemblance with the optimized topologies from Section 5.1.7.1. In order to make it easier to visualize, the similar topology is highlighted from the full rotor (from Fig. 5.89) in Fig. 5.90. Therefore, although it seems that the *full-inlet*-type design is more sensitive to the choice of the initial guess than the *side*-type design from Section 5.1.7.1, it may be able to reach similar optimized topologies.

Figure 5.90 – Interpretation of the optimized blades (*full-inlet*-type design), highlighting the flow between a pair of blades, which resembles the optimized topologies from Section 5.1.7.1.



Source: Author.

5.1.8 **Turbulent 2D swirl flow design (WA2018 model)**

In this section, the topology optimization method is considered for turbulent flows through the Wray-Agarwal model (WA2018), which poses advantages in terms of simulation and also in a topology optimization point-of-view, as shown in Section 2.1.3.2. The TOBS approach is also considered (ALONSO *et al.*, 2022).

In the numerical results of this section, the fluid is considered as water, with a dynamic viscosity (μ) of 0.001 Pa s, and a density (ρ) of 1000.0 kg/m^3. The MINI element is considered for the finite element method (see Section 2.2.2), for less computational cost than Taylor-Hood elements. The implementation considers the use of *FEniCS TopOpt Foam* (ALONSO *et al.*, 2021). The specified fluid volume fraction (f) is chosen as 30%. The porous medium is assumed to be stationary, as well as the reference frame ($\boldsymbol{v}_{\mathrm{mat}} = \boldsymbol{v}$, $\omega_0 = 0$). The parameter $\lambda_{R_{\mathrm{T}}}$ is chosen as 1.0.

The inlet values for the turbulent variable ($R_{\mathrm{T},in}$) are given from Section 2.1.4.2, by considering local inlet velocity values. When considering laminar flow, the inlet velocity profile is set as laminar, whereas, when considering turbulent flow, the inlet velocity profile is set as turbulent. The computation of these profiles is described in Appendix C. The objective function is considered as the relative energy dissipation (eq. (2.51)) with the adjustment mentioned in Section 2.3.1 for turbulent flow. The material model for topology optimization is given by the Brinkman model (Section 2.5.1.1). The TOBS algorithm (Section 3.1.1.2) is used for the optimization in this section. The specified tolerance for the TOBS algorithm is for when the change in the pseudo-density distribution ($\Delta\alpha$) is sufficiently small. In this section, the optimization is progressed until $\Delta\alpha = 0$. Also, the Riesz map adjustment from eq. (3.2) is considered.

In order to accelerate the execution of the optimization, the OpenFOAM® simulation for each optimization step reuses the simulation result from the immediately previous optimization step. A maximum number of SIMPLE iterations per optimization step is also considered, which is set, in this work, as 2000. The Reynolds number ($\mathrm{Re}_{\mathrm{ext},\ell}$) is considered from the external diameter ($2r_{ext}$) in Table 2.1. The post-processing is performed by smoothing by point cloud (Section 2.5.8.2.2), considering the use of the Savitzky-Golay filter (window size of 9, and degree of 2, remeshing resolution set as 128).

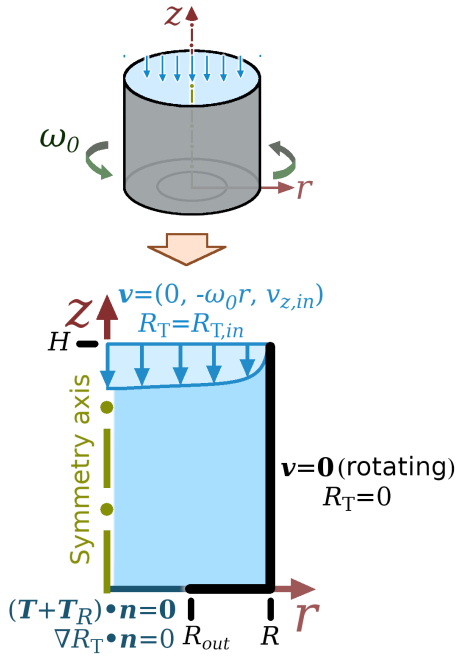
Besides the 2D swirl flow numerical examples presented in this section, Alonso

et al. (2022) also presents two 2D topology optimization cases (a 2D double pipe design and a 2D U-bend channel design), in order to show the Wray-Agarwal model (WA2018) being applied for topology optimization in 2D cases, and also in order to show another type of initial guess being considered for the topology optimization (some distributed circles).

5.1.8.1 Rotating nozzle

The first example is the design of a rotating nozzle. A nozzle is used to control the characteristics of the fluid flow entering or leaving another fluid device. This type of design has been previously evaluated for laminar 2D swirl flow by Alonso *et al.* (2018). Fig. 5.91 shows the design domain that is considered in this case. Since the nozzle is rotating, the solid material distribution is optimized for these rotating walls under the same rotation of the reference frame (ω_0).

Figure 5.91 – Design domain for the rotating nozzle.

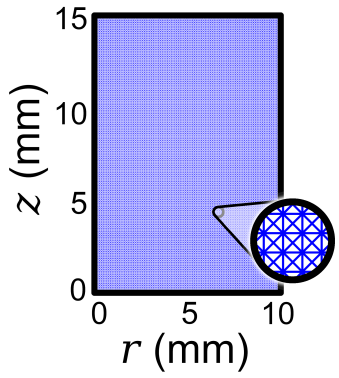


Source: Author (ALONSO *et al.*, 2022).

The mesh consists of 19,401 nodes and 38,400 elements (i.e., 80 radial and 120 axial rectangular partitions of crossed triangular elements, see Fig. 5.92). The input parameters, geometric dimensions and material model parameters that are considered for the design are shown in Table 5.28. In this example, turbulent flow optimized topologies are compared against optimized topologies obtained from laminar flow: The inlet flow

rate for laminar flow corresponds to a maximum inlet Reynolds number of 130, while the inlet flow rate for turbulent flow corresponds to a maximum inlet Reynolds number of 1.3×10^4. Since the TOBS approach considers binary variables, the initial guess has to be chosen to be discrete: In this work, in order to facilitate convergence, a *conical* initial guess is considered (i.e., directly connecting the inlet (R) of the design domain (H) to the outlet (R_{out}) with a straight line – See the leftmost topologies in Fig. 5.95). It can be highlighted that, in any fluid topology optimization problem with TOBS, other discrete initial guesses are also possible, such as a *fully-fluid* initial guess, but with care taken in case there is some undesired vortex generation in the fluid for this initial guess, which may possibly hinder the topology optimization process. The specified fluid volume fraction (f) is set as 30%.

Figure 5.92 – Mesh used in the design of the rotating nozzle.



Source: Author (ALONSO *et al.*, 2022).

Table 5.28 – Parameters used for the topology optimization of the rotating nozzle.

Input parameters (laminar flow)	
Inlet flow rate (Q)	0.06 L/min
Wall rotation (n_0)	0, 25 and 50 rpm
Inlet velocity profile	Parabolic
Input parameters (turbulent flow)	
Inlet flow rate (Q)	10 L/min
Wall rotation (n_0)	0, 2500 and 5000 rpm
Inlet velocity profile	Turbulent
I_T	5.0%
ℓ_T	0.77 mm
Dimensions	
H	15 mm
R	10 mm
Material model parameters (laminar flow)*	
$\kappa_{\max}$ ($\times 10^8 \mu$ (kg/(m^3 s)))	10^3 (for 0 rpm) ** 2.5 (for 25 rpm) 5.0 (for 50 rpm)
q	1.0
Material model parameters (turbulent flow)*	
$\kappa_{\max}$ ($\times 10^{10} \mu$ (kg/(m^3 s)))	2.5 (for 0 rpm) 5.0 (for 2500 rpm) 8.0 (for 5000 rpm)
q	1.0
λ_{R_T}	1.0

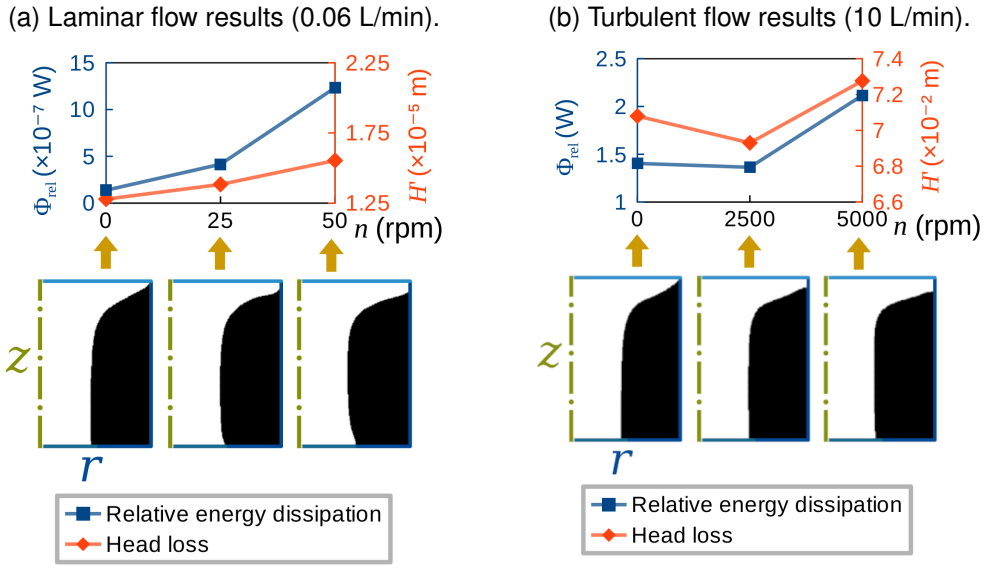
* The optimization considers a Helmholtz pseudo-density filter (Section 2.5.7.1) in order to better stabilize the discrete optimized topologies. The filter length parameter (r_H) is chosen as the value $r_H = 0.0625$ mm for the laminar flow cases, and as the value $r_H = 0.25$ mm for the turbulent flow cases.

** The value of $\kappa_{\max}$ for laminar flow for 0 rpm was chosen to be higher in order to enforce that the inlet is not partially blocked by solid material during topology optimization, which is due to the smaller influence of lower velocity zones during topology optimization, and is a problem that can also be observed in Borrvall and Petersson (2003)'s 2D laminar Stokes nozzle design.

A series of topology optimizations is performed for different rotations, whose results are shown in Fig. 5.93. The maximum local Reynolds numbers are computed as: 479, 526 and 1060 (for the laminar optimized topologies); and 5.9×10^4, 6.5×10^4, and 1.0×10^5 (for the turbulent optimized topologies). In Fig. 5.93a, it can be noticed that the presence of higher fluid flow velocities under laminar flow tends to increase an "inlet zone". This inlet zone seems to help the fluid to make a smoother change in flow direction towards the middle of the nozzle. Fig. 5.93b shows the optimized topologies for turbulent flow. As can be seen, a similar effect to that of laminar flow (Fig. 5.93a) is observed. However, the 0 rpm optimized topology of turbulent flow features a concave transition near the inlet whilst the 0 rpm optimized topology of laminar flow features a more linear transition. This can be seen as a consequence of the different velocity

profiles in both cases (turbulent and laminar velocity profiles), since a turbulent velocity profile features somewhat higher velocities when farther from the symmetry axis, with respect to a laminar velocity profile. It can also be noticed that the “outlet zone” of the turbulent nozzle is straighter than the laminar nozzle when under rotation, in which a “divergent shape” can be noticed. This “divergent shape” creates a small effect of reducing the fluid pressure and increasing the fluid velocity, which may help reducing the dissipated energy due to the fluid acceleration from the rotation effect. However, in the turbulent flow case, the effect of the rotating wall on the velocity seems to be more prominent, leading to a straighter outlet channel shape.

Figure 5.93 – Topology optimization results for the rotating nozzle under different wall rotations, for laminar and turbulent flows.



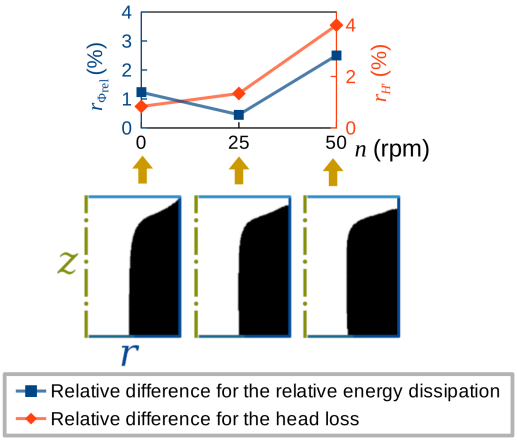
Source: Author (ALONSO *et al.*, 2022).

In order to show the effect of considering the optimized topologies for laminar flow operating under turbulent flow and vice-versa, additional simulations are performed and shown in Fig. 5.94. In Fig. 5.94, the *relative differences* are shown, which correspond to $r_x = \frac{x_{\text{other flow}} - x_{\text{flow}}}{x_{\text{flow}}}$, where x_{flow} is the function being computed in the flow that generated the optimized topology, while $x_{\text{other flow}}$ is the function being computed in the topology that was optimized for the other type of flow. Thus, a positive *relative difference* means that the optimized topology operates better at the flow it was optimized for. It can be noticed that almost all optimized function values are better at the flow that generated the optimized topology, with the exception of the head loss for 5000 rpm (Fig. 5.94b). This may possibly mean the induction of a local minimum, but, since the relative energy

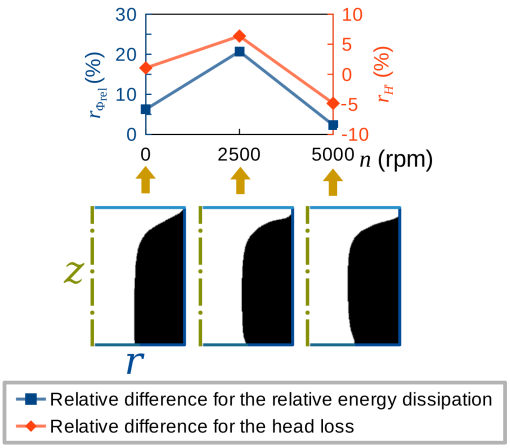
dissipation (objective function) is smaller in the flow that generated the optimized topology, this does not pose an issue for optimization, but may mean that the viscous effects become more apparent in the relative energy dissipation than in the head loss when under higher rotations in turbulent flow (turbulent viscosity).

Figure 5.94 – Laminar and turbulent flow optimized topologies operating under the flow configurations of each other.

(a) Turbulent flow optimized topologies operating under laminar flow (0.06 L/min).



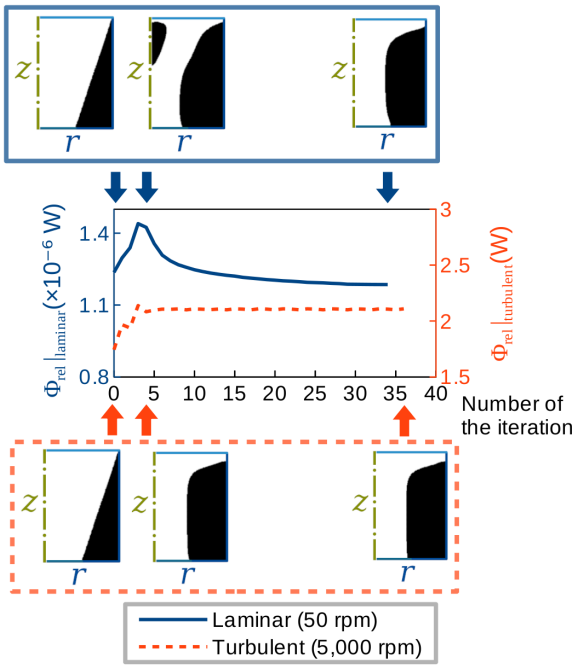
(b) Laminar flow optimized topologies operating under turbulent flow (10 L/min).



Source: Author (ALONSO *et al.*, 2022).

The convergence curves for the laminar and turbulent rotating nozzles are shown in Fig. 5.95. From this figure, it can be promptly noticed that including an island to split the inflow dissipates more energy, such that it disappeared during the optimization iterations. It can also be noticed that the relative energy dissipation values for the turbulent case are lower in the first iterations. This is due to the fact that a limited number of simulation (SIMPLE) iterations is run at each optimization step in order to reduce the computational cost, and the volume constraint is not satisfied at the initial guess.

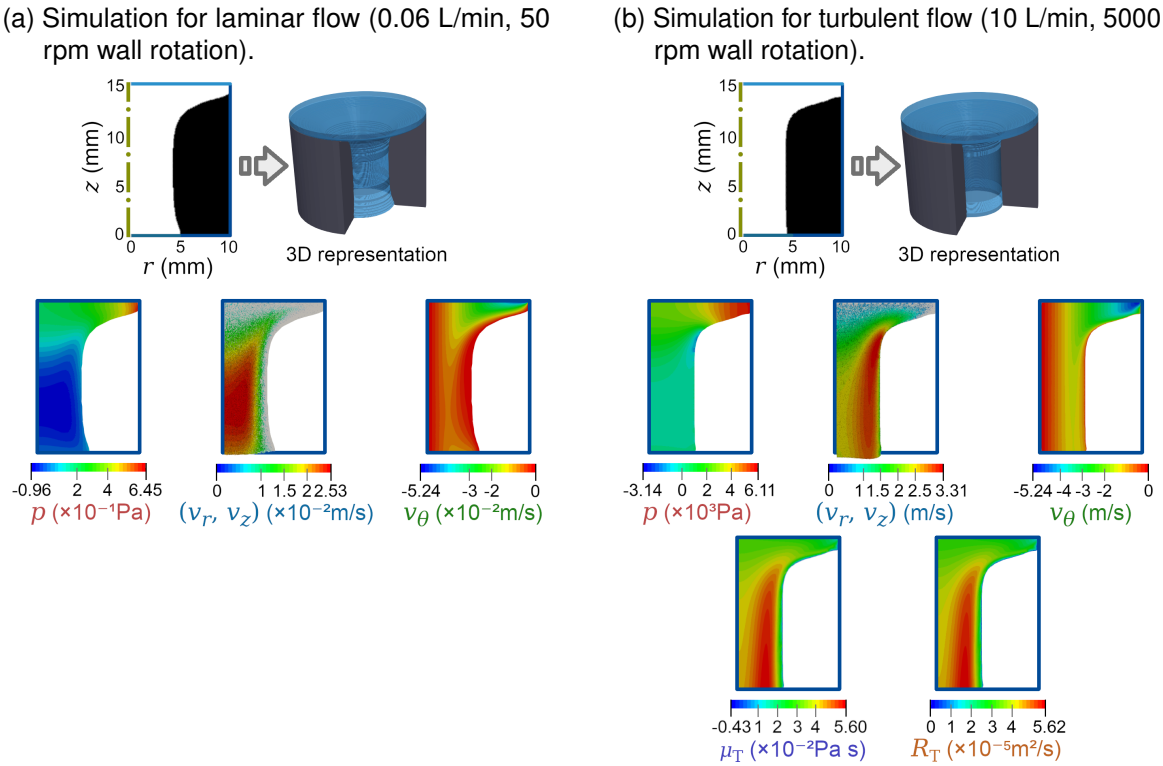
Figure 5.95 – Convergence curve of the topology optimization of the rotating nozzle for laminar (50 rpm wall rotation) and turbulent flows (5000 rpm wall rotation).



Source: Author (ALONSO *et al.*, 2022).

The simulation results for the post-processed meshes for the optimized topologies for their respective flow regimes are shown in Fig. 5.96. As can be noticed in Fig. 5.96b, the turbulent effect (i.e., the turbulent viscosity) causes a higher radial-axial flow acceleration near the rotating wall, which is the opposite from the laminar flow case (Fig. 5.96a), where the radial-axial flow is mainly concentrated in the middle of the nozzle. This may explain the fact that the “outlet zone” is straighter in the turbulent flow optimized topology than in the laminar flow optimized topology.

Figure 5.96 – Optimized topologies and variables for optimized rotating nozzles.

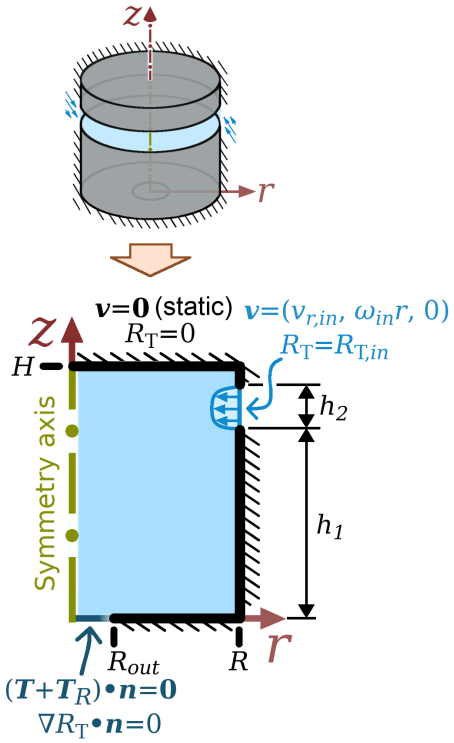


Source: Author (ALONSO *et al.*, 2022).

5.1.8.2 Hydrocyclone-type device

The second example is of a hydrocyclone-type device. With respect to a “real” hydrocyclone device, it differs from the fact that it considers a single-phase flow (instead of a two-phase flow), which enters the fluid flow device from a single inlet under rotation (ω_{in}), and exits it through a single outlet. This type of design has been previously evaluated for laminar 2D swirl flow by Alonso *et al.* (2018). Fig. 5.97 shows the design domain that is considered in this case. Since the hydrocyclone-type device is static, the solid material distribution is optimized for these static walls ($\omega_0 = 0$ rad/s).

Figure 5.97 – Design domain for the hydrocyclone-type device.



Source: Author (ALONSO *et al.*, 2022).

The mesh is considered as the same from Fig. 5.92. The input parameters, geometric dimensions and material model parameters that are considered for the design are shown in Table 5.29. The inlet flow rates correspond to maximum inlet Reynolds numbers 4.0×10^4, 4.5×10^4 and 5.8×10^4. Since the TOBS approach considers binary variables, the initial guess has to be chosen to be discrete: In this work, in order to facilitate convergence, an initial guess featuring a *straight connection between inlet and outlet* is considered. The specified fluid volume fraction (f) is set as 30%. In this case, since the reference frame is stationary, it can be pointed out that the inertial effect terms from the relative energy dissipation (eq. (2.51)) are zero.

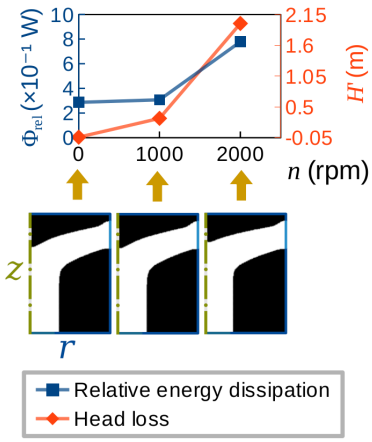
Table 5.29 – Parameters used for the topology optimization of the hydrocyclone-type device.

Input parameters	
Inlet flow rate (Q)	20 L/min
Wall rotation (n_0)	0 rpm
Inlet rotation (n_{in})	0, 1000 and 2000 rpm
Inlet velocity profile	Turbulent
I_T	5.0%
ℓ_T	0.12 mm
Dimensions	
H	15 mm
R	10 mm
h_1	11 mm
h_2	3 mm
Material model parameters*	
$\kappa_{\max}$ ($\times 10^{12}\mu$ (kg/(m^3 s)))	5.0 (for 0 rpm) 5.0 (for 1000 rpm) 50.0 (for 2000 rpm)
q	1.0
λ_{R_T}	1.0

* The optimization considers a Helmholtz pseudo-density filter (Section 2.5.7.1) in order to better stabilize the discrete optimized topologies. The filter length parameter (r_H) is chosen as the value $r_H =$ 0.25 mm.

A series of topology optimizations is performed for different inlet rotations, whose results are shown in Fig. 5.98. The maximum local Reynolds numbers are computed as: 4.18×10^5, 4.42×10^5 and 5.24×10^5. In Fig. 5.98, it can be noticed that the channel slightly raises in position when under higher inlet rotations. This effect can be mostly attributed to the increased flow inertia when under higher inlet rotations, which tends to hinder the change in flow direction to the outlet. It can also be noticed that, as in the turbulent nozzles of Section 5.1.8.1, the downmost part of the channel is straight for less relative energy dissipation.

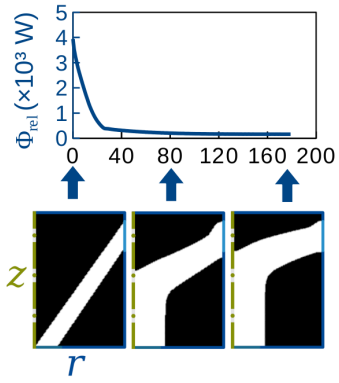
Figure 5.98 – Topology optimization results for the hydrocyclone-type device under different inlet rotations.



Source: Author (ALONSO *et al.*, 2022).

The convergence curve for the hydrocyclone-type device (1000 rpm inlet rotation) is shown in Fig. 5.99. From there, it can be noticed that the optimized channel slowly "rises" to its optimized positioning during topology optimization.

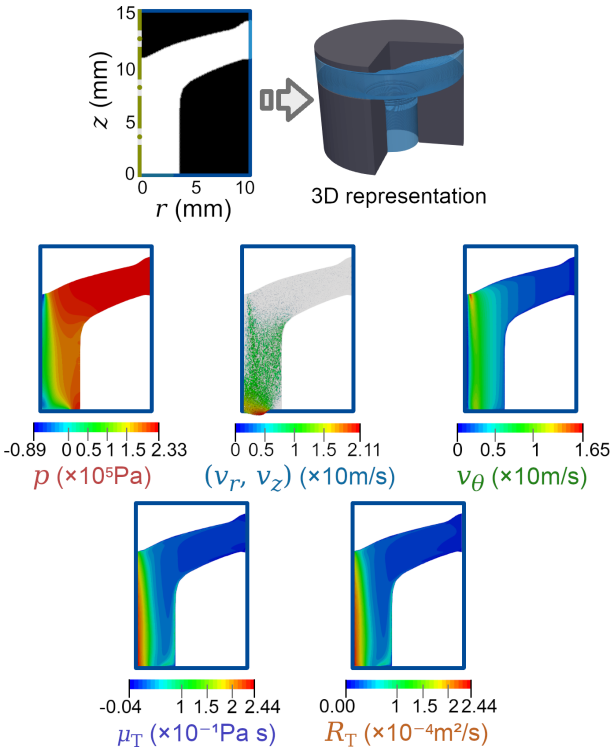
Figure 5.99 – Convergence curve of the topology optimization of the hydrocyclone-type device (1000 rpm inlet rotation).



Source: Author (ALONSO *et al.*, 2022).

The simulation results for the post-processed mesh for the optimized topology for the hydrocyclone-type device (1000 rpm inlet rotation) are shown in Fig. 5.100. As can be noticed in Fig. 5.100, there is a flow acceleration from the inlet towards the outlet, which mostly happens when the fluid reaches the "straight" part of the channel, which is closer to the outlet. This is probably due to the sudden decrease in cross-sectional area near the middle of the channel, which changes it from a *cylinder-like* cross-section ("$2\pi r\Delta z$") to a *disk-like* cross-section ("πr^2").

Figure 5.100 – Optimized topologies and variables for the optimized hydrocyclone-type device (1000 rpm inlet rotation).

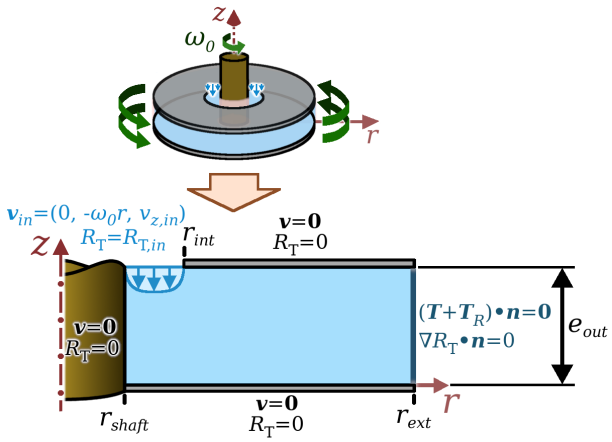


Source: Author (ALONSO *et al.*, 2022).

5.1.8.3 Tesla-type pump device

The design domain for the Tesla-type pump device is shown in Fig. 5.101.

Figure 5.101 – Design domain for the Tesla pump.

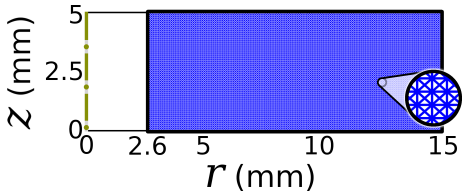


Source: Author (ALONSO *et al.*, 2022).

The mesh consists of 10,277 nodes and 20,240 elements (i.e., 110 radial and 46 axial rectangular partitions of crossed triangular elements, see Fig. 5.102). The input parameters, geometric dimensions and material model parameters that are considered

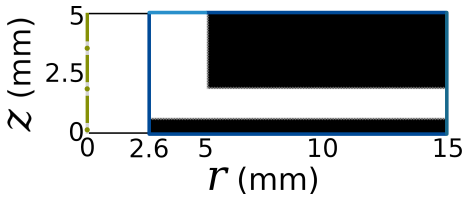
for the design are shown in Table 5.30. In this example, the maximum inlet Reynolds number is given as 4.92×10^4. In this work, in order to facilitate convergence, a *straight disks* initial guess is considered (see Fig. 5.103). The specified fluid volume fraction (f) is set as 30%.

Figure 5.102 – Mesh used in the design of the Tesla pump.



Source: Author (ALONSO *et al.*, 2022).

Figure 5.103 – Straight disks reference design for the Tesla pump.



Source: Author (ALONSO *et al.*, 2022).

Table 5.30 – Parameters used for the topology optimization of the Tesla pump.

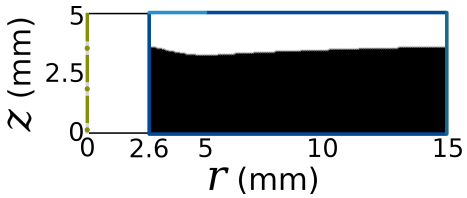
Input parameters	
Inlet flow rate (Q)	5.0 L/min
Wall rotation (n_0)	50,000 rpm
Inlet rotation (n_{in})	0 rpm
Inlet velocity profile	Turbulent
I_T	5.0%
ℓ_T	0.092 mm
Dimensions	
r_{shaft}	2.6 mm
r_{int}	5 mm
e_{out}	5 mm
r_{ext}	15 mm
Material model parameters*	
$\kappa_{\max}$ ($\times 10^{15}\mu$ (kg/(m^3 s)))	2.5
q	1.0
λ_{R_T}	1.0

* The optimization considers a Helmholtz pseudo-density filter (Section 2.5.7.1) in order to better stabilize the discrete optimized topologies. The filter length parameter (r_H) is chosen as the value $r_H =$ 0.22 mm.

The optimized topology is shown in Fig. 5.104, where the maximum local Reynolds number is given as 1.96×10^6. As can be noticed, when under a high flow

rate and rotation, the optimized channel tends to attach itself to the upper surface of the design domain, which, in fact, corresponds to the least distance from the inlet to the outlet. Table 5.31 shows the computed values for the reference (Fig. 5.103) and optimized (Fig. 5.104) designs. As can be noticed, the computed values show that the optimized design is an improvement in relation to the reference design, with the relative energy dissipation (Φ_{rel}) being slightly smaller (-0.53%), the pressure head (H) being slightly higher (+1.21%) and the isentropic efficiency (η_s) also being slightly higher (+1.57%). It can be noticed that the relative differences are not high, because, when considering a fluid flow problem that includes a high rotational effect, the rotation itself poses a high influence in all computed functions. This leads to the effect that, if the reference topology is not chosen as a *poor-performing* topology, the computed functions should be mainly guided by the rotation, meaning that the relative performance improvement from topology optimization may not be so high.

Figure 5.104 – Optimized topology for the Tesla pump.



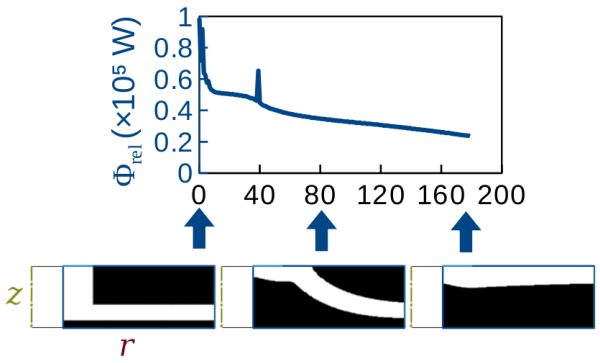
Source: Author (ALONSO *et al.*, 2022).

Table 5.31 – Computed values for the reference and optimized topologies for the Tesla pump device.

Designs	Φ_{rel} ($\times 10^4$ W)	H (m)	η_s (%)
Reference	1.88	57.7	25.4
Optimized	1.87	58.4	25.8

The convergence curve is shown in Fig. 5.105.

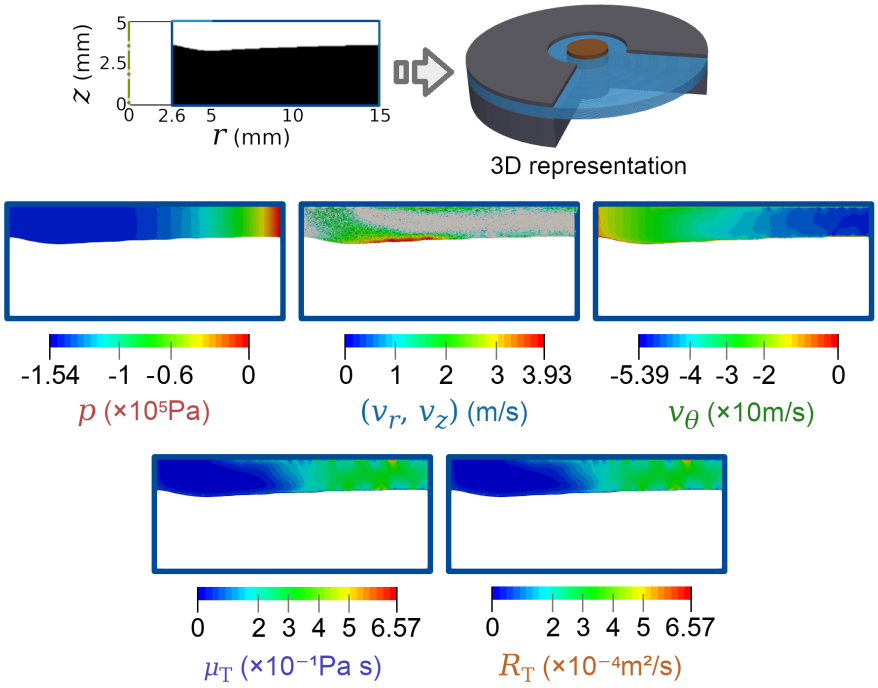
Figure 5.105 – Convergence curve of the topology optimization of the Tesla pump.



Source: Author (ALONSO *et al.*, 2022).

The simulation of the optimized design is shown in Fig. 5.106. From it, it can be noticed that the pressure increases more at higher radii, due to the fluid pumping. From the high rotation, the Tesla principle “dampens” a *possible collision-like* behavior of the inlet flow towards the *horizontal disk-surface*, leading the fluid to accelerate towards the outlet near the walls. This behavior seems to justify the optimized design in relation to the reference (Fig. 5.103), due to the fact that the main difference between the two designs would be that the reference design allows an additional axial rotational acceleration which increases the relative energy dissipation. It can also be noticed that higher velocities are achieved near the walls, due to the higher rotational effect (Tesla principle). The turbulent viscosity increases when the fluid reaches the “outlet channel”, where the fluid is more intensely rotationally accelerated.

Figure 5.106 – Optimized topology and variables for the optimized Tesla pump.



Source: Author (ALONSO *et al.*, 2022).

5.1.9 **Tesla VAD design considering rotor and volute**

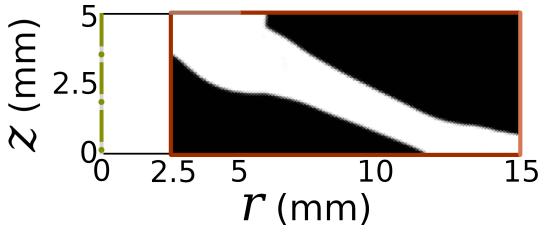
The design of the complete Tesla VAD pump consists of combining the optimized topologies for the rotor and the volute. It may be highlighted that the complete design requires various design choices, from which some are described in Chapter 4. The optimized topologies that are considered are those obtained for a rotation of 2000 rpm and a flow rate of 1 L/min, which are indicated in Table 5.32.

Table 5.32 – Topology optimization results for the volute under different weights in the multi-objective function for the hemolysis index.

Optimized topology	Configuration	Figure
Tesla rotor	2000 rpm, 1 L/min, optimized considering $w_H = 0.9$	Fig. 5.59b (from Section 5.1.5)
Volute	Optimized for the middle of the outlet of the Tesla rotor described above, considering $w_\Phi = 1$	Fig. 5.70 (from Section 5.1.6)
Bladed rotor	2000 rpm, optimized for an approximation of the flow inside the Tesla rotor described above, and considering 5 blades and $w_{PAS} = 0.85$	Fig. 5.81 (from Section 5.1.7)

In order to simplify the design of the prototype when considering the components that are available in the market, more specifically the coupling of the shaft with the rotor, it has been decided to change the internal diameter of the rotor shaft from the Tesla rotor optimized topology from 5.2 mm ($r_{shaft} = 2.6$ mm) to 5 mm ($r_{shaft} = 2.5$ mm) in order to allow using a Ø5 mm shaft instead of a Ø3 mm shaft. Thus, the topology optimization was repeated with the same conditions that were considered for the previous results. The resulting optimized topology for a shaft diameter of 5 mm ($r_{shaft} = 2.5$ mm) is shown in Fig. 5.107. It can be noticed that, as expected from the shaft radius difference of 0.1 mm, the differences in the optimized topologies are almost unnoticeable: visually checking it with Fig. 5.59b ($w_H = 0.9$), the difference would be essentially only a tiny *stretch* near the shaft until reaching the new r_{shaft} value.

Figure 5.107 – Optimized Tesla pump rotor with $r_{shaft} = 2.5$ mm (2000 rpm, 1 L/min, optimized considering $w_H = 0.9$).



Source: Author.

From the definition of the local Reynolds number in relation to the external radius (Table 2.1), by assuming the *Newtonian* viscosity of blood (i.e., $\nu = \frac{\mu_\infty}{\rho}$), $|\boldsymbol{v}_{\text{abs}}| \approx \omega_0 r$, and the definition based on the external diameter ($2r_{ext}$) (i.e., eq. (5.2)),

$$\text{Re}_{\text{ext}} \approx \frac{\rho(\omega_0 r_{\text{ext}})(2r_{ext})}{\mu_\infty} \tag{5.4}$$

In eq. (5.4), by considering $\text{Re}_{ext} \approx 10^6$, which corresponds to the transition Reynolds number in pumps (SABERSKY *et al.*, 1971; WU, 2007), and also $r_{\text{ext}} = 15$ mm (30 mm diameter), $\omega_0 \approx 7,300$ rad/s, which means $n_0 \approx 70,000$ rpm. This means that, in order for the fluid flow to be turbulent in a Tesla pump rotor of radius $r_{\text{ext}} = 15$ mm, the rotation would need to be at least 70,000 rpm. Since the considered rotations are much smaller than 70,000 rpm, laminar flow is assumed in the simulations. It can also be mentioned that commercial bladed VADs operate at a range of rotations such as 3,000$\sim$9,000 rpm (HeartMate III®) (THORATEC, 2017), which is much smaller than 70,000 rpm. Even in the case when $r_{\text{ext}} = 30$ mm (60 mm diameter), the rotation would also need to be quite high for reaching turbulence (35,000 rpm).

5.1.9.1 Prototype designs

Three prototypes are designed for comparing the rotor designs, by considering the optimized volute: *Straight* (with the reference straight disks rotor, reproduced in Fig. 5.57), *Optimized* (with the optimized Tesla pump rotor), and *Optimized (with blades)* (with the optimized Tesla pump rotor and the optimized blades). These designs are summarized in Table 5.33.

Table 5.33 – Prototype designs.

Name of the design	Rotor	Volute
Straight	Straight	Optimized
Optimized	Optimized	Optimized
Optimized (with blades)	Optimized with blades	Optimized

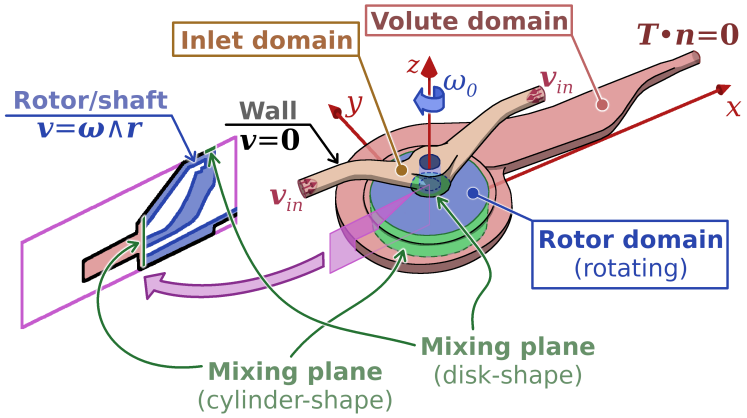
In order to consider the design of the volute in the prototype, it is necessary to interpret (*extrapolate*) it from 2D to 3D. This interpretation requires considering a cross-section (Section 1.1.4) and possibly some other changes, resulting in the shape shown in the next section. Particularly, a rectangular-shaped cross-section with rounded corners is considered (which is also similar to the one considered in the Rotaflow pump), together with a variation of thickness in the first 90°, from 2 mm to 4 mm. The height of the inlet part of the volute is chosen so as to allow it to function with all rotor designs.

5.1.9.2 Simulations of the designed prototypes

For the simulations of the designed prototypes, the CAD models from Section 4.2 are simplified. The simplification consists of removing the seal (i.e., neglecting leakage). The considered rotor and volute shapes are shown in Section 4.2. The blades from Section 4.2 are shown inverted with respect to the optimized designs (when considering an upper view of the components), but their orientation is consistent with the optimized topologies when viewed from below.

The boundary conditions that are considered for the fluid flow simulation are shown in Fig. 5.108. In order to perform the simulations under steady state conditions, the mixing plane approach is considered (see Section 3.5). The rotor domain is considered between $z = 0$ mm and $z = 11$ mm, and for $r \leqslant 15$ mm. The inlet velocity profiles are considered to be parabolic.

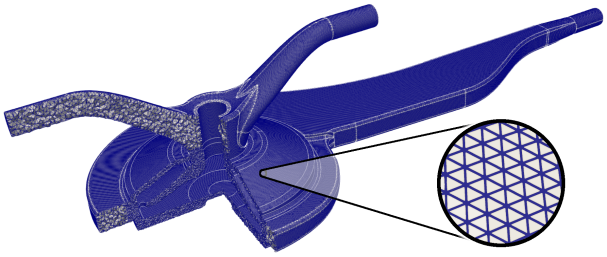
Figure 5.108 – Boundary conditions for the simulations of the designed prototypes.



Source: Author.

The meshes are composed of around 3 million elements (Fig. 5.109), with a higher resolution inside the rotor and on the walls.

Figure 5.109 – Mesh for the simulations of the designed prototypes (exemplified for the optimized rotor).



Source: Author.

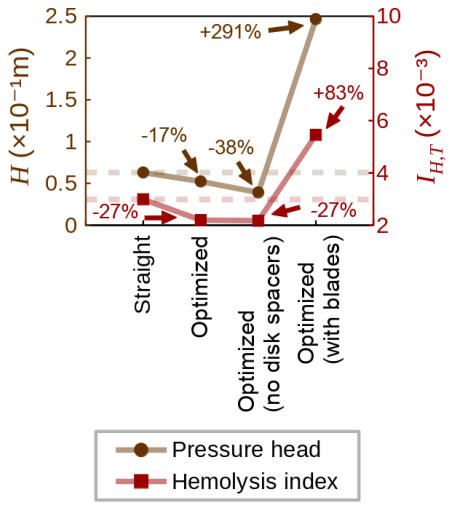
The implementation of the hemolysis and thrombosis models faced some numerical convergence difficulties in the 3D computations. In order to give an idea of how blood damage occurs in the prototypes, the differential equation of the hemolysis model is considered from the simplification presented in Section 2.4.1.1.2, enabling the hemolysis index to be algebraically computed through an integral. Although the performed simplifications may not be entirely correct, the computed value might be able to give a rough idea of how the hemolysis index value should be. As an example, for the optimized Tesla pump rotor in the 2D swirl flow model (2000 rpm, 1 L/min, optimized considering $w_H = 0.9$, from Fig. 5.59b), the hemolysis index is computed as 1.79×10^{-4}, whilst the simplification gives the value 7.01×10^{-4}. Note that, in this specific case, there was an overestimation of about 4 times, which may mean that the approximation is not very precise.

The simulations are performed for 1.0 L/min and 2000 rpm. An additional simulation is also performed when considering the optimized rotor without the disk spacers, and without any arm-like structure that would otherwise be needed for keeping the upper part of the rotor in place. This is done with the aim of checking the influence of the disk spacers in the simulation. The functions computed for the simulations are shown in Fig. 5.110. It can be noticed that the optimized rotor portrays less blood damage than the straight rotor. However, the pressure head is also smaller, which can be attributed to the intermediary flow rates (detailed in the next paragraph), because the intermediary flow rates entering and exiting the straight rotor are slightly higher than their counterparts in the optimized rotor. When considering the hypothetical condition (optimized rotor without the disk spacers), the blood damage was kept the same with respect to the optimized rotor with the disk spacers, whilst the pressure head worsened. This may be attributed to the presence of the spacers, which may act as blades, inducing a higher pressure head. However, the blood damage did not worsen, which may be caused by two combined factors: the first one would be the design of the spacers (*airfoil-like*-shaped), which is, in fact, a “worse” local minimum (with respect to the results from Section 5.1.7.2) that can be achieved in the case of the design of blades (Section 5.1.7.2) by increasing the use of topology optimization filters; the second factor would be the *washout leakage* (flow through the washout hole, detailed in the next paragraph), which is slightly higher in the optimized rotor without the disk spacers. This shows that it is possible for well-designed disk spacers to portray a positive impact in the performance, while keeping the blood

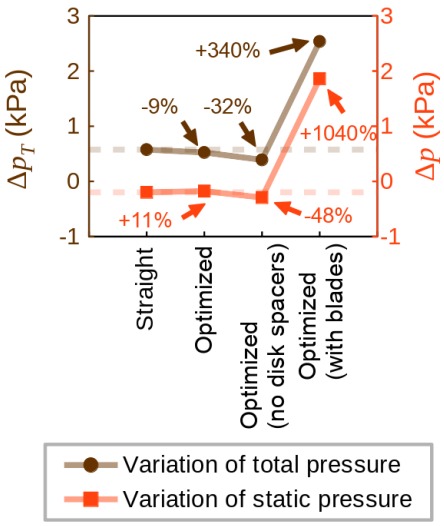
damage low. The optimized rotor with blades shows increased pressure head and blood damage, with the relative increase of the pressure head being about 3.5 times higher than the relative increase of the blood damage. This shows that the presence of blades is capable of significantly increasing the pump performance, also showing, however, a significant negative impact in blood damage. The values for the variation of pressure (Fig. 5.110b) show approximately the same behavior as the pressure head from Fig. 5.110a, with the sole exception of the variation of static pressure in the optimized rotor with the disk spacers.

Figure 5.110 – Functions computed in the simulations for 1.0 L/min and 2000 rpm (the percentages correspond to the relative difference fractions with respect to the values for the straight rotor).

(a) Pressure head and hemolysis index (from eq. (2.98)).



(b) Variations of total and static pressures.



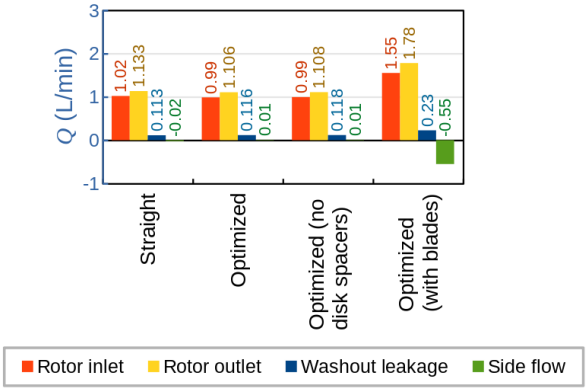
Source: Author.

In the operation of the designed prototype, there is the presence of intermediary flow rates, which may impact differently the overall blood pump operation. These intermediary flow rates are detailed in Fig. 5.111. As shown in Fig. 5.111b, there are mainly four types of intermediary flows: *rotor inlet* (the flow effectively entering the rotor), *rotor outlet* (the flow effectively exiting the rotor), *washout leakage* (flow through the washout hole), and *side flow* (flow that passes over the rotor). The remaining flows (*inflow* and *outflow*) are both equal to the total flow rate (i.e., 1 L/min). The arrows that are shown in Fig. 5.111b correspond to the positive directions for the flow rates that are computed in Fig. 5.111a. The first aspect that can be noticed is that the flow rates that effectively enter the rotor in each case (*rotor inlet*) are different, meaning that flow is passing over

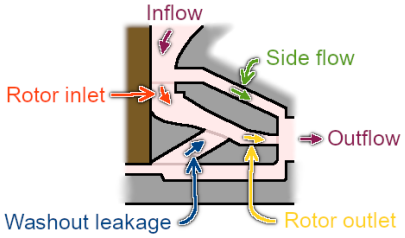
the rotor (*side flow*). This effect (*side flow*) seems to be affected by the capacity of the rotor to pump fluid, where a higher capacity is even able to revert the direction of the side flow, as shown in the cases of the straight rotor and the optimized rotor with blades. The second noticeable aspect are the flow rates that effectively exit the rotor, which are all higher than the inflow, meaning that fluid is entering the rotor through the washout hole. This makes sense, since the rotation of the rotor tends to create high pressure zones farther from the rotating axis, and low pressure zones near the rotating axis (this effect is analogous to the centrifugal effect approximation for the pressure drop, which is shown in the description of eq. (4.1)). This pressure drop happens below the rotor, towards the rotating axis, leading the fluid flow to be *pumped back* (*backflow*), as has been illustrated in Fig. 4.1.7. From there, the fluid is pumped back to the inside of the rotor. The washout leakage can be better visualized from Fig. 5.111c, which, although most of the velocity vectors are pointing outside this sheet of paper, shows the directions of the intermediary flows for the optimized rotor. As can be noticed, the washout hole "suctions" the fluid from below the rotor, avoiding the appearance of a stagnated fluid zone, which is a highly important condition for blood flow devices. From Fig. 5.111a, it can also be noticed that the presence of disk spacers slightly reduced the side flow and the washout leakage, which is consistent with the positive impact of the disk spacers shown in Fig. 5.110a.

Figure 5.111 – Intermediary flow rates around the rotor.

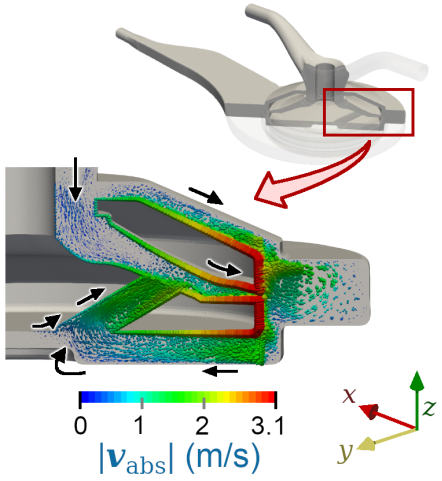
(a) Intermediary flow rate distribution.



(b) Positions of the intermediary flow rates around the rotor.



(c) Velocity vectors in a cross-section that passes through the washout hole for the optimized rotor.



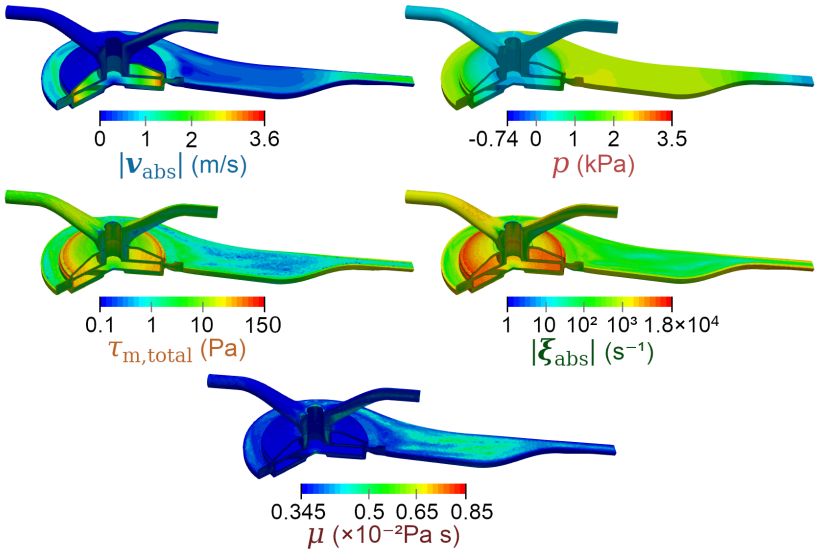
Source: Author.

The simulations are plotted in Figs. 5.112, 5.113, 5.114 and 5.115. Since the local blood damage indices were not computed, in order to give an idea of the blood damage (hemolysis and thrombosis), the scalar shear stress ($\tau_{\mathrm{m,total}}$), which is an important term of the computation of blood damage models, and the vorticity ($|\boldsymbol{\xi}_{\mathrm{abs}}|$), which is indicated in Fig. 1.4, are also plotted. The plots are presented by cutting out a section of the rotor and the volute: This is done in order to show the distribution of the variables inside the rotor, as well as their distribution in the washout hole and before reaching the rotor. There is not any significant change in the variables' distribution inside the section that has been cut. Another cut is also made in the middle height of the volute, in order to show the flow inside the volute. In order to still be able to give an idea of how the flow behaves inside the cross-section of the volute around the rotor, the plots of two of these

cross-sections are shown in the plots.

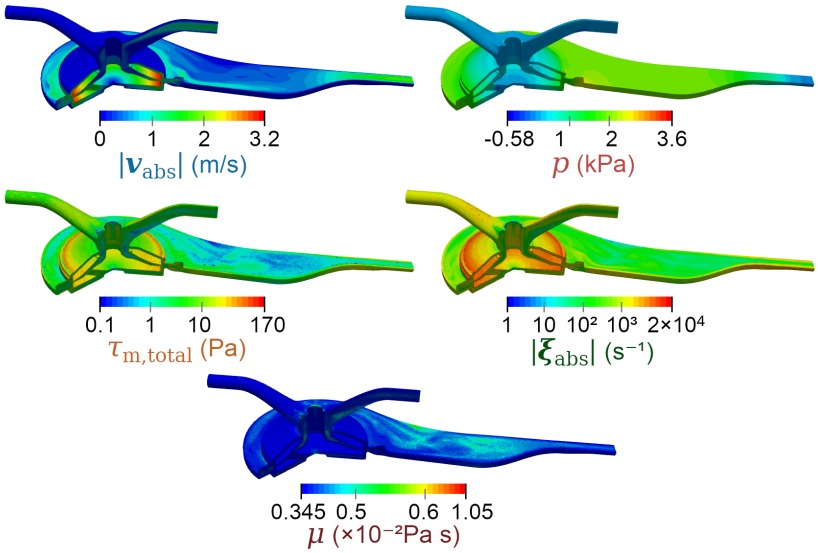
By comparing the scalar shear stress in Figs. 5.112, 5.113, 5.114 and 5.115, it can be noticed that it is much higher in the optimized rotor with blades, which is, in fact, consistent with the higher blood damage shown in Fig. 5.110. In terms of the variation of (static) pressure, it can be noticed that it rises mainly inside the rotor, and drops when the volute cross-section begins to shrink until the outlet.The non-Newtonian viscosity seems to be higher inside the inlet channel, where the fluid flow is slower, and inside the volute, showing that the non-Newtonian effect does not seem to be negligible in the simulations. A high vorticity value can be seen near the external radius of the rotor; however, since the absolute vorticity is being computed, it also includes the rotor rotation itself, and not only the recirculation. Nonetheless, the vorticity seems to be high inside the washout hole, near the outlet, and near the inlet.

Figure 5.112 – Simulation results for the straight rotor (1 L/min, 2000 rpm).



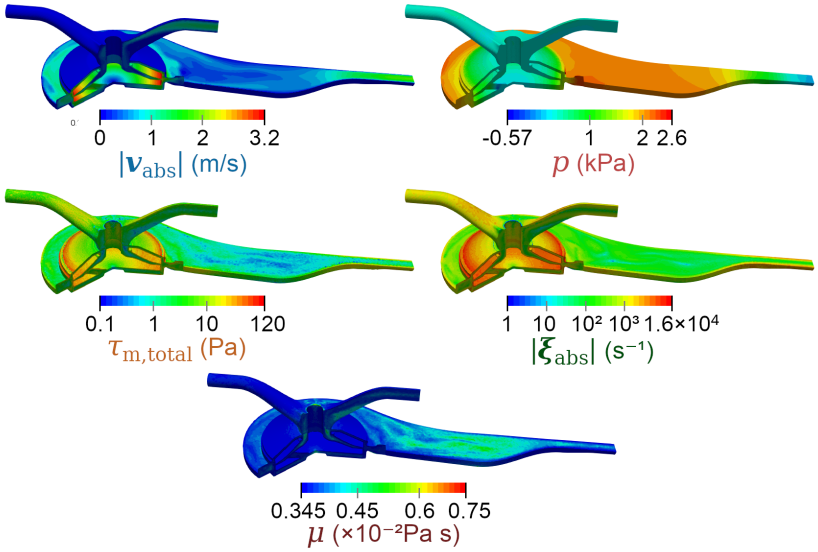
Source: Author.

Figure 5.113 – Simulation results for the optimized rotor (1 L/min, 2000 rpm).



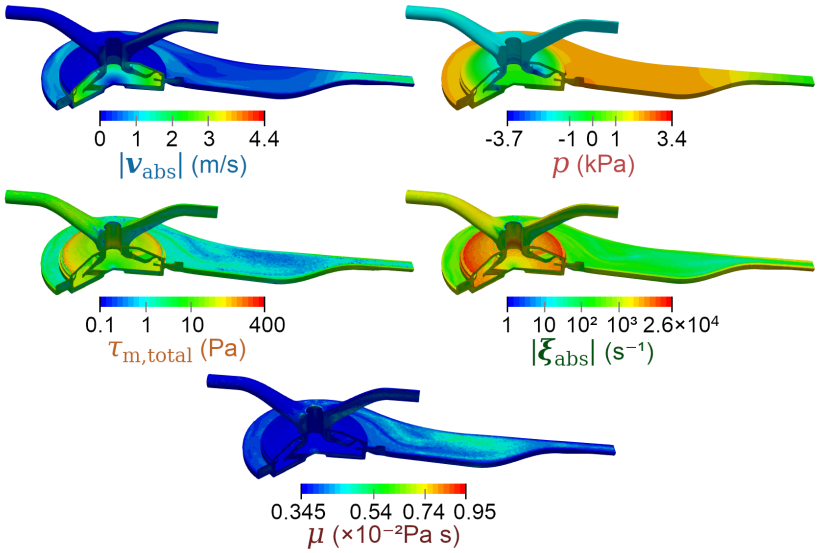
Source: Author.

Figure 5.114 – Simulation results for the optimized rotor (no disk spacers) (1 L/min, 2000 rpm).



Source: Author.

Figure 5.115 – Simulation results for the optimized rotor (with blades) (1 L/min, 2000 rpm).



Source: Author.

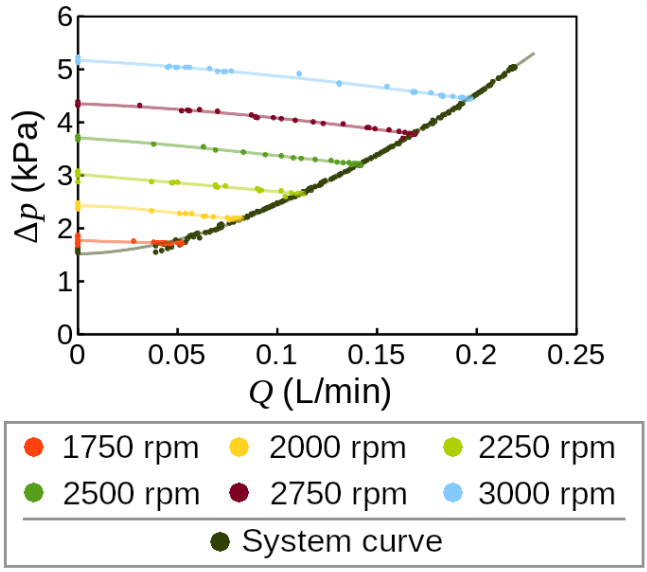
For reference, the hemolysis indices can be converted to standardized values (NIH, mgNIH, MIH) (ASTM F1841-97, 1997), from Table 2.2 and by considering a healthy person, in which $\mathrm{Hb} = 1500$ g/dL and $\mathrm{Ht} = 45\%$ (ARORA *et al.*, 2006b; NAM *et al.*, 2011; BEHBAHANI *et al.*, 2009; CHO; KENSEY, 1991). For example, for the optimized rotor, $I_{H,T} \approx 2.19 \times 10^{-3}$, meaning that NIH $= 1.8$ g/dL, mgNIH $= 1800$ mg/dL and MIH $= 0.0012$. The Reynolds number, considering the characteristic length as being the diameter of the rotor, had its value below 4.3×10^4 in all the simulations, which is smaller than 10^6 (transition Reynolds number in pumps (SABERSKY *et al.*, 1971; WU, 2007)), meaning that the fluid flow in the simulated designs, under the given operating conditions, should not require solving the turbulence phenomenon.

5.2 EXPERIMENTAL RESULTS

The experimental part consists of the experiments performed for the designed prototypes, by considering the use of a blood analogue (Section 4.4). The experimental results for the prototypes described in Chapter 4 are shown in Fig. 5.116. The system curves were obtained from the fluid flow circuit operating with a fully open valve, and continuously decreasing the rotation from 3200 rpm to 0 rpm, with an angular deceleration of 10 rpm/s. Note that, from the experimental results, the flow sensor is unable to measure flow rates below around 0.03 L/min. The uncertainties (error bars) are not indicated in these plots in order to avoid visual clutter, but they can be estimated from the sensors' specifications as ± 0.225 kPa and $\pm 3\% Q$.

Figure 5.116 – Experimental pump curves (expressed as $\Delta p \times Q$).

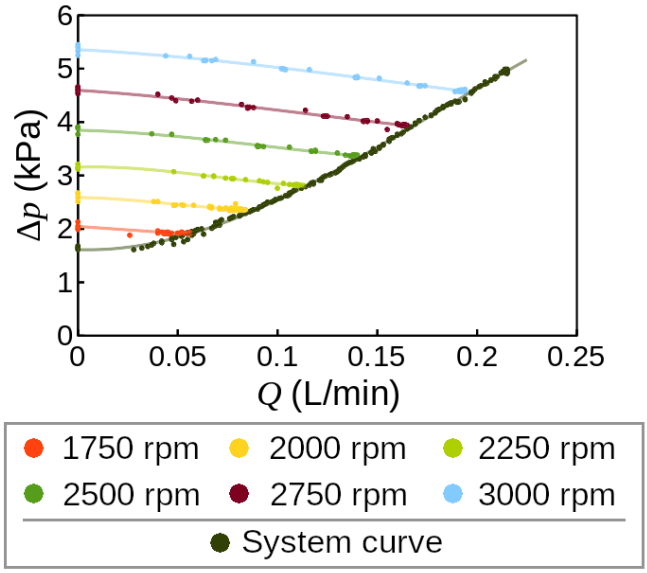
(a) Straight rotor.



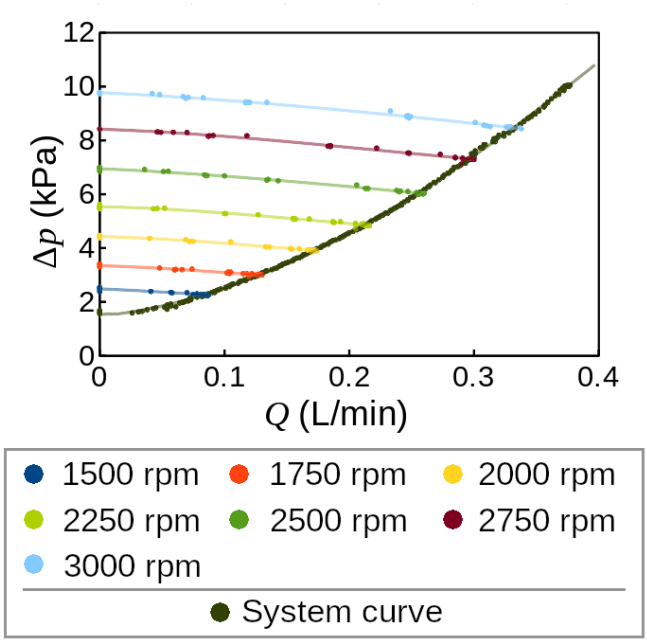
Source: Author.

Figure 5.116 – [Continued] Experimental pump curves (expressed as $\Delta p \times Q$).

(b) Optimized rotor.



(c) Optimized rotor (with blades).



Source: Author.

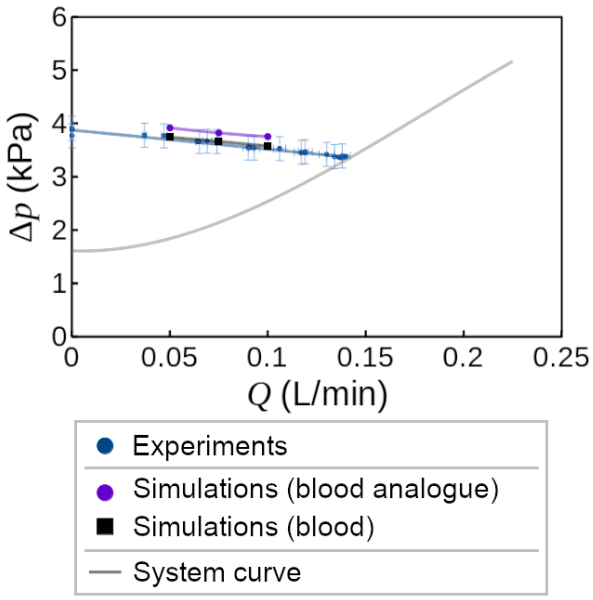
By comparing the three types of rotor, it can be noticed that, in terms of the variation of static pressure, the optimized rotor performs better than the straight rotor. However, the inclusion of blades causes the variation of static pressure to double. This is consistent with the fact that bladed rotors are able to achieve higher variations of static pressure due to the power transmission provided by the variation of linear momentum through the blades.

In the simulations, the Reynolds number, considering the characteristic length as being the diameter of the rotor, had its value below 5×10^4, which is smaller than 10^6 (transition Reynolds number in pumps (SABERSKY *et al.*, 1971; WU, 2007)), meaning that the fluid flow in the simulated designs should be laminar. This is also shown when comparing the simulated results to the experiments, which are consistent.

5.2.1 Comparison of the experiments with simulations for blood and a blood analogue

Fig. 5.117 shows a comparison of the experimental results (considering a blood analogue) with simulations considering blood and a blood analogue, for 2500 rpm. It can be noticed that both simulation results are close to the experiments, and within the error bar.

Figure 5.117 – Comparison of experimental results with simulations for the optimized rotor at 2500 rpm.



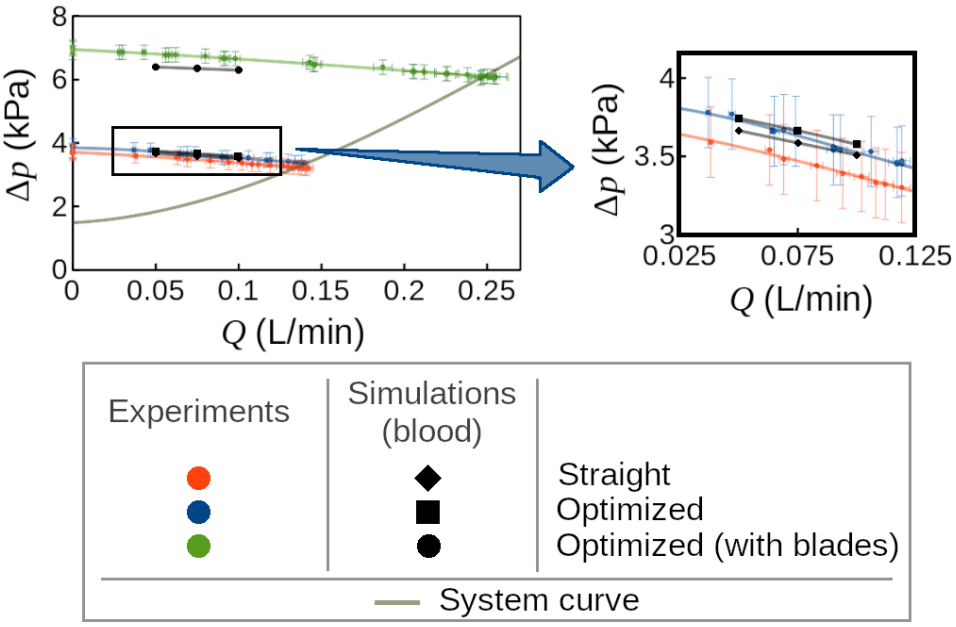
Source: Author.

5.2.2 Comparison of the experiments with simulations for the different types of rotor

The designed prototypes are compared considering experiments and simulations, in Fig. 5.118, for 2500 rpm. The simulated results are consistent with the experiments, which can be seen from their proximity in the plot, and also with respect to the order from lower to higher pressure rises: straight rotor → optimized rotor → optimized rotor

(with blades). The higher difference in some values may be attributed to the neglected aspects of the modeling, such as leakage (through the seal), weight (i.e., gravity), and possibly differences in the inlet velocity profiles.

Figure 5.118 – Comparison of experimental results with simulations for the rotors at 2500 rpm, given by the pump curve expressed as $\Delta p \times Q$.

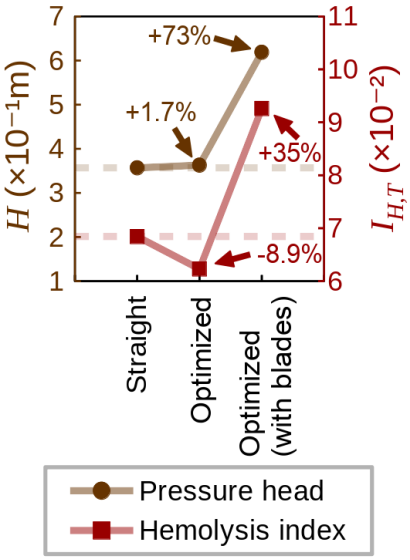


Source: Author.

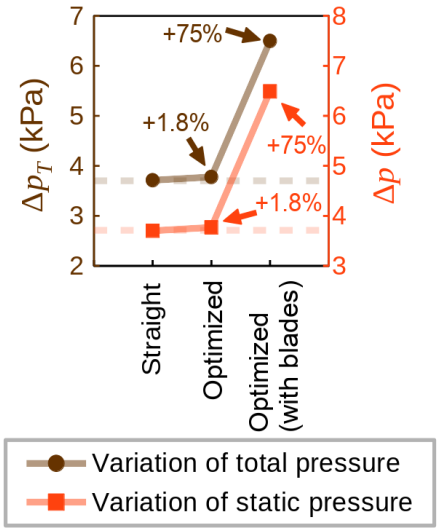
For completeness, Fig. 5.119 shows some computed functions in the simulations. Although the flow rate and rotation are different from the design (mostly due to the experimental apparatus/setup), the obtained results show that the optimized rotor is better in terms of performance and blood damage than the straight rotor. As also shown in Section 5.1.9, the optimized rotor with blades shows increased performance, but worse blood damage.

Figure 5.119 – Functions computed in the simulations for 0.1 L/min and 2500 rpm (the percentages correspond to the relative difference fractions with respect to the values for the straight rotor).

(a) Pressure head and hemolysis index (from eq. (2.98)).



(b) Variations of total and static pressures.



Source: Author.

6 CONCLUSIONS AND FUTURE WORK

The topology optimization method has been applied to the design of Ventricular Assist Devices (VADs) based on the 2D swirl concept. In order to perform the topology optimization for this type of device, various aspects have been progressively considered and evaluated along the research, along five research fronts: *Newtonian 2D swirl flow*, *Non-Newtonian 2D swirl flow*, *Turbulent 2D swirl flow*, *Blood damage* and *VAD design*.

The first research front (*Newtonian 2D swirl flow*) marks the beginning of the investigation of the 2D swirl flow model in topology optimization, for a Newtonian fluid. The presented formulation allows the design of 2D swirl flow devices, such as hydrocyclones and some pumps and turbines. The greatest advantage of the 2D swirl flow model is the reduced computational cost in relation to 3D models. From the initial numerical results, it can be noticed that a sufficiently high flow rotation has the effect of slowing the effect of the radial and axial velocity components in the optimized topologies. Following, the design of Tesla-type pump devices is investigated, while taking more into account: the *extended material model*, which takes into account the different nature of the swirl component of the flow in the 2D swirl flow model, and is shown to lead to better optimized topologies; and an extra term is included in the vorticity objective function, helping to obtain clear discrete topologies. From the numerical results, the isentropic efficiency is shown to increase with smaller flow rates and longer disks; and the energy dissipation is shown to decrease with higher flow rates (starting from a certain rotation), and longer disks. This shows that the performance of a 2D swirl pump should increase with a higher quantity of “channels” (i.e., a higher quantity of disks). Some other aspects (Brinkman-Forchheimer model, power objective function including the effect of the material model, and MINI elements) are further investigated in Alonso and Silva (2022b), for Tesla-type turbine devices.

The second research front (*Non-Newtonian 2D swirl flow*) starts with considering a non-Newtonian fluid (blood) in the design of 2D swirl flow devices, by also taking into account the non-Newtonian penalization, which imposes that the non-Newtonian viscosity is constant inside the solid material, while it also achieves its highest value. This behavior of the non-Newtonian viscosity is shown to be coherent with the expected/desired behavior of the fluid inside a modeled solid material. From the numerical example, the effect of using a non-Newtonian fluid model seems to be more significant

for designs including “bends” and “axial-radial” flows.

The third research front (*Blood damage*) involves the inclusion of blood damage (hemolysis and thrombosis) in the topology optimization formulation, where it is shown that considering them in the objective function leads to different optimized topologies than when considering only the relative energy dissipation. In particular, it shows that they create a tendency for *inclined disk*-like topologies, while the relative energy dissipation function creates a tendency for *straighter disk*-like topologies. The *inclined disk*-like topologies slightly resemble some commercial Tesla pump devices that feature conical-shaped disks. The same developed approach is then applied to the design of blades, and the volute. It may be pointed out that the blood damage is not considered as a requirement during optimization, but the aim to minimize it is considered during the design process.

The fourth research front (*Turbulent 2D swirl flow*) involves considering turbulence in topology optimization. The implementation is based on the *FEniCS TopOpt Foam* library (ALONSO *et al.*, 2021), which enables combining the main advantages of two open source platforms: OpenFOAM® for an efficient fluid flow simulation, and FEniCS/dolfin-adjoint for an automatically generated adjoint model. Although an even higher computational efficiency would be possible to be achieved through manually deriving the continuous adjoint model and adjusting its implementation (such as through reordering the terms/operations, block matrices, local preconditionings etc.), this procedure may become a hard and cumbersome task, especially for complex models. Therefore, this work presents a more convenient and comprehensive approach of obtaining the automatically derived adjoint model in an efficient manner when considering OpenFOAM® . The initial implementation (ALONSO *et al.*, 2021) is extended to the Wray-Agarwal turbulence model (WA2018), which poses advantages in terms of simulation and also in a topology optimization point-of-view, and also extended to consider a binary variables approach for topology optimization (TOBS). Therefore, one of the main aspects is the Wray-Agarwal turbulence model (WA2018), which reduces the number of coefficients that need to be adjusted in topology optimization and does not require the computation of the wall distance, making it easier to perform/calibrate topology optimization. Also, the smaller number of additional equations when using this model (i.e., only one instead of two, with respect to other turbulence models) makes it simpler to implement topology optimization. Another relevant aspect is the TOBS approach,

which allows the use of binary variables, eliminating the problem of a *gray* medium possibly being present in the optimized results or during topology optimization itself.

Following, the fifth research front (*VAD design*) consists of the design of the prototype, from which various design choices have been described and made. Some differences from the simplified models to the 3D model are the different inlet rotation in the design of the blades, the fact that the volute has a thickness, and also the neglected leakage. The simulations of the prototype under 1 L/min and 2500 rpm show that blood damage is reduced in the optimized rotor with respect to the straight rotor, while the pressure head does not face such improvement, most probably due to the negative impact of the disk spacers, which led to a higher side flow. This possibly means that it would be interesting to restrain the side flow, by designing, for example, a tortuous path rather than a straight inclined path (i.e., an inclined labyrinth seal) over the rotor, or improving the design of the disk spacers (i.e., further analyzing it for lower blockage ratios (Section 4.1.5)). The hybrid design (optimized rotor with blades) shows an increase in the pressure head, as well as a worsening in the blood damage aspect due to the presence of blades. The experimental results are consistent with the simulations, and the optimized rotor is shown to be better (in terms of performance and blood damage) than the straight rotor design. It can be highlighted that hemolysis and thrombosis were not experimentally evaluated, since experimental measurements would require specialized equipment, may suffer from imprecisions and may also face safety/ethical issues. Due to convergence difficulties for the blood damage models, an estimation to the hemolysis index is presented, alongside plots of scalar shear stress and vorticity. Due to limitations of the experimental setup, the operating conditions of the prototype resulted smaller than the one from the design. In such case, some ways to increase the measured values would be to perform the design for: *stacking* the rotor profiles for more disks (see Fig. 4.4), pattern repetition for more disks (Section 2.5.6), considering larger radii in the design, or further increasing the rotation.

6.1 FUTURE WORK

As future work, there are various various possibilities that may arise, which include:

- Extending the 2D swirl flow model to thermofluid problems, fluid separators, labyrinth seals, other turbulent flows, Fluid-Structure Interaction (FSI), compressible flow and even transient design (pulsatile);
- Considering other non-Newtonian fluids – For example, other fluids that feature a shear-thinning behavior – such as activated sludge (GARAKANI *et al.*, 2011), ketchup (BAYOD *et al.*, 2008) etc. –, fluids that feature a shear-thickening behavior – such as a mixture of corn starch and water –, fluids that feature a Bingham plastic/pseudoplastic behavior – such as in concrete (FERRARIS; DE LARRARD, 1998) – or even fluids that exhibit viscoelasticity – such as polymers;
- Considering other blood damage models, such as the *mechanical dose infinitesimal damage index* model for hemolysis (GRIGIONI *et al.*, 2005), which comes from a derivation that is more generic than the *asymptotically consistent damage index* model;
- Extending the topology optimization approach for axial blood pumps, which are also quite important in terms of medical applications;
- Considering even higher rotations in topology optimization – Higher rotations mean a higher swirling effect, which poses challenges for simulation and topology optimization;
- Considering other more complex turbulence models in topology optimization, such as the SST k-ω model and the realizable k-ε model, which may be more suitable depending on the application;
- Considering another turbulence modeling approach in topology optimization, which is not based on RANS turbulence models – RANS turbulence models rely on empirical parameters and/or assumptions calibrated for certain conditions in order to give an “artificial dissipation” for turbulence, which means that an approach with less empiricity, e.g. a steady-state LES (GANESAN; AWANG, 2015), may be more interesting, although with a higher computational cost;
- Considering 3D models for VAD topology optimization – Although being more computationally expensive, they may be able to capture effects that are not modelable in 2D, which may possibly play a significant effect in the optimized topology;

- Developing *morphing* (*intelligent*) *blades/disks* – That is, blade/disk shapes that can be changed (such as from an actuator) according to the rotation and flow rate, in order to match the corresponding optimized topologies for each rotation and flow rate;
- Considering a larger internal diameter for the tubes of the fluid circuit in the experiments, which would enable having a lower head loss in the circuit, and possibly a higher flow rate in the experiments;
- Considering experiments for some variations of the design of the whole pump in order to improve it, by considering either a trial-and-error approach, a Design of Experiments (DoE) approach (i.e., defining a reduced set of parameters in the optimized topologies, varying them through experiments and evaluating the results statistically), or even machine learning.

REFERENCES

AARONSON, K. D.; SLAUGHTER, M. S.; MILLER, L. W.; MCGEE, E. C.; COTTS, W. G.; ACKER, M. A.; JESSUP, M. L.; GREGORIC, I. D.; LOYALKA, P.; FRAZIER, O.; JEEVANANDAM, V.; ANDERSON, A. S.; KORMOS, R. L.; TEUTEBERG, J. J.; LEVY, W. C.; NAFTEL, D. C.; BITTMAN, R. M.; PAGANI, F. D.; HATHAWAY, D. R.; BOYCE, S. W. **Use of an intrapericardial, continuous-flow, centrifugal pump in patients awaiting heart transplantation clinical perspective**. Circulation, American Heart Association, Inc., v. 125, n. 25, p. 3191–3200, 2012. ISSN 0009-7322. Available at: http://circ.ahajournals.org/content/125/25/3191. Cited in page 56.

ABBOTT. ***HeartMate 3^{TM} left ventricular assist system***. 2018. Available at: https://www.sjmglobal.com/en-int/patients/heart-failure/our-solutions/left-ventricle-assist-device/heartmate-3?halert=show&clset=92f57278-460e-4300-b7fe-89e52a04194f%3acadddb93-fcc4-47f2-8ceb-fd88f01ca17f. Accessed on: 2018-01-02. Cited in page 58.

ABRAHAM, F.; BEHR, M.; HEINKENSCHLOSS, M. **Shape optimization in steady blood flow: a numerical study of non-Newtonian effects**. Computer methods in biomechanics and biomedical engineering, Taylor & Francis, v. 8, n. 2, p. 127–137, 2005. Cited 4 times in pages 98, 99, 100, and 421.

ABTO. ***Dimensionamento dos transplantes no Brasil e em cada estado (2008-2015)***. [*S.l.*], 2015. Available at: http://www.abto.org.br/abtov03/Upload/file/RBT/2015/anual-n-associado.pdf. Cited 2 times in pages 54 and 55.

ABTO. ***Dimensionamento dos transplantes no Brasil e em cada estado (2009-2016)***. [*S.l.*], 2016. Available at: http://www.abto.org.br/abtov03/Upload/file/RBT/2016/RBT2016-leitura.pdf. Cited 2 times in pages 54 and 55.

ABTO. ***Dimensionamento dos transplantes no Brasil e em cada estado (2010-2017)***. [*S.l.*], 2017. Available at: http://www.abto.org.br/abtov03/Upload/file/RBT/2017/rbt-imprensa-associados-compressed.pdf. Cited 2 times in pages 54 and 55.

ABTO. ***Dimensionamento dos transplantes no Brasil e em cada estado (2011-2018)***. [*S.l.*], 2018. Available at: http://www.abto.org.br/abtov03/Upload/file/RBT/2018/Lv_RBT-2018.pdf. Cited 2 times in pages 54 and 55.

ACUTE MARKET REPORTS. ***Global ventricular assist devices market size, market share, application analysis, regional outlook, growth trends, key players, competitive strategies and forecasts, 2017 to 2025***. [*S.l.*], 2017. Cited in page 55.

ADEPT. ***Adept - A combined automatic differentiation and array library for C++***. 2021. Available at: http://www.met.reading.ac.uk/clouds/adept/. Accessed on: 2021-05-17. Cited in page 195.

AL-AZAWY, M. G.; TURAN, A.; REVELL, A. **Investigating the impact of non-Newtonian blood models within a heart pump**. International journal for numerical methods in biomedical engineering, v. 33, n. 1, 2017. Cited in page 62.

ALEMU, Y.; BLUESTEIN, D. **Flow-induced platelet activation and damage accumulation in a mechanical heart valve: numerical studies**. Artificial organs, Wiley Online Library, v. 31, n. 9, p. 677–688, 2007. Cited 2 times in pages 126 and 139.

ALIMOHAMADI, H.; IMANI, M.; SHOJAEIZADEH, M. **Numerical simulation of porosity effect on blood flow pattern and atherosclerotic plaques temperature**. International journal of technology enhancements and emerging engineering research, v. 2, n. 10, p. 44–49, 2014. Cited 4 times in pages 83, 148, 149, and 150.

ALLEN, G. S.; MURRAY, K. D.; OLSEN, D. B. **The importance of pulsatile and nonpulsatile flow in the design of blood pumps**. Artificial organs, v. 21, n. 8, p. 922–928, 1997. Cited 2 times in pages 56 and 57.

ALMEIDA, S. R. M.; PAULINO, G. H.; SILVA, E. C. N. **A simple and effective inverse projection scheme for void distribution control in topology optimization**. Structural and Multidisciplinary Optimization, v. 39, n. 4, p. 359–371, Oct 2009. ISSN 1615-1488. Available at: https://doi.org/10.1007/s00158-008-0332-6. Cited in page 161.

ALMEIDA, S. R. M.; PAULINO, G. H.; SILVA, E. C. N. **Layout and material gradation in topology optimization of functionally graded structures: a global-local approach**. Structural and Multidisciplinary Optimization, v. 42, n. 6, p. 855–868, Dec 2010. ISSN 1615-1488. Available at: https://doi.org/10.1007/s00158-010-0514-x. Cited 2 times in pages 159 and 248.

ALONSO, D. H. ***Projeto, Fabricação e Caracterização de uma Bomba Tesla***. Graduation Thesis — Universidade de São Paulo, 2017. Cited in page 292.

ALONSO, D. H. **Projeto, Fabricação e Caracterização de uma Bomba Tesla**. Mecatrone (Journal by the “PET Mecatrônica” academic group (Poli-USP)), 2018. Available at: https://www.revistas.usp.br/mecatrone/article/view/143554. Cited in page 292.

ALONSO, D. H.; GARCIA RODRIGUEZ, L. F.; SILVA, E. C. N. **Flexible framework for fluid topology optimization with OpenFOAM® and finite element-based high-level discrete adjoint method (FEniCS/dolfin-adjoint)**. Structural and Multidisciplinary Optimization, 2021. Available at: https://link.springer.com/article/10.1007/s00158-021-03061-4. Cited 13 times in pages 87, 89, 102, 195, 196, 197, 198, 200, 231, 321, 352, 404, and 411.

ALONSO, D. H.; PICELLI, R.; ROMERO SAENZ, J. S.; SILVA, E. C. N. **Topology optimization method based on the Wray-Agarwal turbulence model**. Structural and Multidisciplinary Optimization, v. 65, n. 3, p. 1–24, 2022. Cited 20 times in pages 87, 89, 104, 185, 200, 230, 231, 321, 322, 323, 325, 326, 327, 328, 329, 331, 332, 333, 334, and 335.

ALONSO, D. H.; ROMERO SAENZ, J. S.; SILVA, E. C. N. **Non-newtonian laminar 2D swirl flow design by the topology optimization method**. Structural and Multidisciplinary Optimization, v. 62, n. 1, p. 299–321, 2020. ISSN 1615-1488. Available at: https://link.springer.com/article/10.1007%2Fs00158-020-02499-2. Cited 14 times in pages 83, 84, 86, 88, 100, 152, 159, 230, 266, 267, 268, 269, 271, and 272.

ALONSO, D. H.; SÁ, L. F. N. de; ROMERO SAENZ, J. S.; SILVA, E. C. N. **Topology optimization applied to the design of 2D swirl flow devices**. Structural and Multidisciplinary Optimization, v. 58, n. 6, p. 2341–2364, Dec 2018. ISSN 1615-1488. Available at: https://doi.org/10.1007/s00158-018-2078-0. Cited 21 times in pages 83, 86, 88, 91, 94, 107, 108, 230, 232, 233, 234, 235, 236, 237, 238, 239, 240, 241, 266, 322, and 328.

ALONSO, D. H.; SÁ, L. F. N. de; ROMERO SAENZ, J. S.; SILVA, E. C. N. **Topology optimization based on a two-dimensional swirl flow model of Tesla-type pump devices**. Computers & Mathematics with Applications, v. 77, n. 9, p. 2499–2533, 2019. ISSN 0898-1221. Available at: http://www.sciencedirect.com/science/article/pii/S0898122118307338. Cited 33 times in pages 67, 83, 86, 88, 91, 107, 118, 119, 121, 125, 147, 230, 242, 243, 244, 245, 246, 248, 249, 250, 251, 252, 253, 255, 256, 257, 258, 259, 260, 261, 262, 263, and 273.

ALONSO, D. H.; SILVA, E. C. N. **Topology optimization for blood flow considering a hemolysis model**. Structural and Multidisciplinary Optimization, Springer Science and Business Media LLC, v. 63, n. 5, p. 2101–2123, mar 2021. Available at: https://doi.org/10.1007%2Fs00158-020-02806-x. Cited 15 times in pages 83, 84, 87, 88, 230, 273, 274, 275, 276, 278, 280, 281, 282, 283, and 284.

ALONSO, D. H.; SILVA, E. C. N. **Blood flow topology optimization considering a thrombosis model**. Structural and Multidisciplinary Optimization, 2022. Accepted for publication. Cited 20 times in pages 89, 139, 230, 284, 286, 287, 288, 290, 413, 414, 415, 416, 417, 418, 419, 420, 421, 422, 423, and 425.

ALONSO, D. H.; SILVA, E. C. N. **Topology optimization applied to the design of Tesla-type turbine devices**. Applied Mathematical Modelling, v. 103, p. 764–791, 2022. ISSN 0307-904X. Available at: https://www.sciencedirect.com/science/article/pii/S0307904X21005370. Cited 8 times in pages 83, 86, 89, 119, 120, 149, 231, and 351.

ALVAREZ, D. R. A. ***Influence of outlet boundary conditions on cerebrovascular aneurysm hemodynamics***. Thesis (Master's) — Duke University, 2016. Cited in page 109.

AMESTOY, P. R.; DUFF, I. S.; KOSTER, J.; L'EXCELLENT, J.-Y. **A fully asynchronous multifrontal solver using distributed dynamic scheduling**. SIAM Journal on Matrix Analysis and Applications, v. 23, n. 1, p. 15–41, 2001. Cited in page 177.

AMIGO, R. C. R.; PRADO, D. S.; PAIVA, J. L.; HEWSON, R. W.; SILVA, E. C. N. **Topology optimisation of biphasic adsorbent beds for gas storage**. Structural and Multidisciplinary Optimization, v. 58, n. 6, p. 2431–2454, Dec 2018. ISSN 1615-1488. Available at: https://doi.org/10.1007/s00158-018-2117-x. Cited in page 150.

AMINI, G. **Liquid flow in a simplex swirl nozzle**. International Journal of Multiphase Flow, Elsevier, v. 79, p. 225–235, 2016. Cited in page 65.

ANAND, M.; RAJAGOPAL, K. R. **A short review of advances in the modelling of blood rheology and clot formation**. Fluids, Multidisciplinary Digital Publishing Institute, v. 2, n. 3, 2017. Cited 3 times in pages 96, 97, and 98.

ANDERSON, J.; WOOD, H. G.; ALLAIRE, P. E.; OLSEN, D. B. **Numerical analysis of blood flow in the clearance regions of a continuous flow artificial heart pump**. Artificial organs, Wiley Online Library, v. 24, n. 6, p. 492–500, 2000. Cited in page 220.

ANDRADE, A.; FONSECA, J.; NICOLOSI, D.; BOCK, E.; LEME, J.; VALENTE, P.; PAULISTA, P.; DINKHUYSEN, J.; MANRIQUE, R.; BISCEGLI, J. **Status of brazilian development on blood pumping devices**. *In*: INTERNATIONAL CONGRESS OF MECHANICAL ENGINEERING, 18., 2005, Ouro Preto, MG. *Proceedings of the COBEM 2005*. Ouro Preto, MG: Associação Brasileira de Engenharia e Ciências Mecânicas, 2005. Cited 3 times in pages 55, 56, and 58.

ANDREASEN, C. S.; GERSBORG, A. R.; SIGMUND, O. **Topology optimization of microfluidic mixers**. International Journal for Numerical Methods in Fluids, v. 61, p. 498–513, 2009. Available at: http://dx.doi.org/10.1002/fld.1964. Cited in page 83.

ANSYS, I. ***Modeling Turbulent Flows - Introductory Fluent Training.*** 2006. Available at: http://www.southampton.ac.uk/~nwb/lectures/GoodPracticeCFD/Articles/Turbulence_Notes_Fluent-v6.3.06.pdf. Accessed on: 2017-12-05. Cited in page 102.

ANSYS, I. ***Ansys Fluent Theory Guide – Release 2021 R2***. 2021. Cited in page 204.

ANTAKI, J. F.; GHATTAS, O.; BURGREEN, G. W.; HE, B. **Computational flow optimization of rotary blood pump components**. Artificial Organs, v. 19, n. 7, p. 608–615, 1995. Cited 3 times in pages 63, 81, and 87.

APEL, J.; PAUL, R.; KLAUS, S.; SIESS, T.; REUL, H. **Assessment of hemolysis related quantities in a microaxial blood pump by computational fluid dynamics**. Artificial Organs, v. 25, n. 5, p. 341–347, 2001. Available at: https://onlinelibrary.wiley.com/doi/abs/10.1046/j.1525-1594.2001.025005341.x. Cited in page 61.

ARNOLD, D. N.; BREZZI, F.; FORTIN, M. **A stable finite element method for the Stokes equations**. Calcolo, v. 21, p. 337–344, 1984. Cited in page 114.

ARORA, D.; BEHR, M.; PASQUALI, M. **A tensor-based measure for estimating blood damage**. Artificial Organs, Wiley Online Library, v. 28, n. 11, p. 1002–1015, 2004. Errata in: Arora *et al.* (2012). Cited 3 times in pages 99, 126, and 127.

ARORA, D.; BEHR, M.; PASQUALI, M. **Errata**. Artificial Organs, v. 30, n. 11, p. 892–892, 2006. Available at: https://onlinelibrary.wiley.com/doi/abs/10.1111/j.1525-1594.2006.00318.x. Cited in page 359.

ARORA, D.; BEHR, M.; PASQUALI, M. **Hemolysis estimation in a centrifugal blood pump using a tensor-based measure**. Artificial organs, Wiley Online Library, v. 30, n. 7, p. 539–547, 2006. Errata in: Arora *et al.* (2006a). Cited 5 times in pages 100, 127, 128, 129, and 345.

ARORA, D.; BEHR, M.; PASQUALI, M. **Errata**. Artificial Organs, v. 36, n. 5, p. 500–500, 2012. Available at: https://onlinelibrary.wiley.com/doi/abs/10.1111/j.1525-1594.2012.01491.x. Cited in page 359.

ASTM F1841-97. ***Standard practice for assessment of hemolysis in continuous flow blood pumps***. West Conshohocken, PA, 1997. Available at: http://www.astm.org/cgi-bin/resolver.cgi?F1841-97. Cited 3 times in pages 129, 130, and 345.

ASUAJE, M.; BAKIR, F.; KOUIDRI, S.; KENYERY, F.; REY, R. **Numerical modelization of the flow in centrifugal pump: volute influence in velocity and pressure fields**. International journal of rotating machinery, Hindawi, v. 2005, n. 3, p. 244–255, 2005. Cited in page 78.

AUPOIX, B.; ARNAL, D.; BÉZARD, H.; CHAOUAT, B.; CHEDEVERGNE, F.; DECK, S.; GLEIZE, V.; GRENARD, P.; LAROCHE, E. **Transition and turbulence modeling**. Aerospace Lab, n. 2, p. 1–13, 2011. Cited in page 64.

AXELSSON, O.; HE, X.; NEYTCHEVA, M. **Numerical solution of the time-dependent Navier-Stokes equation for variable density-variable viscosity. Part I**. Mathematical Modelling and Analysis, Taylor & Francis, v. 20, n. 2, p. 232–260, 2015. Available at: https://doi.org/10.3846/13926292.2015.1021395. Cited in page 190.

AYACHIT, U. ***The paraview guide: a parallel visualization application***. [*S.l.*]: Kitware, Inc., 2015. Cited in page 176.

AYDER, E.; BRAEMBUSSCHE, R. Van den; BRASZ, J. **Experimental and theoretical analysis of the flow in a centrifugal compressor volute**. Journal of turbomachinery, American Society of Mechanical Engineers, v. 115, n. 3, p. 582–589, 1993. Cited in page 123.

BAGOT, C. N.; ARYA, R. **Virchow and his triad: a question of attribution**. British Journal of Haematology, v. 143, n. 2, p. 180–190, 2008. Available at: https://onlinelibrary.wiley.com/doi/abs/10.1111/j.1365-2141.2008.07323.x. Cited in page 61.

BALONI, B. D.; CHANNIWALA, S.; MAYAVANSHI, V. **Pressure recovery and loss coefficient variations in the two different centrifugal blower volute designs**. Applied Energy, v. 90, n. 1, p. 335–343, 2012. ISSN 0306-2619. Energy Solutions for a Sustainable World, Special Issue of International Conference of Applied Energy, ICA2010, April 21-23, 2010, Singapore. Available at: http://www.sciencedirect.com/science/article/pii/S0306261911001152. Cited in page 123.

BALONI, B. D.; PATHAK, Y.; CHANNIWALA, S. **Centrifugal blower volute optimization based on Taguchi method**. Computers & Fluids, v. 112, p. 72–78, 2015. ISSN 0045-7930. Available at: http://www.sciencedirect.com/science/article/pii/S0045793015000444. Cited 2 times in pages 80 and 123.

BANSAL, R. K. ***A textbook of fluid mechanics and hydraulic machines***. New Delhi: Laxmi Publications (P) Limited, 2005. ISBN 9788170083115. Cited in page 78.

BAPPOO, N.; KELSEY, L. J.; PARKER, L.; CROUGH, T.; MORAN, C. M.; THOMSON, A.; HOLMES, M. C.; WYRWOLL, C. S.; DOYLE, B. J. **Viscosity and haemodynamics in a late gestation rat feto-placental arterial network**. Biomechanics and modeling in mechanobiology, Springer, v. 16, n. 4, p. 1361–1372, 2017. Cited in page 100.

BARDINA, J. E.; HUANG, P. G.; COAKLEY, T. J. ***Turbulence modeling validation, testing and development***. [*S.l.*], 1997. Cited in page 102.

BARIĆ, D. **Why pulsatility still matters: a review of current knowledge**. Croatian medical journal, Medicinska naklada, v. 55, n. 6, p. 609–620, 2014. Cited in page 58.

BARNES, H. A. **Thixotropy-a review**. Journal of Non-Newtonian Fluid Mechanics, v. 70, n. 1, p. 1–33, 1997. ISSN 0377-0257. Available at: http://www.sciencedirect.com/science/article/pii/S0377025797000049. Cited in page 95.

BARRENECHEA, G. R.; WACHTEL, A. **The inf-sup stability of the lowest order Taylor-Hood pair on affine anisotropic meshes**. IMA Journal of Numerical Analysis, Oxford University Press, v. 40, n. 4, p. 2377–2398, 2020. Cited in page 114.

BARTH, W. L.; CAREY, G. F. **On a boundary condition for pressure-driven laminar flow of incompressible fluids**. International Journal for Numerical Methods in Fluids, v. 54, n. 11, p. 1313–1325, 2007. Available at: https://onlinelibrary.wiley.com/doi/abs/10.1002/fld.1427. Cited in page 108.

BARTHES-BIESEL, D.; RALLISON, J. **The time-dependent deformation of a capsule freely suspended in a linear shear flow**. Journal of Fluid Mechanics, Cambridge University Press, v. 113, p. 251–267, 1981. Cited in page 127.

BASSETT, C. E. **Integral solution for compressible flow through disk turbines**. *In*: IEEE-INST ELECTRICAL ELECTRONICS ENGINEERS INC 345 E 47TH ST, NEW YORK, NY 10017-2394. *IEEE Transactions on Aerospace and Electronic Systems*. [*S.l.*], 1975. v. 11, n. 5, p. 957–958. Cited in page 75.

BAYOD, E.; WILLERS, E. P.; TORNBERG, E. **Rheological and structural characterization of tomato paste and its influence on the quality of ketchup**. LWT-Food Science and Technology, Elsevier, v. 41, n. 7, p. 1289–1300, 2008. Cited 2 times in pages 95 and 354.

BAZAN, O.; ORTIZ, J. P. **Experimental Validation of a Cardiac Simulator for in vitro Evaluation of Prosthetic Heart Valves**. Brazilian Journal of Cardiovascular Surgery, Scielo, v. 31, p. 151–157, 04 2016. ISSN 0102-7638. Available at: http://www.scielo.br/scielo.php?script=sci_arttext&pid=S0102-76382016000200151&nrm=iso. Cited in page 226.

BEANS, E. W. **Investigation into the performance characteristics of a friction turbine.** Journal of Spacecraft and Rockets, v. 3, n. 1, p. 131–134, 1966. Cited 2 times in pages 75 and 216.

BEAR, J. ***Modeling phenomena of flow and transport in porous media***. [*S.l.*]: Springer, 2018. v. 31. Cited in page 149.

BEAUDOIN, M.; NILSSON, H.; PAGE, M.; MAGNAN, R.; JASAK, H. **Evaluation of an improved mixing plane interface for OpenFOAM**. *In*: IOP PUBLISHING. *IOP Conference Series: Earth and Environmental Science*. [*S.l.*], 2014. v. 22, n. 2, p. 022004. Cited in page 205.

BEAVERS, G. S.; SPARROW, E. M. **Non-Darcy flow through fibrous porous media**. Journal of Applied Mechanics, v. 36, p. 711–714, 1969. Cited in page 150.

BECKER, K.-H.; MILLA, P.; HERGT, P.; HELLMANN, H.-D. ***Radial turbine blade system.*** 1981. US 4,383,800. Cited in page 79.

BEHBAHANI, M.; BEHR, M.; HORMES, M.; STEINSEIFER, U.; ARORA, D.; CORONADO, O.; PASQUALI, M. **A review of computational fluid dynamics analysis of blood pumps**. European Journal of Applied Mathematics, Cambridge University Press, v. 20, n. 4, p. 363–397, 2009. Cited 12 times in pages 55, 56, 58, 60, 61, 62, 63, 96, 97, 100, 129, and 345.

BELLAOUAR, A.; KOPEY, B.; ABDELBAKI, N. **Methods of the rational choice of a labyrinth seal design for gas pumping unit**. Mechanics, v. 19, n. 1, p. 81–86, 2013. Cited in page 65.

BENDSØE, M. P.; KIKUCHI, N. **Generating optimal topologies in structural design using a homogenization method**. Computer methods in applied mechanics and engineering, Elsevier, v. 71, n. 2, p. 197–224, 1988. Cited in page 82.

BENDSØE, M. P.; SIGMUND, O. ***Topology optimization: theory, methods, and applications***. 2. ed. [*S.l.*]: Springer Verlag: Berlin Heidelberg, 2003. Cited 2 times in pages 160 and 161.

BHARGAVA, R.; RAWAT, S.; TAKHAR, H. S.; BÉG, O. A. **Pulsatile magneto-biofluid flow and mass transfer in a non-Darcian porous medium channel**. Meccanica, v. 42, n. 3, p. 247–262, Jun 2007. ISSN 1572-9648. Available at: https://doi.org/10.1007/s11012-007-9052-z. Cited in page 150.

BILLETT, H. H. **Hemoglobin and hematocrit**. *In*: *Clinical Methods: The History, Physical, and Laboratory Examinations. 3rd edition*. Boston: Butterworths, 1990. Cited in page 129.

BIRD, R.; STEWART, W.; LIGHTFOOT, E. ***Transport Phenomena***. 2. ed. [*S.l.*]: John Wiley & Sons, 2002. Cited in page 118.

BIRD, R. B.; ARMSTRONG, R. C.; HASSAGER, O. ***Dynamics of polymeric liquids, Volume 1: Fluid mechanics***. 1. ed. [*S.l.*]: John Wiley & Sons, 1987. Cited 2 times in pages 98 and 99.

BITYUKOV, Y. I.; DENISKIN, Y. I. **Chaikin algorithm and its generalization**. *In*: IEEE. *2016 Dynamics of Systems, Mechanisms and Machines (Dynamics)*. [*S.l.*], 2016. p. 1–5. Cited in page 167.

BLUDSZUWEIT, C. **Three-Dimensional numerical prediction of stress loading of blood particles in a centrifugal pump**. Artificial Organs, Wiley Online Library, v. 19, n. 7, p. 590–596, 1995. Cited 2 times in pages 127 and 131.

BLUESTEIN, M.; MOCKROS, L. F. **Hemolytic effects of energy dissipation in flowing blood**. Medical and biological engineering, v. 7, n. 1, p. 1–16, Jan 1969. ISSN 1741-0444. Available at: https://doi.org/10.1007/BF02474665. Cited 2 times in pages 63 and 119.

BOCCHI, E. A. **Heart failure in South America**. Current cardiology reviews, Bentham Science Publishers, v. 9, n. 2, p. 147–156, 2013. Cited in page 54.

BOMMADEVARA, M.; ZHU, L. **Temperature difference between the body core and arterial blood supplied to the brain during hyperthermia or hypothermia in humans**. Biomechanics and modeling in mechanobiology, Springer, v. 1, n. 2, p. 137–149, 2002. Cited in page 62.

BONOW, R. O.; MANN, D. L.; ZIPES, D. P.; LIBBY, P.; BRAUNWALD, E. ***Braunwald's Heart disease: A Textbook of Cardiovascular Medicine***. 9. ed. [*S.l.*]: Elsevier Saunders, 2012. v. 1. Cited 2 times in pages 8 and 60.

BORATE, H. P.; MISAL, N. D. **An effect of surface finish and spacing between discs on the performance of disc turbine**. International Journal of Applied Research in Mechanical Engineering, v. 2, p. 2231–5950, 2012. Cited 3 times in pages 69, 70, and 75.

BORRVALL, T.; PETERSSON, J. **Topology optimization of fluids in Stokes flow**. International Journal for Numerical Methods in Fluids, John Wiley & Sons, Ltd., v. 41, n. 1, p. 77–107, 2003. ISSN 1097-0363. Available at: http://dx.doi.org/10.1002/fld.426. Cited 16 times in pages 9, 82, 83, 85, 86, 108, 118, 119, 144, 145, 146, 235, 245, 260, 270, and 324.

BOYD, J.; BUICK, J. M.; GREEN, S. **Analysis of the Casson and Carreau-Yasuda non-Newtonian blood models in steady and oscillatory flows using the lattice Boltzmann method**. Physics of Fluids, AIP, v. 19, n. 9, 2007. Cited in page 100.

BRAILE BIOMÉDICA. ***Centrifugal blood pump CentriFlux BR-100***. 2017. Available at: http://www.medicalexpo.com/prod/braile-biomedica/product-106890-707115.html. Accessed on: 2017-07-04. Cited in page 75.

BRASS, L. F. **Thrombin and platelet activation**. Chest, Elsevier, v. 124, n. 3, p. 18S–25S, 2003. Cited in page 138.

BREITER, M. C.; POHLHAUSEN, K. ***Laminar flow between two parallel rotating disks***. Wright-Patterson AFB-O: [*s.n.*], 1962. 1–81 p. Aeronautic Research Laboratory Office of Aerospace Research United States Air Force. ISBN 3257227892. Cited 2 times in pages 67 and 125.

BREZZI, F.; FORTIN, M. ***Mixed and hybrid finite element methods***. Berlin, Heidelberg: Springer-Verlag, 1991. ISBN 0-387-97582-9. Cited 2 times in pages 114 and 116.

BRINDISE, M. C.; BUSSE, M. M.; VLACHOS, P. P. **Density-and viscosity-matched Newtonian and non-Newtonian blood-analog solutions with PDMS refractive index**. Experiments in fluids, Springer, v. 59, n. 11, p. 1–8, 2018. Cited in page 227.

BRINKMAN, H. C. **A calculation of the viscous force exerted by a flowing fluid on a dense swarm of particles**. Journal of applied sciences research, A1, p. 27–34, 1947. Cited 3 times in pages 83, 145, and 148.

BROOKSHIER, K. A.; TARBELL, J. M. **Evaluation of a transparent blood analog fluid: aqueous xanthan gum/glycerin**. Biorheology, IOS Press, v. 30, n. 2, p. 107–116, 1993. Cited in page 227.

BUENO-OROVIO, A.; CASTRO, C.; PALACIOS, F.; ZUAZUA, E. **Continuous adjoint approach for the Spalart-Allmaras model in aerodynamic optimization**. AIAA journal, v. 50, n. 3, p. 631–646, 2012. Cited in page 102.

BUMRUNGPETCH, J. ***Mechanism Design of Ventricular Assist Device.*** Thesis (Master's) — Queensland University of Technology, 2016. Cited 3 times in pages 207, 218, and 219.

BURCHAM, R. ***Liquid rocket engine turbopump rotating-shaft seals***. [*S.l.*]: National Aeronautics and Space Administration, 1978. v. 8121. Cited in page 216.

BURGREEN, G. W.; LOREE, H. M.; BOURQUE, K.; DAGUE, C.; POIRIER, V. L.; FARRAR, D.; HAMPTON, E.; WU, Z. J.; GEMPP, T. M.; SCHÖB, R. **Computational fluid dynamics analysis of a maglev centrifugal left ventricular assist device**. Artificial organs, Wiley Online Library, v. 28, n. 10, p. 874–880, 2004. Cited in page 64.

CAMPO-DEAÑO, L.; DULLENS, R. P.; AARTS, D. G.; PINHO, F. T.; OLIVEIRA, M. S. N. **Viscoelasticity of blood and viscoelastic blood analogues for use in polydymethylsiloxane in vitro models of the circulatory system**. Biomicrofluidics, AIP, v. 7, n. 3, 2013. Cited 2 times in pages 226 and 227.

CAREY, V. P. **Assessment of Tesla turbine performance for small scale rankine combined heat and power systems**. Journal of Engineering for Gas Turbines and Power, American Society of Mechanical Engineers, v. 132, n. 12, p. 122301:1–122301:9, 2010. Cited in page 68.

CASE, M.; ERVIN, V.; LINKE, A.; REBHOLZ, L. **A connection between Scott-Vogelius and Grad-Div stabilized Taylor-Hood FE approximations of the Navier-Stokes equations**. SIAM Journal on Numerical Analysis, v. 49, n. 4, p. 1461–1481, 2011. Available at: https://doi.org/10.1137/100794250. Cited in page 190.

CASTAGNO, J.; ATKINS, E. **Polygon extraction from triangular meshes**. arXiv preprint arXiv:2002.01886, 2020. Cited 2 times in pages 172 and 174.

CELIK, I. **RANS/LES/DES/DNS: The Future Prospects of Turbulence Modeling**. Journal of Fluids Engineering, v. 127, n. 5, p. 829–830, 01 2003. ISSN 0098-2202. Available at: https://doi.org/10.1115/1.2033011. Cited in page 101.

CFTURBO. ***VOLUTE | Cross Section***. 2019. Available at: https://en.cfturbo.com/fileadmin/content/manual/en/cross_section.html. Accessed on: 2019-02-03. Cited in page 79.

CHAN, W.; AKAMATSU, T.; LI, H. **Analytical Investigation of Leakage Flow in Disk Clearance of a Magnetically Suspended Centrifugal Impeller**. Artificial Organs, v. 24, p. 734–742, 09 2000. Cited in page 220.

CHAN, W.-K.; WONG, Y.-W. **A Review of Leakage Flow in Centrifugal Blood Pumps**. Artificial Organs, v. 30, n. 5, p. 354–359, 2006. Available at: https://onlinelibrary.wiley.com/doi/abs/10.1111/j.1525-1594.2006.00225.x. Cited 2 times in pages 218 and 220.

CHANDRAN, K. B.; KHALIGHI, B. **A note on the blood analog for in-vitro testing of heart valve bioprostheses**. Journal of biomechanical engineering, American Society of Mechanical Engineers, v. 106, n. 2, p. 112–114, 1984. Cited in page 226.

CHEBBI, R. **Dynamics of blood flow: modeling of the Fåhræus-Lindqvist effect**. Journal of biological physics, Springer, v. 41, n. 3, p. 313–326, 2015. Cited in page 97.

CHEEMA, T. A.; KIM, G. M.; LEE, C. Y.; HONG, J. G.; KWAK, M. K.; PARK, C. W. **Characteristics of blood vessel wall deformation with porous wall conditions in an aortic arch**. Applied Rheology, v. 24, n. 24590, p. 1–8, 2014. Cited in page 150.

CHEN, C.; YAJI, K.; YAMADA, T.; IZUI, K.; NISHIWAKI, S. **Local-in-time adjoint-based topology optimization of unsteady fluid flows using the lattice Boltzmann method**. Mechanical Engineering Journal, The Japan Society of Mechanical Engineers, v. 4, n. 3, p. 17–00120, 2017. Cited in page 83.

CHEN, G.; XIONG, Q.; MORRIS, P. J.; PATERSON, E. G.; SERGEEV, A.; WANG, Y. **OpenFOAM for computational fluid dynamics**. Not. AMS, v. 61, n. 4, p. 354–363, 2014. Cited 3 times in pages 176, 192, and 194.

CHEN, Z.; NGUYEN, V. T. T.; TRAN, N. T. **Optimum design of the volute tongue shape of a low specific speed centrifugal pump**. J Electr Electron Syst, 10.4172/2332-0796.1000226, v. 6, n. 226, 2017. Cited in page 79.

CHENG, A.; WILLIAMITIS, C. A.; SLAUGHTER, M. S. **Comparison of continuous-flow and pulsatile-flow left ventricular assist devices: is there an advantage to pulsatility?** Annals of cardiothoracic surgery, AME Publications, v. 3, n. 6, p. 573–581, 2014. Cited in page 57.

CHENG, R.; LAI, Y. G.; CHANDRAN, K. B. **Three-dimensional fluid-structure interaction simulation of bileaflet mechanical heart valve flow dynamics**. Annals of biomedical engineering, Springer, v. 32, n. 11, p. 1471–1483, 2004. Cited in page 137.

CHILDS, P. R. ***Mechanical design engineering handbook***. 2. ed. [*S.l.*]: Butterworth-Heinemann, 2019. Cited in page 209.

CHMIELINSKI, A.; KOONS, B. **Nursing care for the patient with a left ventricular assist device**. Nursing, LWW, v. 47, n. 5, p. 34–40, 2017. Cited in page 59.

CHO, Y. I.; KENSEY, K. R. **Effects of the non-Newtonian viscosity of blood on flows in a diseased arterial vessel. Part 1: Steady flows**. Biorheology, v. 28, p. 241–262, 1991. Cited 7 times in pages 95, 96, 98, 99, 100, 129, and 345.

CHOON, T. W.; RAHMAN., A. A.; JER, F. S.; AIK, L. E. **Optimization of Tesla turbine using computational fluid dynamics approach**. *In*: *2011 IEEE Symposium on Industrial Electronics and Applications*. [*S.l.: s.n.*], 2011. p. 477–480. Cited 3 times in pages 73, 75, and 81.

CHOPARD, B.; SOUSA, D. R. de; LäTT, J.; MOUNTRAKIS, L.; DUBOIS, F.; YOURASSOWSKY, C.; ANTWERPEN, P. V.; EKER, O.; VANHAMME, L.; PEREZ-MORGA, D.; COURBEBAISSE, G.; LORENZ, E.; HOEKSTRA, A. G.; BOUDJELTIA, K. Z. **A physical description of the adhesion and aggregation of platelets**. Royal Society open science, The Royal Society Publishing, v. 4, n. 4, p. 170219, 2017. Cited in page 137.

CHUA, L. P.; SU, B.; LIM, T. M.; ZHOU, T. **Numerical simulation of an axial blood pump**. Artificial organs, Wiley Online Library, v. 31, n. 7, p. 560–570, 2007. Cited in page 64.

CIMOLIN, F.; DISCACCIATI, M. **Navier-Stokes/Forchheimer models for filtration through porous media**. Applied Numerical Mathematics, Elsevier, v. 72, p. 205–224, 2013. Cited in page 149.

COLVIN-ADAMS, M.; SMITH, J. M.; HEUBNER, B. M.; SKEANS, M. A.; EDWARDS, L. B.; WALLER, C. D.; CALLAHAN, E. R.; SNYDER, J. J.; ISRANI, A. K.; KASISKE, B. L. **OPTN/SRTR 2013 Annual Data Report: Heart**. American Journal of Transplantation, v. 15, n. S2, p. 1–28, 2015. Available at: https://onlinelibrary.wiley.com/doi/abs/10.1111/ajt.13199. Cited 2 times in pages 54 and 55.

CONSOLO, F.; VALERIO, L.; BRIZZOLA, S.; ROTA, P.; MARAZZATO, G.; VINCOLI, V.; REGGIANI, S.; REDAELLI, A.; FIORE, G. **On the use of the platelet activity state assay for the in vitro quantification of platelet activation in blood recirculating devices for extracorporeal circulation**. Artificial organs, Wiley Online Library, v. 40, n. 10, p. 971–980, 2016. Cited in page 138.

COUSINS, B. R.; BORNE, S. L.; LINKE, A.; REBHOLZ, L. G.; WANG, Z. **Efficient linear solvers for incompressible flow simulations using Scott-Vogelius finite elements**. Numerical Methods for Partial Differential Equations, Wiley Online Library, v. 29, n. 4, p. 1217–1237, 2013. Cited in page 115.

COUTO, H. d. S.; BATISTA, J. C. ***Hybrid Tesla-Pelton wheel disc turbine.*** 2011. US 2011/0027069 A1. Cited 3 times in pages 70, 71, and 75.

COUTO, H. S.; DUARTE, J. B. F.; BASTOS-NETTO, D. **The Tesla turbine revisited**. *In*: *Proceedings of the Eighth Asia-Pacific International Symposium on Combustion and Energy Utilization*. [*S.l.: s.n.*], 2006. Cited in page 75.

CRAWFORD, M. E.; RICE, W. **Calculated design data for the multiple-disk pump using incompressible fluid**. Journal of Engineering for Power, American Society of Mechanical Engineers, v. 96, n. 3, p. 274–282, 1974. Cited in page 73.

CROUZEIX, M.; RAVIART, P.-A. **Conforming and nonconforming finite element methods for solving the stationary Stokes equations I**. Revue française d'automatique informatique recherche opérationnelle. Mathématique, EDP Sciences, v. 7, n. R3, p. 33–75, 1973. Cited in page 115.

DARCY, H. P. G. ***Les Fontaines publiques de la ville de Dijon. Exposition et application des principes à suivre et des formules à employer dans les questions de distribution d'eau, etc***. [*S.l.*]: V. Dalamont, 1856. Cited 3 times in pages 83, 145, and 148.

DAVIS, T. A. **Algorithm 832: UMFPACK V4.3—an Unsymmetric-Pattern Multifrontal Method**. ACM Trans. Math. Softw., Association for Computing Machinery, New York, NY, USA, v. 30, n. 2, p. 196–199, Jun. 2004. ISSN 0098-3500. Available at: https://doi.org/10.1145/992200.992206. Cited 3 times in pages 177, 193, and 194.

DE CHANT, L. J. **The venerable 1/7th power law turbulent velocity profile: a classical nonlinear boundary value problem solution and its relationship to stochastic processes**. Journal of Applied Mathematics and Computational Mechanics, v. 161, p. 463–474, 2005. Cited 2 times in pages 410 and 411.

DE WACHTER, D.; VERDONCK, P. **Numerical calculation of hemolysis levels in peripheral hemodialysis cannulas**. Artificial organs, Wiley Online Library, v. 26, n. 7, p. 576–582, 2002. Cited 2 times in pages 129 and 131.

DEARDORFF, J. W. **A numerical study of three-dimensional turbulent channel flow at large Reynolds numbers**. J. Fluid Mech, v. 41, n. 2, p. 453–480, 1970. Cited in page 101.

DEBAKEY, M. E. **The odyssey of the artificial heart**. Artificial Organs, v. 24, n. 6, p. 405–411, 2000. Available at: https://onlinelibrary.wiley.com/doi/abs/10.1046/j.1525-1594.2000.06635.x. Cited in page 56.

DENG, Y.; LIU, Z.; WU, J.; WU, Y. **Topology optimization of steady Navier-Stokes flow with body force**. Computer methods in applied mechanics and engineering, v. 255, n. Supplement C, p. 306–321, 2013. ISSN 0045-7825. Available at: http://www.sciencedirect.com/science/article/pii/S0045782512003532. Cited in page 83.

DENG, Y.; LIU, Z.; WU, Y. **Topology optimization of steady and unsteady incompressible Navier-Stokes flows driven by body forces**. Struct. Multidiscip. Optim., Springer-Verlag New York, Inc., Secaucus, NJ, USA, v. 47, n. 4, p. 555–570, Apr. 2013. ISSN 1615-147X. Available at: http://dx.doi.org/10.1007/s00158-012-0847-8. Cited 3 times in pages 82, 83, and 107.

DEUEL, J. W.; SCHAER, C. A.; BORETTI, F. S.; OPITZ, L.; GARCÍA-RUBIO, I.; BAEK, J.; SPAHN, D. R.; BUEHLER, P. W.; SCHAER, D. J. **Hemoglobinuria-related acute kidney injury is driven by intrarenal oxidative reactions triggering a heme toxicity response**. Cell Death & Disease, Nature Publishing Group, v. 7, n. 1, p. e2064–e2064, 2016. Cited in page 61.

DIA DEVELOPMENT TEAM. ***Dia - Diagram Editor***. Dia Development Team, 2022. Available at: http://dia-installer.de. Accessed on: 2022-01-23. Cited in page 176.

DILGEN, C. B.; DILGEN, S. B.; FUHRMAN, D. R.; SIGMUND, O.; LAZAROV, B. S. **Topology optimization of turbulent flows**. Computer Methods in Applied Mechanics and Engineering, v. 331, p. 363–393, 2018. ISSN 0045-7825. Available at: http://www.sciencedirect.com/science/article/pii/S0045782517307478. Cited 6 times in pages 83, 87, 102, 104, 105, and 108.

DING, J.; CHEN, Z.; NIU, S.; ZHANG, J.; MONDAL, N. K.; GRIFFITH, B. P.; WU, Z. J. **Quantification of shear-induced platelet activation: high shear stresses for short exposure time**. Artificial organs, Wiley Online Library, v. 39, n. 7, p. 576–583, 2015. Cited in page 61.

DINKHUYSEN, J. J.; ANDRADE, A. J. A. P. d.; MANRIQUE, R.; SAITO, C. S. M.; LEME, J.; BISCEGLI, F. **Bomba sangínea espiral: concepção, desenvolvimento e aplicaçã clínica de projeto original**. Brazilian Journal of Cardiovascular Surgery,

Scielo, v. 22, p. 218–223, 06 2007. ISSN 0102-7638. Available at: http://www.scielo.br/scielo.php?script=sci_arttext&pid=S0102-76382007000200012&nrm=iso. Cited in page 58.

DISCFLO. ***Discflo disc pumps for chemical and petroleum processing***. 2000. Brochure. Available at: https://discflo.com/pdf/chembroch.pdf. Accessed on: 2018-05-01. Cited 3 times in pages 8, 66, and 69.

DODGE JR, J. T.; BROWN, B. G.; BOLSON, E. L.; DODGE, H. T. **Lumen diameter of normal human coronary arteries. Influence of age, sex, anatomic variation, and left ventricular hypertrophy or dilation.** Circulation, Am Heart Assoc, v. 86, n. 1, p. 232–246, 1992. Cited in page 224.

DODSWORTH, L.; GROULX, D. **Operational parametric study of a Tesla pump: Disk pack spacing and rotational speed**. *In*: AMERICAN SOCIETY OF MECHANICAL ENGINEERS. *ASME/JSME/KSME 2015 Joint Fluids Engineering Conference*. [*S.l.*], 2015. Cited 3 times in pages 67, 68, and 75.

DODSWORTH, L. J. ***Operational parametric study of a prototype Tesla pump***. Thesis (Master's) — Dalhousie University, 2016. Cited 4 times in pages 68, 76, 217, and 218.

DORMAN, F. D.; MURPHY, T. E.; BLACKSHEAR, P. L. **An application of the Tesla viscous flow turbine to pumping blood: Mechanical devices to assist the failing heart. National Research Council**. *In*: *National Academy of Science*. [*S.l.: s.n.*], 1966. p. 119–128. Cited in page 73.

DOUGLAS, P. S.; FIOLKOSKI, J.; BERKO, B.; REICHEK, N. **Echocardiographic visualization of coronary artery anatomy in the adult**. Journal of the American College of Cardiology, Elsevier, v. 11, n. 3, p. 565–571, 1988. Cited in page 224.

DUAN, X.; LI, F.; QIN, X. **Topology optimization of incompressible Navier-Stokes problem by level set based adaptive mesh method**. Computers & Mathematics with Applications, v. 72, n. 4, p. 1131–1141, 2016. ISSN 0898-1221. Available at: http://www.sciencedirect.com/science/article/pii/S0898122116303662. Cited in page 82.

DUAN, X.-B.; LI, F.-F.; QIN, X.-Q. **Adaptive mesh method for topology optimization of fluid flow**. Applied Mathematics Letters, Elsevier, v. 44, p. 40–44, 2015. Cited in page 84.

EARL, B. ***All About Stepper Motors***. 2021. Available at: https://learn.adafruit.com/all-about-stepper-motors/types-of-steppers. Accessed on: 2021-12-01. Cited in page 225.

EFFENBERGER, U. E. ***Viscosity impeller.*** 1983. US 4,402,647. Cited 2 times in pages 70 and 71.

ELHANAFY, A.; GUAILY, A.; ELSAID, A. **Pressure stabilized finite elements simulation for steady and unsteady Newtonian fluids**. Journal of Applied Mathematics and Computational Mechanics, v. 16, n. 3, p. 17–26, 2017. Cited in page 115.

ELMAN, H. C.; SILVESTER, D. J.; WATHEN, A. J. ***Finite elements and fast iterative solvers: with applications in incompressible fluid dynamics***. 1. ed. New York: Oxford University Press, 2005. Cited in page 107.

ENGIN, T.; ÖZDEMIR, M.; ÇEŞMECI, Ş. **Design, testing and two-dimensional flow modeling of a multiple-disk fan**. Experimental Thermal and Fluid Science, v. 33, n. 8, p. 1180 – 1187, 2009. ISSN 0894-1777. Available at: http://www.sciencedirect.com/science/article/pii/S0894177709001083. Cited in page 68.

ESLAMIAN, E.; SHIRVANI, H.; SHIRVANI, A. **Numerical investigation of swirl flow inside a supersonic nozzle**. Adv Fluid Mech IX, v. 74, p. 131–140, 2012. Cited in page 65.

EVGRAFOV, A. **Topology optimization of Navier-Stokes equations**. *In*: LINKÖPING UNIVERSITY ELECTRONIC PRESS. *Nordic MPS 2004. The Ninth Meeting of the Nordic Section of the Mathematical Programming Society*. [*S.l.*], 2004. p. 37–55. Cited 4 times in pages 82, 83, 92, and 118.

EVGRAFOV, A. **Topology optimization of slightly compressible fluids**. ZAMM-Journal of Applied Mathematics and Mechanics/Zeitschrift für Angewandte Mathematik und Mechanik, v. 86, n. 1, p. 46–62, 2006. Cited in page 83.

EVGRAFOV, A. **On Chebyshev's method for topology optimization of Stokes flows**. Structural and Multidisciplinary Optimization, Springer, v. 51, n. 4, p. 801–811, 2015. Cited in page 84.

EYNON, P. A.; WHITFIELD, A. **Pressure recovery in a turbocharger compressor volute**. Proceedings of the Institution of Mechanical Engineers, Part A: Journal of Power and Energy, v. 214, n. 6, p. 599–610, 2000. Available at: https://doi.org/10.1243/0957650001538137. Cited in page 123.

FANG, F.; PIGGOTT, M.; PAIN, C.; GORMAN, G.; GODDARD, A. **An adaptive mesh adjoint data assimilation method**. Ocean Modelling, v. 15, n. 1, p. 39–55, 2006. ISSN 1463-5003. The Third International Workshop on Unstructured Mesh Numerical Modelling of Coastal, Shelf and Ocean Flows. Available at: http://www.sciencedirect.com/science/article/pii/S1463500306000126. Cited in page 187.

FARINAS, M.-I.; GARON, A.; LACASSE, D.; N'DRI, D. **Asymptotically consistent numerical approximation of hemolysis**. Journal of Biomechanical Engineering, v. 128, n. 5, p. 688–696, 03 2006. ISSN 0148-0731. Available at: https://doi.org/10.1115/1.2241663. Cited 5 times in pages 132, 133, 134, 135, and 142.

FARRELL, P. E.; BEENTJES, C. H.; BIRKISSON, Á. **The computation of disconnected bifurcation diagrams**. arXiv preprint arXiv:1603.00809, 2016. Cited in page 85.

FARRELL, P. E.; HAM, D. A.; FUNKE, S. W.; ROGNES, M. E. **Automated derivation of the adjoint of high-level transient finite element programs**. SIAM Journal on Scientific Computing, v. 35, n. 4, p. C369–C393, 2013. Cited 5 times in pages 10, 177, 181, 187, and 188.

FEDOSOV, D. A.; NOGUCHI, H.; GOMPPER, G. **Multiscale modeling of blood flow: from single cells to blood rheology**. Biomechanics and modeling in mechanobiology, Springer, v. 13, n. 2, p. 239–258, 2014. Cited in page 97.

FERRARIS, C. F.; DE LARRARD, F. ***Testing and modeling of fresh concrete rheology***. [*S.l.*], 1998. Cited 2 times in pages 95 and 354.

FIGUEIRA JÚNIOR, E. A.; OLIVEIRA, C. H. de F.; BORGES, V. L.; CARVALHO, S. R. de. **Design of bladeless impellers for abrasive fluid pumping**. Journal of the Brazilian Society of Mechanical Sciences and Engineering, v. 43, 04 2021. Cited in page 69.

FLATHERS, M. B.; BACHE, G. E.; RAINSBERGER, R. **An experimental and computational investigation of flow in a radial inlet of an industrial pipeline centrifugal compressor**. Journal of turbomachinery, American Society of Mechanical Engineers, v. 118, n. 2, p. 371–384, 1996. Cited in page 79.

FOO, S.; TAN, W. C.; SHARIL, M. **Development of Tesla turbine for green energy applications**. *In*: LINKÖPING UNIVERSITY ELECTRONIC PRESS. *2nd NCMER 2010. National Conference in Mechanical Engineering Research and Postgraduate Studies*. [*S.l.*], 2010. Cited in page 125.

FORCHHEIMER, P. **Wasserbewegung durch boden**. Z. Ver. Deutsch, Ing., v. 45, p. 1782–1788, 1901. Cited 3 times in pages 83, 148, and 149.

FORD, D. ***Tubular adhesion turbine or pump.*** 2018. US 2018 / 0216463 A1. Cited 2 times in pages 65 and 72.

FOSTER, M. ***The potential of a Tesla type device as a non pulsatile blood pump***. Thesis (PhD) — Middlesex University, 2006. Cited 5 times in pages 70, 71, 73, 75, and 76.

FRANCA, L. P. **Stabilized finite element methods: II. The incompressible Navier-Stokes equations**. Computer Methods in Applied Mechanics and Engineering, v. 99, n. 258, p. 209–233, 1992. Cited in page 115.

FRASER, K.; TASKIN, M.; ZHANG, T.; GRIFFITH, B.; WU, Z. **Comparison of shear stress, residence time and lagrangian estimates of hemolysis in different ventricular assist devices**. *In*: SPRINGER. *26th Southern Biomedical Engineering Conference SBEC 2010, April 30-May 2, 2010, College Park, Maryland, USA*. [*S.l.*], 2010. p. 548–551. Cited 6 times in pages 127, 128, 131, 132, 133, and 137.

FRASER, K. H.; TASKIN, M. E.; GRIFFITH, B. P.; WU, Z. J. **The use of computational fluid dynamics in the development of ventricular assist devices**. Medical Engineering & Physics, v. 33, n. 3, p. 263–280, April 2011. Available at: http://opus.bath.ac.uk/43258/. Cited 8 times in pages 56, 57, 60, 62, 63, 64, 127, and 295.

FULLER, H. J. ***Wind turbine for generation of electric power.*** 2010. US 7,695,242 B2. Cited 3 times in pages 8, 68, and 69.

FUNKE, S. ***The automation of PDE-constrained optimisation and its applications***. Thesis (PhD) — Imperial College London, 2013. Cited 3 times in pages 10, 186, and 187.

FÜRST, J.; STRAKA, P.; PRÍHODA, J.; SIMURDA, D. **Comparison of several models of the laminar/turbulent transition**. EPJ Web of Conferences, v. 45, p. 01032, 2013. Available at: https://doi.org/10.1051/epjconf/20134501032. Cited in page 64.

GALVIN, K. J. ***Advancements in finite element methods for Newtonian and non-Newtonian flows***. Thesis (PhD) — Clemson University, 2013. Cited in page 116.

GANESAN, T.; AWANG, M. **Large Eddy Simulation (LES) for Steady-State Turbulent Flow Prediction**. *In*: ____. *Engineering Applications of Computational Fluid Dynamics*. Cham: Springer International Publishing, 2015. p. 17–32. ISBN 978-3-319-02836-1. Available at: https://doi.org/10.1007/978-3-319-02836-1_2. Cited in page 354.

GANUSHCHAK, Y.; LICHTENBELT, W. van M.; NAGEL, T. V. D.; JONG, D. D. **Hydrodynamic performance and heat generation by centrifugal pumps**. Perfusion, Sage Publications Sage CA: Thousand Oaks, CA, v. 21, n. 6, p. 373–379, 2006. Cited 2 times in pages 62 and 226.

GAO, R.; SPAKOVSZKY, Z.; RUSCH, D.; HUNZIKER, R. **Area schedule based design of high-pressure recovery radial diffusion systems**. Journal of Turbomachinery, American Society of Mechanical Engineers, v. 139, n. 1, p. 011012:1–011012:9, 2017. Cited 2 times in pages 123 and 124.

GARAKANI, A. H. K.; MOSTOUFI, N.; SADEGHI, F.; HOSSEINZADEH, M.; FATOURECHI, H.; SARRAFZADEH, M. H.; MEHRNIA, M. R. **Comparison between different models for rheological characterization of activated sludge**. Iranian journal of environmental health science & engineering, v. 8, n. 3, p. 255–264, 2011. Cited 2 times in pages 95 and 354.

GARON, A.; FARINAS, M.-I. **Fast three-dimensional numerical hemolysis approximation**. Artificial Organs, Wiley Online Library, v. 28, n. 11, p. 1016–1025, 2004. Cited 7 times in pages 61, 127, 129, 130, 132, 133, and 135.

GAUR, M.; GUPTA, M. K. **Steady slip blood flow through a stenosed porous artery**. Advances in Applied Science Research, Pelagia Research Library, v. 5, n. 5, p. 549–259, 2014. Cited in page 150.

GEERTSMA, J. **Estimating the coefficient of inertial resistance in fluid flow through porous media**. Society of Petroleum Engineers Journal, Society of Petroleum Engineers, v. 14, n. 05, p. 445–450, 1974. Cited 2 times in pages 148 and 149.

GERSBORG-HANSEN, A.; SIGMUND, O.; HABER, R. B. **Topology optimization of channel flow problems**. Structural and multidisciplinary optimization, Springer, v. 30, n. 3, p. 181–192, 2005. Cited 2 times in pages 82 and 83.

GEUZAINE, C.; REMACLE, J.-F. **Gmsh: A 3-D finite element mesh generator with built-in pre- and post-processing facilities**. International Journal for Numerical Methods in Engineering, v. 79, n. 11, p. 1309–1331, 2009. Available at: https://onlinelibrary.wiley.com/doi/abs/10.1002/nme.2579. Cited in page 176.

GHATTAS, O.; HE, B.; ANTAKI, J. F. ***Shape optimization of Navier-Stokes flows with application to optimal design of artificial heart components***. [*S.l.*], 1995. Cited in page 61.

GIERSIEPEN, M.; WURZINGER, L.; OPITZ, R.; REUL, H. **Estimation of shear stress-related blood damage in heart valve prostheses-in vitro comparison of 25 aortic valves**. The International journal of artificial organs, SAGE Publications Sage UK: London, England, v. 13, n. 5, p. 300–306, 1990. Cited 2 times in pages 131 and 139.

GIJSEN, F. J. H.; VOSSE, F. N. van de; JANSSEN, J. D. **The influence of the non-Newtonian properties of blood on the flow in large arteries: steady flow in a carotid bifurcation model**. Journal of Biomechanics, v. 32, n. 6, p. 601–608, 1999. ISSN 0021-9290. Available at: http://www.sciencedirect.com/science/article/pii/S0021929099000159. Cited in page 98.

GILL, B.; COX JR., C. S.; AROOM, K. R. ***Centrifugal pump.*** 2009. US 2009/0317271 A1. Cited in page 74.

GILLIAM, C. D. ***Disc pump.*** 2012. US 2012/0014779 A1. Cited in page 66.

GIRAULT, V.; RAVIART, P. ***Finite element methods for Navier-Stokes equations: Theory and algorithms***. [*S.l.*]: Springer Berlin Heidelberg, 2012. (Springer Series in Computational Mathematics). ISBN 9783642616235. Cited 2 times in pages 114 and 116.

GOUBERGRITS, L. **Numerical modeling of blood damage: current status, challenges and future prospects**. Expert review of medical devices, Taylor & Francis, v. 3, n. 5, p. 527–531, 2006. Cited 2 times in pages 130 and 131.

GRANDE III, S. F.; DRAPER, D. R. ***Bladeless conical radial turbine and method.*** 2005. US 2005/0214109 A1. Cited 3 times in pages 66, 70, and 71.

GRAW, J. A.; HILDEBRANDT, P.; KRANNICH, A.; BALZER, F.; SPIES, C.; FRANCIS, R. C.; KUEBLER, W. M.; WEBER-CARSTENS, S.; MENK, M.; HUNSICKER, O. **The role of cell-free hemoglobin and haptoglobin in acute kidney injury in critically ill adults with ARDS and therapy with VV ECMO**. Critical Care, Springer, v. 26, n. 1, p. 1–10, 2022. Cited in page 61.

GREYSON, C. R. **The Right Ventricle and Pulmonary Circulation: Basic Concepts**. Revista Española de Cardiología (English Edition), v. 63, n. 1, p. 81–95, 2010. ISSN 1885-5857. Available at: http://www.sciencedirect.com/science/article/pii/S1885585710700128. Cited 2 times in pages 8 and 60.

GRIEWANK, A. ***Evaluating derivatives: Principles and techniques of algorithmic differentiation***. Philadelphia, PA, USA: Society for Industrial and Applied Mathematics, 2000. ISBN 0-89871-451-6. Cited in page 181.

GRIGIONI, M.; DANIELE, C.; MORBIDUCCI, U.; D'AVENIO, G.; BENEDETTO, G. D.; BARBARO, V. **The power-law mathematical model for blood damage prediction: analytical developments and physical inconsistencies**. Artificial organs, Wiley Online Library, v. 28, n. 5, p. 467–475, 2004. Cited 3 times in pages 128, 130, and 132.

GRIGIONI, M.; MORBIDUCCI, U.; D'AVENIO, G.; BENEDETTO, G. D.; GAUDIO, C. D. **A novel formulation for blood trauma prediction by a modified power-law mathematical model**. Biomechanics and Modeling in Mechanobiology, Springer, v. 4, n. 4, p. 249–260, 2005. Cited 3 times in pages 130, 132, and 354.

GUEST, J. K.; PRÉVOST, J. H. **Topology optimization of creeping fluid flows using a Darcy-Stokes finite element**. International Journal for Numerical Methods in Engineering, John Wiley & Sons, Ltd., v. 66, n. 3, p. 461–484, 2006. ISSN 1097-0207. Available at: http://dx.doi.org/10.1002/nme.1560. Cited 2 times in pages 82 and 108.

GUEST, J. K.; PRÉVOST, J. H.; BELYTSCHKO, T. **Achieving minimum length scale in topology optimization using nodal design variables and projection functions**. International Journal for Numerical Methods in Engineering, v. 61, n. 2, p. 238–254, 2004. Available at: https://onlinelibrary.wiley.com/doi/abs/10.1002/nme.1064. Cited in page 161.

GÜLICH, J. F. ***Centrifugal Pumps***. Springer Berlin Heidelberg, 2014. ISBN 9783642401145. Available at: https://books.google.com.br/books?id=d74UBQAAQBAJ. Cited 4 times in pages 78, 209, 213, and 214.

GUPTA, D. K.; KEULEN, F. van; LANGELAAR, M. **Design and analysis adaptivity in multiresolution topology optimization**. International Journal for Numerical Methods in Engineering, v. 121, n. 3, p. 450–476, 2020. Available at: https://onlinelibrary.wiley.com/doi/abs/10.1002/nme.6217. Cited in page 84.

GURTIN, M. E. ***An introduction to continuum mechanics***. 1. ed. New York: Academic Press, 1981. Cited 2 times in pages 92 and 99.

GUZMÁN, J.; SALGADO, A. J.; SAYAS, F.-J. **A Note on the Ladyženskaja-Babuška-Brezzi Condition**. J. Sci. Comput., Plenum Press, New York, NY, USA, v. 56, n. 2, p. 219–229, aug 2013. ISSN 0885-7474. Available at: http://dx.doi.org/10.1007/s10915-012-9670-z. Cited 2 times in pages 114 and 116.

HABHAB, M.-B.; ISMAIL, T.; LO, J. F. **A laminar flow-based microfluidic Tesla pump via lithography enabled 3D printing**. Sensors, v. 16, n. 11, 2016. ISSN 1424-8220. Available at: http://www.mdpi.com/1424-8220/16/11/1970. Cited in page 68.

HALLGREN, L.; TAKAGI, S.; TILLIANDER, A.; YOKOYA, S.; JÖNSSON, P. **Effect of nozzle type and swirl on flow pattern for initial filling conditions in the mould for up-hill teeming**. steel research international, Wiley Online Library, v. 78, n. 3, p. 254–259, 2007. Cited in page 65.

HAN, X.; RAHMAN, M.; AGARWAL, R. K. **Development and Application of Wall-Distance-Free Wray-Agarwal Turbulence Model (WA2018)**. *In*: *2018 AIAA Aerospace Sciences Meeting*. [*S.l.: s.n.*], 2018. p. 0593. Cited 2 times in pages 104 and 105.

HAN, X.; WRAY, T.; AGARWAL, R. K. **Application of a new DES model based on wray-agarwal turbulence model for simulation of wall-bounded flows with separation**. *In*: *47th AIAA Fluid Dynamics Conference*. [*S.l.: s.n.*], 2017. p. 3966. Cited in page 104.

HAN, X.; WRAY, T. J.; FIOLA, C.; AGARWAL, R. K. **Computation of Flow in S Ducts With Wray–Agarwal One-Equation Turbulence Model**. Journal of Propulsion and Power, American Institute of Aeronautics and Astronautics, v. 31, n. 5, p. 1338–1349, 2015. Cited in page 104.

HANSEN, K. B.; ARZANI, A.; SHADDEN, S. C. **Mechanical platelet activation potential in abdominal aortic aneurysms**. Journal of biomechanical engineering, American Society of Mechanical Engineers Digital Collection, v. 137, n. 4, 2015. Cited in page 141.

HASINGER, S. H.; KEHRT, L. G. **Investigation of a shear-force pump**. Journal of Engineering for Power, American Society of Mechanical Engineers, v. 85, n. 3, p. 201–206, 1963. Cited 3 times in pages 66, 68, and 73.

HASUND, K. E. S. ***Topology optimization for unsteady flow with applications in biomedical flows***. Thesis (Master's) — NTNU, 2017. Cited 2 times in pages 107 and 109.

HE, P.; MADER, C. A.; MARTINS, J. R. R. A.; MAKI, K. J. **An aerodynamic design optimization framework using a discrete adjoint approach with OpenFOAM**. Computers & Fluids, v. 168, p. 285–303, 2018. Cited in page 195.

HE, P.; MADER, C. A.; MARTINS, J. R. R. A.; MAKI, K. J. **DAFoam: An open-source adjoint framework for multidisciplinary design optimization with OpenFOAM**. AIAA Journal, 2020. Cited in page 195.

HEINRICH, M. ***Genetic optimization of turbomachinery components using the volute of a transonic centrifugal compressor as a case study***. Thesis (PhD) — Technische Universität Bergakademie Freiberg, 2016. Cited in page 80.

HEINRICH, M.; SCHWARZE, R. **Genetic algorithm optimization of the volute shape of a centrifugal compressor**. International Journal of Rotating Machinery, Hindawi, v. 2016, 2016. Cited in page 80.

HELLUMS, J. D. **1993 Whitaker Lecture: biorheology in thrombosis research**. Annals of biomedical engineering, Springer, v. 22, n. 5, p. 445–455, 1994. Cited 4 times in pages 139, 140, 141, and 142.

HILTON, A.; TANSLEY, G. **Magnetic drive system for a new centrifugal rotary blood pump**. Artificial organs, Wiley Online Library, v. 32, n. 10, p. 772–777, 2008. Cited 2 times in pages 207 and 208.

HINGHOFER-SZALKAY, H.; GREENLEAF, J. **Continuous monitoring of blood volume changes in humans**. Journal of applied physiology, Am Physiological Soc, v. 63, n. 3, p. 1003–1007, 1987. Cited 8 times in pages 62, 96, 210, 227, 266, 273, 294, and 306.

HOLLAND, K. ***Design, construction and testing of a Tesla Turbine***. Thesis (Master's) — The Faculty of Graduate Studies, Laurentian University, 2015. Cited 2 times in pages 76 and 209.

HORNE, D.; CONWAY, J.; REBEYKA, I. M.; BUCHHOLZ, H. **Mechanical circulatory support in univentricular hearts: Current management**. Seminars in Thoracic and Cardiovascular Surgery: Pediatric Cardiac Surgery Annual, v. 18, p. 17–24, 12 2015. Cited in page 57.

HOSHI, H.; KATAKOA, K.; OHUCHI, K.; ASAMA, J.-i.; SHINSHI, T.; SHIMOKOHBE, A.; TAKATANI, S. **Magnetically suspended centrifugal blood pump with a radial magnetic driver**. ASAIO journal, LWW, v. 51, n. 1, p. 60–64, 2005. Cited in page 207.

HUANG, H.; AYOUB, J. A. **Applicability of the Forchheimer equation for non-Darcy flow in porous media**. *In*: SOCIETY OF PETROLEUM ENGINEERS. *SPE Annual Technical Conference and Exhibition*. [*S.l.*], 2006. Cited 2 times in pages 83 and 148.

HUANG, X.; XIE, Y. **Convergent and mesh-independent solutions for the bi-directional evolutionary structural optimization method**. Finite Elements in Analysis and Design, v. 43, n. 14, p. 1039–1049, 2007. ISSN 0168-874X. Available at: http://www.sciencedirect.com/science/article/pii/S0168874X07000777. Cited 3 times in pages 84, 183, and 185.

HUNTER, J. D. **Matplotlib: A 2D graphics environment**. Computing in Science & Engineering, IEEE COMPUTER SOC, v. 9, n. 3, p. 90–95, 2007. Cited 2 times in pages 176 and 275.

HYUN, J.; WANG, S.; YANG, S. **Topology optimization of the shear thinning non-Newtonian fluidic systems for minimizing wall shear stress**. Computers & Mathematics with Applications, v. 67, n. 5, p. 1154–1170, 2014. ISSN 0898-1221. Available at: http://www.sciencedirect.com/science/article/pii/S0898122113007074. Cited 7 times in pages 83, 84, 86, 95, 96, 98, and 151.

IBGE. ***Estatísticas do Registro Civil 2016***. [*S.l.*], 2016. Available at: https://biblioteca.ibge.gov.br/visualizacao/periodicos/135/rc_2016_v43_informativo.pdf. Cited in page 54.

IKEDA, T.; YAMANE, T.; ORITA, T.; TATEISHI, T. **A quantitative visualization study of flow in a scaled-up model of a centrifugal blood pump**. Artificial organs, Wiley Online Library, v. 20, n. 2, p. 132–138, 1996. Cited in page 219.

INCOR. ***Dispositivo de Assistência Ventricular InCor***. 2018. Available at: http://www.incor.usp.br/sites/bioengenharia/pt-br/index2.html?content=dav. Accessed on: 2018-04-06. Cited in page 58.

INCROPERA, F. P.; DEWITT, D. P.; BERGMAN, T. L.; LAVINE, A. S. ***Fundamentals of heat and mass transfer***. [*S.l.*]: John Wiley & Sons, 2011. Cited in page 118.

IZRAELEV, V.; WEISS, W. J.; FRITZ, B.; NEWSWANGER, R. K.; PATERSON, E. G.; SNYDER, A.; MEDVITZ, R. B.; CYSYK, J.; PAE, W. E.; HICKS, D.; LUKIC, B.; ROSENBERG, G. **A passively-suspended Tesla pump left ventricular assist device**. ASAIO journal (American Society for Artificial Internal Organs: 1992), NIH Public Access, v. 55, n. 6, p. 556–561, 2009. Cited 2 times in pages 72 and 73.

JACK, A.; MECROW, B.; MADDISON, C. **Combined radial and axial permanent magnet motors using soft magnetic composites**. *In*: *1999. Ninth International Conference on Electrical Machines and Drives (Conf. Publ. No. 468)*. [*S.l.: s.n.*], 1999. p. 25–29. Cited in page 207.

JENKINS, E. W.; PARIBELLO, C.; WILSON, N. E. **Mass conserving schemes for saturated groundwater flow**. *In*: *XIX International Conference on Water Resources*. [*S.l.: s.n.*], 2012. Cited in page 190.

JENSEN, K. E. ***Structural optimization of non-Newtonian microfluidics***. Thesis (PhD) — Technical University of Denmark, 2013. Cited in page 95.

JENSEN, K. E.; SZABO, P.; OKKELS, F. **Topology optimization of viscoelastic rectifiers**. Applied Physics Letters, AIP, v. 100, n. 23, p. 234102:1–234102:3, 2012. Cited in page 83.

JIAN SHI, G. ***Filamentous turbine.*** 2016. US 9.260,967 B2. Cited in page 72.

JIANG, L.; CHEN, S.; SADASIVAN, C.; JIAO, X. **Structural topology optimization for generative design of personalized aneurysm implants: Design, additive manufacturing, and experimental validation**. *In*: IEEE. *2017 IEEE Healthcare Innovations and Point of Care Technologies (HI-POCT)*. [*S.l.*], 2017. p. 9–13. Cited in page 95.

JIAO, K.; SUN, H.; LI, X.; WU, H.; KRIVITZKY, E.; SCHRAM, T.; LAROSILIERE, L. M. **Numerical simulation of air flow through turbocharger compressors with dual volute design**. Applied Energy, v. 86, n. 11, p. 2494–2506, 2009. ISSN 0306-2619. Available at: http://www.sciencedirect.com/science/article/pii/S0306261909000774. Cited in page 79.

JOSEPH, D. D.; NIELD, D. A.; PAPANICOLAOU, G. **Nonlinear equation governing flow in a saturated porous medium**. Water Resources Research, v. 18, n. 4, p. 1049–1052, 1982. Available at: https://agupubs.onlinelibrary.wiley.com/doi/abs/10.1029/WR018i004p01049. Cited 2 times in pages 149 and 150.

JOSHI, K. N.; SANGHVI, M. N.; DAVE, T. D. **Hybrid Tesla Pelton wheel Turbine**. International Journal of Scientific & Engineering Research, v. 7, n. 9, p. 1702–1707, 2016. Cited in page 70.

JOY, K. I. **Chaikin's algorithms for curves**. Visualization and Graphics Re, 1999. Cited in page 167.

KAMENEVA, M. V.; BURGREEN, G. W.; KONO, K.; REPKO, B.; ANTAKI, J. F.; UMEZU, M. **Effects of turbulent stresses upon mechanical hemolysis: experimental and computational analysis**. ASAIO journal, v. 50, n. 5, p. 418–423, 2004. Cited in page 64.

KAWAMOTO, A.; MATSUMORI, T.; KONDOH, T. **Regularization in topology optimization**. ROKS 2013, Leuven, 2013. Cited 2 times in pages 160 and 161.

KHAIRY, P.; POIRIER, N.; MERCIER, L.-A. **Univentricular Heart**. Circulation, v. 115, n. 6, p. 800–812, 2007. Available at: https://www.ahajournals.org/doi/abs/10.1161/CIRCULATIONAHA.105.592378. Cited in page 57.

KHODAK, A. ***Warming therapy device including tesla pump air circulation system.*** 2009. WO 2009/131936 A1. Cited in page 68.

KIAN, J. d. M. ***Topology optimization method applied to design channels considering non-newtonian fluid flow.*** Thesis (Master's) — Universidade de São Paulo, 2017. Available at: http://www.teses.usp.br/teses/disponiveis/3/3152/tde-16032017-103709/en.php. Cited 2 times in pages 95 and 96.

KIM, J. H.; OH, K. T.; PYUN, K. B.; KIM, C. K.; CHOI, Y. S.; YOON, J. Y. **Design optimization of a centrifugal pump impeller and volute using computational fluid dynamics**. IOP Conference Series: Earth and Environmental Science,

IOP Publishing, v. 15, n. 3, p. 032025:1–032025:9, nov 2012. Available at: https://doi.org/10.1088%2F1755-1315%2F15%2F3%2F032025. Cited in page 80.

KINI, V.; BACHMANN, C.; FONTAINE, A.; DEUTSCH, S.; TARBELL, J. **Integrating particle image velocimetry and laser Doppler velocimetry measurements of the regurgitant flow field past mechanical heart valves**. Artificial organs, Wiley Online Library, v. 25, n. 2, p. 136–145, 2001. Cited in page 137.

KLETSCHKA, H. D.; RAFFERTY, E. H. ***Pumps capable of use as heart pumps and blood pumps.*** 1975. US 3,864,055. Cited in page 74.

KO, J. ***Numerical modelling of highly swirling flows in a cylindrical through-flow hydrocyclone***. Thesis (PhD) — KTH, 2005. Cited in page 65.

KOGA, A. A.; LOPES, E. C. C.; VILLA NOVA, H. F.; LIMA, C. R. de; SILVA, E. C. N. **Development of heat sink device by using topology optimization**. International Journal of Heat and Mass Transfer, v. 64, p. 759–772, 2013. ISSN 0017-9310. Available at: http://www.sciencedirect.com/science/article/pii/S0017931013003979. Cited in page 83.

KOURI, D. P.; RIDZAL, D.; VON WINCKEL, G. ***Rapid Optimization Library.*** 2017. Available at: https://www.osti.gov/servlets/purl/1481491. Cited in page 177.

KRISHNAN, V. ***Design and Fabrication of cm-scale Tesla Turbines***. Thesis (Master's) — Electrical Engineering and Computer Sciences, University of California at Berkeley, 2015. Cited 2 times in pages 76 and 216.

KUKREJA, N.; LOUBOUTIN, M.; VIEIRA, F.; LUPORINI, F.; LANGE, M.; GORMAN, G. **Devito: automated fast finite difference computation**. CoRR, abs/1608.08658, 2016. Available at: http://arxiv.org/abs/1608.08658. Cited in page 176.

KUMAR, A.; CHANDEL, R. S.; SHRIVASTAVA, R.; SHRIVASTAVA, K.; KUMAR, S. **Mathematical modeling of blood flow in an inclined tapered artery under MHD effect through porous medium**. International Journal of Pure and Applied Mathematical Sciences, v. 9, p. 75–88, 2016. Cited in page 150.

KUNDU, P.; KUMAR, V.; MISHRA, I. M. **Experimental and numerical investigation of fluid flow hydrodynamics in porous media: Characterization of pre-Darcy, Darcy and non-Darcy flow regimes**. Powder Technology, Elsevier, v. 303, p. 278–291, 2016. Cited in page 148.

KUSTERS, R. W. J.; SIMONS, A. P.; LANCÉ, M. D.; GANUSHCHAK, Y. M.; BEKERS, O.; WEERWIND, P. W. **Blood warming, pump heating and haemolysis in low-flow extracorporeal life support; an in vitro study using freshly donated human blood**. Perfusion, SAGE Publications Sage UK: London, England, v. 32, n. 1, p. 27–34, 2017. Cited in page 62.

KUSZTELAN, A.; YAO, Y. F.; MARCHANT, D. R.; WANG, Y. **A review of novel turbocharger concepts for enhancements in energy efficiency**. Int. J. of Thermal & Environmental Engineering, v. 2, n. 2, p. 75–82, 2011. Cited in page 79.

LAHPOR, J. R. **State of the art: implantable ventricular assist devices**. Current opinion in organ transplantation, LWW, v. 14, n. 5, p. 554–559, 2009. Cited in page 56.

LAI, W. M.; RUBIN, D.; KREMPL, E. ***Introduction to continuum mechanics***. [*S.l.*]: Butterworth-Heinemann, 2009. Cited 5 times in pages 94, 99, 121, 203, and 412.

LAMICHHANE, B. P. **A nonconforming finite element method for the Stokes equations using the Crouzeix-Raviart element for the velocity and the standard linear element for the pressure**. International Journal for Numerical Methods in Fluids, Wiley Online Library, v. 74, n. 3, p. 222–228, 2014. Cited in page 114.

LAMPART, P.; KOSOWSKI, K.; PIWOWARSKI, M.; JĘDRZEJEWSKI, Ł. **Design analysis of Tesla micro-turbine operating on a low-boiling medium**. Polish Maritime Research, v. 16, n. Special, p. 28–33, 2009. Cited in page 68.

LAND, A. H.; DOIG, A. G. **An automatic method of solving discrete programming problems**. Econometrica, v. 28, p. 497–520, 1960. Cited in page 185.

LANGTANGEN, H. P.; LOGG, A. ***Solving PDEs in Minutes - The FEniCS tutorial Volume I***. [*s.n.*], 2016. Available at: https://fenicsproject.org/book/. Cited 2 times in pages 114 and 115.

LANGTANGEN, H. P.; MARDAL, K.-A.; WINTHER, R. **Numerical methods for incompressible viscous flow**. Advances in water Resources, Elsevier, v. 25, n. 8-12, p. 1125–1146, 2002. Cited in page 115.

LANGTRY, R. B.; MENTER, F. R.; LIKKI, S. R.; SUZEN, Y. B.; HUANG, P. G.; VO¨LKER, S. **A correlation-based transition model using local variables: Part I: Test Cases and Industrial Applications**. J. Turbomach, v. 128, n. 3, p. 423–434, 2006. Cited in page 64.

LASSEUX, D.; VALDÉS-PARADA, F. J. **On the developments of Darcy's law to include inertial and slip effects**. Comptes Rendus Mécanique, v. 345, n. 9, p. 660–669, 2017. ISSN 1631-0721. A century of fluid mechanics: 1870-1970. Available at: http://www.sciencedirect.com/science/article/pii/S1631072117300979. Cited in page 149.

LAZAROV, B. S.; SIGMUND, O. **Filters in topology optimization based on Helmholtz-type differential equations**. International Journal for Numerical Methods in Engineering, Wiley Online Library, v. 86, n. 6, p. 765–781, 2010. Cited 10 times in pages 161, 162, 199, 254, 257, 259, 261, 284, 414, and 423.

LEAMAN, A. B. ***The design, construction and investigation of a Tesla turbine***. Thesis (PhD) — University of Maryland, 1950. Cited in page 216.

LEE, S. P.; BARRANS, S. M.; JUPP, M. L.; NICKSON, A. K. **The impact of volute aspect ratio on the performance of a mixed flow turbine**. Aerospace, Multidisciplinary Digital Publishing Institute, v. 4, n. 4, p. 56–77, 2017. Cited in page 79.

LEE, S. S.; AHN, K. H.; LEE, S. J.; SUN, K.; GOEDHART, P. T.; HARDEMAN, M. R. **Shear induced damage of red blood cells monitored by the decrease of their deformability**. Korea-Australia Rheology Journal, Korean Society of Rheology, v. 16, n. 3, p. 141–146, 2004. Cited in page 61.

LEMMA, E.; DEAM, R.; TONCICH, D.; COLLINS, R. **Characterisation of a small viscous flow turbine**. Experimental Thermal and Fluid Science, v. 33, n. 1, p. 96–105, 2008. ISSN 0894-1777. Available at: http://www.sciencedirect.com/science/article/pii/S0894177708001015. Cited in page 66.

LENNEMANN, E. **Aerodynamic aspects of disk files**. IBM J. Res. Dev., IBM Corp., Riverton, NJ, USA, v. 18, n. 6, p. 480–488, Nov. 1974. ISSN 0018-8646. Available at: http://dx.doi.org/10.1147/rd.186.0480. Cited in page 67.

LEONDES, C. ***Biomechanical systems: Techniques and applications, Volume II: Cardiovascular techniques***. 1. ed. [*S.l.*]: CRC Press, 2000. (Biomechanical Systems: Techniques and Applications). ISBN 9781420049534. Cited in page 98.

LETOURNEAU, G. L. ***Rotor assembly for disc turbine.*** 1981. US 6,692,232 B1. Cited in page 76.

LEVINE, B. D.; CORNWELL, W. K.; DRAZNER, M. H. **Factors influencing the rate of flow through continuous-flow left ventricular assist devices at rest and with exercise**. JACC: Heart Failure, JACC: Heart Failure, v. 2, n. 4, p. 331–334, 2014. ISSN 2213-1779. Available at: http://heartfailure.onlinejacc.org/content/2/4/331. Cited in page 59.

LI, B. Q. ***Discontinuous finite elements in fluid dynamics and heat transfer***. [*S.l.*]: Springer Science & Business Media, 2006. Cited in page 115.

LI, R.; WANG, H.; YAO, E.; LI, M.; NAN, W. **Experimental study on bladeless turbine using incompressible working medium**. Advances in Mechanical Engineering, SAGE Publications Sage UK: London, England, v. 9, n. 1, p. 1687814016686935, 2017. Cited in page 76.

LIMA, J. S.; PAULINO, R. H.; SAENZ, J. S. R. **Bomba centrífuga de multiplos discos giratórios - tecnologia a ser utilizada na área biomédica**. ENCICLOPÉDIA BIOSFERA, Centro Científico Conhecer - Goiânia, v. 9, n. 17, p. 3069–3088, 2013. Cited in page 54.

LIN, S.; ZHAO, L.; GUEST, J. K.; WEIHS, T. P.; LIU, Z. **Topology optimization of fixed-geometry fluid diodes**. Journal of Mechanical Design, American Society of Mechanical Engineers, v. 137, n. 8, p. 081402:1–081402:8, 2015. Cited in page 118.

LINKE, A.; REBHOLZ, L. G.; WILSON, N. E. **On the convergence rate of grad-div stabilized Taylor-Hood to Scott-Vogelius solutions for incompressible flow problems**. Journal of Mathematical Analysis and Applications, v. 381, n. 2, p. 612–626, 2011. ISSN 0022-247X. Available at: http://www.sciencedirect.com/science/article/pii/S0022247X1100240X. Cited in page 190.

LIU, R.; LIU, J.; YU, Y. **Effects of axial inclined guide vanes on a turbo air classifier**. Powder Technology, Elsevier, v. 280, p. 1–9, 2015. Cited in page 79.

LIU, Z.; GAO, Q.; ZHANG, P.; XUAN, M.; WU, Y. **Topology optimization of fluid channels with flow rate equality constraints**. Structural and Multidisciplinary Optimization, Springer, v. 44, n. 1, p. 31–37, 2011. Cited in page 118.

LOBANOFF, V. S.; ROSS, R. R. ***Centrifugal pumps: design and application***. 2. ed. Massachusetts: Elsevier Butterworth-Heinemann, 1910. Cited 4 times in pages 77, 78, 79, and 213.

LOGAN Jr, E. ***Handbook of turbomachinery***. [*S.l.*]: CRC Press, 2003. Cited 3 times in pages 66, 73, and 81.

LOGG, A.; MARDAL, K.-A.; WELLS, G. ***Automated solution of differential equations by the finite element method: The FEniCS book***. Berlin: Springer, 2012. v. 84. Available at: https://fenicsproject.org/book/. Cited 6 times in pages 114, 115, 176, 181, 194, and 314.

LU, P.; LAI, H.; LIU, J. **A reevaluation and discussion on the threshold limit for hemolysis in a turbulent shear flow**. Journal of biomechanics, Elsevier, v. 34, n. 10, p. 1361–1364, 2001. Cited in page 131.

MA, Z.-D.; WANG, H.; KIKUCHI, N.; PIERRE, C.; RAJU, B. **Experimental validation and prototyping of optimum designs obtained from topology optimization**. Structural and Multidisciplinary Optimization, Springer, v. 31, n. 5, p. 333–343, 2006. Cited in page 169.

MACKAY, R. ***The practical pumping handbook***. [*S.l.*]: Elsevier, 2004. Cited in page 213.

MAGNETIC INNOVATIONS. ***Radial flux permanent magnet motor***. 2021. Available at: https://www.magneticinnovations.com/faq/radial-flux-permanent-magnet-motor/. Accessed on: 2021-08-27. Cited in page 207.

MAJIDI, K.; SIEKMANN, H. E. **Numerical calculation of secondary flow in pump volute and circular casings using 3D viscous flow techniques**. International Journal of Rotating Machinery, Hindawi, v. 6, n. 4, p. 245–252, 2000. Cited in page 78.

MALONEY, J. V.; BUCKBERG, G. D. ***Mass and thermal transfer means for use in heart lung machines, dialyzers, and otherapplications.*** 1999. US 5,900,142. Cited 2 times in pages 66 and 67.

MANN, D.; TARBELL, J. **Flow of non-Newtonian blood analog fluids in rigid curved and straight artery models**. Biorheology, v. 27, p. 711–33, 02 1990. Cited in page 227.

MANNING, K. B.; MILLER, G. E. **Shaft/shaft-seal interface characteristics of a multiple disk centrifugal blood pump**. Artificial Organs, v. 23, n. 6, p. 552–558, 1999. Available at: https://onlinelibrary.wiley.com/doi/abs/10.1046/j.1525-1594.1999.06402.x. Cited in page 74.

MAQUET. ***RotaFlow centrifugal pump***. 2018. Available at: https://www.maquet.com/int/products/rotaflow-centrifugal-pump/. Accessed on: 2018-01-02. Cited in page 75.

MARTONIK, H. **Caring for patients with a left ventricular assist device**. American Nurse Today, v. 12, n. 5, p. 22–23, 2017. Cited 4 times in pages 54, 55, 58, and 59.

MARUYAMA, O.; NISHIDA, M.; TSUTSUI, T.; JIKUYA, T.; YAMANE, T. **The hemolytic characteristics of monopivot magnetic suspension blood pumps with washout holes**. Artificial organs, Wiley Online Library, v. 29, n. 4, p. 345–348, 2005. Cited in page 219.

MATSUI, J.; NAGAHAMA, K.; KAGAWA, S.; KUROKAWA, J.; CHOI, Y.-D. **Application of circular casing to the centrifugal pump of low specific speed and the internal flow**. Turbomachinery, v. 34, n. 8, p. 463–470, 2006. Cited in page 78.

MAYER, E. ***Mechanical seals***. [*S.l.*]: Butterworth-Heinemann, 2013. Cited in page 213.

MC NALLY INSTITUTE. ***Circular casing***. 2019. Available at: http://www.mcnallyinstitute.com/c-html/c039.htm. Accessed on: 2019-02-03. Cited in page 79.

MCARDLE, C. R.; PRITCHARD, D.; WILSON, S. K. **The Stokes boundary layer for a thixotropic or antithixotropic fluid**. Journal of Non-Newtonian Fluid Mechanics, v. 185-186, p. 18–38, 2012. ISSN 0377-0257. Available at: http://www.sciencedirect.com/science/article/pii/S0377025712001358. Cited in page 95.

MCMILLAN, D. E.; UTTERBACK, N. G.; NASRINASRABADI, M.; LEE, M. M. **An instrument to evaluate the time dependent flow properties of blood at moderate shear rates**. Biorheology, IOS Press, v. 23, n. 1, p. 63–74, 1986. Cited in page 97.

MECHMATE FORUM. ***Why Mariss uses 32 X SQRT(Inductance) to calculate voltage of power supply***. 2009. Available at: http://www.mechmate.com/forums/showthread.php?t=1618. Accessed on: 2021-12-01. Cited in page 225.

MEDVITZ, R. B.; BOGER, D. A.; IZRAELEV, V.; ROSENBERG, G.; PATERSON, E. G. **A passively-suspended Tesla pump left ventricular assist device**. Artificial Organs, v. 35, n. 5, p. 522–533, 2011. Cited 2 times in pages 68 and 71.

MENTER, F. R.; LANGTRY, R. B.; LIKKI, S. R.; SUZEN, Y. B.; HUANG, P. G.; VO¨LKER, S. **A correlation-based transition model using local variables: Part I: Model formulation**. J. Turbomach, v. 128, n. 3, p. 413–422, 2006. Cited in page 64.

MEURER, A.; SMITH, C. P.; PAPROCKI, M.; ČERTÍK, O.; KIRPICHEV, S. B.; ROCKLIN, M.; KUMAR, A.; IVANOV, S.; MOORE, J. K.; SINGH, S.; RATHNAYAKE, T.; VIG, S.; GRANGER, B. E.; MULLER, R. P.; BONAZZI, F.; GUPTA, H.; VATS, S.; JOHANSSON, F.; PEDREGOSA, F.; CURRY, M. J.; TERREL, A. R.; ROUČKA, Š.; SABOO, A.; FERNANDO, I.; KULAL, S.; CIMRMAN, R.; SCOPATZ, A. **SymPy: symbolic computing in Python**. PeerJ Computer Science, v. 3, p. e103, jan 2017. ISSN 2376-5992. Available at: https://doi.org/10.7717/peerj-cs.103. Cited in page 187.

MILLER, G. E.; ETTER, B. D.; DORSI, J. M. **A multiple disk centrifugal pump as a blood flow device**. IEEE Transactions on Biomedical Engineering, v. 37, n. 2, p. 157–163, Feb 1990. ISSN 0018-9294. Cited in page 66.

MILLER, G. E.; MADIGAN, M.; FINK, R. **A preliminary flow visualization study in a multiple disk centrifugal artificial ventricle**. Artificial Organs, v. 19, n. 7, p. 680–684, 1995. Available at: https://onlinelibrary.wiley.com/doi/abs/10.1111/j.1525-1594.1995.tb02402.x. Cited in page 73.

MILLER, G. E.; RAINER, F. **Analysis of optimal design configurations for a multiple disk centrifugal blood pump**. Artificial Organs, v. 23, n. 6, p. 559–565, 1999. Available at: https://onlinelibrary.wiley.com/doi/abs/10.1046/j.1525-1594.1999.06403.x. Cited in page 74.

MILLER, G. E.; SIDHU, A.; FINK, R.; ETTER, B. D. **Evaluation of a multiple disk centrifugal pump as an artificial ventricle**. Artificial Organs, v. 17, n. 7, p. 590–592, 1993. Available at: https://onlinelibrary.wiley.com/doi/abs/10.1111/j.1525-1594.1993.tb00599.x. Cited 2 times in pages 73 and 226.

MILLER, L. W.; PAGANI, F. D.; RUSSELL, S. D.; JOHN, R.; BOYLE, A. J.; AARONSON, K. D.; CONTE, J. V.; NAKA, Y.; MANCINI, D.; DELGADO, R. M.; MACGILLIVRAY, T. E.; FARRAR, D. J.; FRAZIER, O. **Use of a continuous-flow device in patients awaiting heart transplantation**. New England Journal of Medicine, v. 357, n. 9, p. 885–896, 2007. PMID: 17761592. Available at: https://doi.org/10.1056/NEJMoa067758. Cited in page 55.

MITOH, A.; YANO, T.; SEKINE, K.; MITAMURA, Y.; OKAMOTO, E.; KIM, D.-W.; YOZU, R.; KAWADA, S. **Computational fluid dynamics analysis of an intra-cardiac axial flow pump**. Artificial Organs, v. 27, n. 1, p. 34–40, 2003. Available at: https://onlinelibrary.wiley.com/doi/abs/10.1046/j.1525-1594.2003.07190.x. Cited 2 times in pages 63 and 132.

MITUSCH, S.; FUNKE, S.; DOKKEN, J. **dolfin-adjoint 2018.1: automated adjoints for FEniCS and Firedrake**. Journal of Open Source Software, The Open Journal, v. 4, n. 38, p. 1292, 2019. Available at: https://doi.org/10.21105/joss.01292. Cited in page 177.

MOHITE, A. S. ***Investigations of the flow in a blower volute casing***. Thesis (PhD) — The Maharaja Sayajirao University of Baroda, 2013. Cited in page 79.

MONROE, D. M.; HOFFMAN, M.; ROBERTS, H. R. **Platelets and thrombin generation**. Arteriosclerosis, thrombosis, and vascular biology, Am Heart Assoc, v. 22, n. 9, p. 1381–1389, 2002. Cited in page 138.

MONTEVECCHI, F.; INZOLI, F.; REDAELLI, A.; MAMMANA, M. **Preliminary design and optimization of an ECC blood pump by means of a parametric approach**. Artificial organs, v. 19, n. 7, p. 685–690, 1995. Cited 2 times in pages 84 and 136.

MOODY, K. ***Efficiency evaluation of a magnetically driven multiple disk centrifugal blood pump***. Thesis (Master's) — Baylor University, 2016. Cited 3 times in pages 73, 76, and 226.

MOON, J. Y.; SUH, D. C.; LEE, Y. S.; KIM, Y. W.; LEE, J. S. **Considerations of blood properties, outlet boundary conditions and energy loss approaches in computational fluid dynamics modeling**. Neurointervention, v. 9, n. 1, p. 1–8, 2014. Cited in page 109.

MORTENSEN, M. ***CBC.RANS***. Launchpad repository, 2011. Available at: https://launchpad.net/cbc.rans. Accessed on: 2020-07-03. Cited in page 195.

MORTENSEN, M. ***CBC.PDESys***. Launchpad repository, 2013. Available at: https://code.launchpad.net/cbcpdesys. Accessed on: 2020-07-03. Cited in page 195.

MORTENSEN, M. ***CBC.PDESys***. Bitbucket repository, 2016. Available at: https://bitbucket.org/simula_cbc/cbcpdesys. Accessed on: 2020-07-03. Cited in page 195.

MORTENSEN, M.; LANGTANGEN, H. P.; WELLS, G. N. **A FEniCS-based programming framework for modeling turbulent flow by the Reynolds-averaged Navier-Stokes equations**. Advances in Water Resources, v. 34, n. 9, p. 1082–1101, 2011. ISSN 0309-1708. New Computational Methods and Software Tools. Available at: http://www.sciencedirect.com/science/article/pii/S030917081100039X. Cited 4 times in pages 193, 194, 195, and 196.

MOSCATELLI, E.; ALONSO, D. H.; SÁ, L. F. N.; PICELLI, R.; SILVA, E. C. N. **Topology optimisation for rotor-stator fluid flow devices**. Structural and Multidisciplinary Optimization, Springer Science and Business Media LLC, v. 65, n. 5, apr 2022. Available at: https://doi.org/10.1007%2Fs00158-022-03233-w. Cited in page 89.

MOTIN, A. ***Theoretical and numerical study of swirling flow separation devices for oil-water mixtures***. Thesis (PhD) — Michigan State University, 2015. Cited in page 65.

MUNSON, B. R.; YOUNG, D. F.; OKIISHI, T. H. ***Fundamentals of fluid mechanics***. 6. ed. [*S.l.*]: John Wiley & Sons, Inc., 2009. Cited 7 times in pages 92, 120, 122, 295, 411, 426, and 427.

MXQ. ***Disk pumps***. 2000. Brochure. Available at: http://jamestownindustries.com/wp-content/uploads/2017/03/MXQ-DISC-PUMP.pdf. Accessed on: 2018-05-01. Cited in page 69.

NADARAJAH, S.; JAMESON, A. **A comparison of the continuous and discrete adjoint approach to automatic aerodynamic optimization**. *In*: *38th Aerospace Sciences Meeting and Exhibit*. [*S.l.: s.n.*], 2000. p. 667–687. Cited in page 186.

NAGIB, H. M.; JR, L. W.; LAVAN, Z.; FEJER, A. A. ***On the stability of flow in rotating pipes***. [*S.l.*], 1969. Cited in page 234.

NAJJARI, M. R.; HINKE, J. A.; BULUSU, K. V.; PLESNIAK, M. W. **On the rheology of refractive-index-matched, non-Newtonian blood-analog fluids for PIV experiments**. Experiments in Fluids, Springer, v. 57, n. 6, p. 96, 2016. Cited in page 227.

NAKAHARA, T.; YOSHIDA, F. **Mechanical effects on rates of hemolysis**. Journal of Biomedical Materials Research, v. 20, n. 3, p. 363–374, 1986. Available at: https://onlinelibrary.wiley.com/doi/abs/10.1002/jbm.820200308. Cited 2 times in pages 63 and 119.

NAM, J.; BEHR, M.; PASQUALI, M. **Space-time least-squares finite element method for convection-reaction system with transformed variables**. Computer methods in applied mechanics and engineering, Elsevier, v. 200, n. 33-36, p. 2562–2576, 2011. Cited 7 times in pages 100, 127, 129, 133, 134, 135, and 345.

NASA. ***Turbulence Modeling Resource - The Spalart-Allmaras Turbulence Model .*** 2019. Available at: https://turbmodels.larc.nasa.gov/spalart.html. Accessed on: 2020-07-19. Cited in page 102.

NAZ, S.; LOCKHART, D.; HARWOOD, P.; KOMRAKOVA, A. E. **Numerical study of turbulent rotating flow in a tesla disc pump**. *In*: AMERICAN SOCIETY OF MECHANICAL ENGINEERS. *ASME 2017 International Mechanical Engineering Congress and Exposition*. [*S.l.*], 2017. Cited in page 74.

NDF. ***Recursos Computacionais - Cluster Mintrop***. 2022. Available at: http://ndf.poli.usp.br/recursos-computacionais. Accessed on: 2022-03-17. Cited in page 231.

NIH. ***Glycerol***. 2021. Available at: https://pubchem.ncbi.nlm.nih.gov/compound/Glycerol. Accessed on: 2021-09-29. Cited in page 227.

NISHIDA, M.; YAMANE, T.; ASZTALOS, B. **Washout hole flow measurement for the development of a centrifugal blood pump**. Artificial organs, Wiley Online Library, v. 22, n. 5, p. 386–392, 1998. Cited in page 219.

NIST. ***What is a ventricular assist device?*** 2016. Available at: https://www.nhlbi.nih.gov/health/health-topics/topics/vad. Accessed on: 2016-10-16. Cited in page 55.

NOBILI, M.; SHERIFF, J.; MORBIDUCCI, U.; REDAELLI, A.; BLUESTEIN, D. **Platelet activation due to hemodynamic shear stresses: damage accumulation model and comparison to in vitro measurements**. ASAIO journal (American Society for Artificial Internal Organs: 1992), NIH Public Access, v. 54, n. 1, p. 64, 2008. Cited 5 times in pages 138, 139, 140, 141, and 142.

NONAKA, K.; LINNEWEBER, J.; ICHIKAWA, S.; YOSHIKAWA, M.; KAWAHITO, S.; MIKAMI, M.; MOTOMURA, T.; ISHITOYA, H.; NISHIMURA, I.; OESTMANN, D.; GLUECK, J.; SCHIMA, H.; WOLNER, E.; SHINOHARA, T.; NOSÉ, Y. **Development of the Baylor Gyro permanently implantable centrifugal blood pump as a biventricular assist device**. Artificial Organs, v. 25, n. 9, p. 675–682, 2001. Available at: https://onlinelibrary.wiley.com/doi/abs/10.1046/j.1525-1594.2001.06855.x. Cited in page 55.

NØRGAARD, S.; SIGMUND, O.; LAZAROV, B. **Topology optimization of unsteady flow problems using the lattice boltzmann method**. J. Comput. Phys., Academic Press Professional, Inc., San Diego, CA, USA, v. 307, n. C, p. 291–307, Feb. 2016. ISSN 0021-9991. Available at: https://doi.org/10.1016/j.jcp.2015.12.023. Cited in page 83.

NØRGAARD, S. A. ***Topology optimization and lattice Boltzmann methods***. Thesis (PhD) — Technical University of Denmark (DTU), 2017. Cited 2 times in pages 91 and 92.

NOSÉ, Y.; YOSHIKAWA, M.; MURABAYASHI, S.; TAKANO, T. **Development of rotary blood pump technology: Past, present, and future**. Artificial Organs, v. 24, n. 6, p. 412–420, 2000. Available at: https://onlinelibrary.wiley.com/doi/abs/10.1046/j.1525-1594.2000.06634.x. Cited in page 55.

O'HEAREN, S. D. ***Radial turbine blade system.*** 2003. US 2003/0053909. Cited 2 times in pages 70 and 71.

OKUBO, C.; SÁ, L. F. N. de; KIYONO, C.; SILVA, E. C. N. **A discrete adjoint approach based on finite differences applied to topology optimization of flow problems**. Computer Methods in Applied Mechanics and Engineering, v. 389, p. 114406, 02 2022. Cited 2 times in pages 83 and 195.

OKUBO, C. M.; KIYONO, C. Y.; SÁ, L. F. N. de; SILVA, E. C. N. **Topology optimization applied to 3D rotor flow path design based on the continuous adjoint approach**. Computers & Mathematics with Applications, v. 96, p. 16–30, 2021. ISSN 0898-1221. Available at: https://www.sciencedirect.com/science/article/pii/S0898122121001863. Cited 4 times in pages 118, 119, 122, and 302.

OLESEN, L. H.; OKKELS, F.; BRUUS, H. **A high-level programming-language implementation of topology optimization applied to steady-state Navier-Stokes flow**. International Journal for Numerical Methods in Engineering, Wiley Online Library, v. 65, n. 7, p. 975–1001, 2006. Cited 3 times in pages 82, 83, and 147.

OLSEN, D. B. **Rotary blood pumps: A new horizon**. Artificial Organs, v. 23, n. 8, p. 695–696, 1999. Available at: https://onlinelibrary.wiley.com/doi/abs/10.1046/j.1525-1594.1999.00778.x. Cited in page 56.

OLSEN, D. B. **The history of continuous-flow blood pumps**. Artificial Organs, v. 24, n. 6, p. 401–404, 2000. Available at: https://onlinelibrary.wiley.com/doi/abs/10.1046/j.1525-1594.2000.06652.x. Cited in page 56.

OLSHANSKII, M.; LUBE, G.; HEISTER, T.; LÖWE, J. **Grad-div stabilization and subgrid pressure models for the incompressible Navier-Stokes equations**. Computer Methods in Applied Mechanics and Engineering, v. 198, n. 49, p. 3975–3988, 2009. ISSN 0045-7825. Available at: http://www.sciencedirect.com/science/article/pii/S004578250900303X. Cited in page 190.

OLSHANSKII, M.; REUSKEN, A. **Grad-div stablilization for Stokes equations**. Mathematics of Computation, v. 73, n. 248, p. 1699–1718, 2004. Cited in page 190.

OPENFOAM FOUNDATION. ***Official OpenFOAM Repository***. GitHub repository, 2020. Available at: https://github.com/OpenFOAM. Accessed on: 2020-03-17. Cited 2 times in pages 102 and 192.

OPENFOAM WIKI. ***OpenFOAM guide/The SIMPLE algorithm in OpenFOAM***. 2014. Available at: http://openfoamwiki.net/index.php/The_SIMPLE_algorithm_in_OpenFOAM. Accessed on: 2020-04-13. Cited 2 times in pages 201 and 404.

ORSZAG, S. A. **Analytical theories of turbulence**. Journal of Fluid Mechanics, Cambridge University Press, v. 41, n. 2, p. 363–386, 1970. Cited in page 101.

OSEI, H.; AL-KAYIEM, H.; AHMED, O. **Flow dynamics behaviour of a novel liquid-liquid hydrocyclone with varying upper cylindrical lengths and number of inlets**. ARPN J Eng Appl Sci, v. 11, p. 12159–12164, 01 2016. Cited in page 65.

OSHER, S.; SETHIAN, J. A. **Fronts propagating with curvature-dependent speed: algorithms based on Hamilton-Jacobi formulations**. Journal of computational physics, Elsevier, v. 79, n. 1, p. 12–49, 1988. Cited in page 82.

OTHMER, C. **A continuous adjoint formulation for the computation of topological and surface sensitivities of ducted flows**. International Journal for Numerical Methods in Fluids, v. 58, n. 8, p. 861–877, 2008. Available at: https://onlinelibrary.wiley.com/doi/abs/10.1002/fld.1770. Cited in page 108.

PACELLO, J.; HANAS, P. **Disc pump-type pump technology for hard-to-pump applications**. *In*: TEXAS A&M UNIVERSITY. TURBOMACHINERY LABORATORIES. *Proceedings of the 17th International Pump Users Symposium*. [*S.l.*], 2000. Cited 2 times in pages 69 and 76.

PACKHAM, M. A. **Role of platelets in thrombosis and hemostasis**. Canadian journal of physiology and pharmacology, NRC Research Press, v. 72, n. 3, p. 278–284, 1994. Cited in page 61.

PALADINO, E.; AGUIRRE, J. a.; QUINTELLA, E. **Developing multiphase models for liquid-liquid hydrocyclone flow**. *In*: *6th International Conference on Multiphase Flow, S6 Wed C*. [*S.l.: s.n.*], 2007. v. 37. Cited in page 65.

PAPADOPOULOS, I.; FARRELL, P. E.; SUROWIEC, T. M. **Computing multiple solutions of topology optimization problems**. arXiv preprint arXiv:2004.11797, 2020. Cited in page 85.

PAPOUTSIS-KIACHAGIAS, E.; ZYMARIS, A.; KAVVADIAS, I.; PAPADIMITRIOU, D.; GIANNAKOGLOU, K. **The continuous adjoint approach to the k-ϵ turbulence model for shape optimization and optimal active control of turbulent flows**. Engineering Optimization, Taylor & Francis, v. 47, n. 3, p. 370–389, 2015. Available at: https://doi.org/10.1080/0305215X.2014.892595. Cited in page 195.

PAPOUTSIS-KIACHAGIAS, E. M.; GIANNAKOGLOU, K. C. **Continuous adjoint methods for turbulent flows, applied to shape and topology optimization: industrial applications**. Archives of Computational Methods in Engineering, Springer, v. 23, n. 2, p. 255–299, 2016. Cited 2 times in pages 102 and 104.

PAPOUTSIS-KIACHAGIAS, E. M.; KONTOLEONTOS, E. A.; ZYMARIS, A. S.; PAPADIMITRIOU, D.; GIANNAKOGLOU, K. C. **Constrained topology optimization for laminar and turbulent flows, including heat transfer**. CIRA, editor, EUROGEN, Evolutionary and Deterministic Methods for Design, Optimization and Control, Capua, Italy, 2011. Cited in page 83.

PATANKAR, S. V. ***Numerical heat transfer and fluid flow***. 1. ed. [*S.l.*]: McGraw-Hill, 1980. Cited 2 times in pages 201 and 404.

PATLOLLA, V.; PATTEN, R. D.; DENOFRIO, D.; KONSTAM, M. A.; KRISHNAMANI, R. **The effect of ventricular assist devices on post-transplant mortality: An analysis of the united network for organ sharing thoracic registry**. Journal of the American College of Cardiology, v. 53, n. 3, p. 264–271, 2009. ISSN 0735-1097. Available at: http://www.sciencedirect.com/science/article/pii/S073510970803458X. Cited in page 55.

PAULI, L.; NAM, J.; PASQUALI, M.; BEHR, M. **Transient stress-based and strain-based hemolysis estimation in a simplified blood pump**. International journal for numerical methods in biomedical engineering, Wiley Online Library, v. 29, n. 10, p. 1148–1160, 2013. Cited 4 times in pages 127, 128, 132, and 134.

PERUMAL, D. A.; DASS, A. K. **A review on the development of lattice Boltzmann computation of macro fluid flows and heat transfer**. Alexandria Engineering Journal, v. 54, n. 4, p. 955–971, 2015. ISSN 1110-0168. Available at: http://www.sciencedirect.com/science/article/pii/S1110016815001362. Cited in page 92.

PESHLAKAI, A. ***Challenging the Versatility of the Tesla Turbine: Working Fluid Variations and Turbine Performance***. Thesis (Master's) — Arizona State University, 2012. Cited in page 74.

PFLEIDERER, C.; PETERMANN, H. ***Máquinas de fluxo***. 4. ed. Rio de Janeiro: Livros Técnicos e Científicos Editora S.A., 1979. Cited 5 times in pages 209, 210, 213, 214, and 215.

PFLEIDERER, C.; PETERMANN, H. ***Strömungsmaschinen***. 6. ed. Berlin-Heidelberg: Springer-Verlag, 1991. Cited in page 213.

PHILIPPI, B.; JIN, Y. **Topology optimization of turbulent fluid flow with a sensitive porosity adjoint method (SPAM)**. arXiv:1512.08445, 2015. Cited 4 times in pages 83, 86, 148, and 150.

PHILLIPS, G. O.; WILLIAMS, P. A. ***Handbook of hydrocolloids***. [*S.l.*]: CRC press Boca Raton, FL, 2000. Cited in page 227.

PICELLI, R.; RANJBARZADEH, S.; SIVAPURAM, R.; GIORIA, R.; SILVA, E. C. N. S. **Topology optimization of binary structures under design-dependent fluid-structure interaction loads**. Structural and Multidisciplinary Optimization, v. 62, p. 2101–2116, 10 2020. Cited in page 85.

PICELLI, R.; SIVAPURAM, R.; XIE, Y. M. **A 101-line MATLAB code for topology optimization using binary variables and integer programming**. Structural and Multidisciplinary Optimization, v. 63, p. 935–954, 2020. Cited 2 times in pages 84 and 85.

PICELLI, R.; SOUZA, E. M.; YAMABE, P. V. M.; ALONSO, D. H.; RANJBARZADEH, S.; GIORIA, R. d. S. **Topology optimization of turbulent fluid flow via the TOBS method and a geometry trimming procedure**. Structural and Multidisciplinary Optimization, v. 65, p. 34, 2021. Cited 3 times in pages 85, 89, and 167.

PINGEN, G.; MAUTE, K. **Optimal design for non-Newtonian flows using a topology optimization approach**. Computers & Mathematics with Applications, Elsevier, v. 59, n. 7, p. 2340–2350, 2010. Cited 7 times in pages 83, 84, 86, 94, 96, 99, and 151.

PINOTTI, M. **Is there correlation between the turbulent eddies size and mechanical hemolysis?** Journal of the Brazilian Society of Mechanical Sciences, Scielo, v. 22, p. 565–569, 00 2000. ISSN 0100-7386. Available at: http://www.scielo.br/scielo.php?script=sci_arttext&pid=S0100-73862000000400006&nrm=iso. Cited in page 64.

PINOTTI, M.; ROSA, E. S. **Computational prediction of hemolysis in a centrifugal ventricular assist device**. Artificial Organs, Wiley Online Library, v. 19, n. 3, p. 267–273, 1995. Cited in page 127.

PODER, T. G.; NONKANI, W. G.; LEPONKOUO, É. T. **Blood warming and hemolysis: a systematic review with meta-analysis**. Transfusion medicine reviews, Elsevier, v. 29, n. 3, p. 172–180, 2015. Cited in page 62.

POLISETTI, S.; VENKATRAMAN, S.; MIRYALA, M. **Fabrication and Study of the Parameters Affecting the Efficiency of a Bladeless Turbine**. *In*: . [*S.l.: s.n.*], 2017. p. 78–82. Cited in page 76.

PONTAZA, J.; REDDY, J. **Least-squares finite element formulations for viscous incompressible and compressible fluid flows**. Computer Methods in Applied Mechanics and Engineering, Elsevier, v. 195, n. 19-22, p. 2454–2494, 2006. Cited in page 115.

PRATUMWAL, Y.; LIMTRAKARN, W.; MUENGTAWEEPONGSA, S.; PHAKDEESAN, P.; DUANGBURONG, S.; EIAMARAM, P.; INTHARAKHAM, K. **Whole blood viscosity modeling using power law, Casson, and Carreau Yasuda models integrated with image scanning U-tube viscometer technique.** Songklanakarin Journal of Science & Technology, v. 39, n. 5, p. 625–631, 2017. Cited in page 98.

PUZYREWSKI, R.; TESCH, K. **1D Model calibration based on 3D calculations for Tesla turbine**. TASK QUARTERLY, v. 14, n. 3, p. 237–248, 2010. Cited in page 75.

QUARTERONI, A.; ROZZA, G. **Optimal control and shape optimization of aorto-coronaric bypass anastomoses**. Mathematical Models and Methods in Applied Sciences, v. 13, n. 12, p. 1801–1823, 2003. Available at: https://doi.org/10.1142/S0218202503003124. Cited in page 107.

QUARTERONI, A.; TUVERI, M.; VENEZIANI, A. **Computational vascular fluid dynamics: problems, models and methods**. Computing and Visualization in Science, Springer, v. 2, n. 4, p. 163–197, 2000. Cited 4 times in pages 95, 96, 97, and 98.

RAFFERTY, E. H.; KLETSCHKA, H. D. ***Electrically driven pumps capable of use as heart pumps.*** 1972. US 3,647,324. Cited in page 74.

RAFFERTY, E. H.; KLETSCHKA, H. D. ***Pumping apparatus and process characterized by gentle operation.*** 1976. US 3,957,389. Cited in page 74.

RAJE, A.; SINGH, B.; CHURAI, R.; BORWANKAR, P. **A review of Tesla turbine**. International Journal of Mechanical Engineering and Technology, v. 6, n. 10, p. 28–31, 2015. Cited 2 times in pages 68 and 69.

RAMALINGOM, D.; COCQUET, P.-H.; BASTIDE, A. **A new interpolation technique to deal with fluid-porous media interfaces for topology optimization of heat transfer**. Computers & Fluids, v. 168, p. 144–158, 2018. ISSN 0045-7930. Available at: http://www.sciencedirect.com/science/article/pii/S0045793018301932. Cited in page 83.

RATHGEBER, F.; HAM, D. A.; MITCHELL, L.; LANGE, M.; LUPORINI, F.; MCRAE, A. T. T.; BERCEA, G.-T.; MARKALL, G. R.; KELLY, P. H. J. **Firedrake: Automating the finite element method by composing abstractions**. ACM Trans. Math. Softw., ACM, New York, NY, USA, v. 43, n. 3, p. 24:1–24:27, Dec. 2016. ISSN 0098-3500. Available at: http://doi.acm.org/10.1145/2998441. Cited in page 176.

RAZ, S.; EINAV, S.; ALEMU, Y.; BLUESTEIN, D. **DPIV prediction of flow induced platelet activation-comparison to numerical predictions**. Annals of biomedical engineering, Springer, v. 35, n. 4, p. 493–504, 2007. Cited in page 138.

REDDY, J. N. ***An introduction to continuum mechanics***. 2. ed. [*S.l.*]: Cambridge university press, 2013. Cited in page 190.

REDDY, J. N.; GARTLING, D. K. ***The finite element method in heat transfer and fluid dynamics***. 3. ed. [*S.l.*]: CRC press, 2010. Cited 4 times in pages 92, 114, 115, and 116.

REINKE, W.; GAEHTGENS, P.; JOHNSON, P. **Blood viscosity in small tubes: effect of shear rate, aggregation, and sedimentation**. American Journal of Physiology-Heart and Circulatory Physiology, American Physiological Society Bethesda, MD, v. 253, n. 3, p. H540–H547, 1987. Cited in page 97.

REMPFER, D. **On boundary conditions for incompressible Navier-Stokes problems**. Applied Mechanics Reviews, v. 59, n. 3, p. 107–125, 05 2006. ISSN 0003-6900. Available at: https://doi.org/10.1115/1.2177683. Cited in page 201.

REUL, H. M.; AKDIS, M. **Blood pumps for circulatory support**. Perfusion, Sage Publications Sage CA: Thousand Oaks, CA, v. 15, n. 4, p. 295–311, 2000. Cited in page 58.

REY LADINO, A. F. ***Numerical simulation of the flow field in a friction-type turbine (Tesla Turbine)***. Thesis (Diploma thesis) — Institute of Thermal Powerplants, Vienna University of Technology, 2004. Cited 8 times in pages 65, 66, 74, 76, 79, 123, 125, and 216.

REYNOLDS, O. **IV. On the dynamical theory of incompressible viscous fluids and the determination of the criterion**. Philosophical transactions of the royal society of london.(a.), The Royal Society London, n. 186, p. 123–164, 1895. Cited in page 101.

RICE, W. **Tesla turbomachinery**. *In*: *Proc. IV International Nikola Tesla Symposium*. [*S.l.: s.n.*], 1991. Cited 2 times in pages 68 and 73.

RODRIGUES, A. ***Volute shaped pump casing for a centrifugal pump.*** 2011. EP 2 397 700 A2. Cited in page 79.

RODRIGUES, S. S.; MARTA, A. C. **Discrete adjoint mixing-plane formulation for multi-stage turbomachinery design**. *In*: *Proceedings of the 2015 Congress on Numerical Methods in Engineering, Lisbon, Portugal*. [*S.l.: s.n.*], 2015. Cited in page 204.

ROMERO SAENZ, J.; SILVA, E. C. N. **A topology optimization approach applied to laminar flow machine rotor design**. Computer Methods in Applied Mechanics and Engineering, v. 279, n. Supplement C, p. 268–300, 2014. ISSN 0045-7825. Available at: http://www.sciencedirect.com/science/article/pii/S0045782514002151. Cited 10 times in pages 83, 92, 93, 118, 121, 122, 302, 304, 305, and 307.

ROMERO SAENZ, J.; SILVA, E. C. N. **Non-newtonian laminar flow machine rotor design by using topology optimization**. Structural and Multidisciplinary Optimization, Springer, v. 55, n. 5, p. 1711–1732, 2017. Cited 9 times in pages 83, 84, 87, 95, 96, 302, 305, 307, and 312.

ROZVANY, G. **Aims, scope, methods, history and unified terminology of computer-aided topology optimization in structural mechanics**. Structural and Multidisciplinary Optimization, v. 21, n. 2, p. 90–108, Apr 2001. ISSN 1615-1488. Available at: https://doi.org/10.1007/s001580050174. Cited in page 82.

ROZVANY, G. I. N.; ZHOU, M.; BIRKER, T. **Generalized shape optimization without homogenization**. Structural optimization, v. 4, n. 3, p. 250–252, Sep 1992. ISSN 1615-1488. Available at: https://doi.org/10.1007/BF01742754. Cited in page 82.

RYKE, D. A.; IGARASHI, C. ***Expandable boundary layer turbine.*** 2015. US 2015/0330234 A1. Cited in page 76.

SÁ, L. F. N. ***Topology optimization method applied to laminar flow machine rotor design.*** Thesis (Master's) — Universidade de São Paulo, 2016. Available at: http://www.teses.usp.br/teses/disponiveis/3/3152/tde-16032017-103709/en.php. Cited 2 times in pages 83 and 207.

SÁ, L. F. N. ***Topology optimization method applied to ventricular assist device impeller and volute design.*** Thesis (PhD) — Universidade de São Paulo, 2019. Available at: http://www.teses.usp.br/teses/disponiveis/3/3152/tde-16032017-103709/en.php. Cited 4 times in pages 207, 208, 292, and 407.

SÁ, L. F. N.; AMIGO, R. C. R.; NOVOTNY, A. A.; SILVA, E. C. N. **Topological derivatives applied to fluid flow channel design optimization problems**. Structural and Multidisciplinary Optimization, v. 54, n. 2, p. 249–264, Aug 2016. ISSN 1615-1488. Available at: https://doi.org/10.1007/s00158-016-1399-0. Cited in page 82.

SÁ, L. F. N.; NOVOTNY, A. A.; ROMERO SAENZ, J.; SILVA, E. C. N. **Design optimization of laminar flow machine rotors based on the topological derivative concept**. Structural and Multidisciplinary Optimization, Springer, v. 56, n. 5, p. 1013–1026, 2017. Cited 2 times in pages 302 and 305.

SÁ, L. F. N.; OKUBO JR, C. M.; SILVA, E. C. N. **Topology Optimization of Subsonic Compressible Flows**. Structural and Multidisciplinary Optimization, Springer, 2021. Cited in page 83.

SÁ, L. F. N.; ROMERO SAENZ, J.; HORIKAWA, O.; SILVA, E. C. N. **Topology optimization applied to the development of small scale pump**. Structural and Multidisciplinary Optimization, Springer-Verlag, Berlin, Heidelberg, v. 57, n. 5, p. 2045–2059, May 2018. ISSN 1615-147X. Available at: https://doi.org/10.1007/s00158-018-1966-7. Cited 6 times in pages 83, 207, 208, 302, 304, and 305.

SÁ, L. F. N.; YAMABE, P. V. M.; SOUZA, B. C.; SILVA, E. C. N. **Topology optimization of turbulent rotating flows using Spalart-Allmaras model**. Computer Methods in Applied Mechanics and Engineering, v. 373, p. 113551, 2021. ISSN 0045-7825. Available at: http://www.sciencedirect.com/science/article/pii/S0045782520307362. Cited 6 times in pages 9, 83, 103, 117, 302, and 305.

SAAD, T. ***Turbulence modeling for beginners***. 2007. Available at: https://www.cfd-online.com/W/images/3/31/Turbulence_Modeling_For_Beginners.pdf. Accessed on: 2017-12-05. Cited in page 101.

SABERSKY, R. H.; ACOSTA, A. J.; HAUPTMANN, E. G.; GATES, E. M. ***Fluid flow: a first course in fluid mechanics***. [*S.l.*]: Macmillan, 1971. v. 299. Cited 9 times in pages 64, 276, 285, 295, 307, 315, 337, 345, and 348.

SADEK, S. H.; RUBIO, M.; LIMA, R.; VEGA, E. J. **Blood Particulate Analogue Fluids: A Review**. Materials, v. 14, n. 9, 2021. ISSN 1996-1944. Available at: https://www.mdpi.com/1996-1944/14/9/2451. Cited in page 227.

SAGEBAUM, M.; ALBRING, T.; GAUGER, N. R. **Expression templates for primal value taping in the reverse mode of algorithmic differentiation**. Optimization Methods and Software, Taylor & Francis, v. 33, n. 4-6, p. 1207–1231, 2018. Available at: https://doi.org/10.1080/10556788.2018.1471140. Cited in page 195.

SAHU, G. ***Pumps: Rotodynamic and positive displacement types: Theory, design and applications***. 1. ed. [*S.l.*]: New Age International, 2000. ISBN 9788122412246. Cited 2 times in pages 77 and 209.

SAITOH, T. S. ***Centrifugal reverse flow disk turbine and method to obtain rotational power thereby.*** 2011. US 2011/0164958 A1. Cited 2 times in pages 70 and 71.

SALVI, P. ***Pulse waves - How vascular hemodynamics affects blood pressure***. 1. ed. [*S.l.*]: Springer, 2012. Cited in page 59.

SASTRY, S.; KADAMBI, J. R.; SANKOVIC, J. M.; IZRAELEV, V. **Study of flow field in an advanced bladeless rotary blood pump using Particle Image Velocimetry**. *In*: INTERNATIONAL SYMPOSIUM ON APPLICATIONS OF LASER TECHNIQUES TO FLUID MECHANICS, 13., 2005. [*S.l.*], 2006. Abstract, 1095. Cited 3 times in pages 61, 66, and 72.

SATO, Y.; YAJI, K.; IZUI, K.; YAMADA, T.; NISHIWAKI, S. **Topology optimization of a no-moving-part valve incorporating Pareto frontier exploration**. Structural and Multidisciplinary Optimization, v. 56, n. 4, p. 839–851, Oct 2017. ISSN 1615-1488. Available at: https://doi.org/10.1007/s00158-017-1690-8. Cited in page 155.

SATO, Y.; YAJI, K.; IZUI, K.; YAMADA, T.; NISHIWAKI, S. **An optimum design method for a thermal-fluid device incorporating multiobjective topology optimization with an adaptive weighting scheme**. Journal of Mechanical Design, American Society of Mechanical Engineers, v. 140, n. 3, p. 031402:1–031402:12, 2018. Cited in page 83.

SATOH, H.; UCHIDA, K.; CAO, Y. **Designing an ultra-low specific speed centrifugal pump**. *In*: TEXAS A&M UNIVERSITY. TURBOMACHINERY LABORATORIES. *Proceedings of the 22nd International Pump Users Symposium*. [*S.l.*], 2005. Cited in page 78.

SAVITZKY, A.; GOLAY, M. J. **Smoothing and differentiation of data by simplified least squares procedures.** Analytical chemistry, ACS Publications, v. 36, n. 8, p. 1627–1639, 1964. Cited in page 167.

SBC. ***Cardiômetro***. 2020. Available at: http://www.cardiometro.com.br/anteriores.asp. Accessed on: 2020-06-14. Cited in page 54.

SCHIBILSKY, D.; TAKATANI, S.; SCHIBILSKY, B.; GRAF, T.; SILVA, D. M. da; WENDEL, H. P.; AVCI-ADALI, M.; SCHLENSAK, C. **Hemocompatibility of new magnetically-levitated centrifugal pump technology compared to the CentriMag adult pump**. Scientific Reports, Nature Publishing Group, v. 10, n. 1, p. 1–8, 2020. Cited in page 219.

SCHLICHTING, H. ***Boundary-layer theory***. 7. ed. [*S.l.*]: McGraw-Hill, 1979. Cited in page 201.

SCHLÖMER, N. ***meshio***. 2021. Available at: https://github.com/nschloe/meshio. Accessed on: 2021-09-3. Cited in page 176.

SCHOSSER, C.; LECHELER, S.; PFITZNER, M. **A test rig for the investigation of the performance and flow field of Tesla friction turbines**. *In*: AMERICAN SOCIETY OF MECHANICAL ENGINEERS. *ASME Turbo Expo 2014: Turbine Technical Conference and Exposition*. [*S.l.*], 2014. p. 1–11. Cited in page 75.

SCHOSSER, C.; LECHELER, S.; PFITZNER, M. **Analytical and numerical solutions of the rotor flow in Tesla turbines**. Periodica Polytechnica. Engineering. Mechanical Engineering, Periodica Polytechnica, Budapest University of Technology and Economics, v. 61, n. 1, p. 12–22, 2017. Cited in page 75.

SCHULER, C. A.; USRY, W.; WEBER, B.; HUMPHREY, J. A. C.; GREIF, R. **On the flow in the unobstructed space between shrouded corotating disks**. Physics of Fluids A: Fluid Dynamics, v. 2, n. 10, p. 1760–1770, 1990. Cited in page 66.

SCHWEDES, T.; HAM, D. A.; FUNKE, S. W.; PIGGOTT, M. D. ***Mesh dependence in PDE-constrained optimisation – An Application in Tidal Turbine Array Layouts***. 1. ed. [*S.l.*]: Springer, 2017. Cited in page 178.

SCOTT, L. R.; VOGELIUS, M. **Norm estimates for a maximal right inverse of the divergence operator in spaces of piecewise polynomials**. ESAIM: Mathematical Modelling and Numerical Analysis, EDP Sciences, v. 19, n. 1, p. 111–143, 1985. Cited in page 115.

SECOMB, T. W. **Hemodynamics**. *In*: ____. *Comprehensive Physiology*. American Cancer Society, 2016. p. 975–1003. ISBN 9780470650714. Available at: https://onlinelibrary.wiley.com/doi/abs/10.1002/cphy.c150038. Cited in page 97.

SHAN, X.; YUAN, X.-F.; CHEN, H. **Kinetic theory representation of hydrodynamics: a way beyond the Navier-Stokes equation**. Journal of Fluid Mechanics, Cambridge University Press, v. 550, p. 413–441, 2006. Cited in page 92.

SHERIFF, J.; BLUESTEIN, D.; GIRDHAR, G.; JESTY, J. **High-shear stress sensitizes platelets to subsequent low-shear conditions**. Annals of biomedical engineering, Springer, v. 38, n. 4, p. 1442–1450, 2010. Cited 3 times in pages 137, 139, and 140.

SHERIFF, J.; GIRDHAR, G.; CHIU, W.-C.; JESTY, J.; SLEPIAN, M. J.; BLUESTEIN, D. **Comparative efficacy of in vitro and in vivo metabolized aspirin in the DeBakey ventricular assist device**. Journal of thrombosis and thrombolysis, Springer, v. 37, n. 4, p. 499–506, 2014. Cited in page 138.

SHERIFF, J.; SOARES, J. a. S.; XENOS, M.; JESTY, J.; BLUESTEIN, D. **Evaluation of shear-induced platelet activation models under constant and dynamic shear stress loading conditions relevant to devices**. Annals of biomedical engineering, Springer, v. 41, n. 6, p. 1279–1296, 2013. Cited 5 times in pages 55, 132, 137, 139, and 140.

SHI, D.-y.; WANG, H.-m. **The Crouzeix-Raviart type nonconforming finite element method for the nonstationary Navier-Stokes equations on anisotropic meshes**. Acta Mathematicae Applicatae Sinica, English Series, Springer, v. 30, n. 1, p. 145–156, 2014. Cited in page 115.

SHI, Z.-C. **Nonconforming finite element methods**. Journal of computational and applied mathematics, Elsevier, v. 149, n. 1, p. 221–225, 2002. Cited in page 115.

SHIM, H.-S.; AFZAL, A.; KIM, K.-Y.; JEONG, H.-S. **Three-objective optimization of a centrifugal pump with double volute to minimize radial thrust at off-design conditions**. Proceedings of the Institution of Mechanical Engineers, Part A: Journal of Power and Energy, v. 230, n. 6, p. 598–615, 2016. Available at: https://doi.org/10.1177/0957650916656544. Cited in page 80.

SHIMELES, S. ***Design, simulation of fluid flow and optimization of operational parameters in Tesla multiple-disk turbine***. Thesis (Master's) — Addis Ababa University, 2014. Cited 3 times in pages 73, 76, and 79.

SHU, F.; VANDENBERGHE, S.; ANTAKI, J. F. **The importance of dQ/dt on the flow field in a turbodynamic pump with pulsatile flow**. Artificial organs, Wiley Online Library, v. 33, n. 9, p. 757–762, 2009. Cited in page 57.

SHWARTZ, J.; PROBSTEIN, R. F. **Experimental study of slurry separators for use in desalination**. Desalination, v. 6, n. 2, p. 239–266, 1969. ISSN 0011-9164. Available at: http://www.sciencedirect.com/science/article/pii/001191646980007X. Cited in page 150.

SIDDIQUI, M. S.; AHMED, H.; AHMED, S. **Numerical simulation of a compressed air driven Tesla Turbine**. *In*: AMERICAN SOCIETY OF MECHANICAL ENGINEERS. *ASME 2014 Power Conference*. [*S.l.*], 2014. Cited in page 74.

SIESS, T.; REUL, H. **Basic design criteria for rotary blood pumps**. *In*: ____. *Rotary blood pumps : New developments and current applications / Matsuda, H. Hrsg*. Tokyo [u.a.]: Springer, 2000. p. 69–83. Cited in page 57.

SIGMUND, O. **A 99 line topology optimization code written in Matlab**. Structural and Multidisciplinary Optimization, v. 21, n. 2, p. 120–127, Apr 2001. ISSN 1615-1488. Available at: https://doi.org/10.1007/s001580050176. Cited in page 160.

SIGMUND, O. **Morphology-based black and white filters for topology optimization**. Structural and Multidisciplinary Optimization, v. 33, n. 4, p. 401–424, Apr 2007. ISSN 1615-1488. Available at: https://doi.org/10.1007/s00158-006-0087-x. Cited 3 times in pages 153, 160, and 161.

SIGMUND, O.; PETERSSON, J. **Numerical instabilities in topology optimization: a survey on procedures dealing with checkerboards, mesh-dependencies and**

local minima. Structural optimization, Springer, v. 16, n. 1, p. 68–75, 1998. Cited in page 160.

SIN, D.; TAN, A. C.; KELSON, N.; CHADWICK, G. **Blood flow in a double output centrifugal artificial heart pump as a biventricular assist device**. ANZIAM Journal, v. 48, p. C949–C962, 2006. Cited in page 219.

SIN, D.-C.; KEI, H.-L.; MIAO, X. **Surface coatings for ventricular assist devices**. Expert Review of Medical Devices, Taylor & Francis, v. 6, n. 1, p. 51–60, 2009. Cited in page 60.

SIVAPURAM, R.; PICELLI, R. **Topology optimization of binary structures using Integer Linear Programming**. Finite Elements in Analysis and Design, v. 139, p. 49–61, 2018. ISSN 0168-874X. Available at: http://www.sciencedirect.com/science/article/pii/S0168874X17305619. Cited 5 times in pages 84, 85, 183, 184, and 186.

SIVAPURAM, R.; PICELLI, R. **Topology design of binary structures subjected to design-dependent thermal expansion and fluid pressure loads**. Structural and Multidisciplinary Optimization, v. 61, p. 1877–1895, 2020. Cited in page 185.

SIVAPURAM, R.; PICELLI, R.; XIE, Y. M. **Topology optimization of binary microstructures involving various non-volume constraints**. Computational Materials Science, v. 154, p. 405–425, 2018. ISSN 0927-0256. Available at: http://www.sciencedirect.com/science/article/pii/S0927025618305123. Cited 3 times in pages 84, 85, and 183.

SLAUGHTER, M. S.; PAGANI, F. D.; MCGEE, E. C.; BIRKS, E. J.; COTTS, W. G.; GREGORIC, I.; FRAZIER, O. H.; ICENOGLE, T.; NAJJAR, S. S.; BOYCE, S. W.; ACKER, M. A.; JOHN, R.; HATHAWAY, D. R.; NAJARIAN, K. B.; AARONSON, K. D. **HeartWare ventricular assist system for bridge to transplant: combined results of the bridge to transplant and continued access protocol trial**. The Journal of Heart and Lung Transplantation, Elsevier, v. 32, n. 7, p. 675–683, 2013. Cited in page 55.

SLAUGHTER, M. S.; PAGANI, F. D.; ROGERS, J. G.; MILLER, L. W.; SUN, B.; RUSSELL, S. D.; STARLING, R. C.; CHEN, L.; BOYLE, A. J.; CHILLCOTT, S.; ADAMSON, R. M.; BLOOD, M. S.; CAMACHO, M. T.; IDRISSI, K. A.; PETTY, M.; SOBIESKI, M.; WRIGHT, S.; MYERS, T. J.; FARRAR, D. J. **Clinical management of continuous-flow left ventricular assist devices in advanced heart failure**. The Journal of Heart and Lung Transplantation, v. 29, n. 4, Supplement, p. S1–S39, 2010. ISSN 1053-2498. Clinical Management of Continuous-flow Left Ventricular Assist Devices in Advanced Heart Failure. Available at: http://www.sciencedirect.com/science/article/pii/S1053249810000434. Cited in page 96.

SMAGORINSKY, J. **General circulation experiments with the primitive equations: I. The basic experiment**. Monthly weather review, American Meteorological Society, v. 91, n. 3, p. 99–164, 1963. Cited in page 101.

SMITH, W. A.; ALLAIRE, P.; ANTAKI, J.; BUTLER, K. C.; KERKHOFFS, W.; KINK, T.; LOREE, H.; REUL, H. **Collected nondimensional performance of rotary dynamic blood pumps**. ASAIO journal, LWW, v. 50, n. 1, p. 25–32, 2004. Cited in page 64.

SOARES, J. S.; SHERIFF, J.; BLUESTEIN, D. **A novel mathematical model of activation and sensitization of platelets subjected to dynamic stress histories**. Biomechanics and modeling in mechanobiology, Springer, v. 12, n. 6, p. 1127–1141, 2013. Cited 6 times in pages 126, 137, 139, 140, 141, and 142.

SOKOLOWSKI, J.; ZOCHOWSKI, A. **On the topological derivative in shape optimization**. SIAM journal on control and optimization, SIAM, v. 37, n. 4, p. 1251–1272, 1999. Cited in page 82.

SONG, X.; THROCKMORTON, A. L.; WOOD, H. G.; ANTAKI, J. F.; OLSEN, D. B. **Computational fluid dynamics prediction of blood damage in a centrifugal pump**. Artificial Organs, v. 27, n. 10, p. 938–941, 2003. Available at: https://onlinelibrary.wiley.com/doi/abs/10.1046/j.1525-1594.2003.00026.x. Cited 2 times in pages 63 and 132.

SONG, X.; THROCKMORTON, A. L.; WOOD, H. G.; ANTAKI, J. F.; OLSEN, D. B. **Quantitative evaluation of blood damage in a centrifugal VAD by computational fluid dynamics**. Journal of fluids engineering, American Society of Mechanical Engineers, v. 126, n. 3, p. 410–418, 2004. Cited in page 63.

SONG, X.; THROCKMORTON, A. L.; WOOD, H. G.; ALLAIRE, P. E.; OLSEN, D. B. **Transient and quasi-steady computational fluid dynamics study of a left ventricular assist device**. ASAIO journal, LWW, v. 50, n. 5, p. 410–417, 2004. Cited in page 57.

SONG, X.; UNTAROIU, A.; WOOD, H. G.; ALLAIRE, P. E.; THROCKMORTON, A. L.; DAY, S. W.; OLSEN, D. B. **Design and transient computational fluid dynamics study of a continuous axial flow ventricular assist device**. ASAIO journal, LWW, v. 50, n. 3, p. 215–224, 2004. Cited in page 57.

SONG, X.; WOOD, H. G.; OLSEN, D. **Computational fluid dynamics (CFD) study of the 4th generation prototype of a continuous flow ventricular assist device (VAD)**. Journal of biomechanical engineering, American Society of Mechanical Engineers, v. 126, n. 2, p. 180–187, 2004. Cited in page 63.

SONG, X. G.; WANG, L.; BAEK, S. H.; PARK, Y. C. **Multidisciplinary optimization of a butterfly valve**. ISA transactions, Elsevier, v. 48, n. 3, p. 370–377, 2009. Cited in page 83.

SONNTAG, R. E.; BORGNAKKE, C. ***Fundamentals of thermodynamics***. 8. ed. [*S.l.*]: Wiley, 2013. Cited in page 123.

SOUZA, B. C.; YAMABE, P. V. M.; SÁ, L. F. N.; RANJBARZADEH, S.; PICELLI, R.; SILVA, E. C. N. **Topology optimization of fluid flow by using Integer Linear Programming**. Structural and Multidisciplinary Optimization, Springer, 2021. Cited 2 times in pages 85 and 184.

SOUZA, B. C. de. ***Topology optimization of fluid diodes based on integer linear programming.*** Thesis (PhD) — Universidade de São Paulo, 2021. Available at: https://www.teses.usp.br/teses/disponiveis/3/3152/tde-18052021-134145/en.php. Cited in page 172.

SPALART, P. R. A.; ALLMARAS, S. **A one-equation turbulence model for aerodynamic flows**. Cla Recherche Aérospatiale, n. 1, p. 5–21, 1994. Cited in page 102.

STEINES, D.; WESTPHAL, D.; GÖBEL, C.; REUL, H.; RAU, G. **Platelet function and hemolysis in centrifugal pumps: in vitro investigations**. The International journal of artificial organs, SAGE Publications Sage UK: London, England, v. 22, n. 8, p. 559–565, 1999. Cited in page 130.

STERN, R. M.; RAY, W. J.; QUIGLEY, K. S. ***Psychophysiological recording***. 2. ed. [*S.l.*]: Oxford University Press, USA, 2001. Cited in page 59.

SUSAN-RESIGA, R. F.; MUNTEAN, S.; TĂNASĂ, C.; BOSIOC, A. **Three-dimensional versus two-dimensional axisymmetric analysis for decelerated swirling flows**. *In*: DEPARTMENT OF FLUID MECHANICS, FACULTY OF MECHANICAL ENGINEERING, BUDAPEST UNIVERSITY OF TECHNOLOGY AND ECONOMICS. *Conference on Modelling Fluid Flow (CMFF'06)*. [*S.l.*], 2006. Cited 2 times in pages 65 and 216.

SVANBERG, K.; SVARD, H. **Density filters for topology optimization based on the geometric harmonic means**. *In*: *10th world congress on structural and multidisciplinary optimization. Orlando*. [*S.l.: s.n.*], 2013. Cited in page 161.

SVANBERG, K.; WERME, M. **Sequential integer programming methods for stress constrained topology optimization**. Structural and Multidisciplinary Optimization, Springer, v. 34, n. 4, p. 277–299, 2007. Cited in page 183.

TAKAMI, Y.; NAKAZAWA, T.; MAKINOUCHI, K.; GLUECK, J.; BENKOWSKI, R.; NOSÉ, Y. **Mapping of pump efficiency on the pressure-flow curve of a centrifugal blood pump**. Artificial organs, Wiley Online Library, v. 21, n. 8, p. 953–957, 1997. Cited in page 62.

TANG, J. ***Wiring Basics: Unipolar vs Bipolar***. 2020. Available at: https://blog.orientalmotor.com/wiring-basics-unipolar-vs-bipolar. Accessed on: 2021-12-01. Cited in page 225.

TASKIN, M. E.; FRASER, K. H.; ZHANG, T.; GELLMAN, B.; FLEISCHLI, A.; DASSE, K. A.; GRIFFITH, B. P.; WU, Z. J. **Computational characterization of flow and hemolytic performance of the UltraMag blood pump for circulatory support**. Artificial organs, Wiley Online Library, v. 34, n. 12, p. 1099–1113, 2010. Cited in page 219.

TASKIN, M. E.; FRASER, K. H.; ZHANG, T.; WU, C.; GRIFFITH, B. P.; WU, Z. J. **Evaluation of Eulerian and Lagrangian models for hemolysis estimation**. ASAIO journal, LWW, v. 58, n. 4, p. 363–372, 2012. Cited 7 times in pages 63, 127, 128, 130, 131, 132, and 133.

TERREL, A. R. ***Finite element method automation for non-newtonian fluid models***. Thesis (PhD) — University of Chicago, 2010. Cited in page 114.

TESCH, K. **On invariants of fluid mechanics tensors**. Task Quarterly, v. 17, n. 3-4, p. 228–230, 2013. Cited 2 times in pages 99 and 127.

TESLA, N. ***Fluid propulsion.*** 1913. US 1,061,142. Cited 5 times in pages 8, 65, 66, 67, and 76.

TESLA, N. ***Turbine.*** 1913. US 1,061,206. Cited 4 times in pages 65, 76, 213, and 216.

TESLA, N. ***Improved process of and apparatus for production of high vacua.*** 1921. GB 179,043. Cited in page 68.

THE DOCUMENT FOUNDATION. ***LibreOffice***. The Document Foundation, 2022. Available at: https://www.libreoffice.org. Accessed on: 2022-01-23. Cited in page 176.

THE GIMP DEVELOPMENT TEAM. ***GIMP - GNU Image Manipulation Program***. The GIMP Development Team, 2022. Available at: https://www.gimp.org. Accessed on: 2022-01-23. Cited in page 176.

THORATEC. ***HEARTMATE 3™LEFT VENTRICULAR ASSIST SYSTEM - Instructions for Use***. 2017. Available at: https://www.accessdata.fda.gov/cdrh_docs/pdf16/P160054C.pdf. Accessed on: 2021-04-28. Cited in page 337.

THORATEC. ***HeartMate II LVAD***. 2018. Available at: http://www.thoratec.com/medical-professionals/vad-product-information/heartmate-ll-lvad.aspx. Accessed on: 2018-04-06. Cited in page 58.

THROCKMORTON, A. L.; UNTAROIU, A.; ALLAIRE, P. E.; WOOD, H. G.; MATHERNE, G. P.; LIM, D. S.; PEELER, B. B.; OLSEN, D. B. **Computational analysis of an axial flow pediatric ventricular assist device**. Artificial organs, v. 28, n. 10, p. 881–891, 2004. Cited in page 59.

THROCKMORTON, A. L.; WOOD, H. G.; DAY, S. W.; SONG, X.; CLICK, P. C.; ALLAIRE, P. E.; OLSEN, D. B. **Design of a continuous flow centrifugal pediatric ventricular assist device**. The International journal of artificial organs, SAGE Publications Sage UK: London, England, v. 26, n. 11, p. 1015–1031, 2003. Cited in page 59.

THURSTON, G. B. **Rheological parameters for the viscosity viscoelasticity and thixotropy of blood**. Biorheology, IOS Press, v. 16, n. 3, p. 149–162, 1979. Cited in page 97.

TIMMS, D. L. ***Design, development and evaluation of centrifugal ventricular assist devices***. Thesis (PhD) — Queensland University of Technology, 2005. Cited 2 times in pages 216 and 219.

TOSCO, T.; MARCHISIO, D. L.; LINCE, F.; SETHI, R. **Extension of the Darcy-Forchheimer law for shear-thinning fluids and validation via pore-scale flow simulations**. Transport in Porous Media, v. 96, n. 1, p. 1–20, Jan 2013. ISSN 1573-1634. Available at: https://doi.org/10.1007/s11242-012-0070-5. Cited in page 150.

TOWARA, M.; NAUMANN, U. **A Discrete Adjoint Model for OpenFOAM**. Procedia Computer Science, v. 18, p. 429–438, 2013. ISSN 1877-0509. 2013 International Conference on Computational Science. Available at: http://www.sciencedirect.com/science/article/pii/S1877050913003499. Cited in page 195.

TRAVIS, B. R.; MARZEC, U. M.; LEO, H. L.; MOMIN, T.; SANDERS, C.; HANSON, S. R.; YOGANATHAN, A. P. **Bileaflet aortic valve prosthesis pivot geometry influences platelet secretion and anionic phospholipid exposure**. Annals of biomedical engineering, Springer, v. 29, n. 8, p. 657–664, 2001. Cited in page 137.

TSUKAMOTO, Y.; ITO, K.; SAWAIRI, T.; KONISHI, Y.; YAMANE, T.; NISHIDA, M.; MASUZAWA, T.; TSUKIYA, T.; ENDO, S.; TAENAKA, Y. **Computational fluid dynamics analysis of a centrifugal blood pump with washout holes**. Artificial organs, Wiley Online Library, v. 24, n. 8, p. 648–652, 2000. Cited in page 219.

TSUKIYA, T.; TAENAKA, Y.; TATSUMI, E.; TAKANO, H. **Improvement of washout flow in a centrifugal blood pump by a semi-open impeller**. ASAIO journal, LWW, v. 48, n. 1, p. 76–82, 2002. Cited in page 219.

TUZSON, J. ***Centrifugal pump design***. 1. ed. Massachusetts: John Wiley & Sons, Inc., 2000. Cited 2 times in pages 79 and 292.

ÜNDAR, A. **Myths and truths of pulsatile and nonpulsatile perfusion during acute and chronic cardiac support**. Artificial Organs, v. 28, n. 5, p. 439–443, 2004. Available at: https://onlinelibrary.wiley.com/doi/abs/10.1111/j.1525-1594.2004.00086.x. Cited in page 56.

USP MULTI. ***Central Multiusuários - RCGI - CM-RCGI***. 2022. Available at: https://uspmulti.prp.usp.br/public/centrais/94. Accessed on: 2022-03-17. Cited in page 223.

VAFAI, K. ***Handbook of porous media***. 2. ed. [*S.l.*]: Crc Press, 2005. Cited 2 times in pages 145 and 149.

VALEN-SENDSTAD, K.; MORTENSEN, M.; LANGTANGEN, H. P.; REIF, B.; MARDAL, K.-A. **Implementing a k-ϵ Turbulence Model in the FEniCS Finite Element Programming Environment**. *In*: . [*S.l.: s.n.*], 2013. p. 1–13. Cited in page 195.

VANDERBEI, R. J. ***Linear Programming: Foundations and Extensions***. 4. ed. [*S.l.*]: Springer US, 2014. Cited in page 185.

VARCHANIS, S.; SYRAKOS, A.; DIMAKOPOULOS, Y.; TSAMOPOULOS, J. **A new finite element formulation for viscoelastic flows: Circumventing simultaneously the LBB condition and the high-Weissenberg number problem**. Journal of Non-Newtonian Fluid Mechanics, Elsevier, v. 267, p. 78–97, 2019. Cited in page 115.

VARELA, R. A. S. ***Design of electrothermomechanical (ETM) MEMS using topology optimization method (TOM) considering the thermal transient response.*** Thesis (Master's) — Universidade de São Paulo, 2012. Available at: https://teses.usp.br/teses/disponiveis/3/3152/tde-04072012-174915/en.php. Cited in page 169.

VARSAKELIS, C.; PAPALEXANDRIS, M. V. **On the well-posedness of the Darcy–Brinkman–Forchheimer equations for coupled porous media-clear fluid flow**. Nonlinearity, IOP Publishing, v. 30, n. 4, p. 1449–1464, feb 2017. Available at: https://doi.org/10.1088%2F1361-6544%2Faa5ecf. Cited in page 150.

VATANABE, S. L.; LIPPI, T. N.; LIMA, C. R. de; PAULINO, G. H.; SILVA, E. C. N. **Topology optimization with manufacturing constraints: A unified projection-based approach**. Advances in Engineering Software, v. 100, p. 97–112, 2016. ISSN 0965-9978. Available at: http://www.sciencedirect.com/science/article/pii/S0965997816301703. Cited in page 161.

VIGNON-CLEMENTEL, I. E.; FIGUEROA, C. A.; JANSEN, K. E.; TAYLOR, C. A. **Outflow boundary conditions for three-dimensional finite element modeling of blood flow and pressure in arteries**. Computer methods in applied mechanics and engineering, Elsevier, v. 195, n. 29-32, p. 3776–3796, 2006. Cited in page 109.

VLACHOPOULOS, C.; O'ROURKE, M.; NICHOLS, W. W. ***McDonald's blood flow in arteries: theoretical, experimental and clinical principles***. 6. ed. London: Hodder Arnold, 2011. Cited 3 times in pages 96, 97, and 100.

WÄCHTER, A.; BIEGLER, L. T. **On the implementation of an interior-point filter line-search algorithm for large-scale nonlinear programming**. Mathematical programming, Springer, v. 106, n. 1, p. 25–57, 2006. Cited 4 times in pages 177, 182, 183, and 228.

WAGNER, W. R.; SCHAUB, R. D.; SORENSEN, E. N.; SNYDER, T. A.; WILHELM, C. R.; WINOWICH, S.; BOROVETZ, H. S.; KORMOS, R. L. **Blood biocompatibility analysis in the setting of ventricular assist devices**. Journal of Biomaterials Science, Polymer Edition, Taylor & Francis, v. 11, n. 11, p. 1239–1259, 2000. Cited in page 60.

WAKISAKA, Y.; TAENAKA, Y.; ARAKI, K.; CHIKANARI, K.-i.; NAKATANI, T.; BABA, Y.; ANAI, H.; EYA, K.; TODA, K.; TAKANO, H. **Effects of self washout structure on the antithrombogenicity and the hemolytic properties of a centrifugal pump**. Artificial organs, Wiley Online Library, v. 21, n. 2, p. 148–153, 1997. Cited in page 219.

WALBURN, F. J.; SCHNECK, D. J. **A constitutive equation for whole human blood**. Biorheology, IOS Press, v. 13, n. 3, p. 201–210, 1976. Cited in page 100.

WAMPLER, R. K. ***Sealless rotary blood pump with passive magnetic radial bearings and blood immersed axial bearings.*** 1997. US 5,695,471. Cited in page 207.

WANG, L.; TORRES, A.; XIANG, L.; FEI, X.; NAIDO, A.; WU, W. **A technical review on shale gas production and unconventional reservoirs modeling**. Natural Resources, Scientific Research Publishing, v. 6, n. 03, p. 141–151, 2015. Cited in page 148.

WARD, J. C. **Turbulent flow in porous media**. Journal of the Hydraulics Division, ASCE, v. 90, n. 5, p. 1–12, 1964. Cited in page 150.

WAYLAND, H. **Rheology and the microcirculation**. Gastroenterology, v. 52, n. 2, p. 342–355, 1967. Cited in page 97.

WELLER, H. G.; TABOR, G.; JASAK, H.; FUREBY, C. **A tensorial approach to computational continuum mechanics using object-oriented techniques**. Computers in physics, American Institute of Physics, v. 12, n. 6, p. 620–631, 1998. Cited 3 times in pages 176, 192, and 194.

WHITAKER, S. **The Forchheimer equation: A theoretical development**. Transport in Porous Media, v. 25, n. 1, p. 27–61, Oct 1996. ISSN 1573-1634. Available at: https://doi.org/10.1007/BF00141261. Cited in page 150.

WHITE, F. M. ***Fluid Mechanics***. 7. ed. [*S.l.*]: McGraw-Hill, 2011. Cited 3 times in pages 92, 93, and 118.

W.H.O. ***Cardiovascular diseases (CVDs)***. 2017. Available at: https://www.who.int/en/news-room/fact-sheets/detail/cardiovascular-diseases-(cvds). Accessed on: 2020-06-14. Cited in page 54.

WIEGMANN, L.; BOËS, S.; ZÉLICOURT, D. de; THAMSEN, B.; DANERS, M. S.; MEBOLDT, M.; KURTCUOGLU, V. **Blood pump design variations and their influence on hydraulic performance and indicators of hemocompatibility**. Annals of biomedical engineering, v. 46, n. 3, p. 417–428, 2018. Cited 2 times in pages 62 and 63.

WIKER, N.; KLARBRING, A.; BORRVALL, T. **Topology optimization of regions of Darcy and Stokes flow**. International journal for numerical methods in engineering, v. 69, n. 7, p. 1374–1404, 2007. Cited in page 82.

WILCOX, D. C. ***Turbulence Modeling for CFD***. 3. ed. [*S.l.*]: DCW Industries, Inc, 2006. Cited in page 102.

WILSON, E. A. ***Fluid flow channels in bladeless compressors, turbines and pumps.*** 2006. US 2006/0216149 A1. Cited in page 71.

WOLF DYNAMICS. ***A Crash Introduction to the Finite Volume Method and Discretization Schemes in OpenFOAM® .*** 2020. Available at: http://www.wolfdynamics.com/tutorials.html?id=158. Accessed on: 2020-08-23. Cited in page 405.

WRAY, T.; AGARWAL, R. K. **Application of the Wray-Agarwal Model to Compressible Flows**. *In*: *46th AIAA Fluid Dynamics Conference*. [*S.l.: s.n.*], 2016. p. 3641. Cited in page 104.

WRAY, T. J.; AGARWAL, R. K. **Low-Reynolds-Number One-Equation Turbulence Model Based on k-ω Closure**. AIAA Journal, American Institute of Aeronautics and Astronautics, v. 53, n. 8, p. 2216–2227, 2015. Cited in page 104.

WU, J. **Letter to the editor: A possible major mistake in the paper entitled "Collected nondimensional performance of rotary dynamic blood pump": Smith WA, Allaire P, Antaki J, Butler KC, Kerkhoffs W, Kink T, Loree H, Reul H. ASAIO Journal 50: 25–32, 2004**. Asaio Journal, LWW, v. 53, n. 2, p. 255–256, 2007. Cited 10 times in pages 64, 65, 276, 285, 295, 307, 315, 337, 345, and 348.

WU, J.; ANTAKI, J. F.; SNYDER, T. A.; WAGNER, W. R.; BOROVETZ, H. S.; PADEN, B. E. **Design optimization of blood shearing instrument by computational fluid dynamics**. Artificial organs, Wiley Online Library, v. 29, n. 6, p. 482–489, 2005. Cited in page 126.

WU, J.; PADEN, B. E.; BOROVETZ, H. S.; ANTAKI, J. F. **Computational fluid dynamics analysis of blade tip clearances on hemodynamic performance and blood damage in a centrifugal ventricular assist device**. Artificial organs, Wiley Online Library, v. 34, n. 5, p. 402–411, 2010. Cited in page 216.

WU, Z.; ZHANG, J.; CHEN, X.; FRASER, K.; TASKIN, M. E.; GRIFFITH, B. P. **Computational study of the blood flow in three types of 3D hollow fiber membrane bundles**. Journal of biomechanical engineering, v. 135, p. 21009:1–21009:11, 10 2013. Cited in page 62.

WYATT, N. B.; LIBERATORE, M. W. **Rheology and viscosity scaling of the polyelectrolyte xanthan gum**. Journal of Applied Polymer Science, Wiley Online Library, v. 114, n. 6, p. 4076–4084, 2009. Cited in page 227.

YAJI, K.; YAMADA, T.; YOSHINO, M.; MATSUMOTO, T.; IZUI, K.; NISHIWAKI, S. **Topology optimization in thermal-fluid flow using the lattice Boltzmann method**. Journal of Computational Physics, v. 307, p. 355–377, 2016. ISSN 0021-9991. Available at: http://www.sciencedirect.com/science/article/pii/S0021999115008244. Cited 2 times in pages 83 and 92.

YANG, S.; KONG, F.; CHEN, B. **Research on pump volute design method using CFD**. International Journal of Rotating Machinery, Hindawi, v. 2011, 2011. Cited 2 times in pages 78 and 79.

YANO, T.; SEKINE, K.; MITOH, A.; MITAMURA, Y.; OKAMOTO, E.; KIM, D.-W.; NISHIMURA, I.; MURABAYASHI, S.; YOZU, R. **An estimation method of hemolysis within an axial flow blood pump by computational fluid dynamics analysis**. Artificial organs, Wiley Online Library, v. 27, n. 10, p. 920–925, 2003. Cited in page 132.

YELESWARAPU, K. K.; ANTAKI, J. F.; KAMENEVA, M. V.; RAJAGOPAL, K. R. **A mathematical model for shear-induced hemolysis**. Artificial Organs, Wiley Online Library, v. 19, n. 7, p. 576–582, 1995. Cited in page 132.

YEOW, Y. L.; WICKRAMASINGHE, S. R.; LEONG, Y.-K.; HAN, B. **Model-independent relationships between hematocrit, blood viscosity, and yield stress derived from Couette viscometry data**. Biotechnology progress, Wiley Online Library, v. 18, n. 5, p. 1068–1075, 2002. Cited in page 100.

YOGANATHAN, A. P.; CHANDRAN, K. B.; SOTIROPOULOS, F. **Flow in prosthetic heart valves: State-of-the-art and future directions**. Annals of Biomedical Engineering, v. 33, n. 12, p. 1689–1694, Dec 2005. ISSN 1573-9686. Available at: https://doi.org/10.1007/s10439-005-8759-z. Cited in page 63.

YOON, G. H. **Topology optimization for turbulent flow with Spalart-Allmaras model**. Computer methods in applied mechanics and engineering, v. 303, p. 288–311, 2016. ISSN 0045-7825. Available at: http://www.sciencedirect.com/science/article/pii/S004578251630007X. Cited 9 times in pages 9, 83, 87, 102, 103, 104, 105, 106, and 117.

YOON, G. H. **Topology optimization method with finite elements based on the k-ε turbulence model**. Computer Methods in Applied Mechanics

and Engineering, v. 361, p. 112784, 2020. ISSN 0045-7825. Available at: http://www.sciencedirect.com/science/article/pii/S0045782519306760. Cited 3 times in pages 83, 87, and 105.

YU, M. ***Flow design optimization of blood pumps considering hemolysis***. Thesis (PhD) — Otto-von-Guericke-Universität Magdeburg, 2015. Cited 5 times in pages 63, 67, 70, 72, and 73.

YUN, S.-H.; SIM, E.-H.; GOH, R.-Y.; PARK, J.-I.; HAN, J.-Y. **Platelet activation: the mechanisms and potential biomarkers**. BioMed research international, Hindawi, v. 2016, 2016. Cited in page 137.

ZAUDERER, E. ***Partial differential equations of applied mathematics***. 2. ed. [*S.l.*]: John Wiley & Sons, 1989. Cited in page 162.

ZHANG, B.; LIU, X. **Topology optimization study of arterial bypass configurations using the level set method**. Struct. Multidiscip. Optim., Springer-Verlag New York, Inc., Secaucus, NJ, USA, v. 51, n. 3, p. 773–798, Mar. 2015. ISSN 1615-147X. Available at: http://dx.doi.org/10.1007/s00158-014-1175-y. Cited 5 times in pages 83, 84, 95, 96, and 421.

ZHANG, B.; LIU, X.; SUN, J. **Topology optimization design of non-Newtonian roller-type viscous micropumps**. Structural and Multidisciplinary Optimization, Springer, v. 53, n. 3, p. 409–424, 2016. Cited 2 times in pages 95 and 96.

ZHANG, H.; JIA, X.; PAN, X.; JIANG, B.; ZHENG, Q. **Interaction between rotor and annular seals: interlaced and straight-through labyrinth seals**. Journal of Propulsion and Power, American Institute of Aeronautics and Astronautics, v. 32, n. 6, p. 1483–1493, 2016. Cited in page 65.

ZHANG, J.; GELLMAN, B.; KOERT, A.; DASSE, K. A.; GILBERT, R. J.; GRIFFITH, B. P.; WU, Z. J. **Computational and experimental evaluation of the fluid dynamics and hemocompatibility of the CentriMag blood pump**. Artificial organs, Wiley Online Library, v. 30, n. 3, p. 168–177, 2006. Cited in page 64.

ZHANG, J.; KOERT, A.; GELLMAN, B.; GEMPP, T. M.; DASSE, K. A.; GILBERT, R. J.; GRIFFITH, B. P.; WU, Z. J. **Optimization of a miniature maglev ventricular assist device for pediatric circulatory support**. Asaio Journal, LWW, v. 53, n. 1, p. 23–31, 2007. Cited in page 64.

ZHANG, T.; TASKIN, M. E.; FANG, H.-B.; PAMPORI, A.; JARVIK, R.; GRIFFITH, B. P.; WU, Z. J. **Study of flow-induced hemolysis using novel Couette-type blood-shearing devices**. Artificial organs, Wiley Online Library, v. 35, n. 12, p. 1180–1186, 2011. Cited in page 131.

ZHANG, X.; WRAY, T.; AGARWAL, R. K. **Application of a New Simple Rotation and Curvature Correction to the Wray-Agarwal Turbulence Model**. *In*: *46th AIAA Fluid Dynamics Conference*. [*S.l.: s.n.*], 2016. p. 3475. Cited in page 104.

ZHOU, S.; LI, Q. **A variationals level set method for the topology optimization of steady-state Navier-Stokes flow**. Journal of Computational Physics, Elsevier, v. 227, n. 24, p. 10178–10195, 2008. Cited in page 82.

ZHU, B.; ZHANG, X.; FATIKOW, S. **A multi-objective method of hinge-free compliant mechanism optimization**. Structural and Multidisciplinary Optimization, v. 49, n. 3, p. 431–440, Mar 2014. ISSN 1615-1488. Available at: https://doi.org/10.1007/s00158-013-1003-9. Cited in page 156.

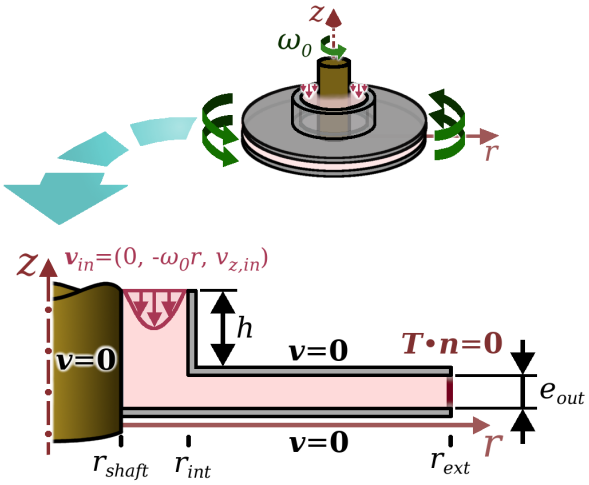
ZHU, B.; ZHANG, X.; FATIKOW, S. **Structural topology and shape optimization using a level set method with distance-suppression scheme**. Computer Methods in Applied Mechanics and Engineering, v. 283, n. Supplement C, p. 1214–1239, 2015. ISSN 0045-7825. Available at: http://www.sciencedirect.com/science/article/pii/S0045782514002874. Cited in page 156.

APPENDIX A – VERIFICATION OF THE SIMULATION IMPLEMENTED IN FEniCS

A simulation has been performed in order to check the finite element implementation for laminar flow in FEniCS with another software (OpenFOAM®). Particularly, the following verification makes use of the *FEniCS TopOpt Foam* library (ALONSO *et al.*, 2021) in order to easily set up the OpenFOAM® simulation from the setup performed in FEniCS.

The simulations are performed in the computational domain shown in Fig. A.1, where r_{shaft} = 2.6 mm, r_{int} = 5 mm, e_{out} = 1.196 mm, h = 3.152 mm, and r_{ext} = 15 mm. The finite element mesh is the same considered in Fig. 5.45.

Figure A.1 – Computational domain for a vertical inlet Tesla pump with two disks.

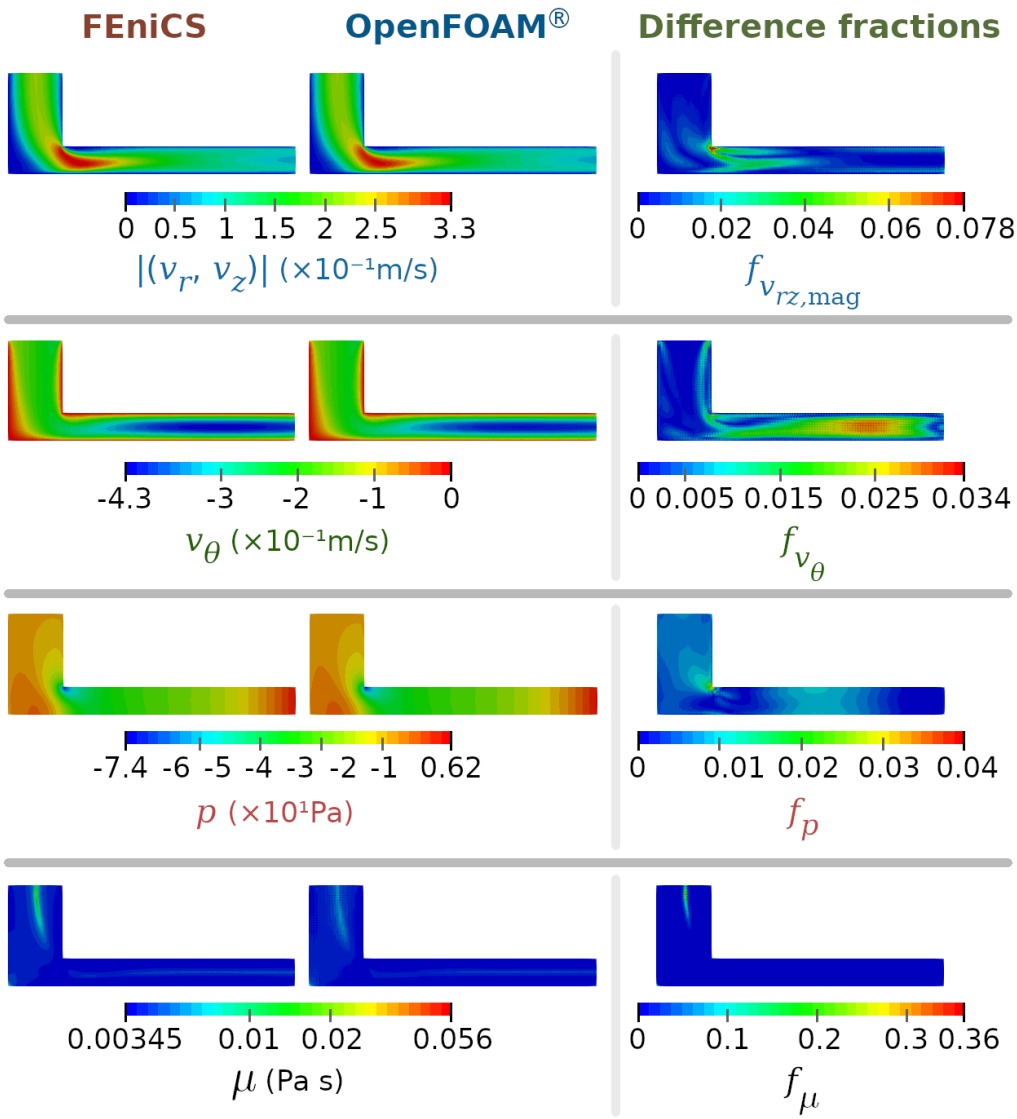


Source: Author.

In this verification, the fluid is considered as blood, for 500 rpm and 0.5 L/min. The FEniCS implementation is considered for Taylor-Hood elements. The boundary conditions shown in Fig. A.1 are considered in OpenFOAM® according to Fig. 3.8, and the mesh is considered in OpenFOAM® according to Fig. 3.6, being generated from transforming the 2D mesh into a *wedge* format. The fluid flow problem is solved in OpenFOAM® from the SIMPLE algorithm (PATANKAR, 1980; OPENFOAM WIKI, 2014) for a rotating reference frame (Single Rotating Frame, SRF) ("`SRFSimpleFoam`" solver). The fluid flow model for blood (Carreau-Yasuda) is referred in OpenFOAM® as "`BirdCarreau`", requiring setting the values of model coefficients. Particularly, the OpenFOAM® simulation is set to use a vector-coupled solver (i.e., a matrix solver) for

the velocity field, instead of the default segregated solver, because the vector-coupled solver is said to be able to improve stability (WOLF DYNAMICS, 2020), and also because it led to faster convergence in simulations performed by the author of this work. The simulation results are shown in Fig. A.2, where the simulation results from OpenFOAM® have already been projected to FEniCS variables, as described in Section 3.3.

Figure A.2 – Comparison of simulation results for the vertical inlet Tesla pump with two disks.



Source: Author.

The first column in Fig. A.2 shows the results of the simulation performed in FEniCS for the radial-axial velocity ((v_r, v_z)), the relative tangential velocity (v_θ), the pressure (p) and the non-Newtonian viscosity (μ). The second column shows the corresponding simulation results achieved in OpenFOAM® , where the Non-Newtonian

viscosity of the OpenFOAM® simulation is computed by using FEniCS from the velocity and pressure computed by OpenFOAM® . As can be seen, the simulation results from FEniCS are consistent with the simulation results from OpenFOAM® . In order to get a better insight of the difference between both results, the relative differences (*difference fractions*) are plotted in the third column of Fig. A.2. The relative differences between FEniCS and OpenFOAM® are computed as:

$$f_{v_{rz,\mathrm{mag}}} = \frac{\|\boldsymbol{v}_{rz,\text{FEniCS}} - \boldsymbol{v}_{rz,\text{OpenFOAM®}}\|}{\max(\|\boldsymbol{v}_{rz,\text{OpenFOAM®}}\|) - \min(\|\boldsymbol{v}_{rz,\text{OpenFOAM®}}\|)} \tag{A.1}$$

$$f_{v_\theta} = \frac{|v_{\theta,\text{FEniCS}} - v_{\theta,\text{OpenFOAM®}}|}{\max(v_{\theta,\text{OpenFOAM®}}) - \min(v_{\theta,\text{OpenFOAM®}})} \tag{A.2}$$

$$f_p = \frac{|p_{\text{FEniCS}} - p_{\text{OpenFOAM®}}|}{\max(p_{\text{OpenFOAM®}}) - \min(p_{\text{OpenFOAM®}})} \tag{A.3}$$

$$f_\mu = \frac{|\mu_{\text{FEniCS}} - \mu_{\text{OpenFOAM®}}|}{\mu_0 - \mu_{\inf}} \tag{A.4}$$

where $v_{rz,\mathrm{mag}} = \|\boldsymbol{v}_{rz}\| = \|(v_r, v_z)\| = \sqrt{v_r^2 + v_z^2}$.

As can be seen in Fig. A.2, the highest relative difference is less than 8%, which confirms the fact that both simulations are consistent. Among the factors that may cause the small observed difference, there are the tolerances used in the OpenFOAM® simulation, which may be further reduced if deemed necessary. There is also the fact that the same discretization has been used in both simulations, because FEniCS is using a quadratic interpolation for the velocity and a linear interpolation for the pressure (Taylor-Hood elements), and OpenFOAM® is using an element-wise interpolation for both the velocity and the pressure. This difference in interpolation degrees for the velocity is most probably the cause of the differences observed in the non-Newtonian viscosity and near the edge of the bend in the computational domain (due to higher velocity gradients). Some other factors that may cause differences are the different simulation methods (finite elements and finite volumes), the different boundary conditions and discretization schemes for the differential operators.

APPENDIX B – MESH SMOOTHING BY CONTOUR FILTERING

The mesh smoothing technique by contour filtering consists of changing the coordinates of the vertices of the contour of the optimized topology by the average of the coordinates of the vertices around each vertex. This is similar to a topology optimization filter/projection scheme (Section 2.5.7), but applied to the coordinates of the vertices instead of the values of the design variable (α). It is extended from the scheme implemented by Sá (2019), by considering the presence of generic contours and a different filtering scheme. If the interpolation of the design variable is not linear, it needs to be converted to a linear interpolation in order to apply the technique described in this section, because of the assumption that every node with a design variable value corresponds to a vertex of the mesh. After the closed contours of the optimized topology have been determined in the mesh, the averaging is performed by taking into account the neighbor vertices that are in the same closed contour, in the form of a linear averaging:

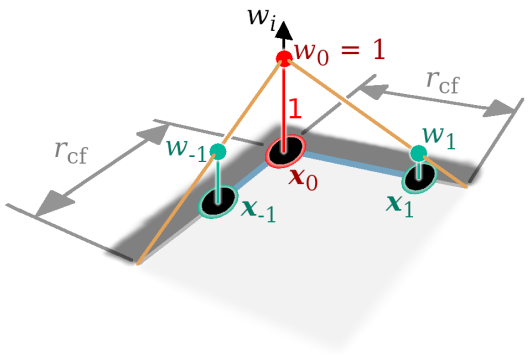
$$\begin{aligned} \boldsymbol{s}_{0,\mathrm{new}} &= \frac{\sum_{i=-n_{\mathrm{cf}}}^{n_{\mathrm{cf}}} w_{\mathrm{cf},i}\boldsymbol{s}_i}{\sum_{i=-n_{\mathrm{cf}}}^{n_{\mathrm{cf}}} w_{\mathrm{cf},i}} \\ w_{\mathrm{cf},i} &= \frac{r_{\mathrm{cf}} - \|\boldsymbol{s}_0 - \boldsymbol{s}_i\|}{r_{\mathrm{cf}}}, i \in \mathbb{Z} \end{aligned} \tag{B.1}$$

where $w_{\mathrm{cf},i}$ is the *smoothing* weight of each vertex (cf stands for contour filtering), $\boldsymbol{s}_0$ are the coordinates of the vertex, $\boldsymbol{s}_{0,\mathrm{new}}$ are the coordinates of the vertex after applying the linear averaging, and n_{cf} is the number of vertices that are considered in the smoothing around the vertex of the contour (one can use, for example, $n_{\mathrm{cf}} = 1$). The indices i are given in relation to the current vertex index ($i = 0$) in an ordered closed contour: previous vertex indices in the closed contour are given by $i < 0$, and next vertex indices in the closed contour are given by $i > 0$. The variable r_{cf} is the averaging radius of contour filtering, which is shown in Fig. B.1 and is given by (for a vertex "0"):

$$r_{\mathrm{cf}} = \max\left[\|\boldsymbol{s} - \boldsymbol{s}_{-n_{\mathrm{cf}}}\|, \|\boldsymbol{s} - \boldsymbol{s}_{-n_{\mathrm{cf}}+1}\|, ..., \|\boldsymbol{s} - \boldsymbol{s}_{n_{\mathrm{cf}}-1}\|, \|\boldsymbol{s} - \boldsymbol{s}_{n_{\mathrm{cf}}}\|\right] + d_{\mathrm{adjust}} \tag{B.2}$$

where d_{adjust} is an adjustment distance, that may be adjusted according to the case. One may consider, for example, $d_{\mathrm{adjust}} = \frac{1}{8}\max\left[d_{\mathrm{element}}\right]$, where d_{element} is the maximum size of the elements of the mesh (maximum distance between two vertices of each element).

Figure B.1 – Representation of the linear averaging around a vertex "0" on the closed contour, considering $n_{\mathrm{cf}} = 1$.



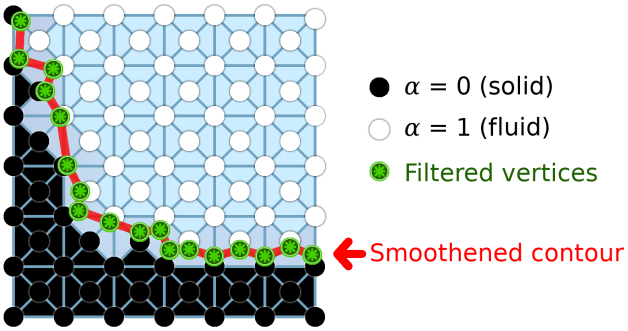
Source: Author.

Note that eq. (B.1) may also be used with other types of interpolation, such as a quadratic interpolation ($w_{\mathrm{cf},i} = \left(\frac{r_{\mathrm{cf}} - \|\boldsymbol{s} - \boldsymbol{s}_i\|}{r_{\mathrm{cf}}}\right)^2$). The mesh smoothing technique by contour filtering is detailed in Algorithm B.1 and illustrated in Fig. B.2. Note that the first steps of the algorithm are the same as in the thresholding technique (Algorithm 2.1).

Algorithm B.1 Pseudocode of mesh smoothing by contour filtering.

1: **Input parameters:** Mesh, optimized topology (i.e., the optimized α), the threshold limit ($\alpha_{\mathrm{th,lim}}$), n_{cf} and d_{adjust}.
2: **Result:** Smoothened mesh obtained by contour filtering.
3: **1** Apply thresholding in the design variable values (eq. (2.159)).
4: **2** Cut the mesh in order to remove the solid material ($\alpha = 0$) from the computational domain (in FEniCS, this is done with the functions `SubDomain` and `SubMesh`).
5: **3** Identify the boundary vertices of the *cut mesh*.
6: **4** Go through all these boundary vertices and create lists of closed contours, marking **if** each contour is to be subtracted or added to the final domain.
7: **5** Apply eq. (B.1) to each vertex of the closed contours, creating the new vertices in new lists of closed contours.
8: **6** Generate the mesh from the new lists of closed contours (in FEniCS, this can be done by creating `Polygon`'s (from the mshr module) for each closed contour and summing/subtracting them (CSG (Constructive Solid Geometry) operations), and then generating a non-structured mesh with a given mesh discretization/resolution (`generate_mesh`). Note that, for mshr, the closed contours have to be given in the counterclockwise order.)

Figure B.2 – Illustration of an example of mesh smoothing by contour filtering (for a nodal design variable).



Source: Author.

It can be noticed that the contour filtering technique needs less parameters to adjust (two: n_{cf} and d_{adjust}), whereas the generation of contours technique requires the adjustment of more parameters (four: $\gamma_{\mathrm{ic,int,min}}$, $\gamma_{\mathrm{ic,int,max}}$, $\gamma_{\mathrm{ec,int,min}}$ and $\gamma_{\mathrm{ec,int,max}}$). This may mean that the contour filtering technique is easier to use. Also, the contour filtering technique changes the coordinates of all contour vertices, which may be interesting depending on the optimized topology, whereas the generation of contours technique changes only the corner vertices' coordinates.

APPENDIX C – COMPUTATION OF FLUID FLOW VELOCITY PROFILES

Under fully developed flow in a circular pipe, the fluid flow velocity profile is different when under laminar and turbulent flows. The computation of these velocity profiles is described as follows.

C.1 LAMINAR VELOCITY PROFILE

Under fully developed laminar flow in circular pipes, the velocity profile is parabolic. The parabolic inlet velocity profile may be computed as

$$v_{in} = v_{in,max}\left[1 - \left(\frac{x - x_{\text{middle}}}{x_1}\right)^2\right] \tag{C.1}$$

where x is the coordinate on the line in which the parabola is located; $x_{\text{middle}} = \frac{x_{max}+x_{min}}{2}$; $x_1 = \frac{x_{max}-x_{min}}{2}$; and x_{max} and x_{min} are the boundaries of the interval in which the parabola is defined ($v_{in}(x_{max}) = v_{in}(x_{min}) = 0$). The maximum value of the inlet parabola ($v_{in,max}$) is obtained from the flow rate Q, which means that the following equation should be computed:

$$\begin{aligned} Q &= \int_{\Gamma_{\Pi_{\text{in}}}} v_{in} d\Gamma_{\Pi_{\text{in}}} \\ \implies v_{in,max} &= \frac{Q}{\int_{\Gamma_{\Pi_{\text{in}}}}\left[1 - \left(\frac{x-x_{\text{middle}}}{x_1}\right)^2\right] d\Gamma_{\Pi_{\text{in}}}} \end{aligned} \tag{C.2}$$

For 2D flow, $d\Gamma_{\Pi_{\text{in}}} = d\Gamma_{\text{in}}$, while for 2D swirl flow, $d\Gamma_{\Pi_{\text{in}}} = 2\pi r d\Gamma_{\text{in}}$. The value of $d\Gamma_{\text{in}}$ depends on the line in which this boundary condition is applied: when the line is horizontal (vertical inlet velocity profile), $d\Gamma_{\text{in}} = dx$ (2D) or $d\Gamma_{\text{in}} = dr$ (2D swirl); when the line is vertical (horizontal inlet velocity profile), $d\Gamma_{\text{in}} = dy$ (2D) or $d\Gamma_{\text{in}} = dz$ (2D swirl). The integration is then performed from x_{min} to x_{max}, and may be analytical, or numerical (by using numerical integration, such as the trapezoidal rule).

C.2 TURBULENT VELOCITY PROFILE

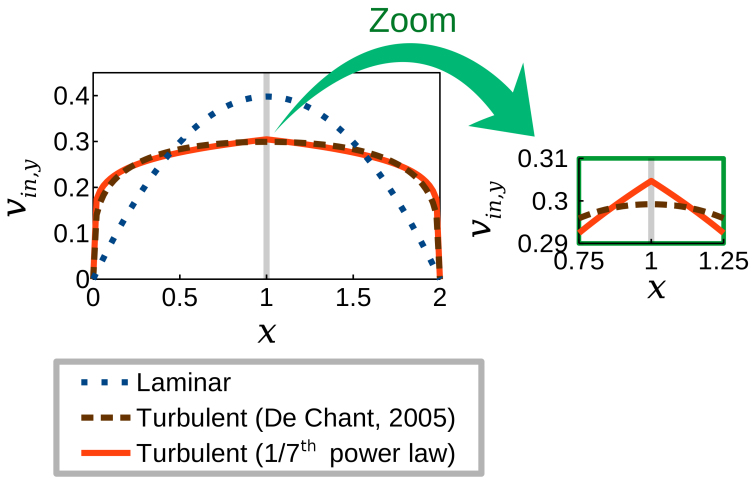
Under fully developed turbulent flow in circular pipes, the velocity profile is not parabolic (see Fig. C.1). Particularly, in this work, the turbulent velocity profiles are implemented according to De Chant (2005), in which the velocity profile is analytically

deduced from a simplified fluid flow model. The resulting difference of this turbulent velocity profile with respect to the 1/7$^{\text{th}}$ power law (MUNSON *et al.*, 2009) is that the derivative is zero in the middle of the velocity profile, which can be seen in the highly enlarged view of the difference in derivatives in Fig. C.1. It can be pointed out that this zero derivative in the middle of the turbulent velocity profile is expected for turbulent fluid flows (MUNSON *et al.*, 2009). For reference, a turbulent velocity profile in the y direction, between a minimum ($x_{\min}$) and a maximum ($x_{\max}$) coordinate becomes (DE CHANT, 2005):

$$v_{in,y} = v_{in,y,\max}\sqrt{\sin\left(\frac{\pi}{2}\sqrt{1-\left|\frac{x-x_{\text{middle}}}{x_1}\right|}\right)} \tag{C.3}$$

where $x_{\text{middle}} = \frac{x_{\max}+x_{\min}}{2}$ is the coordinate of the middle of the velocity profile, $x_1 = \frac{x_{\max}-x_{\min}}{2}$ is an auxiliary coordinate, and $v_{in,y,\max}$ is the maximum velocity of the turbulent velocity profile (computed from numerical integration for a given flow rate). The turbulent velocity profile may be computed similarly as in Section C.1.

Figure C.1 – Laminar and turbulent velocity profiles for the same *2D flow rate* (area below the curves).



Source: Author (ALONSO *et al.*, 2021).

APPENDIX D – RELATIVE REFERENCE FRAME IN THE 2D SWIRL FLOW MODEL

In order to consider a relative reference frame for the solution of the equations, it is necessary to consider the formula of the reference frame change, which is given as follows, by also considering the material derivative, and $\boldsymbol{v}$ as the relative velocity (velocity with respect to the moving reference frame):

- For a scalar variable "a":

$$\left.\frac{Da}{Dt}\right|_{\text{abs}} = \left.\frac{Da}{Dt}\right|_{\text{rel}} = \frac{\partial a}{\partial t} + (\boldsymbol{v}\bullet\nabla)a \tag{D.1}$$

- For a vector variable "$\boldsymbol{a}$":

$$\left.\frac{D\boldsymbol{a}}{Dt}\right|_{\text{abs}} = \left.\frac{D\boldsymbol{a}}{Dt}\right|_{\text{rel}} + \boldsymbol{\omega}\wedge\boldsymbol{a} = \frac{\partial \boldsymbol{a}}{\partial t} + (\boldsymbol{v}\bullet\nabla)\boldsymbol{a} + \boldsymbol{\omega}\wedge\boldsymbol{a} \tag{D.2}$$

Eq. (D.2) can be deduced by considering that $\boldsymbol{a} \xrightarrow{\text{Indicial notation}} a_i\boldsymbol{e}_i$, where $\boldsymbol{e}_i$ is a unit vector from the coordinate system of the relative reference frame. Therefore, the derivative becomes $\frac{D\boldsymbol{a}}{Dt} \xrightarrow{\text{Indicial notation}} \frac{Da_i}{Dt}\boldsymbol{e}_i + a_i\frac{D\boldsymbol{e}_i}{Dt}$, where $\frac{D\boldsymbol{e}_i}{Dt}$ is given as $\boldsymbol{\omega}\wedge\boldsymbol{e}_i$. From eq. (D.2) applied to $\boldsymbol{a} = \boldsymbol{v}_{\text{abs}}$ (from eq. (2.4)), eq. (2.5) is achieved. In eq. (D.1), for a scalar variable, when considering the differential operators for cylindrical coordinates (LAI *et al.*, 2009),

$$(\boldsymbol{v}\bullet\nabla)a = \left(v_r\frac{\partial a}{\partial r},\ v_\theta\frac{1}{r}\frac{\partial a}{\partial \theta},\ v_z\frac{\partial a}{\partial z}\right) \tag{D.3}$$

In the 2D swirl flow model, when assuming axisymmetry ($\frac{\partial(\,)}{\partial\theta} = 0$), eq. (D.3) will not depend on v_θ anymore. Therefore, for the 2D swirl flow model, eq. (D.3) is independent of the reference frame (i.e., $\boldsymbol{v}_{\text{abs}}$ may be used instead of $\boldsymbol{v}$). If $\frac{D\boldsymbol{v}_{\text{abs}}}{Dt}$ is computed by "simply" substituting eq. (2.4), instead of considering eq. (D.2) (i.e., $\frac{D\boldsymbol{v}_{\text{abs}}}{Dt} = \frac{\partial \boldsymbol{v}_{\text{abs}}}{\partial t} + (\boldsymbol{v}_{\text{abs}}\bullet\nabla)\boldsymbol{v}_{\text{abs}}$), the following equation is achieved in cylindrical coordinates

$$\frac{D\boldsymbol{v}_{\text{abs}}}{Dt} = \frac{D\boldsymbol{v}}{Dt} + \frac{D\boldsymbol{v}_{\text{ref}}}{Dt} + \frac{\partial\boldsymbol{\omega}}{\partial t}\wedge\boldsymbol{r} + 2\boldsymbol{\omega}\wedge\boldsymbol{v} + \boldsymbol{\omega}\wedge(\boldsymbol{\omega}\wedge\boldsymbol{r}) + (\boldsymbol{\omega}\bullet\boldsymbol{e}_z)\frac{\partial\boldsymbol{v}}{\partial\theta} \tag{D.4}$$

By reordering and using the same notation from eq. (2.5),

$$\boldsymbol{a}_{\text{abs}} = \boldsymbol{a}_{\text{ref}} + \boldsymbol{a} + 2\boldsymbol{\omega}\wedge\boldsymbol{v} + \boldsymbol{\omega}\wedge(\boldsymbol{\omega}\wedge\boldsymbol{r}) + \dot{\boldsymbol{\omega}}\wedge\boldsymbol{r} + (\boldsymbol{\omega}\bullet\boldsymbol{e}_z)\frac{\partial\boldsymbol{v}}{\partial\theta} \tag{D.5}$$

Therefore, only if the 2D swirl flow model is assumed, eqs. (2.5) and (D.5) are equivalent (from the axisymmetry assumption ($\frac{\partial(\,)}{\partial\theta} = 0$)). This shows that, in the 2D swirl flow model, the reference frame transformation reduces itself to simply a conversion between absolute and relative velocities.

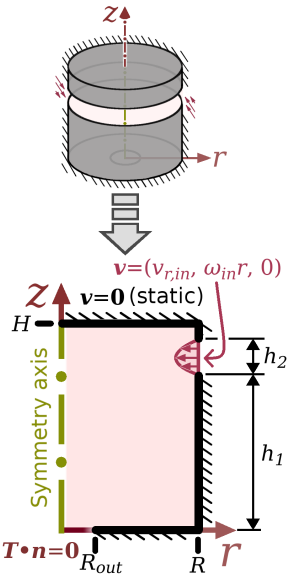
APPENDIX E – OTHER NUMERICAL RESULTS FOR THROMBOSIS

In order to show the effect of considering blood damage in topology optimization, two more numerical examples are presented as follows (ALONSO; SILVA, 2022a). An observation is that, with respect to Section 5.1.5, in the post-processing, the Savitzky-Golay filter is repeated 2 times only in the case of the bypass numerical example; the other case, including the Tesla pump case from Section 5.1.5, does not consider repetition.

E.1 HYDROCYCLONE-TYPE DEVICE

The first example considers the design of a hydrocyclone-type device. This type of device is different from a real hydrocyclone device, because it models a flow with a single phase (instead of considering two phases) entering with a rotation (ω_{in}) from a single inlet towards a single outlet. The design domain considered for the 2D swirl flow model is selected as shown in Fig. E.1. The solid material distribution is considered to be optimized for the static walls ($\omega_0 = 0$ rad/s).

Figure E.1 – Design domain considered for the hydrocyclone-type device.

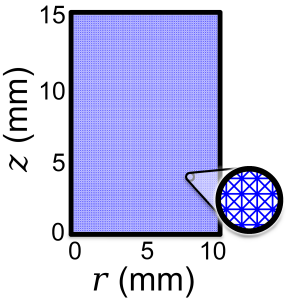


Source: Author (ALONSO; SILVA, 2022a).

The mesh is composed of 19,401 nodes and 38,400 elements (see Fig. E.2). The input parameters, geometric dimensions and material model parameters being

considered in the design are shown in Table E.1. The specified fluid volume fraction (f) is set as 30%.

Figure E.2 – Mesh considered in the design of the hydrocyclone-type device.



Source: Author (ALONSO; SILVA, 2022a).

Table E.1 – Parameters considered for the topology optimization of the hydrocyclone-type device.

Input parameters	
Inlet flow rate (Q)	0.05 L/min
Wall rotation (n_0)	0 rpm
Inlet rotation (n_{in})	20 rpm
Inlet velocity profile	Parabolic
Dimensions	
H	15 mm
R	10 mm
h_1	11 mm
h_2	3 mm
Material model parameters*	
$\kappa_{\max}$ ($\times 10^7 \mu_\infty$ (kg/(m^3 s)))	8.0
q	1.0
$\kappa_{PAS,\max}$ (s^{-1})	10^3

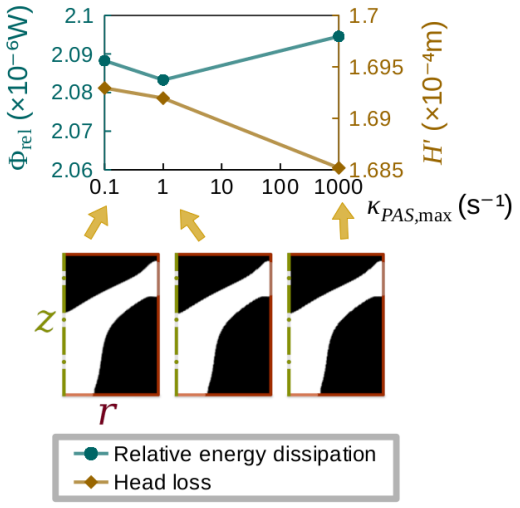
* The optimization considers a Helmholtz pseudo-density filter (LAZAROV; SIGMUND, 2010) in order to better stabilize the discrete optimized topologies, with a filter length parameter of 0.0625 mm.

In this numerical example, some of the factors that influence the topology optimization for hemolysis and thrombosis are illustrated separately. In the optimized topologies, the maximum local Reynolds number is 177, which means that the flow is laminar. Fig. E.3 shows the effect of the additional penalization from the thrombosis model ($\kappa_{PAS,\max}$), by considering $w_{PAS} = 0.5$. The corresponding contours are shown enlarged in Fig. E.4. The optimized topologies mainly show slight differences near the outlet, and near the solid material that is near the rotation axis. Particularly, the optimized topology for $\kappa_{PAS,\max} = 10^3$ s^{-1} is slightly more inclined to the right and is straighter near the outlet, with respect to the optimized topology for $\kappa_{PAS,\max} = 0.1$ s^{-1}. The fact that it is

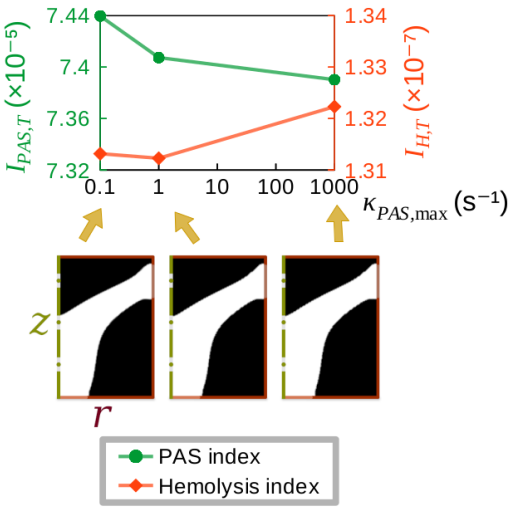
straighter near the outlet (with respect to the optimized topology for $\kappa_{PAS,\max} = 0.1$ s^{-1}) seems contribute to further reducing the low velocity values that appear near the wall that is next to the outlet (thus helping to reduce thrombosis), and the small differences with respect to the optimized topology for $\kappa_{PAS,\max} = 1$ s^{-1} ended up leading to a slight increase in the velocity gradients near the "start" of the straighter part of the outlet, thus helping to slightly increase hemolysis alongside the small curvature changes in the overall topology. These small differences seem to lead to a slight increase in velocity gradients, worsening the relative energy dissipation, while the head loss is reduced from a straighter fluid flow velocity exiting the fluid flow device. From Fig. E.3, it can be noticed that higher $\kappa_{PAS,\max}$ values lead to worse relative energy dissipation (Fig. E.3a), better head loss (Fig. E.3a) and worse hemolysis (Fig. E.3b). However, there is some improvement in thrombosis (Fig. E.3b).

Figure E.3 – Topology optimization results for the hydrocyclone-type device for $w_{PAS} = 0.5$, considering different $\kappa_{PAS,\max}$ values.

(a) Relative energy dissipation (Φ_{rel}) and head loss (H').

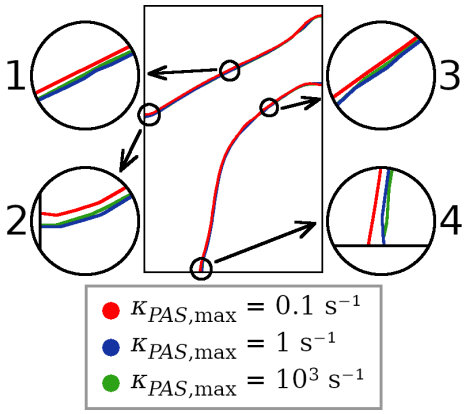


(b) PAS index (I_{PAS}) and hemolysis index (I_H).



Source: Author (ALONSO; SILVA, 2022a).

Figure E.4 – Contours of the optimized topologies from Fig. E.3.



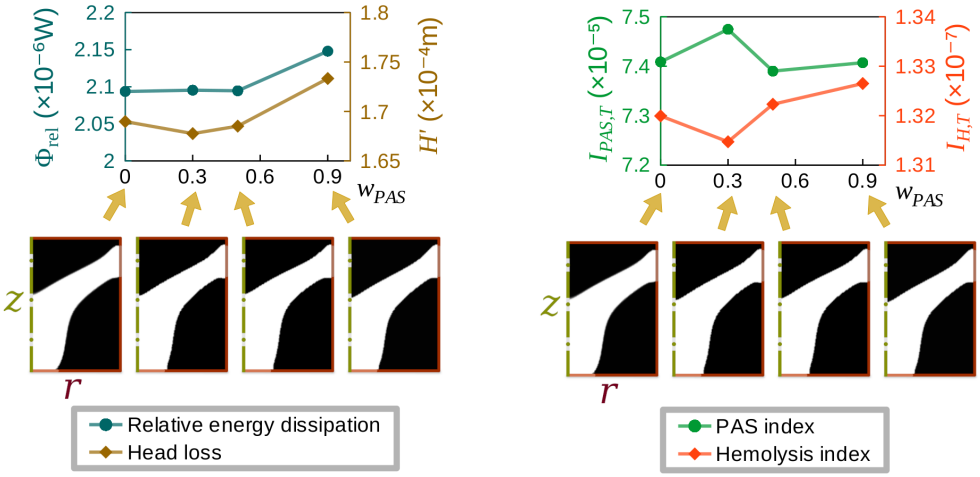
Source: Author (ALONSO; SILVA, 2022a).

By considering $\kappa_{PAS,\max} = 10^3$ s^{-1}, which showed the best PAS index value in Fig. E.3b, the effect of the thrombosis weight (w_{PAS}) is evaluated. The results are shown in Fig. E.5 and the corresponding contours are shown enlarged in Fig. E.6. In Fig. E.5b, it can be noticed that there may be induction of local minima depending on the w_{PAS} value, such as for $w_{PAS} = 0.3$, which improved hemolysis while worsening thrombosis. In Fig. E.5b, it can be noticed that "overprioritizing" thrombosis, such as in $w_{PAS} = 0.9$, may lead to significantly worse relative energy dissipation and head loss. In particular, the main aspect of the optimized topology for $w_{PAS} = 0.9$ is that it is more inclined to the right than the other optimized topologies, which means that the fluid flow path is slightly larger (due to the axisymmetric volume) than the other optimized topologies (more inclined to the left), leading to a higher energy dissipation. The hemolysis is also higher, which is possibly due to the upper solid material boundary (located lower than the other topologies).

Figure E.5 – Topology optimization results for the hydrocyclone-type device for different w_{PAS} values ($\kappa_{PAS,\max} = 10^3$ s^{-1}).

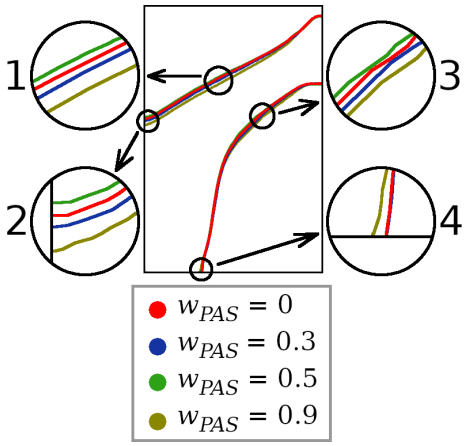
(a) Relative energy dissipation (Φ_{rel}) and head loss (H').

(b) PAS index ($I_{PAS,T}$) and hemolysis index ($I_{H,T}$).



Source: Author (ALONSO; SILVA, 2022a).

Figure E.6 – Contours of the optimized topologies from Fig. E.5.



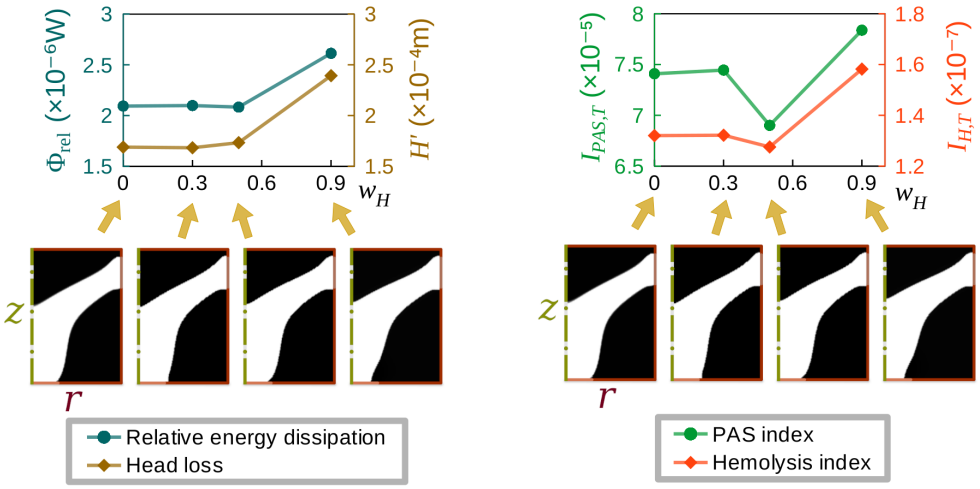
Source: Author (ALONSO; SILVA, 2022a).

The effect of the hemolysis weight (w_H) is shown in Fig. E.7. The effect is similar to the one shown for w_{PAS} (Fig. E.5) and the corresponding contours are shown enlarged in Fig. E.8. However, a better local minimum was induced when $w_H = 0.5$ (better hemolysis and thrombosis), and a worse local minimum was induced when $w_H = 0.9$ (worse hemolysis and thrombosis). As can be noticed, the optimized topology for $w_H = 0.9$ shows a more inclined path near the outlet, which reduces the fluid volume flowing near the outlet (remembering that the fluid volume is axisymmetric), possibly increasing the corresponding velocity gradients and, therefore, hemolysis and thrombosis.

Figure E.7 – Topology optimization results for the hydrocyclone-type device for different w_H values.

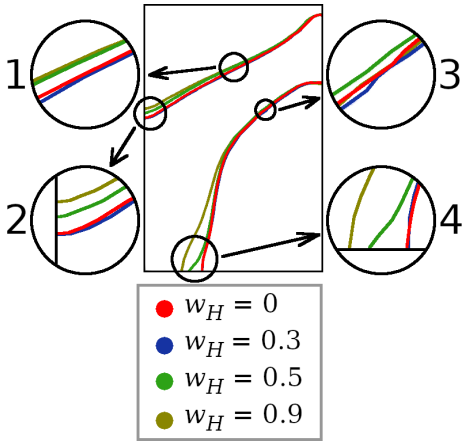
(a) Relative energy dissipation (Φ_{rel}) and head loss (H').

(b) PAS index ($I_{PAS,T}$) and hemolysis index ($I_{H,T}$).



Source: Author (ALONSO; SILVA, 2022a).

Figure E.8 – Contours of the optimized topologies from Fig. E.7.



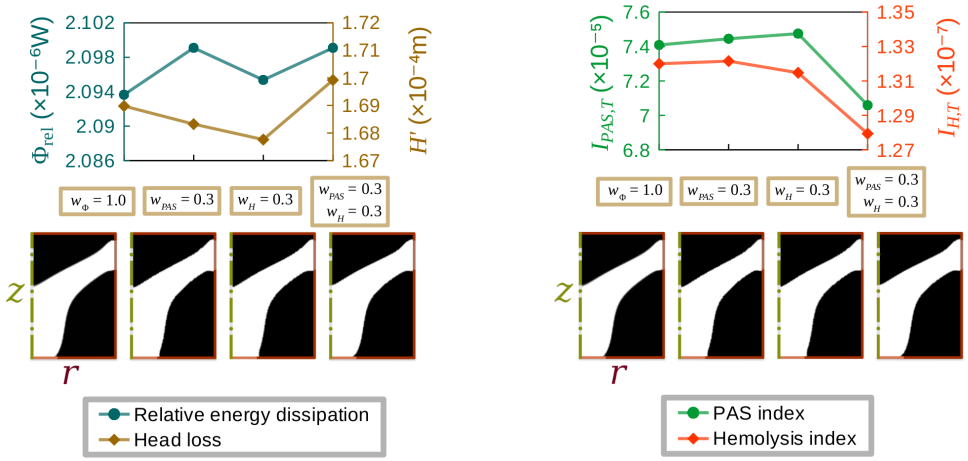
Source: Author (ALONSO; SILVA, 2022a).

An additional analysis is performed by combining hemolysis ($w_H = 0.3$) and thrombosis ($w_{PAS} = 0.3$) in the same multi-objective function. Figs. E.9 and E.10 show a comparison between the optimized topologies for $w_\Phi = 1$, $w_{PAS} = 0.3$, $w_H = 0.3$ and "$w_{PAS} = 0.3$ and $w_H = 0.3$". It can be seen that considering both hemolysis and thrombosis may lead to a better optimized topology for both quantities. In particular, the optimized topology for "$w_{PAS} = 0.3$ and $w_H = 0.3$" shows a curve near the outlet, which reduced thrombosis, and the upper part of the "channel" is located at a higher position.

Figure E.9 – Topology optimization results for the hydrocyclone-type device considering w_{PAS} and w_H.

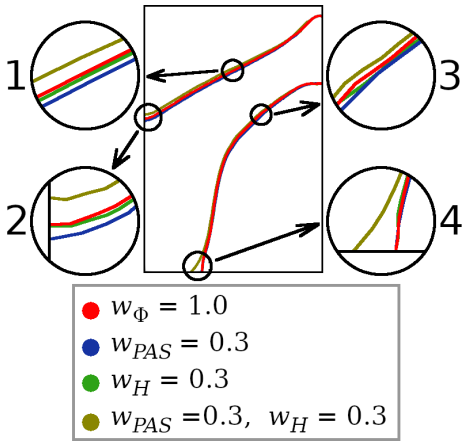
(a) Relative energy dissipation (Φ_{rel}) and head loss (H').

(b) PAS index ($I_{PAS,T}$) and hemolysis index ($I_{H,T}$).



Source: Author (ALONSO; SILVA, 2022a).

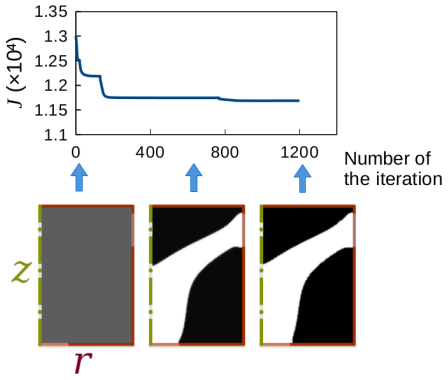
Figure E.10 – Contours of the optimized topologies from Fig. E.9.



Source: Author (ALONSO; SILVA, 2022a).

In the overall, the best result is the one for $w_H = 0.5$. Nonetheless, the result for $w_{PAS} = 0.5$ ($\kappa_{PAS,\max} = 10^3$ s^{-1}) is not far. The convergence curve for $w_{PAS} = 0.5$ ($\kappa_{PAS,\max} = 10^3$ s^{-1}) is shown in Fig. E.11.

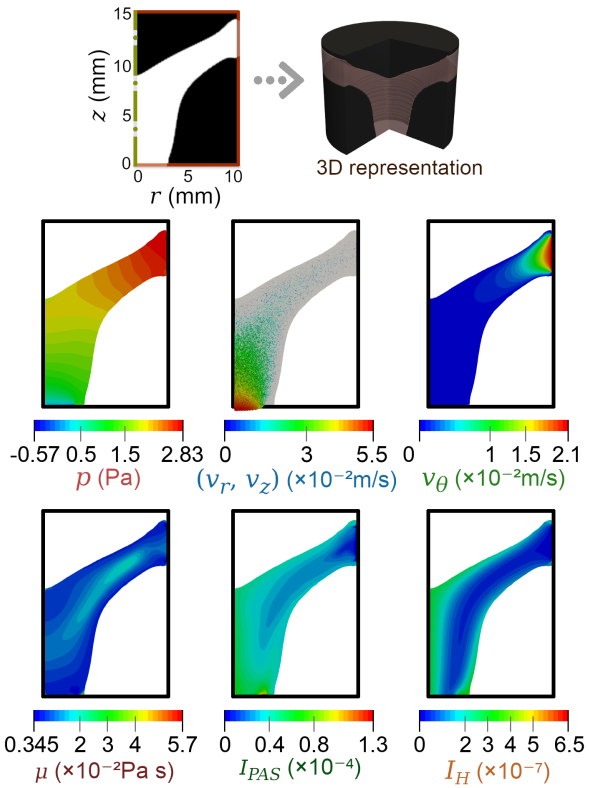
Figure E.11 – Convergence curve of the topology optimization of the hydrocyclone-type device ($w_{PAS} = 0.5$, $\kappa_{PAS,\max} = 10^3$ s^{-1}).



Source: Author (ALONSO; SILVA, 2022a).

The optimized topology for $w_{PAS} = 0.5$ ($\kappa_{PAS,\max} = 10^3$ s^{-1}) is simulated in Fig. E.12. As can be seen, the tangential velocity (v_θ) is dissipated/converted to radial-axial velocity (v_r, v_z) in the first part of the optimized topology from the inlet. The non-Newtonian effect can be observed mainly near the middle of the fluid flow cross-section. It can be noticed that the non-Newtonian viscosity $\mu(\dot{\gamma}_{\mathrm{m}})$ slightly rises next to the outlet due to the formation of a small stagnated zone. Moreover, the plots of local PAS index (I_{PAS}) and local hemolysis index (I_H) show similar behaviors in the sense that both quantities are small near the inlet and increase as the fluid flows through the device. However, it can be noticed that the local PAS index (I_{PAS}) is more “spread” towards the outlet. It can also be pointed out that the local PAS index (I_{PAS}) and local hemolysis index (I_H) plots can be viewed as maps of the potential blood damage that can happen to blood flow.

Figure E.12 – Optimized topology, pressure, velocity, dynamic viscosity, PAS index and hemolysis index for the optimized hydrocyclone-type device ($w_{PAS} = 0.5$, $\kappa_{PAS,\max} = 10^3$ s^{-1}).

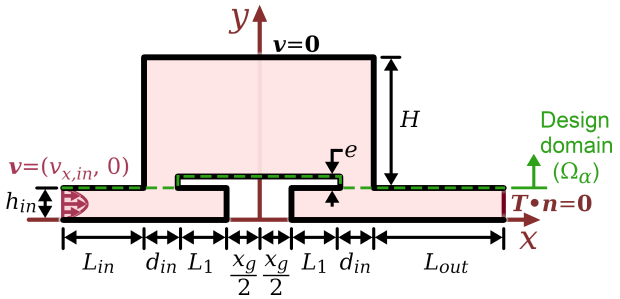


Source: Author (ALONSO; SILVA, 2022a).

E.2 BYPASS GRAFT

The second example is the design of a bypass graft, considered through a 2D model. A bypass graft is used to allow blood to bypass blocked coronary arteries, in order to restore the normal blood flow. The design of some bypass configurations has already been previously evaluated for shape optimization (ABRAHAM *et al.*, 2005) and topology optimization through the *level-set approach* (ZHANG; LIU, 2015), by considering an energy dissipation objective function. In this work, a similar bypass configuration is considered for topology optimization through the *pseudo-density approach*, while also considering hemolysis and thrombosis in the optimization process. The computational domain is shown in Fig. E.13, where the design domain does not include the inlet and outlet channels (which would represent the arteries). The configuration is non-rotating ($\omega = 0$ rad/s, $\omega_0 = 0$ rad/s).

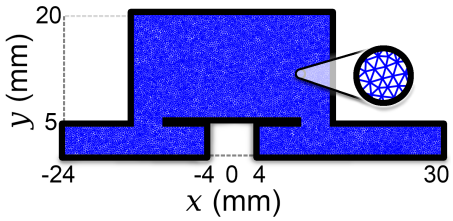
Figure E.13 – Design domain considered for the bypass graft.



Source: Author (ALONSO; SILVA, 2022a).

The mesh is unstructured, composed of 10,815 nodes and 20,888 elements (see Fig. E.14). The input parameters, dimensions of the computational domain, and material model parameters that are used are shown in Table E.2. The specified fluid volume fraction (f) is set as 35.3%.

Figure E.14 – Mesh considered in the design of the bypass graft.



Source: Author (ALONSO; SILVA, 2022a).

Table E.2 – Parameters considered for the topology optimization of the bypass graft.

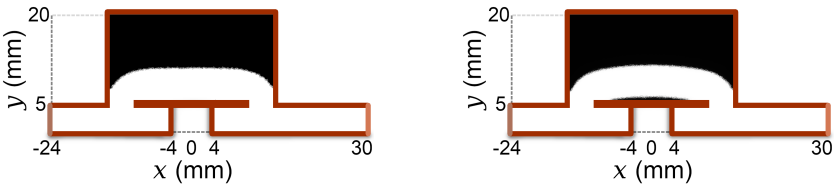
Input parameters	
Inlet flow rate (Q)	5.0 mL/min*
Inlet velocity profile	Parabolic
Dimensions	
H	20 mm
h_{in}	4 mm
r_i	30 mm
L_{in}	10 mm
L_{out}	16 mm
d_{in}	4 mm
L_1	6 mm
x_g	8 mm
e	1.5 mm
Material model parameters**	
κ_{max} ($\times 10^7 \mu_\infty$ (kg/(m^3 s)))	8.0
q	0.1
$\kappa_{PAS,\text{max}}$ (s^{-1})	10^3

* The flow rate is computed assuming that the width of the inlet (h_{in}) corresponds to an *inlet diameter* (in 3D).
** The optimization considers a Helmholtz pseudo-density filter (LAZAROV; SIGMUND, 2010) to better stabilize the discrete optimized topologies, with a filter length parameter of 0.315 mm.

The bypass configuration is considered at a low maximum Reynolds number (6.4), which corresponds to laminar flow. The topology optimization resulted in one optimized topology for $w_\Phi = 1$, while the optimized topology for $w_{PAS} = 0.9$ and the optimized topology for $w_H = 0.9$ resulted the same (Fig. E.15). The computed values in both topologies are shown in Table E.3. As can be noticed, the optimized topology for $w_{PAS} = 0.9$ (or $w_H = 0.9$) is better for hemolysis and thrombosis than the optimized topology for $w_\Phi = 1.0$ – i.e., the energy dissipation is slightly worse (0.9% higher), the thrombosis is slightly better (2.6% lower), the hemolysis is slightly better (1.8% lower), and the head loss is slightly worse (1.0% higher).

Figure E.15 – Optimized topologies for the bypass graft.

(a) For $w_\Phi = 1$. (b) For $w_H = 0.9$ or $w_{PAS} = 0.9$.



Source: Author (ALONSO; SILVA, 2022a).

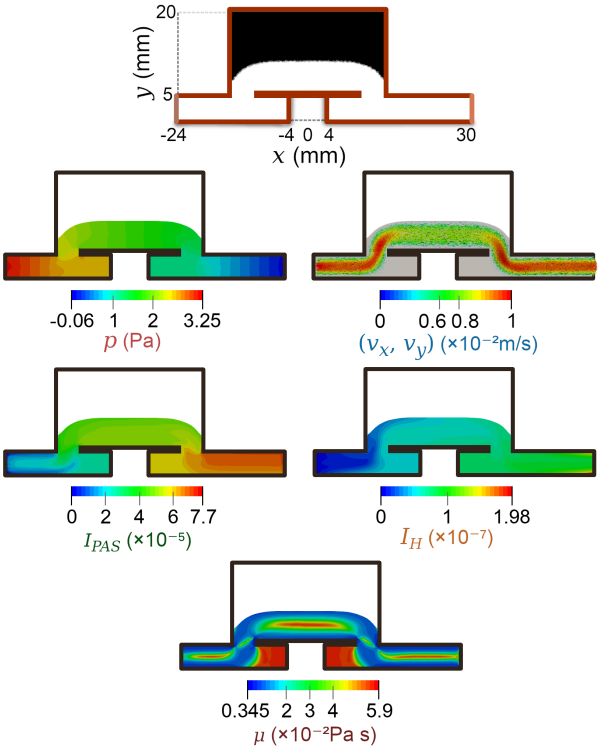
Table E.3 – Computed values in the optimized topologies for the bypass design.

Designs	Φ_{rel} ($\times 10^{-4}$ W/m)	$I_{PAS,T}$ ($\times 10^{-5}$ 1/m)	$I_{H,T}$ ($\times 10^{-8}$ 1/m)	H' ($\times 10^{-4}$ m)
$w_\Phi = 1$	1.13	7.17	9.89	3.12
$w_{PAS} = 0.9$ (or $w_H = 0.9$)	1.14	6.98	9.71	3.15

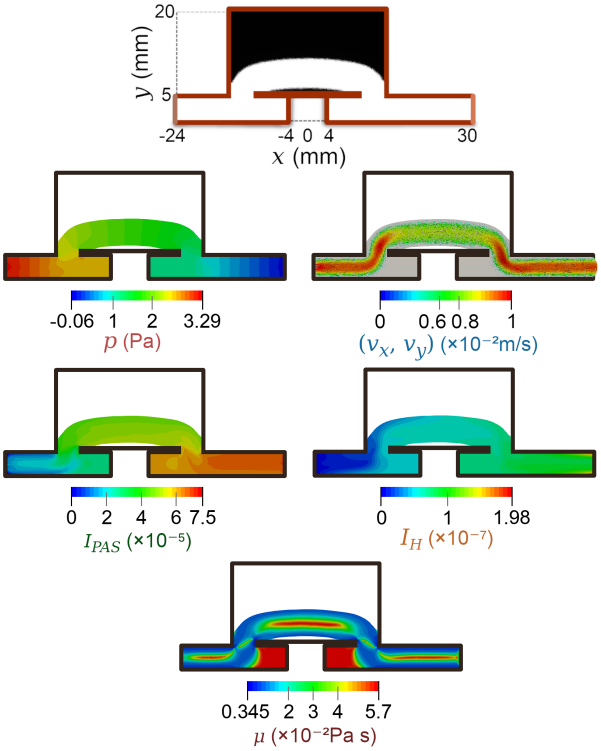
Both optimized topologies are simulated in Fig. E.16. As can be seen, there is not much difference in the fluid flow behavior in both cases, but the the slightly detached channel (Fig. E.16b) leads to a smaller change in flow direction, which, in turn, reduces velocity gradients and improves hemolysis and thrombosis. This, however, worsens the energy dissipation (and the head loss), because the flow has to undergo a slightly larger path, which dissipates slightly more energy. The dynamic viscosity plots show that the non-Newtonian behavior is more significant in the middle of the flow cross-section and also inside the *stagnated flow zones* (indicated by L_1 in Fig. E.13).

Figure E.16 – Optimized topology, pressure, velocity, PAS index, hemolysis index and dynamic viscosity for the optimized bypass grafts.

(a) For $w_\Phi = 1$.



(b) For $w_H = 0.9$ or $w_{PAS} = 0.9$.

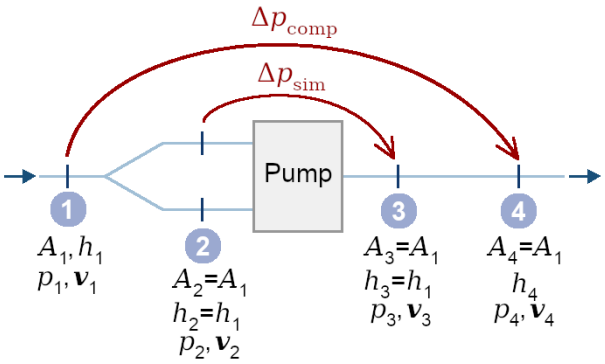


Source: Author (ALONSO; SILVA, 2022a).

APPENDIX F – ADJUSTMENT FOR COMPARING WITH THE EXPERIMENTAL RESULTS

The compensation of the simulated (static) pressure values mentioned in Section 3.5.1 is illustrated in Fig. F.1, and the considered effects are described as follows.

Figure F.1 – Schematic illustration of the compensation of the simulated (static) pressure for comparing with the experiments.



Source: Author.

The first effect consists on the fact that the variation of (static) pressure in the simulations (Δp_{sim}) is computed for two inlets. However, in the experiments, the pressure measurement probe (indicated as “1” in Fig. F.1) is placed before the Y-joint that splits the fluid flow to the aforementioned two inlets (indicated as “2” in Fig. F.1). In order to compensate the effect of the Y-joint (except for losses), two equations are considered: the conservation of volume (i.e., flow rate), and the energy equation for control volumes (MUNSON *et al.*, 2009) (assuming steady state regime, no losses, same heights, no heat transfer, parabolic velocity profiles, and constant pressure levels on each cross section). They are given as:

$$\overline{|\boldsymbol{v}_1|}A_1 = \overline{|\boldsymbol{v}_2|}A_2 + \overline{|\boldsymbol{v}_2|}A_2 \tag{F.1}$$

$$\int_{A_1}\left(\frac{p_1}{\rho}+\frac{|\boldsymbol{v}_1|^2}{2}+gh_1\right)\rho\boldsymbol{v}_1\bullet\boldsymbol{n}dA_1 = 2\int_{A_2}\left(\frac{p_2}{\rho}+\frac{|\boldsymbol{v}_2|^2}{2}+gh_2\right)\rho\boldsymbol{v}_2\bullet\boldsymbol{n}dA_2 \tag{F.2}$$

where $A_1 = \pi R_{\mathrm{tube}}^2$ is the internal area of the tube used in the experiments, R_{tube} is the internal radius of the tubes used in the experiments, g is the gravitational acceleration, $\boldsymbol{v}_1\bullet\boldsymbol{n} = |\boldsymbol{v}_1|$, $\boldsymbol{v}_2\bullet\boldsymbol{n} = |\boldsymbol{v}_2|$, the parabolic velocity profile is given from eq. (C.1) (by

considering $x = r$ (radius from the center of the tube), $x_{\text{middle}} = 0$, and $x_1 = R_{\text{tube}}$), and the remaining assumptions illustrated in Fig. F.1 are considered. Therefore,

$$p_2 - p_1 = \frac{3}{4}\rho\left(\frac{Q}{\pi R_{\text{tube}}^2}\right)^2 \tag{F.3}$$

where Q is the flow rate.

The second effect consists on the fact that the two pressure measurement probes from the experiments are slightly displaced in height. This can be compensated through the energy equation for control volumes (MUNSON *et al.*, 2009) (assuming steady state regime, different heights, no heat transfer, parabolic velocity profiles, and constant pressure levels on each cross section):

$$\int_{A_3}\left(\frac{p_3}{\rho} + \frac{|\boldsymbol{v}_3|^2}{2} + gh_3\right)\rho\boldsymbol{v}_3\bullet\boldsymbol{n}dA_3 = \int_{A_4}\left(\frac{p_4}{\rho} + \frac{|\boldsymbol{v}_4|^2}{2} + gh_4\right)\rho\boldsymbol{v}_4\bullet\boldsymbol{n}dA_4 \tag{F.4}$$

where $\overline{|\boldsymbol{v}_3|} = \overline{|\boldsymbol{v}_4|}$ (from the conservation of volume). Therefore,

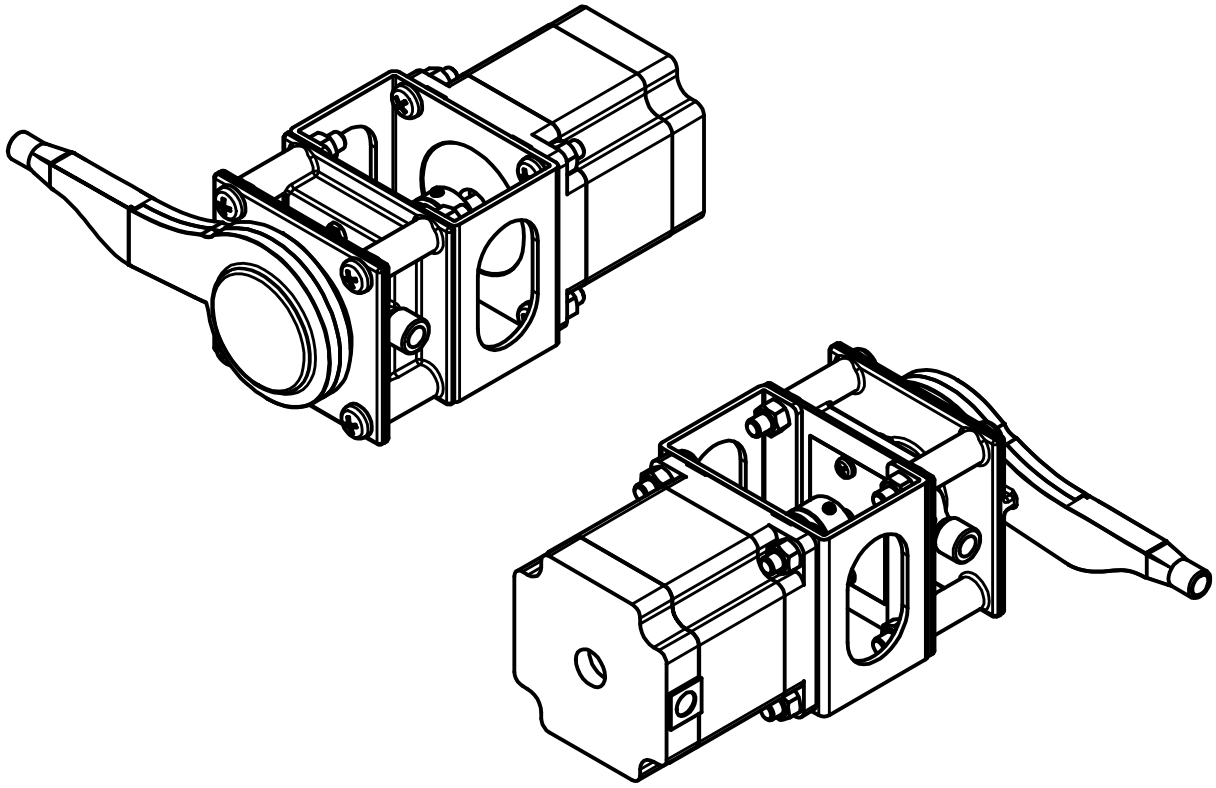
$$p_4 - p_3 = -\rho g(h_3 - h_4) \tag{F.5}$$

By considering $\Delta h_{\text{probes}} = h_3 - h_4$ (variation of height between the pressure measurement probes), $\Delta p_{\text{sim}} = p_3 - p_2$ (variation of (static) pressure from the simulation) and $\Delta p_{\text{comp}} = p_4 - p_1$ (which would correspond to the experimental measurements),

$$\Delta p_{\text{comp}} = \Delta p_{\text{sim}} + \frac{3}{4}\rho\left(\frac{Q}{\pi R_{\text{tube}}^2}\right)^2 - \rho g\Delta h_{\text{probes}} \tag{F.6}$$

APPENDIX G – TECHNICAL DRAWINGS

In this section, the technical drawings pertaining the fabricated prototype are presented. The fabrication drawings are only presented for the effectively fabricated parts. For the parts are fabricated through additive manufacturing, only some dimensions are presented.



NUMBER	NAME	QUANTITY	MATERIAL
18	Nut - ISO 4033 - M5	8	Steel
17	Nut - ISO 4032 - M3	2	Steel
16	Bolt - ISO 7045 - M5 x 16	4	Steel
15	Bolt - ISO 7045 - M5 x 40	4	Steel
14	Bolt - ISO 7045 - M3 x 16	2	Steel
13	Bolt - ISO 4027 - M3 x 8	2	Steel
12	Flexible coupling Ø6.35×Ø5	1	Steel
11	U-bracket	1	Steel
10	Step motor - SM1.8-D12-CS	1	-
9	Shaft	3	Brass
8	Seal block 4	1	Polymer
7	Seal block 3	1	Rubber
6	Seal block 2	1	Rubber
5	Seal block 1	1	Polymer
4	Volute (part 2)	1	Polymer
3	Volute (part 1)	1	Polymer
2	Rotor	3	Polymer
1	Base	1	Polymer

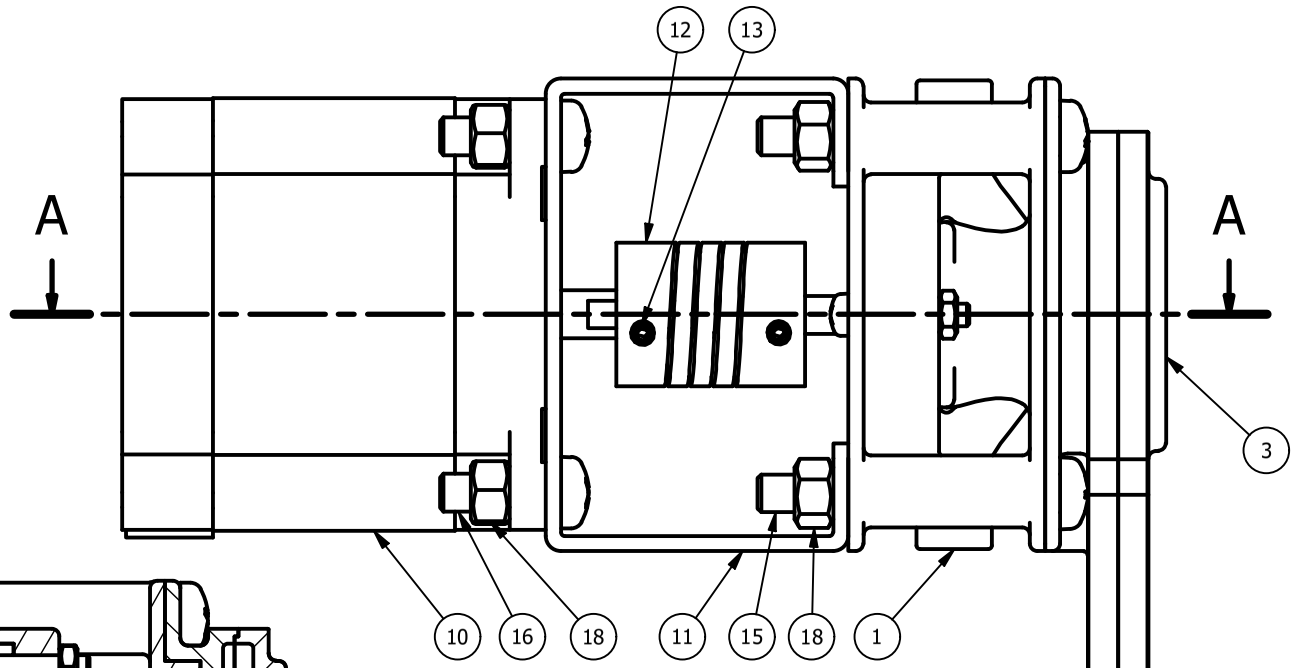
TITLE:

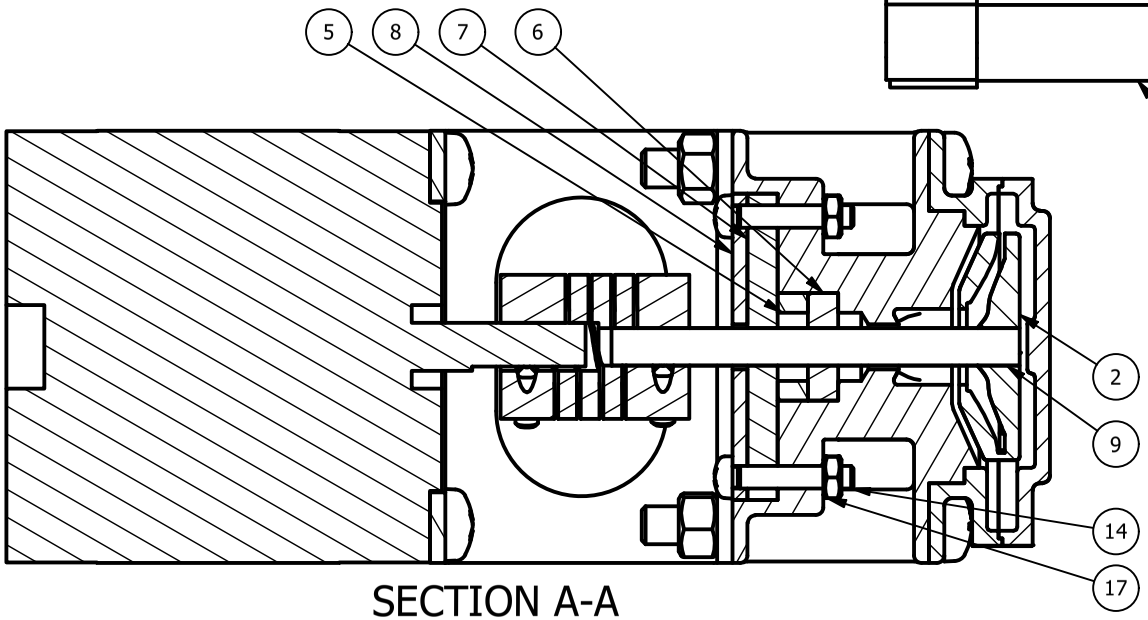
SET DRAWING (PART 1/2)

NAME:

DIEGO HAYASHI ALONSO

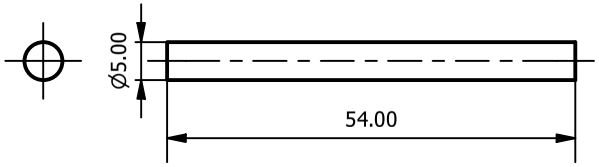
SHEET:	SCALE:	UNITS:	DATE:	SHEET NUMBER:	MATERIAL:	QUANTITY:	1st DIHEDRON:
A4	1:2	mm	2021/11/20	1	-	-	

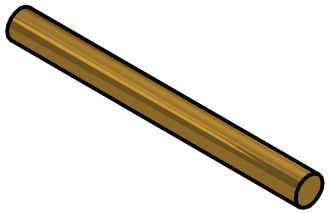




SECTION A-A

TITLE: SET DRAWING (PART 2/2)							
NAME: DIEGO HAYASHI ALONSO							
SHEET: A4	SCALE: 1:1	UNITS: mm	DATE: 2021/11/20	SHEET NUMBER: 2	MATERIAL: -	QUANTITY: -	1st DIHEDRON:

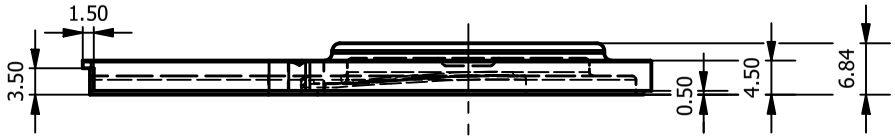


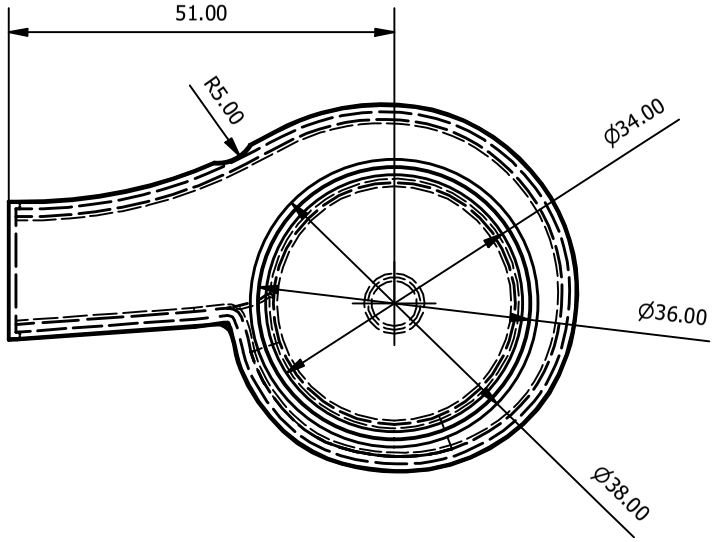


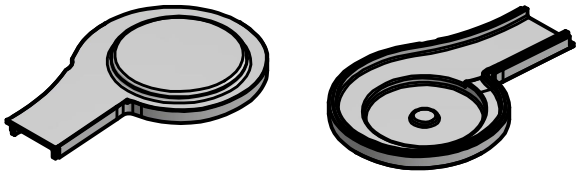
General roughness tolerance (when there is no indicated value): 1.6
(Manfé et al., "Desenho técnico mecânico", vol. 3, 2004, p.22)

General dimension tolerance (when there is no indicated value): ±0.02

TITLE:							
SHAFT							
NAME:							
DIEGO HAYASHI ALONSO							
SHEET:	SCALE:	UNITS:	DATE:	SHEET NUMBER:	MATERIAL:	QUANTITY:	1st DIHEDRON:
A4	1:1	mm	2021/07/13	3	**BRASS**	3	



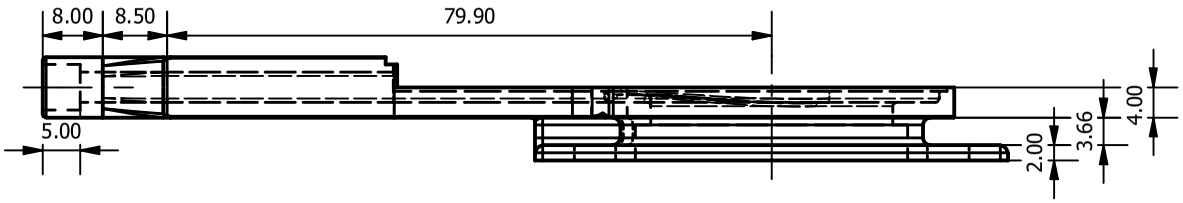


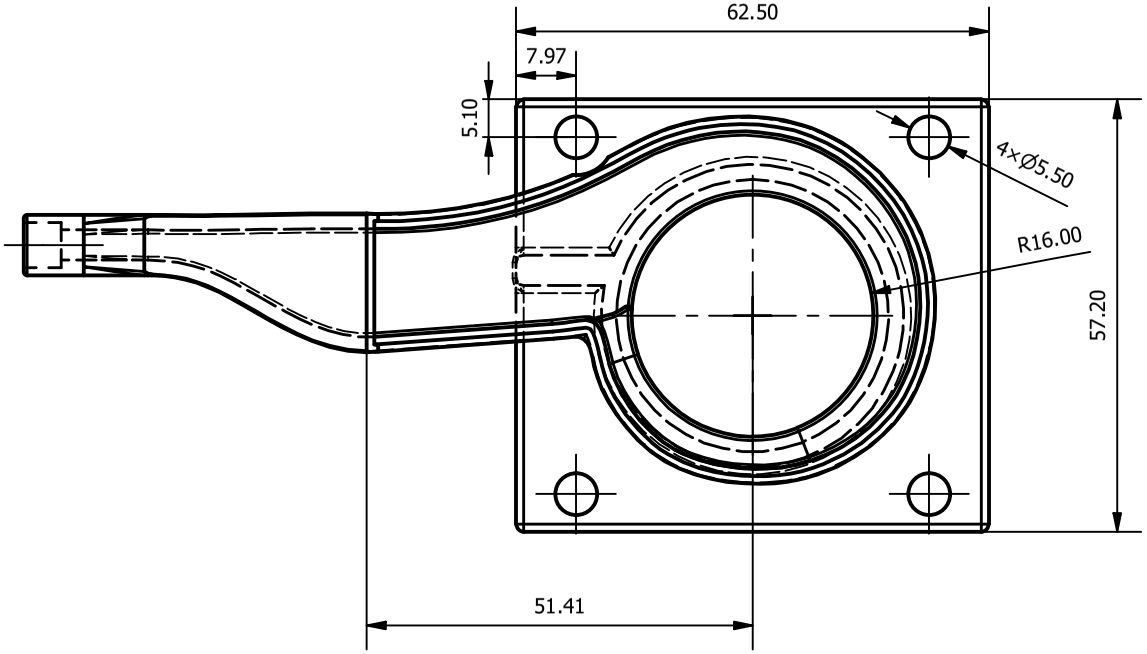


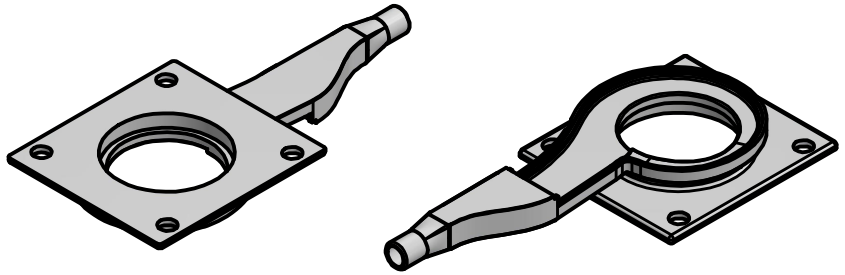
General roughness tolerance (when there is no indicated value): 1.6
(Manfé et al., "Desenho técnico mecânico", vol. 3, 2004, p.22)

General dimension tolerance (when there is no indicated value): ±0.02

TITLE: VOLUTE (PART 1)							
NAME: DIEGO HAYASHI ALONSO							
SHEET: A4	SCALE: 1:1	UNITS: mm	DATE: 2021/11/20	SHEET NUMBER: 4	MATERIAL: **POLYMER**	QUANTITY: 1	1st DIHEDRON:



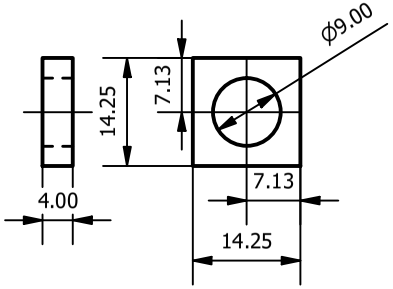


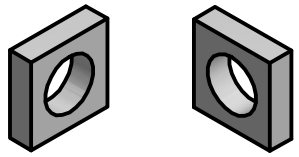


General roughness tolerance (when there is no indicated value): 1.6
(Manfé et al., "Desenho técnico mecânico", vol. 3, 2004, p.22)

General dimension tolerance (when there is no indicated value): ±0.02

TITLE: VOLUTE (PART 2)							
NAME: DIEGO HAYASHI ALONSO							
SHEET: A4	SCALE: 1:1	UNITS: mm	DATE: 2021/11/20	SHEET NUMBER: 5	MATERIAL: **POLYMER**	QUANTITY: 1	1st DIHEDRON:

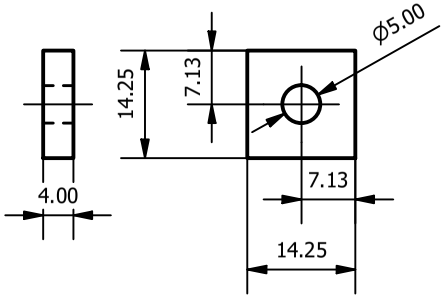


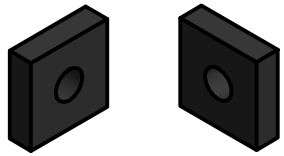


General roughness tolerance (when there is no indicated value): 1.6
(Manfé et al., "Desenho técnico mecânico", vol. 3, 2004, p.22)

General dimension tolerance (when there is no indicated value): ±0.02

TITLE: SEAL BLOCK 1							
NAME: DIEGO HAYASHI ALONSO							
SHEET: A4	SCALE: 1:1	UNITS: mm	DATE: 2021/11/20	SHEET NUMBER: 6	MATERIAL: **POLYMER**	QUANTITY: 1	1st DIHEDRON:

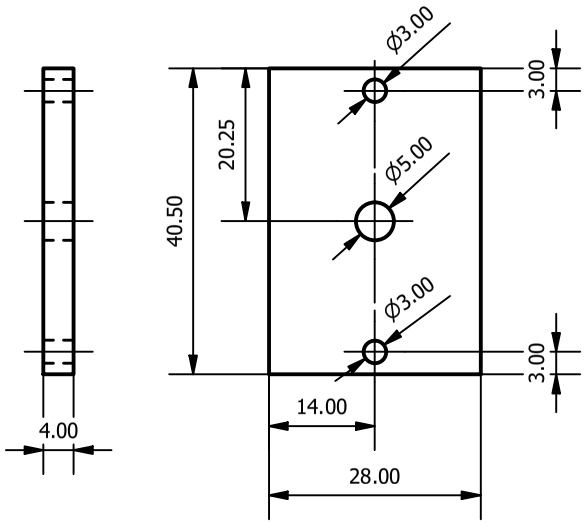


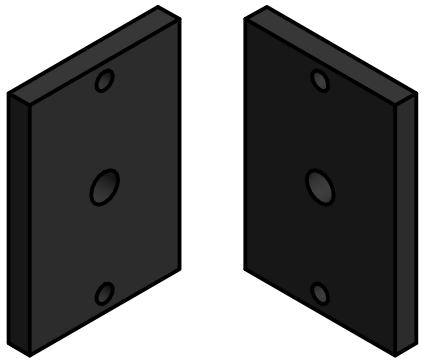


General roughness tolerance (when there is no indicated value): 1.6
(Manfé et al., "Desenho técnico mecânico", vol. 3, 2004, p.22)

General dimension tolerance (when there is no indicated value): ±0.02

TITLE:							
SEAL BLOCK 2							
NAME:							
DIEGO HAYASHI ALONSO							
SHEET:	SCALE:	UNITS:	DATE:	SHEET NUMBER:	MATERIAL:	QUANTITY:	1st DIHEDRON:
A4	1:1	mm	2021/11/20	7	**RUBBER**	1	

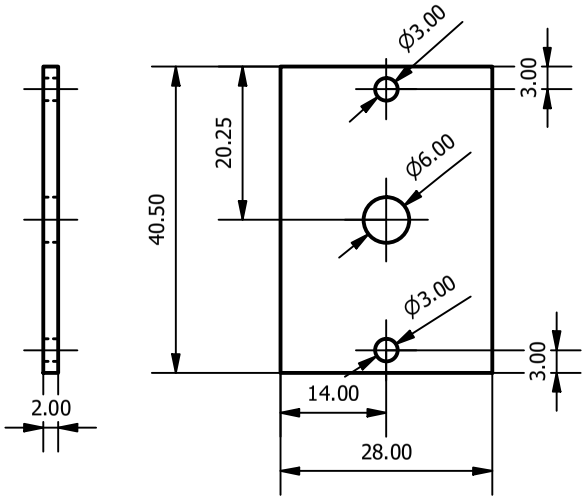


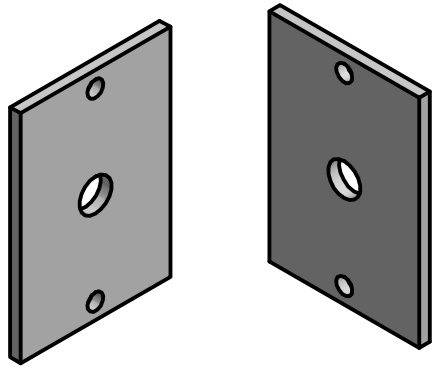


General roughness tolerance (when there is no indicated value): 1.6
(Manfé et al., "Desenho técnico mecânico", vol. 3, 2004, p.22)

General dimension tolerance (when there is no indicated value): ±0.02

TITLE: SEAL BLOCK 3							
NAME: DIEGO HAYASHI ALONSO							
SHEET: A4	SCALE: 1:1	UNITS: mm	DATE: 2021/11/20	SHEET NUMBER: 8	MATERIAL: **RUBBER**	QUANTITY: 1	1st DIHEDRON:

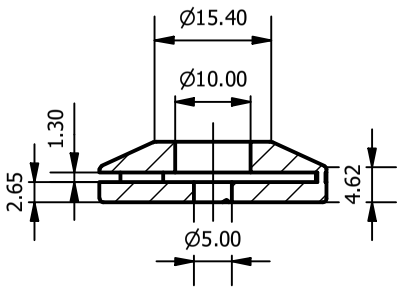




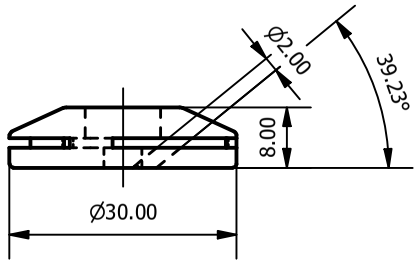
General roughness tolerance (when there is no indicated value): 1.6
(Manfé et al., "Desenho técnico mecânico", vol. 3, 2004, p.22)

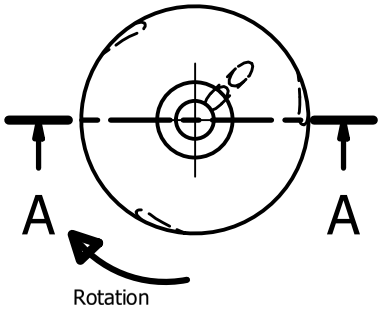
General dimension tolerance (when there is no indicated value): ±0.02

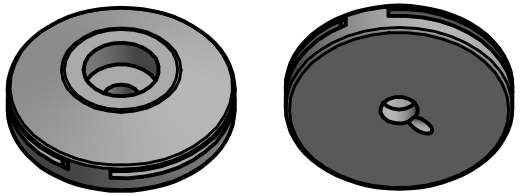
TITLE: SEAL BLOCK 4							
NAME: DIEGO HAYASHI ALONSO							
SHEET: A4	SCALE: 1:1	UNITS: mm	DATE: 2021/11/20	SHEET NUMBER: 9	MATERIAL: **POLYMER**	QUANTITY: 1	1st DIHEDRON:



SECTION A-A



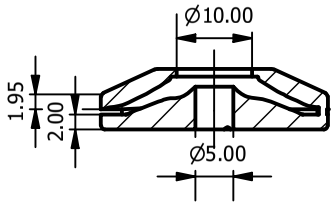




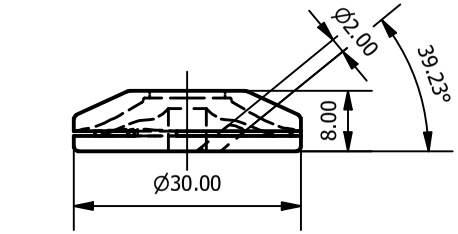
General roughness tolerance (when there is no indicated value): 1.6
(Manfé et al., "Desenho técnico mecânico", vol. 3, 2004, p.22)

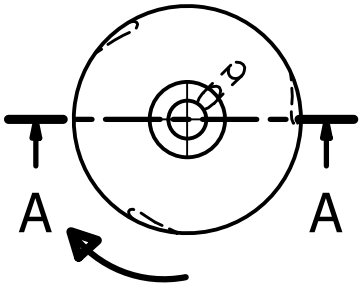
General dimension tolerance (when there is no indicated value): ±0.02

TITLE: TESLA ROTOR - STRAIGHT							
NAME: DIEGO HAYASHI ALONSO							
SHEET: A4	SCALE: 1:1	UNITS: mm	DATE: 2021/11/20	SHEET NUMBER: 10	MATERIAL: **POLYMER**	QUANTITY: 1	1st DIHEDRON:

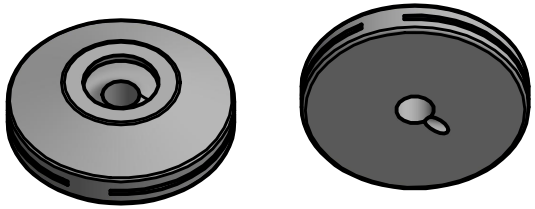


SECTION A-A





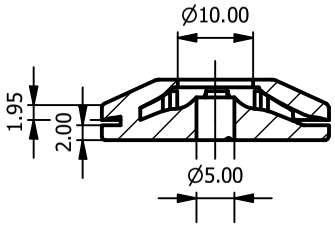
Sentido de rotação



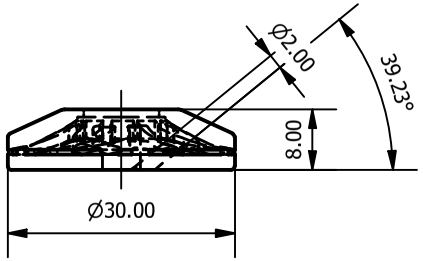
General roughness tolerance (when there is no indicated value): 1.6
(Manfé et al., "Desenho técnico mecânico", vol. 3, 2004, p.22)

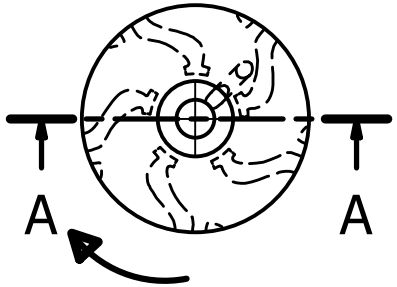
General dimension tolerance (when there is no indicated value): ±0.02

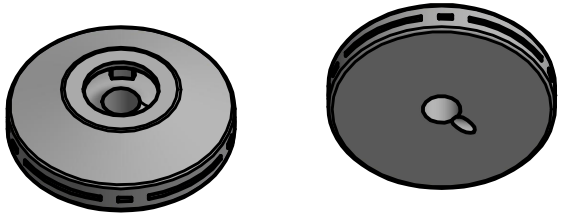
TITLE: TESLA ROTOR - OPTIMIZED							
NAME: DIEGO HAYASHI ALONSO							
SHEET: A4	SCALE: 1:1	UNITS: mm	DATE: 2021/11/20	SHEET NUMBER: 11	MATERIAL: **POLYMER**	QUANTITY: 1	1st DIHEDRON:



SECTION A-A



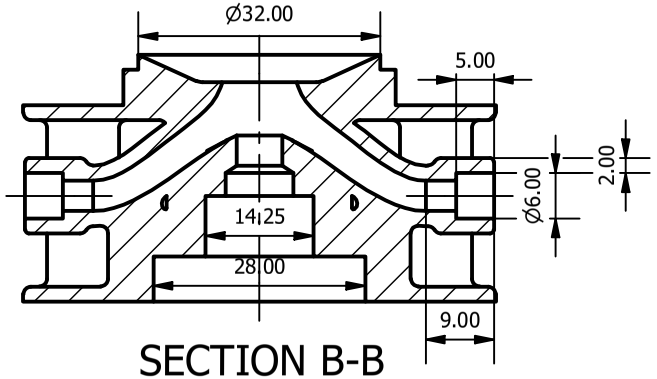




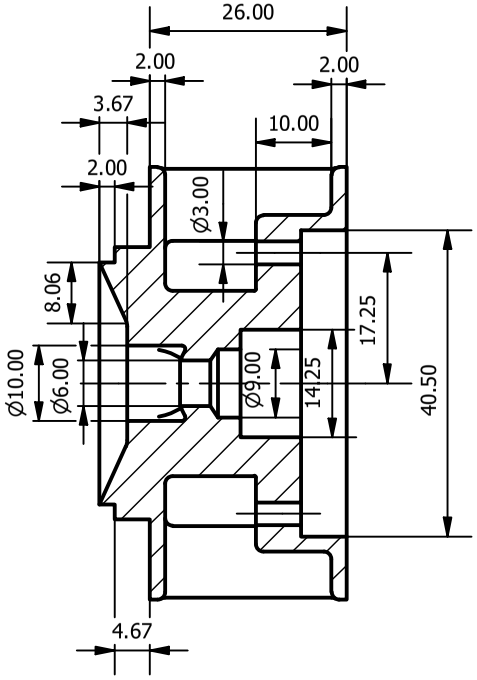
General roughness tolerance (when there is no indicated value): 1.6
(Manfré et al., "Desenho técnico mecânico", vol. 3, 2004, p.22)

General dimension tolerance (when there is no indicated value): ±0.02

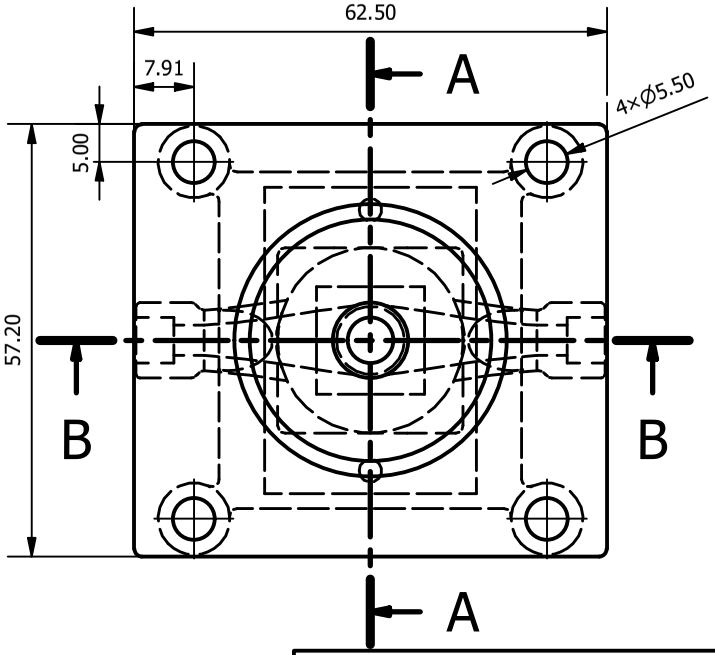
TITLE: TESLA ROTOR - OPTIMIZED (WITH BLADES)							
NAME: DIEGO HAYASHI ALONSO							
SHEET: A4	SCALE: 1:1	UNITS: mm	DATE: 2021/11/20	SHEET NUMBER: 12	MATERIAL: **POLYMER**	QUANTITY: 1	1st DIHEDRON:

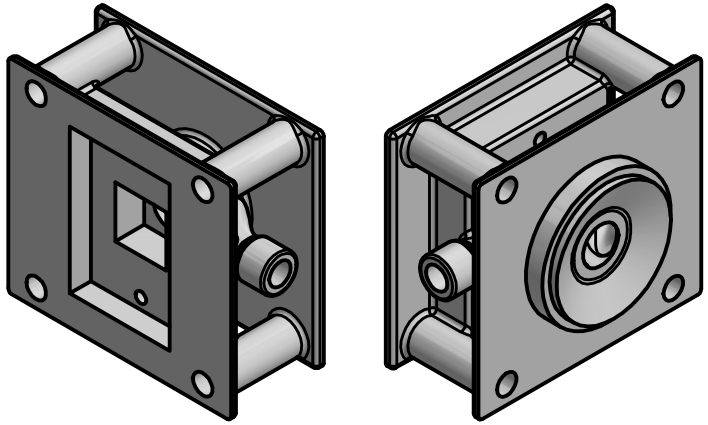


SECTION B-B



SECTION A-A





General roughness tolerance (when there is no indicated value): 1.6
(Manfé et al., "Desenho técnico mecânico", vol. 3, 2004, p.22)

General dimension tolerance (when there is no indicated value): ±0.02

TITLE: BASE							
NAME: DIEGO HAYASHI ALONSO							
SHEET: A4	SCALE: 1:1	UNITS: mm	DATE: 2021/11/20	SHEET NUMBER: 13	MATERIAL: **POLYMER**	QUANTITY: 1	1st DIHEDRON: